Transactions of the ASME, Journal of Heat Transfer (ISSN 0022-1481) is published monthly by The American Society of Mechanical Engineers, Three Park Avenue, New York, NY 10016. Periodicals postage paid at New York, NY and additional mailing offices. POSTMASTER: Send address changes to Transactions of the ASME, Journal of Heat Transfer, c/o THE AMERICAN SOCIETY OF MECHANICAL ENGINEERS, 22 Law Drive, Box 2300, Fairfield, NJ 07007-2300. **CHANGES OF ADDRESS** must be received at Society headquarters seven weeks before they are to be effective. Please send old label and new address. **STATEMENT from By-Laws.** The Society shall not be responsible for statements or opinions advanced in papers or ... printed in its publications (B7.1, Para. 3).

Journal of Heat Transfer

Published Monthly by ASME

VOLUME 130 • NUMBER 10 • OCTOBER 2008

RESEARCH PAPERS

101001 **Thermal-Boundary-Layer Response to Convected Far-Field Fluid Temperature Changes**
Hongwei Li and M. Razi Nalim

Conduction

101301 **Fractal Model for Thermal Contact Conductance**
Mingqing Zou, Boming Yu, Jianchao Cai, and Peng Xu

101302 **Small and Large Time Solutions for Surface Temperature, Surface Heat Flux, and Energy Input in Transient, One-Dimensional Conduction**
A. S. Lavine and T. L. Bergman

Evaporation, Boiling, and Condensation

101501 **Droplet and Bubble Dynamics in Saturated FC-72 Spray Cooling on a Smooth Surface**
Ruey-Hung Chen, David S. Tan, Kuo-Chi Lin, Louis C. Chow, Alison R. Griffin, and Daniel P. Rini

101502 **Flow Boiling in Minichannels Under Normal, Hyper-, and Microgravity: Local Heat Transfer Analysis Using Inverse Methods**
Sébastien Luciani, David Brutin, Christophe Le Niliot, Ouamar Rahli, and Lounès Tadrist

Experimental Techniques

101601 **Experimental Study of a Curved Rotating Heat Pipe**
T. A. Jankowski, F. C. Prenger, and A. Razani

Heat Exchangers

101801 **High Performance Recuperator With Oblique Wavy Walls**
Kenichi Morimoto, Yuji Suzuki, and Nobuhide Kasagi

Heat Transfer in Manufacturing

102101 **Comparison of Two-Dimensional and Three-Dimensional Thermal Models of the LENS® Process**
H. Yin, L. Wang, and S. D. Felicelli

Jets, Wakes, and Impingement Cooling

102201 **Modeling of Convective Cooling of a Rotating Disk by Partially Confined Liquid Jet Impingement**
Jorge C. Lallave and Muhammad M. Rahman

Micro/Nanoscale Heat Transfer

102401 **Experimental Investigation on the Heat Transfer Between a Heated Microcantilever and a Substrate**
Keunhan Park, Graham L. W. Cross, Zhuomin M. Zhang, and William P. King

102402 **Measurement of the Thermal Conductivity and Heat Capacity of Freestanding Shape Memory Thin Films Using the 3ω Method**
Ankur Jain and Kenneth E. Goodson

Porous Media

102601 **Flows Between Rotating Cylinders With a Porous Lining**
M. Subotic and F. C. Lai

(Contents continued on inside back cover)

This journal is printed on acid-free paper, which exceeds the ANSI Z39.48-1992 specification for permanence of paper and library materials. ♾™
♻ 85% recycled content, including 10% post-consumer fibers.

Journal of Heat Transfer Volume 130, Number 10 OCTOBER 2008

Radiative Heat Transfer

102701 The Solution of Transient Radiative Transfer With Collimated Incident Serial Pulse in a Plane-Parallel Medium by the DRESOR Method
Qiang Cheng, Huai-Chun Zhou, Zhi-Feng Huang, Yong-Lin Yu, and De-Xiu Huang

Two-Phase Flow and Heat Transfer

102901 Two-Phase Flow Simulation of Mist Film Cooling on Turbine Blades With Conjugate Internal Cooling
Xianchang Li and Ting Wang

TECHNICAL BRIEFS

104501 Assessment of the Single-Mixture Gas Assumption for the Correlated *K*-Distribution Fictitious Gas Method in H_2O-CO_2-CO Mixture at High Temperature
C. Caliot, G. Flamant, M. El Hafi, and Y. Le Maoult

104502 Effect of Velocity and Temperature Boundary Conditions on Convective Instability in a Ferrofluid Layer
C. E. Nanjundappa and I. S. Shivakumara

104503 Modeling the Natural Convection Heat Transfer and Dryout Heat Flux in a Porous Debris Bed
R. Sinha, A. K. Nayak, and B. R. Sehgal

104504 Soret and Dufour Effects on Free Convection Heat and Mass Transfer From a Horizontal Flat Plate in a Darcy Porous Medium
P. A. Lakshmi Narayana and P. V. S. N. Murthy

104505 Heating and Ignition of Metal Particles in the Transition Heat Transfer Regime
Salil Mohan, Mikhaylo A. Trunov, and Edward L. Dreizin

104506 Experiments in Single-Phase Natural Circulation Miniloops With Different Working Fluids and Geometries
Pietro Garibaldi and Mario Misale

The ASME Journal of Heat Transfer is abstracted and indexed in the following:

Applied Science and Technology Index, Chemical Abstracts, Chemical Engineering and Biotechnology Abstracts (Electronic equivalent of Process and Chemical Engineering), Civil Engineering Abstracts, Compendex (The electronic equivalent of Engineering Index), Corrosion Abstracts, Current Contents, E & P Health, Safety, and Environment, Ei EncompassLit, Engineered Materials Abstracts, Engineering Index, Enviroline (The electronic equivalent of Environment Abstracts), Environment Abstracts, Environmental Engineering Abstracts, Environmental Science and Pollution Management, Fluidex, Fuel and Energy Abstracts, Index to Scientific Reviews, INSPEC, International Building Services Abstracts, Mechanical & Transportation Engineering Abstracts, Mechanical Engineering Abstracts, METADEX (The electronic equivalent of Metals Abstracts and Alloys Index), Petroleum Abstracts, Process and Chemical Engineering, Referativnyi Zhurnal, Science Citation Index, SciSearch (The electronic equivalent of Science Citation Index), Theoretical Chemical Engineering

Thermal-Boundary-Layer Response to Convected Far-Field Fluid Temperature Changes

Hongwei Li
School of Mechanical Engineering,
Purdue University,
West Lafayette, IN 47907

M. Razi Nalim[1]
Department of Mechanical Engineering,
Indiana University-Purdue University
Indianapolis,
Indianapolis, IN 46202
e-mail: mnalim@iupui.edu

Fluid flows of varying temperature occur in heat exchangers, nuclear reactors, nonsteady-flow devices, and combustion engines, among other applications with heat transfer processes that influence energy conversion efficiency. A general numerical method was developed with the capability to predict the transient laminar thermal-boundary-layer response for similar or nonsimilar flow and thermal behaviors. The method was tested for the step change in the far-field flow temperature of a two-dimensional semi-infinite flat plate with steady hydrodynamic boundary layer and constant wall temperature assumptions. Changes in the magnitude and sign of the fluid-wall temperature difference were considered, including flow with no initial temperature difference and built-up thermal boundary layer. The equations for momentum and energy were solved based on the Keller-box finite-difference method. The accuracy of the method was verified by comparing with related transient solutions, the steady-state solution, and by grid independence tests. The existence of a similarity solution is shown for a step change in the far-field temperature and is verified by the computed general solution. Transient heat transfer correlations are presented, which indicate that both magnitude and direction of heat transfer can be significantly different from predictions by quasi-steady models commonly used. The deviation is greater and lasts longer for large Prandtl number fluids. [DOI: 10.1115/1.2953239]

Keywords: thermal boundary layer, transient heat transfer, nonsteady flow, wave rotor

Introduction

Nonsteady heat convection occurs in many natural and engineered systems. Of particular interest is the flow of gases of varying temperatures in energy conversion devices. In such practical applications, classical steady heat transfer correlations are widely used, with an assumption of quasisteadiness. This may cause significant heat transfer prediction errors in both direction and magnitude due to the transient thermal response. For example, Annand and Pinfold [1] measured the heat transfer rate to the internal surface of an operating internal combustion engine and found that the heat transfer rate is out of phase with the bulk-gas wall temperature difference. Kornhauser and Smith [2] derived a complex Nusselt number for the in-cylinder heat transfer during the compression and expansion to account for the unsteady thermal effect on heat transfer. These studies of gross heat transfer did not examine details of the boundary-layer transients.

Accurate knowledge of the time-varying thermal response is necessary in the design and transient operation of unsteady systems, such as regeneration heat exchangers, nuclear reactors, combustion engines, shock tubes, and wave rotors. Significant fuel efficiency and emission reduction benefits are offered by machines that exploit nonsteady flow, such as wave rotors and pulsed combustion devices [3–5]. These machines require an accurate prediction of heat transfer in passages with varying gas temperatures.

The convection of nonuniform fluid with a moving temperature-step contact surface has important engineering application in the channels of regenerative heat exchangers and wave rotors. These machines are typically constructed as rotating drums with a number of flow channels that admit different gases alternately. The wave rotor, in particular, has been shown to have potential to improve aircraft and gas turbine energy efficiency and to reduce emission of greenhouse gases by 10–25%. Regenerative heat exchangers also have important energy conversion benefits [6].

Using pressure waves like a shock tube [7] and possibly confined pressure-gain combustion, the wave rotor affects direct pressure exchange and work transfer between inert or reacting fluids [8]. By rotation, each channel is periodically charged from or discharged to inlet and outlet partial annular ports. The alignment of the rotating channel with an inlet port creates a pressure wave that travels rapidly into the gas inside the channel, equalizing pressure and velocity. More slowly, the channel ingests fresh gas flow that has a different composition and temperature, but now shares the same velocity as the gas inside the channel.

The fundamental behavior of such transient thermal problems can be well modeled as an external boundary-layer problem on a two dimensional (2D) semi-infinite flat plate using standard boundary-layer assumptions. The present study is limited to laminar flow conditions with a steady-flow velocity field.

Changes in a thermal boundary layer can be induced through different actions, such as imposing a heat flux at the wall [9–11], change in wall surface temperature [12], or change in fluid temperature [13,14]. This paper focuses on the transient laminar thermal boundary layer due to a moving incompressible fluid of varying temperatures. A general methodology was developed for the simulation of unsteady thermal-boundary-layer behavior subject to uniform or nonuniform flow and thermal boundary conditions [15]. The method is illustrated for the cases of an initial steady state subject to a sudden step temperature change as the fluid of different temperature sweeps over the plate, with unchanged velocity. As the contact surface between the two fluids travels down the plate, the upstream boundary layer asymptotically approaches a new steady state.

The cases studied here include flows with and without an initial

[1]Corresponding author.

Contributed by the Heat Transfer Division of ASME for publication in the JOURNAL OF HEAT TRANSFER. Manuscript received August 7, 2007; final manuscript received December 23, 2007; published online August 7, 2008. Review conducted by Louis C. Burmeister. Paper presented at the 2007 ASME International Mechanical Engineering Congress (IMECE2007), Seattle, WA, November 10–16, 2007.

thermal boundary layer, subject to a step change in far-field fluid temperature. A range of Prandtl number is considered to illustrate the effect of the relative size of the thermal boundary layer, which must be accommodated in the numerical method.

The governing incompressible laminar 2D unsteady-boundary-layer equations were solved using Keller's box method [16]. This is an implicit finite-difference method with second-order accuracy for both spatial and temporal variables and can be improved to higher orders of accuracy [17]. The method has been applied to forced-convection problems such as two-dimensional [18] and three-dimensional steady flows [19,20] as well as two-dimensional time-dependent flow [21], in addition to thermal-boundary-layer problems [22]. It has also been applied to free-convection flow [23] and combined forced and free-convection flow [24]. According to the Keller-box method, the high-order differential equations are rewritten as a system of first-order equations by introducing new dependent variables. The system is then linearized using Newton's method, and the resulting system is solved effectively by using the block-elimination method [25]. A marching procedure along the flow direction (x) at each time step requires iteration at each x-station until some convergence criterion is satisfied.

General Equations

A steady hydrodynamic boundary layer is established, the fluid moving with constant velocity u_∞ far from the plate. At time $t<0$, the bulk fluid temperature is constant at $T_{\infty 1}$. In the general case when $T_{\infty 1}$ is different from the plate temperature T_w, a steady initial thermal boundary layer is also established. At time $t=0$, the incoming far-field fluid temperature at the leading edge is suddenly changed to $T_{\infty 2}$. For $t>0$, the far-field fluid at $T_{\infty 2}$ is convected down the plate at speed u_∞. The appropriate far-field temperature boundary condition is applied on each side of the contact surface between the fluids, while the plate temperature remains constant. The fluid is assumed incompressible, and the density and other fluid properties are assumed constant, so that the 2D boundary-layer equations are uncoupled. Viscous dissipation is neglected and the Eckert number is assumed small due to low fluid velocity [26].

The boundary-layer continuity and momentum equations for the 2D laminar incompressible flow have the following time-steady form:

$$\frac{\partial u}{\partial x}+\frac{\partial v}{\partial y}=0 \tag{1}$$

$$u\frac{\partial u}{\partial x}+v\frac{\partial u}{\partial y}=\nu\frac{\partial^2 u}{\partial y^2} \tag{2}$$

The boundary conditions applied to Eqs. (1) and (2) are

$$u(x,0)=v(x,0)=0 \quad \text{and} \quad u(x,\infty)=u_\infty \tag{3}$$

The time-dependent energy equation

$$\frac{\partial T}{\partial t}+u\frac{\partial T}{\partial x}+v\frac{\partial T}{\partial y}=\alpha\frac{\partial^2 T}{\partial y^2} \tag{4}$$

is subject to the initial condition

$$T(x,y>0,t<0)=T_{\infty 1}$$

and boundary conditions

$$\begin{aligned} T(x\leqslant u_\infty t, y\to\infty, t\geqslant 0)&=T_{\infty 2}\\ T(x>u_\infty t, y\to\infty, t\geqslant 0)&=T_{\infty 1}\\ T(x,y=0,t)&=T_w \end{aligned} \tag{5}$$

where $T_{\infty 2}$ can be equal to, greater than, or less than $T_{\infty 1}$.

Equations (2) and (4) are nondimensionalized as

$$\bar{U}\frac{\partial \bar{U}}{\partial X}+\bar{V}\frac{\partial \bar{U}}{\partial Y}=\frac{\partial^2 \bar{U}}{\partial Y^2} \tag{6}$$

$$\frac{\partial \theta}{\partial \tau}+\bar{U}\frac{\partial \theta}{\partial X}+\bar{V}\frac{\partial \theta}{\partial Y}=\frac{1}{\mathrm{Pr}}\frac{\partial^2 \theta}{\partial Y^2} \tag{7}$$

where

$$\begin{aligned} X&=\frac{x}{L}, \quad Y=\frac{y}{L}\sqrt{\mathrm{Re}_L}, \quad \bar{U}=\frac{u}{u_\infty}, \quad \bar{V}=\frac{v}{u_\infty}\sqrt{\mathrm{Re}_L}\\ \theta&=\frac{T-T_\infty}{T_w-T_\infty}, \quad \tau=\frac{tu_\infty}{L} \end{aligned} \tag{8}$$

T_∞ is $T_{\infty 1}$ if a thermal boundary layer exists initially. T_∞ is $T_{\infty 2}$ if $T_{\infty 1}=T_w$.

Using the standard definition of the stream function, ψ ($\bar{U}=\partial\psi/\partial Y$, $\bar{V}=-\partial\psi/\partial X$), the boundary layer similarity transformation is introduced,

$$\eta=\frac{Y}{\sqrt{X}}, \quad f(X,\eta)=\frac{\psi}{\sqrt{X}} \tag{9}$$

where η is the similarity variable and f is the nondimensional reduced stream function. Unlike for some steady boundary layers with constant velocity or power-law velocity variation, the X-dependence is not eliminated by this step for a general far-field temperature variation, only reduced.

The nondimensional momentum equation and the time-dependent energy equation can be written as

$$f'''+\frac{1}{2}ff''=X\left[f'\frac{\partial f'}{\partial X}-f''\frac{\partial f}{\partial X}\right] \tag{10}$$

$$\frac{1}{\mathrm{Pr}}\theta''+\frac{1}{2}f\theta'=X\left[f'\frac{\partial \theta}{\partial X}-\theta'\frac{\partial f}{\partial X}+\frac{\partial \theta}{\partial \tau}\right] \tag{11}$$

The number of prime marks on f and θ denotes the degree of differentiation with respect to η, the first derivative being f'. The boundary conditions for the steady momentum equation are rewritten as

$$f(X,0)=f'(X,0)=0, \quad f'(X,\infty)=1 \tag{12}$$

With the above definition of θ, when the initial fluid temperature is different from the wall temperature, the boundary conditions are

$$\begin{aligned} \theta(X\leqslant\tau,\infty,\tau\geqslant 0)&=\frac{T_{\infty 2}-T_{\infty 1}}{T_w-T_{\infty 1}}=R\\ \theta(X\geqslant\tau,\infty,\tau\geqslant 0)&=0, \quad \theta(X,0,\tau)=1 \end{aligned} \tag{13}$$

When the initial fluid and wall temperatures are equal, the boundary conditions become

$$\begin{aligned} \theta(X\leqslant\tau,\infty,\tau\geqslant 0)&=0\\ \theta(X>\tau,\infty,\tau\geqslant 0)&=1 \end{aligned} \tag{14}$$

Regional Self-Similar Solution

Although Eqs. (10) and (11) indicate the solution dependency on X and τ, the thermal boundary layer can be shown to be self-similar with respect to a dimensionless ratio, $\tau^+=\tau/X=u_\infty t/x$, for any far-field temperature variation that is purely convected at a constant u_∞, given a uniform wall boundary condition. The solutions with respect to η collapse to a single curve for a given value of τ^+, which, in the case of a step change in far-field temperature, represents the distance traveled by the contact surface from the leading edge, relative to the distance x of any location of interest.

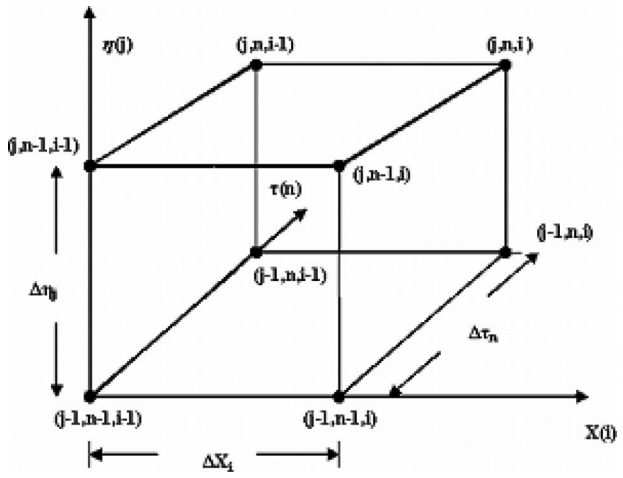

Fig. 1 Finite-difference grid for the Keller-box scheme

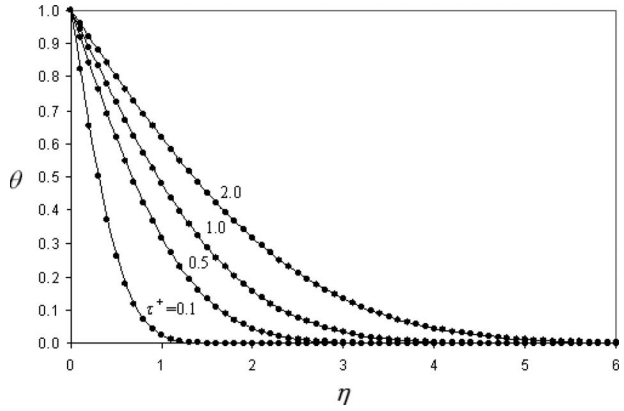

Fig. 2 Present-method numerical (dots) and analytical (line) solutions of the heat equation for a range of τ^+

The elapsed time after the contact surface passes a given location is represented by τ^+-1. This self-similar character can be shown by introducing a similar transformation with the definition of τ^+, reducing Eqs. (2) and (4) to

$$f''' + \tfrac{1}{2} f f'' = 0 \tag{15}$$

and

$$\frac{1}{\mathrm{Pr}}\theta'' + \frac{1}{2} f\theta' = \frac{\partial\theta}{\partial\tau^+}(1 - f'\tau^+) \tag{16}$$

The transformation in Eqs. (15) and (16) now eliminates the X-dependency in the equations. If the boundary conditions are also independent of X, the solutions will be functions of η and τ^+ only. In the undisturbed region with $\tau^+ < 1$, the self-similar boundary-layer solution remains as a function of η alone.

Note that when the temporal coefficient $(1-f'\tau^+)$ changes sign from positive for locations close to the plate (where $f' \ll 1$) to negative for locations close to the upper boundary layer, a combination of different finite-difference schemes is required. Equations (15) and (16) have been solved for other X-independent boundary conditions, using appropriate numerical methods [12].

Numerical Discretization and Method Validation

In this study, a general methodology is presented for problems with similar or nonsimilar flow and thermal behaviors. The similarity character for the special case above is verified. The Keller-box numerical discretization is based on the idea of expressing all functions and derivatives in terms of quantities at the corners of one computational block. All derivatives are approximated by simple centered-difference and two-point averages using only values at the corners of the three-dimensional box (or rectangle mesh) [16]. The box schematic is shown in Fig. 1, with $X_i = X_{i-1} + \Delta X_i$, $\tau_n = \tau_{n-1} + \Delta\tau_n$, and $\eta_j = \eta_{j-1} + \Delta\eta_j$. The spacings ΔX_i, $\Delta\eta_j$, and $\Delta\tau_n$ are independently variable.

New dependent variables g, h, and e are introduced to eliminate all higher-order derivatives, and a system of first-order partial differential equations is formed. The transformed Eqs. (10) and (11) are rewritten as

$$g = \frac{\partial f}{\partial\eta} = f' \tag{17}$$

$$h = \frac{\partial g}{\partial\eta} = g' \tag{18}$$

$$e = \frac{\partial\theta}{\partial\eta} = \theta' \tag{19}$$

$$h' + \frac{1}{2} f h = X\left(g\frac{\partial g}{\partial X} - h\frac{\partial f}{\partial X}\right) \tag{20}$$

$$\frac{1}{\mathrm{Pr}}e' + \frac{1}{2} f e = X\left(g\frac{\partial\theta}{\partial X} - e\frac{\partial f}{\partial X} + \frac{\partial\theta}{\partial\tau}\right) \tag{21}$$

The first-order partial differential equations (Eqs. (17)–(19)) are discretized about the point $(x_i,\ \eta_{j-1/2})$, Eq. (20) is discretized at $(x_{i-1/2},\ \eta_{j-1/2})$, and Eq. (21) is discretized at $(x_{i-1/2},\ \eta_{j-1/2},\ \tau_{n-1/2})$.

The transformed laminar boundary-layer thickness is nominally constant; the computation domain extends to $\eta_{\max}=8$, and the velocity attains 0.999 of its freestream value around $\eta=6$. The velocity and temperature field were calculated using uniform grid spacings $\Delta\tau=0.001$, $\Delta X=0.001$, and $\Delta\eta=0.01$ for smooth high-resolution solutions. Grid sensitivity was examined by choosing successively finer grids, and they showed no significant improvement on the solution accuracy.

The time accuracy of the described methodology and its computer coding were validated by a comparison with the known analytical solution of a problem with a sudden temperature change of an *infinite* flat plate. At time $t=0$, the plate temperature has a sudden change, while the far-field fluid temperature remains constant. This problem is mathematically expressed as the heat diffusion equation

$$\frac{\partial\theta}{\partial t} = a\frac{\partial^2\theta}{\partial y^2} \tag{22}$$

with initial and boundary conditions

$$\begin{aligned} &\theta = \theta_w = 1 \quad \text{at} \quad y = 0, \quad t \geqslant 0 \\ &\theta = \theta_\infty = 0 \quad \text{at} \quad y \to \infty, \quad t \geqslant 0 \\ &\theta = \theta_\infty = 0 \quad \text{at} \quad 0 \leqslant y < \infty, \quad t < 0 \end{aligned} \tag{23}$$

The analytical solution [27] is

$$\theta = 1 - \mathrm{erf}\left(\frac{y}{\sqrt{4at}}\right) = 1 - \mathrm{erf}\left(\eta\sqrt{\frac{X\,\mathrm{Pr}}{4\tau}}\right) \tag{24}$$

using the error function

$$\mathrm{erf}(\xi) = \frac{2}{\sqrt{\pi}}\int_0^\xi e^{-z^2} dz \tag{25}$$

The numerical solution for Pr=1, shown in Fig. 2, matches the analytical solution quite well, using $\Delta\eta=0.1$ and $\Delta\tau=0.001$.

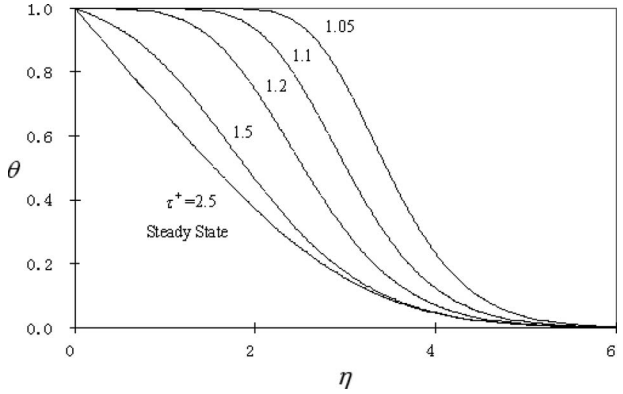

Fig. 3 Temperature response to the step change in incoming fluid temperature, with no initial thermal boundary layer

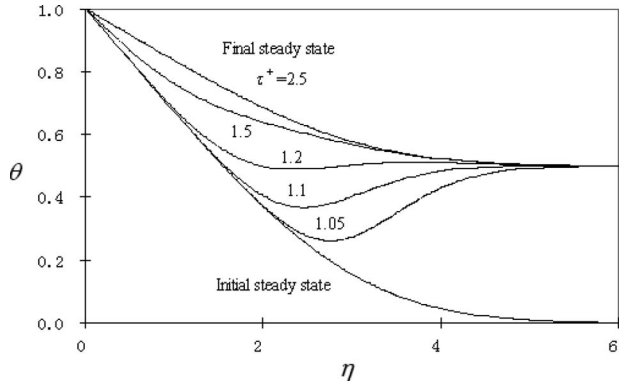

Fig. 4 Temperature response to a step change in incoming fluid temperature, with an initial thermal boundary layer (*R* =0.5)

Solution for Nonuniform Convected Flow

The convected nonuniform fluid or moving contact-surface problem is governed by a different mechanism from previous transient heat transfer analyses for uniform plate or fluid temperature changes [13]. The far-field temperature disturbance is convected with freestream velocity and diffuses across the boundary layer [28,29] only after the disturbance travels to a given position, so that locally $\tau^+ \geq 1$.

The final steady-state solution was separately calculated through the steady energy equation, so as to provide an independent verification of the asymptotic approach of the transient solution to the steady solution for large τ^+. When Pr=1.0, the steady momentum equation serves as an additional verification, as the numerical solution of $1-f'$ and θ are then identical.

Qualitatively, there are four possible nontrivial transitions: (1) no initial thermal boundary layer, (2) increase or (3) decrease in magnitude of fluid-plate temperature difference, but with the same direction of heat transfer, and (4) change in direction of fluid-plate temperature difference and heat transfer. Case (2) is not presented for brevity.

The transient temperature profile is shown in Fig. 3 for a step change in incoming fluid temperature when there is no initial thermal boundary layer and Pr=1.0 for increasing $\tau^+ > 1$. A steep temperature gradient occurs in the middle range of the developed thermal boundary layer, but the temperature gradient at the wall does not change significantly until after τ^+ exceeds 1.2. The final steady solution computed directly from the steady form of the equations is indistinguishable from the solution computed from the unsteady equations for $\tau^+=2.5$. The solution was computed at different *X* locations away from the leading edge and was verified to be similar for given $\tau^+ > 1$.

It is more general for the initial fluid and wall temperatures to differ, with an initial existing thermal boundary layer subject to a step change in incoming fluid temperature. The change in temperature difference is expressed as a ratio *R*, as defined in Eq. (13). The transient thermal response for a step change $R=0.5$ is shown in Fig. 4. For the early transient states, the temperature changes rapidly in the outer region of the boundary layer, asymptotic to the changed upper boundary value, but near the wall remains asymptotically close to the initial steady state. A temperature extremum appears at some location along the η direction, and bidirectional heat conduction exists temporarily within the boundary layer. As time passes, the extremum moves toward the wall and disappears; thereafter heat transfer is unidirectional and the temperature ultimately reaches a new steady state.

At the wall, the direction of heat transfer remains the same, but the magnitude changes; the conventional heat transfer coefficient as defined by the far-field temperature remains positive.

The temperature history for a step change of incoming fluid temperature, with $R=2.0$, is shown in Fig. 5, so that the fluid-wall temperature difference changes sign. Similar to the $R=0.5$ case, the transient temperature profile has an extremum at some η but becomes monotone again in the final steady state as the extremum reaches the wall and disappears. In this case, both the magnitude and direction of the heat transfer change, and the conventional heat transfer coefficient based on the local far-field temperature becomes *temporarily negative*.

The local Nusselt number is defined as $\mathrm{Nu}_x = q_w(x)x/\lambda(T_w - T_{\infty 2})$, where the heat flux is expressed as $q_w(x) = -\lambda\,(\partial T/\partial y)|_{y=0}$. After nondimensionalization and application of the similarity transformation, the local Nusselt number is expressed as

$$\mathrm{Nu}_x\,\mathrm{Re}_x^{-1/2} = -\frac{\partial\theta}{\partial\eta}(x,0,\tau)\frac{T_w - T_{\infty 1}}{T_w - T_{\infty 2}} = -\frac{e(x,0,\tau)}{1-R} \qquad (26)$$

This common definition of Nu using the local far-field temperature $T_{\infty 2}$ anticipates a Newtonian heat transfer direction, which may sometimes be negated by the temperature gradient at the wall during the transient. Thus for $R=2.0$, the initial heat transfer direction is dominated by the prior far-field temperature, and Nu is initially negative.

The relative thickness of momentum and thermal boundary layers in the steady parallel laminar flow is related to the Prandtl number by $\delta/\delta_t = \mathrm{Pr}^{1/3}$ [26] for large Pr. For a given flow condition, Pr has a direct effect on temperature profile. In the transient boundary layer, Pr also determines the response time of the change as it expresses the rate of thermal diffusion relative to the momentum diffusion. The transition of the local Nusselt number

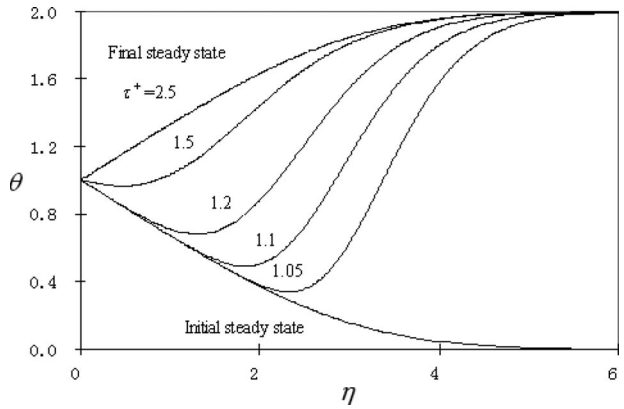

Fig. 5 Temperature response to a step change in incoming fluid temperature with an initial thermal boundary layer (*R* =2.0)

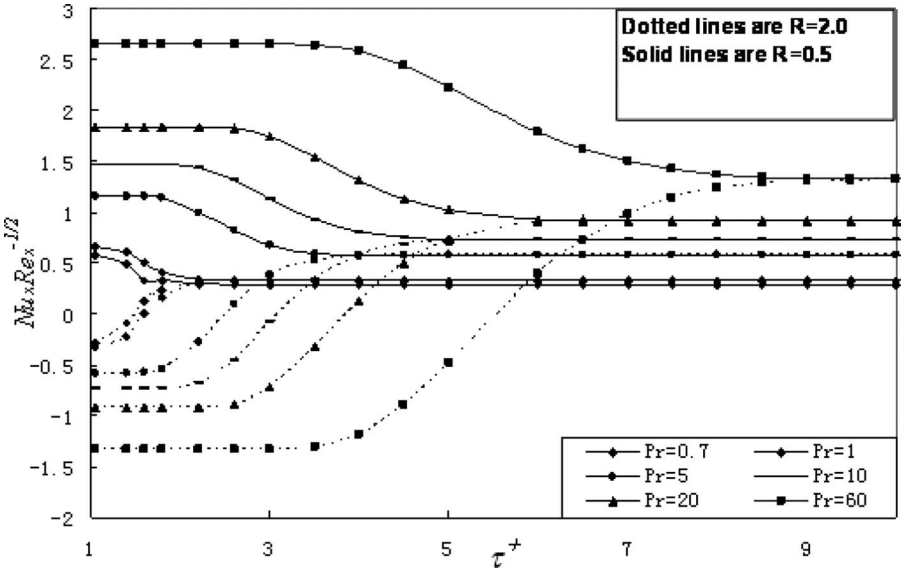

Fig. 6 Transitions of the local Nusselt number for step changes $R=0.5$ and $R=2.0$ at different Pr

is shown in Fig. 6 for incoming fluid temperature-step changes of $R=0.5$ and $R=2.0$ for a range of Prandtl numbers. For $R=0.5$, the local Nusselt number decreases over time until the final steady state while remaining positive. This corresponds to the change in temperature gradient seen in Fig. 4. For $R=2.0$, the local Nusselt number is negative initially as the heat transfer rate at the wall remains in the initial direction, but the wall-fluid temperature difference that defines Nu changes sign. For the Pr=1 case of Fig. 5, the location of the temperature extremum reaches the wall at approximately $\tau^+=1.6$, whereupon the direction of heat transfer at the wall changes sign. Thus, there is a period of time for which the heat transfer predicted here differs in direction (not just in magnitude) from any quasisteady model that follows the classical Newton cooling law. There will be a serious qualitative prediction error if the steady heat transfer correlation is applied immediately after the far-field temperature changes, especially for larger Pr.

This error may be important in unsteady-flow device models, such as a widely used quasi-one-dimensional model for wave rotor flows [30]. In this code, the steady-state Reynolds–Colburn analogy is invoked to model heat transfer based on the local bulk-gas temperature without regard to the changing temperature history of the flow.

The effect of the Prandtl number on local Nusselt numbers is shown in Fig. 6. For larger Pr, the transition from an initial to a final steady state occurs later and takes longer than that for smaller Pr due to the smaller diffusivity of heat relative to momentum. A range of Pr is explored from 0.7 for typical gases and air to 60 for some oils, which includes many useful fluids such as liquid water ($\mathrm{Pr}\approx 5$) and water vapor ($\mathrm{Pr}\approx 1$). For Pr=0.7, the wall heat transfer change occurs over a range of τ^+ from near 1 to 2.5, whereas for Pr=60, the change occurs over a range of τ^+ from 4 to 9 approximately. The larger Pr also results in a higher absolute value of the local Nusselt number. The Nu curves for $R=0.5$ and $R=2.0$ asymptotically reach the same value, as the final temperature profile only depends on the final temperatures and fluid properties.

Conclusions

The transient thermal boundary-layer response due to a convected nonuniform temperature fluid was numerically investigated for an incompressible laminar flow under the assumption of a steady hydraulic boundary layer on a semi-infinite plate. Far-field temperature changes that result in changes in the magnitude and/or direction of the fluid-plate heat transfer were considered, including the case where no thermal boundary layer exists initially. Unlike the problems of uniform change of fluid or plate temperature, the boundary layer experiences no changes until the convected far-field variation or contact surface arrives at a given plate location. A time-accurate boundary-layer flow and temperature computation methodology was developed, verified against some analytical solutions and prior work, and then applied to predict the boundary-layer temperature profiles in response to a convected step change in fluid temperature. The analysis of the local instantaneous Nusselt number shows that the use of steady-state heat transfer correlations in transient thermal states can cause both magnitude and direction of heat transfer rate to be incorrectly predicted during the transition. The response time and thermal boundary-layer thickness are correlated with the fluid Prandtl number.

It is anticipated that the numerical methodology developed here will be extended to compressible and turbulent flows. The errors related to quasisteady assumptions may be less significant for turbulent flow in gases but must be quantified for either justification or relaxation of this assumption. Practical nonsteady devices such as the wave rotor subject to complex temperature variations of a flowing gas may then be modeled with a realistic transient heat transfer prediction. This will enable important technologies to be improved for energy conversion efficiency and other benefits.

Acknowledgment

H.L. was partially supported by a fellowship from Indiana University–Purdue University Indianapolis (IUPUI) and by the Indiana 21st Century Fund for Research and Technology managed by Rolls Royce Liberty Works during this effort. The advice of Dr. C. Merkle is gratefully acknowledged.

Nomenclature

e = dependent differential variable
f = nondimensional reduced stream function
g = dependent differential variable
h = dependent differential variable
L = characteristic length
Nu = Nusselt number
Pr = Prandtl number
q = heat flux

R = temperature difference ratio
Re = Reynolds number
T = temperature
t = time
$\bar{U}$ = nondimensional velocity
u = longitudinal velocity
$\bar{V}$ = nondimensional velocity
v = transverse velocity
X = nondimensional streamwise distance
x = streamwise distance from the leading edge
Y = nondimensional transverse distance
y = transverse distance from the plate

Greek Symbols

α = thermal diffusivity
η = similarity variable
θ = dimensionless temperature
λ = thermal conductivity
τ = dimensionless time
τ^+ = dimensionless ratio of τ to X
ν = kinematic viscosity
ψ = stream function

Subscripts

i = grid index in the longitudinal direction
j = grid index in the transverse direction
n = grid index in the temporal direction
w = wall
∞ = far-field flow

References

[1] Annand, W. J. D., and Pinfold, D., 1980, "Heat Transfer in the Cylinder of a Motored Reciprocating Engine," SAE Paper No. 800457.
[2] Kornhauser, A. A., and Smith, J. L. Jr., 1994, "Application of a Complex Nusselt Number to Heat Transfer During Compression and Expansion," ASME J. Heat Transfer, **116**, pp. 536–542.
[3] Wilson, J., and Paxson, D. E., 1996, "Wave Rotor Optimization for Gas Turbine Engine Topping Cycles," J. Propul. Power, **12**, pp. 778–785.
[4] Nalim, M. R., and Paxson, D. E., 1997, "A Numerical Investigation of Premixed Combustion in Wave Rotors," ASME J. Eng. Gas Turbines Power, **119**, pp. 668–675.
[5] Kailasanath, K., 2002, "Recent Developments in the Research on Pulse Detonation Engines," J. Propul. Power, **18**, pp. 77–83.
[6] Klein, H., and Eigenberger, G., 2001, "Approximate Solutions for Metallic Regenerative Heat Exchanger," Int. J. Heat Mass Transfer, **44**, pp. 3553–3563.
[7] Fujii, N., Koshi, M., Ando, H., and Asaba, T., 1979, "Evaluation of Boundary-Layer Effects in Shock-Tube Studies of Chemical Kinetics," Int. J. Chem. Kinet., **11**, pp. 285–304.
[8] Nalim, M. R., 2000, "Longitudinally Stratified Combustion in Wave Rotors," J. Propul. Power, **16**, pp. 1060–1068.
[9] Rebay, M., and Padet, J., 2005, "Parametric Study of Unsteady Forced Convection With Pressure Gradient," Int. J. Eng. Sci., **43**, pp. 655–667.
[10] Harris, S. D., Ingham, D. B., and Pop, I., 2001, "Transient Boundary-Layer Heat Transfer From a Flat Plate Subjected to a Sudden Change in Heat Flux," Eur. J. Mech. B/Fluids, **20**, pp. 187–204.
[11] Polidori, G., Lachi, M., and Padet, J., 1998, "Unsteady Convective Heat Transfer on a Semi-Infinite Flat Surface Impulsively Heated," Int. Commun. Heat Mass Transfer, **25**, pp. 33–42.
[12] Rebay, M., and Padet, J., 1999, "Laminar Boundary-Layer Flow Over a Semi-Infinite Plate Impulsively Heated or Cooled," Eur. Phys. J.: Appl. Phys., **7**, pp. 263–269.
[13] Kurkal, K. R., and Munukutla, S., 1989, "Thermal Boundary Layer Due to Sudden Heating of Fluid," J. Thermophys. Heat Transfer, **3**, pp. 470–472.
[14] Munukutla, S., and Kurkal, K. R., 1988, "Computational Analysis of Unsteady Heat Transfer in a Pulsed High Energy Laser Flow Loop," Paper No. AIAA-88-2745.
[15] Li, H., and Nalim, M. R., 2007, "Thermal Boundary Layer Response to Far-Field Flow Temperature Transitions," IMECE Paper No. 2007-41288.
[16] Keller, H. B., 1978, "Numerical Methods in Boundary-Layer Theory," Annu. Rev. Fluid Mech., **10**, pp. 417–433.
[17] Cimbala, J. M., 1980, "Fourth-Order Keller Box Solution of the Incompressible Axisymmetric Boundary Layer Equations," Paper No. AIAA-80-0864.
[18] Keller, H. B., and Cebeci, T., 1972, "Accurate Numerical Methods for Boundary-Layer Flows. II: Two-Dimensional Turbulent Flows," AIAA J., **10**, pp. 1193–1199.
[19] Cebeci, T., Khattab, A. A., and Stewartson, K., 1980, "Studies on Three-Dimensional Boundary Layers on Bodies of Revolution. II. Three-Dimensional Laminar Boundary Layers and the OK of Accessibility," Douglas Aircraft Co., Long Beach, CA, Report No. MDC J8716.
[20] Vadyak, J., and Hoffman, J. D., 1984, "Three-Dimensional Flow Simulations for Supersonic Mixed-Compression Inlets and Incidence," AIAA J., **22**, pp. 873–881.
[21] Cebeci, T., 1977, "Calculation of Unsteady Two-Dimensional Laminar and Turbulent Boundary Layers With Fluctuations in External Velocity," Proc. R. Soc. London, Ser. A, **355**, pp. 22–238.
[22] Rebay, M., Padet, J., and Kakac, S., 2007, "Forced Convection From a Microstructure on a Flat Plate," Heat Mass Transfer, **43**, pp. 309–317.
[23] Rees, D. A. S., 1997, "Three-Dimensional Free Convection Boundary Layers in Porous Media Induced by a Heated Surface With Spanwise Temperature Variations," ASME J. Heat Transfer, **119**, pp. 792–798.
[24] Ishak, A., Nazar, R., and Pop, I., 2007, "Mixed Convection on the Stagnation Point Flow Toward a Vertical, Continuously Stretching Sheet," ASME J. Heat Transfer, **129**, pp. 1087–1090.
[25] Cebeci, T., and Bradshaw, P., 1984, *Physical and Computational Aspects of Convective Heat Transfer*, Springer, Berlin.
[26] Schlichting, H., and Gersten, K., 2001, *Boundary Layer Theory*, Springer-Verlag, New York.
[27] White, F. M., 1991, *Viscous Fluid Flow*, McGraw-Hill, New York.
[28] Telionis, D. P., 1981, *Unsteady Viscous Flow*, Springer-Verlag, New York.
[29] Smith, S. H., 1972, "On the Impulsive Flow of a Viscous Liquid Past a Semi-Infinite Flat Plate," SIAM J. Appl. Math., **22**, pp. 148–154.
[30] Paxson, D. E., 1995, "A Comparison Between Numerically Modelled and Experimentally Measured Loss Mechanisms in Wave Rotors," J. Propul. Power, **11**, pp. 908–914.

Fractal Model for Thermal Contact Conductance

Mingqing Zou

Boming Yu[1]
e-mail: yuboming2003@yahoo.com.cn

Jianchao Cai

Peng Xu

Department of Physics,
Huazhong University of Science and Technology,
1037 Luoyu Road,
Wuhan, 430074 Hubei, P.R.C.

A random number model based on fractal geometry theory is developed to calculate the thermal contact conductance (TCC) of two rough surfaces in contact. This study is carried out by geometrical and mechanical investigations. The present study reveals that the fractal parameters D and G have important effects on TCC. The predictions by the proposed model are compared with existing experimental data, and good agreement is observed by fitting parameters D and G. The results show that the effect of the bulk resistance on TCC, which is often neglected in existing models, should not be neglected for the relatively larger G and D. The main advantage of this model is the randomization of roughness distributions on rough surfaces. The present results also show a better agreement with the practical situation than the results of other models. The proposed technique may have the potential in prediction of other phenomena such as friction, radiation, wear and lubrication on rough surfaces. [DOI: 10.1115/1.2953304]

Keywords: rough surfaces, fractal, thermal contact conductance

1 Introduction

It is known that real surfaces are usually not perfectly smooth, and most surfaces (such as engineering surfaces) appear rough when viewed microscopically. As a result, when a rough surface is placed in mechanical contact, real contact occurs only at a few discrete spots separated by relatively large gaps. Therefore, if the thermal radiation and conductance across the gap are neglected, the heat flow would only be through the contact spots, as illustrated in Fig. 1. The real contact area, A_r, which is the sum of areas of actual contact spots, typically forms a few percent of the nominal contact area A_a. The constriction of heat flow lines at the contacting surfaces gives rise to thermal resistance, which is defined as the temperature difference across the contact divided by the total heat flow rate through the contact. This resistance is used as a basis for defining thermal contact conductance (TCC) as follows:

$$h_c = \frac{1}{A_a R_c} = \frac{Q}{A_a \Delta T_c} \tag{1}$$

where h_c is the TCC, R_c is the thermal contact resistance (TCR), Q is the total heat transfer across the joint, A_a is the apparent area, and ΔT_c is the temperature drop across a joint.

The TCR or TCC plays an important role in many engineering applications such as microelectronics cooling, spacecraft structures, satellite bolted joints, nuclear engineering, ball bearings, and heat exchangers [1]. A large number of theoretical or experimental investigations [1–17] have been performed to predict the TCR or TCC since the 1950s. It is evident from the literature review that TCR or TCC depends on the mechanical and thermophysical properties of contacting materials, the geometrical characteristics of contacting surfaces, and the applied pressure and temperature condition of a joint.

Although many studies have been carried out, there seems to be no fully comprehensive theory or method to predict the TCC with sufficient accuracy in practical engineering applications. As shown schematically in Fig. 1, most engineering surfaces in contact exhibit both microscopic bulk resistance and constriction resistance; the former is related to the roughness deformation, and the latter arises from the constriction of heat flow lines at the contacting spots. In this situation, heat flows experience two stages of resistance in series: bulk resistance and constriction resistance. Many of previous studies on TCC were basically concerned with the constriction resistance. However, real engineering surfaces are very rough, implying that the influence of the bulk resistance should not be ignored. Moreover, the effect of bulk resistance may become more significant if the contact pressure acting on the substrate is low, as is usually the case in spacecraft and microelectronics applications.

In this work, a random number model based on fractal geometry theory is developed to calculate the TCC, bulk resistance, and constriction resistance of rough surfaces. The geometrical and mechanical investigations are carried out. The theoretical results are then compared with the existing experimental data.

2 Model Development

2.1 Characterization of Surface Topography. The theoretical formulation for an estimation of the TCC primarily simulates the contacting surfaces. Conventionally, statistical parameters such as the standard deviation of asperity height, slope, and radius of curvature have been used to characterize surfaces [18,19]. However, due to the multiscale nature of surfaces, it is found that such parameters depend on the resolution of the surface measuring apparatus and sample length, and hence no unique description exists for a surface [20–22]. In order to overcome this drawback, fractal geometry [23] has been utilized to characterize the surface topography and has been employed in contact mechanics models [5,22,24–26]. Scale-invariant parameters are used based on fractal geometry to describe the realistic multiscale roughness and to maintain the self-affinity property of real surfaces over a wide range of length scales.

In view of the self-affinity property, the real surface profile can usually be described by the Weierstrass–Mandelbrot (WM) function [27],

$$z(x) = G^{(D-1)} \sum_{n=n_1}^{\infty} \frac{\cos 2\pi \gamma^n x}{\gamma^{(2-D)n}}, \quad 1 < D < 2, \quad \gamma > 1 \tag{2}$$

where the parameter D is the fractal dimension of the profile, which is related to the surface fractal dimension D_s by $D = D_s - 1$. G is a characteristic length scale of the surface, and γ^n determines the frequency spectrum of surface roughness. n_1 is related to γ and the sample length, L_s, by $\gamma^{n_1} \approx 1/L_s$. The values of G and D

[1]Corresponding author.

Contributed by the Heat Transfer Division of ASME for publication in the JOURNAL OF HEAT TRANSFER. Manuscript received August 12, 2007; final manuscript received March 5, 2008; published online August 8, 2008. Review conducted by A. Haji-Sheikh.

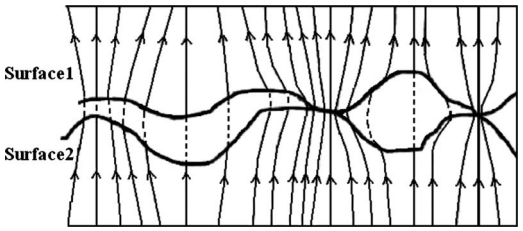

Fig. 1 Constriction of heat flow lines through contacting spots

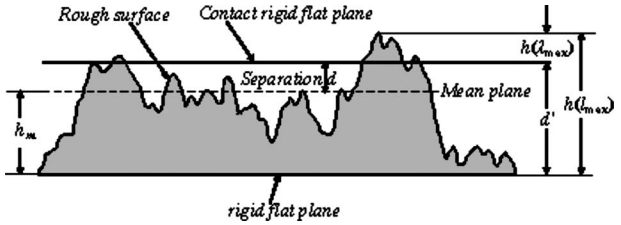

Fig. 2 Contact between a rough surface and a flat producing isolated contact spots

can be determined from a log-log plot of the structure function of $z(x)$ versus wavelength [28]. This function suggests that a rough surface is composed of a large number of length scales of asperities that are superimposed on each other in a self-affine fashion and that the function satisfies a scaling relation of the form [5,21,22]

$$z_i = G^{(D-1)} l_i^{(2-D)} \tag{3}$$

where the asperity amplitude z and the lateral length scale l_i can be obtained from the WM function for a single frequency mode of $\gamma^{n_i} = 1/l_i$. The amplitude z represents the local mean value over a sample length l_i.

Based on Eqs. (2) and (3), it is seen that the roughness height h_i for a certain length scale l_i can be obtained by

$$h_i = G^{(D-1)} l_i^{(2-D)} + \sum_{j=1}^{i-1} h_j \tag{4}$$

where the asperity diameters l_i ascends from l_1 to l_n, the value of D controls the relative amplitude of roughness at different length scales, and the value of G controls the absolute amplitude of the roughness over all length scales [29].

Equation (4) will be used in this investigation to simulate the surface topography once the fractal parameters G and D and asperity diameter l_i have been determined.

2.2 Analysis of the Asperity Size Distribution. According to the fractal geometry theory, it is well known that the cumulative size distribution of pores or islands (on earth) or spots (on engineering surfaces) whose sizes, L, are greater than or equal to the size l have been proven to follow the fractal scaling law [5,21–23,30–32],

$$N(L \geqslant l) = \left(\frac{l_{\max}}{l} \right)^D \tag{5}$$

where L is the length scale of asperities and $l_{\min} \leqslant L \leqslant l_{\max}$, D is the fractal dimension, $1 < D < 2$ in two dimensions, and $l_{\max}$ is the maximum asperity diameter. Equation (5) implies that there is only one maximum roughness on an engineering surface or one maximum island on earth, and this is consistent with the practical situation.

The total number of islands or asperities, from the smallest diameter $l_{\min}$ to the largest diameter $l_{\max}$, can be obtained from Eq. (5) as [30,31]

$$N_t(L \geqslant l_{\min}) = \left(\frac{l_{\max}}{l_{\min}} \right)^D \tag{6}$$

An asperity diameter l_i is analogous to a pore diameter in fractal porous media. The asperity diameter l_i can thus be generated according to the Monte Carlo simulation method [33] and is expressed as

$$l_i = \frac{l_{\min}}{(1 - \text{rand}_i)^{1/D}} \tag{7}$$

where rand_i is a random number of 0–1, $i = 1, 2, 3, \ldots, n$ (equal to N_t determined by Eq. (6)), and n is the total number of Monte Carlo simulations in one run for a given D and G. In general, Eq. (7) holds approximately if $l_{\min}/l_{\max} < 10^{-2}$ (for more details, readers may consult Refs. [33,43]). Equation (7) presents an explicit model for simulating the randomness and fractal distribution of asperity diameters on rough surfaces, whereas the conventional solutions cannot provide such an explicit model for asperity diameter distribution.

Equation (7) is a probability model for asperity diameter in the present simulations. Therefore, we can choose a random number rand_i and determine the asperity diameters by using Eq. (7) if $l_{\min}$ is known for a rough surface.

From the diameter distribution by Eq. (5), we can also see that when the asperity diameters (produced by Eq. (7)) are sorted from small to big, the number of the ith roughness can be obtained by

$$n_i = N(L \geqslant l_i) - N(L \geqslant l_{i+1}) = l_{\max}^D (l_i^{-D} - l_{i+1}^{-D}) \tag{8}$$

The apparent area A_a is defined by

$$A_a = \frac{A_l}{\phi} = \frac{\sum_{i=1}^{n} n_i \pi \left(\frac{l_i}{2} \right)^2}{\phi} \tag{9}$$

where A_l is the total area of the cross sections of all asperities and ϕ is determined by [30]

$$\phi = \left(\frac{l_{\min}}{l_{\max}} \right)^{d_E - D} \tag{10}$$

where ϕ is the effective porosity or pore volume fraction since the asperities on a surface are analogous to the pores in fractal porous media, d_E is the Euclidean dimension, and $d_E = 2$ and $1 < D < 2$ in the two-dimensional space.

2.3 Contact Mechanics and Pressure Distribution. Similar to some previous models [5,7,18,21,34,35], the contact between two surfaces in this work is modeled by that between an equivalent fractal rough surface and a perfectly smooth surface. The equivalent rough surface is assumed to be isotropic, and asperities are far apart so that there is no interaction between them, and no bulk deformation occurs in contact. The combined effective rms surface roughness σ, the absolute surface slopes m, and the equivalent Hertzian elastic modulus are related by

$$\sigma = \sqrt{\sigma_1^2 + \sigma_2^2} \quad \text{and} \quad m = \sqrt{m_1^2 + m_2^2} \tag{11}$$

where the parameters σ_1 and σ_2 are the roughnesses and m_1 and m_2 are the slopes of contacting surfaces. The absolute mean surface slopes can be easily obtained from roughness measurements using the method given in Ref. [2].

Figure 2 schematically shows the contacting process, which has widely been used for the geometric modeling of the actual contact between two rough surfaces. In the past, different approaches have been proposed to analyze the deformation of asperities by assuming plastic [2], elastic [18], or elastoplastic [8,26] regimes at microcontacts. The fundamental difference between these models is the contact deformation model used.

The scale independence of contact surfaces motivated the application of the fractal description of the multiscale nature of con-

tacting rough surfaces. Archard [36] showed that even for a purely elastic contact, a linear relationship between load and contact area can be established when a Hertzian contact is assumed. Ciavarella and Demelio [37] revisited Archard's model for an elastic multiscale contact of rough surfaces and compared it with modern fractal models. Majumdar and Bhushan [22] used the WM function to develop a fractal contact model. In their model, they assumed that when the two surfaces are brought into contact, the rigid flat forms a "truncation plane" on which the contact spots are spread. Then the isolated contact spots will be of different diameters and will spread randomly over the contact joint, as shown in Fig. 2. According to this model, all contact spots of areas smaller than a critical area are in plastic deformation. When load is increased, these plastically deformed spots join to form elastic spots. The concept of fractal roughness has also been implemented to thermal [5] and electrical [38] contact resistances. However, Morag and Etsion [39] criticized this model because the results presented by Ref. [22] contradict classical contact mechanics. They revisited the critical contact area and load-area relation in model [22],

$$a_c = \frac{1}{\pi}\left(\frac{K\sigma_y}{2E}\right)^2\left(\frac{\lambda^D}{G^{(D-1)}}\right)^2 \tag{12}$$

$$F = \frac{4E\pi^{1/2}G^{D-1}}{3\lambda^D}a^{3/2} \quad (a < a_c \text{ for plastic contact}) \tag{13a}$$

$$F = K\sigma_y a \quad (a > a_c \text{ for elastic contact}) \tag{13b}$$

where λ is the base diameter for the deformed asperity, σ_y is the yield strength of the softer material, K is a factor relating the hardness H to the yield strength by $H=K\sigma_y$, and F is the load on the contact area a. The parameter E is the equivalent Hertzian elastic modulus expressed in the form of

$$\frac{1}{E} = \frac{1-\nu_1^2}{E_1} + \frac{1-\nu_2^2}{E_2} \tag{14}$$

where E_1 and E_2 and ν_1 and ν_2 are Young's modulus and Poisson's ratios of the contacting surfaces 1 and 2, respectively.

Due to Eqs. (12), (13*a*), and (13*b*), the critical contact spot diameter and load-diameter relation for a deformed asperity having a contact diameter λ_i are expressed as

$$\lambda_c = \frac{G}{(H/2E)^{1/(D-1)}} \tag{15}$$

$$F_i = \frac{4\pi^{1/2}E}{3}G^{D-1}\lambda_i^{3-D} \quad (\lambda_i > \lambda_c \text{ for the elastic contact}) \tag{16a}$$

$$F_i = H\frac{\pi}{4}\lambda_i^2 \quad (\lambda_i < \lambda_c \text{ for the plastic contact}) \tag{16b}$$

From Eqs. (16*a*) and (16*b*), the dimensionless contact pressure applied at two contacting surfaces can be found to be

$$P^* = \frac{1}{HA_a}\sum_{i=i_1}^{n} F_i \tag{17}$$

Here n represents the number of contacting asperities with different diameters and i_1 corresponds to the asperity that has the smallest spot.

The present model can be obtained by using the contact model described above to define the contact pressure, P, in terms of load, mechanical properties, and surface geometry. The value of λ_i is obtained from the geometry of contacting surfaces and surface parameters. See the following sections for details.

2.4 Model for Thermal Contact Conductance. As shown in Fig. 1, the heat flow under steady state conditions across the joints are constrained through the individual microcontact. Therefore in addition to the bulk resistance due to roughness itself (r_{bi}) for a given roughness (i), there is an additional constrained resistance (r_{ci}) due to the constriction of heat flow lines. The total thermal resistance r_{ti} of roughness (i) is thus given by (see Fig. 3)

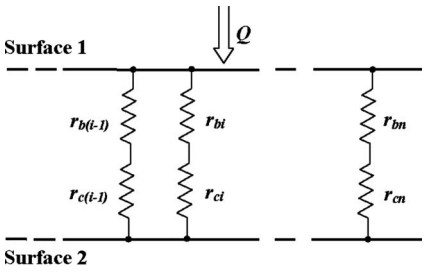

Fig. 3 The thermal resistance network of two contacting rough surfaces

$$r_{ti} = r_{bi} + r_{ci} \tag{18}$$

Note that each contact spot imposes a certain resistance to the heat flow across the surface. However, as shown in Fig. 2, since all the spots coexit at the contact plane, these series of resistances act in parallel (see Fig. 3). Obviously, when the TCC is analyzed, r_{bi} and r_{ci} should be first calculated.

2.4.1 Bulk Resistance. According to Mandelbrot [23], the diameter distribution of contact spots also follows the fractal scaling law [5,21,22],

$$N(L' \geqslant \lambda) = \left(\frac{\lambda_{\max}}{\lambda}\right)^D \tag{19}$$

From Eq. (19), the probability density function $n(\lambda)$ for spot diameters on a rough surface can be obtained from Eq. (19) as

$$n(\lambda) = -\frac{dN(\lambda)}{d\lambda} = D\lambda_{\max}^D\lambda^{-(D+1)} \tag{20}$$

Therefore, the total area of all the contact spots, A_r, can be found to be

$$A_r = \int_0^{\lambda_{\max}} n(\lambda)\lambda^2 d\lambda = \frac{D}{2-D}\lambda_{\max}^2 \tag{21}$$

Then, the dimensionless contact area A^* is

$$A^* = \frac{A_r}{A_a} = \frac{D}{2-D}\left(\frac{\lambda_{\max}}{L_s}\right)^2 \tag{22}$$

Once A^* is given, the largest contact spot diameter,$\lambda_{\max}$, can be determined from Eq. (22),

$$\lambda_{\max} = L_s\sqrt{\frac{2-D}{D}A^*} \tag{23}$$

Based on Eq. (4), it is seen in Fig. 2 that all asperities with height h greater than $d' = h(l_{\max}) - h(\lambda_{\max})$ will contact.

For a given roughness (i), the resistance is composed of a series of resistances due to small asperities stacked on bigger ones in a self-similar fashion. Figure 4(*a*) shows a model of stacked asperities. The present contact model is based on volume conservation in an assumed plastically deformed region of asperity. It is assumed that asperity deformation is localized mainly near contact. The truncated cone segment of height d' (see Fig. 4(*b*)) remains in a self-affine fashion, as shown in Fig. 4(*a*). We can also see that the basic element of either a series or a parallel network is the resistance of a single asperity. As suggested in Eq. (3) the amplitude z of an asperity of diameter l is $G^{(D-1)}l^{(2-D)}$. The resistance, r, of a single asperity is

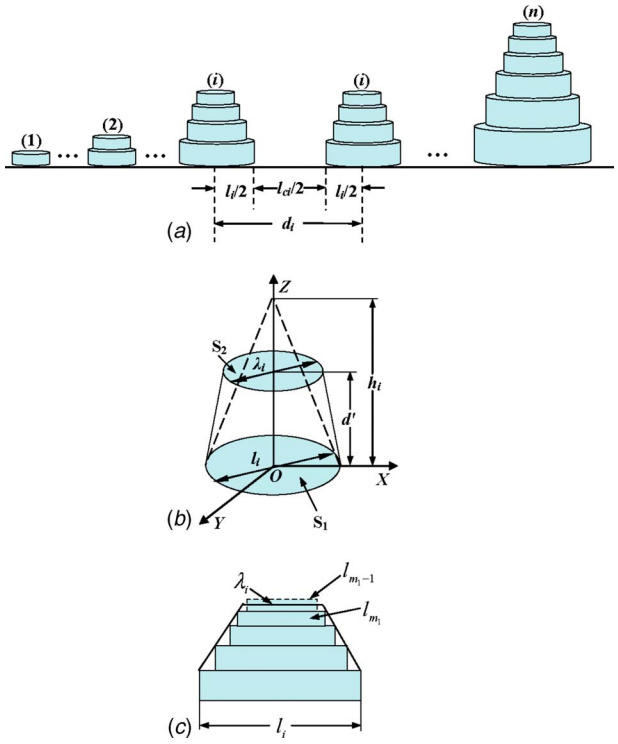

Fig. 4 Geometry model in this work: (*a*) model for stacked asperities, (*b*) geometry of an asperity with deformation, and (*c*) schematic for the determination of m_1

$$r = \frac{z}{k\pi\left(\frac{l}{2}\right)^2} = \frac{4G^{D-1}}{\pi k} l^{-D} = Cl^{-D} \tag{24}$$

where k is the effective conductivity of the two surfaces in series, $C=4G^{D-1}/\pi k$, and the characteristic lateral length l of an asperity is chosen such that its base area follows $a=\pi l^2/4$.

Then, the total series resistance of roughness (i) after deformation is given by

$$r_{bi} = C \sum_{m=m_1}^{i} l_m^{-D} \tag{25}$$

where m_1 is an integer and is determined by $l_{m_1} \geq \lambda_i > l_{m_1-1}$ (see Fig. 4(c)), and λ_i is the contact spot diameter corresponding to the roughness, which has the base diameter l_i (see Fig. 4(b)), and it can be found to be

$$\lambda_i = \left(\sqrt{\frac{h_i}{d'} - 0.75} - 0.5\right) l_i \tag{26}$$

The general derivation of Eq. (26) is given in the Appendix (Eq. (A7)).

2.4.2 Constrained Resistance. For heat flow through two contacting roughnesses, as shown in Fig. 5, Cooper et al. [2] developed a model for the constriction resistance,

$$R_c = \frac{\Delta T_c}{Q} = \frac{\psi(c/b)}{2kc} \tag{27}$$

where k is the harmonic mean of the conductivities of the two contacting materials and ψ is a geometrical factor equal to unity for a single contact belonging to an infinite apparent area.

For properly distributed contacts having contact points at the center of the corresponding roughnesses, the term $\psi(c/b)$ in Eq. (27) is approximated by [2]

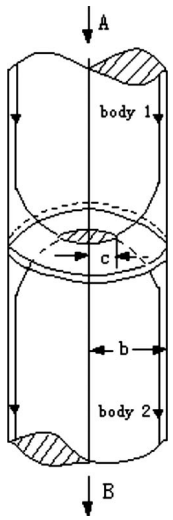

Fig. 5 Elemental flow channel [2]

$$\psi(c/b) \approx \left(1 - \frac{c}{b}\right)^{1.5} \tag{28}$$

Therefore, based on Eqs. (27) and (28), once the individual contact spot diameter, λ_i, is known, the constriction resistance for the contact spot can be written as

$$r_{ci} = \frac{1}{2k\lambda_i}\left(1 - \frac{\lambda_i}{d_i}\right)^{1.5} \tag{29}$$

where $d_i=l_i+l_{ci}$, as shown in Fig. 4(a).

The parameter l_{ci} is the cavity diameter according to Majumdar and Tien [5],

$$l_{ci} = l_i\left(\frac{1}{\phi} - 1\right)^{1/2} \tag{30}$$

where $\phi=A_l/A_a$ is determined by Eq. (10).

So, the effective resistance R_{ti}, which represents the total series-parallel network for the whole set of ith roughnesses, can be determined by dividing the total series resistance of each strand r_{ti} by the number of parallel strands, as given in Eq. (8). The expression for R_{ti} is

$$R_{ti} = \frac{r_{ti}}{n_i} \tag{31}$$

The contact conductance can be obtained from Eqs. (1) and (31) as

$$h_c = \frac{1}{A_a R_c} = \frac{1}{A_a}\sum_{i=i_1}^{n}\frac{1}{R_{ti}} = \frac{1}{A_a}\sum_{i=i_1}^{n}\frac{n_i}{r_{bi}+r_{ci}} \tag{32}$$

Multiplying by $(\sigma/m)/k$, the dimensionless conductance across the contacting solid spots is obtained,

$$h^* = \frac{h_c\sigma}{mk} \tag{33}$$

where the height variance σ and the slope variance of the surface profile are obtained from Eq. (11) and the power spectrum function as follows [40]:

$$\sigma_1 = \frac{1}{\sqrt{2}} G^{D-1}\sqrt{\sum_{i=1}^{n} l_i^{4-2D}} \tag{34}$$

and

$$m_1 = \sqrt{2}\pi G^{D-1}\sqrt{\sum_{i=1}^{n} l_i^{2-2D}} \tag{35}$$

Table 1 Material parameters of stainless steel

Thermal conductivity k (W/m K)	Young's modulus E (Pa)	Poisson's ratio υ	Microhardness H (Pa)
54	2.07×10^{11}	0.29	2.295×10^{9}

By substituting Eqs. (32), (34), and (35) into Eq. (33), the dimensionless contact conductance can be obtained as

$$h^* = \frac{l_{\max}^D}{A_a}\sqrt{\frac{\sum_{i=1}^{n} l_i^{4-2D}}{\sum_{i=1}^{n} l_i^{2-2D}}\sum_{i=i_1}^{n}\frac{l_i^{-D}-l_{i+1}^{-D}}{\frac{\pi}{\lambda_i}\left(1-\frac{\lambda_i}{d_i}\right)^{1.5}+8G^{D-1}\sum_{m=m_1}^{i} l_m^{-D}}} \tag{36}$$

The above expression is the Monte Carlo model for dimensionless contact conductance h^*. Equation (36) reveals that the dimensionless contact conductance h^* resulted from constriction and bulk resistances, and this is expected and is consistent with the physical situation. Equation (36) also indicates that the dimensionless contact conductance is a function of parameters A_a, $l_{\min}$, $l_{\max}$, D, G, and rand_i (see Eq. (7)). Once these parameters are determined, the dimensionless contact conductance h^* can be calculated from Eq. (36) by choosing a set of random numbers rand_i.

3 Results and Discussion

In the present investigation, the stainless steel surface is chosen, and the material parameters are listed in Table 1, where contact microhardness, H, and equivalent elastic modulus, E, for stainless steel refer to the effective values.

The random numbers used in this analysis were generated by using the Microsoft FORTRAN uniform random number generator subroutine RANDOM. The subroutine returns a value between 0 and 1 for an input seed value. Figure 6 gives the asperity diameters randomly chosen by the probability model (Eq. (7)) under the given parameters G and D. In Fig. 6 it is seen that the number of larger asperities is much less than that of smaller asperities. This is qualitatively consistent with the fractal geometry theory.

Based on Eqs. (4) and (7), a three-dimensional isotropic rough surface of 1000×1000 nm^2 square plate can be constructed, as shown in Fig. 7(*a*), under the given parameters D, G, and $l_{\min}$. Figure 7(*b*) shows the cutaway views of Fig. 7(*a*). These reproduce the intuitionistic images of the fine surface roughness distribution with high randomness.

Figure 8 compares the dimensionless contact conductance predicted by the present model (Eq. (36)) and the MT model [5] at a fixed value of $G=9.46\times10^{13}$ m with the existing experiment data [17]. Table 2 lists the effective rms surface roughnesses and the absolute surface slopes of the test pieces [17]. From this figure, the fractal MT model underestimates the values compared to the experimental results. While it is worth pointing out that when a proper value of $D(=1.6)$ at a fixed value of G is taken, an excellent agreement between the present analytical expression Eq. (36) and the existing experimental data [17] can be obtained. See the solid line in Fig. 8. It is also found that at a fixed value of G, a lower value of the fractal dimension D yields a lower value of dimensionless contact conductance. This is expected since the surface will become smoother as D increases at a fixed value of G. This phenomenon can be explained by examining the effects of D in Eq. (4), which indicates that D affects the roughness amplitude in terms of a designated power (i.e., $2-D$). Furthermore, as D becomes larger, the number of the asperities increases and their heights decrease. By this definition, as D approaches 2.0 ($D_s \rightarrow 3.0$), the surface becomes smoother (the results are in accord with those reported in Refs. [41–43]). The two factors D and G result in a higher value of h^* as D increases. This verifies the validity of the present model. It is also worth pointing out that the value of $D=1.6$ compares well with the data in Ref. [17] for a fixed value of G. This value of D may be changed when different values of G are taken for data from other different sources.

Dimensionless conductance of a typical joint is shown in Fig. 9 in a wide range of the dimensionless pressure $P^*=P/H$. Five values of $G=10^{-9}$ m, 10^{-10} m, 10^{-11} m, 10^{-12} m, and 10^{-13} m are selected to investigate the effect of G on TCC. Other contact parameters are shown in the figure and are kept constant as G is changed. It can be seen in Fig. 9 that the dimensionless conduc-

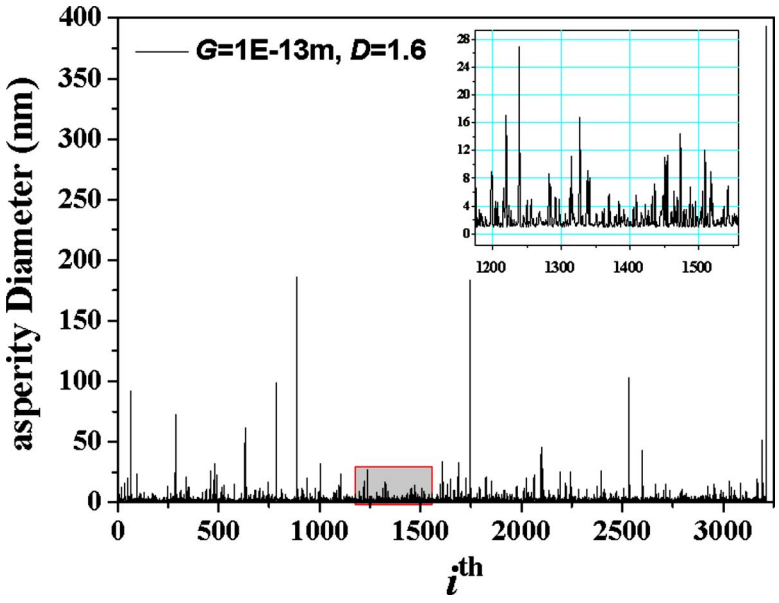

Fig. 6 The asperity diameters simulated by the present method at $l_{\min}$ =1 nm

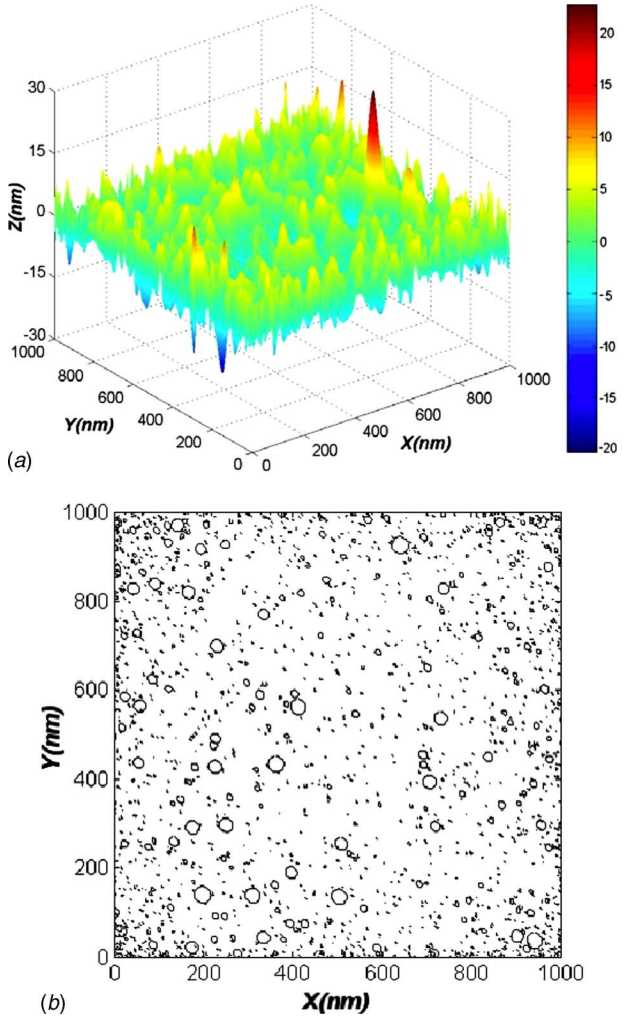

Fig. 7 (*a*) A typical three-dimensional surface as $D=1.44$, $G=9.46\times10^{-13}$ m, and $l_{min}=0.1$ nm, and (*b*) the cutaway view of (*a*)

tance decreases as G increases. This is also expected because the dimensionless conductance is inversely proportional to the value of G (see Eq. (36)).

Figure 10 illustrates the effect of the fractal parameter G on separation d. The figure shows that the separation decreases with the decrease in the fractal parameter G. This is expected because the lower the fractal parameter G, the lower the height of roughness, causing a shorter separation between the two contacting surfaces and thus a larger pressure. The latter can be found in Eqs. (16*a*), (16*b*), (17), and (26).

Table 2 The effective rms surface roughnesses and the absolute surface slopes of the test pieces [17]

Test no.	Test pieces	rms surface roughnesses: Upper test piece (μm)	rms surface roughnesses: Lower test piece (μm)	Absolute surface slopes
1	Steel and steel	5.00	5.13	0.0352
2	Steel and steel	1.57	4.78	0.0139
3	Steel and steel	5.76	5.36	0.0362
4	Steel and steel	2.26	2.80	0.0098
5	Steel and steel	4.00	5.56	0.0757
17	Steel and steel	0.59	3.92	0.0593
26	Steel and steel	2.28	3.31	0.0130

To illustrate the physical significance of fractal parameters G on the contact resistance, the comparisons of the bulk resistance, the constrain resistance, and the total contact resistance at $G=1\times10^{-13}$ m, 1×10^{-11} m, and 1×10^{-9} m are shown in Figs. 11(*a*)–11(*c*), respectively. It is seen that the constrained resistance often predominates, and the bulk resistance is almost negligible as the value of G is relatively small. The bulk resistance increases as G increases, and finally the bulk resistance is larger than the value of the constrained resistance. This is expected since G affects the amplitude in Eq. (4). Moreover, it can be found that as the mean separation between the two contacting surfaces decreases, more microcontacts are formed, which in turn leads to a higher real contact area that is equivalent to a lower TCR, and this is consistent with the practical situation.

4 Summary and Conclusion

The TCC and its components have been studied in this work. The modeling process is divided into two aspects: geometrical and mechanical. The random numbers are used to model the asperity diameters on surfaces and the pressure distribution, and then TCC has been studied. A good agreement has been observed by properly choosing G and D when compared with the exiting experimental data. The present results show that the fractal parameters D and G are two important factors that are to be taken into account for a realistic TCC calculation. A higher value of D leads to a lower TCC, while a higher value of G results in a higher TCC. The effect of G on the bulk resistance (which is often neglected in most existing models) is found to be important and could not be negligible as the value of G is relatively large.

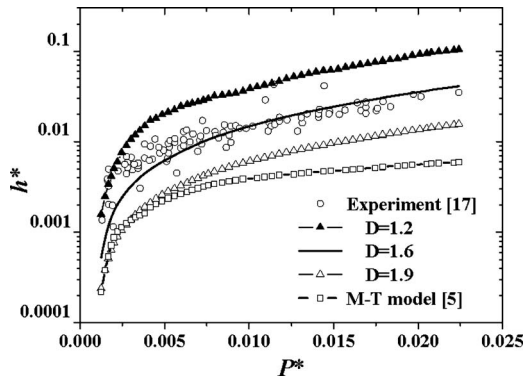

Fig. 8 Dimensionless conductance across the contacting solid spots versus dimensionless pressure

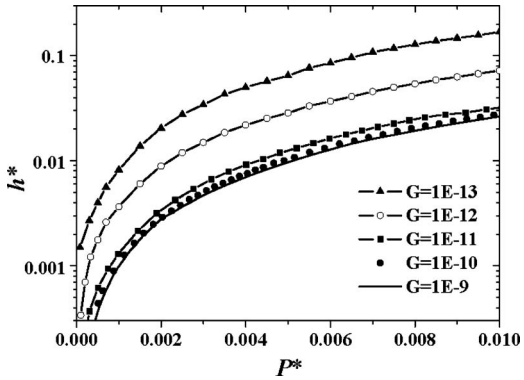

Fig. 9 Variation of dimensionless conductance with dimensionless pressure at various values of G when $D=1.6$

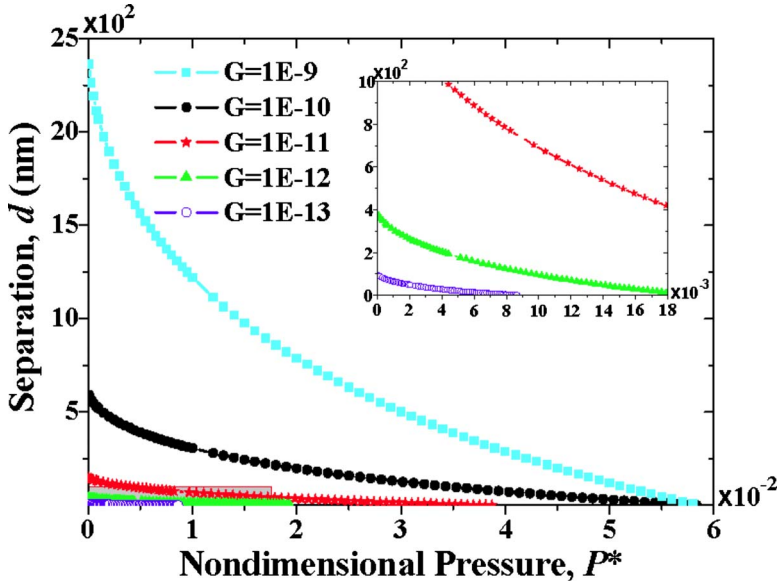

Fig. 10 The separation d versus dimensionless pressure at different values of G (as D=1.6)

In addition, the present model may also have the potential in analyzing other phenomena such as friction, radiation, wear, and lubrication on rough surfaces.

Acknowledgment

This work was supported by the National Natural Science Foundation of China through Grant No. 10572052.

Nomenclature

A_r = real contact area (m^2)
A_a = nominal contact area (m^2)
d = separation between the mean plane and contact rigid flat plane (m)
d' = separation between the mean plane and rigid flat plane (m)
D = fractal dimension
E = Young's modulus (Pa)
F = load (N)
G = characteristic length of rough surface (m)
h = roughness height (m)
h_c = TCC (W/m^2 K)
h^* = dimensionless TCC
H = hardness (Pa)
k = conductivity (W/m K)
K = factor relating to the yield strength and hardness
l = diameter of asperity (m)
L_s = sample length (m)
m = absolute surface slope
P = contact pressure (Pa)
P^* = dimensionless contact pressure
Q = total heat transfer across the joint (W)
r_b = bulk resistance of roughness (K/W)
r_c = contact resistance of roughness (K/W)
r_t = total resistance of roughness (K/W)
R_c = TCR (K/W)
V = volume (m^3)
z = asperity amplitude (m)

Greek Symbols

γ^n = frequency spectrum parameter of surface roughness (1/m)
ΔT_c = temperature drop across the joint (K)
λ = contact spot diameter (m)
ν = Poisson's ratio
σ = rms surface roughness (m)
σ_y = yield strength (Pa)
ϕ = effective porosity
ψ = geometrical factor

Appendix

This appendix is devoted to the derivation of the contact spot diameter on a fractal surface.

The mean height of all the asperities can be calculated by

$$h_m = \frac{1}{n}\sum_{i=1}^{n} h_i \tag{A1}$$

Therefore, in Fig. 2 we can see that the contact height d' can be determined by

$$d' = d + h_m \tag{A2}$$

here d is the separation between the contact rigid flat plane and the mean plane of the rough surface.

The roughness, which has the base diameter l_i, can be thought of as a cone before deformation, and its volume is given by

$$V_c = \frac{1}{3}h_i S_1 = \frac{1}{3}h_i \pi \left(\frac{l_i}{2}\right)^2 \tag{A3}$$

The deformed asperity model can be approximated without considering its accurate shape. It is assumed that asperity deformation is localized mainly near contact, as shown in Fig. 4(b), and the volume of the truncated cone segment is

$$V_t = \frac{1}{3}d'(S_2 + \sqrt{S_2 S_1} + S_1) = \frac{1}{3}d'\pi\left[\left(\frac{\lambda_i}{2}\right)^2 + \frac{\lambda_i}{2}\frac{l_i}{2} + \left(\frac{l_i}{2}\right)^2\right] \tag{A4}$$

where λ_i is the contact spot diameter of a deformed asperity at a given height d', as shown in Figs. 2 and 4(b).

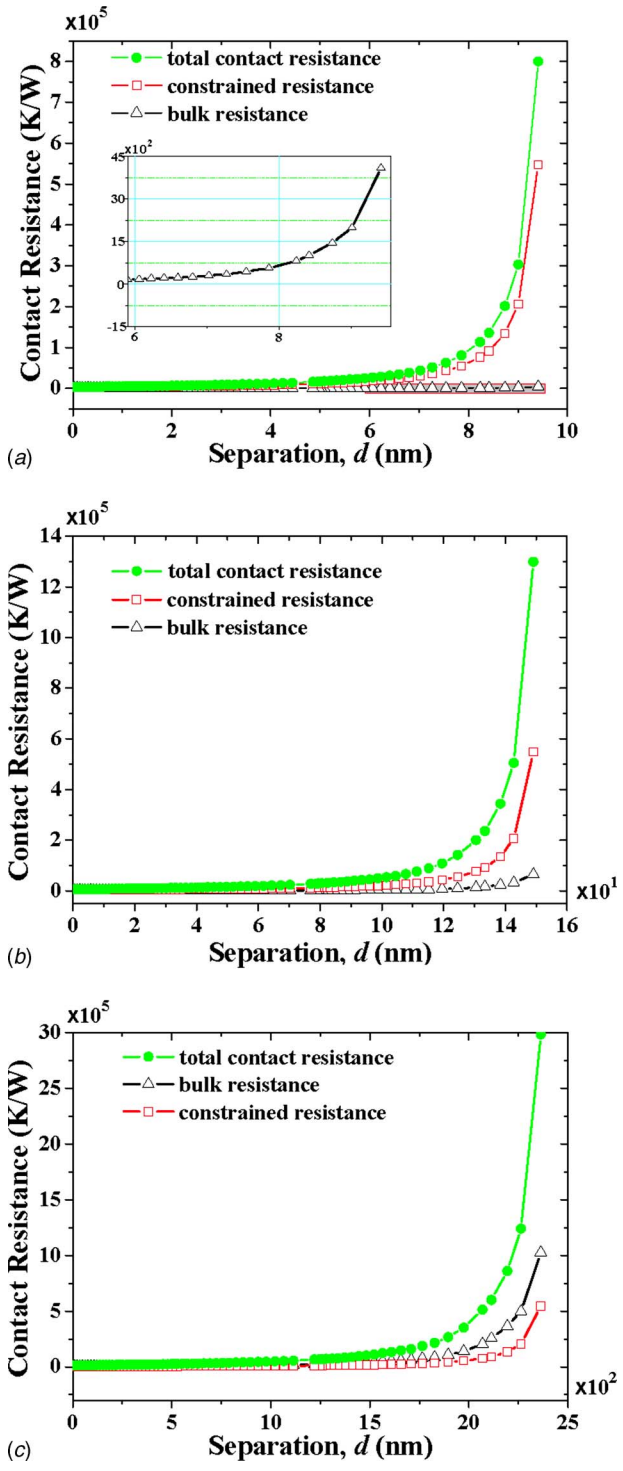

Fig. 11 Effect of G on contact resistance (D=1.6): (a) G=1 $\times 10^{-13}$ m, (b) G=1$\times 10^{-11}$ m, and (c) G=1$\times 10^{-9}$ m

Based on Eqs. (A3) and (A4) and on the assumption of volume conservation, the following relationship is obtained:

$$\frac{1}{3}h_i\pi\left(\frac{l_i}{2}\right)^2 = \frac{1}{3}d'\pi\left[\left(\frac{\lambda_i}{2}\right)^2 + \frac{\lambda_i}{2}\frac{l_i}{2} + \left(\frac{l_i}{2}\right)^2\right] \tag{A5}$$

and

$$\frac{h_i}{d'} = \frac{\lambda_i^2}{l_i^2} + \frac{\lambda_i}{l_i} + 1 = \left(\frac{\lambda_i}{l_i} + 0.5\right)^2 + 0.75 \tag{A6}$$

Therefore, λ_i can be found from the initial height h_i and the initial diameter l_i at a given height d' as

$$\lambda_i = \left(\sqrt{\frac{h_i}{d'} - 0.75} - 0.5\right)l_i \tag{A7}$$

which is Eq. (26).

References

[1] Cong, P. Z., Zhang, X., and Fujii, M., 2006, "Estimation of Thermal Contact Resistance Using Ultrasonic Waves," Int. J. Thermophys., **27**, pp. 171–183.
[2] Cooper, M. G., Mikic, B. B., and Yovanovich, M. M., 1969, "Thermal Contact Conductance," Int. J. Heat Mass Transfer, **12**, pp. 279–300.
[3] Mikic, B. B., 1974, "Thermal Contact Conductance; Theoretical Considerations," Int. J. Heat Mass Transfer, **17**, pp. 205–214.
[4] Johnson, K. L., 1985, *Contact Mechanics*, Cambridge University Press, Cambridge.
[5] Majumdar, A., and Tien, C. L., 1991, "Fractal Network Model for Contact Conductance," ASME J. Heat Transfer, **113**, pp. 516–525.
[6] Nishino, K., Yamashita, S., and Torii, K., 1995, "Thermal Contact Conductance Under Low Applied Load in a Vacuum Environment," Exp. Therm. Fluid Sci., **10**, pp. 258–271.
[7] Madhusudana, C. V., 1996, *Thermal Contact Conductance*, Springer-Verlag, New York, pp. 4–5.
[8] Jeng, Y. R., Chen, J. T., and Cheng, C. Y., 2003, "Theoretical and Experimental Study of a Thermal Contact Conductance Model for Elastic, Elastoplastic and Plastic Deformation of Rough Surfaces," Tribol. Lett., **14**, pp. 251–259.
[9] Bahrami, M., Culham, J. R., Yovanovich, M. M., and Schneider, G. E., 2003, "Review of Thermal Joint Resistance Models for Non-Conforming Rough Surfaces in a Vacuum," ASME Paper No. HT2003-47051.
[10] Bahrami, M., Culham, J. R., and Yovanovich, M. M., 2004, "Thermal Contact Resistance: A Scale Analysis Approach," ASME J. Heat Transfer, **126**, pp. 896–905.
[11] Wahid, S. M. S., Madhusudana, C. V., and Leonardi, E., 2004, "Solid Spot Conductance at Low Contact Pressure," Exp. Therm. Fluid Sci., **28**, pp. 489–494.
[12] Xiao, Y. M., Sun, H., Xu, L., Feng, H. D., and Zhu, H. M., 2004, "Thermal Contact Conductance Between Solid Interfaces Under Low Temperature and Vacuum," Rev. Sci. Instrum., **75**, pp. 3074–3076.
[13] Kumar, S. S., Abilash, P. M., and Ramamurthi, K., 2004, "Thermal Contact Conductance for Cylindrical and Spherical Contacts," Heat Mass Transfer, **40**, pp. 679–688.
[14] Bahrami, M., Yovanovich, M. M., and Culham, J. R., 2005, "Thermal Contact Resistance at Low Contact Pressure: Effect of Elastic Deformation," Int. J. Heat Mass Transfer, **48**, pp. 3284–3293.
[15] Bahrami, M., Culham, J. R., Yananovich, M. M., and Schneider, G. E., 2006, "Review of Thermal Joint Resistance Models for Nonconforming Rough Surfaces," Appl. Mech. Rev., **59**, pp. 1–11.
[16] Zhang, X., Cong, P. Z., and Fujii, M., 2006, "A Study on Thermal Contact Resistance at the Interface of Two Solids," Int. J. Thermophys., **27**, pp. 880–895.
[17] Yüncü, H., 2006, "Thermal Contact Conductance of Nominaly Flat Surfaces," Heat Mass Transfer, **43**, pp. 1–5.
[18] Greenwood, J. A., and Williamson, J. B. P., 1966, "Contact of Nominally Flat Surfaces," Proc. R. Soc. London, Ser. A, **295**, pp. 300–319.
[19] Patir, N., 1978, "A Numerical Procedure for Random Generation of Rough Surfaces," Wear, **47**, pp. 263–277.
[20] Majumdar, A., and Tien, C. L., 1990, "Fractal Characterization and Simulation of Rough Surfaces," Wear, **136**, pp. 313–327.
[21] Majumdar, A., and Bhushan, B., 1990, "Role of Fractal Geometry in Roughness Characterization and Contact Mechanics of Surfaces," ASME J. Tribol., **112**, pp. 205–216.
[22] Majumdar, A., and Bhushan, B., 1991, "Fractal Model of Elastic-Plastic Contact Between Rough Surfaces," ASME J. Tribol., **113**, pp. 1–11.
[23] Mandelbrot, B. B., 1983, *The Fractal Geometry of Nature*, Freeman, New York.
[24] Warren, T. L., and Krajcinovic, D., 1995, "Fractal Models of Elastic-Perfectly Plastic Contact of Rough Surfaces Based on the Cantor Set," Int. J. Solids Struct., **32**, pp. 2907–2922.
[25] Yan, W., and Komvopoulos, K., 1998, "Contact Analysis of Elastic-Plastic Fractal Surfaces," J. Appl. Phys., **84**, pp. 3617–3624.
[26] Willner, K., 2004, "Elasto-Plastic Normal Contact of Three-Dimensional Fractal Surfaces Using Halfspace Theory," ASME J. Tribol., **126**, pp. 28–33.
[27] Berry, M. V., and Lewis, Z. V., 1980, "On the Weierstrass-Mandelbrot Fractal Function," Proc. R. Soc. London, Ser. A, **370**, pp. 459–484.
[28] Komvopoulos, K., 2000, "Head-Disk Interface Contact Mechanics for Ultrahigh Density Magnetic Recording," Wear, **238**, pp. 1–11.
[29] Liou, J. L., and Lin, J. F., 2006, "A New Method Developed for Fractal Dimension and Topothesy Varying With the Mean Separation of Two Contact Surfaces," ASME J. Tribol., **128**, pp. 515–524.
[30] Yu, B. M., and Li, J. H., 2001, "Some Fractal Characters of Porous Media," Fractals, **9**, pp. 365–372.
[31] Yu, B. M., and Cheng, P., 2002, "A Fractal Permeability Model for Bidispersed Porous Media," Int. J. Heat Mass Transfer, **45**, pp. 2983–2993.

[32] Yu, B. M., Lee, L. J., and Cao, H. Q., 2002, "A Fractal In-Plane Permeability Model for Fabrics," Polym. Compos., **23**, pp. 201–221.
[33] Yu, B. M., Zou, M. Q., and Feng, Y. J., 2005, "Permeability of Fractal Porous Media by Monte Carlo Simulations," Int. J. Heat Mass Transfer, **48**, pp. 2787–2794.
[34] Greenwood, J. A., and Tripp, J. H., 1970–1971, "The Contact of Two Nominally Flat Rough Surfaces," Proc. Inst. Mech. Eng., **185**, pp. 625–633.
[35] Sahoo, P., and Banerjee, A., 2005, "Asperity Interaction in Adhesive Contact of Metallic Rough Surfaces," J. Phys. D, **38**, pp. 4096–4103.
[36] Archard, J. F., 1957, "Elastic Deformation and the Laws of Friction," Proc. R. Soc. London, Ser. A, **243**, pp. 190–205.
[37] Ciavarella, M., and Demelio, G., 2001, "Elastic Multiscale Contact of Rough Surfaces: Archard's Model Revisited and Comparisons With Modern Fractal Models," ASME J. Appl. Mech., **68**, pp. 496–498.
[38] Lumbantobing, A., Kogut, L., and Komvopoulos, K., 2004, "Electrical Contact Resistance as a Diagnostic Tool for MEMS Contact Interfaces," J. Microelectromech. Syst., **13**, pp. 977–987.
[39] Morag, Y., and Etsion, I., 2007, "Resolving the Contradiction of Asperities Plastic to Elastic Mode Transition in Current Contact Models of Fractal Rough Surfaces," Wear, **262**, pp. 624–629.
[40] Yang, A. J., and Komvopoulos, K., 2005, "Mechanics Approach to Static Friction of Elastic-Plastic Fractal Surfaces," ASME J. Tribol., **127**, pp. 315–324.
[41] Komvopoulos, K., and Ye, N., 2001, "Three-Dimensional Contact Analysis of Elastic-Plastic Layered Media With Fractal Surface Topographies," ASME J. Tribol., **123**, pp. 632–640.
[42] Kogut, L., and Komvopoulos, K., 2003, "Electrical Contact Resistance Theory for Conductive Rough Surfaces," J. Appl. Phys., **94**, pp. 3153–3162.
[43] Zou, M. Q., Yu, B. M., Feng, Y. J., and Xu, P., 2007, "A Monte Carlo Method for Simulating Fractal Surfaces," Physica A, **386**, pp. 176–186.

Small and Large Time Solutions for Surface Temperature, Surface Heat Flux, and Energy Input in Transient, One-Dimensional Conduction

A. S. Lavine
Mechanical and Aerospace Engineering Department,
University of California,
Los Angeles,
Los Angeles, CA 90095-1597
e-mail: lavine@seas.ucla.edu

T. L. Bergman
Department of Mechanical Engineering,
University of Connecticut,
191 Auditorium Road,
Unit 3139,
Storrs, CT 06269
e-mail: tberg@engr.uconn.edu

This paper addresses one-dimensional transient conduction in simple geometries. It is well known that the transient thermal responses of various objects, or of an infinite medium surrounding such objects, collapse to the same behavior as a semi-infinite solid at small dimensionless time. At large dimensionless time, the temperature reaches a steady state (for a constant surface temperature boundary condition) or increases linearly with time (for a constant heat flux boundary condition). The objectives of this paper are to bring together existing small and large time solutions for transient conduction in simple geometries, put them into forms that will promote their usage, and quantify the errors associated with the approximations. Approximate solutions in the form of simple algebraic expressions are derived (or compiled from existing solutions) for use at both small and large times. In particular, approximate solutions, which are accurate for Fo <0.2 and which bridge the gap between the large Fo (single-term) approximation and the semi-infinite solid solution (valid only at very small Fo), are presented. Solutions are provided for the surface temperature when there is a constant surface heat flux boundary condition, or for the surface heat flux when there is a constant surface temperature boundary condition. These results are provided in terms of a dimensionless heat transfer rate. In addition, the dimensionless energy input is given for the constant surface temperature cases. The approximate expressions may be used with good accuracy over the entire Fourier number range to rapidly estimate important features of the transient thermal response. With the use of the approximations, it is now a trivial matter to calculate the dimensionless heat transfer rate and dimensionless energy input, using simple closed-form expressions. [DOI: 10.1115/1.2945902]

Keywords: conduction, mass diffusion, approximate solutions

Introduction

Analytical solutions for one-dimensional, constant property, transient conduction (or species diffusion) within objects having simple geometries (plane wall, infinite cylinder, and sphere) have been known for decades and are presented in various heat transfer texts [1–6]. Because the internal temperature distributions are predicted with these solutions, these cases will be referred to as "interior" in this paper. As is well known, higher-order terms in the infinite series expressions for either temperature distributions or heat transfer rates may be neglected at large dimensionless times, as expressed by the Fourier number. The approximate results associated with large Fo are reported graphically in terms of the well-known Heisler–Gröber charts.

At small dimensionless times, however, evaluation of the analytical solutions can be surprisingly difficult, with the need to include many terms in the infinite series to achieve convergence [3]. This can be particularly problematic when the analytical solutions are applied to mass diffusion problems through the use of the heat and mass transfer analogy. In situations involving ordinary diffusion in solids or liquids, mass diffusivities are usually many orders of magnitude smaller than thermal diffusivities, leading to small values of Fo and rendering the exact solutions difficult to use, even in practical problems involving moderate time and length scales [1].

In addition to these interior cases, one can also consider the "exterior" cases of transient conduction from a body into a surrounding infinite medium [5–7]. Yovanovich et al. [7] considered the cases of transient conduction from isothermal convex bodies of various shapes into a surrounding infinite medium held at uniform temperature a large distance away from the body. They showed that, with proper nondimensionalization, the dimensionless heat flow rate, q^*(Fo), can be well approximated over the *entire* Fo range by a function that asymptotes to the semi-infinite solid solution for small times and to the steady-state solution for large times. The agreement between the q^*(Fo) behavior of the semi-infinite solid and the q^*(Fo) behavior of arbitrary shapes reflects the fact that, at small times, thermal penetration depths within the surrounding medium are small relative to the characteristic dimension of the object, and spatially averaged heat transfer rates are therefore independent of the object shape. The study of Yovanovich et al. suggests that, with proper nondimensionalization, the transient thermal response might be described by simple expressions over the *entire* Fo range, obviating the need for cumbersome evaluation of many terms in the infinite series expressions associated with the exact solutions. Carslaw and Jaeger [5] also presented several exterior cases, including providing

Contributed by the Heat Transfer Division of ASME for publication in the JOURNAL OF HEAT TRANSFER. Manuscript received May 8, 2007; final manuscript received February 8, 2008; published online August 8, 2008. Review conducted by A. Haji-Sheikh.

small time approximations derived using Laplace transform techniques.

The idea of approximating transient conduction solutions for small and large times is explored in a book and various papers by Beck et al. [6,8,9] and McMasters et al. [10], where it is referred to as time partitioning. The small and large time solutions are introduced in the context of Green's functions; numerical integration of the Green's functions over time must be carried out, and efficiency is greatly enhanced by using the small and large time approximations. In an earlier paper by Beck et al. [11], small and large time solutions are presented for some transient conduction problems with constant heat flux boundary conditions. The solutions are presented in the context of the unsteady surface element method, for which Duhamel's theorem is employed with influence functions that are the constant heat flux solutions.

The objectives of this paper are to bring together existing small and large time solutions for transient conduction in simple geometries, put them into forms that will promote their usage, and quantify the errors associated with the approximations. Specifically, the geometries considered in this study are as follows (see Fig. 1):

- semi-infinite solid
- interior of plane wall
- interior of infinite cylinder
- interior of sphere
- exterior of sphere

The exterior of an infinite cylinder is omitted because it is not amenable to the asymptotic approaches considered here. Information about this case can be found in Refs. [5,12].

For each geometry, we consider the transient thermal response of the object subject to both constant surface temperature (species concentration) and constant surface heat flux (species flux) boundary conditions. Following Ref. [7], the predicted thermal responses are reported in terms of a dimensionless heat rate

$$q^* \equiv \frac{q_s'' L_c}{k(T_s - T_i)} \tag{1}$$

as a function of the Fourier number, $\mathrm{Fo} = \alpha t / L_c^2$ (where L_c is a characteristic length defined in Table 1 for each of the geometries). For a constant surface temperature boundary condition, this is equivalent to reporting the surface heat flux, whereas for a constant surface heat flux boundary condition this is equivalent to reporting the surface temperature. It is also useful to consider the total energy (or species) input to each of the interior objects up to a given time. The total energy input is typically normalized by the total energy which will have entered the object at steady state, that is,

$$\frac{Q}{Q_o} = \frac{\int_0^t q_s'' A_s dt}{\rho c (T_s - T_i) V} = \frac{A_s L_c}{V} \int_0^{\mathrm{Fo}} q^* d\mathrm{Fo} = p \int_0^{\mathrm{Fo}} q^* d\mathrm{Fo} \tag{2}$$

where $p = 1, 2, 3$ for plane wall, infinite cylinder, and sphere, respectively.

For each of the cases, we provide the following.

- The analytical solution for $q^*(\mathrm{Fo})$, assuming constant thermophysical properties. Of course, many of these solutions are already known [1–6].
- Analytically derived approximations for small and large Fo, which take the form of simple algebraic expressions. By using the small time solution for $\mathrm{Fo} < 0.2$ and the large time

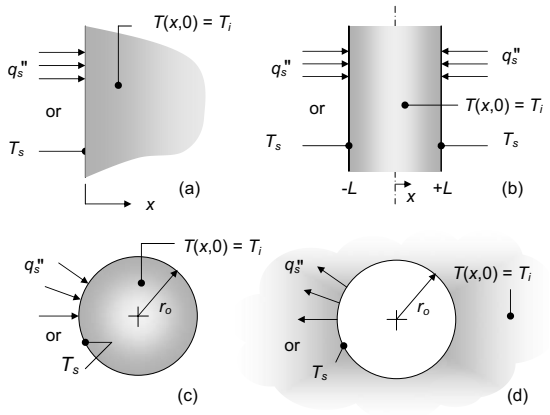

Fig. 1 Physical system: (*a*) semi-infinite solid, (*b*) plane wall, (*c*) sphere or infinite cylinder, and (*d*) sphere embedded in an infinite medium

Table 1 Summary of transient heat transfer results for constant surface temperature cases. $q^* \equiv q_s'' L_c / k(T_s - T_i)$ and $\mathrm{Fo} \equiv \alpha t / L_c^2$, where L_c is the length scale given in the table, T_s is the object surface temperature, and T_i is (a) the initial object temperature for the interior cases and (b) the temperature of the infinite medium for the exterior case.

		$q^*(\mathrm{Fo})$			
			Approximate solutions		
Geometry	Length scale, L_c	Exact solutions	$\mathrm{Fo} < 0.2$	$\mathrm{Fo} \geq 0.2$	Maximum error (%)
Semi-infinite	L (arbitrary)	$\frac{1}{\sqrt{\pi \mathrm{Fo}}}$	Use exact solution		None
Interior cases					
Plane wall of thickness $2L$	L	$2\sum_{n=1}^{\infty} \exp(-\zeta_n^2 \mathrm{Fo}), \quad \zeta_n = \left(n - \frac{1}{2}\right)\pi$	$\frac{1}{\sqrt{\pi \mathrm{Fo}}}$	$2\exp(-\zeta_1^2 \mathrm{Fo}),\ \zeta_1 = \pi/2$	1.7
Infinite cylinder	r_o	$2\sum_{n=1}^{\infty} \exp(-\zeta_n^2 \mathrm{Fo}), \quad J_0(\zeta_n) = 0$	$\frac{1}{\sqrt{\pi \mathrm{Fo}}} - \frac{1}{2} - 0.65\mathrm{Fo}$	$2\exp(-\zeta_1^2 \mathrm{Fo}),\ \zeta_1 = 2.4050$	0.8
Sphere	r_o	$2\sum_{n=1}^{\infty} \exp(-\zeta_n^2 \mathrm{Fo}), \quad \zeta_n = n\pi$	$\frac{1}{\sqrt{\pi \mathrm{Fo}}} - 1$	$2\exp(-\zeta_1^2 \mathrm{Fo}),\ \zeta_1 = \pi$	6.3
Exterior case Sphere	r_o	$\frac{1}{\sqrt{\pi \mathrm{Fo}}} + 1$	Use exact solution		None

Table 2 Summary of transient heat transfer results for constant surface heat flux cases. $q^* \equiv q_s'' L_c / k(T_s - T_i)$ and $\mathrm{Fo} \equiv \alpha t / L_c^2$, where L_c is the length scale given in the table, T_s is the object surface temperature, and T_i is (a) the initial object temperature for the interior cases and (b) the temperature of the infinite medium for the exterior case.

Geometry	Length scale, L_c	$q^*(\mathrm{Fo})$ Exact solutions	Approximate solutions $\mathrm{Fo}<0.2$	Approximate solutions $\mathrm{Fo}\geq 0.2$	Maximum error (%)
Semi-infinite	L (arbitrary)	$\frac{1}{2}\sqrt{\frac{\pi}{\mathrm{Fo}}}$	Use exact solution		None
Interior cases					
Plane wall of thickness $2L$	L	$\left[\mathrm{Fo}+\frac{1}{3}-2\sum_{n=1}^{\infty}\frac{\exp(-\zeta_n^2\mathrm{Fo})}{\zeta_n^2}\right]^{-1}$, $\zeta_n = n\pi$	$\frac{1}{2}\sqrt{\frac{\pi}{\mathrm{Fo}}}$	$\left[\mathrm{Fo}+\frac{1}{3}\right]^{-1}$	5.3
Infinite cylinder	r_o	$\left[2\mathrm{Fo}+\frac{1}{4}-2\sum_{n=1}^{\infty}\frac{\exp(-\zeta_n^2\mathrm{Fo})}{\zeta_n^2}\right]^{-1}$, $J_1(\zeta_n)=0$	$\frac{1}{2}\sqrt{\frac{\pi}{\mathrm{Fo}}}-\frac{\pi}{8}$	$\left[2\mathrm{Fo}+\frac{1}{4}\right]^{-1}$	2.1
Sphere	r_o	$\left[3\mathrm{Fo}+\frac{1}{5}-2\sum_{n=1}^{\infty}\frac{\exp(-\zeta_n^2\mathrm{Fo})}{\zeta_n^2}\right]^{-1}$, $\tan(\zeta_n)=\zeta_n$	$\frac{1}{2}\sqrt{\frac{\pi}{\mathrm{Fo}}}-\frac{\pi}{4}$	$\left[3\mathrm{Fo}+\frac{1}{5}\right]^{-1}$	4.5
Exterior case Sphere	r_o	$[1-\exp(\mathrm{Fo})\mathrm{erfc}(\mathrm{Fo}^{1/2})]^{-1}$	$\frac{1}{2}\sqrt{\frac{\pi}{\mathrm{Fo}}}+\frac{\pi}{4}$	$\frac{0.77}{\sqrt{\mathrm{Fo}}}+1$	3.2

solution for $\mathrm{Fo}>0.2$, approximate solutions are available over the entire range, $0<\mathrm{Fo}<\infty$. In some cases, new numerical approximations which are preferable to the asymptotic solutions are presented.

- Maximum errors associated with the use of the approximate solutions. The error is defined as the percentage difference between predicted and exact dimensionless heat transfer rates. Maximum errors are less than 6.3%, with the error significantly smaller over most of the Fo range.
- Approximate solutions for the total, normalized energy input, Q/Q_o, as a function of Fo, and the associated errors relative to the exact solution, for the interior cases. These solutions are presented only for the constant surface temperature boundary condition, since it is a trivial matter to find Q/Q_o for constant surface heat flux. Maximum errors are less than approximately 0.2%.

All of these results are summarized in Tables 1–3. The remainder of this paper is devoted to deriving, presenting, and discussing the results in these tables and giving examples using the approximate results. As will become evident, the approximate results are valuable, in that they can be used to very rapidly estimate, to a high degree of accuracy, relevant thermal responses (surface heat fluxes or temperatures and total energy inputs) over the entire time range, $0<\mathrm{Fo}<\infty$. In addition, these solutions can be used as the influence functions in Duhamel's theorem, to generate surface temperatures (or surface heat fluxes) for situations in which the surface heat flux (or surface temperature) is a specified function of time.

Problem Statement

For each of the cases, the heat diffusion equation can be written as

$$\frac{\partial\theta}{\partial \mathrm{Fo}} = \frac{1}{r^{*n}}\frac{\partial}{\partial r^*}\left(r^{*n}\frac{\partial\theta}{\partial r^*}\right) \tag{3}$$

In this equation, $\theta=(T-T_i)/\Delta T_c$, where T_i is the initial temperature of the object and $\Delta T_c=(T_s-T_i)$ for constant surface temperature boundary conditions and $\Delta T_c=q_s''L_c/k$ for constant surface heat flux boundary conditions. In addition, $r^*=r/L_c$, where r is the dimensional spatial coordinate (x for Cartesian coordinates), and $n=0,1,2$ for Cartesian, cylindrical radial, and spherical radial coordinates, respectively. The initial condition is $\theta(r^*,\mathrm{Fo}=0)=0$, and the boundary conditions are as follows.

Semi-infinite solid:

$$\theta(r^*\rightarrow\infty,\mathrm{Fo})=0 \tag{4}$$

and one of the following:

$$\text{constant } T_s: \quad \theta(r^*=0,\mathrm{Fo})=1 \tag{5}$$

Table 3 Formulas for total heat input for constant surface temperature interior cases, using approximate solutions, and maximum errors

Geometry	Length scale, L_c	$Q/Q_o(\mathrm{Fo})$ $\mathrm{Fo}<0.2$	$\mathrm{Fo}\geq 0.2$	Maximum error (%)
Interior cases				
Plane wall of thickness $2L$	L	$2\sqrt{\frac{\mathrm{Fo}}{\pi}}$	$1-\frac{2}{\zeta_1^2}\exp(-\zeta_1^2\mathrm{Fo})$, $\zeta_1=\pi/2$	0.21
Infinite cylinder	r_o	$4\sqrt{\frac{\mathrm{Fo}}{\pi}}-\mathrm{Fo}-0.65\mathrm{Fo}^2$	$1-\frac{4}{\zeta_1^2}\exp(-\zeta_1^2\mathrm{Fo})$, $\zeta_1=2.4050$	0.22
Sphere	r_o	$6\sqrt{\frac{\mathrm{Fo}}{\pi}}-3\mathrm{Fo}$	$1-\frac{6}{\zeta_1^2}\exp(-\zeta_1^2\mathrm{Fo})$, $\zeta_1=\pi$	0.18

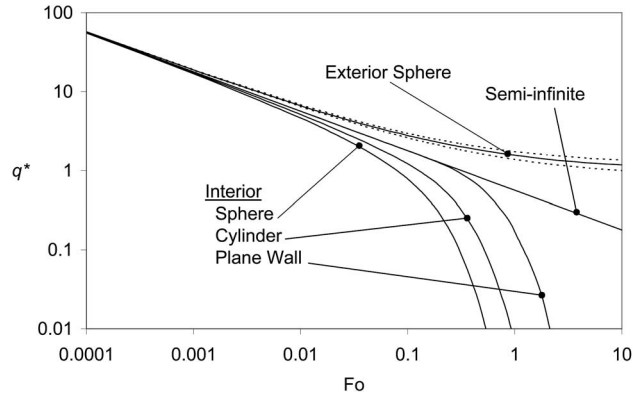

Fig. 2 Transient thermal response, q^*(Fo), for constant surface temperature boundary conditions. The dotted lines approximately bound exterior objects in Ref. [7].

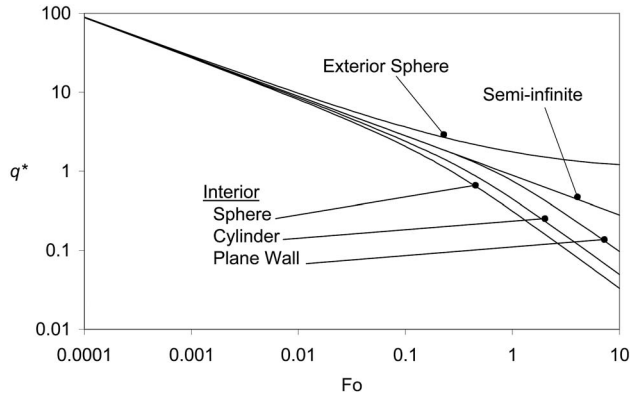

Fig. 3 Transient thermal response, q^*(Fo), for constant surface heat flux boundary conditions

$$\text{constant } q_s'': \quad \left.\frac{\partial\theta}{\partial r^*}\right|_{r^*=0} = -1 \tag{6}$$

All interior cases:

$$\left.\frac{\partial\theta}{\partial r^*}\right|_{r^*=0} = 0 \tag{7}$$

and one of the following:

$$\text{constant } T_s: \quad \theta(r^*=1,\text{Fo}) = 1 \tag{8}$$

$$\text{constant } q_s'': \quad \left.\frac{\partial\theta}{\partial r^*}\right|_{r^*=1} = 1 \tag{9}$$

Exterior sphere:

$$\theta(r^*\to\infty,\text{Fo}) = 0 \tag{10}$$

and one of the following:

$$\text{constant } T_s: \quad \theta(r^*=1,\text{Fo}) = 1 \tag{11}$$

$$\text{constant } q_s'': \quad \left.\frac{\partial\theta}{\partial r^*}\right|_{r^*=1} = -1 \tag{12}$$

Exact Results and Discussion

The resulting analytical expressions for q^*(Fo) are listed in Tables 1 and 2 for constant temperature and constant heat flux boundary conditions, respectively. The exact solutions, in dimensionless form, are shown graphically in Figs. 2 and 3, and are discussed below.

Constant Surface Temperature Boundary Conditions. For the semi-infinite solid, the value of q^* is independent of the characteristic length and $q^* \propto \text{Fo}^{-1/2}$, as evident in Fig. 2. In particular, the thermal response of the semi-infinite solid is

$$q^* = \frac{1}{\sqrt{\pi\text{Fo}}} \tag{13}$$

Results for heat transfer to the interior of a plane wall, infinite cylinder, and sphere are also shown in Fig. 2, using characteristic lengths of $L_c = L$ or r_o for a plane wall of thickness $2L$ or a sphere (or infinite cylinder) of radius r_o. As is evident in the figure, for each geometry q^* initially follows the semi-infinite solid behavior but at some point decreases rapidly as the objects approach their equilibrium temperature and, in turn, $q^*(\text{Fo}\to\infty)=0$. The value of q^* decreases more rapidly for geometries that possess large surface area to volume ratios, as expected.

Figure 2 also shows the solution for the exterior sphere case, namely,

$$q^* = \frac{1}{\sqrt{\pi\text{Fo}}} + 1 \tag{14}$$

Note that the dotted lines surrounding the response of the sphere approximately bound the other exterior geometries as derived computationally and reported in Ref. [7]. For these exterior heat transfer cases, the length scale is $L_c = (A_s/4\pi)^{1/2}$, where A_s is the surface area of the embedded object (which reduces to $L_c = r_o$ for a sphere). It was shown in Ref. [7] that a length scale proportional to the square root of the surface area most effectively collapses the behavior of the various geometries. Note that for *any* convex geometry for the exterior heat transfer cases, the initial response of the surrounding medium is identical to that of a semi-infinite solid, and a steady-state solution is reached where $q^*(\text{Fo}\to\infty) \approx 1$. (The infinite cylinder exterior case, not considered here, is an exception that does not reach a steady state.)

Constant Surface Heat Flux Boundary Conditions. When a constant heat flux is applied to the surface of the object, the numerator of Eq. (1) is fixed and the temperature difference in the denominator evolves with time. Thus, the dimensionless heat rate represents the surface temperature history. The results for the various geometries are shown in Fig. 3. For the semi-infinite solid, the dimensionless heat rate is given by

$$q^* = \frac{1}{2}\sqrt{\frac{\pi}{\text{Fo}}} \tag{15}$$

For heat transfer to the interior of the one-dimensional plane wall, infinite cylinder, or sphere, the q^*(Fo) response is initially the same as that of the semi-infinite solid, as was seen for the constant temperature boundary condition cases. Compared to the constant surface temperature cases of Fig. 2, however, the rate at which q^* decreases is more modest, since steady-state conditions are never reached. At large times for objects of finite size, $q^* \propto \text{Fo}^{-1}$, as expected from consideration of lumped thermal capacitance behavior [1]. For the exterior sphere case, the thermal response is given by the exact solution

$$q^* = [1 - \exp(\text{Fo})\text{erfc}(\text{Fo}^{1/2})]^{-1} \tag{16}$$

As for the constant temperature boundary condition responses, the sphere reaches a steady-state condition for which $q^*(\text{Fo}\to\infty)=1$.

Approximate Solutions

The discussion in the preceding section illustrates the benefits associated with the use of the dimensionless heat rate. However,

the oftentimes cumbersome task associated with evaluating the infinite series expressions for q^* at small times remains. To this end, the asymptotic behavior at small Fo suggests that the exact infinite series solutions might be readily replaced with simpler expressions, just as approximate solutions can be applied at large Fo. Indeed, small time approximations are available in the literature, as discussed previously, although they are not as widely known as the large time approximations. In this paper, the small time approximations will be derived by making use of the Euler–Maclaurin summation formula. This is an alternative to the Laplace transform method used in some of the references, and has the attractive feature of beginning from the exact series solutions (which is not to detract from the power of the Laplace transform method). It will be shown that the small and large time approximations taken together can be used to provide very accurate approximations of the exact solutions with minor errors restricted to very narrow ranges of Fo. In addition, an approximate solution will be provided for the exterior sphere with constant heat flux, since evaluation of the complementary error function can be problematic.

Small Fourier Number Limit for Interior Cases. Considering first the constant T_s cases in Table 1, the exact solutions for all of the interior cases can be written as

$$q^* = 2\sum_{n=1}^{\infty} \exp(-\zeta_n^2 \mathrm{Fo}) \tag{17}$$

where

$$\zeta_n = \begin{cases} \left(n-\frac{1}{2}\right)\pi & \text{plane wall} \\ \text{roots of } J_0 & \text{infinite cylinder} \\ n\pi & \text{sphere} \end{cases} \tag{18}$$

and J_0 is the Bessel function of the first kind of order 0. The cylinder solution is significantly more complicated than the other two and will be addressed later. Continuing with the plane wall and sphere, it is convenient to separate the first term in Eq. (17), that is,

$$q^* = 2\exp(-\zeta_1^2 \mathrm{Fo}) + 2\sum_{k=1}^{\infty} \exp(-\zeta_{k+1}^2 \mathrm{Fo}) \tag{19}$$

Next, the summation over k is approximated using the Euler–Maclaurin summation formula (13),

$$S = \sum_{k=1}^{\infty} f_k = \int_{k=0}^{\infty} f(k)dk - \frac{1}{2}f(0) - \frac{1}{12}f'(0) + \frac{1}{720}f'''(0) + \cdots \tag{20}$$

where $f_k = 2\exp(-\zeta_{k+1}^2 \mathrm{Fo})$, the prime denotes differentiation with respect to k (treating f as a continuous function of k), and use has been made of the fact that f and all its derivatives go to zero as $k \to \infty$. We now proceed to evaluate each of the terms in S.

$$I = \int_{k=0}^{\infty} f(k)dk = 2\int_{k=0}^{\infty} \exp(-\zeta_{k+1}^2 \mathrm{Fo})dk$$

$$= \frac{2}{\pi \mathrm{Fo}^{1/2}} \int_{\eta_0}^{\infty} \exp(-\eta_k^2)d\eta_k = \frac{1}{\sqrt{\pi \mathrm{Fo}}} \mathrm{erfc}(\zeta_1 \mathrm{Fo}^{1/2}) \tag{21}$$

where the transformation $\eta_k = \zeta_{k+1}\mathrm{Fo}^{1/2}$ was used. Continuing with the remaining terms,

$$f(0) = 2\exp(-\zeta_1^2 \mathrm{Fo}) \tag{22}$$

$$f'(0) = -4\pi\zeta_1 \mathrm{Fo}\exp(-\zeta_1^2 \mathrm{Fo}) \tag{23}$$

$$f'''(0) = (24\zeta_1 \mathrm{Fo}^2 - 16\zeta_1^3 \mathrm{Fo}^3)\pi^3 \exp(-\zeta_1^2 \mathrm{Fo}) \tag{24}$$

Note that higher-order derivatives of f would involve the same or higher powers of Fo. Since we seek a small Fo approximation for q^*, we drop terms that are higher than linear in Fo. Thus, we will omit $f'''(0)$ and all higher derivatives. Finally, we can write

$$q^* = 2\exp(-\zeta_1^2 \mathrm{Fo}) + \frac{1}{\sqrt{\pi \mathrm{Fo}}} \mathrm{erfc}(\zeta_1 \mathrm{Fo}^{1/2}) - \exp(-\zeta_1^2 \mathrm{Fo})$$

$$+ \frac{1}{3}\pi\zeta_1 \mathrm{Fo}\exp(-\zeta_1^2 \mathrm{Fo}) \tag{25}$$

For small Fo, the complementary error function and exponential terms can be expanded in Taylor series. Retaining only terms up to order Fo, the result is

$$q^* = 1 - \zeta_1^2 \mathrm{Fo} + \frac{1}{\sqrt{\pi \mathrm{Fo}}}\left(1 - \frac{2}{\pi^{1/2}}\zeta_1 \mathrm{Fo}^{1/2} + \frac{2}{3\pi^{1/2}}\zeta_1^3 \mathrm{Fo}^{3/2}\right) + \frac{\pi}{3}\zeta_1 \mathrm{Fo}$$

$$= \frac{1}{\sqrt{\pi \mathrm{Fo}}} + \left(1 - \frac{2}{\pi}\zeta_1\right) + \left(-\zeta_1^2 + \frac{2}{3\pi}\zeta_1^3 + \frac{\pi}{3}\zeta_1\right)\mathrm{Fo} \tag{26}$$

With $\zeta_1 = (1-a)\pi$ ($a = 1/2$ for the plane wall and $a = 0$ for the sphere), this simplifies to

$$q^* = \frac{1}{\sqrt{\pi \mathrm{Fo}}} - b, \quad b = 1 - 2a = \begin{cases} 0 & \text{plane wall} \\ 1 & \text{sphere} \end{cases} \tag{27}$$

The first term is the semi-infinite solid solution, the second term is a constant (different for the two different geometries), and the terms that are linear in Fo cancel out.

For the cylinder solution, the roots of J_0 can be approximated for large n as [13]

$$\zeta_n = \beta_n + \frac{1}{8\beta_n} - \frac{4 \times 31}{3(8\beta_n)^3} + \cdots \tag{28}$$

where $\beta_n = (n - 1/4)\pi$. The fact that $d\zeta_n/dn$ is a function of n makes the cylinder solution much more complicated than the other two cases. A derivation which uses the first two terms of the expansion for ζ_n yields the following result for q^*:

$$q^* = \frac{1}{\sqrt{\pi \mathrm{Fo}}} - \frac{1}{2} - \frac{1}{4}\sqrt{\frac{\mathrm{Fo}}{\pi}} - \frac{1}{8}\mathrm{Fo} \tag{29}$$

Because the objective is to approximate the exact solution over the range $0 < \mathrm{Fo} < 0.2$, the asymptotic solution above will be replaced with the numerical approximation below, in which the last two terms are replaced with a single term proportional to Fo, chosen to give good agreement over the desired range. The asymptotic solution gives better agreement for very small Fo, as expected, but for very small Fo the last two terms are relatively unimportant anyway. Over the entire desired range, the fitted solution is a better approximation. Thus, it is recommended to use

$$q^* = \frac{1}{\sqrt{\pi \mathrm{Fo}}} - \frac{1}{2} - 0.65\mathrm{Fo} \tag{30}$$

Turning next to the constant q_s'' interior cases in Table 2, they each contain a summation term of the form

$$S = 2\sum_{n=1}^{\infty} \frac{\exp(-\zeta_n^2 \mathrm{Fo})}{\zeta_n^2} \tag{31}$$

where

$$\zeta_n = \begin{cases} n\pi & \text{plane wall} \\ \text{roots of } J_1 & \text{infinite cylinder} \\ \text{solutions of } \zeta_n = \tan(\zeta_n) & \text{sphere} \end{cases} \tag{32}$$

For large n, these each take the form

$$\zeta_n = (n+c)\pi, \quad c = \begin{cases} 0 & \text{plane wall} \\ \frac{1}{4} & \text{infinite cylinder} \\ \frac{1}{2} & \text{sphere} \end{cases} \tag{33}$$

We will take a somewhat different approach here and split the sum, S, into two portions, such that the second portion is for sufficiently large n so that the above approximations are good. (This was the approach used for the infinite cylinder constant surface temperature case above.) That is,

$$S = 2\sum_{n=1}^{N} \frac{\exp(-\zeta_n^2 \mathrm{Fo})}{\zeta_n^2} + 2\sum_{k=1}^{\infty} \frac{\exp(-\zeta_{N+k}^2 \mathrm{Fo})}{\zeta_{N+k}^2} \tag{34}$$

For the second sum, the Euler–Maclaurin summation formula, Eq. (20), is used, with

$$f(k) = 2\frac{\exp(-\zeta_{N+k}^2 \mathrm{Fo})}{\zeta_{N+k}^2} \tag{35}$$

resulting in

$$S = 2\sum_{n=1}^{N} \frac{\exp(-\zeta_n^2 \mathrm{Fo})}{\zeta_n^2} + 2\left(\frac{\exp(-\zeta_N^2 \mathrm{Fo})}{\pi \zeta_N} - \frac{\mathrm{Fo}^{1/2}}{\pi^{1/2}} \operatorname{erfc}(\zeta_N \mathrm{Fo}^{1/2}) \right) + \left[-\frac{1}{\zeta_N^2} + \frac{\pi}{3}\left(\frac{\mathrm{Fo}}{\zeta_N} + \frac{1}{\zeta_N^3} \right) - \frac{\pi^3}{15}\left(\frac{\mathrm{Fo}}{\zeta_N^3} + \frac{1}{\zeta_N^5} \right) \right] \exp(-\zeta_N^2 \mathrm{Fo}) + \cdots \tag{36}$$

where Fo^2 and Fo^3 terms have been omitted in $f'''(0)$. Expanding for small Fo and retaining terms up to linear in Fo, this becomes

$$S = \left[2\sum_{n=1}^{N} \frac{1}{\zeta_n^2} + \frac{2}{\pi \zeta_N} - \frac{1}{\zeta_N^2} + \frac{\pi}{3\zeta_N^3} - \frac{\pi^3}{15\zeta_N^5} \right] - \frac{2\mathrm{Fo}^{1/2}}{\pi^{1/2}} + \left(\frac{2\zeta_N}{\pi} - 2N + 1 \right) \mathrm{Fo} \tag{37}$$

Thus,

$$q^{*-1} = \left[e - 2\sum_{n=1}^{N} \frac{1}{\zeta_n^2} - \frac{2}{\pi \zeta_N} + \frac{1}{\zeta_N^2} - \frac{\pi}{3\zeta_N^3} + \frac{\pi^3}{15\zeta_N^5} \right] + \frac{2\mathrm{Fo}^{1/2}}{\pi^{1/2}} + \left(d - \frac{2\zeta_N}{\pi} + 2N - 1 \right) \mathrm{Fo} \tag{38}$$

where (from Table 2)

$$d = \begin{cases} 1 & \text{plane wall} \\ 2 & \text{infinite cylinder} \\ 3 & \text{sphere} \end{cases}, \quad e = \begin{cases} 1/3 & \text{plane wall} \\ 1/4 & \text{infinite cylinder} \\ 1/5 & \text{sphere} \end{cases} \tag{39}$$

Recalling that the summation was split into two pieces, with N defined to be large enough so that Eq. (33) holds, the coefficient of the Fo term comes out to be 0, 1/2, and 1 for the plane wall, cylinder, and sphere, respectively. The constant term (in square brackets) is numerically found to converge to zero in all three cases, as $N \to \infty$. Thus, inverting Eq. (38) for small Fo results in

$$q^* = \frac{1}{2}\sqrt{\frac{\pi}{\mathrm{Fo}}} - g, \quad g = \begin{cases} 0 & \text{plane wall} \\ \pi/8 & \text{infinite cylinder} \\ \pi/4 & \text{sphere} \end{cases} \tag{40}$$

for the interior cases with constant heat flux boundary conditions.

Large Fourier Number Limit for Interior Cases. For the interior cases with constant surface temperature boundary condition, the large Fourier number limit is the well-known approximation of retaining only the first term in the infinite series solution (see Table 1). For the constant heat flux boundary condition, the entire infinite series can be neglected relative to the linear function of Fo (see Table 2).

Small and Large Fourier Number Limits for Exterior Case. For the exterior sphere case with a constant temperature boundary condition, the exact solution (see Table 1) is already a simple algebraic expression, which (as pointed out in Ref. [7]) is the superposition of the small time, semi-infinite solid solution and the steady-state solution. For the exterior sphere with a constant heat flux boundary condition (not addressed in Ref. [7]), the exact solution is given in Table 2. It is trivial to evaluate using modern computational tools, but approximations which can be evaluated using a handheld calculator are provided. The small Fourier number limit is readily obtained by expanding the exact solution in a Taylor series, as given in Table 2. The large Fourier number asymptote is $q^* = (\pi \mathrm{Fo})^{-1/2} + 1$. However, over the desired range of $0.2 < \mathrm{Fo} < \infty$, a better overall fit is found by using $q^* = 0.77\mathrm{Fo}^{-1/2} + 1$, as given in Table 2.

Approximate Solutions for Q/Q_o. Equation (2) provides an expression that can be evaluated to yield Q/Q_o. It is convenient to use in this form for $\mathrm{Fo} < 0.2$, making use of the approximate solutions for q^* in Table 1. For $\mathrm{Fo} > 0.2$, the integral in Eq. (2) can be calculated in two pieces, using the small and large Fo approximations. Alternatively, and preferably so as to ensure the correct large Fo limiting behavior, the integral can be rewritten as

$$\frac{Q}{Q_o} = p\left[\int_0^{\infty} q^* d\mathrm{Fo} - \int_{\mathrm{Fo}}^{\infty} q^* d\mathrm{Fo} \right] = 1 - p\int_{\mathrm{Fo}}^{\infty} q^* d\mathrm{Fo} = 1 - \frac{2p}{\zeta_1^2} \exp(-\zeta_1^2 \mathrm{Fo}), \quad \mathrm{Fo} > 0.2 \tag{41}$$

where the large Fo approximation has been used, and $p = 1, 2, 3$ for plane wall, infinite cylinder, and sphere, respectively. While the existing large Fo one-term approximations for q^* can be used to evaluate Eq. (41) as indicated, the results are of limited utility, since at the recommended limit for their applicability ($\mathrm{Fo} = 0.2$), the Q/Q_o values are already large (0.50, 0.78, and 0.92 for the plane wall, infinite cylinder, and sphere respectively). At least half of the maximum energy transfer has already occurred by the time corresponding to $\mathrm{Fo} = 0.2$; results for Q/Q_o for $\mathrm{Fo} < 0.2$ are likely to be of greater interest.

Discussion and Usage of Approximate Solutions

The approximate solutions for q^* are all compiled in Tables 1 and 2 (for constant surface temperature and constant heat flux boundary conditions, respectively), along with the maximum errors associated with their use. As an example, Fig. 4 shows the exact solution (solid line) and three approximations for the interior sphere with constant surface temperature boundary condition. The three approximations are the semi-infinite solution (long dashed line), the small Fo approximation (short dashed line, which coincides with the exact solution for small Fo), and the large Fo approximation (dash-dot line, which coincides with the exact solution for large Fo). First, consider the semi-infinite solid solution and the large Fo approximation. The semi-infinite solution is seen to be valid only for very small Fo; it visibly deviates from the exact solution for Fo near 0.001, where the error is already 6.0%. The large Fo approximation is indistinguishable from the exact solution for $\mathrm{Fo} \gtrsim 0.1$, but as Fo decreases, the large Fo approximation rapidly deviates from the exact solution. At $\mathrm{Fo} = 0.1$, the error in the large Fo approximation is 4.9%. Thus, in the broad range of $0.001 < \mathrm{Fo} < 0.1$, neither of these approximations is very accurate. If we attempted to use these approximations with a transition at around $\mathrm{Fo} = 0.03$, the maximum error would be

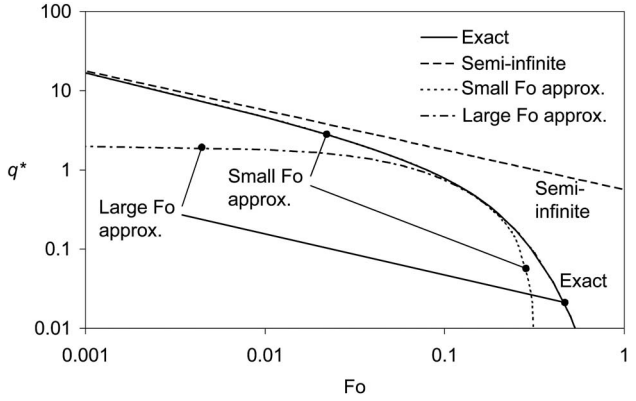

Fig. 4 Exact and approximate solutions for interior sphere with constant surface temperature boundary condition

a clearly unacceptable 40%. Instead, the full series solution should be calculated until converged. We next focus on the small Fo approximation. This hugs the exact solution from small Fo up to around Fo=0.2, where it begins to visibly deviate. Thus, it fills in the entire range where neither the semi-infinite nor the large Fo approximations are accurate. Using the small Fo approximation and the large Fo approximation, with a transition at Fo=0.2, the largest error is 6.3% and occurs at Fo=0.2. (This is the largest error of all the cases, see Tables 1 and 2.) A smaller maximum error could be obtained by choosing a different transition point between the small and large Fo solutions. For this particular case, a transition at around Fo=0.15 is optimal, and yields a maximum error of 1.1%. Unfortunately, the optimal transition point is different for each case; in the interest of simplicity, the common transition point of Fo=0.2 has been chosen.

The approximate solutions for q^* in Table 1 have been used to calculate Q/Q_o. For Fo$<$0.2, Eq. (2) has been used directly, whereas for Fo$>$0.2, the form given in Eq. (41) has been utilized. The resulting formulas and the associated maximum errors relative to the exact solutions are provided in Table 3. The results for Q/Q_o are more accurate than for q^* itself (since errors in q^* are significant only in a small Fo range). Maximum errors are seen to be less than approximately 0.2%.

The following example illustrates the value of the small Fo approximation for q^*. Consider the microwave heating of a nominally dielectric material. The material's radius and length are 2.5 and 15 cm, respectively, and the thermal conductivity and diffusivity are 1.0 W/m K and 1×10^{-6} m^2/s, respectively. In order to heat the material, it is wrapped in a thin susceptor that absorbs microwave radiation and results in 400 W of power being deposited at the outer surface of the object. If the object is initially at 2°C and heat losses to the environment can be neglected, how long will it take for the material's outer surface to reach 140°C?

Treating the object as an infinite cylinder, this problem is one in which the value of q^* is known, $q^*=(q/A_s)r_o/k(T_s-T_i)=q/[2\pi Lk(T_s-T_i)]=3.08$, and the value of Fo must be determined. Using the small Fo approximate solution, $q^*=1/2\sqrt{\pi/\mathrm{Fo}}-\pi/8$, we can directly solve for Fo, yielding Fo=0.0653 and t=40.8 s. Utilizing the exact solution, we would need to solve iteratively for Fo, using $q^*=[2\mathrm{Fo}+1/4-2\Sigma_{n=1}^{\infty}\exp(-\zeta_n^2\mathrm{Fo})/\zeta_n^2]^{-1}$, with the need to determine the eigenvalues, which are the solutions of $J_1(\zeta_n)=0$. Starting from guessed values of Fo=0.2 and Fo=0.01, which yield q^* values of 1.56 and 8.42 (bounding the desired result), and using bisection, 12 different q^* evaluations are needed. Fortunately, each requires only between one and four terms in the infinite series for acceptable accuracy. Nonetheless, this solution approach is a significant burden. The exact solution yields Fo=0.0645, t=40.3 s. Thus, the error in the approximate solution is around 1%.

The next example illustrates the utility of the Q/Q_o approximation. Spherical air bubbles of radius 1 mm rise through water at 25°C. The mass diffusivity of water vapor in air is $D_{AB}=0.26\times10^{-4}$ m^2/s. How long should the bubbles remain in the water to achieve an average water vapor concentration inside the bubble that is 50% of the maximum value? Using the heat and mass transfer analogy, with a constant species concentration at the bubble boundary, and assuming negligible advection within the bubble, the ratio of average concentration to maximum possible concentration is analogous to Q/Q_o as follows:

$$\frac{C}{C_o}=0.5=\begin{cases}6\sqrt{\dfrac{\mathrm{Fo}_m}{\pi}}-3\mathrm{Fo}_m, & \mathrm{Fo}_m<0.2\\ 1-\dfrac{6}{\zeta_1^2}\exp(-\zeta_1^2\mathrm{Fo}_m), & \mathrm{Fo}_m>0.2\end{cases}$$

where $\mathrm{Fo}_m=D_{AB}t/r_o^2$, and $\zeta_1=\pi$. Utilizing the expression for $\mathrm{Fo}_m<0.2$ yields $\mathrm{Fo}_m=0.0305$ (and a second root, 0.909, which does not lie within the range of validity). Thus, t=1.17 ms. (If we had begun with the assumption $\mathrm{Fo}_m>0.2$, we would have found $\mathrm{Fo}_m=0.0198$, revealing that the initial assumption was incorrect.) To solve the problem exactly using the infinite series solution would require tedious iteration to solve for the value of Fo_m, with each evaluation of the infinite series for Q/Q_o requiring a few terms for acceptable accuracy in this range.

Conclusion

This paper has considered a range of simple "interior" and "exterior" geometries, with constant surface temperature and constant surface heat flux boundary conditions. In each case, the exact solution for dimensionless heat transfer rate was provided. A small Fo approximate solution, accurate for Fo$<$0.2, was then derived for each case. This approximation bridges the gap between the large Fo (single-term) approximation, which is accurate for Fo $>$0.2, and the semi-infinite solid solution, valid at very small Fo. With the use of these approximations, it is now a trivial matter to calculate the dimensionless heat transfer rate for $0<\mathrm{Fo}<\infty$, for all of these cases, using simple expressions that can be evaluated with a handheld calculator. In addition, for the interior cases with constant surface temperature, expressions have been provided for the dimensionless energy input, Q/Q_o, which can be very accurately approximated over the entire Fo range.

Nomenclature

A_s = surface area, m^2
c = specific heat, J/kg K
C = average species concentration
C_o = average species concentration at steady state
D_{AB} = mass diffusivity, m^2/s
Fo = Fourier number for heat transfer, $\alpha t/L_c^2$
Fo_m = Fourier number for mass transfer, $D_{AB}t/L_c^2$
k = thermal conductivity, W/m K
L = plane wall half-width, m
L_c = characteristic length, m
q^* = dimensionless heat rate
q_s'' = surface heat flux, W/m^2
r = cylindrical or spherical radial coordinate, m
r_o = cylinder or sphere radius, m
r^* = dimensionless spatial coordinate, r/L_c
n = $n=0,1,2$ for Cartesian, cylindrical, spherical coordinates (also summation index)
p = $p=1,2,3$ for Cartesian, cylindrical, spherical coordinates

Q = total energy input into an interior object up to time t
Q_o = total energy input into an interior object at steady state
t = time, s
T = temperature, K
T_i = initial temperature, K
T_s = surface temperature, K
V = volume, m^3
α = thermal diffusivity, m^2/s
ΔT_c = characteristic temperature difference $(T_s - T_i)$ for constant T_s boundary condition $q_s'' L_c/k$ for constant q_s'' boundary condition
ζ_n = nth eigenvalue, defined in Tables 1 and 2
θ = dimensionless temperature, $(T - T_i)/\Delta T_c$
ρ = density, kg/m^3

References

[1] Incropera, F. P., DeWitt, D. P., Bergman, T. L., and Lavine, A. S., 2007, *Fundamentals of Heat and Mass Transfer*, Wiley, Hoboken, NJ, Chap. 5.

[2] Kreith, F., and Bohn, M. S., *Principles of Heat Transfer*, West, St. Paul, MN, Chap. 2.

[3] Mills, A. F., 1995, *Heat and Mass Transfer*, Irwin, Chicago, Chap. 3.

[4] Poulikakos, D., 1994, *Conduction Heat Transfer*, Prentice Hall, Englewood Cliffs, NJ, Chap. 5.

[5] Carslaw, H. S., and Jaeger, J. C., 1959, *Conduction of Heat in Solids*, Clarendon, Oxford.

[6] Beck, J. V., Cole, K. D., Haji-Sheikh, A., and Litkouhi, B., 1992, *Heat Conduction Using Green's Functions*, Hemisphere, Washington, DC.

[7] Yovanovich, M. M., Teertstra, P., and Culham, J. R., 1995, "Modeling Transient Conduction From Isothermal Convex Bodies of Arbitrary Shape," J. Thermophys. Heat Transfer, **9**(3), pp. 385–390.

[8] Beck, J. V., Haji-Sheikh, A., Amos, D. E., and Yen, D., 2004, "Verification Solution for Partial Heating of Rectangular Solids," Int. J. Heat Mass Transfer, **47**, pp. 4243–4255.

[9] Beck, J. V., McMasters, R., Dowding, K. J., and Amos, D. E., 2006, "Intrinsic Verification Methods in Linear Heat Conduction," Int. J. Heat Mass Transfer, **49**, pp. 2984–2994.

[10] McMasters, R. L., Dowding, K. J., Beck, J. V., and Yen, D. H. Y., 2002, "Methodology to Generate Accurate Solutions for Verification in Transient Three-Dimensional Heat Conduction," Numer. Heat Transfer, Part B, **41**, pp. 521–541.

[11] Beck, J. V., Keltner, N. R., and Schisler, I. P., 1985, "Influence Functions for the Unsteady Surface Element Method," AIAA J., **23**(12), pp. 1978–1982.

[12] Cooper, L. Y., 1976, "Heating of a Cylindrical Cavity," Int. J. Heat Mass Transfer, **19**, pp. 575–577.

[13] Abramowitz, M., and Stegun, I. A., eds., 1970, *Handbook of Mathematical Functions*, Dover, New York, pp. 16 and 371.

Droplet and Bubble Dynamics in Saturated FC-72 Spray Cooling on a Smooth Surface

Ruey-Hung Chen[1]
Professor
e-mail: chenrh@mail.ucf.edu

David S. Tan

Kuo-Chi Lin

Louis C. Chow

Alison R. Griffin

Daniel P. Rini

Department of Mechanical, Materials and Aerospace Engineering,
University of Central Florida,
Orlando, FL 32816-2450

Droplet and bubble dynamics and nucleate heat transfer in saturated FC-72 spray cooling were studied using a simulation model. The spray cooling system simulated consists of three droplet fluxes impinging on a smooth heater, where secondary nuclei outnumber the surface nuclei. Using the experimentally observed bubble growth rate on a smooth diamond heater, submodels were assumed based on physical reasoning for the number of secondary nuclei entrained by the impinging droplets, bubble puncturing by the impinging droplets, bubble merging, and the spatial distribution of secondary nuclei. The predicted nucleate heat transfer was in agreement with experimental findings. Dynamic aspects of the droplets and bubbles, which had been difficult to observe experimentally, and their ability in enhancing nucleate heat transfer were then discussed based on the results of the simulation. These aspects include bubble merging, bubble puncturing by impinging droplets, secondary nucleation, bubble size distribution, and bubble diameter at puncture. Simply increasing the number of secondary nuclei is not as effective in enhancing nucleate heat transfer as when it is also combined with increased bubble puncturing frequency by the impinging droplets. For heat transfer enhancement, it is desirable to have as many small bubbles and as high a bubble density as possible.
[DOI: 10.1115/1.2953237]

Keywords: spray cooling, cooling, spray, bubbles, droplets

1 Introduction

This article presents results from computer simulations of nucleate heat transfer in FC-72 spray cooling. Due to the multitude of complex and interacting multiphase events in spray cooling [1,2], the simulation is phenomenological without invoking conservation equations. However, an energy balance is achieved by matching the simulated nucleate heat flux with the experimental value. This is intended to illuminate dynamic aspects of bubble and droplet behaviors and their effects during spray cooling. Experimental studies of spray cooling were previously conducted [2–7]; the results include the heat transfer curve, bubble growth rate, bubble density, and estimation of relative importance of phase-change versus single-phase heat transfer. However, some questions are more difficult to answer using an experimental approach, for example, how many bubbles are punctured by the impinging droplets, is there a preferred bubble size at puncturing, and what is the bubble merging mechanism in spray cooling. On the other hand, the experimental spray cooling results obtained in the nucleate boiling regime along with those of pool boiling [8–14] can be used for the various submodels in this simulation study, helping to answer these questions.

Figure 1 schematically depicts the events during spray cooling using either a pressure- or air-assisted atomizer. The droplets arrive at the heater surface and form a thin liquid film on the heater. Due to continuity, the liquid drains off the edges of the heater, resulting in convective flow over the heater surface. Direct evaporation from the free surface of the liquid film also contributes to the overall heat transfer. Within the liquid film, two types of nuclei exist. The first type is the surface nuclei, similar to those found in pool boiling when sufficient surface superheat exists. The other type of nuclei is the so-called secondary nuclei [15–18]. In spray cooling, they are generated as the droplets entrain air or vapor into the thin liquid film [1]. It was shown that for a smooth diamond heater, these secondary nuclei tend to reside in the liquid layer without attaching to the heater surface and therefore move with the convective fluid current within the film [2]. Furthermore, the smoothness does not favor surface nucleation. Such an observation differs from that for most practical heater surfaces, where nuclei tend to be anchored on the surface and the roughness provides ample sites for surface nucleation. Both surface and secondary nuclei may merge with neighboring bubbles during their lifetime. Although bubble merging has been visualized in pool boiling with relative ease [14], it has not been documented in spray cooling, primarily due to the turbulent nature of the liquid layer caused by droplet impingement [2,14] that prevents clear visualization of merging events. The lifetime (τ_b) of a bubble ends upon departure from the heater surface (as in pool boiling), growing to reach the free surface of the liquid layer where it is ruptured or being punctured by the impinging droplets [1]. This is true whether the bubble is a surface or secondary nucleus or results from merging. It is known that the lifetimes of spray cooling bubbles are ended most likely by the puncturing action of the impinging droplets [2].

The heat transfer in spray cooling over a smooth heater consists of three mechanisms [1]: (1) nucleate boiling, (2) convective heat transfer due to the liquid motion within the liquid layer, and (3) direct evaporation from the surface of the liquid layer. There exists evidence that the liquid-vapor-surface contact line length correlates with the heat transfer [19]. Over a smooth heater, this correlation may not completely explain the amount of nucleate heat transfer, as secondary nuclei generate no contact lines. More than half of the heat transfer could be due to the participation of both surface and secondary nuclei in nucleate boiling [2]. This contribution from nucleate boiling was found to increase with an increase in the spray droplet number flux (N) and with the associated increase in secondary nuclei [2]. An increase in droplet flux (N) is also expected to enhance the single-phase convection heat

[1]Corresponding author.

Manuscript received June 29, 2007; final manuscript received April 1, 2008; published online August 7, 2008. Review conducted by Satish G. Kandlikar. Paper presented at the 2005 ASME International Mechanical Engineering Congress (IMECE2005), Orlando, FL, November 5–11, 2005.

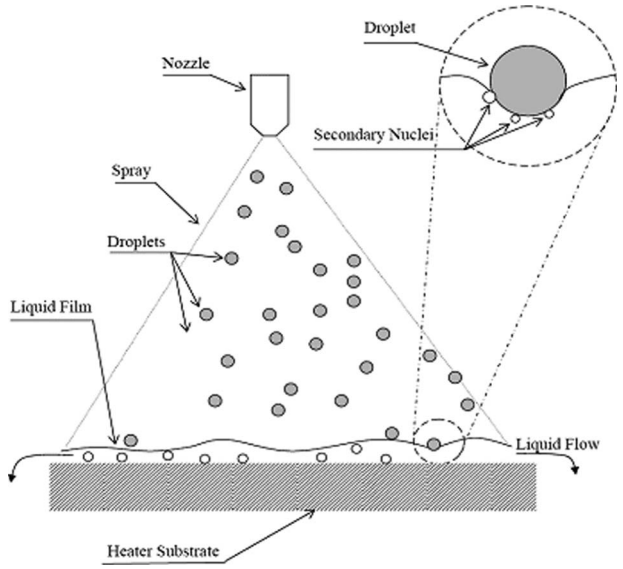

Fig. 1 Schematic of spray cooling system

transfer due to the turbulent convective flow within the liquid layer caused by the impinging action. As a consequence, the heat flux is greater than that in pool boiling for similar surface temperatures [2,14].

In a recent spray cooling study using saturated FC-72 liquid [2], the following results were reported. The average departure diameter in pool boiling is approximately 800 μm [14]. However, the average bubble size at puncture (d_p) in spray cooling rarely exceeds 500 μm with an average of approximately 180–280 μm, depending on the droplet flux (N) [2]. Therefore, the average bubble size when punctured (d_p) during spray cooling is appreciably smaller than the departure diameter under pool boiling conditions. This is believed to occur because the impinging droplets are the primary factor that determines bubble lifetime (τ_b) [2].

The above observations were made with the aid of a high-speed charge-coupled device (CCD) camera and a 70% transparent heater, with the surface temperature ranging from 62 to 67 K, well below the Leidenfrost value [2]. Three values of N, $2.0\times10^6/\mathrm{cm}^2\,\mathrm{s}$, $4.4\times10^6/\mathrm{cm}^2\,\mathrm{s}$, and $8.2\times10^6/\mathrm{cm}^2\,\mathrm{s}$, were examined in the experiment. Bubble parameters included average bubble size (d_b), bubble density (n_b), bubble lifetime (τ_b), waiting time (τ_w), and growth rate (diameter versus time); the heat flux due to nucleation (q''_N) could also be calculated [2]. A microscopic lens system was used to observe a $1\times1\ \mathrm{mm}^2$ area from the underside of the heater ($1\times1\ \mathrm{cm}^2$). Several locations were observed and were found to yield essentially the same values of bubble parameters. A secondary nucleus was not attached to the heater surface and was therefore moving with the estimated bulk fluid velocity. It was found that the number of moving bubbles increased with an increase in N and could be as many as four times the bubbles observed during saturated pool boiling using the same experimental setup. As reported in Table 3 of Ref. [2], the number of bubbles (n_b) increases with increasing N in spite of an associated decrease in the superheat. Classical pool boiling theories predict that $n_b\propto(\Delta T)^\alpha$, where ΔT is the superheat and α falls between 4 and 6. These conflicting results lend support to the existence of secondary nuclei and to the simulation model used in this study, described in the following section.

Several questions remain regarding the dynamic aspects of spray cooling and how they affect q''_N, such as (1) how many bubbles are punctured by the impinging droplets and at what size are they mostly likely to be punctured, (2) what is the bubble size distribution, and (3) how would the answers to these two questions depend on the droplet flux N. A simulation model was proposed to answer these questions. The model and its submodels are described in the following section, followed by the simulation results and further discussion.

Simulation Model

The simulation model consists of submodels including bubble growth, surface and secondary nucleation, bubble merging, bubble-droplet interaction (bubble puncturing by impinging droplets), and distribution of secondary nuclei. They are based on results from previous experimental observations of spray cooling [2] or derived from relevant pool boiling results [8–14]. The model is then validated by the agreement of the simulated results and the experimental values of nucleate heat transfer.

Bubble Formation. The distribution of the surface nuclei is described by the following:

$$\mathbf{F}_{\mathrm{fix}}=\mathbf{X}_{\mathrm{fix}}(x_i,y_i)f_{\mathrm{fix}}(t) \tag{1}$$

It should be noted that $\mathbf{X}_{\mathrm{fix}}$ is an array representing the random locations of the surface nuclei. Because of the surface imperfections, there are preferred sites for the surface nuclei. Their locations are "fixed" on the surface and do not change with time. At any instant, its number density is designated as n_{fix}.

Impinging droplets and secondary nuclei are randomly generated at varying locations. The random functions for the secondary nuclei and the droplets, respectively, are

$$\mathbf{F}_{\mathrm{sec}}=\mathbf{X}_{\mathrm{sec}}(x_j,y_j)f_{\mathrm{sec}}(t) \tag{2}$$

$$\mathbf{F}_{d}=\mathbf{X}_{d}(x_k,y_k)f_{d}(t) \tag{3}$$

where $f_d(t)=\delta(t-m\Delta t)$, a delta function where $m=1,2,\ldots$ and Δt is the simulation time step. Due to the randomness, each location on the heater surface has an equal likelihood for a droplet to land on it. In other words, both $\mathbf{X}_d$ and $\mathbf{X}_{\mathrm{sec}}$ are themselves random functions. Because the number of droplets arriving at the heater surface during each time step is $NA\Delta t$, where A is the heater area, $\mathbf{X}_d$ is an array representing $NA\Delta t$ positions during the time step. Similarly, $f_{\mathrm{sec}}(t)=\delta(t-m\Delta t)$ and $\mathbf{X}_{\mathrm{sec}}$ is an array representing $C_{\mathrm{sec}}NA\Delta t$ positions of the secondary nuclei generated by the impinging droplets, where C_{sec} is the number of secondary nuclei generated per droplet.

Once generated (or "planted" for secondary nuclei), the boundary of the ith nucleus is represented by (x,y), such that

$$[(x-x_i)^2+(y-y_i)^2]^{1/2}=R(t) \tag{4}$$

where $R(t)=d(t)/2$ is the radius of the bubble, described by Eq. (5) in the following section. Equation (4) applies to both the surface and secondary nuclei once they come into existence.

Bubble Growth. The bubble growth rate is based on experimental observations [2]. The results of the average bubble diameter (d) versus time are shown in Fig. 2 by the solid line fitting the data, where the growth of the bubble is seen to follow a $\sqrt{t}$ curve, resembling that of the heat-transfer-controlled growth in an extensive pool [20]. The curve in Fig. 2 can be represented by

$$d(t)=0.0100618\sqrt{t} \tag{5}$$

where d is in meters and t is in seconds. In spray cooling, the average bubble growth rate is not sensitive to q'' or T_w over a small range of surface superheat [2], making Eq. (5) suitable for the present simulation as the values of N and q'' vary. This could be due to the fact that most nuclei are secondary and they do not attach to the surface.

The typical scatter of data shown in Fig. 2 is approximately 50 μm. The maximum diameter at the end of the bubble lifetime (τ_b) rarely exceeded 500 μm for the values of N in this study [2].

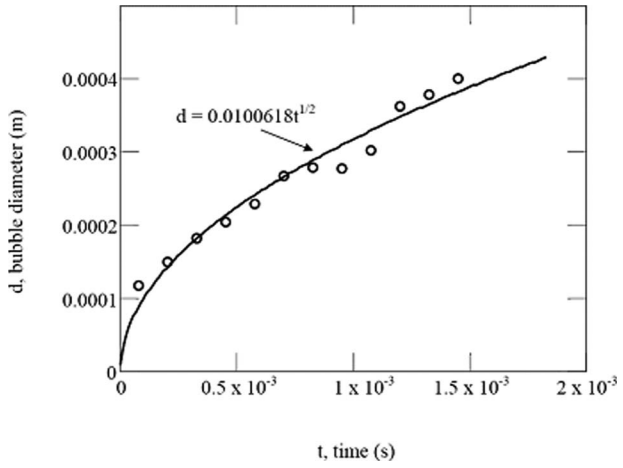

Fig. 2 Average bubble diameter versus time based on experimental observations. The curve fit is $d(t)=C\sqrt{t}$, with $C=0.0100618$ m and t in seconds. Note that the experimental growth rates are nearly equal and the curve was therefore used for all three values of N in the simulation. The typical scatter of the experimental data is approximately 50 μm.

Bubble Puncture. In the present model, a bubble was punctured if its perimeter and that of the impinging droplet overlapped on a two-dimensional plane (i.e., the heater surface). This criterion is expressed by

$$|\mathbf{X}_d(x,y) - \mathbf{X}_i(x,y)| \leq R(t) + 50\ \mu\text{m} \tag{6}$$

where 50 μm is the droplet radius used in this study. Punctured bubbles also consist of those resulting from merging (discussed in detail below). Once a bubble was punctured, its vapor volume was included in the calculation of q''_N. The vapor volume was collected over a period of 2 s for heat transfer calculations to ensure that sufficient data were recorded after the simulation reached steady state. The dynamic steady state condition is defined in a later section.

Surface and Secondary Nuclei. Unlike pool boiling, the number of nuclei in spray cooling does not depend on T_w. This again is because impinging droplets bring secondary nuclei that far outnumber surface nuclei [2]. Furthermore, within the turbulent liquid film, the thermal boundary layer may not favor surface nucleation [21] even if a measured T_w may dictate otherwise. The diminished role of surface nuclei as N is increased is described in the Results and Discussion section. Based on the results, n_{fix} was chosen to be zero for most of the cases studied except those noted otherwise.

The number of secondary nuclei generated by each impinging droplet (C_{sec}) was varied over a wide range to examine its effect on q''_N. The results are shown for $C_{\text{sec}}=1$, 2, 5, and 15 in Table 1, where the center of the secondary nuclei were located at a distance of one droplet radius from the center of the droplet impact ($R_d=1$; the effect of R_d is discussed below). It is noted that over this range of C_{sec}, the value of q''_N does not vary more than 25%. As shown in Table 1, n_b increases with C_{sec} by a factor of nearly 2 (Table 1). However, this increase is accompanied with a decrease in d_b, resulting in a relatively small net change in the vapor volume and q''_N produced.

The value of C_{sec} is difficult to determine experimentally, as tracing the identity of each droplet is difficult. It was known that water droplets having a diameter of 400 μm could entrain two to three bubbles and the number of bubbles entrained decreased with the droplet size [15]. The droplet diameter used for the simulation was 100 μm, similar to the experimental conditions [2]. It was decided that $C_{\text{sec}}=1$ was suitable for the simulation.

Table 1 Effect of number of secondary nuclei (C_{sec}) on nucleate heat transfer ($R_d=1$, $\Delta t=0.01$ ms, $n_{\text{fix}}=0$)

C_{sec}	q''_N (W/cm^2)	d_b (μm)	n_b (1/cm^2)
	$N=2.0\times10^6$/cm^2 s		
1	11.88	178	662
2	12.48	173	716
5	13.41	163	826
15	13.84	145	975
	$N=4.4\times10^6$/cm^2 s		
1	14.25	143	989
2	15.21	139	1095
5	16.75	128	1322
15	17.62	111	1652
	$N=8.2\times10^6$/cm^2 s		
1	16.20	121	1346
2	17.62	116	1531
5	20.20	106	1943
15	21.67	90	2557

Secondary nuclei, upon entering the liquid film, may be scattered around the impinging droplet. The distance from the center of the impinging droplet over which secondary nuclei can reach was expressed in terms of the droplet radius. The ratio (designated as R_d) of this distance to the droplet radius ranging from 1 to 5 was investigated, with the results shown in Table 2 for $C_{\text{sec}}=1$. It was found that the value of q''_N does not change more than 0.5%. The effect of R_d is not expected to be significant due to the random droplet impingement location.

Summarizing the above observations, the values of C_{sec} and R_d were chosen to be 1, except where noted. It is also noted that the initial size of secondary nuclei was assumed to be zero, because secondary nuclei are typically an order of magnitude smaller than the impinging droplets [15–18].

Merging. Bubble merging has been experimentally observed in FC-72 pool boiling [14]. In the present study, two neighboring i and j bubbles were assumed to merge when they came into contact. This criterion is expressed as the following:

$$|\mathbf{X}_i - \mathbf{X}_j| \leq R_i(t) + R_j(t) \tag{7}$$

No merging of bubbles in the direction normal (or vertical) to the heater was considered. In this case, the upper bubble is most likely generated by an impinging droplet, which would puncture

Table 2 Effect of spatial distribution of secondary nuclei (R_d) on nucleate heat transfer. ($C_{\text{sec}}=1$, $\Delta t=0.01$ ms, $n_{\text{fix}}=0$)

R_d	q''_N (W/cm^2)
	$N=2.0\times10^6$/cm^2 s
1	11.88
2	11.87
5	11.87
	$N=4.4\times10^6$/cm^2 s
1	14.24
2	14.20
5	14.20
	$N=8.2\times10^6$/cm^2 s
1	16.20
2	16.22
5	16.20

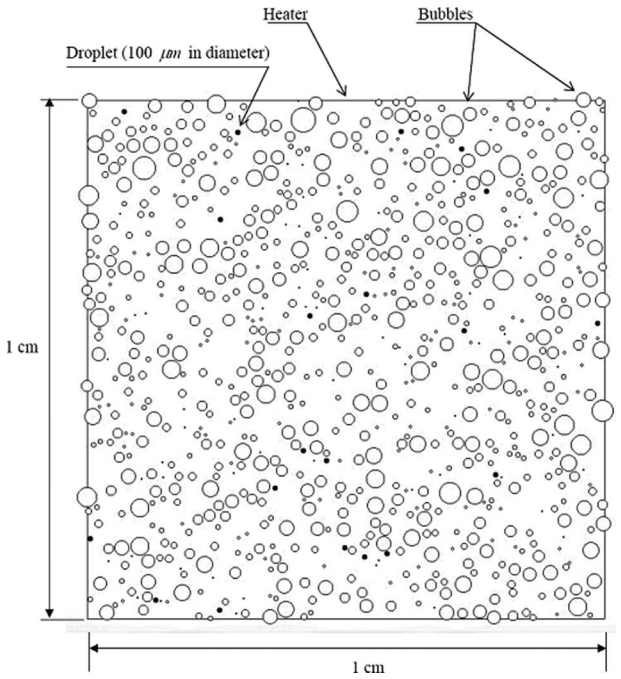

Fig. 3 A snapshot (with on exposure time equal to 0.01 ms) of bubbles and droplets arriving at the heater based on simulation result. Note that open circles represent bubbles having various diameters and solid dots represent droplets, which have a uniform size of 100 μm in diameter. $N=2.0\times10^6/\text{cm}^2\,\text{s}$; $C_{\text{sec}}=1$; $R_d=1$; $n_{\text{fix}}=0$.

the existing bubble, eliminating the possibility of vertical merging.

Once two bubbles had merged, their new size/diameter was calculated based on their combined volume. The new bubble would then move forward one or more simulation time steps corresponding to the d versus t curve shown in Fig. 2 and continue its growth from that point of time following the growth curve. The new bubble assumed a new location $\mathbf{X}=([x_i+x_j]/2,[y_i+y_j]/2)$.

Snapshots of Bubbles and Droplets. A typical "snapshot" of the bubbles and impinging droplets distributed on the heater (1×1 cm^2) is shown in Fig. 3 (for $N=2.0\times10^6/\text{cm}^2\,\text{s}$, $C_{\text{sec}}=1$ and $n_{\text{fix}}=0$) with the "exposure time" equal to 0.01 ms (i.e., the simulation time step). The open circles (of various sizes) and black dots (all with diameters equal to 100 μm) represent bubbles and impinging droplets on the heater surface, respectively. This choice of N and Δt resulted in 20 droplets arriving at the heater during each time step, as can be counted in Fig. 3. The effect of the step size on convergence and nucleate heat transfer is described below.

It should be noted in Fig. 3 that bubbles have discrete sizes due to the finite value of Δt. To reach the maximum d of 500 μm, approximately 250 simulation time steps are needed. This suggests that there might be up to 250 different bubble sizes in any snapshot such as the one shown in Fig. 3. Puncturing or merging activities eliminate some of the sizes.

Dynamic Steady State. Employing all of the submodels described earlier, it took some time after the calculation was initiated (at $t=0$) for the system to reach a steady state. As can be seen in Fig. 4(a), the surface bubble density (n_b) from the initiation of the simulation can be seen to reach a steady state after approximately $t=1.0$ ms. Similar results of n_{pd} (the number of bubbles punctured per cm^2 during a time step) can be seen in Fig. 4(b). It can be seen that n_{pd} may still vary with time even after $t=1.0$ ms. This is due to the random locations of the bubbles and the impinging droplets. However, the variation appears to reach a stationary state of a random process. For example, for $N=4.4\times10^6/\text{cm}^2$ s in Fig. 4(b), $15/\text{cm}^2<n_{pd}<40/\text{cm}^2$. For this value of N, at most 44 bubbles can be punctured during a time step, assuming every droplet lands on an existing bubble.

Once the dynamic steady state was reached, the numerical simulation was continued for a period of time (chosen to be 2 s for this study) so that time-averaged droplet and bubble parameters along with q''_N could be calculated.

Convergence. Convergence is said to exist if the value of q''_N converged as Δt was reduced. Results of a typical test are shown in Table 3, where the value of q''_N changes by less than 1% for $\Delta t<0.02$ ms for the three values of N. Unless otherwise specified, $\Delta t=0.01$ ms and m (as shown in Eq. (3)) =20,000 were chosen.

Outputs From Simulation. The simulation was performed using a desktop computer. The results consist of (1) the vapor of removed bubbles over 2 ms for the q''_N calculation, (2) probability densities of bubble size and bubble size at puncturing and the resulting average values of these two characteristic sizes, and (3) bubble density (n_b). These results are then used to analyze the dynamic process of puncturing, merging, droplet-bubble interaction, and the effect of secondary nucleation, as described earlier.

Results and Discussion

Effects of Surface Nuclei. Table 4 shows the results of varying the density of the surface nuclei (n_{fix}). It can be seen that by varying the value of n_{fix} from $0/\text{cm}^2$ to $500/\text{cm}^2$, the values of the bubble density, bubble diameter, bubble diameter when punctured, the number of bubble punctured per unit area per second (n_b, d_b, d_p, and n_p, respectively), and the heat flux due to nucleation (q''_N) fall within very narrow ranges (within less than 1%). These results over the three values of N ($2\times10^6/\text{cm}^2\,\text{s}$, $4.4\times10^6/\text{cm}^2\,\text{s}$, and $8.2\times10^6/\text{cm}^2\,\text{s}$) suggest that the effect of the surface nucleation is overwhelmed by secondary nuclei, justifying the choice of $n_{\text{fix}}=0$ for the model.

It is noted that n_p differs from n_{pd}, the latter being the number of punctured bubbles during one simulation time step. Depending on the size of the simulation time step, n_{pd} is several orders of magnitude smaller than n_p, as can be seen from Table 4 and Fig. 4(b).

Overall Performance of the Simulation. The overall performance of the simulation is examined by comparing the predicted value of q''_N as a function of n_b with that from the experimental results [2], as shown in Fig. 5. This is to ensure that the energy balance due to the phase-change heat transfer is satisfied. For the simulation results, the values of bubble parameters were obtained from snapshots like the typical one shown in Fig. 3. For comparison, the critical heat flux (CHF) for $N=2.1\times10^6/\text{cm}^2\,\text{s}$, $2.1\times10^6/\text{cm}^2\,\text{s}$, and $2.1\times10^6/\text{cm}^2\,\text{s}$ are, respectively, approximately 67 W/cm^2, 70 W/cm^2, and 80 W/cm^2 [2], with T_w within the range of 67–69 K.

It should first be noted that the simulation results shown in Fig. 5 were carried out for $C_{\text{sec}}=1$, 2, 5, 10, and 15, to examine the effect of n_b on q''_N. As shown in Fig. 5, the present simulation yielded good agreement with the experimental results (with an experimental scatter of q''_N approximately 8%). It is noted that the experimental and the simulation results overlap for n_b up to $\approx2500/\text{cm}^2$. As described earlier and in Fig. 3, the simulated bubble distribution is two dimensional and merge when touching each other. In experiment, bubbles may stack in the vertical direction (i.e., three dimensional) without merging. This may explain why the simulated value of q''_N can be smaller than the experimental one. It is noted that the simulation captures the experimental trend of q''_N versus n_b and helps to explain the contribution of nucleate heat transfer. The poorest agreement was found for $n_b\approx1400/\text{cm}^2$, with the difference between the experiment and the

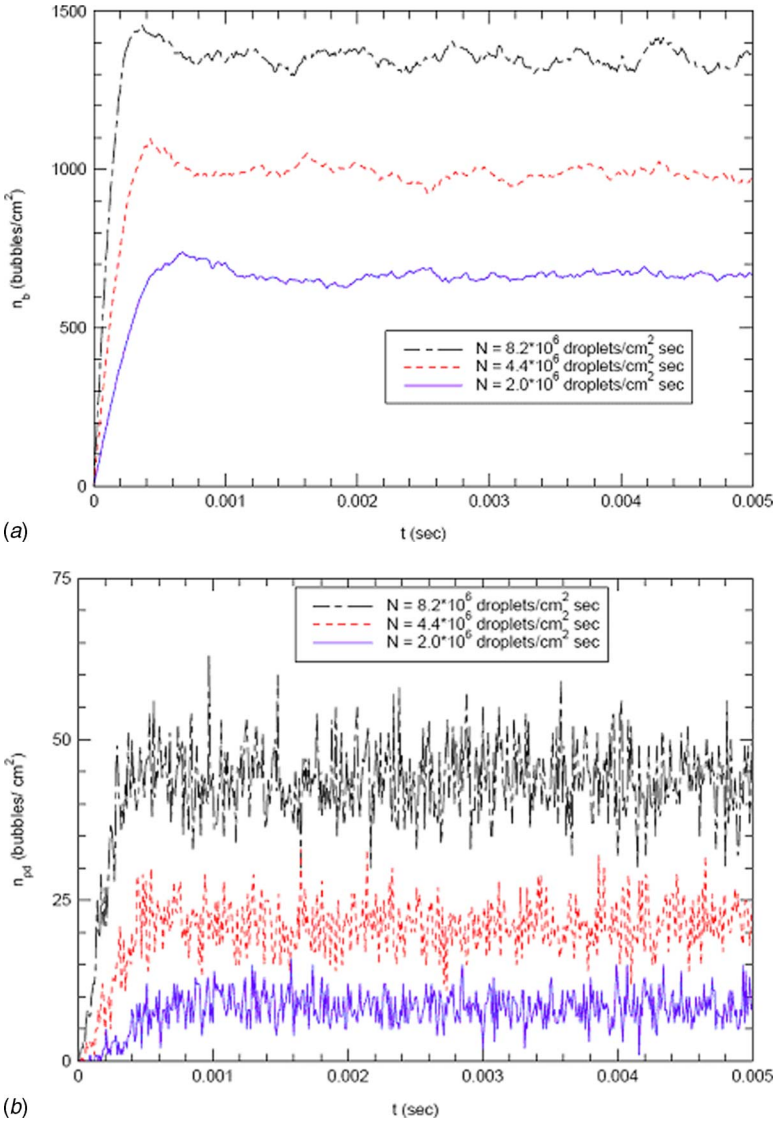

Fig. 4 (*a*) **For $N=2.0\times10^6/\text{cm}^2$ s to $4.4\times10^6/\text{cm}^2$ s and $8.2\times10^6/\text{cm}^2$ s, with $\Delta t=0.01$ ms, $C_{\text{sec}}=1$, $R_d=1$, and $n_{\text{fix}}=0$: surface bubble density (n_b) as a function of time.** (*b*) **For $N=2.0\times10^6/\text{cm}^2$ s to $4.4\times10^6/\text{cm}^2$ s and $8.2\times10^6/\text{cm}^2$ s, with $\Delta t=0.01$ ms, $C_{\text{sec}}=1$, $R_d=1$, and $n_{\text{fix}}=0$: the number of bubbles punctured per cm^2 per time step. Note that the simulation quickly reaches steady state after $t\geqslant0.01$ s (i.e., after 1000 time steps).**

simulation approximately 30–40% (see Fig. 5). Experimentally, n_b was varied for each given N by varying the overall surface heat flux, q'' (40 W/cm^2, 50 W/cm^2, and 60 W/cm^2); for a given N, as q'' was increased, both n_b and q''_N increased [2]. The simulation also captured the experimental trend that q''_N increases with N, which is really responsible for the increase in n_b. Other features based on the simulation of spray cooling are described in the following sections.

Bubble Size Characteristics. Figure 6 shows the fraction of bubbles having a diameter d (denoted by $P(d)$), determined using average values of many snapshots similar to that shown in Fig. 3. The "bin" size used in Figs. 6 and 7 was 25 μm. For example, all bubbles in the size range of 76–100 μm were counted as 100 μm. It can be noted that there exists a value of d (denoted by d^*) at which the value of $P(d)$ peaks for each given N. This can be explained as follows.

Figure 6 suggests that $d^*\approx125$ μm for the three values of N. It can be seen that for $d>d^*$, the value of $P(d)$ decreases with

Table 3 Results of convergence test for $N=2.0\times10^6/\text{cm}^2$ s, $4.4\times10^6/\text{cm}^2$ s, and $8.2\times10^6/\text{cm}^2$ s ($C_{\text{sec}}=1$, $R_d=1$, $n_{\text{fix}}=0$)

Time step (Δt, ms)	q''_N (W/cm^2)
$N=2.0\times10^6/\text{cm}^2$ s	
0.02	11.79
0.01	11.88
0.005	11.88
0.0025	11.85
0.001	11.85
0.0005	11.84
$N=4.4\times10^6/\text{cm}^2$ s	
0.02	14.18
0.01	14.25
0.0025	14.22
$N=8.2\times10^6/\text{cm}^2$ s	
0.02	16.12
0.01	16.19
0.005	16.20

Table 4 Bubble characteristics and nucleate heat transfer (C_{sec}=1, Δt=0.01 ms)

n_{fix} (1/cm^2)	n_b (1/cm^2)	d_b (μm)	n_p (1/cm^2 s)	d_p (μm)	q''_N (W/cm^2)
		Case 1	(N=2.0×10^6/cm^2 s)		
				268–282[a]	
0	662	177.5	863,400	237.6	11.81
100	669	177.6	868,900	237.9	11.95
300	682	177.4	855,200	238.1	12.17
500	683	177.0	883,900	238.0	12.13
		Case 2	(N=4.4×10^6/cm^2 s)		
				195–205[a]	
0	989	143.8	2,133,100	185.6	14.20
100	994	143.6	2,143,000	185.6	14.26
300	998	143.6	2,157,000	185.1	14.30
500	1013	143.7	2,163,600	185.5	14.41
		Case 3	(N=8.2×10^6/cm^2 s)		
				174–181[a]	
0	1346	121.4	4,374,700	152.3	16.21
100	1351	121.3	4,409,200	152.2	16.25
300	1358	121.3	4,418,200	152.4	16.34
500	1364	121.2	4,428,200	152.5	16.40

[a]Experimental values from Ref. [2].

increased d. This is because larger bubbles are more likely to be punctured due to both longer periods of time spent under bombardment and larger cross sections over which impinging droplets can land on. For $d<d^*$, $P(d)$ increases with increased d. This is attributable to the fact that smaller bubbles have smaller cross sections and are likely to survive droplet bombardment and grow for a period of time, until they reach larger sizes.

As N is increased, more bubbles are expected to be punctured at earlier stages of their growth with an increased frequency. Consequently, as N is increased, the value of $P(d)$ is increased in the range of $d<d^*$. As can be seen from Fig. 6, the values of $P(d)$ in the range of $d=125\pm25$ μm were approximately 0.11, 0.15, and 0.18% for $N=2.0\times10^6$/cm^2 s, 4.4×10^6/cm^2 s, and 8.2×10^6/cm^2 s, respectively. The opposite is true for $d>d^*$. The fraction of bubbles in the range of larger diameters $d=276-300$ μm were approximately 0.04, 0.02, and 0.01 for $N=2.0\times10^6$/cm^2 s, 4.4×10^6/cm^2 s, and 8.2×10^6/cm^2 s, respectively. The effect of increased bombardment frequency reduces the number of larger bubbles as N is increased, as discussed above.

Bubbles of all sizes may be punctured. The probability of them being punctured at diameter d_p, $P(d_p)$, is shown in Fig. 7. Let d_p^* denote the value of d_p for maximum $P(d_p)$. Unlike d^*, the values

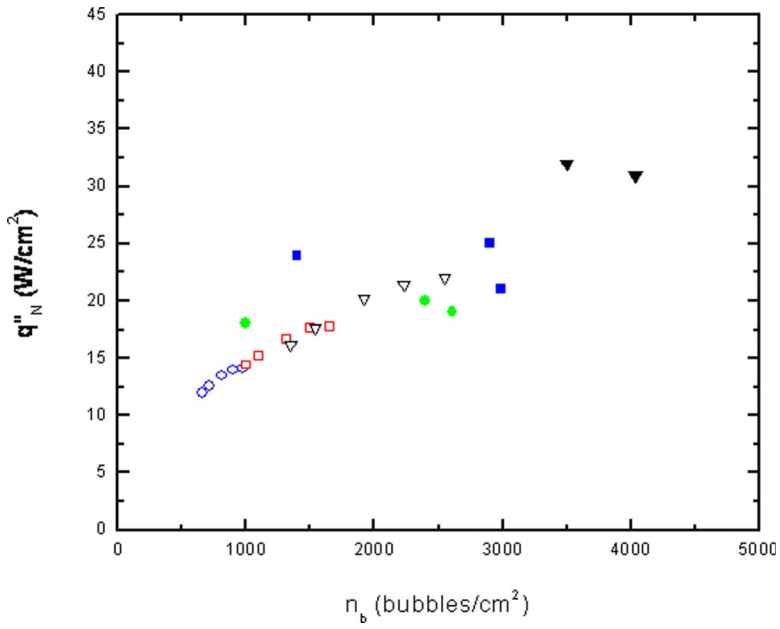

Fig. 5 Nucleate heat transfer (q''_N) versus bubble density (n_b); Δt=0.01 ms, C_{sec}=1, 2, 5, 10, and 15, n_{fix}=0, and R_d=1. Circles, squares and inverted triangles are for N=2.0×10^6/cm^2 s, 4.4×10^6/cm^2 s, and 8.2×10^6/cm^2 s, respectively. Solid symbols are experimental results and open symbols represent simulated results. The typical scatter of the experimental heat transfer data is approximately ±8%.

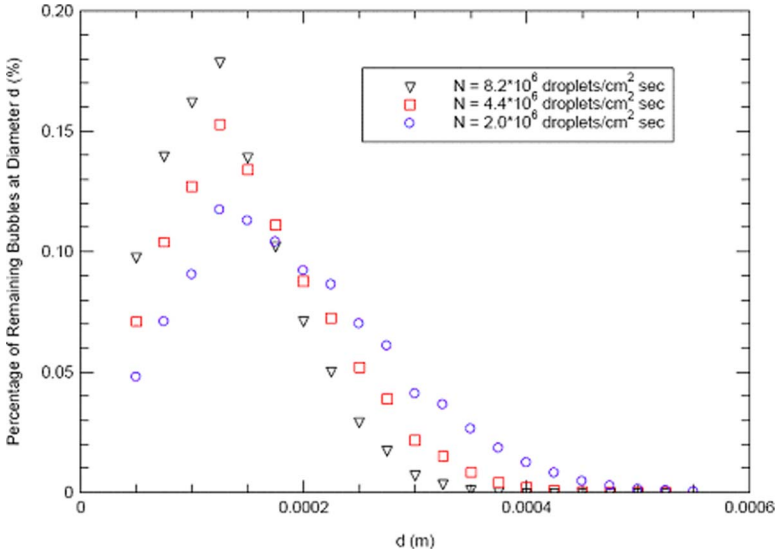

Fig. 6 Fraction of bubbles with diameter d, $P(d)$; $\Delta t=0.01$ ms, $C_{sec}=1$, $n_{fix}=0$, and $R_d=1$

of d_p^* are different for the three values of N ($d_p^* \approx 225$ μm, 175 μm, and 125 μm, respectively, for $N=2.0\times10^6/\text{cm}^2$ s, $4.4\times10^6/\text{cm}^2$ s, and $8.2\times10^6/\text{cm}^2$ s). It can be seen that the probability of puncturing bubbles with $d_p > d_p^*$ decreases with an increase in diameter. For $d_p < d_p^*$, $P(d_p)$ increases with an increase in diameter. These results appear to correlate with the general trend of $P(d)$ shown in Fig. 6. Therefore, there is a preferred size range, near d_p^*, where the bubbles are punctured, with d_p^* depending on the value of N. The dependence of d_p^* on N is explained in the following section on bubble puncturing.

It is noted that values of d_p^* and d_p (mean bubble size at puncturing, shown in Table 4) are different. It is seen that d_p values for $N=2.0\times10^6/\text{cm}^2$ s, $4.4\times10^6/\text{cm}^2$ s, and $8.2\times10^6/\text{cm}^2$ s are approximately 240 μm, 185 μm, and 152 μm, respectively. The quantitative agreement with corresponding experimental results (also listed in Table 4) is encouraging, with the qualitative trend well predicted by the simulation. However, these values of d_p are larger than their respective values of d_p^*, mainly because the $P(d_p)$ function has long tails in the region of large d_p (see Fig. 7). The decreasing trend of d_p with increasing N is expected, in a manner similar to the trend of d_p^* with N.

Dynamics of Bubble Puncturing. As discussed above, the peaks in Fig. 7 indicate preferred ranges of bubble size for puncture. The following offers a quantitative explanation. As shown in Table 4, the density of remaining bubbles (n_b) for $N=2.0\times10^6/\text{cm}^2$ s is approximately $670/\text{cm}^2$. Assuming these bubbles form approximately a 26×26 array on the square heater, the distances between the centers of two adjacent bubbles are approximately $l=380$ μm and 540 μm along the sides and the diagonal of the heater, respectively. Because the droplet size in this simulation is uniform at 100 μm, the smallest bubble that is to be hit by an impinging droplet has a diameter $d=(l-100)/2$, if the droplets land between bubbles. Therefore, this diameter lies between 140 μm and 220 μm for the bubble density of $670/\text{cm}^2$. This preferred range of bubble diameter agrees with the broad peak in

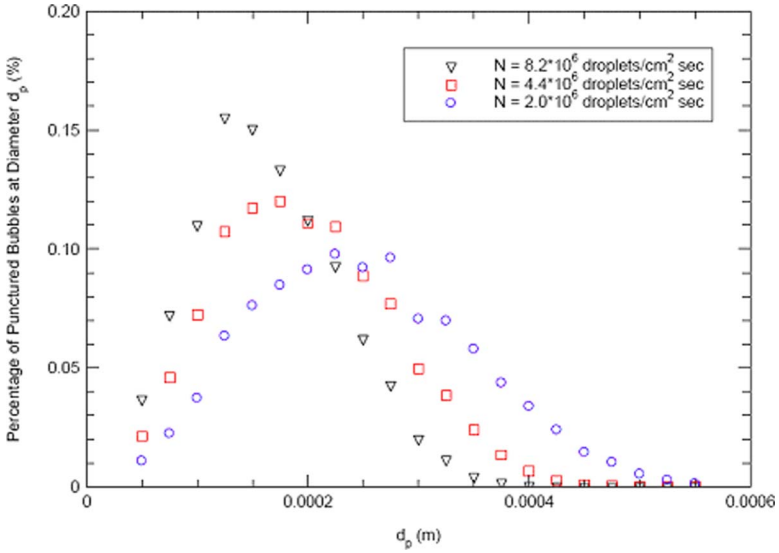

Fig. 7 Fraction of bubbles punctured at diameter d, $P(d_b)$; $\Delta t=0.01$ ms, $C_{sec}=1$, $n_{fix}=0$, and $R_d=1$

Fig. 7 ($d_p^* \approx 225$ μm).

Similar observations can be made for $N=4.4\times10^6/\text{cm}^2$ s and $8.2\times10^6/\text{cm}^2$ s. Consider $N=8.2\times10^6/\text{cm}^2$ s, for which $n_b=1346/\text{cm}^2$ (Table 4). If these bubbles form a 37×37 array on the square heater, one finds $l\approx270-385$ μm. Then the smallest diameter at which bubbles are more likely to be punctured would lie approximately between 85 μm and 140 μm, agreeing with $d_p^* \approx 125$ μm for $N=8.2\times10^6/\text{cm}^2$ s. Similarly, for $N=4.4\times10^6/\text{cm}^2$ s, the bubbles form a 32×32 array, with the smallest bubble to be hit lying within 105–171 μm, agreeing with $d_p^* \approx 175$ μm from simulation results. As discussed above, bubbles are punctured more frequently and at an earlier stage of their growth as N is increased. As a result of increasing N, smaller bubbles remain to be punctured, leading to a decrease in d_p^*.

Cross examination of the results from Table 4 further reveals the dominant role of secondary nuclei. Consider n_b, for example. The result of Table 4 indicates that while n_{fix} was increased from $0/\text{cm}^2$ to $500/\text{cm}^2$, n_b changed less than 1% and are approximately $670/\text{cm}^2$, $1000/\text{cm}^2$, and $1350/\text{cm}^2$, respectively, for $N=2.0\times10^6/\text{cm}^2$ s, $4.4\times10^6/\text{cm}^2$ s, and $8.2\times10^6/\text{cm}^2$ s. This suggests that nearly all surface nuclei were punctured and were replaced by secondary nuclei, whose number is insensitive to the surface temperature. Therefore, $n_{\text{fix}}=0$ is further justified in the simulation and the array may well represent up to 500 random locations while affecting the simulation results by less than 1%, as discussed earlier.

Dynamics of Bubble Merging. Consider the case of $N=2.0\times10^6/\text{cm}^2$ s, which yields $n_{\text{sec}}=2.0\times10^6/\text{cm}^2$ s for $C_{\text{sec}}=1$. A snapshot for this case (as in Fig. 3) would produce $n_b \approx 670/\text{cm}^2$ bubbles on the heater (see Table 4). For this case, the number of bubbles punctured per second (n_p) is approximately $864{,}000/\text{cm}^2$ s (shown in Table 4), less than $2.0\times10^6/\text{cm}^2$ s. This suggests that many bubbles merge before they are punctured and that slightly more than half (57%) of the droplets do not land on bubbles to cause them to rupture. For $N=4.4\times10^6/\text{cm}^2$ s and $8.2\times10^6/\text{cm}^2$ s, $n_p \approx 2.15\times10^6/\text{cm}^2$ s, and $4.40\times10^6/\text{cm}^2$ s, respectively (Table 4); approximately half of the impinging droplets do not cause puncturing.

It is interesting to note from Table 4 that as N is quadrupled from $2.0\times10^6/\text{cm}^2$ s to $8.2\times10^6/\text{cm}^2$ s, n_b only doubles from $664/\text{cm}^2$ to $1346/\text{cm}^2$. Increasing N by a factor of 4 (and thus increasing n_{sec} by the same factor) leads to a more crowded field of bubbles. This leads to more merging according to Eq. (7), and a higher probability of a droplet puncturing according to Eq. (6) and also a higher probability of a droplet impinging upon multiple bubbles. This may help to explain why quadrupling N only approximately doubles n_b.

Mean Bubble Size. With all the bubble activities of growing, merging, and puncturing, the snapshot such as that in Fig. 3 can be used to calculate the mean bubble size (d_b). Its values are shown in Table 4. As N was increased from $2.0\times10^6/\text{cm}^2$ s to $4.4\times10^6/\text{cm}^2$ s and to $8.2\times10^6/\text{cm}^2$ s, d_b was reduced from 177 μm to approximately 144 μm and to 121 μm, respectively. This is consistent with results shown in Fig. 6, where the bubble population skewed toward smaller diameters as N was increased.

Effect of Secondary Nucleation on Nucleate Heat Transfer. It can be seen from Table 1 that for a given value of C_{sec}, increasing N leads to an increase in n_b and a decrease in d_b, d_p, and d_p^*, as a result of more frequent puncturing of bubbles at earlier stages of growing. As this is associated with an increase in q_N'', it can be concluded that a large number of small bubbles and their early removal, which is achieved by a large value of N, are desirable for enhanced nucleate heat transfer.

Because $d \propto t^{1/2}$, as shown in Fig. 2, the volume scales as $t^{3/2}$, meaning that a single bubble removes more heat in the later stages of its growth. However, the number of bubbles that can be packed into the two-dimensional heater surface is proportional to $d^{-1/2} \propto (t^{-1/2})^2 \propto t^{-1}$. It is understood that as bubbles grow in size to touch each other, they merge and the number of them decreases with time. Therefore, the amount of heat transferred from the heater surface due to nucleation is proportional to $t^{3/2}t^{-1} \propto t^{1/2}$. The *rate* of the heat transfer from the heater surface is the derivative of $t^{1/2}$, which is $t^{-1/2} \propto 1/d$.

Conclusions

The simulation model properly captured the experimental trends of nucleate heat flux and was extended to predict the dynamics of bubble and droplet interactions. The predicted results include the following:

1. The values of n_b and d_b increase and decrease, respectively, with an increase in N. Nucleate heat transfer is enhanced with an increasing number of bubbles with decreasing bubble size, which can be achieved by increasing N.
2. The values of n_b are not sensitive to the number of surface nuclei. This is attributed to the large values of N in the simulation, which entrains large numbers of secondary nuclei. The contribution from surface nuclei to the nucleate heat transfer is overwhelmed by the secondary nuclei.
3. d_p and d_p^* decrease with an increase in N due to the increased puncturing frequency and bubble removal at an increasingly earlier stage during bubble growth. Bubble merging frequency increases with N, as more secondary nuclei are packed on the heater surface.

Acknowledgment

This research was supported by the National Science Foundation (NSF) Division of Chemical and Thermal Systems (Grant Nos. CTS-9813959 and CTS-9616344). A.R.G. was supported by a NSF Graduate Fellowship.

Nomenclature

A = heater area
C_{sec} = number of secondary nuclei generated per spray droplet (dimensionless)
d = bubble diameter (μm or m)
d^* = bubble diameter for peak $P(d)$ (μm or m)
d_b = mean bubble diameter (μm or m)
d_p = mean bubble diameter when punctured (μm or m)
d_p^* = mean bubble diameter when punctured for peak $P(d_p)$ (μm or m)
$\mathbf{F}$ = random function of locations (see Eqs. (1)–(3))
f = temporal function (see Eqs. (1)–(3))
i,j,k,m = integers
l = distance between the center of two adjacent bubbles (μm or m)
N = droplet flux ($=nv$) ($1/\text{cm}^2$ s)
n = droplet number density ($1/\text{cm}^3$)
n_b = bubble density ($1/\text{cm}^2$)
n_{fix} = bubble density due to surface nucleation ($1/\text{cm}^2$)
n_m = number of bubbles merged per unit area per unit time ($1/\text{cm}^2$ s)
n_p = number of bubbles punctured/terminated per unit area per unit time ($1/\text{cm}^2$ s)
n_{pd} = number of bubbles punctured/terminated per unit area during a time step ($1/\text{cm}^2$)
n_{sec} = generation rate or flux of secondary nuclei ($1/\text{cm}^2$ s)
q'' = heat flux (W/cm^2)

q''_N = nucleate heat flux (W/cm^2)
P = probability density function ($1/m$)
R = bubble radius (μm or m)
R_d = ratio of distance from the center of droplet impingement to the perimeter over which secondary nuclei are distributed to the droplet radius
T_w = surface temperature (°C or K)
t = time (μs or s)
$\mathbf{X}$ = location of bubble or droplet impingement (see Eqs. (1)–(4))
v = droplet velocity (cm/s or m/s)
Δt = simulation time step (μs or)
τ_b = bubble lifetime (μs or s)
τ_w = waiting time (μs or s)

Subscripts

d = droplet
fix = surface nuclei
sec = secondary nuclei

References

[1] Chow, L. C., Sehmbey, M. S., and Pais, M. R., 1997, "High Heat Flux Spray Cooling," Annu. Rev. Heat Transfer, **8**, pp. 291–318.
[2] Rini, D. P., Chen, R.-H., and Chow, L. C., 2002, "Bubble Behavior and Nucleate Boiling Heat Transfer in Saturated FC-72 Spray Cooling," ASME J. Heat Transfer, **124**, pp. 63–72.
[3] Estes, K. A., and Mudawar, I., 1995, "Comparison of Two-Phase Electronic Cooling Using Free Jets and Sprays," ASME J. Electron. Packag., **117**, pp. 323–332.
[4] Mudawar, I., and Estes, K. A., 1996, "Optimizing and Predicting CHF in Spray Cooling of a Square Surface," J. Heat Transfer, **118**, pp. 672–670.
[5] Bernardin, J. D., and Mudawar, I., 1997, "Film Boiling Heat Transfer of Droplet Streams and Sprays," Int. J. Heat Mass Transfer, **40**, pp. 2579–2593.
[6] Sehmbey, M. S., Chow, L. C., Hahn, O. J., and Pais, M. R., 1995, "Spray Cooling of Power Electronics at Cryogenic Temperatures," J. Thermophys. Heat Transfer, **9**(1), 123–128.
[7] Sehmbey, M. S., Chow, L. C., Hahn, O. J., and Pais, M. R., 1995, "Spray Cooling of Power Electronics at Cryogenic Temperatures," J. Thermophys. Heat Transfer, **9**(1), 123–128.
[8] Judd, R. L., and Hwang, K. S., 1976, "A Comprehensive Model for Nucleate Pool Boiling Heat Transfer Including Microlayer Evaporation," ASME J. Heat Transfer, **98**, pp. 623–629.
[9] Yu, C. L., and Mesler, R., 1977, "A Study of Nucleate Boiling Near the Heat Flux Through Measurement of Transient Surface Temperature," Int. J. Heat Mass Transfer, **20**, pp. 827–840.
[10] Cooper, M. G., and Lloyd, A. J. P., 1969, "The Microlayer in Nucleate Pool Boiling," Int. J. Heat Mass Transfer, **12**, pp. 895–913.
[11] Cooper, M. G., 1969, "The Microlayer and Bubble Growth in Nucleate Pool Boiling," Int. J. Heat Mass Transfer, **12**, pp. 915–933.
[12] Kirby, D. B., and Westwater, J. W., 1965, "Bubble and Vapor Behavior on a Heated Horizontal Plate During Pool Boiling Near Burnout," Chem. Eng. Prog., Symp. Ser., **61**, pp. 238–248.
[13] Nishio, S., Gotoh, T., and Nagai, N., 1998, "Observation of Boiling Structure in High-Flux Boiling," Int. J. Heat Mass Transfer, **41**, pp. 3191–3201.
[14] Rini, D. P., Chen, R.-H., and Chow, L. C., 2001, "Bubble Behavior and Heat Transfer Mechanism in FC-72 Pool Boiling," Exp. Heat Transfer, **14**, pp. 27–44.
[15] Sigler, J., and Mesler, R., 1990, "The Behavior of the Gas Film Formed Upon Drop Impact With a Liquid Surface," J. Colloid Interface Sci., **134**, pp. 459–474.
[16] Esmailizadeh, L., and Mesler, R., 1986, "Bubble Entrainment With Drops," J. Colloid Interface Sci., **110**, pp. 561–573.
[17] Mesler, R., 1982, "Research on Nucleate Boiling," Chem. Eng. Educ., **16**(4), pp. 152–156.
[18] Bergman, T., and Mesler, R., 1981, "Bubble Nucleation Studies, Part 1: Formation of Bubble Nuclei in Superheated Water by Bursting Bubbles," AIChE J., **27**(5), 851–856.
[19] Horacek, B., Kiger, K. T., and Kim, J., 2005, "Single Nozzle Spray Cooling Heat Transfer Mechanisms," Int. J. Heat Mass Transfer, **48**, pp. 1425–1438.
[20] I.Scriven, E., 1959, "On the Dynamics of Phase Growth," Chem. Eng. Sci., **90**, pp. 1–13.
[21] Hsu, Y. Y., 1962, "On the Size Range of Active Nucleation Cavities on a Heating Surface," ASME J. Heat Transfer, **84**, pp. 207–213.

Flow Boiling in Minichannels Under Normal, Hyper-, and Microgravity: Local Heat Transfer Analysis Using Inverse Methods

Sébastien Luciani
e-mail: sebastien.luciani@polytech.univ-mrs.fr

David Brutin

Christophe Le Niliot

Ouamar Rahli

Lounès Tadrist

Ecole Polytechnique Universitaire de Marseille,
Technopôle de Château-Gombert,
5, rue Enrico Fermi,
13453 Marseille, France

Boiling in microchannels is a very efficient mode of heat transfer since high heat and mass transfer coefficients are achieved. Here, the objective is to provide basic knowledge on the systems of biphasic cooling in mini- and microchannels during hyper- and microgravity. The experimental activities are performed in the frame of the MAP Boiling project founded by ESA. Analysis using inverse methods allows us to estimate local flow boiling heat transfers in the minichannels. To observe the influence of gravity level on the fluid flow and to take data measurements, an experimental setup is designed with two identical channels: one for the visualization and the other one for the data acquisition. These two devices enable us to study the influence of gravity on the temperature and pressure measurements. The two minichannels are modeled as a rectangular rod made up of three materials: a layer of polycarbonate ($\lambda = 0.2\ W\,m^{-1}\,K^{-1}$) used as an insulator, a cement rod ($\lambda = 0.83\ W\,m^{-1}\,K^{-1}$) instrumented with 21 K-type thermocouples, and in the middle a layer of Inconel® ($\lambda = 10.8\ W\,m^{-1}\,K^{-1}$) in which the minichannel is engraved. Pressure and temperature measurements are carried out simultaneously at various levels of the minichannel. Above the channel, we have a set of temperature and pressure gauges and inside the cement rods, five heating wires provide a power of 11 W. The K-type thermocouple sensors enable us to acquire the temperature in various locations (x, y, and z) of the device. With these temperatures and the knowledge of the boundary conditions, we are able to solve the problem using inverse methods and obtain local heat fluxes and local surface temperatures on several locations. The experiments are conducted with HFE-7100 as this fluid has a low boiling temperature at the cabin pressure on Board A300. We applied for each experiment a constant heat flux ($Qw = 33\ kW\,m^{-2}$) for the PF52 campaigns (Parabolic Flights). The mass flow rate varies in the range of $1 < Qm < 4\ g\,s^{-1}$ and the fluid saturation temperature (T_{sat}) is 54°C at $P_{sat} = 820$ mbars. [DOI: 10.1115/1.2953306]

Keywords: convective flow boiling, microchannel, microgravity, inverse methods, truncated S.V.D., local heat transfer coefficient

1 Introduction

On convective boiling in microchannels, studies are limited and under investigation Kandlikar [1]. Unsteady flows and flow boiling instabilities are related to the confined effects on bubble behavior in the microducts. Yan and Kenning [2] observed high surface temperature fluctuations in a minichannel with hydraulic diameter of 1.33 mm. Surface temperature fluctuations (1–2°C) are caused by gray level fluctuations of liquid crystals. The authors evidenced a coupling between flow and heat transfer by obtaining the same fluctuation frequencies between the surface temperature and two-phase flow pressure fluctuations. Kennedy et al. [3] studied convective boiling in circular minitubes of 1.17 mm diameter and focused on the nucleate boiling and unsteady flow thresholds using distilled water. They obtained these results experimentally analyzing the pressure drop curves of the inlet mass flow rate for several heat fluxes. Qu and Mudawar [4] found two kinds of unsteady flow boiling. In their parallel microchannel arrays, they observed either a spatial global fluctuation of all the two-phase zones for all the microchannels or anarchistic fluctuations of the two-phase zones: overpressure in one microchannel and underpressure in another. However, it is important to have a constant mass flow rate at each microchannel entrance. Flow visualization analysis has previously been realized by Brutin and Tadrist [5]. They developed a model based on a vapor slug expansion and defined a nondimensioned number to characterize the flow stability transition. Based on this criterion, they proposed pressure loss, heat transfer, and oscillation frequency scaling laws. These characteristic numbers allow us to analyze quite well the experimental results. It highlights the coupling phenomena between the liquid-vapor phase change and the inertia effects.

It is of interest to further understand these instabilities. Indeed, two-phase and boiling flow instabilities are complex, due to phase change and the presence of several interfaces. To fully understand the high heat transfer potential of boiling flows in microscale's geometry, it is vital to quantify the heat transfer occurring in the microchannel. To perform this, analysis is made up by using an inverse method, which allows us to estimate the local heat coefficient. In the past few years, it has appeared that the resolution of inverse heat conduction problems could be applied to many industrial applications when the direct measurement of the fluxes or the heat sources is impossible, for instance, because the direct mea-

Contributed by the Heat Transfer Division of ASME for publication in the JOURNAL OF HEAT TRANSFER. Manuscript received August 20, 2007; final manuscript received March 18, 2008; published online August 8, 2008. Review conducted by Satish G. Kandlikar. Paper presented at the Fifth International Conference on Nanochannels, Microchannels and Minichannels (ICNMM2007), Puebla, Mexico, June 18–20 2007.

surement would impair the accuracy of the searched variable or because the sensor would not survive on a boundary exposed to a severe environment.

In our configuration, the use of inverse methods is essential since it is impossible to place a thermocouple on the surface of the studied minichannels without disturbing the established flow. The direct problem in heat conduction consists in the resolution of the fundamental heat transfer equation in order to calculate the temperature variations in time and space. From the point of view of the experiments, in most cases the numerical solutions of the direct problem are compared to experimental values in a validation procedure. The resolution is inverse when one of the conditions necessary to solve the direct problem is missing. For instance, we can find some inverse problems devoted to the estimation of thermal parameters, unknown initial or boundary conditions (here the local heat transfer coefficient), and unknown heat source terms. The latter problems are called inverse heat conduction problems (IHCPs).

For IHCP resolution, the measurements are necessary to estimate the unknown parameters or functions. Such a procedure is based on an inverse formulation of the classical scheme "causes $\rightarrow$effects." The latter is an ill-posed problem in the sense of Hadamard [6]; actually, the obtained solution is highly sensitive to measurement errors and in some cases the obtained solution might be nonunique. This means that the experimental design and the associated measurement procedure are the main factors in the quality of the results. In this paper, we will present a multidimensional IHCP, which consists of the unknown boundary condition using data measurements. For the IHCP related to unknown boundary estimation, the main variable is the heat flux history applied on a surface unsuited to direct measurement. Of course in some simple geometries, it is possible to apply some analytical methods but most of the time a numerical method has to be applied to cope with transient multidimensional problems.

An alternative to finite element method (FEM) is the boundary element method (BEM), which permits a direct connection between the measurements and the unknown boundary condition. This method is described in detail by Brebbia et al. [7] and applied by some authors for IHCP resolution [8–11]. Compared to the FEM, BEM gives a direct solution of the IHCP replacing the usual iterative process with the resolution of a linear system. One consequence of using a Green function as the weighting function T^* is that the calculation code does not require any internal mesh but allows the computation of singularities as internal points and point heat sources. Because of these particularities, BEM is well adapted to cope with internal measurements provided by thermocouples and surface measurements obtained by infrared thermography. Here, the use of inverse methods will enable us to estimate the local heat transfer and more especially the local heat transfer coefficient. Actually, we do not find in literature some examples of 3D inverse problems using BEM [12,13] and also FEM [14,15] using the adjoint method. None of them use real experiments. However, the main difficulties for inverse problem are their ill-posed problem character. As a consequence, the solution might become unstable considering measurement errors. In order to obtain a stable solution, we use some regularization procedures; here, we used the truncated singular value decomposition (SVD) method.

For this purpose, an experimental rack has been designed to observe flow patterns depending on the mass flow rate. With regard to applications, the expected results will contribute to the development of microgravity models for heat transfer coefficients and pressure loss. The fluid flow is temporally stored in the compressible volume (damper). When the minichannel pressure loss is too high and when the pressure in the buffer is higher than the minichannel pressure loss, the fluid is reinjected. A constant mass flow rate condition is considered in front of the buffer. We applied for each experiments a constant heat flux ($Qw=33$ kW m^{-2}). The mass flow rate varies in the range of $1<Qm<4$ g s^{-1} and the fluid saturation temperature (T_{sat}) is 54 °C at $P_{sat}=820$ mbars.

The objective of this paper is to acquire better knowledge of the boundary conditions that influence the two-phase flow and the local heat transfer in the minichannel. The expected results will contribute to the development of microgravity models and create a database for convective boiling in minichannels and microgravity conditions, which is necessary to elaborate future two-phase systems on board space vehicles and stations. In this line, this paper aims to complete the actual studies by analyzing and explaining the phenomena of heat transfer suitable in minichannels during microgravity. The original feature of this experiment consists in providing new results for local heat transfer using an inverse method coupled with experimental data.

2 Conception

2.1 Description of the Experiment. For safety purposes, the main experiment is kept inside a confinement box, where we store the fluid needed to perform the experiments during the flight. The rack is divided into four areas: the confinement box, the material storage zone below it, the visualization zone with Computer 2, and the loop control zone with Computer 1. The entire fluid loop is inside the confinement box in order to avoid any fluid leakage inside the cabin during microgravity. The heating system is composed of a small cement rod of dimensions $16\times10\times70$ mm^3 with five heating wires (0.4 mm diameter). The cooling system is made using Peltier elements with heat sinks and the investigated fluid is HFE-7100. It is chosen for its many advantages: This fluid has a low boiling temperature (54 °C at 835 mbars) and a low latent heat of vaporization (20 times less than water), and is compatible with almost all materials. Channels (Fig. 1) with three hydraulic diameters are investigated: 0.49 mm (6×0.254 mm^2), 0.84 mm (6×0.454 mm^2), and 1.18 mm (6×0.654 mm^2). The width of the channel is kept constant to allow comparison of the influence with regard to the thickness.

The channels are engraved in a thin Inconel® plate ($2\times16\times70$ mm^3) to obtain a measurable temperature gradient under the heating surface needed in the use of the inverse methods. A transparent polycarbonate cover plate is used to close the geometry and to perform the flow visualization. Two preheaters are used to warm up the fluid to 2 °C below its saturation temperature. Pressure measurements are acquired at 133 Hz to allow observation of nonstationary flow. Fluid temperatures are also acquired at this frequency, and the gravity level is given by an accelerometer. Flow visualization is performed using a Photron® FastCam.

2.2 Dimension of the Minichannel. The dimensions are as follows: 50 mm long, 6 mm width, and 254 μm deep (Fig. 2). Above the channel, there is a series of temperature and pressure sensors and inside the cement rod, 21 thermocouples (of Chromel-Alumel type) are located at a height of 9 mm and are also distributed lengthwise (1 mm under the minichannel), as shown in Fig. 3. These K-type thermocouples (140 μm diameter) are used to measure the temperatures of the cement rod at several locations under the minichannel heating surface. To observe the influence of gravity on the flow and the behavior of the convective boiling, two instrumented test tubes are embarked during the parabolic flights: one for the visualization using a high speed camera and the other one for the data acquisition using thermocouples and pressure gauges. They make it possible to check the influence of gravity on the temperature and pressure measurements for three levels of gravity: terrestrial gravity ($1g$), hypergravity ($1.8g$), and microgravity (μg).

3 Sensitivity Analysis and Inverse Problem

3.1 Overdetermined Problem. The inverse problem described in this paper (21 temperature measurements to inverse) is an underdetermined problem [9]: it presents fewer equations than

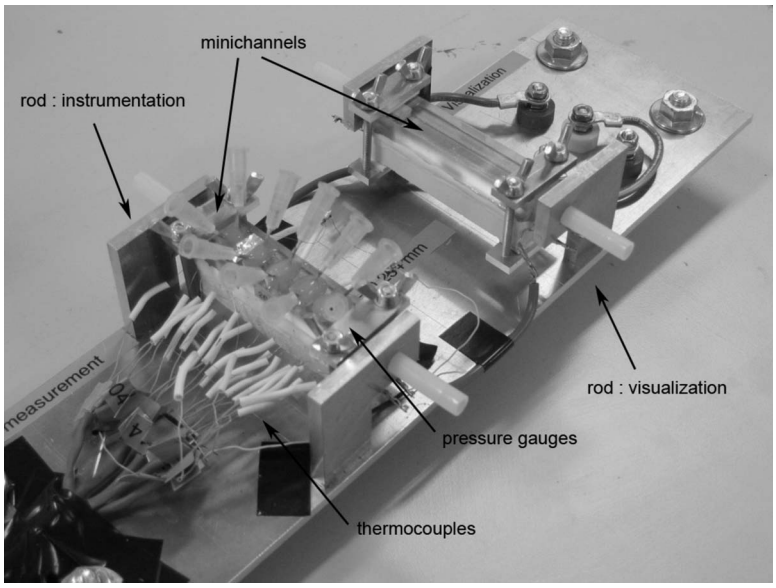

Fig. 1 Coupling of the two rods used during parabolic flights (the left minichannel is used for measurements and the right minichannel for visualization). The thermocouples are located along the minichannel and the pressure gauges on top of it.

unknowns. In other words, there is not enough information in the system, and this lack of temperature measurements is increased in this case. Indeed, let us suppose that some of the sensors are broken during the process: it is not possible to recover these measurements. The number of equations (one per sensor) is no longer 21 and must be brought down to a lower number. It is thus necessary to deal with this problem by increasing the number of measurements. We transform the inverse underdetermined problem in order to have an overdetermined inverse problem. We use the property that our geometrical model has a symmetry axis in the cross section (x,z): Each thermocouple measurement is thus duplicated by taking the symmetrical one from a preset mirror axis according to y. As a result, we obtain 42 (21×2) measurements, which are not all independent (see Fig. 4).

3.2 Noises and Locations. The main point is to identify the parameters that affect the solution of our inverse problem. To perform this task, we test the following:

1. the influence of the noise with regard to thermocouples' temperatures on the surface minichannel temperature

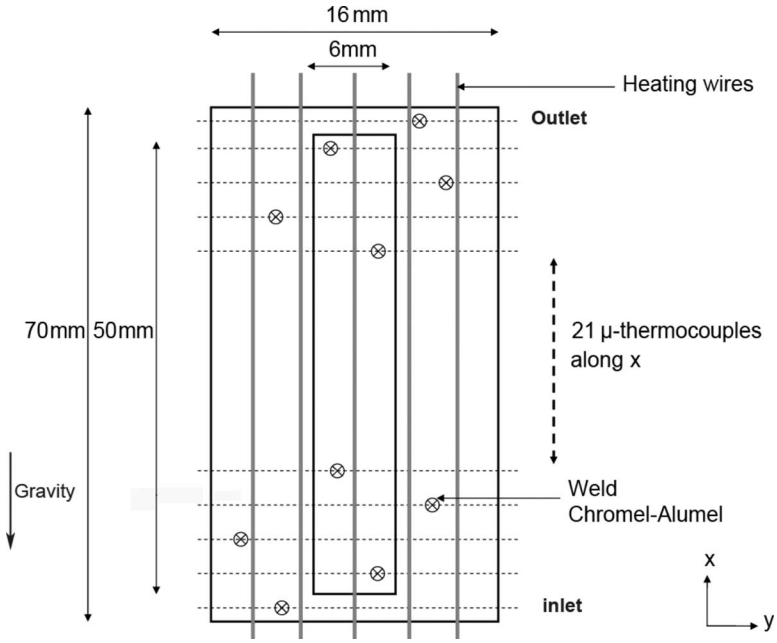

Fig. 2 Top view of the minichannel cross-sectional components. The minichannels are engraved in the Inconel plate. The gravity direction is opposite to *x*.

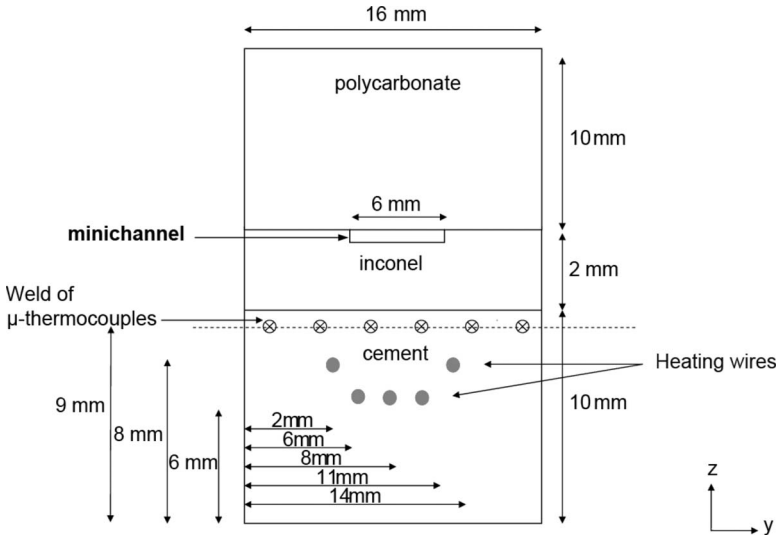

Fig. 3 Front view of the minichannel cross-sectional components. We can see the five heating wires and the several thermocouples weld represented in circles.

2. the influence of the estimation error on thermocouples' locations

For the first step, we inverse the thermocouples' temperature by adding some Gaussian noise to the measurements. We compare then it with two profiles: one obtained without noise and the other one obtained by solving a direct problem. First results show that the direct and the inverse profile obtained without noise are similar (Fig. 5), which means that our numerical model is well adapted. A second result highlights that the noise of our measurement has an influence on the resolution process. Indeed, there is a difference around 4 °C in some sections of the curves that change the estimated value of the local coefficient (Eq. (5)). Second, we test the influence of the location of the thermocouples. Actually, the locations of the sensors are given using pictures that were taken before we cast the cement rod. During this process, the coordinates of the thermocouples may have changed so that it can influence the solution. From our study, we assume that there is no influence of the location with the (x,y) location since the heat transfers are located on the z-axis. It is on this axis that we have to estimate the sensitivity to the location errors. In order to calculate the influence, we change the coordinates of the sensors by shifting the coordinates (± 0.5 mm and ± 0.75 mm). Then, we inverse the modified temperature profile and compare the result to the original one.

Figure 6 highlights the fact that the z-coordinate is a critical parameter since the different profiles present important variations from one to another. Compared to the original profile, we obtain some differences of 6 °C. This variation is very high and causes some instability in our numerical solution. As the sensitivity of the solution to measurements is high, theses errors will have to be well estimated.

3.3 Meshing. We studied the convergence meshing for several cases. We made a first meshing with N elements (N=184) then we double it ($2N$, $4N$, and $6N$) and compare with a direct simulation (boundary conditions known) the solution for each meshing. When we put side by side the heat flux and the wall temperature on the minichannel for each mesh, we observe that the profiles for $2N$ elements and N elements are the same. This

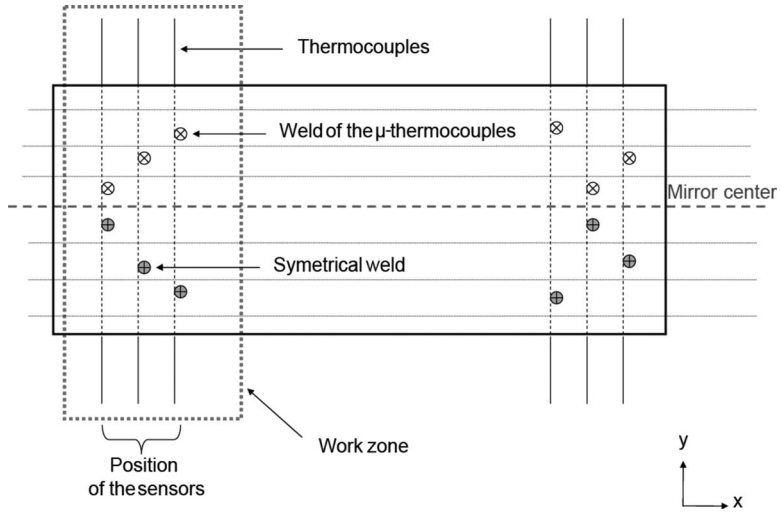

Fig. 4 Doubling of the sensors. We copy the symmetrical weld thermocouple trough the *x*-axis and pass from 21 thermocouples to 42.

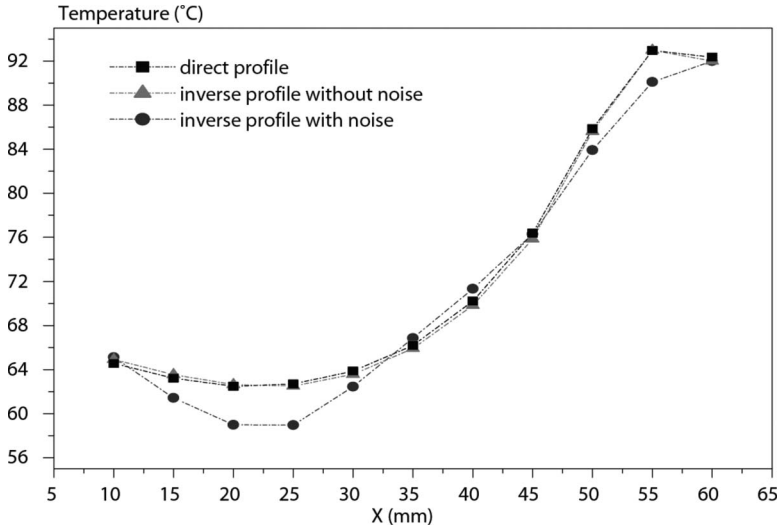

Fig. 5 Influence of the thermocouples' noise measurements on the predicted wall

result validates the fact that the N meshing is well adapted for the 2D model (in Fig. 7). Moreover, using the 2D analysis, we mesh only domains (cement-Inconel) and we found the same solution with the three domains meshed (cement-Inconel-Polycarbonate). These two results validate the assumptions concerning the boundary conditions of the system (the polycarbonate has no influence) as well as the step of the meshing (N is sufficient). We made the same convergence meshing study for the 3D model (Fig. 8).

3.4 Inverse Heat Conduction Problem With BEM. The inverse problem under investigation deals with the resolution of IHCP [16], where we want to estimate the unknown boundary conditions on the modeled minichannel. The numerical scheme used here is based on the BEM. BEM is attractive for our inverse problem resolution because it provides a direct connection between the unknown boundary heat flux and the measurements (thermocouples). The other advantage of the BEM is to take into account singularities such as point line heat sources or internal points (thermocouple) without domain mesh. In the case of linear heat conduction, the solution can be obtained by solving a linear system of simultaneous equations without any iterative process.

3.5 Boundary Condition Estimation. As N' is the number of domain Ω interior points given here by the thermocouples and N the number of boundary elements on our rod, the system has got $(N+N')$ equations. The number of unknowns, noted M, is a function of the boundary conditions applied on the different elements of Γ (Fig. 9). Namely, for element Γi, we have at least one unknown per element for the following boundary conditions:

1. first kind condition for which heat flux φ_i is unknown and temperature θ_i is imposed
2. second kind condition for which temperature θ_i is unknown and heat flux φ_i is imposed
3. third kind condition $\varphi_i = f(\theta_i)$

The elements, for which we have one equation, where the boundary condition is missing, let appear two unknowns. The only way to solve the fundamental heat transfer equation is to find some extra information, provided by measurements. In our case, we have interior measurements, given by thermocouples. They enable us to solve the problem and to calculate local heat flux and

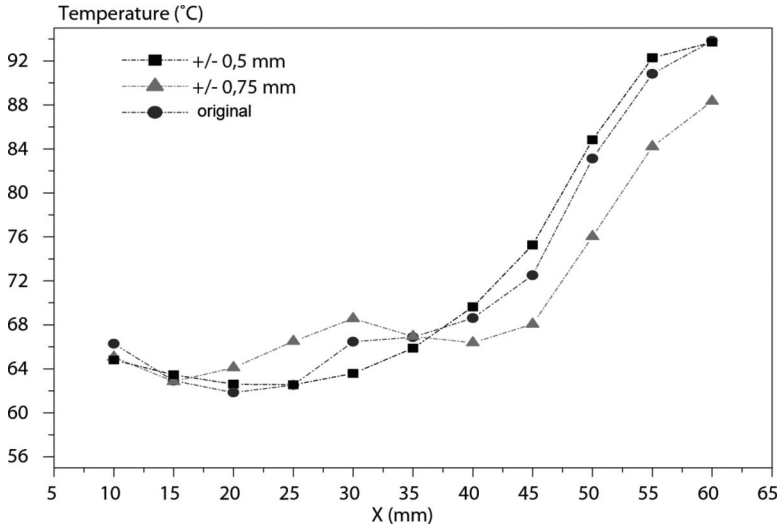

Fig. 6 Influence of the error estimation induced by the thermocouples' locations on the surface temperature

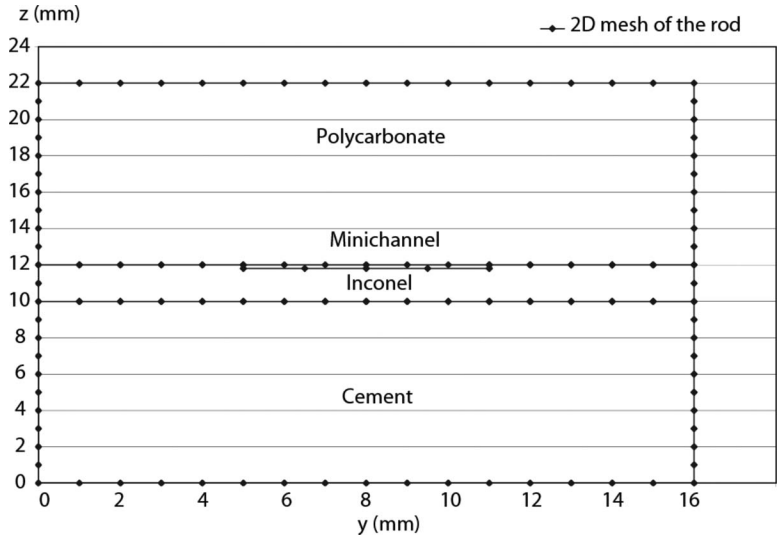

Fig. 7 2D meshing of the minichannel—the three domains are meshed but due to the adiabatic condition on the polycarbonate; we work with only two domains, the cement rod and the Inconel where the minichannel is engraved

local surface temperatures along the minichannel with the knowledge of the boundary conditions. This estimation procedure consists in inversing the temperature measurements under the minichannel in order to estimate the local boiling heat transfer coefficient $h(x)$, knowing the local heat flux and the local surface temperatures (ϕ_{surface}, T_{surface}). Those functions of space are the results of the inverse problem. The estimation of the solution is obtained using the BEM as the solution of the following optimization problem:

$$\hat{T}_{\text{surface}}, \hat{\phi}_{\text{surface}} = \arg\{\min(\|T_{\text{mod}} - T_{\text{meas}}\|)\} \tag{1}$$

In this last expression, the vectors T_{meas} and T_{mod}, respectively, represent the vector of temperature measurements and the vector of the calculated temperatures. The unknown factors (ϕ_{surface}, T_{surface}) are obtained by minimizing the difference between measurements and a mathematical modeling. Taking into account the specificity of formulation BEM, this minimization is not obtained explicitly but done through a function utilizing a linear combination of the measurements. This formulation leads to a system of simultaneous equation

$$\boldsymbol{A}X = B \tag{2}$$

In this last equation, $\boldsymbol{A}$ is a matrix of dimension $((N+N') \times M)$, X the vector of the M unknowns including (ϕ_{surface}, T_{surface}), and B a vector of dimension $(N+N')$ gathering a linear combination of the data measurements and the contribution of the

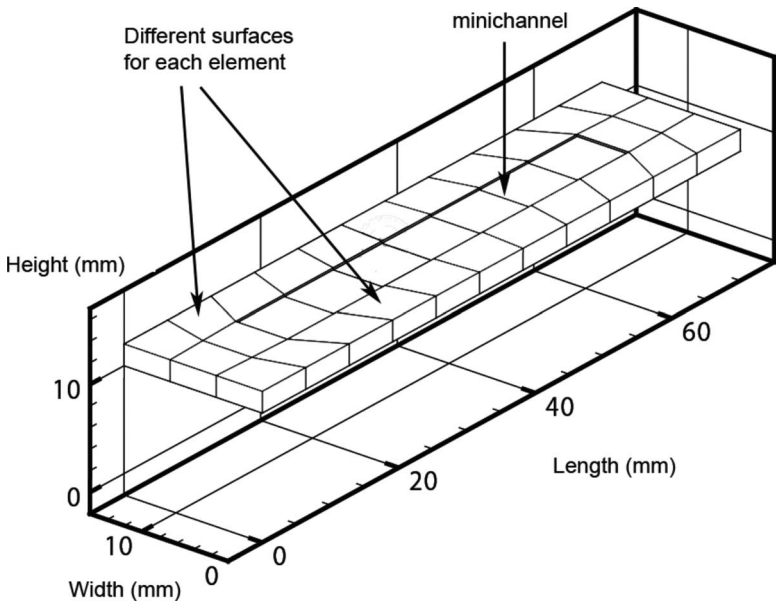

Fig. 8 3D Inconel meshing—only the faces are meshed with the BEM. All the elements are connected with each other. The minichannel is divided into seven parts in order to have good correspondence with three thermocouples located in the cement rod. We have then for each mesh, three thermocouples to have significant gradient to solve the inverse problem.

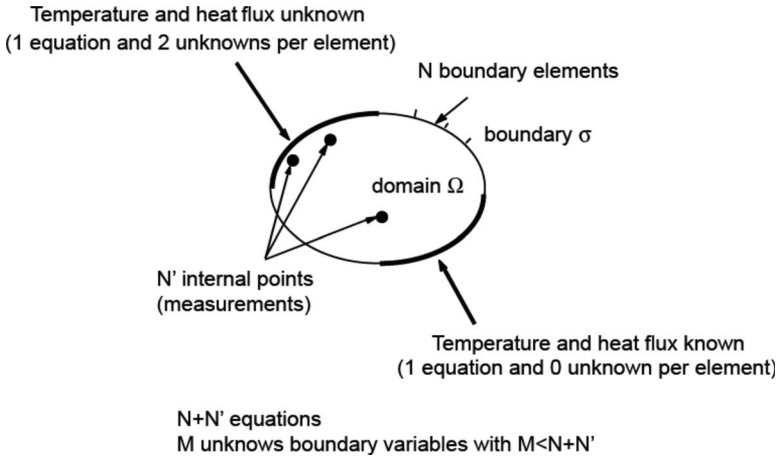

Fig. 9 The problem of the unknown boundary conditions. We have N' internal points (42 thermocouples) and we want to obtain the temperature and the heat flux density on the minichannel boundary where we have one equation and two unknowns.

heat sources. If $M=N+N'$, we obtain a square system of linear equation but most of the time we have $M<N+N'$ and has more equations than unknown (see Sec. 3): Our system presents 270 equations for 255 unknown factors (overdetermined system). A solution can be found by minimizing the distance between vector $\boldsymbol{A}X$ and vector B. In order to find out an estimation $\hat{X}$ of the unknown exact solution X, we have to solve the optimization problem using a cost function (Eq. (3)). Assuming that the difference between $\boldsymbol{A}X$ and B can be considered as distributed according to a Gaussian law, we can find $\hat{X}$ solution of the matricial system in the meaning of the least squares. Using this last property leads to the ordinary least squared solution as follows:

$$\hat{X} = \arg\{\min(\|AX - B\|^2)\} \tag{3}$$

$$\boldsymbol{A}\hat{X} = B \tag{4}$$

As As a result, the estimated vector $\hat{X}$ contains all the estimated surface temperatures ($\hat{T}_{\text{surface}}$) and the surface heat flux ($\hat{\phi}_{\text{surface}}$), so that we can calculate the local boiling coefficient $\hat{h}(x)$ in the minichannel knowing the saturation temperature of the liquid (T_{sat}) as follows:

$$\hat{h}(x) = \frac{\hat{\phi}_{\text{surface}}(x)}{\hat{T}_{\text{surface}}(x) - T_{\text{sat}}} \tag{5}$$

Actually, the inverse heat condition problem is ill posed and very sensitive to the measurements errors. Thus, we observe for the system numerical resolution instabilities of the solution $\hat{X}$ with regard to the measurement errors introduced into the vector B. As a consequence, we need to obtain a stable solution of this system by using regularization tools such as the truncated SVD solution [17] or Tikhonov regularization method [18–20]. We propose in the following paragraph an example of regularization procedure, which can be applied. In order to smooth the solution, we used in our study the truncated SVD solution.

3.6 Troncature Using SVD (Singular Value Decomposition). The regularization of an inverse problem consists in adding information to improve the stability of the solution with regard to the measurement noise and/or to select a type of solution among all those possibilities. The ill-conditioned character of matrix $\boldsymbol{A}$ results in the presence of low singular values. They are a consequence of linear dependent equations: indication of a strong correlation between the unknown factors. Actually, the SVD method makes it possible to deal with 3D inverse problem where the mesh is structured, i.e., the pavements of the elements do not have all the same surfaces and thus the same sensitivity (Fig. 8). This property increased the ill posedness of the problem. Indeed, the solution is much more unstable when the space discretization is refined. This singular behavior is due to the fact that the conditioning number of the linear system (see Sec. 3.7) is a function of the power of the meshing step.

In our problem, the truncated SVD method consists in removing the too small singular values that affect the stability of the system in order to find one solution among several, which best fits. It can seem contradictory to improve the system by removing equations and thus information: The suppression of the equations involves a reduction in the rank of our system and consequently an increase in the space of the plausible solutions. However, the action of removing these equations improves the stability because it deliberately removes the equations that disturb the solution. Matrix $\boldsymbol{A}$ can be built into a product of square matrices (U and V are orthogonal matrices and W is the diagonal matrix of the singular values w_j) as follows:

$$\begin{aligned} \hat{A} &= UWV^T \\ \hat{X} &= \left(V \operatorname{diag}\left(\frac{1}{w_j}\right) U^T\right) B \end{aligned} \tag{6}$$

$\boldsymbol{A}$ is ill conditioned when some singular values $w_j \to 0 (1/w_j \to \infty)$. As a result, the errors are increased. By using SVD, W^{-1} is truncated from the too high $(1/wj)$.

$$W = \begin{bmatrix} w_1 & \cdots & \cdots & 0 & \\ \vdots & \ddots & & \vdots & \\ \vdots & & \ddots & \vdots & 0 \\ \vdots & & & \ddots & \\ 0 & \cdots & \cdots & \cdots & w_n \end{bmatrix} \tag{7}$$

The truncated matrix can be built up as in

$$W_t = \begin{bmatrix} w_1 & \cdots & \cdots & 0 & \\ \vdots & \ddots & & \vdots & \\ \vdots & & \ddots & \vdots & 0 \\ 0 & \cdots & \cdots & w_p & \\ & & 0 & & \end{bmatrix} \tag{8}$$

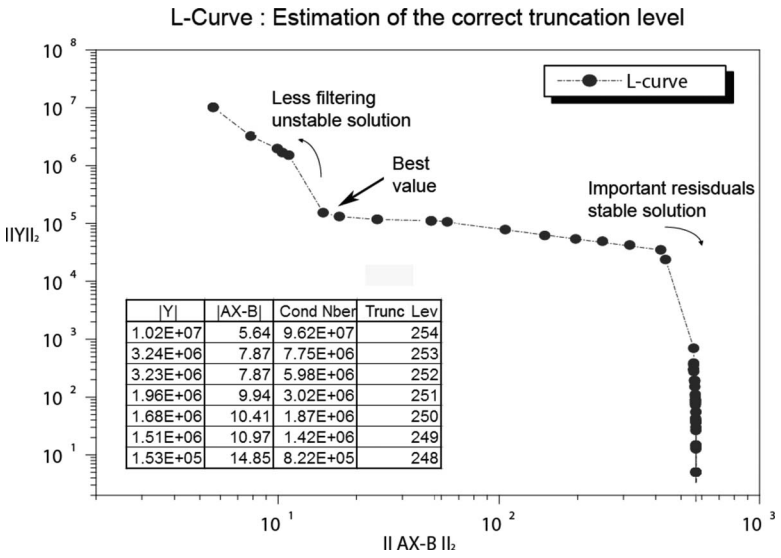

Fig. 10 The L-curve approach applied to the BEM. The optimal value is in the bend of the L where the best compromise is between stable results and low residuals (on the distinct corner separating the vertical and the horizontal part of the curve). It is around this corner at the maximum curvature that we find the best compromise.

The estimate solution vector $\hat{X}_t$ is a function of the new truncated matrix W_t^{-1} as follows:

$$\hat{X}_t = (U^T W_t^{-1} V)B \tag{9}$$

We observe a smoothing of the solution like in the regularization method by modifications of the functions to be minimized (for example, see Ref. [18]). However, it is necessary to explain how is carried out the choice of the ignored singular values. There is a "criterion" making it possible to quantify the balance between a stable solution and low residuals: the condition number. It is defined by the ratio of the highest to the weakest of the singular values of matrix $\boldsymbol{A}$. All the singular values lower than a limit value are eliminated. The numerical procedure can be found in the LAPACK [21]. This technique requires the use of a threshold, which allows the choice of values to be canceled. The level of truncation is determined by the technique known as the L-curve [17].

3.7 L-Curve Analysis. The obtained solution $\hat{X}$ depends on the best truncated value selected by the user. To avoid entering extremes and losing information, a tool called L-curve is introduced to estimate the correct condition number. The goal is to trace on a logarithmic scale the norm of the solution on the norm of the residuals $\|A\hat{X}-B\|$ (Fig. 10). The optimal value is in the hollow of the L where the best compromise is between stable results and low residuals (on the distinct corner separating the vertical and the horizontal part of the curve). It is around this corner that we find the best compromise. Thus, this value makes it possible to define the truncation level and the number of conditioning associated. In our problem, this value is around 10^7, which is very high and illustrates the ill posedness of our problem.

4 Results Concerning Heat Transfer

4.1 Boundary Reduction. The modeled system was made up of three domains. According to our 2D study, we consider only two domains: the cement and the Inconel. We made this choice simply because the polycarbonate had no influence on the studied zone (adiabatic condition). A variation in the different coefficients on the edge of the device does not change the output temperature profiles (Fig. 11). Concerning the thermal conduction, we work with a cement rod to have a significant temperature gradient necessary for the inversion and as we work in a stationary state, we did not take into account the accumulation term due to the heat capacity.

4.2 Processing. The following results were obtained during the PF52 CNES flight. The inversion of the temperature measurements is made for an x-coordinate. The local boiling coefficient $\hat{h}(x)$ is calculated as a function of the heat flux and the wall temperature according to Eq. (5). The profiles obtained are made up of seven points, as shown in Fig. 13. Indeed, as the system is very resistive, the assumption of an isolated system (adiabatic) is correct since a variation in the different coefficients on the edge of the device does not change the output temperature profiles. It is thus reasonable not to model the polycarbonate. A direct result is that the system is no longer overloaded. The computing time is shorter and the matrix containing the parameters of the meshing is

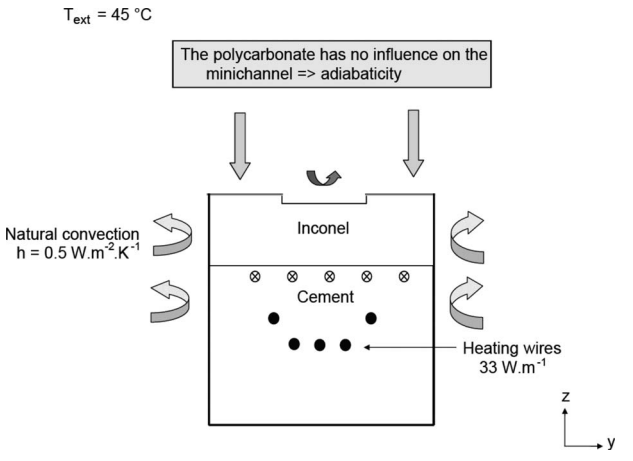

Fig. 11 Boundary conditions. According to our study, we consider only two domains: the cement and the Inconel. We made this choice simply because the polycarbonate had no influence on the studied zone (adiabatic condition). A variation in the different coefficients on the edge of the device does not change the output temperature profiles.

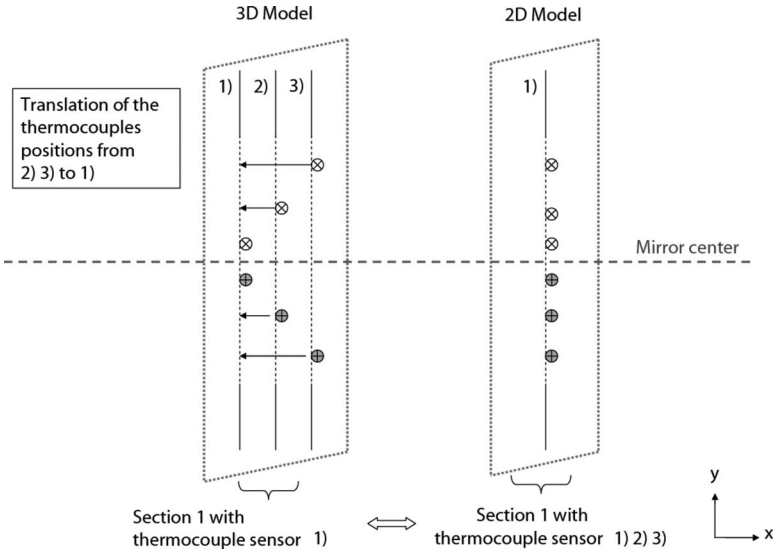

Fig. 12 Grouping of the sensors by section. As we work on different sections of the bar, it is necessary that they contain the inversed information. However, the cutting cannot contain the real positions of the thermocouples and the temperatures. An additional step is required to bring the sensors to the edges of the cutout sections. Their grouping is done by translating the three closer (and their symmetrical) next to the section.

of a smaller size. This saving of time and space (smaller rank of matrix) is significant since the matrix is ill conditioned (any action decreasing its component count is beneficial). Moreover, within the framework of our next studies concerning a nonstationary state, this simplification will be useful because during the resolution, the matrix is calculated every other second and requires significant resources for calculations (allowance of a great range of memory).

4.3 2D Analysis. For the 2D approach, we cut the minichannel into seven sections. The choice of this cutting is due to the fact that our model is optimized so that we want to obtain seven values of the heat flux and the wall temperature on the minichannel. Among these seven cross sections, only five are directly below the studied zone. The two others, located at $x=5$ mm and $x=65$ mm, are not useful to us in the 2D model since they describe positions, respectively, exceeding the minichannel. Nevertheless, their presence is necessary because they characterize the transfers on the edges. Moreover, to be able to take into account the 21 sensors duplicated along the bar, it is necessary to align them 3×3 for each portion in order best to fit our model. The error introduced is minimized since the disparity between the sensors, noted as d, is very low compared to the overall length L of the minichannel ($d/L<0.1$). The bar is thus cut into seven parts and on each part we have six sensors (described in Sec. 4.4).

As we work on different sections of the bar, it is necessary that they contain the inversed information. However, the cutting cannot contain the real locations of the thermocouples. An additional step is required to bring the sensors to the edges of the cutout sections. Their grouping is done by translating the three closer (and their symmetrical) next to the section (see Fig. 12). It is then necessary to repeat this operation for the seven sections with various values of x. The various x-positions are as follows ($x=10,15,25,35,45,50,55$). Then, the local heat transfer coefficient is calculated (Fig. 13) as a function of the heat flux and the wall temperature related to Eq. (5). The profiles obtained are made up of seven points corresponding to the couples ($x\ \varepsilon\ [10;\ 60]$; $y=8$; $z=11.8$), which are independent of each other.

A first result validating the use of the inverse methods is the fact that the wall temperature is higher than the saturation temperature ($T_{sat}=54\,^{\circ}C$), which is in agreement with the fact that the liquid boils. Moreover, the rising temperature profile is coherent: It confirms the overheating due to the vapor pockets, which are visible on the edge of the minichannel. To conclude, this 2D approach mades it possible to validate the assumptions concerning the boundary conditions of the system as well as the step of the meshing. However, considering the geometry of the minichannel, it seems more logical to work with a 3D model, which shows the real influence of the thermocouples and particularly the diffusive effects.

4.4 3D Analysis. This 3D study presents the results obtained in normal gravity during the PF53 ESA flight campaign. The interest of 3D modeling lies in the fact that it is better adapted to the geometry of the problem since in our case the longitudinal effects intervene. However, the conditioning number is higher (because of the denser meshing), which accentuates the ill-posed character of the system. It is thus necessary to pay particular attention to the regularization of the solution, which is much more unstable than in two dimensions. The temperature profiles obtained in the minichannel are in agreement with the inversed values of the thermocouples. As regards the surface flow, the power injected by the heating wires equals to 11 W minus losses (delivered by the heating wires). In the cement, the power is 10.8 W and in the Inconel 10.3 W. All the power delivered by the heating wires in the cement rod are transmitted to the upper surface in contact with the Inconel and pumped directly via the minichannel.

The lost power is used to heat the surrounding air (about 0.7 W). The cement temperature is of the same order of magnitude as the profile of the inversed temperatures (approximately $70\,^{\circ}C$) and in the Inconel the temperature is higher than the saturation temperature of the boiling fluid ($T_{sat}=54\,^{\circ}C$). Indeed, in the cement rod, the temperature distribution is high on the edges and low on the top surface (Fig. 14) because the heat is pumped by the minichannel. Moreover, concerning the heat flux, all the power of the heating wires are injected into the minichannel, which validates the choice of the materials (the total power of the heating wire is well pumped by the minichannel due to the low heat conductivity of the cement). However, on the edges of the minichannel, the estimation of the flux presents significant variations in

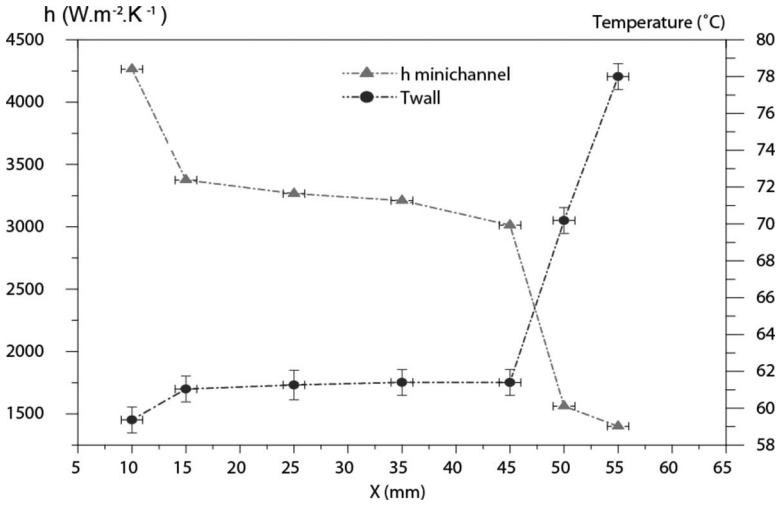

Fig. 13 Profile of the heat transfer coefficient *h* and the wall temperature along the minichannel obtained with a 2D model (Qw=32 kW m^{-2}, Qm =0.45 g s^{-1}, χ=0.66). The sharp decrease at the inlet and the outlet of the minichannel is due to the edge effects, which are not taken into account in the 2D model.

spite of the regularization tools. This result is mainly due to the errors contained in the thermocouples, which cannot be corrected here. The profiles of the wall temperature and heat flux (Fig. 15) are less accurate to those evaluated in the 2D model. Indeed, the precision of the 3D model is greater especially in the evaluation of the transfers. Furthermore, with regard to the transfer coefficient, its profile is different (higher values) from that in two dimensions since we take into account the diffusive effects of the rod. This leads to a modification of the values of the flux especially on the edges of the minichannel. Indeed, there are much instabilities here due to edge effects.

4.5 Influence of Gravity on Heat Transfer. To analyze the flow boiling heat transfer coefficient profile, the measurements are continuously taken at three gravity levels. The differences induced by gravity level on the heat transfer coefficient are obtained using the data of parabolic flights for three ranges; corresponding to μg, $1g$, and $1.8g$ levels. The local heat transfer coefficient in Fig. 16 is higher in the inlet minichannel. This is in agreement with the analysis of the recorded movies, which highlights that on the minichannel inlet the flow has a low percentage of insulated bubbles. The more significant the sizes of the bubbles are, the larger is the surface of the superheated liquid is. Besides, concerning the microgravity phase, the results present variations by ratio to the terrestrial gravity and the hypergravity, which evidence an influence of the gravity level on the confined flow boiling. During the phase of microgravity, at the inlet of the minichannel (x=12 mm), the heat transfer coefficient is higher with a value around 5500 W m^{-2} K^{-1} in comparison with the $1.8g$ and the $1g$, where it is equal to 3500 W m^{-2} K^{-1}.

Furthermore, as soon as the vapor completely fills the pipe, the heat exchange strongly decreases because there is no more phase change (Fig. 17), only heat transfer through the vapor (heat insulator). The study of the transfers confirms a higher heat transfer coefficient at the inlet minichannel during the phase of microgravity. This is due to the decrease in size of the vapor bubbles. In Fig. 17, the local quality increases along the main axis from the inlet to the outlet of the channel. This result is in good agreement with the temperature profile we have on the boundary minichannel since at the outlet the temperature is higher. Second result shows that the evolution is not linear because in our case the heat flux density is

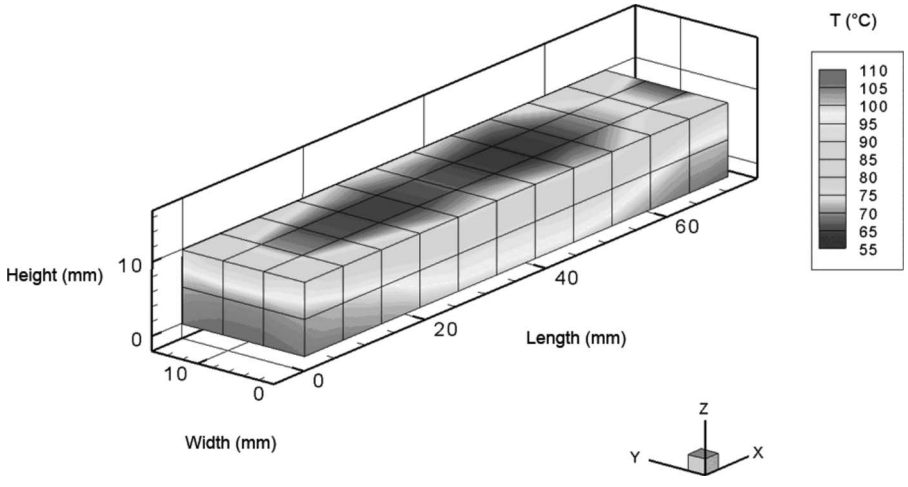

Fig. 14 3D temperature distribution inside the cement rod. The temperature decreases on top in the cement surface because the heat is pumped directly to the minichannel.

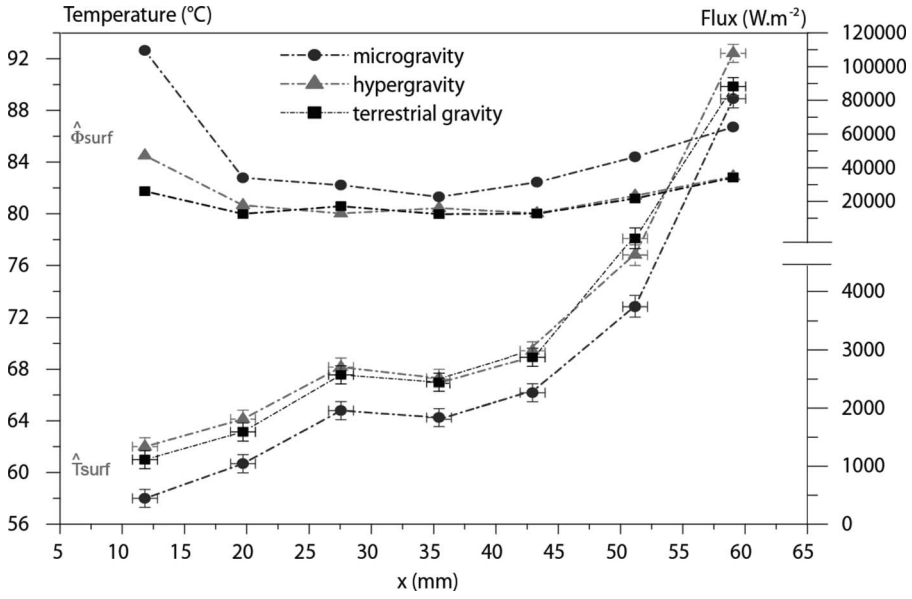

Fig. 15 Local wall temperature and local heat flux along the minichannel (Qw = 32 kW m^{-2}, Qm=0.26 g s^{-1}, χ=0.26) depending on the gravity level

not constant. Indeed, the heat flux calculated on the wall minichannel varies around 2%. This result is explicit at the inlet minichannel where we observe a short decrease since the error estimation is higher around these points. Besides, at the outlet minichannel, the local vapor quality (x=60 mm) tends to reach a value corresponding to the outlet vapor quality.

Another result shows that the heat transfer coefficient decreases along the x length in the flow direction. Whatever the choice of gravity, as soon as the vapor occupies the whole of the minichannel, the boiling coefficient falls strongly to reach a level that characterizes a kind of heat transfer with only a vapor phase. Concerning the temperature profile (Fig. 15), the temperature in the minichannel increases according to x (increase around 30°C–x =15 mm, T=62°C and x=60 mm, T=92°C). This phenomenon translates a heating at the origin of convective boiling (formation of the bubbles). First point, the results in terrestrial gravity and hypergravity are similar (less than one degree of difference). Second, in microgravity, we notice a variation of 4°C (a value higher than uncertainties of measurements). Concerning the heat flux, it remains constant except at the inlet and outlet of the minichannel since we have edge effects in these two zones.

5 Conclusions and Perspectives

In this study, we highlighted the influence of gravity on convective boiling in minichannels. The microgravity generates vapor pocket structures, which fill the width of the minichannel and the heat transfer coefficient is locally higher. Consequently, we can assume that μg influences the appearance of the vapor bubbles whose size varies depending on parameter g. In the case of hypergravity, a classical bubble structure is observed. The analysis of temperature as a function of parameter g evidences that gravity has an influence on the flow. However, as the profiles of the temperatures of the thermocouples do not present enough variations (difference of less than 1°C between the temperatures at hypergravity and microgravity), in the future it will be important to

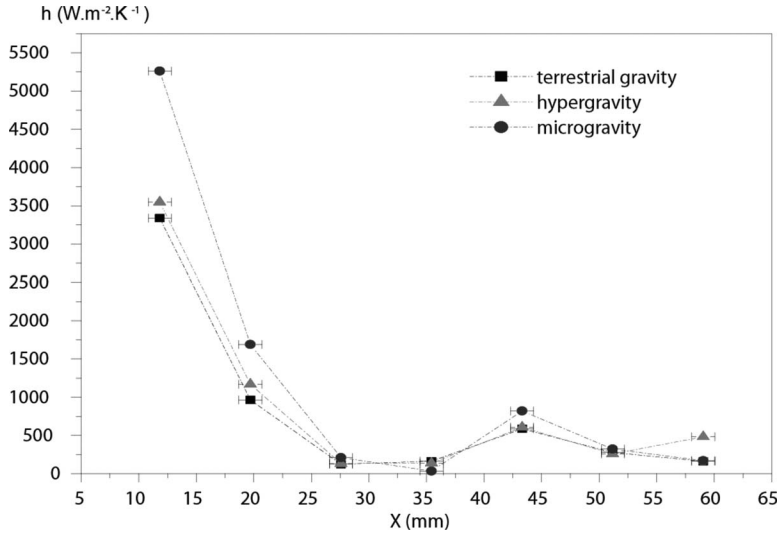

Fig. 16 Local heat transfer coefficient as a function of the main flow axis (Qw=32 kW m^{-2}, Qm=0.26 g s^{-1}, χ=0.26)

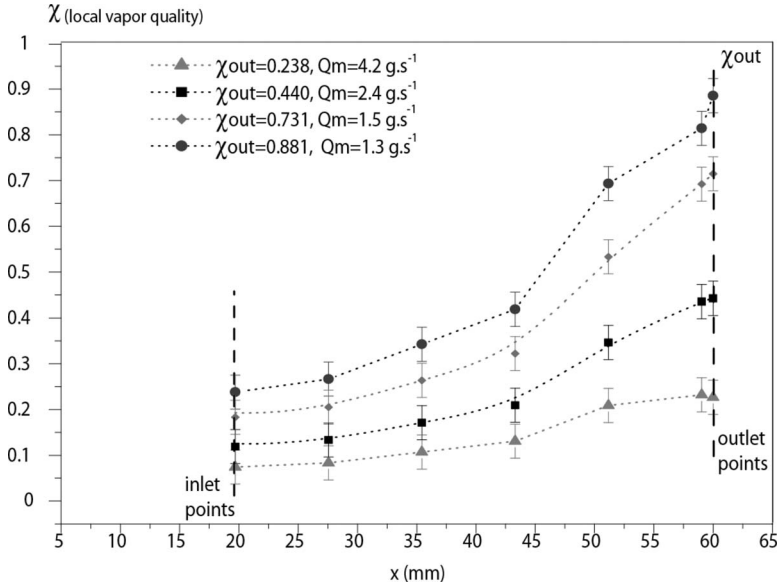

Fig. 17 Local vapor quality as a function of the main flow axis (*Qw* = 32 kW m^{-2}) depending on the mass flow rate. We plot the curves for seven points. The profiles increase from the inlet to the outlet minichannel. We observe that the final point corresponds to the outlet vapor quality, which is a way to validate our results. The error estimation is here around 2%.

determine their precise locations. For the inverse methods, the sensors induce too many disturbances and accentuate the ill-posed character. In our case, the temperatures cannot be evaluated without taking into account the relative error due to the accuracy of the measurements (noise) and to the position of the thermocouples (z-axis). These uncertainties lead to clear variations in the solution and particularly in the surface heat flux. It has been also shown that combined application of the known measurement errors leads to substantial errors in our numerical calculation. One solution would be to use an X-ray tomography of our cement rod in order to estimate with accuracy the exact locations of the thermocouples and the heating wires. Besides, an additional issue would be to add infrared (IR) measurements while painting the lower face of the cement in black and placing a camera directly below.

Acknowledgment

We would especially like to thank the CNES (793/2002/CNES/8665) and ESA (MAP Boiling) for their financial support. We thank them for giving us access to the experimentation in microgravity on Board A300 Zero-G. We would also like to express our gratitude to Novespace® and more especially to Mr. Mora and Mr. Gai for their technical assistance during the Campaigns PF52/CNES and PF53/ESA.

Nomenclature

Symbols

A = matrix
B = right hand vector
X = vector of the unknowns
U, V = orthogonal matrices
W = diagonal matrix
T = temperature, K
h = local heat transfer coefficient, W m^{-2} K^{-1}
Qw = heat flux density, W s^{-2}
Qm = mass flow rate, kg s^{-1}

Indices

mod = model
meas = measurements
sat = saturated

Superscript

$\hat{}$ = estimated variable

Subscript

i, j = heat flux, temperature indices

Greek Symbols

ϕ = heat flux, W m^{-2}
λ = heat conductivity, W m^{-1} K^{-1}
Γ = boundary of the domain
Ω = diffusive domain
θ = temperature on the boundary, K
χ = vapor quality

References

[1] Kandlikar, S. G., 2004, "Heat Transfer Mechanisms During Flow Boiling in Microchannels," ASME J. Heat Transfer, **126**, pp. 8–16.
[2] Yan, Y., and Kenning, D. B. R., 1998, "Pressure Fluctuations During Boiling in a Narrow Channel," HTFS Research Symposium 1998.
[3] Kennedy, J. E., Roach, G. M., Dowling, M. F., Abdel-Khalik, S. I., Ghiaasiaan, S. M., Jeter, S. M., and Quershi, Z. H., 2000, "The Onset of Flow Instability in Uniformly Heated Horizontal Microchannels," ASME J. Heat Transfer, **122**, pp. 118–125.
[4] Qu, W., and Mudawar, I., 2003, "Measurement and Prediction of Pressure Drop in Two-Phase Micro-Channels Heat Sinks," Int. J. Heat Mass Transfer, **46**, pp. 2737–2753.
[5] Brutin, D., and Tadrist, L., 2003, "Destabilization Mechanisms and Scaling Laws of Convective Boiling in a Minichannel," J. Thermophys. Heat Transfer, **20**, pp. 851–855.
[6] Hadamard, J., 1932, *Le Probème de Cauchy et les Équations aux Dérivées Partielles Linéaires Hyperboliques*, Hermann, Paris.
[7] Brebbia, C. A., Telles, J. C. F., and Wrobel, L. C., 1984, *Boundary Element Techniques*, Springer-Verlag, Berlin.
[8] Pasquetti, R., and Le Niliot, C., 1991, "Boundary Element Approach for Inverse Conduction Problems: Application to a Bidimensional Transient Numerical Experiment," Numer. Heat Transfer, Part B, **20**, pp. 169–189.
[9] Martin, T. J., Dulikravitch, and G. S., 1996, "Inverse Determination of Boundary Conditions and Sources in Steady Heat Conduction With Heat Generation," ASME J. Heat Transfer, **118**, pp. 546–554.
[10] Lesnic, D., Elliott, L., and Ingham, D. B., 1996, "Application of The Boundary Element Method to Inverse Heat Conduction Problems," Int. J. Heat Mass Transfer, **39**, pp. 1503–1517.
[11] Lagier, G. L., 1999, "Application de la méthode des éléments de frontière à la résolution du problème inverse de diffusion de la chaleurmultidimensionnel:

régularisation par troncature de spectre," Ph.D. thesis, Institut National Polytechnique de, Grenoble, France.
[12] Dulikravitch, G. S., and Martin, T. J., 1996, "Inverse Determination of Boundary Conditions and Sources in Steady Heat Conduction With Heat Generation," ASME J. Heat Transfer, **118**, pp. 546–554.
[13] Le Niliot, C., and Lefèvre, F., 2001, "A Method for Multiple Steady Line Heat Sources Identification in a Diffusive System: Application to an Experimental 2D Problem," Int. J. Heat Mass Transfer, **44**, pp. 1425–1438.
[14] Yang, C.-Y., 1999, "The Determination of Two Heat Sources in an Inverse Heat Conduction Problem," Int. J. Heat Mass Transfer, **42**, pp. 345–356.
[15] Silva Neto, A. J., and Ozisik, M. N., 1992, "Two-Dimensional Inverse Heat Conduction Problem of Estimating the Time-Varying Strength of a Line Heat Source," J. Appl. Phys., **71**, pp. 5357–5362.
[16] Beck, J. V., Blackwell, B., and St. Clair, C. R., 1985, *Inverse Heat Conduction, Ill-Posed Problems*, Wiley Interscience, New York.
[17] Hansen, P. C., 1998, *Rank-Deficient and Discrete Ill-Posed Problems*, SIAM, Philadelphia PA.
[18] Tikhonov, A. N., and Arsenin, V. Y., 1977, *Solutions of Ill-Posed Problems*, V. H. Winston & Sons, Washington, DC.
[19] Alifanov, O. M., 1977, *Inverse Heat Transfer Problems*, Springer, Washington, DC.
[20] Le Niliot, C., 2002, *La Méthode des Eléments de Frontière Pour la Résolution de Problèmes Inverses en Conduction de la Chaleur: Applications Numériques et Expérimentales*, Hdr, Marseilles.
[21] Press, W. H., Flannery, B. P., Teulossky, S. A., and Vetterling, W. T., 1990, *Numerical Recipes*, Cambridge University Press, Cambridge.

Experimental Study of a Curved Rotating Heat Pipe

T. A. Jankowski[1]
e-mail: jankowski@lanl.gov

F. C. Prenger

Mechanical and Thermal Engineering Group
(AET-1),
Los Alamos National Laboratory,
MS J580,
Los Alamos, NM 87545

A. Razani
Department of Mechanical Engineering,
University of New Mexico,
MSC01 1150,
Albuquerque, NM 87131

A curved rotating heat pipe for use in motor and generator applications is studied experimentally. The heat pipe is built so that both the condenser and evaporator sections are parallel to the axis of rotation. The condenser section is close to the axis of rotation while the evaporator section can be placed in contact with off-axis heat sources in the rotating machine. The geometry is achieved by incorporating an S-shaped curve between the on-axis rotating condenser section and the off-axis revolving evaporator section. The curved rotating heat pipe allows for a direct coupling of the rotating condenser section to an on-axis stationary refrigeration system, while allowing the revolving evaporator section to intercept off-axis heat sources in the rotating machine. An experimental rotating heat pipe test apparatus was built and operated. The test data indicate that the working fluid continued to circulate, resulting in heat transfer with a high effective thermal conductivity, with the curved rotating heat pipe operating under the influence of centrifugal accelerations approaching 400g. Furthermore, the experimental results were used to validate a heat pipe thermal model that can be used in the design of rotating machines that rely on the curved rotating heat pipe as part of the thermal management system.
[DOI: 10.1115/1.2953303]

Keywords: experimental heat transfer, rotating heat pipe, revolving heat pipe

1 Introduction

On-axis rotating heat pipes have been used extensively to cool the heat generating components in a variety of rotating machines [1,2]. In a typical on-axis rotating heat pipe, the working fluid, which is a two-phase liquid-vapor mixture, is confined in a sealed cylindrical container rotating about the longitudinal axis. At sufficiently high rotation speeds, the liquid phase of the working fluid, under the action of the centrifugal force, forms a thin liquid layer against the outer wall of the heat pipe container. When the evaporator end of the heat pipe is heated, a portion of the liquid phase vaporizes at the liquid-vapor interface. A difference in pressure, in the vapor phase, created by a temperature difference between the evaporator and condenser ends of the heat pipe, is used to drive the vapor flow through the adiabatic section and into the condenser. In the condenser section, a portion of the vapor condenses at the liquid-vapor interface as heat is rejected to the heat sink. A pressure difference between the condenser and evaporator sections, in the liquid phase, is then used to drive the liquid flow from the condenser toward the evaporator. In on-axis rotating heat pipes, a variable thickness liquid film, and the resulting hydrostatic head caused by the rotation, provides the pressure difference for liquid return to the evaporator. This liquid return mechanism can also be augmented by tapering the outer container, from small diameter at the condenser endcap to larger diameter at the evaporator endcap, or by including a porous wick structure in the rotating heat pipe. For most on-axis rotating heat pipes, the only significant thermal resistances are for radial heat transfer across the thin liquid films in the condenser and evaporator sections [3].

In applications where heat sources are located at some radial distance from the axis of rotation, designs have been suggested using radially rotating and revolving heat pipes [4,5]. In the radially rotating heat pipe, the longitudinal axis of the heat pipe is perpendicular to the axis of rotation, with the evaporator section farthest away from the axis and the condenser section close to the axis. This orientation allows for the centrifugal force to be used for liquid return to the evaporator. The longitudinal axis of the revolving heat pipe is parallel to, but displaced from, the axis of rotation, so that the evaporator can be placed in direct contact with off-axis heat sources.

A curved rotating heat pipe that combines many of the features of rotating, radially rotating, and revolving heat pipes is studied here. The heat pipe geometry is shown in Fig. 1. The heat pipe consists of an on-axis rotating condenser section, an S-shaped transition section, and an off-axis revolving evaporator section.

A cross-sectional view of the heat pipe is shown in Fig. 1(*b*). The heat pipe uses an annular gap composite wick structure. The presence of the annular gap wick structure allows the heat pipe to be used in stationary operation (with no rotation). The unique geometry of the heat pipe allows the evaporator section to be in contact with heat sources that are located at some distance from the axis of rotation, while the condenser section can be easily coupled to an on-axis heat sink.

Using the curved heat pipe shown in Fig. 1 in applications where off-axis heat sources must be cooled offers many advantages when compared to the use of conventional rotating and revolving heat pipes. For example, in the case of large-diameter superconducting rotating machines operating at cryogenic temperatures, external heat in leak, which occurs at the periphery of the machine, is a significant portion of the total heat load that must be removed from the machine. To ensure proper operation, this heat load must be removed from the machine both when the machine is rotating and when the machine is stationary (for example, during cooldown periods) [6,7]. While the evaporator section of a revolving heat pipe could easily be placed in contact with the off-axis heated components of a rotating machine, coupling the eccentrically rotating condenser section to a stationary on-axis heat sink can be difficult. The on-axis condenser section of a rotating heat pipe, on the other hand, could more easily be coupled to a heat sink. Coupling the evaporator section of the rotating heat pipe to the off-axis heat sources, however, often requires longer conduction heat transfer paths though solid components of the machine, raising the operating temperature of the machine's components well above the temperature of the heat sink.

[1]Corresponding author.

Contributed by the Heat Transfer Division of ASME for publication in the JOURNAL OF HEAT TRANSFER. Manuscript received August 10, 2007; final manuscript received March 13, 2008; published online August 8, 2008. Review conducted by Louis C. Chow.

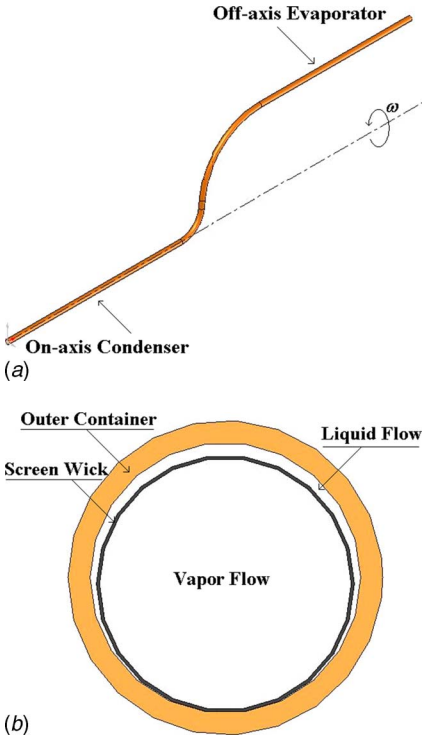

Fig. 1 The curved rotating heat pipe. The layout of the rotating heat pipe in (*a*) shows the on-axis rotating condenser section and the off-axis revolving evaporator section, while the cross-sectional view in (*b*) shows the annular gap wick structure.

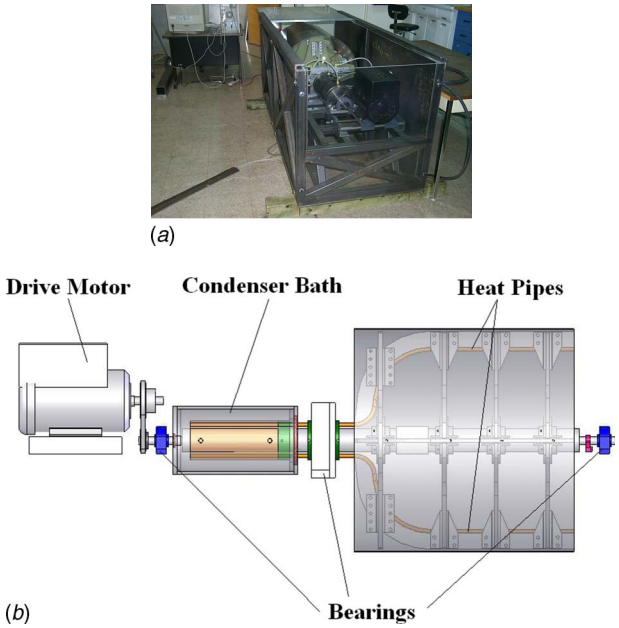

Fig. 2 The experimental apparatus used to test the rotating heat pipes. A picture is shown in (*a*) and a solid model of the components mounted to the frame is shown in (*b*).

Both the liquid and vapor phases of the working fluid in the curved rotating heat pipe are subjected to significant rotation induced acceleration loads during rotating operation, which may interrupt the circulation of the working fluid in the heat pipe. Additionally, we found that fabricating the long, small-diameter heat pipe with an annular gap wick structure was a significant technical challenge. For these reasons, a series of experiments were performed with the heat pipe, both in rotating and nonrotating operation, (1) to determine whether the flexible annular gap wick structure would meet performance expectations in stationary and low-speed rotating operation, (2) to ensure that the working fluid continues to circulate with the heat pipe operating at rotation speeds typically encountered in motors and generators, and (3) to validate a thermal model of the rotating heat pipe. The design and construction of the heat pipes and a rotating test apparatus are described in Sec. 2, along with a description of the data collected during the experiments and an estimation of the experimental uncertainties. In Sec. 3, data are presented for the heat pipe operating in both stationary (nonrotating) and rotating operation. Comparisons of the rotating heat pipe data to the thermal model are discussed in Sec. 4. Finally, conclusions are given in Sec. 5.

2 Experimental Setup

2.1 Experimental Hardware. The heat pipes used throughout the experiments were fabricated from a 1.27 cm (0.5 in.) outside diameter, 0.089 cm (0.035 in.) wall thickness copper tube. Before bending into the curved configuration shown in Fig. 1, each heat pipe had a straight length of 140 cm (55 in.). The cylindrical wick was made from two layers of 200×200 mesh stainless steel screen wound on 10 mm (0.393 in.) diameter mandrel to form the annular gap wick structure shown in Fig. 1.

Before inserting the wick into the heat pipe container, the effective pore radius of the wick was measured by immersing the cylindrical wick structure in a methanol bath and pressurizing the interior vapor space with nitrogen gas until vapor bubbles were observed breaking through the wick. The nitrogen pressure in the vapor space was measured and was used to calculate an effective pore radius of 44 μm (± 3 μm) for the wrapped annular gap wick structure. This value compares well to the 42 μm expected pore radius for the screen [8].

After bubble testing, the wick structure was inserted into the heat pipe container and the outer container was bent twice to form the curved configuration, with a radial distance of 24 cm (9.5 in.) between the off-axis evaporator and the on-axis condenser. After bending, the heat pipes were first evacuated and then filled by pulling a known volume of liquid methanol into the heat pipe. For the results reported here, each heat pipe was charged with 15.7g ($\pm 0.4g$) of methanol working fluid.

A substantial rotating test apparatus, which allows for simultaneous testing of two rotating heat pipes, was designed, built, and safety approved. The configuration of the test apparatus is shown in Fig. 2. A 5 hp variable speed motor is used to drive a 1.8 m (6 ft.) long, 7.6 cm (3 in.) diameter solid steel shaft, on which the rotating heat pipes and a G-10 support structure are mounted, up to 1200 rpm. 46 cm (18 in.) of each heat pipe at the off-axis evaporator ends, which are in contact with the G-10 support structure, are heated with tape heaters that supply up to 200 W. The condenser sections are cooled in a stationary water bath with water circulated by a chiller. Measurements taken throughout the rotating tests include the power into the tape heaters, the condenser bath temperature, and six temperatures at locations in the condenser, curved adiabatic, and evaporator sections.

Temperatures along the length of the heat pipes are measured using type K thermocouples that are recorded using two eight channel remote data loggers [9]. The manufacturer's reported overall instrument error for the calibrated thermocouples and data loggers is ± 1.2 K. Point calibration tests were performed with the data loggers and thermocouples to further quantify the uncertainty in the temperature measurements. The thermocouples were immersed in an ice-water bath and in boiling water. Data were taken every 10 s from all eight thermocouples for 20 min, giving a sample size of 960 readings. Both the ice-water and boiling water tests showed normal frequency distributions, with the boiling water test having the largest standard deviation. A band of ± 0.5 K,

corresponding to a 99% (±3 standard deviations) confidence interval for the boiling water test, is used as an estimate of the temperature measurement uncertainty throughout the experimental study.

2.2 Experimental Uncertainties. Two major sources of uncertainty in reporting the test results for the rotating heat pipe in the test apparatus have been identified. Temperature values along the length of the heat pipe and temperature differences between two locations on the heat pipe are reported. As was mentioned in the previous section, all individual thermocouple readings are assumed to have an uncertainty of ±0.5 K. Additionally, heat transfer rates are reported. The maximum value of the heat transfer rate into the evaporator section is given by the power dissipated in the resistance heater. The heater resistance and voltage drop across the heater are measured with a multimeter, allowing for a calculation of the maximum heat transfer rate to within 1%. The major source of uncertainty in the heat transfer rate into the heat pipe is due to heat loss through the insulation and G-10 supports. A conservative (high) estimate of the conduction loss has been made by assuming that the outer surfaces of the insulation and G-10 in contact with the evaporator and adiabatic sections are at room temperature, and that the surface temperature of the heat pipe is equal to the temperature of the evaporator. These calculated values are used as an estimate of the uncertainty in reporting the heat transfer rate.

Uncertainties for results calculated from the measured values are determined with standard formulas for uncertainty propagation (i.e., the Kline–McClintock second power law) [10].

3 Heat Pipe Test Data and Comparisons to a Heat Pipe Thermal Model

3.1 Heat Pipe Thermal Model. An extensive numerical model of the rotating heat pipe has been developed [3]. The model is based on a two-dimensional (symmetry about the longitudinal axis) finite-difference model of laminar liquid flow coupled to a one-dimensional model of vapor flow in a rotating heat pipe.

In the finite-difference calculation of the liquid flow, liquid is allowed to either fill the annular space between the wick and the outer wall of the heat pipe, or the liquid can form a variable-thickness liquid film against the wall of the heat pipe. In this way, the model can predict the performance of rotating heat pipes without a wick structure as well as heat pipes with an annular gap wick.

With the annular gap full of liquid, the thermal model calculates a pressure difference (as a function of axial length) supported by the annular gap wick. If, at any axial location, the pressure difference supported by the annular gap wick exceeds the maximum capillary pressure difference that can be supported by the wick, the model predicts a dryout failure of the heat pipe. This pressure balance calculation is typically how stationary heat pipes are modeled [11,12].

For the heat pipe rotating at high speed and with liquid forming a variable-thickness liquid film, the thermal model calculates liquid-film thickness as a function of axial length in the heat pipe. In most models of rotating heat pipes, simplified forms of the governing equations, referred to as a Nusselt-type film flow analysis, are applied to the liquid layer [13,14]. In the Nusselt-type film flow analysis, acceleration in the liquid flow (axial) direction is ignored and both convection and diffusion are ignored in the cross-stream direction. Rather than solving simplified versions of the governing equations in the liquid flow, the heat pipe thermal model used here solves the full discretized Navier–Stokes and energy equations, subject to the appropriate free-surface boundary conditions, in the liquid layer. To model the liquid flow, we found that the axial acceleration terms must be included because as the liquid flows through the S-shaped curve in the curved rotating heat pipe, the orientation of the centrifugal force changes, causing an acceleration of the liquid. In the analysis, the liquid and vapor flows are treated separately, and a coordinate transformation and mapping procedure is used to determine the varying location of the liquid-vapor interface when the liquid forms a film on the wall of the heat pipe. The coordinate transformation and the method used for application of the free-surface boundary conditions have been extensively used and tested in previous investigations of free-surface flows [15–17]. After calculating the liquid layer thickness, the heat pipe thermal model then calculates temperature differences in the heat pipe by considering thermal resistances across the liquid films in the evaporator and condenser sections.

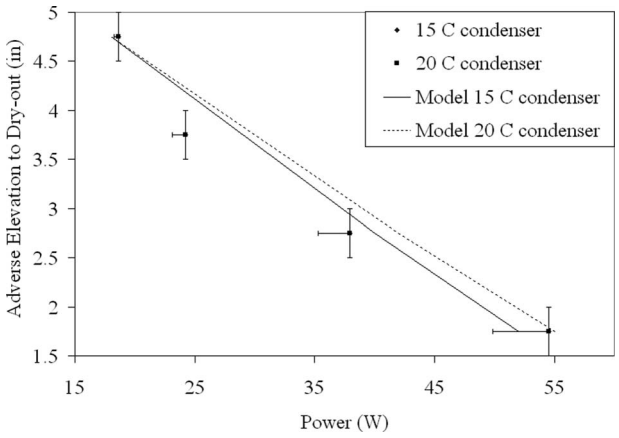

Fig. 3 Stationary dryout tests with the heat pipes installed in the rotating test apparatus

The thermal model described above has been validated by comparing the predictions for a stationary (nonrotating) heat pipe to results generated by another extensively benchmarked heat pipe design code [12]. Additionally, straight on-axis rotating wickless heat pipes were simulated and the results were compared to previous analyses [13,18]. For the numerical predictions presented here, discretization errors have been assessed and minimized using the grid convergence index (GCI) method [19].

The verified and validated heat pipe thermal model was used to simulate the performance of the curved rotating heat pipe shown in Fig. 1 in both stationary and rotating operation. Parametric studies with the heat pipe thermal model show that the curved rotating heat pipe operates in two distinct operating regimes depending on the magnitude of the rotation speed and the centrifugal force acting on the liquid [3]. Specifically, in stationary operation and at low speed, the annular gap wick is full of liquid and is used for liquid return to the evaporator section. However, as the rotation speed is increased, the centrifugal forces, which assist liquid return to the evaporator, overwhelm the capillary forces generated by the porous wick. At high rotation speed, the liquid is forced out of the wick and forms a thin variable-thickness liquid film along the wall of the heat pipe and the excess liquid is forced into the evaporator section.

Additionally, from the thermal model we find that at high rotation speeds, radial heat transfer across the liquid film in the evaporator is significantly affected by buoyancy-driven convection. The heat pipe thermal model includes a number of buoyancy-driven convection correlations for bottom-heated liquid layers (in the revolving heat pipe evaporator, the centrifugal force pushes the liquid into the heated wall) [20,21].

3.2 Stationary Tests. Stationary (nonrotating) tests were performed with the heat pipes in the rotating test apparatus to ensure that the heat pipe would perform as expected. For these long (140 cm), small-diameter (1.3 cm) heat pipes with the annular gap wick, the numerical model suggests that the capacities of the heat pipes are limited by the capillary limit.

The results of the stationary tests in the rotating apparatus are shown in Fig. 3, where the dryout data are compared to predic-

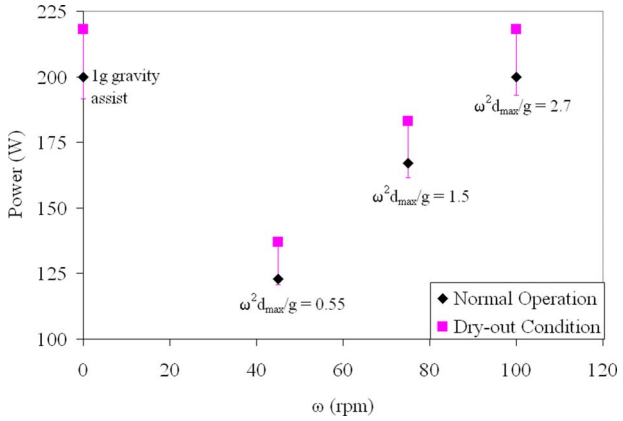

Fig. 4 Low-speed dryout tests

tions from the thermal model. The data compare well (within 12%) to the model predictions of the capillary limit (assuming a pore size of 44 μm in the numerical simulations, which was determined in the methanol-immersion pore size test), indicating that the wick structure was not damaged during assembly or bending of the heat pipes.

3.3 Low-Speed Dryout Tests. Low-speed tests ($\omega \leq 100$ rpm) were performed to determine how the capillary limit is affected by the centrifugal force. For the heat pipe with the off-axis evaporator section, the centrifugal force helps with liquid return to the evaporator. The capillary limit, therefore, should increase with increasing rotation speed. The results of the low-speed test with a condenser set point of 25°C are shown in Fig. 4. The data point for the 0 rpm case is taken with the heat pipe operating in 1g gravity assist with the evaporator 24.1 cm below the condenser. The centrifugal acceleration, $\omega^2 d_{max}$, where $d_{max} = 24.1$ cm is the distance from the axis of rotation to the off-axis evaporator section, increases as the rotation speed is increased. For $\omega^2 d_{max}/g < 2$, the data indicate that the capillary limit for the rotating heat pipe is less than the capillary limit for the nonrotating heat pipe with 1g gravity assist. Recognizing that gravity is superimposed on the rotating heat pipe allows for an explanation of this behavior. At the top of the rotation cycle (with the evaporator above the condenser) and with $\omega^2 d_{max}/g < 2$, the net acceleration assisting liquid return is less than 1g, resulting in a capillary limit lower than the 1g gravity assist case. With the current experimental setup, the capillary limit could not be found after the rotation speed was increased beyond 100 rpm due to the limitation on the maximum power that could be supplied to the heat pipe (~200 W).

3.4 High-Speed Test Data. Although performance limits could not be determined at high rotational speeds, temperatures along the length of the heat pipe were measured while varying the rotational speed and heat load. The rotational speed was varied from 210 rpm to 1170 rpm and the heat load was varied from 38 W to 198 W. An example data file is shown in Fig. 5.

The high-speed test data in Fig. 5 indicate that as the rotation speed is increased to 1170 rpm, no performance limitations are reached, and the working fluid continues to circulate in the rotating heat pipe. At the highest rotation speed (1170 rpm), the effective thermal conductivity of the heat pipe is approximately 150 kW/m K. Furthermore, the figure shows that as the rotational speed is increased from 210 rpm to 550 rpm, the temperatures in the adiabatic and evaporator sections decrease. This temperature decrease indicates that the excess liquid, which in a nonrotating horizontal heat pipe is swept to the condenser section by the

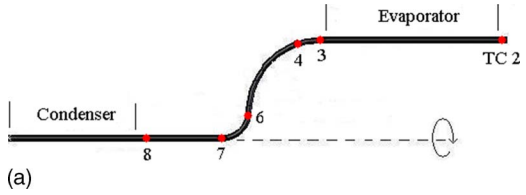

(a)

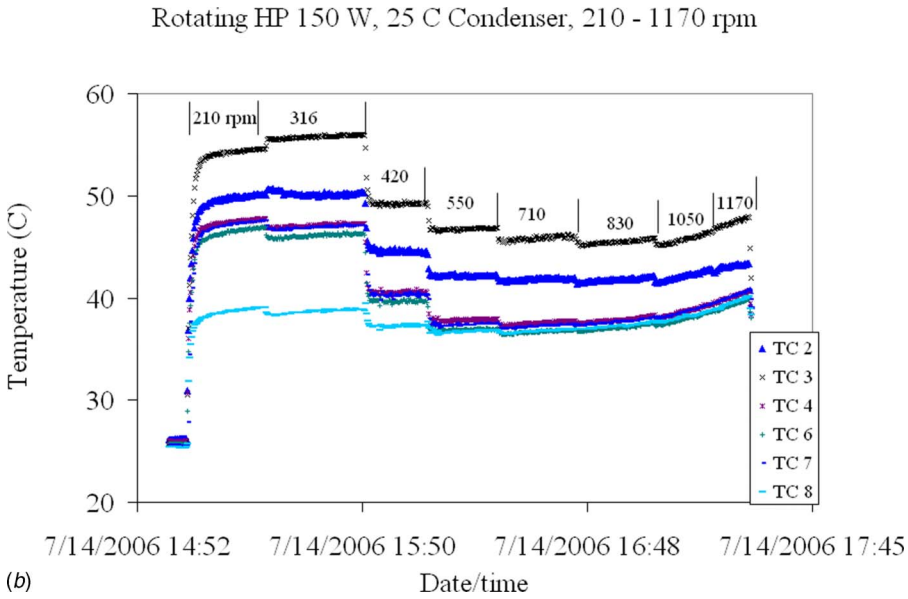

(b)

Fig. 5 Example data file for a rotating test with a 150 W heat load and a condenser temperature of 25°C

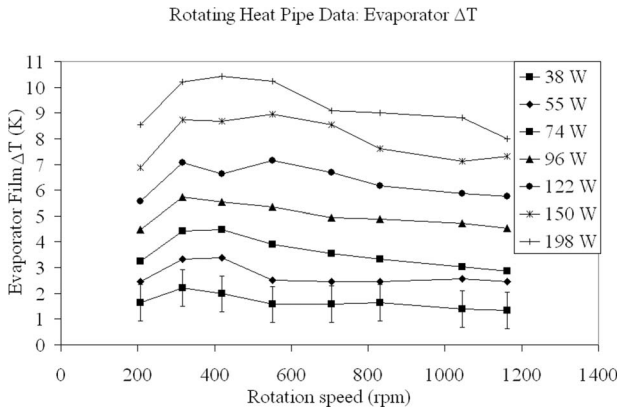

Fig. 6 Measured temperature difference across the evaporator liquid film for the rotating tests. All uncertainties are the same as the 38 W case.

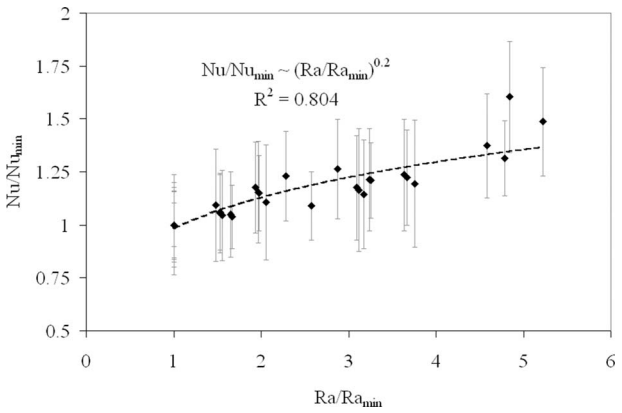

Fig. 8 Nusselt number for heat transfer across the evaporator film in the rotating heat pipe

counter flowing vapor, is being redistributed into the evaporator by the centrifugal force leading to a tighter coupling of the condenser section to the heat sink.

As shown in Fig. 5, TC3 measures the heat pipe wall temperature at the entrance to the evaporator section, while TC4 measures the temperature in the adiabatic section. Therefore, the temperature difference, TC3−TC4, is representative of the radial temperature difference across the evaporator liquid film. The measured temperature difference across the liquid film in the evaporator section (TC3−TC4) for the heat pipe rotating up to 1170 rpm is shown in Fig. 6. The figure shows that the temperature difference across the liquid film in the evaporator increases with rotation speed at low (<420 rpm) speed, then decreases as the rotation speed is increased. The data from these tests with increasing heater power are collapsed to a single curve, shown in Fig. 7, by evaluating the thermal conductance ($G=Q/\Delta T$) across the liquid film. As the temperatures differences in Fig. 6 would suggest, at low rotation speed, the conductance decreases with increasing rotation speed. The decrease in thermal conductance across the liquid film in the evaporator is caused by the redistribution of liquid in the heat pipe due to the centrifugal force. As the excess liquid charge drains from the condenser into the evaporator, the liquid film in the evaporator becomes thicker, decreasing the conductance. Once the rotation speed (and centrifugal force) is large enough to force all of the excess liquid into the evaporator (>420 rpm), further increases in rotation speed result in an increased thermal conductance across the liquid film. The increase in thermal conductance is likely due to an increase in the Nusselt number in the liquid film as the centrifugal force and Rayleigh number are increased.

From the conductance values shown in Fig. 7, the scaling between Nusselt number and Rayleigh number for the liquid film in the evaporator can be approximated. Assuming that the fluid properties are constant, the Rayleigh number increases as $\omega^2\Delta T$. Taking $(\omega^2\Delta T)_{\min}$ and $G_{\min}$ as the values from the 420 rpm data points, the ratios $G/G_{\min}$ and $(\omega^2\Delta T)/(\omega^2\Delta T)_{\min}$ are representative of $\mathrm{Nu}/\mathrm{Nu}_{\min}$ and $\mathrm{Ra}/\mathrm{Ra}_{\min}$, respectively, for the data points with a rotation speed greater than 420 rpm. This relationship is shown in Fig. 8. The figure indicates a power law relationship with an exponent of 0.2. Similar power law relationships have been suggested for buoyancy-driven convection in rotating boilers and in the evaporator sections of on-axis rotating heat pipes [20,21], as well as in laminar and turbulent natural convection in bottom heated cavities [22]. This observation would suggest that heat transfer across the liquid film in the evaporator section is influenced by buoyancy-driven convection.

4 Comparing Experimental Results to the Rotating Heat Pipe Model

The experimental results for heat transfer across the liquid film in the evaporator section and predictions from the rotating heat pipe thermal model discussed in Sec. 3.1 are compared in Fig. 9. The simulations qualitatively capture the behavior of the heat pipe. In particular, both model and experimental results suggest

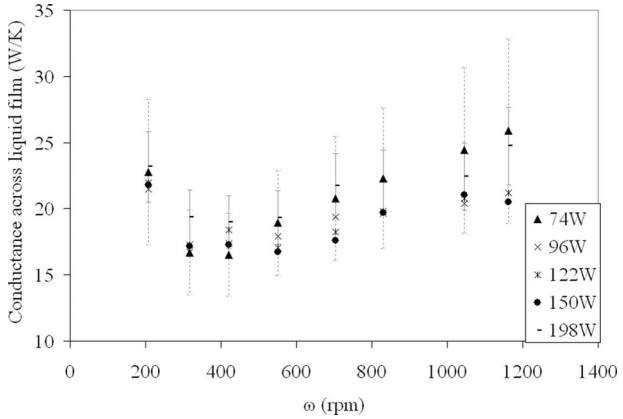

Fig. 7 Conductance across the liquid film in the evaporator section of the rotating heat pipe. The 74 W case gave the largest (dashed) error bar and the 198 W case gave the smallest (solid) error bar when calculating the conductance.

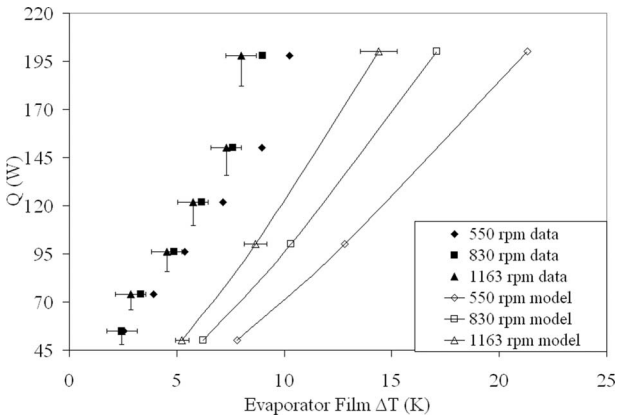

Fig. 9 Comparing measured temperature difference across the evaporator liquid film to the numerical model. Model predictions are shown as lines and experimental data as points.

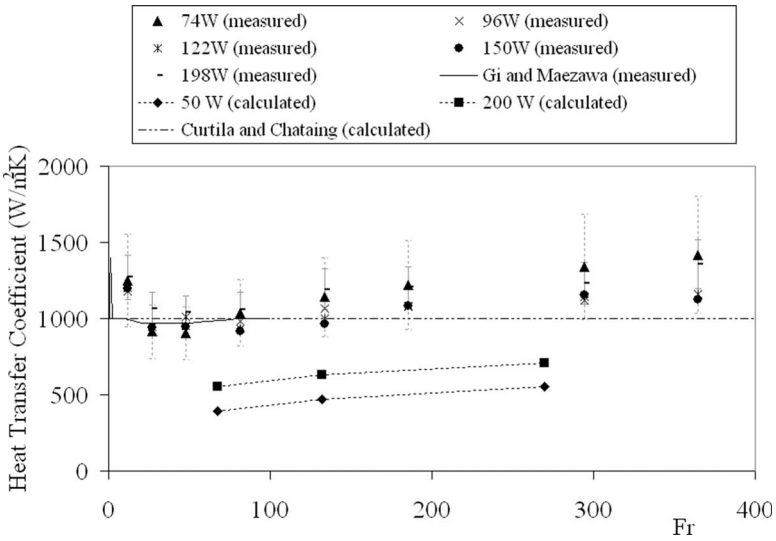

Fig. 10 Comparing heat transfer coefficients in the evaporator. Data labeled (measured) were measured heat transfer coefficients in the experiments performed here, and data labeled (calculated) are calculated values from the heat pipe thermal model described in Sec. 3.1. The dashed error bars are for the 74 W data and the 198 W error bars are solid.

that increases in rotation speed and decreases in heat transfer rate reduce the temperature difference across the liquid film in the evaporator section. Additionally, the slopes of the curves generated by the model are close to those observed in the experiments, suggesting that the model properly predicts the transition from operation with the wick full of liquid and the free-liquid flow regime and the associated redistribution of the working fluid. The model results, however, are overly conservative (that is, predicting higher temperature differences across the film for a given heat transfer rate).

The comparisons shown in Fig. 9 indicate that the model predicts lower heat transfer coefficients across the liquid film in the evaporator than are observed in the experiments. As discussed in Sec. 3.1, the liquid flow was assumed laminar and two dimensional (symmetry about the longitudinal axis) in the development of the numerical heat pipe model. Additionally, the effects of mixed convection, due to the liquid flow from the condenser to the evaporator, on the heat transfer coefficient in the evaporator were ignored. As we discuss below, these simplifying assumptions may contribute to the low estimates of the heat transfer coefficient in the evaporator section produced by the model.

4.1 Mixed Convection and Turbulence in the Liquid. When calculating the heat transfer coefficient in the evaporator, the heat pipe model ignores the presence of mixed convection in the liquid film by using a Nusselt number correlation for pure buoyancy-driven convection. A considerable amount of work has been done to assess the effect of buoyancy on forced convection between horizontal parallel plates [23,24] and in horizontal tubes [25,26]. Nusselt numbers for these mixed convection cases are calculated from the well-known formula for mixed convection, in general [27],

$$\mathrm{Nu}^n = \mathrm{Nu}_F^n + \mathrm{Nu}_N^n \tag{1}$$

where subscripts F and N represent Nusselt numbers for pure forced or natural convection, respectively, and $n=3$ is suggested to provide a best fit to the experimental data [24,25]. The relative importance of buoyancy to forced convection is assessed with the ratio $\mathrm{Gr}/\mathrm{Re}^2$, where the liquid film Reynolds number is based on the average velocity in the liquid layer and on the liquid layer thickness in the evaporator. Film Reynolds numbers developed in rotating heat pipes are typically very low (<100) because of the low flow rates required and the small film thickness. As a consequence, $\mathrm{Gr}/\mathrm{Re}^2 >> 1$ in the evaporator, and natural convection in the liquid film will dominate. In this situation, the forced convection component in Eq. (1) can be ignored.

Although the heat transfer coefficient in the evaporator can be calculated from a natural convection correlation, the transition to thermal turbulence in the heated liquid film may affect the dynamics of the liquid flow. Although Reynolds numbers in the liquid film are well below the transition value to induce hydrodynamic turbulence [13], as the Rayleigh number in the liquid film increases, the flow can transition due to thermal turbulence [26]. When calculating the liquid film thickness in the evaporator, the heat pipe thermal model assumes a laminar liquid flow. If thermal effects are significant enough to develop a turbulent flow in the evaporator, the velocity profile and liquid layer thickness will differ from the values calculated by the laminar flow model.

4.2 Three-Dimensional Pool Flow. The heat pipe thermal model assumes that the liquid flow is two dimensional, with the liquid forming a constant thickness annulus around the circumference of the heat pipe. In the experiment, however, the centrifugal force is large enough to overcome the circumferential pumping force of the porous wick in the off-axis evaporator section [28]. Therefore, the liquid will be forced to pool into a crescent shaped liquid layer on the outer wall, and only a portion of the circumference of the evaporator section will be covered with liquid. This three-dimensional behavior has not been captured in the numerical model and may explain the discrepancies observed when comparing predictions to the experiments.

When the liquid is forced to pool on the surface of the evaporator, the evaporator section behaves as a revolving heat pipe. Only a limited number of studies devoted to the heat transfer in revolving heat pipes have been carried out [4,29–31]. All of these studies had an experimental component, but only Curtila and Chataing [30] attempted to characterize the performance of their revolving heat pipe with a heat pipe model based on a thermal resistance network. In the model by Curtila and Chataing, the thermal resistance in the evaporator section of the revolving heat pipe is crudely estimated by assuming that half of the evaporator surface is covered by liquid with a boiling heat transfer coefficient of 2000 $\mathrm{W/m^2\,K}$. The heat transfer coefficient over the entire evaporator surface area is then estimated as 1000 $\mathrm{W/m^2\,K}$.

In Fig. 10, the measured heat transfer coefficients across the evaporator film from the heat pipe tested here are compared to the measured heat transfer coefficients reported by Gi and Maezawa [29]. The calculated heat transfer coefficient of Curtila and Chataing and the heat transfer coefficient calculated with the two-dimensional axisymmetric model described in Sec. 3.1, which assumes that the liquid is evenly distributed around the circumference, are also shown in the figure. The figure clearly shows that the heat pipe thermal model underestimates the heat transfer coefficient in the evaporator section, resulting in the high estimates of the temperature difference across the evaporator film shown in Fig. 10. Although the simple correlation provided by Curtila and Chataing does agree with both the experimental data collected here and the data of Gi and Maezawa, it does not account for the variations in heat transfer coefficient with rotation speed, fluid charge, working fluid properties, and heat pipe geometry.

Observations from experiments with rotating (on-axis) heat pipes at low speed also indicate that the annular flow assumption used here would underestimate the heat transfer coefficient when the liquid forms a pool in the evaporator section [32–34]. These experimental studies have shown that when the liquid in the on-axis rotating heat pipe transitions from pool flow to annular flow, the heat transfer coefficients in the condenser and evaporator decrease by typically an order of magnitude. The numerical model used here assumes that, regardless of the rotation speed, the liquid in the evaporator forms a continuous annulus around the circumference of the heat pipe. Although heat transfer coefficients in the pool flow regime have been measured, no correlations or theories are available to use in a design calculation.

The heat transfer coefficient in the evaporator section may also be enhanced (over the values observed in smooth-walled tubes) by the presence of the wick. Experimental investigations have found that shallow grooves on the inside wall of revolving heat pipes tend to spread the liquid over a larger area and increase the heat transfer coefficient [4,35,36]. The screen wick pressed against the wall by the centrifugal force may have the same effect as a grooved wall.

It is clear from the comparisons of the numerical and experimental results that more work is needed to characterize and quantify the heat transfer in revolving heat pipes and rotating heat pipes operating in the pool flow regime. The limited data available, however, do seem to confirm the presumption that the differences between the calculated and observed performance for the heat pipe studied here are in large part due to the three-dimensional nature of the flow in the revolving evaporator section. Furthermore, the comparisons of the heat transfer coefficients in pool flow and annular flow indicate that by assuming two-dimensional annular flow, the heat pipe thermal model will consistently overpredict the temperature difference across the evaporator liquid film.

5 Conclusions

A curved rotating heat pipe for use in rotating machines has been developed and tested. The heat pipe allows for a direct thermal coupling between an on-axis stationary refrigeration system and the off-axis heat generating components in a rotating machine. The heat pipe uses an annular gap wick structure for stationary (nonrotating) operation. A prototypical curved rotating heat pipe operating with methanol working fluid at room temperature was tested to ensure that the expected performance could be achieved in stationary operation and that the heat pipe would continue to perform at high rotation speeds. From the experimental studies, we found that the working fluid in the curved rotating heat pipe continued to circulate and did not suggest that a heat transfer limitation was encountered with rotation speeds up to 1200 rpm (corresponding centrifugal force in the off-axis evaporator section of nearly $400g$) and for heat transfer rates up to 200 W. The data collected in the experiments were shown to meet or exceed the performance expectations predicted by a two-dimensional rotating heat pipe thermal model [3], indicating that the numerical model is conservative and will overpredict the temperature difference between the heated off-axis evaporator section and the cooled on-axis condenser section.

Acknowledgment

Funding was provided by the Superconductivity Technology Center at the Los Alamos National Laboratory. Los Alamos National Laboratory is operated by Los Alamos National Security LLC for the Department of Energy.

Nomenclature

English

d_{max} = radial distance between the on-axis condenser and the off-axis evaporator
Fr = Froude number, $\omega^2 d_{max}/g$
g = acceleration due to gravity
G = thermal conductance
Gr = Grashof number
Nu = Nusselt number
Q = heat transfer rate
Ra = Rayleigh number
Re = Reynolds number

Greek

ΔT = temperature difference across the evaporator film
ω = rotation speed

Subscripts

F = forced convection component
loss = heat loss
min = minimum value
N = natural convection component
wall = evaluated at the wall of the heat pipe

References

[1] Ponnappan, R., and Leland, J. E., 1998, "Rotating Heat Pipe for High Speed Motor/Generator Cooling," Aerospace Power Systems Conference, Williamsburg, VA.
[2] Thoren, F., 1984, "Heat Pipe Cooled Induction Motors," 5th International Heat Pipe Conference, Tsukuba, Japan.
[3] Jankowski, T. A., 2007, "Numerical and Experimental Investigations of a Rotating Heat Pipe," Ph.D. thesis The University of New Mexico, Albuquerque, NM.
[4] Niekawa, J., Matsumoto, K., Koizumi, T., Hasegawa, K., Kaneko, H., and Mizoguchi, Y., 1981, "Performance of Revolving Heat Pipes and Application to a Rotary Heat Exchanger," 4th International Heat Pipe Conference, London, UK.
[5] Maezawa, S., Takuma, M., and Tsuchida, A., 1984, "Application of Disk-Shaped Rotating Heat Pipe to Brake Cooling," *Heat and Mass Transfer in Rotating Machinery*, Hemisphere, Washington, DC, pp. 659–668.
[6] Nerowski, G., Frauenhofer, J., Ries, G., Nick, W., and Neumuller, H. W., 2004, "Advances and Prospects of HTS Rotating Machine Development at Siemens," *IEEE Power Engineering Society General Meeting*, Vols. 1 and 2, pp. 2052–2055.
[7] Urbahn, J. A., Ackermann, R. A., Huang, X., Laskaris, E. T., Sivasubramaniam, K., and Steinbach, A., 2004, "The Thermal Performance of a 1.5 MVA HTS Generator," *Advances in Cryogenic Engineering: Transactions of the Cryogenic Engineering Conference*, Vol. 49, pp. 849–858.
[8] Unique Wire Weaving Co., Inc., 762 Ramsey Ave., Hillside, NJ 07205, SS Type 316 Plain Weave.
[9] Omega Engineering Inc., One Omega Drive, P.O. Box 4047, Stamford, CT 06907-0047.
[10] Figliola, R. S., and Beasley, D. E., 1995, *Theory and Design for Mechanical Measurements*, 2nd ed., Wiley, New York.
[11] Cotter, T. P., 1965, "Theory of Heat Pipes," Los Alamos National Laboratory, Report No. LA-3246-MS.
[12] Woloshun, K. A., Merrigan, M. A., and Best, E. D., 1988, "HTPIPE: A Steady-State Heat Pipe Analysis Program," Los Alamos National Laboratory, Report No. LA-11324-M.
[13] Daniels, T. C., and Al-Jumaily, F. K., 1975, "Investigations of the Factors Affecting the Performance of a Rotating Heat Pipe," Int. J. Heat Mass Transfer, **18**, pp. 961–973.
[14] Marto, P. J., 1976, "Performance Characteristics of Rotating, Wickless Heat

Pipes," 2nd International Heat Pipe Conference, Bologna, Italy.
[15] Sim, B. C., Kim, W. S., and Zebib, A., 2004, "Axisymmetric Thermocapillary Convection in Open Cylindrical Annuli With Deforming Interfaces," Int. J. Heat Mass Transfer, **47**, pp. 5365–5373.
[16] Pacheco, J. R., and Peck, R. E., 2000, "Nonstaggered Boundary-Fitted Coordinate Method for Free Surface Flows," Numer. Heat Transfer, Part B, **37**, pp. 267–291.
[17] Faghri, M., Sparrow, E. M., and Prata, A. T., 1984, "Finite-Difference Solutions of Convection-Diffusion Problems in Irregular Domains, Using a Non-orthogonal Coordinate Transformation," Numer. Heat Transfer, **7**, pp. 183–209.
[18] Song, F., Ewing, D., and Ching, C. Y., 2003, "Fluid Flow and Heat Transfer Model for High-Speed Rotating Heat Pipes," Int. J. Heat Mass Transfer, **46**, pp. 4393–4401.
[19] Roache, P. J., 1998, *Verification and Validation in Computational Science and Engineering*, Hermosa, Albuquerque, NM.
[20] Marto, P. J., 1984, "Rotating Heat Pipes," *Heat and Mass Transfer in Rotating Machinery*, Hemisphere, Washington, DC, pp. 609–632.
[21] Körner, W., 1970, "Effect of High Acceleration on Heat Transfer During Boiling," Chem.-Ing.-Tech., **42**, pp. 409–414.
[22] Bejan, A., 1995, *Convection Heat Transfer*, Wiley, New York, pp. 219–267.
[23] Osborne, D. G., and Incropera, F. P., 1985, "Experimental Study of Mixed Convection Heat Transfer for Transitional and Turbulent Flow Between Horizontal, Parallel Plates," Int. J. Heat Mass Transfer, **28**, pp. 1337–1344.
[24] Osborne, D. G., and Incropera, F. P., 1985, "Laminar, Mixed Convection Heat Transfer for Flow Between Horizontal Parallel Plates With Asymmetric Heating," Int. J. Heat Mass Transfer, **28**, pp. 207–217.
[25] Hieber, C. A., 1982, "Laminar Mixed Convection in an Isothermal Horizontal Tube: Correlation of Heat Transfer Data," Int. J. Heat Mass Transfer, **25**, pp. 1737–1746.
[26] Nagendra, H. R., 1973, "Interaction of Free and Forced Convection in Horizontal Tubes in the Transition Regime," J. Fluid Mech., **57**, pp. 269–288.
[27] Churchill, S. W., 1977, "A Comprehensive Correlating Equation for Laminar, Assisting, Forced and Free Convection," AIChE J., **23**, pp. 10–16.
[28] Semena, M. G., Khmelev, Y. A., and Shevel, E. V., 1991, "Distribution of Heat Transfer Agent in the Capillary Structure of Rotating Heat Pipes With a Displaced Axis of Rotation," J. Eng. Phys., **60**, pp. 642–645.
[29] Gi, K., and Maezawa, S., 1990, "Heat Transfer Characteristics of a Parallel Rotating Heat Pipe," 7th International Heat Pipe Conference, Minsk, USSR.
[30] Curtila, R., and Chataing, T., 1984, "Experimental Study of a Revolving Heat Pipe," 5th International Heat Pipe Conference, Tsukuba, Japan.
[31] Pokorny, B., Polasek, F., Schneller, J., and Stulc, P., 1984, "Heat Transfer in Co-Axial and Parallel Rotating Heat Pipes," 5th International Heat Pipe Conference, Tsukuba, Japan.
[32] Jian, C., Lou, D. Y. S., and Chuanjing, T., 1990, "Investigation of the Evaporation Heat Transfer in the Rotating Heat Pipes," 7th International Heat Pipe Conference, Minsk, USSR.
[33] Krivosheev, B. N., Kukharskii, M. P., and Portnov, V. D., 1979, "Heat Transfer in the Evaporator Section of a Rotating Heat Pipe at Low Rotational Speeds," J. Eng. Phys. Thermophys., **37**, pp. 773–778.
[34] Reddy, R. S., Venkateswarlu, P., and Sastri, V. M. K., 1990, "Effect of Inclination on the Performance of Rotating Heat Pipe," 7th International Heat Pipe Conference, Minsk, USSR.
[35] Castle, R. M., Thomas, S. K., and Yerkes, K. L., 2001, "The Effect of Working Fluid Inventory on the Performance of Revolving Helically Grooved Heat Pipes," ASME J. Heat Transfer, **123**, pp. 120–129.
[36] Klasing, K. S., Thomas, S. K., and Yerkes, K. L., 1999, "Prediction of the Operating Limits of Revolving Helically Grooved Heat Pipes," ASME J. Heat Transfer, **121**, pp. 213–217.

High Performance Recuperator With Oblique Wavy Walls

Kenichi Morimoto[1]
Mem. ASME
e-mail: kmrmt@se.ritsumei.ac.jp

Yuji Suzuki
Mem. ASME
e-mail: ysuzuki@thtlab.t.u-tokyo.ac.jp

Nobuhide Kasagi
Fellow ASME
e-mail: kasagi@thtlab.t.u-tokyo.ac.jp

Department of Mechanical Engineering,
The University of Tokyo,
Hongo 7-3-1, Bunkyo-ku,
Tokyo 113-8656, Japan

A series of numerical simulation of the flow and heat transfer in modeled counterflow heat exchangers with oblique wavy walls has been made toward optimal shape design of recuperators. The effects of oblique angles and amplitudes of the wavy walls are systematically evaluated, and the heat transfer and pressure loss characteristics are investigated. It is found that counter-rotating streamwise vortices are induced by the wavy walls, and the flow field has been drastically modified due to the intense secondary flow. By using the optimum set of oblique angle and wave amplitude, significant heat transfer enhancement has been achieved at the cost of relatively small pressure loss, and the j/f factor becomes much larger than that of straight square duct or conventional compact recuperators. When thermal coupling of hot and cold fluid passages is considered, the heat transfer is found to be strongly dependent on the arrangement of counterflow passages. The total heat transfer surface area required for a given pumping power and heat transfer rate can be reduced by more than 60% if compared to the straight square duct.
[DOI: 10.1115/1.2884187]

Keywords: recuperator, heat transfer enhancement, wavy wall, secondary flow, j/f factor

Introduction

With the increasing demand for high-efficiency energy utilization and low environmental impact, small-scale distributed energy systems with micro-gas-turbines have attracted growing attention. Recently, Uechi et al. [1] proposed a conceptual design of a 30 kW hybrid system of a micro-gas-turbine and a solid oxide fuel cell, which gives a power generation efficiency over 65%. It is shown in their cycle analysis that one of the most important technical issues for the system efficiency is to enhance the effectiveness of recuperator, which enables the heat recovery for improving the system performance.

Up to now, a number of compact heat exchangers have been proposed with various types of heat transfer enhancement technologies (e.g., Refs. [2–4]). Conventional heat augmentation methods are roughly grouped into four categories: (1) leading-edge effect through successive interruption of the thermal boundary layers, (2) vortex generator for offering streamwise vortical motions, (3) surface roughness for flow separation and reattachment, and (4) modification of primary heat transfer surfaces for inducing secondary flow. Among them, the former three are mainly effective for turbulent flows at the cost of relatively large pressure loss. On the other hand, for the gas turbine recuperators, the air flow Reynolds number is expected to be in the range of 100–500, when allowable pressure loss penalty is considered. Thus, the most rational way for the heat transfer enhancement in recuperators is presumably to employ the primary surface heat exchanger. McDonald [5] reported that the primary surface heat exchangers will satisfy the industrial requirements for design simplicity, material cost, maintenance cost, etc., and are in practical use in recuperated turbine systems.

In heat-exchanger passages with modified heat transfer surfaces, considerable heat transfer enhancement is attained because of the change of the streamline curvature and associated secondary flow. The cross-corrugated surface, which is called the chevron plate, and the wavy-plate-fin type of heat exchangers are widely used in many applications [3,4]. The flow-passage geometry is characterized by sinusoidal wavy surfaces, and the effects of geometrical parameters and flow conditions on the thermal-hydraulic performance have been extensively investigated both experimentally and numerically [6–9]. Recently, other heat exchangers with wavy-fin cores [10,11], cross-wavy [12], and corrugated undulated surfaces [13] have also been investigated based on computational fluid dynamics techniques, and fundamental characteristics of various types of compact heat exchangers have been accumulated. It is shown by Utriainen and Sundén [14] that the heat exchanger with cross-corrugated surface is expected to be more advantageous for the gas turbine recuperators than any other type of primary surface heat exchangers. However, the optimal shape of the flow passage, which maximizes the heat transfer at the cost of minimum pressure loss, has not been obtained even in the laminar flow regime due to the complexity of heat and fluid flow phenomena. Furthermore, constant wall temperature or constant heat flux conditions were employed in previous studies, and the effect of thermal coupling between adjacent flow passages was not taken into account.

The objectives of the present study are to propose a new design concept for compact recuperators and to obtain general strategy for heat transfer enhancement in laminar flows. In the present work, the flow-passage geometry based on a square duct and modified with oblique wavy top/bottom walls has been proposed in order to obtain heat transfer augmentation by deliberate use of the secondary flow. The heat-exchanger performances are evaluated through a series of numerical simulation of the momentum and heat transfer in modeled counterflow recuperators. The effects of oblique angles and amplitudes of the wavy walls upon the pressure loss and heat transfer characteristics are systematically investigated. In the present study, we focus on the heat-exchanger performances of the oblique-wave recuperator, and the thermal coupling effect between the hot and cold fluid passages.

Recuperator With Oblique Wavy Walls

Recuperator Configuration. Figure 1 shows the surface geometry of the passage with oblique wavy walls over one pitch, and computational grids with the boundary-fitted coordinate system. The top and bottom walls of a straight square duct are replaced

[1]Present address: Department of Micro System Technology, Faculty of Science and Engineering, Ritsumeikan University, Shiga 525-8577, Japan.

Contributed by the Heat Transfer Division of ASME for publication in the JOURNAL OF HEAT TRANSFER. Manuscript received September 27, 2006; final manuscript received July 22, 2007; published online August 7, 2008. Review conducted by Raj M. Manglik.

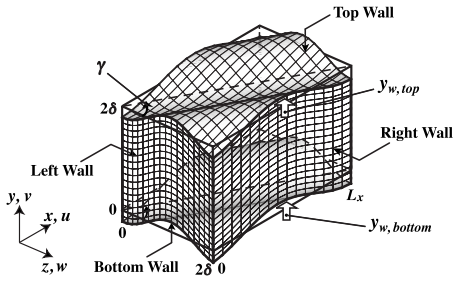

Fig. 1 Surface geometry of the passage with oblique wavy walls and computational grids with boundary-fitted coordinate system

with a pair of oblique wavy walls with the same geometry, while the left and right walls are kept flat. Surface shapes of the top and bottom walls are given by the following equation:

$$y_{w,\text{top}} = y_{w,\text{bottom}} = -A \cos \frac{2\pi}{L_x}(x - z \tan \gamma) \tag{1}$$

where A, L_x, and $\gamma(=\tan^{-1}(L_x/2\delta))$, respectively, denote the height amplitude, the streamwise length of one pitch, and the oblique angle of the wavy walls. Here, δ represents the half height of the straight square duct. The ridge/valley lines of the top and bottom walls are tilted from the main flow direction, and the angle is constant at γ. With the top/bottom walls defined by Eq. (1), the streamwise pitch L_x is given by $L_x=2\delta\tan\gamma$. The wall undulation of the top and bottom walls is parallel to each other, and its distance is 2δ. It is noted that the present flow-passage geometry confined with the sidewalls is different from that formed by the cross-corrugated plates [6–9] or other heat-exchanger passages previously proposed.

As shown in Fig. 2, two types of counterflow heat-exchanger configurations with staggered arrangement of hot and cold fluids are assumed. Each passage is surrounded by oblique wavy walls and flat sidewalls. The oblique angles of adjacent passages in Case 1 are identical in the spanwise (z) direction, while those in Case 2 are the same in magnitude, but opposite in sign. Thus, in Case 2, the top/bottom walls in the neighboring passages are mirror symmetry with respect to the dividing flat sidewalls (see Plane 2 in Fig. 2). Thermal resistance of the heat conduction in dividing walls is generally much smaller than that of the heat convection, and neglected throughout this study.

Numerical Procedure. The governing equations are the incompressible Navier–Stokes, continuity, and energy equations with constant physical properties. The present numerical scheme is based on the finite difference method with a generalized coordinate system [15]. A second-order finite difference scheme is used for the spatial discretization with the collocated grid system [16]. The flow is advanced in time by employing a second-order Adams–Bashforth scheme and a second-order Crank–Nicolson scheme for the nonlinear and viscous terms, respectively. The coupling of the velocity and pressure fields is based on the SMAC method [17], in which the pressure field is corrected by solving the Poisson equation to ensure the continuity at every time step. Air flows with the Prandtl number Pr=0.71 are assumed for both of the counterflowing fluids. After the velocity field is obtained, the energy equation is solved by a successive over-relaxation (SOR) method with the bulk mean temperature being constant at each inlet. When examining the heat transfer performance of an isolated passage, isothermal heated walls are assumed.

In the present study, thermal coupling between the neighboring passages is also considered in order to evaluate their heat-exchange performances; temperature and heat flux are assumed to be continuous at the dividing walls, i.e.,

$$T_{w,H} = T_{w,C}, \qquad \left.\frac{\partial T}{\partial n}\right|_{w,H} = \left.\frac{\partial T}{\partial n}\right|_{w,C} \tag{2}$$

where n refers to the wall-normal direction. A periodic boundary condition, similar to that of Patankar et al. [18], is imposed in the streamwise (x) direction for both flow and thermal fields. The dimensionless temperature which satisfies the periodic condition is described as

$$\theta(x,y,z) = \frac{T(x,y,z) - T_{w,m}(x)}{T_b(x) - T_{w,m}(x)} \tag{3}$$

with the mean wall temperature around the periphery of the duct,

$$T_{w,m}(x) = \int_\Gamma T_w d\Gamma \Big/ \int_\Gamma d\Gamma \tag{4}$$

and the bulk mean temperature,

$$T_b(x) = \int_{A_c} uTdA_c \Big/ \int_{A_c} udA_c \tag{5}$$

The hydraulic diameter D_h of the duct is defined by its volume V and the wall surface area A_s as

$$D_h = \frac{4V}{A_s} \tag{6}$$

in order to compensate the change of the heat transfer surface area and examine the effect of the geometrical change of the surfaces. The surface extension ratio of wavy ducts for different oblique angles at $A/\delta=0.25$ is tabulated in Table 1. The increase of the heat transfer surface area from straight square ducts is shown

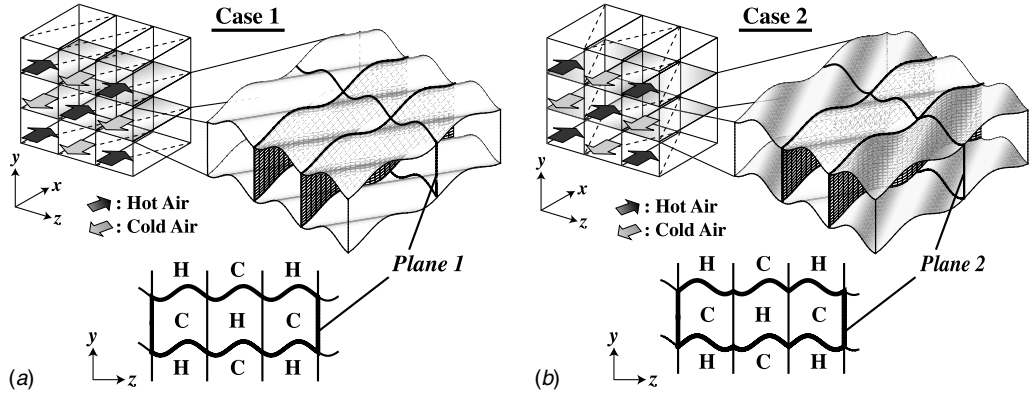

Fig. 2 Configurations of modeled counterflow heat exchangers: (*a*) Case 1 and (*b*) Case 2

Table 1 Surface extension ratio of wavy ducts for different oblique angles ($A/\delta=0.25$)

γ (deg)	38	45	50	56	60	66	72	78
$A_x/(A_s)_0\|_{\text{top,bottom}}$	1.32	1.26	1.22	1.19	1.18	1.16	1.15	1.14
$A_s/(A_s)_0(=1/D_h)$	1.16	1.13	1.11	1.10	1.09	1.08	1.08	1.07

separately for the wavy surface (top and bottom walls) and the total area including the sidewalls.

Unless otherwise mentioned, the Reynolds number Re_δ based on the bulk mean streamwise velocity U_b and 2δ is set constant at 200, while the Reynolds number Re based on the hydraulic diameter is 170–190 in the case of $A/\delta=0.25$ depending on the angle of the oblique walls. The Fanning friction factor f and the area-averaged wall shear stress are, respectively, given by

$$f=\frac{(\Delta p/L_x)D_h}{2\rho U_b^2} \tag{7}$$

and

$$\tau_{w,m}=\frac{1}{A_s}\int_S \tau_w dS=\frac{1}{A_s}\frac{\mathrm{Re}}{\frac{1}{2}\rho U_b^2}\int_S \mu\left.\frac{\partial u}{\partial n}\right|_w dS \tag{8}$$

where the pressure loss Δp represents the mean pressure difference between the inlet and outlet of the duct, and n corresponds to the inward normal direction on the wall. When δ is used for the length scale, the local wall shear stress is expressed as

$$\tau_w^*=\tau_w\frac{\delta}{2D_h} \tag{9}$$

The heat transfer coefficient and the mean Nusselt number averaged over the wall surface are, respectively, defined as follows:

$$h=\frac{q_{w,m}}{\Delta T_{\mathrm{lm}}}=\frac{1}{A_s\Delta T_{\mathrm{lm}}}\int_S -\lambda\left.\frac{\partial T}{\partial n}\right|_w dS, \tag{10}$$

$$\mathrm{Nu}=\frac{hD_h}{\lambda} \tag{11}$$

where the logarithmic-mean temperature difference is given by

$$\Delta T_{\mathrm{lm}}=\frac{T_b(L_x)-T_b(0)}{\ln\{T_{w,m}(0)-T_b(0)\}-\ln\{T_{w,m}(L_x)-T_b(L_x)\}} \tag{12}$$

The local heat flux on the wall is expressed in a nondimensional form as

$$q_w^*=\frac{q_w\delta}{\lambda\Delta T_{in}}=\frac{\delta}{\Delta T_{in}}\left(-\left.\frac{\partial T}{\partial n}\right|_w\right) \tag{13}$$

where ΔT_{in} corresponds to $(T_{b,I}-T_w)$ in the isothermal-wall condition and $(T_{b,I}|_H-T_{b,I}|_C)/2$ in the thermal coupling condition, respectively.

The goodness factor of the present heat-exchanger design is chosen as

$$\frac{j}{f}=\frac{\mathrm{Nu}\,\mathrm{Pr}^{-1/3}}{f\,\mathrm{Re}} \tag{14}$$

A uniform mesh is used in the x direction, while nonuniform meshes with a hyperbolic tangent distribution are used in the y and z directions to prepare denser grid points near the wall. The number of grid points is $32\times37\times37$ in the x, y, and z directions, respectively. The grid spacing in each direction is given in Table 2. In a straight square duct, the difference of the present computational results and the analytical solutions [19] is less than 0.3% both for the friction factor and the Nusselt number. It is shown in our grid refinement study that the computational results converge toward the analytical solution with the observed order of accuracy 2.0, and thus the second-order accuracy of the spatial discretization in the present numerical code was confirmed. We have also examined the effect of the grid number on the computational results for a wavy duct, as shown in Table 3. The difference between computed values of $f\mathrm{Re}$ and Nu is less than 1%. In the present simulations, the coarsest grid density is adopted.

The time step Δt, nondimensionalized by U_b and δ, is 0.01. The initial flow field is given by the analytical solution in a straight square duct. Most simulation required about 4000 time steps ($t=40$) to reach the steady state, where the convergence criterion defined by the residual of the continuity equation being less than 10^{-6} is satisfied. Although unsteady flows can be simulated with the present numerical method, laminar steady states have been reached in the Reynolds number range presently investigated.

Results and Discussion

Effect of Oblique Angle. Figure 3 shows the pressure loss and the friction drag normalized with those in a straight square duct versus the oblique angle γ. Here, the wave amplitude is kept constant at $A/\delta=0.25$. The pressure loss and friction drag characteristics are strongly affected by γ. As γ decreases, the $f\mathrm{Re}$ factor increases monotonically to $\gamma\sim45$ deg. When $\gamma<45$ deg, the mean pressure drop, i.e., $\Delta p/L_x$ in Eq. (7), continues to increase, but the value of D_h decreases considerably for small oblique angles because of the increase of the surface area. Thus, the $f\mathrm{Re}$ factor, which is proportional to the square of D_h, is maximized at $\gamma\sim45$ deg. The friction drag, on the other hand, has a different tendency with the oblique angle and takes its maximum value at $\gamma\sim55$ deg.

Figure 4 shows the mean Nusselt number defined by Eq. (11) versus γ. The Nusselt number also exhibits significant dependency on γ and becomes much larger than that in a straight square duct. Under the isothermal-wall condition, the peak value is 2.2 times as large as Nu in the straight square duct. Note that, since the increase of heat transfer surface area has been compensated in Eq. (6), the net amount of heat transfer rate and pressure loss is

Table 2 Number of grid points with the grid spacing in each direction (Δx is shown for $\gamma=1$ deg)

(N_x,N_y,N_z)	$\Delta x/\delta$	$\Delta y/\delta$	$\Delta z/\delta$
(32,37,37)	1.08×10^{-1}	$(4.65-6.10)\times10^{-2}$	$(4.65-6.10)\times10^{-2}$

Table 3 Computed values in a wavy wall with $A/\delta=0.25$ and $\gamma=60$ deg ($\mathrm{Re}_\delta=200$) for different grid densities

Number of grid points N_x, N_y, N_z	$f\mathrm{Re}$	$\mathrm{Nu_r}$	$\mathrm{Nu_{Case1}}$	$\mathrm{Nu_{Case2}}$
32,37,37	1.540	1.936	1.584	1.863
32,73,37	1.547	1.941	1.587	1.865
48,49,49	1.551	1.943	1.590	1.867

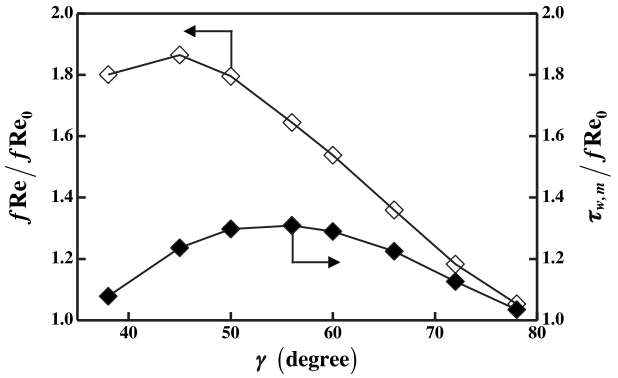

Fig. 3 Pressure loss and friction drag versus the oblique angle for Re_δ=200 and A/δ=0.25

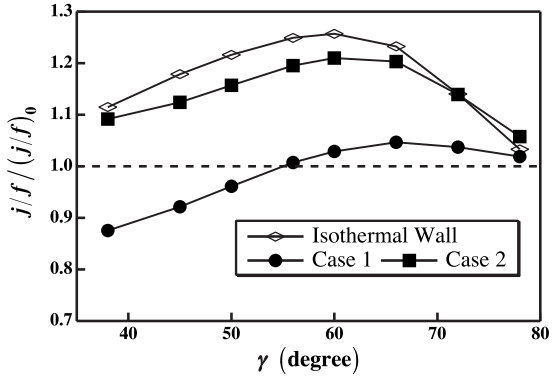

Fig. 5 j/f factor versus the oblique angle for Re_δ=200 and A/δ=0.25

further increased depending on the geometrical parameters. When γ=45 deg, the absolute values of the pressure drop and the heat transfer coefficient under the isothermal-wall condition are, respectively, 2.4 and 2.8 times as large as the corresponding ones in the straight square duct.

Although Nu has its peak at $\gamma\sim$45 deg under all the thermal boundary conditions, the maximum value is sensitive to the thermal boundary condition; Nu for Case 1 is 22% lower than that for the isothermal-wall condition. On the other hand, Nu for Case 2 is only 5% lower at most. This drastic change can be explained by the flow and thermal fields in the duct described later. Since the mean temperature difference defined by Eq. (12) is within 2% for different boundary conditions, the change of Nu is mainly due to the change of the wall heat flux averaged over the surface.

Figure 5 shows the j/f factor versus γ. Under the isothermal-wall condition, the j/f factor becomes larger than that of the corresponding straight square duct by up to 25%. Although the Nusselt number is maximized at $\gamma\sim$45 deg, the j/f factor has its peak at $\gamma\sim$60 deg. This is because the pressure drag, which corresponds to the deviation of fRe over τ_w, is also very large at $\gamma\sim$45 deg due to intense flow separation, as shown in Fig. 3. Therefore, in the present wavy duct, the heat transfer augmentation with flow separation/reattachment is not effective from the viewpoint of increasing the j/f factor. On the other hand, the friction drag is maximized at $\gamma\sim$60 deg as shown in Fig. 3. It is conjectured that the wall shear flow has significant contribution to large j/f, and this fact is examined later in Figs. 8–10.

Effect of Wave Amplitude. The effects of wave amplitude A are examined for the oblique angles of γ=50 deg and 60 deg.

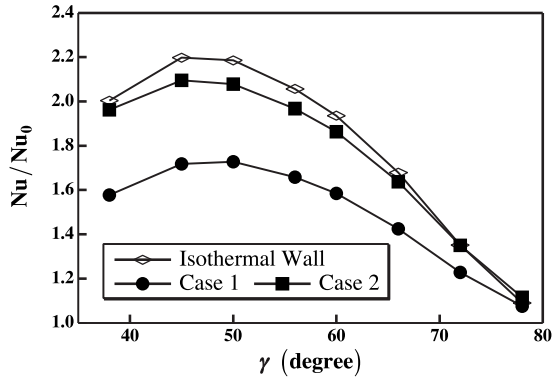

Fig. 4 Averaged Nusselt numbers versus the oblique angle for Re_δ=200 and A/δ=0.25

Figures 6 and 7 show the profiles of fRe, τ_w, Nu, and j/f factor under the thermal coupling condition of Case 2. Each quantity is normalized by that in a straight square duct. With increasing the wave amplitude, fRe, τ_w, and Nu are increased monotonically. The friction drag for γ=50 deg is almost the same as that for γ=60 deg, while the total pressure loss for γ=50 deg is much larger than that for γ=60 deg. This is due to the increase of pressure drag associated with enlarged flow separation bubble (not shown).

As shown in Fig. 7(*a*), the Nusselt number for γ=50 deg is larger than that for γ=60 deg regardless of the wave amplitude. On the other hand, it is seen from Fig. 7(*b*) that the j/f factor has its peak at A/δ=0.20 and 0.25, respectively for γ=50 deg and 60 deg. Although no significant difference is observed in the region of small wave amplitudes, at $A/\delta>$0.20, the j/f factor for γ=60 deg becomes appreciably larger than that for γ=50 deg. This is because the flow separation becomes less significant with larger oblique angle of γ=60 deg, where the j/f factor character-

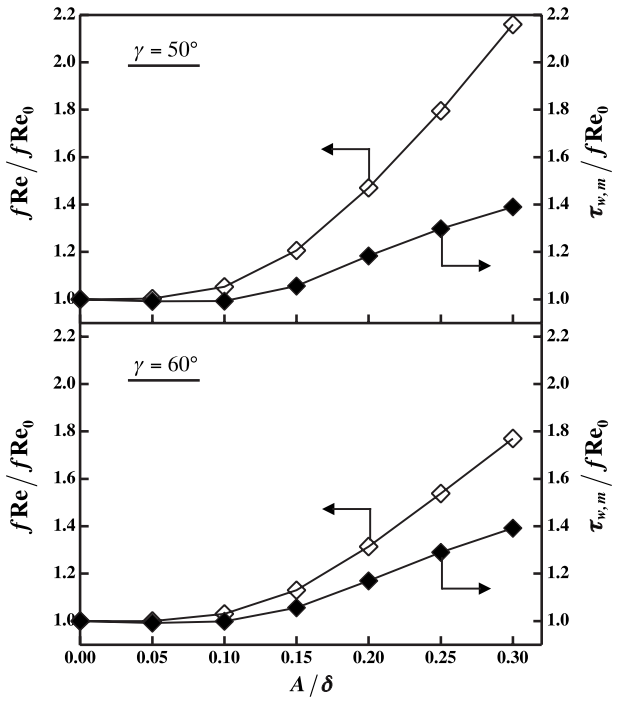

Fig. 6 Pressure loss and friction drag versus the wave amplitude for γ=50 deg and 60 deg (Re_δ=200)

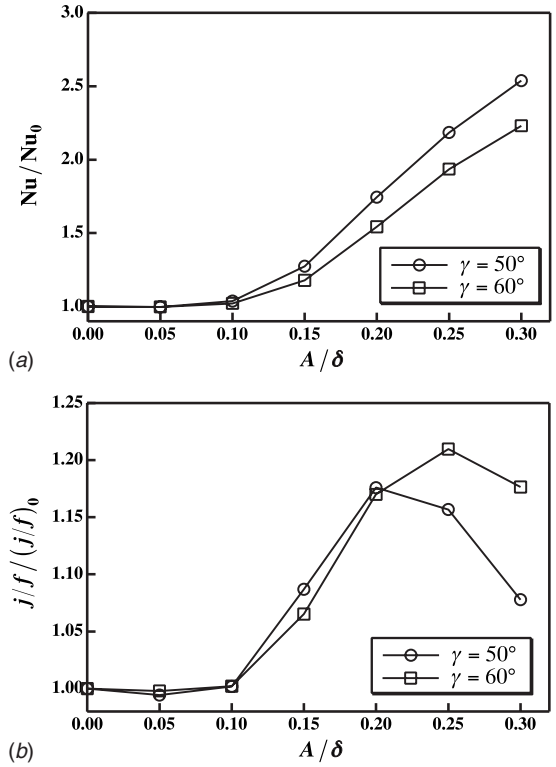

Fig. 7 Effect of wave amplitudes on the heat transfer in Case 2 (Re_δ=200): (*a*) averaged Nusselt number and (*b*) *j*/*f* factor

istic is improved. When γ=50 deg, on the other hand, the sensitivity of the pressure loss with respect to the wave amplitude, which corresponds to the slope of the *f*Re profile in Fig. 6, is more pronounced than that of the Nusselt number. In the following section, we investigate the detailed mechanism of heat transfer enhancement in the present heat-exchanger passages, mainly for γ=60 deg.

Mechanism of Heat Transfer Enhancement. Hereafter, the wave amplitude is kept constant at A/δ=0.25. Figures 8 and 9 show the wall shear stress vectors on the bottom wall, and the velocity vectors in the cross-stream planes at different streamwise positions with contours of the streamwise velocity. As shown in Fig. 8(*a*), the oblique wavy wall induces a flow along the valley (A) and a flow over the hill toward the left wall (B), which is caused by the pressure difference across the wavy wall. There exists a small separation bubble (C) near the left wall. Its size is dependent on the magnitude of the flow over the hill near the left wall (D), and increases with decreasing γ. The flow along the valley changes its direction upward by the interaction with the

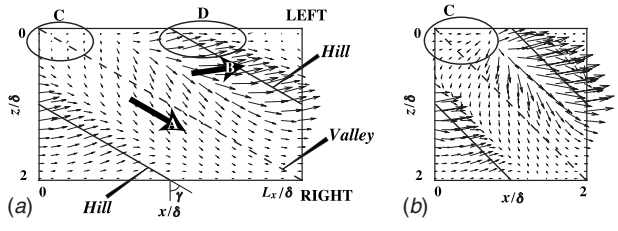

Fig. 8 Wall shear stress vectors on the bottom wall projected onto the *x*-*z* plane (Re_δ=200 and A/δ=0.25). The vector corresponds to ($\partial u/\partial n, \partial w/\partial n$), nondimensionalized by U_b and δ: (*a*) γ=60 deg and (*b*) γ=45 deg

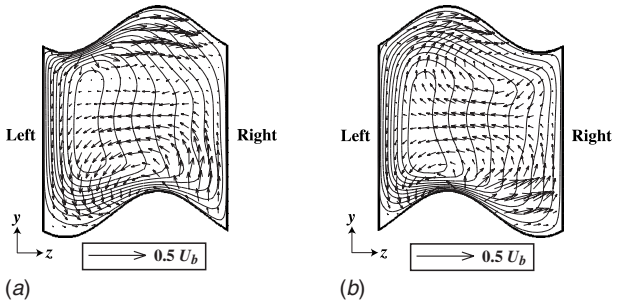

Fig. 9 Velocity vectors and isocontours of the streamwise velocity in the *y*-*z* planes (Re_δ=200 with A/δ=0.25 and 60 deg): (*a*) x/δ=0.43 and (*b*) x/δ=3.0. The contour increment is $0.2U_b$. Refer to Fig. 10 for the streamwise positions.

right wall. In combination with the vigorous flow over the hill toward the low-pressure valley region, a pair of counter-rotating vortices is formed, as shown in Fig. 9. The magnitude of this secondary flow induced by the vortices is extremely large, and the wall-normal velocity reaches up to 25% of the bulk mean velocity. The high-speed region is shifted to the left wall by the secondary flow.

Figure 10 shows the streamwise vortices extracted with the second invariant of the deformation tensor [20], defined by $\Pi = u_{i,j}u_{j,i}$. Its negative value indicates the region where the rotation of a fluid element exceeds the strain in strength. It is observed that a pair of vortical structures is formed on the top and bottom walls. Although the vortex formation mechanism near the top and bottom walls is the same, the vortices are displaced in the streamwise direction, because the hill/valley of the walls is shifted by $L_x/2$, as can be seen in Fig. 10. Figure 11 shows contours of the wall shear stress on each wall calculated from Eq. (9). On the top and bottom walls, the wall shear stress just upstream the ridge of the hill becomes large. The magnitude of the wall shear stress on the left wall is considerably larger than that on the right wall, because the high-speed fluid is shifted to the left side of the duct.

Figure 12 shows the velocity vectors and contours of temperature in the cross-stream plane at x/δ=3.0 under the thermal coupling condition. The thermal fields in two types of counterflow configurations exhibit appreciably different patterns, depending on the spanwise allocation of neighboring cold fluids. In Case 1, the sidewalls having higher heat transfer performances share the left wall of the central duct. Therefore, the heat transfer is remarkably enhanced across the dividing wall. On the other hand, the walls having lower performances share the right wall, and thus the heat transfer there is markedly deteriorated. In Case 2, each of the

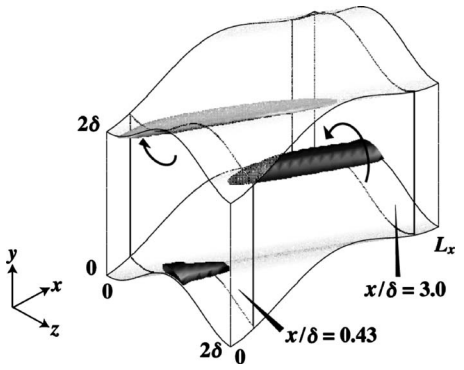

Fig. 10 Isosurfaces of the second invariant of the deformation tensor (Π<−5.0) for Re_δ=200 with A/δ=0.25 and γ=60 deg: black, streamwise vorticity ω_x<0; gray, ω_x>0

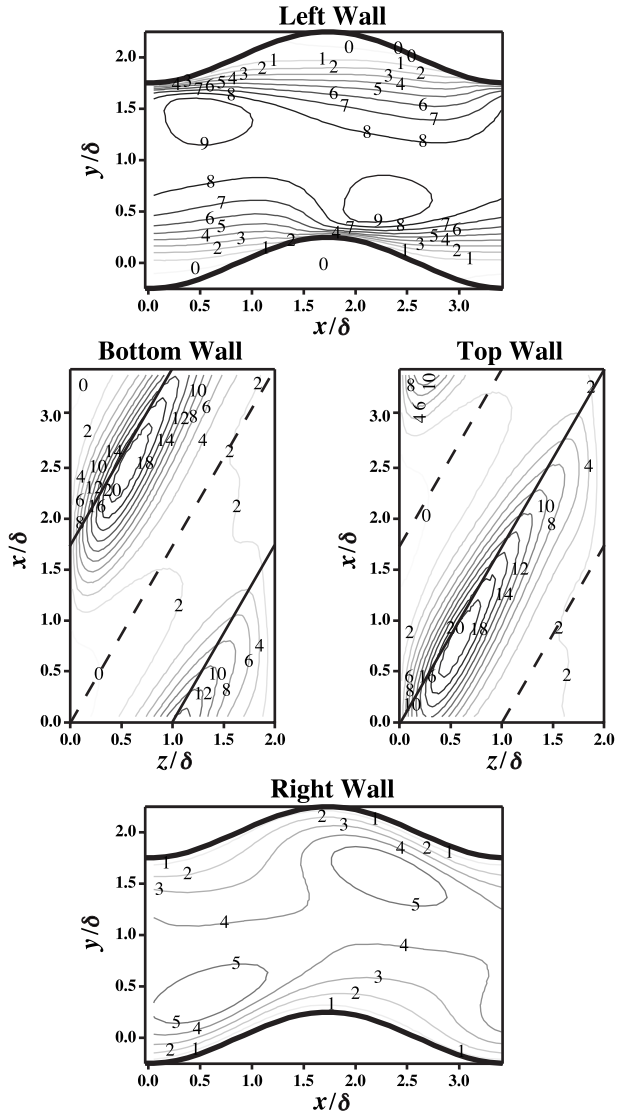

Fig. 11 Distribution of the streamwise wall shear stress for Re_δ=200 with A/δ=0.25 and γ=60 deg

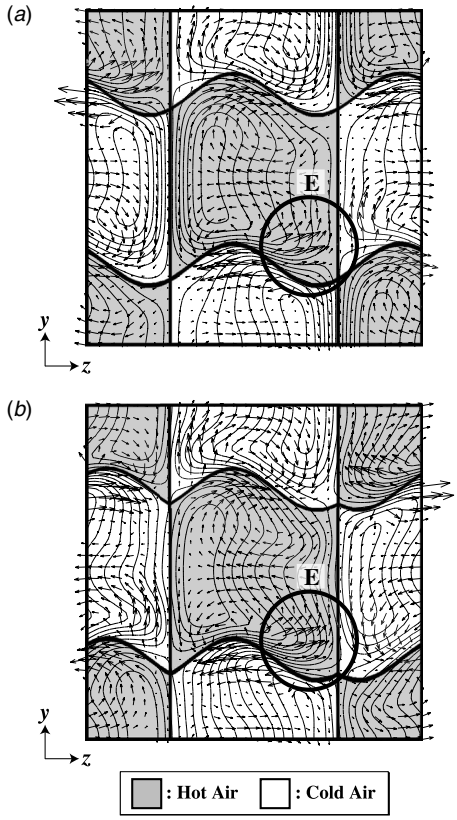

Fig. 12 Velocity vectors and isocontours of temperature under thermal coupling condition in the *y-z* plane at x/δ=3.0 for Re_δ =200 with A/δ=0.25 and γ=60 deg: (*a*) Case 1 and (*b*) Case 2. The contour increment is $0.1\times(T_{b,l}|_H - T_{b,l}|_C)$

sidewalls shares the walls with higher and lower performances in a similar way, so that the total heat transfer is the same on the left and right walls. However, in Case 2, contours of the temperature near the right wall are located closer to the wavy wall (E), which makes the temperature gradient much steeper than in Case 1.

Figure 13 shows wall heat flux distributions on the bottom wall under different thermal boundary conditions calculated from Eq. (13). Under the isothermal-wall condition, distribution of the wall heat flux is similar to that of the wall shear stress shown in Fig. 11. Therefore, the similarity between the momentum and heat transfer holds. On the other hand, the wall heat flux distributions in Cases 1 and 2 are significantly changed due to the thermal coupling effect; whereas the heat flux on the bottom wall is decreased near the left wall ($z/\delta<1$), the heat flux is markedly increased near the right wall ($z/\delta>1$) if compared with that of the isothermal wall, which causes the dissimilarity between the wall shear stress and wall heat flux distributions. The net amount of heat transfer on the sidewalls is almost the same in Cases 1 and 2, as shown later. However, in Case 2, the heat transfer is augmented in broader regions over the top and bottom walls, and this results in larger total heat transfer.

Reynolds Number Dependency. Figure 14 shows Nu and j/f for different Reynolds numbers. The performance of conventional compact heat exchangers, which is derived from the correlations provided by Utriainen and Sundén [14,21], is also plotted for comparison. Here, the data sets for cross-corrugated, cross wavy, and cross undulated surfaces are extrapolated from available data [7,12] by using the least squares method. The data for the plate-fin surface refer to the offset strip fin heat exchanger (1/10–19.74), of which correlations are obtained from Manglik and Bergles [22]. It is seen that the Nusselt number of the present recuperator is almost similar to that of the heat exchanger with cross-wavy surfaces. On the other hand, the friction factor for the same Nu is much smaller in the present recuperator. Therefore, the j/f factor becomes much larger than that of the cross-wavy exchanger, and, in Case 2, even exceeds the value of cross-corrugated-type heat exchanger. It is also found that the j/f factor is strongly dependent on the Reynolds number. When Re_δ=100, the j/f factor for Cases 1 and 2 remains below the value of the straight duct. The j/f factor is increased with Re_δ, but gradually saturated. With the present duct, the superiority of Case 2 over Case 1 is the most significant at Re_δ=200.

Figure 15 shows the heat flux integrated over the bottom and top walls (denoted by BT) and sidewalls (LR) for different Reynolds numbers. Each quantity is normalized with its corresponding value in a straight square duct. Regardless of the thermal boundary condition, the contribution of BT to the total heat transfer is larger than that of LR. The amount of heat fluxes on LR is the largest on the isothermal wall for all the Reynolds numbers examined here. On the other hand, the difference between BT and

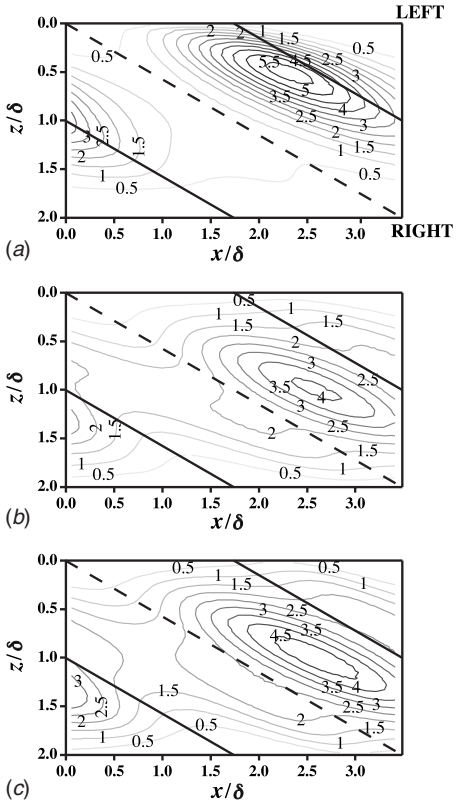

Fig. 13 Distribution of the heat flux on the bottom wall under each thermal boundary condition for Re_δ=200 with A/δ=0.25 and γ=60 deg: (*a*) isothermal heated condition, (*b*) coupling condition (Case 1), and (*c*) coupling condition (Case 2)

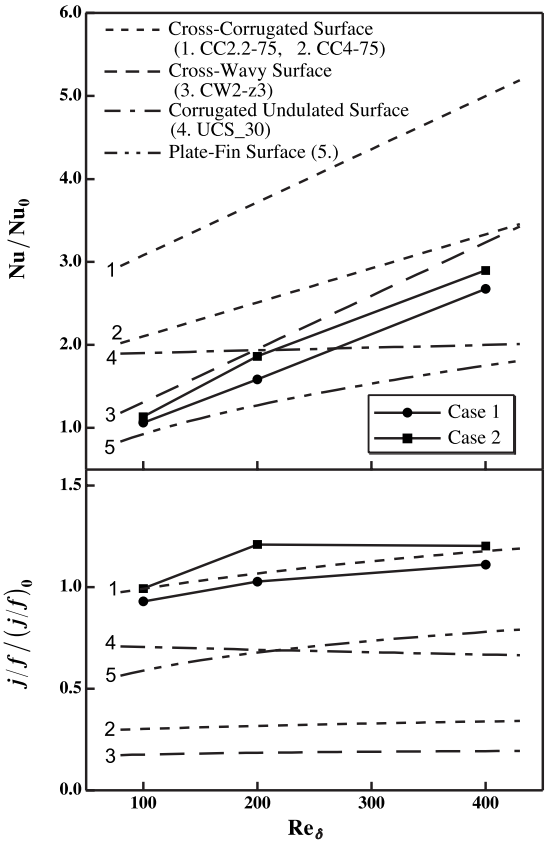

Fig. 14 Effect of Reynolds numbers on the Nusselt number and *j*/*f* factor with A/δ=0.25 and γ=60 deg. Reference data for conventional compact heat exchangers are plotted from the correlations provided in Refs. [14,21].

LR is increased with increasing Reynolds number. The increase of heat flux on BT has a dominant contribution to the heat transfer performance of the present recuperator. When Re_δ=100 and 200, the heat transfer on BT becomes largest under the thermal coupling condition of Case 2. The difference of the heat transfer on BT between Cases 1 and 2 is largest at Re_δ=200, where the effect of thermal coupling condition on the overall heat transfer is the most significant with the present duct geometry. When Re_δ=400, on the other hand, the heat transfer becomes largest under the isothermal-wall condition.

Figure 16 shows contours of the streamwise velocity and temperature under the thermal coupling condition for Re_δ=400. At this Reynolds number, the velocity and thermal fields are altered by more intense secondary flow than those for Re_δ=200. It is seen from Fig. 16(*a*) that the velocity contours in the central region of the duct are distorted drastically toward the left wall. The high-speed regions near the left wall are split off in the *y* direction, and become broader above the wavy wall along the *z* direction (F). The mean wall shear stress on the top and bottom walls is increased to about 188% of that of the straight duct, which is 1.5 times as large as that for Re_δ=200. Moreover, since high-speed regions also approach closer to the right wall (G), the wall shear stress there is increased significantly. The distributions of the wall heat flux under each thermal boundary condition exhibit more similar patterns than those for Re_δ=200 (not shown).

Recuperator Compactness. Finally, the compactness of the present recuperator is examined after Cowell [23]. Among various heat transfer performance indices for evaluating different compact heat exchangers (e.g., Webb [3]), the net amount of heat transfer surface area under the fixed pumping power is employed here. It is assumed that the heat transfer rate Q is achieved at the mass flow rate $\dot{m}$ under the effective temperature difference ΔT. Hereafter, ρ, c_p, and μ denote the fluid density, specific heat capacity, and viscosity, respectively. For simplicity, the thickness of the wall is assumed to be zero, and thus the heat-exchanger frontal area A_{fr} is equivalent to the heat-exchanger minimum free flow area.

The total heat transfer surface area A_s is given by

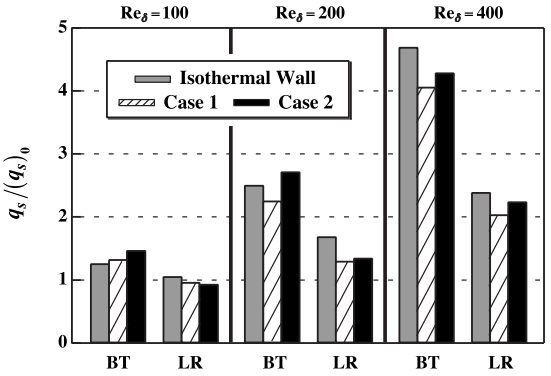

Fig. 15 Effect of Reynolds numbers on the total amount of heat flux of the bottom and top walls (BT) and the sidewalls (LR) with A/δ=0.25 and γ=60 deg.

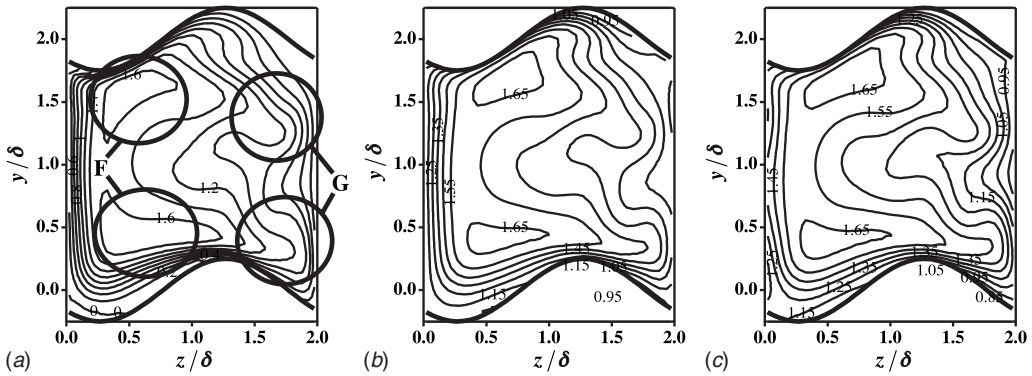

Fig. 16 Isocontours of velocity and thermal fields in the *y-z* plane at $x/\delta=3.0$ for $\mathrm{Re}_\delta=400$ ($A/\delta=0.25$ and $\gamma=60$ deg): (*a*) streamwise velocity, (*b*) temperature in Case 1, and (*c*) temperature in Case 2. Velocity and temperature are scaled by U_b and $T_{b,i}|_H - T_{b,i}|_C$, respectively.

$$A_s = \frac{Q}{h\Delta T} \tag{15}$$

where the mean heat transfer coefficient h is expressed from the Colburn heat transfer modulus j as

$$h = \frac{\dot{m}c_p}{A_{\mathrm{fr}}} j\,\mathrm{Pr}^{-2/3} \tag{16}$$

From the definition of the Reynolds number with $\dot{m}$ and A_{fr}, the hydraulic diameter D_h is expressed as

$$D_h = \frac{A_{\mathrm{fr}}\mu}{\dot{m}}\,\mathrm{Re} \tag{17}$$

By using Eq. (17), the total volume of the heat exchanger V and the pumping power P are, respectively, rearranged as follows:

$$V = \frac{A_s}{4}D_h = \frac{A_s}{4}\frac{A_{\mathrm{fr}}\mu}{\dot{m}}\,\mathrm{Re} \tag{18}$$

and

$$P = f\frac{2L}{D_h}\frac{\dot{m}^3}{\rho^2 A_{\mathrm{fr}}^2} = f\frac{2L\dot{m}^4}{\mu\rho^2 A_{\mathrm{fr}}^3\,\mathrm{Re}} \tag{19}$$

By substituting Eqs. (15) and (16) into Eq. (18), the length of the heat exchanger L can be written as

$$L = \frac{V}{A_{\mathrm{fr}}} = \frac{Q\mu\,\mathrm{Pr}^{2/3}}{4\dot{m}^2 c_p\Delta T}\frac{\mathrm{Re}}{j}A_{\mathrm{fr}} \tag{20}$$

The length L for a given Q and P is deduced by eliminating A_{fr} from Eqs. (19) and (20), and finally expressed as

$$L^2 = \frac{Q^3\mu^2\,\mathrm{Pr}^2}{32\dot{m}^2 c_p^3\Delta T^3\rho^2 P}\frac{f\,\mathrm{Re}^2}{j^3} \tag{21}$$

For a given Q and P, the first term of the right-hand side of Eq. (21) is kept constant with constant fluid properties. Moreover, A_s is proportional to L for a given A_{fr}. Therefore, for a constant Reynolds number, the amount of heat transfer surface area compared to that of the straight square duct can be derived as

$$\frac{A_s}{(A_s)_0} = \frac{L}{L_0} = \frac{1}{j/j_0}\frac{1}{\sqrt{j/f/(j/f)_0}} \tag{22}$$

See Ref. [23] for further information in deriving such indices based on the number of heat transfer units N_{tu}.

In Fig. 17, contours of the heat transfer surface area given by Eq. (22) is shown as a function of the j and j/f factors for $\mathrm{Re}_\delta=200$. The j factor is calculated based on $D_h=2\delta$, in order to examine the net increase of the heat transfer rate. Performances of the present recuperator with different wave amplitudes are also plotted, where the oblique angle of each computational result is displayed. It is seen that, for large oblique angles, the heat transfer surface area is almost the same regardless of the wave amplitude. For small oblique angles, on the other hand, the behavior of each profile is significantly affected by the wave amplitude. When $(A/\delta,\gamma)=(0.25,60\ \mathrm{deg})$, or $(0.30,66\ \mathrm{deg})$, the maximum j/f factor is obtained. With these design parameters, the heat transfer surface area can be reduced to ~40% compared to the straight square duct. For $(A/\delta,\gamma)=(0.30,45\ \mathrm{deg})$, where the largest j factor is obtained, the surface area can be further reduced to ~30%. It is obvious from Eq. (22) that the power of the j factor is twice as large as that of the j/f factor, so that the j factor plays a dominant role in determining the compactness.

It is also noted that the profiles of the heat transfer surface area with $A/\delta=0.20$ and 0.25 have a kink at small γ. This corresponds to the existence of the minimum value in $A_s/(A_s)_0$, as can be expected from the j/f factor characteristics shown in Figs. 5 and 7. The minimum values of $A_s/(A_s)_0$ are, respectively, 0.45 and 0.35 for $A/\delta=0.20$ and 0.25. Although the focus of the present study is on the maximization of the j/f factor, which is crucial for recuperators of gas turbines, the present recuperator exhibits extremely high performance also in the context of compactness of the core size of the heat exchanger, when the smaller oblique angle is employed.

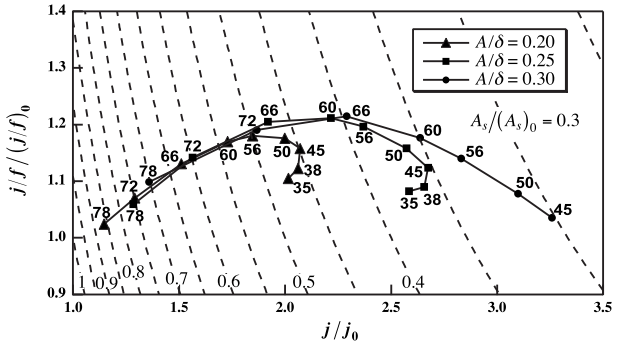

Fig. 17 Contour plot of heat transfer surface area required for constant heat-exchanger performances for $\mathrm{Re}_\delta=200$. Each symbol is marked with the indices representing the oblique angle of the wavy wall.

Conclusions

A series of numerical simulation of the flow and heat transfer in modeled counterflow heat exchangers with oblique wavy walls has been made toward optimal shape design of recuperators. The effects of oblique angles and amplitudes of the wavy walls are systematically evaluated, and the heat transfer and pressure loss characteristics are investigated. The following conclusions are derived.

1. The flow structures are drastically modified due to the counter-rotating streamwise vortices induced by the oblique wavy walls. The heat transfer is significantly enhanced by the strong secondary flows, while the flow separation is suppressed at the minimum level. The j/f factor becomes 1.2 times as large as that in the straight square duct.
2. With increasing wave amplitude, the j factor is monotonically increased in the range presently examined, while the flow separation becomes more significant. Thus, the optimum wave amplitude exists for maximizing the j/f factor with fixed oblique angle.
3. Since the flow field becomes highly asymmetric in the spanwise direction, heat transfer characteristics are strongly dependent on the heat-exchanger configurations of counterflowing hot and cold fluid passages. Heat-exchanger performance is maximized when the sidewalls having larger and smaller heat transfer coefficients share the same dividing wall. Hence, it is critically important to take the thermal coupling effect into account in order to make quantitative assessment of the performances of this type of heat exchangers.
4. Although the heat transfer and pressure loss characteristics are strongly dependent on the Reynolds number, the present recuperator exhibits extremely large j/f factors for $\mathrm{Re}_\delta = 200$. Due to the large values of both j and j/f factors, the total heat transfer surface area required for achieving the prescribed overall performance can be reduced by more than 60% if compared with the straight square duct.

Acknowledgment

The authors are grateful to Professor Naoki Shikazono of the University of Tokyo for valuable discussions during the course of this work. One of the authors (K.M.) appreciates generous support from Dr. Takanori Hino and his colleagues at the National Maritime Research Institute (NMRI), Japan, in completing the manuscript. The financial support through the Grant-in-Aid for JSPS Fellows (No. 15-11654) by the Ministry of Education, Culture, Sports, Science, and Technology of Japan (MEXT) is also acknowledged.

Nomenclature

A = wave amplitude
A_c = cross-sectional area of the duct
A_{fr} = heat-exchanger frontal area
A_s = total heat transfer surface area
D_h = hydraulic diameter of the flow passage
f = Fanning friction factor
h = averaged heat transfer coefficient
j = Colburn heat transfer modulus
L = length of the total heat exchanger
L_x = length of the periodic duct in the streamwise direction
$\dot{m}$ = mass flow rate
n = wall-normal direction
Nu = averaged Nusselt number
p = pressure
P = pumping power
Pr = Prandtl number
q_s = total amount of wall heat flux
q_w = wall heat flux
Q = heat transfer rate
Re = Reynolds number ($=U_b D_h/\nu$)
Re_δ = Reynolds number ($=U_b 2\delta/\nu$)
S = heat transfer surface
T = temperature
T_b = bulk mean temperature
$T_{w,m}$ = mean wall temperature
ΔT_{lm} = logarithmic-mean temperature difference
u,v,w = velocity components in x, y, and z directions, respectively
U_b = bulk mean velocity
V = volume of the heat exchanger
x,y,z = Cartesian coordinates
y_w = wall deformation in the y direction

Greek Symbols

δ = half duct height of the base line square duct
γ = oblique angle of the wavy wall
Γ = periphery of the duct
λ = thermal conductivity
μ = viscosity
ν = kinematic viscosity
Π = second invariant of the deformation tensor
ρ = fluid density
τ_w = wall shear stress
ω_x = streamwise vorticity

Subscripts

H,C = hot and cold air, respectively
I,O = inlet and outlet, respectively
0 = straight square duct
m = area-averaged quantity

References

[1] Uechi, H., Kimijima, S., and Kasagi, N., 2004, "Cycle Analysis of Gas Turbine-Fuel Cell Cycle Hybrid Micro Generation System," ASME J. Eng. Gas Turbines Power, **126**(4), pp. 755–762.
[2] Kays, W. M., and London, A. L., 1984, *Compact Heat Exchangers*, 3rd ed., McGraw-Hill, New York.
[3] Webb, R. L., 1994, *Principles of Enhanced Heat Transfer*, Wiley, New York.
[4] Manglik, R. M., 2003, "Heat Transfer Enhancement," *Heat Transfer Handbook*, A. Bejan and A. D. Kraus, eds., Wiley, New York, Chap. 14.
[5] McDonald, C. F., 2000, "Low-Cost Compact Primary Surface Recuperator Concept for Microturbines," Appl. Therm. Eng., **20**(5), pp. 471–497.
[6] Focke, W. W., Zachariades, J., and Olivier, I., 1985, "The Effect of the Corrugation Inclination Angle on the Thermohydraulic Performance of Plate Heat Exchangers," Int. J. Heat Mass Transfer, **28**(8), pp. 1469–1479.
[7] Stasiek, J., Collins, M. W., Ciofalo, M., and Chew, P. E., 1996, "Investigation of Flow and Heat Transfer in Corrugated Passages—I. Experimental Results," Int. J. Heat Mass Transfer, **39**(1), pp. 149–164.
[8] Ciofalo, M., Stasiek, J., and Collins, M. W., 1996, "Investigation of Flow and Heat Transfer in Corrugated Passages—II. Numerical Simulations," Int. J. Heat Mass Transfer, **39**(1), pp. 165–192.
[9] Blomerius, H., Holsken, C., and Mitra, N. K., 1999, "Numerical Investigation of Flow Field and Heat Transfer in Cross-Corrugated Ducts," ASME J. Heat Transfer, **121**(2), pp. 314–321.
[10] Metwally, H. M., and Manglik, R. M., 2004, "Enhanced Heat Transfer Due to Curvature-Induced Lateral Vortices in Laminar Flows in Sinusoidal Corrugated-Plate Channels," Int. J. Heat Mass Transfer, **47**(10–11), pp. 2283–2292.
[11] Manglik, R. M., Zhang, J., and Muley, A., 2005, "Low Reynolds Number Forced Convection in Three Dimensional Wavy-Plate-Fin Compact Channels: Fin Density Effects," Int. J. Heat Mass Transfer, **48**(8), pp. 1439–1449.
[12] Utriainen, E., and Sundén, B., 2002, "A Numerical Investigation of Primary Surface Rounded Cross Wavy Ducts," Heat Mass Transfer, **38**(7–8), pp. 537–542.
[13] Yin, J., Li, G., and Feng, Z., 2006, "Effects of Intersection Angles on Flow and Heat Transfer in Corrugated-Undulated Channels With Sinusoidal Waves," ASME J. Heat Transfer, **128**(8), pp. 819–828.
[14] Utriainen, E., and Sundén, B., 2002, "Evaluation of the Cross Corrugated and Some Other Candidate Heat Transfer Surface for Microturbine Recuperators," ASME J. Eng. Gas Turbines Power, **124**(3), pp. 550–560.
[15] Kajishima, T., Ohta, T., Okazaki, K., and Miyake, Y., 1998, "High-Order Finite-Difference Method for Incompressible Flows Using Collocated Grid System," JSME Int. J., Ser. B, **41**(4), pp. 830–839.
[16] Rhie, C. M., and Chow, W. L., 1983, "Numerical Study of the Turbulent Flow

Past an Airfoil With Trailing Edge Separation," AIAA J., **21**(11), pp. 1525–1532.
[17] Amsden, A. A., and Harlow, F. H., 1970, "A Simplified MAC Technique for Incompressible Fluid Flow Calculation," J. Comput. Phys., **6**, pp. 322–325.
[18] Patankar, S. V., Liu, C. H., and Sparrow, E. M., 1977, "Fully Developed Flow and Heat-Transfer in Ducts Having Streamwise-Periodic Variations of Cross-Sectional Area," ASME J. Heat Transfer, **99**(2), pp. 180–186.
[19] Shah, R. K., and London, A. L., 1978, *Laminar Flow Forced Convection in Ducts* (Advances in Heat Transfer Supplement 1), Academic, New York.
[20] Chong, M. S., Perry, A. E., and Cantwell, B. J., 1990, "A General Classification of Three-Dimensional Flow Fields," Phys. Fluids A, **2**(5), pp. 765–777.
[21] Utriainen, E., and Sundén, B., 2001, "A Comparison of Some Heat Transfer Surfaces for Small Gas Turbine Recuperators," ASME Paper No. 2001-GT-0474.
[22] Manglik, R. M., and Bergles, B. E., 1995, "Heat Transfer and Pressure Drop Correlations for the Rectangular Offset Strip Fin Compact Heat Exchanger," Exp. Therm. Fluid Sci., **10**(2), pp. 171–180.
[23] Cowell, T. A., 1990, "A General Method for the Comparison of Compact Heat Transfer Surfaces," ASME J. Heat Transfer, **112**(2), pp. 288–294.

Comparison of Two-Dimensional and Three-Dimensional Thermal Models of the LENS® Process

H. Yin
Mechanical Engineering Department,
Mississippi State University,
Mississippi State, MS 39762

L. Wang
Center for Advanced Vehicular Systems,
Mississippi State University,
Mississippi State, MS 39762

S. D. Felicelli
Mechanical Engineering Department,
Mississippi State University,
Mississippi State, MS 39762
e-mail: felicelli@me.msstate.edu

A new two-dimensional (2D) transient finite element model was developed to study the thermal behavior during the multilayer deposition by the laser engineered net shaping rapid fabrication process. The reliability of the 2D model was evaluated by comparing the results obtained from the 2D model with those computed by a previously developed three-dimensional (3D) model. It is found that the predicted temperature distributions and the cooling rates in the molten pool and its surrounding area agree well with the experiment data available in literature and with the previous results calculated with the 3D model. It is also concluded that, for the geometry analyzed in this study, the 2D model can be used with good accuracy, instead of the computationally much more expensive 3D model, if certain precautions are taken to compensate for the 3D effects of the substrate. In particular, a 2D model could be applied to an in situ calculation of the thermal behavior of the deposited part during the fabrication, allowing dynamic control of the process. The 2D model is also applied to study the effects of substrate size and idle time on the thermal field and size of the molten pool. [DOI: 10.1115/1.2953236]

1 Introduction

Laser engineered net shaping (LENS®) is a rapid fabrication process, through which near-net-shaped three-dimensional (3D) components are built by the successive overlapping of layers of laser melted powder by the computer-guided movement of the substrate or the laser in 3D space. The LENS fabrication technique was developed by Sandia National Laboratories in the late 1990s and is gaining popularity as a rapid prototyping and repair technology because of its cost saving potentials and high cooling rates leading to fine microstructures similar to those observed in rapid solidification [1–3].

Because the process is not yet fully understood, the selection of process parameters is often based on previous experience and trial and error experimentation. Appropriate tuning of the laser power, travel speed, powder flow rate, and several other parameters is essential to avoid defects and undesired microstructures. Kurz [4], Kelly and Kampe [5], and Colaco and Vilar [6,7], among others, have shown that the microstructure and mechanical properties obtained with the LENS process partly depend on the solid-state transformations during cool down to room temperature. However, the transformations are mainly driven by the consecutive thermal cycles during the LENS process when the laser beam moves along the part surface line by line and layer by layer. Therefore, it is critical to understand the local thermal cycles and temperature history in order to predict the solid phase transformations and thus the final microstructure in the part.

Only a few experimental works have been done to characterize the thermal behavior during LENS deposition [8–13]. Hofmeister et al. [9] employed a digital 64×64 pixel charge coupled device (CCD) video camera with thermal imaging techniques to observe the molten pool. These experiments were conducted on stainless steel 316 (SS316), using two different particle size distributions. The molten pool size was analyzed from the thermal images, and the temperature gradients and cooling rates in the vicinity of the molten pool were also obtained. Griffith et al. [12] inserted a thermocouple directly into the sample to obtain the thermal history during the LENS fabrication. Fine diameter (10 μm) Type C thermocouple wire was used for the measurements to ensure no reaction during deposition, and the thermocouple bead was inserted into the deposition zone for accurate temperature measurements. They obtained in situ temperature data for 20 deposition layers from a representative thermocouple inserted during the fabrication of an H13 tool steel part. Wei et al. [13] employed a two-wavelength imaging pyrometer to capture the thermal images of the stationary molten pool for different laser powers without powder delivery and substrate movement. The thermal images of the moving molten pool were also taken at the beginning state of deposition for two conditions with different laser power and travel velocity settings. The molten pool size, temperature distribution, temperature gradient, and cooling rate in the molten pool were analyzed. It was found that the cooling rate is on the order of 10^2–10^4 K/s in the processed zone.

However, the experimental measurement of a detailed thermal history in the part is difficult to achieve because the required experiments would be very costly and time consuming. An alternative approach is to use numerical simulation with appropriate mathematical models. Several models have been developed to try to establish an understanding of the thermal behavior in the LENS process [14–22]. Grujicic et al. [14,15] developed a two-dimensional (2D) finite element model to calculate the temperature profiles, obtaining the minimum power of the laser needed to initiate the melting of the part surface. Ye et al. [16] developed a finite element model to predict the temperature distribution during the process, especially near the molten pool. Their results showed good agreement with experimental observations. Costa et al. [17] developed and applied a 3D finite element model to calculate the thermal history in a single-wall plate. They also studied the influence of substrate size and idle time on the temperature field of the fabricated parts. Wang and Felicelli [21] predicted the temperature distribution during deposition of SS316 as a function of time and process parameters by developing a 2D thermal model, but only for one layer of deposition. Later, they developed a 3D finite element model [22] using the commercial software SYSWELD to study the molten pool size by analyzing the temperature and phase evolution in stainless steel 410 (SS410) during the LENS deposition of a thin-walled structure.

As with most 3D models, the computational time greatly exceeds that of equivalent 2D models. This is even so when only

Contributed by the Heat Transfer Division of ASME for publication in the JOURNAL OF HEAT TRANSFER. Manuscript received May 24, 2007; final manuscript received January 29, 2008; published online August 8, 2008. Review conducted by Anthony M. Jacobi.

simple heat conduction is being calculated. The computational cost of a 3D model becomes impractical when more complex phenomena of interest are simulated, such as solidification, segregation, porosity, molten pool convection, solid phase transformations, strain and stresses, and others. The single-wall build, in which a thin plate is deposited layer by layer, is the geometry of choice to study the LENS process because of its relative simplicity for modeling and experimental trials. The fact that both 2D and 3D models have been used in literature to simulate this simple geometry indicates that it is not clear whether a 2D model can capture the thermal phenomena of interest. The situation has not been analyzed and, when in doubt, authors resort to 3D modeling at the expense of analysis time and simplified physics. Because the thermal history is the key to predict the microstructure and the mechanical response, the determination of the conditions under which a 2D model can be used to calculate the temperature field with acceptable accuracy would be very useful to undertake combined numerical/experimental studies of the LENS process that go beyond thermal-only aspects.

In the present paper, a 2D finite element model is developed to calculate the temperature distribution during the deposition of multiple layers of SS410. The thermal characteristics and molten pool size predicted with this 2D model is then compared with those calculated with the 3D model developed by Wang et al. [22] and with experimental data. The conditions under which the 2D simulations produce acceptable results are identified, as well as the cases in which 3D effects cannot be captured by the 2D model. The influence of the idle time between the depositions of consecutive layers of material and of substrate size on the thermal cycle/history is also illustrated.

2 Finite Element Mathematical Model

In this section, we describe the 2D finite element model developed to simulate the transient temperature field during the deposition of ten consecutive layers of a single-wall plate of SS410. The schematic of the geometry is shown in Fig. 1(*a*). A fixed finite element mesh is constructed for the substrate and the ten layers of the plate. A uniform layer thickness is used, whose value is set consistently with the powder deposition rate and the travel speed of the laser/nozzle head. Initially, the substrate is at room temperature, and the layer elements are inactive. When a new layer is being deposited, the elements of that layer are activated and they remain active for the rest of the simulation. The boundary conditions (Fig. 1(*b*)) include convection heat loss on the top and sides, a prescribed temperature at the bottom of the substrate, and convection/radiation on the top plus a heat flux due to the incident laser power. The boundary conditions are updated dynamically as layers are activated and new sections of the boundary become active. After finishing depositing one layer and before beginning depositing the next layer, there is a time interval called the idle time, during which the laser/nozzle head is returned to the left end of the plate so that all layers are deposited from left to right. During the idle time, the laser and powder injection are turned off and the corresponding heat flux boundary condition is inactive.

In order to compare the results of the 2D model with those from the 3D model by Wang et al. [22], the same material properties and process parameters are employed. The plate is built by depositing ten layers of material, each with a length of 10.0 mm and a height of 0.5 mm, on top of a substrate with dimensions 5.0 mm high and 10.0 mm long. For comparison purposes, the geometry of the 3D model of Ref. [22] is shown in Fig. 1(*c*). The travel speed of the laser beam is 7.62 mm/s, and the laser beam moves from left to right for each layer deposition. SS410 was used for both the deposited plate layers and the substrate. The thermal properties of SS410 are presented in Table 1, where it is assumed, due to lack of better available data, that the thermal properties of the resolidified SS410 powder are similar to those of the bulk material.

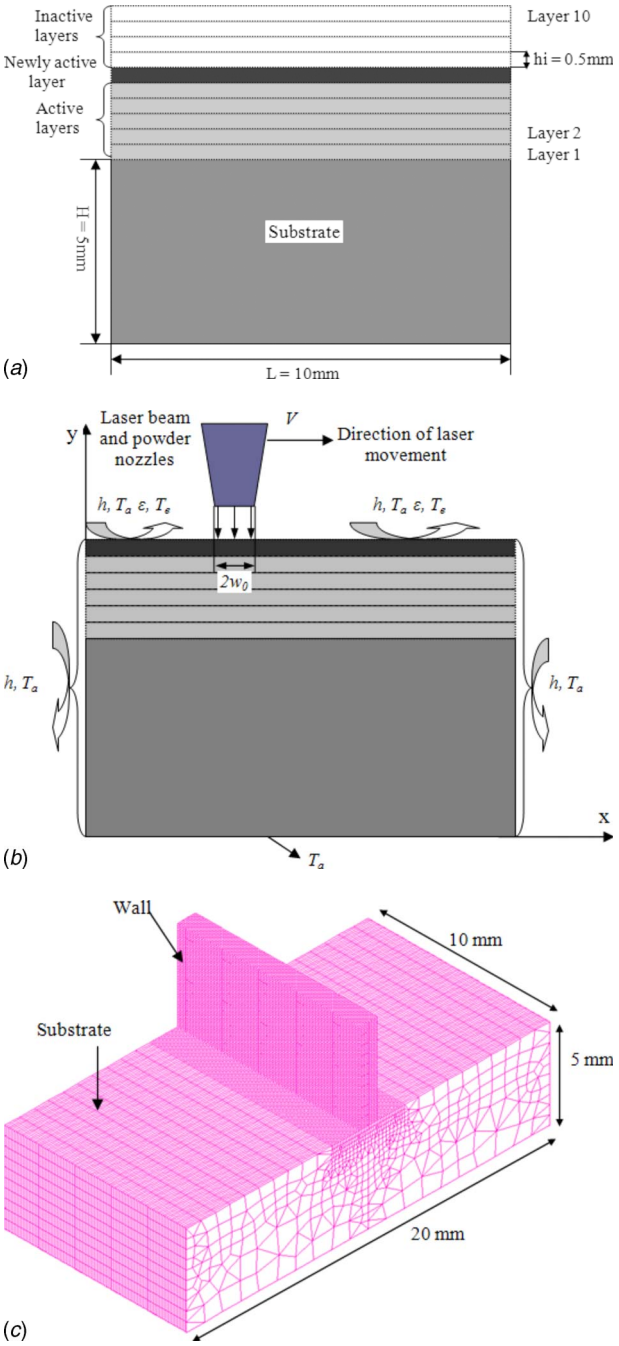

Fig. 1 (*a*) Sketch of the element activation to illustrate the laser powder deposition with multipasses, (*b*) schematic of the model showing the boundary conditions used for the temperature calculation, and (*c*) 3D model of Ref. [22]

2.1 Heat Transfer Equation. The 2D transient equation of heat conduction describing the heat transfer within the plate during the LENS process is

$$\frac{\partial T}{\partial t} = \kappa\left(\frac{\partial^2 T}{\partial x^2} + \frac{\partial^2 T}{\partial y^2}\right) - \frac{L}{C_p}\frac{\partial \phi}{\partial t} \tag{1}$$

where T is the temperature, t is the time, x and y are the horizontal and vertical coordinates, respectively, κ is the thermal diffusivity, L is the latent heat of melting, C_p is the specific heat, and ϕ is the volume fraction of liquid, approximated as $\phi \approx (T-T_s)/(T_l-T_s)$, where T_l is the liquidus temperature and T_s is the solidus temperature of the alloy. This is a reasonable approximation in view of the

Table 1 SS410 thermal properties and LENS process parameters

Parameter	Symbol	Units	Value	Ref.
Density	ρ	kg/m^3	7400	[22]
Thermal conductivity	k	W/m K	25.5	[22]
Specific heat of solid	C_p	J/kg K	650	[22]
Latent heat	L	J/kg	3×10^5	[21]
Liquidus	T_l	K	1723	[21]
Solidus	T_s	K	1693	[21]
Emissivity	ε	N/A	0.8	[21]
Convective heat transfer coefficient	h	W/m^2 K	100	[21]
Radius of the laser beam	w_0	mm	0.5	[21]

very thin mushy zone that forms around the pool [23].

2.2 Initial and Boundary Conditions. The boundary conditions are shown in Fig. 1(*b*). A forced boundary condition is prescribed on the bottom of the substrate:

$$T(x,y,t)|_{y=0} = T_a \tag{2}$$

where T_a is the ambient temperature around the part, in this work considered to be equal to room temperature. The initial temperature of the substrate is also assumed at room temperature,

$$T(x,y,t)|_{t=0} = T_a, \quad y \le H \tag{3}$$

where H is the height of the substrate. The initial condition of the newly deposited material for each layer is set equal to the melting temperature.

$$T(x,y,t)|_{t=0} = T_l, \quad y > H \tag{4}$$

The boundary condition on the section of the top layer under the laser beam is [22]

$$-k\frac{\partial T}{\partial y} = h(T-T_a) + \varepsilon\sigma(T^4 - T_e^4) - Q_r \tag{5}$$

where k is the thermal conductivity, h is the convective heat transfer coefficient, ε is the emissivity of the part surface, σ is the Stefan–Boltzmann constant ($\sigma=5.67\times10^{-8}$ W/m^2 K^4), and T_e is the temperature of the internal wall of the glovebox (taken equal to T_a in this work). In Eq. (5), Q_r is a distributed heat source with a Gaussian profile

$$Q_r = A_0 \exp\left(-\frac{2(x-x_0)^2}{w_0^2}\right) \tag{6}$$

where $A_0=-2\alpha P_1/\sqrt{2\pi}w_0$, being α the effective absorption coefficient of the laser-beam energy, P_l the laser-beam power, w_0 the beam radius, and x_0 the x coordinate of the laser-beam axis.

The boundary condition for the new elements of the top surface, other than the elements beneath the laser beam, considers only the effects of convection and radiation heat loss,

$$-k\frac{\partial T}{\partial y} = h(T-T_a) + \varepsilon\sigma(T^4 - T_e^4) \tag{7}$$

For the two vertical sides, the heat loss due to heat convection is assumed

$$-k\frac{\partial T}{\partial x} = h(T-T_a), \quad x = L \tag{8a}$$

$$+k\frac{\partial T}{\partial x} = h(T-T_a), \quad x = 0 \tag{8b}$$

where L is the width of the plate.

The parameter A_0 in Eq. (6) is used to set the level of power entering the calculation domain. This parameter is necessary because it is not known how much of the nominal laser power is actually absorbed by the material. A similar parameter is used in the 3D model. Because of the limitation of 2D modeling, it is not possible to establish a direct correlation between the actual 3D absorbed power distribution and the idealized 2D power profile used in this work. Ye et al. [20] investigated the thermal behavior in the LENS process with the finite element method. In their work, the temperatures of the nodes where the laser beam focused on were set as the melting point temperatures; thus the laser power did not actually play a role. In this study, the coefficient A_0 is determined by matching the maximum calculated temperature in the molten pool with the measured value reported by Hofmeister et al. [9]. By adjusting A_0, we can calibrate the model to a particular experimental setting. The calibration is done only for one experimental temperature measurement point, then the rest of the temperature profile must result from the model prediction; i.e., A_0 is used to adjust the level of the temperature profile but not the shape of the profile.

By using a 2D model, it is also assumed that there is no significant heat loss through the front and back surfaces of the part. The time evolution of the isotherms is calculated as the laser beam travels across the top surface of the part and layers are deposited. The model dynamically updates the thermal boundary conditions with the laser position and newly added layers; hence it is able to calculate temperature profiles both far from and near the side edges of the plate.

3 Results and Discussions

Due to lack of available experimental data for SS410, we used the experiments of Hofmeister et al. [9] for correlation purposes. In these experiments, ultrahigh speed digital imaging techniques were employed to analyze the image of the molten pool and the temperature gradient on the surface surrounding the molten pool in SS316 samples fabricated using LENS. SS316 and SS410 have similar thermal properties, and in our calculations, we use process parameters (laser power and travel speed) that approximate the conditions of Hofmeister's experiments, in a similar way as it was done in our previous study on the sensitivity of LENS process parameters [21]. To compare the 2D model with the Hofmeister's measurements, a first calculation is performed for the deposition of the top layer (the tenth layer), using the experimental temperature data as the initial condition for the previously built layers.

Figure 2 shows the temperature contours when the laser beam is at the center of the top layer. The travel speed of the laser beam is 7.62 mm/s. It is observed that the temperature profiles predicted by the 2D model (Fig. 2(*a*)) and the 3D model (Fig. 2(*b*)) of Ref. [22] are very similar. Note that the scale of temperature is the same in both figures. The size of the molten pool predicted by the 2D model (Fig. 2(*a*)) is slightly larger than the one predicted by the 3D model (Fig. 2(*b*)) because the heat loss along the z-direction is not considered in the 2D model. Figure 2(*c*) shows the profile of the temperature and cooling rate from the center of the molten pool to a position 4 mm away, opposite to the laser moving direction (indicated in Figs. 2(*a*) and 2(*b*)). The temperature profile calculated by the 2D model qualitatively agrees with the experimental data of Ref. [9] and with the results calculated by the 3D model of Liang et al. [22]. However, the 2D model predicts two small kinks in the temperature and cooling rate curves, which are missed by the 3D model but are consistent with the trend shown in the experiment data. Here by "trend" we mean the qualitative observation that the experimental data show a change in the slope of the temperature and cooling rate profiles at the edge of the molten pool, due to latent heat effect and which is reflected in the 2D model results but not in the 3D (which did not consider latent heat term). The location of these kinks corresponds to a very thin mushy zone surrounding the molten pool and is a consequence of the effect of the latent heat of fusion. The 3D

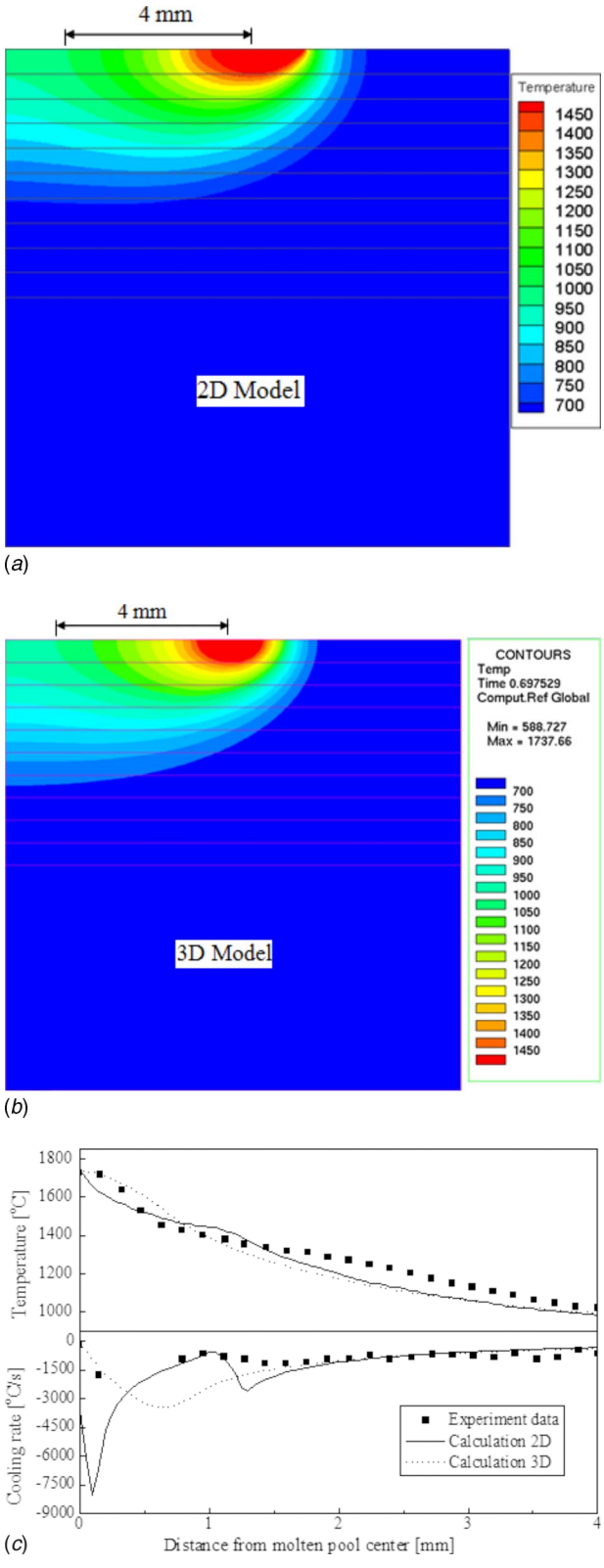

Fig. 2 Temperature distribution predicted (*a*) by the 2D model and (*b*) the 3D mode; molten pool is indicated by the 1450°C isotherm; (*c*) Comparison of calculated results by the 2D and 3D models and experimental data of Hofmeister et al. [9]

model of Ref. [22], based on the commercial software SYSWELD, did not include latent heat effects and hence could not capture this trend.

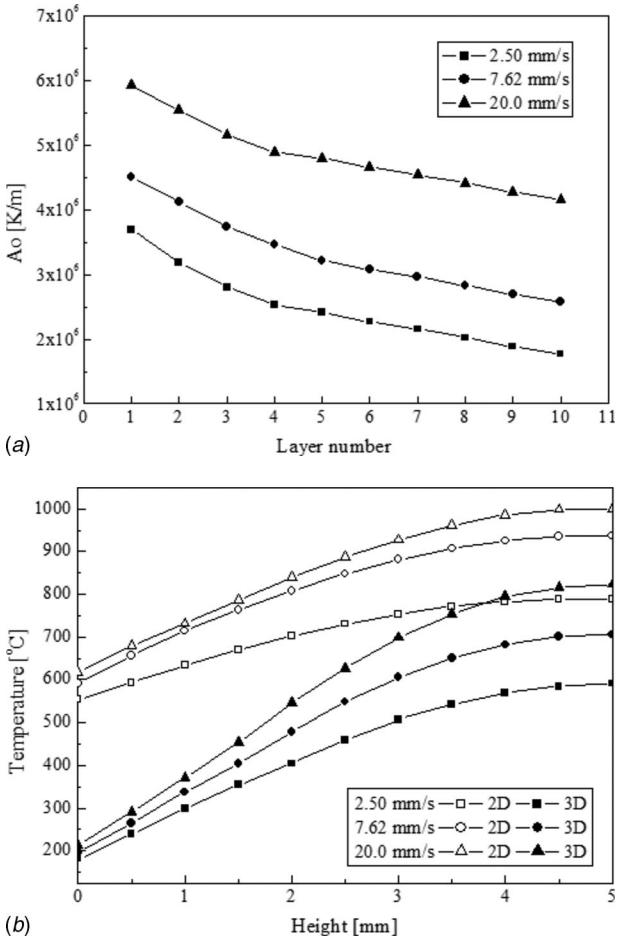

Fig. 3 (*a*) Profiles of the A_0 power coefficient of the 2D model and (*b*) temperature profiles calculated by the 2D and 3D models along the plate centerline for various scanning speeds of the laser beam

In the next simulations, we compare the 2D and 3D models for multilayer deposition for three different travel speeds of the laser beam. In the 3D simulations of Ref. [22], the power program during the deposition of different layers was optimized to obtain a steady molten pool size. In order to reproduce this feature with a 2D model, the power coefficient A_0 needs to be selected accordingly. For each travel speed, the power coefficient A_0 is first determined by matching the maximum temperature in the mid-point of the first layer with the one calculated by the 3D model. For subsequent layers, we assume that A_0 follows the same profile of the power curve of the 3D model, which was optimized for a steady pool size. The A_0—curves for different travel speeds as a function of layer number are shown in Fig. 3(*a*). As explained in Ref. [22], in order to maintain the same pool size from layer to layer, the applied power must decrease as layers are deposited in order to account for the thermal energy storage of the material of the added layers and to compensate for less heat transfer loss to the substrate. The corresponding temperature profiles along the plate centerline, calculated with the 2D and the 3D models, are indicated for three different travel speeds in Fig. 3(*b*), at the time when the tenth layer has been deposited. Higher speeds correspond with higher temperature because less time is available for the layers to cool down between laser scans. In Fig. 3(*b*), we can observe the consequence of having used the same shape of power profile of the 3D part in the 2D calculation. Because the heat loss in the *z*-direction is not considered in the 2D model (and particularly, the heat loss from a 3D substrate), the temperature of the lower portion of the part becomes higher as layers are deposited,

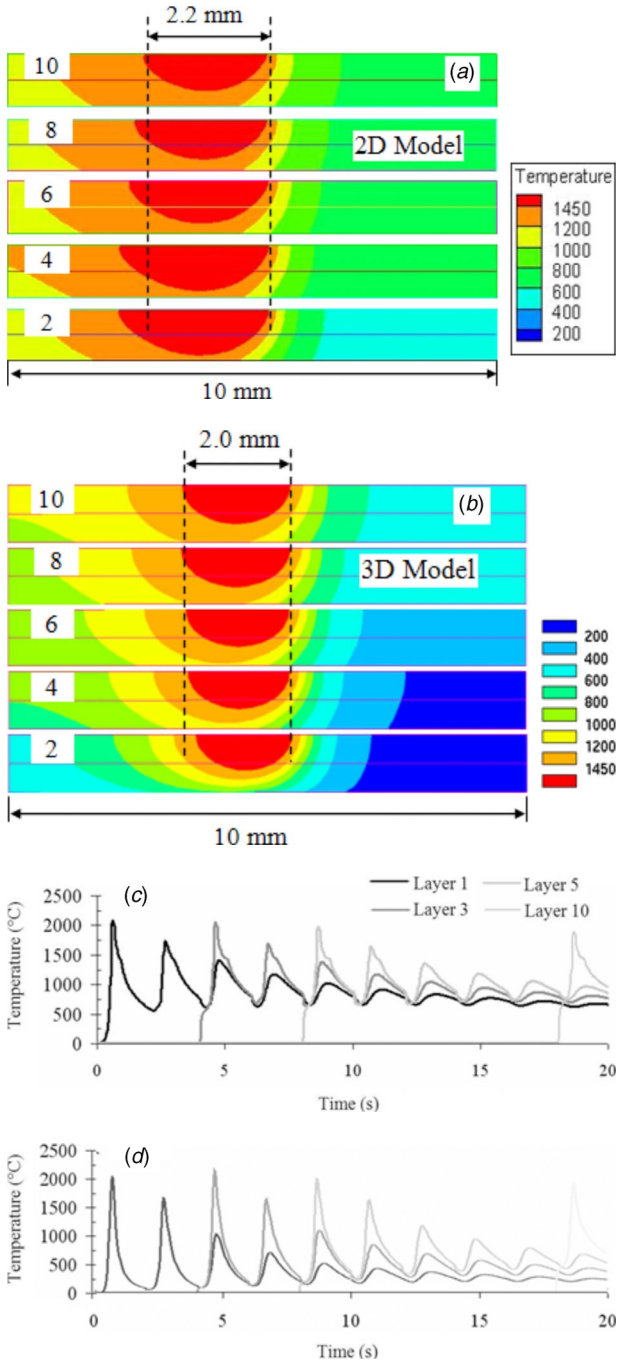

Fig. 4 Temperature distribution when the laser beam is at the center of layers 2, 4, 6, 8, and 10 calculated by the (*a*) 2D and (*b*) 3D models; the molten pool is indicated by the 1450°C isotherm. Temperature cycles at the midpoints of layers 1, 3, 5, and 10 as ten layers are deposited for the (*c*) 2D and (*d*) 3D models. V=7.62 mm/s. In (*d*), M_s is the martensite start temperature (350°C).

in comparison with the 3D plate. At the end of the deposition of the tenth layer, the bottom temperature of the 2D plate has increased to 600°C, while the 3D part remained at 200°C. For the upper layers, the temperature is more sensitive to travel speed, but the temperature difference between the 2D and 3D parts becomes less pronounced as the dissipation of the substrate is less dominant.

Figures 4(*a*) and 4(*b*) show the temperature contours in and around the molten pool for Layer Numbers 2, 4, 6, 8, and 10, predicted by the 2D and 3D models, when the laser is at the midpoint of the layer. The laser travel speed is 7.62 mm/s. The molten pool size of the tenth layer is very similar to that predicted by Wang et al. [22]. The discrepancy in pool size between the 2D and 3D models increases as we move down closer to the substrate, as expected from the thermal profiles observed in Fig. 3.

Figure 4(*c*) shows the thermal cycles at the midpoints of deposited Layers 1, 3, 5, and 10 for the 2D model. Figure 4(*d*), extracted from Ref. [22], shows the same cycles calculated with the 3D model. The temperature of each layer reaches a peak every time the laser goes over the midpoint of the plate, and then decreases to a minimum value before the laser starts scanning a new layer (the idle time between layers also affects the minimum temperature). The calculated thermal cycles look similar for the 2D and 3D models, with the discrepancies already observed in Fig. 3, which show higher temperature for the lower layers of the 2D model at the end of the deposition because of the extra heat loss by the 3D substrate. Note also that the cooling part of the cycle curves in the 2D model shows the effect of latent heat, which is missed by the 3D model.

A comparison of the temperature contours predicted by the 2D and 3D models is shown in Fig. 5 for the two other values of travel speed, 2.5 mm/s and 20 mm/s, when the laser is at the midpoint of the tenth layer. It is observed that the molten pool size in this layer is very similar for both 2D and 3D calculations, but the 2D substrate is hotter than the 3D one, the difference being more pronounced for higher travel speed. The elongation effect of the pool for higher speed is similarly captured by the 2D and 3D models.

Figure 6 illustrates the influence of the idle time elapsed between finishing depositing one layer and starting the next layer. Figure 6(*a*) shows the temperature profile along the plate centerline after the tenth layer has been deposited. It is observed that the idle time does not change the shape of the profiles but only displace the curves toward a lower temperature for a longer idle time. The thermal cycles for the case of an idle time of 4.4 s are shown in Fig. 6(*b*). This figure should be compared with Fig. 4(*c*), where the idle time was 0.82 s. It can be seen that a longer idle time allows the midpoint to cool down to a lower temperature, in particular, below the martensite start temperature (350°C). Hence, the idle time can play an important role when trying to control the final microstructure.

The substrate size has an obvious influence on the thermal cycles of depositions. More heat is lost from a larger substrate, which causes a higher temperature gradient along the height of the plate and leads to a lower average temperature. Because of the restricted heat loss in a 2D substrate, increasing the height of the substrate will lead to opposite results, i.e., a higher temperature in the part, if we use a 2D model. This is contrary to the prediction of the 3D model and also opposes the results published by Costa et al. [17]. Actually, in order to approximate the effect of a larger 3D substrate, either the height of the 2D substrate has to be reduced or a lower temperature must be applied as a boundary condition at the bottom of the 2D substrate. The first option is illustrated in Fig. 7 for a travel speed of 7.62 mm/s. Figure 7(*a*) shows the molten pool in different layers for a substrate height of 2 mm. Note the smaller pool size compared with Fig. 4(*a*), in which the substrate height was 5 mm. The temperature profiles along the centerline of the plate are shown in Fig. 7(*b*) for different substrate sizes. Observe that a smaller substrate size tends to better approximate the temperature profiles in Fig. 3(*b*) calculated with the 3D model.

4 Conclusions

A new 2D finite element model was developed to simulate the temperature history during multilayer deposition by the LENS process. This model is an extension of a 2D model previously developed by the authors for one-layer deposition [21]. The objective of the paper was to investigate the applicability of this new

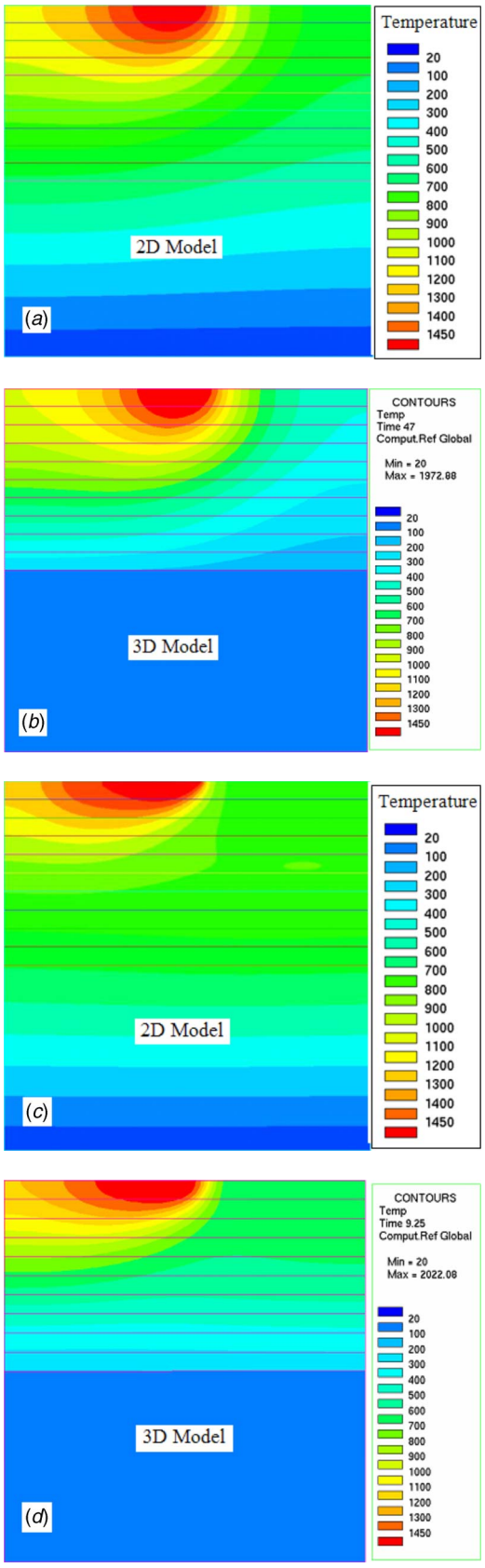

Fig. 5 Temperature distribution when the laser beam is at the center of the tenth layer as predicted by the (*a*) 2D model and (*b*) 3D model for *V*=2.50 mm/s. Temperature distribution when the laser beam is at the center of the tenth layer as predicted by the (*c*) 2D model and (*d*) 3D model for *V*=20.0 mm/s.

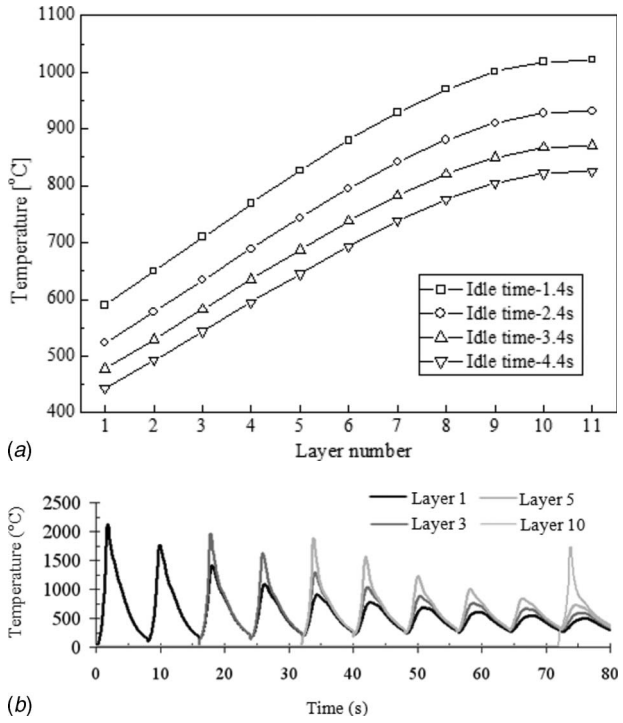

Fig. 6 (*a*) Temperature along the plate centerline for four different idle times after the tenth layer is deposited. (*b*) Temperature cycles at the midpoints of layers 1, 3, 5, and 10 calculated with the 2D model as ten layers are deposited. Idle time is 4.4 s and travel speed *V*=2.5 mm/s.

multilayer model to capture thermal phenomena observed in experiments and previously simulated by a 3D commercial software. The deposition of a thin plate made of ten layers of SS410 built over a substrate of the same material was analyzed. The temperature distribution, temperature history, molten pool size and shape, and cooling rates were calculated with both the 2D and 3D models, comparing the predicted results under variations of process parameters such as laser travel speed, power program, substrate size, and idle time. It was found that the 2D model can reasonably reproduce the results of the 3D model for most cases. It is important to calibrate the power coefficient A_0 of the 2D model so that it reflects an equivalent power level as in a 3D configuration. Also, care must be taken when analyzing the optimization of the power program for steady molten pool size, as well as the effect of changes in the substrate size. Perhaps, the main drawback of the 2D model is that it cannot capture the actual effect of the substrate; hence, 2D and 3D results will differ more pronouncedly in the first deposited layers. A consequent feature is that the 2D model cannot be used, at least in a direct way, to study the effect of different substrate sizes. The higher heat loss produced by a 3D substrate can lead to large discrepancies between the two models, particularly at the lower layers of the part. However, it is possible to design an equivalent 2D model that uses a shorter substrate and produces a thermal response of the part similar to the one observed in the 3D model. Because of the inherent savings in computational time of 2D simulations, more phenomena of interest can be added to a LENS 2D model, such as solidification, pool convection, segregation, and porosity, while still keeping the computational costs at manageable levels. A validated equivalent 2D model can also constitute an improved alternative for online control of the process, which is currently based only on monitoring of the pool size.

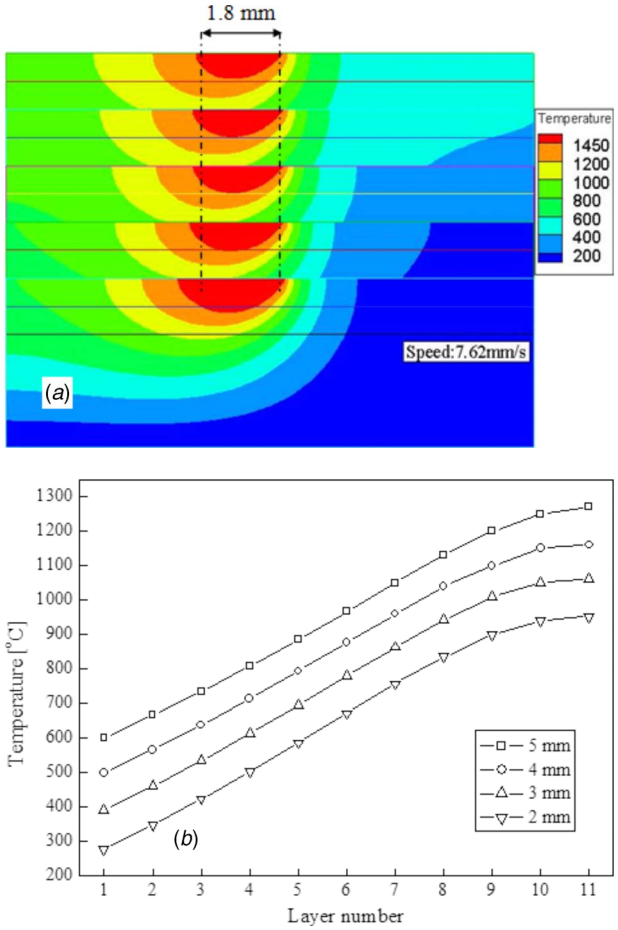

Fig. 7 (*a*) Molten pool size and shape when the laser beam moves to the center of the part for layers 2, 4, 6, 8, and 10, with a substrate height of 2 mm and (*b*) temperature along the plate centerline for four different substrate sizes

Acknowledgment

The authors appreciate the sponsorship of the Center for Advanced Vehicular Systems (CAVS) of Mississippi State University.

Nomenclature

C_p = specific heat
h = convective heat transfer coefficient
H = height of the substrate
k = thermal conductivity
L_0 = width of the plate
L = latent heat of melting
P_l = power of the laser beam
Q_r = distributed heat source with a Gaussian profile
t = time
T = temperature
T_l = liquidus temperature
T_s = solidus temperature
T_a = ambient temperature around the part
T_e = temperature of the internal wall of the glove box
w_0 = radius of the laser beam
x_0 = x coordinate of the laser beam axis
x, y = horizontal and vertical coordinates

Greek Symbols

α = effective absorption coefficient of the laser beam
ε = emissivity of the part surface
κ = thermal diffusivity
ϕ = volume fraction of the liquid
σ = Stefan–Boltzmann constant

References

[1] Atwood, C. L., Griffith, M. L., Schlienger, M. E., Harwell, L. D., Ensz, M. T., Keicher, D. M., Romero, J. A., and Smugeresky, J. E., 1998, "Laser Engineered Net Shaping (LENS®): A Tool for Direct Fabrication of Metal Parts," *Proceedings of ICALEO'98*, Orlando, FL, Nov. 16–19, pp. E-1–E-7.

[2] Lewis, G. K., and Schlienger, M. E., 2003, "Practical Considerations and Capabilities for Laser Assisted Direct Metal Deposition," Mater. Des., **21**, pp. 417–423.

[3] Sears, J. W., 2001, "Solid Freeform Fabrication Technologies: Rapid Prototyping-Rapid Manufacturing," Int. J. Powder Metall., **37**, pp. 417–423.

[4] Kurz, W., 2001, "Solidification Microstructure—Processing Maps: Theory and Application," Adv. Eng. Mater., **3**, pp. 443–452.

[5] Kelly, S. M., and Kampe, S. L., 2004, "Microstructural Evolution in Laser-deposited Multilayer Ti-6A1–4V Builds: Part II. Thermal Modeling," Metall. Mater. Trans. A, **35**, pp. 1869–1879.

[6] Colaco, R., and Vilar, R., 1998, "Effect of the Processing Parameters on the Proportion of Retained Austenite in Laser Surface Melted Tool Steels," J. Mater. Sci. Lett., **17**, pp. 563–567.

[7] Colaco, R., and Vilar, R., 1998, "Effect of Laser Surface Melting on the Tempering Behavior of DIN X42Cr13 Stainless Tool Steel," Scr. Mater., **38**, pp. 107–113.

[8] Hofmeister, W., Griffith, M., Ensz, M., and Smugeresky, J., 2001, "Solidification in Direct Metal Deposition by LENS® Processing," JOM, **53**, pp. 30–34.

[9] Hofmeister, W., Wert, M., Smugeresky, J., Philliber, J., Griffith, M., and Ensz, M., 1999, "Investigation of Solidification in the Laser Engineered Net Shaping (LENS) Process," JOM-e online, **51**(7) www.tms.org/pubs/journals/JOM/9907/Hofmeister/Hofmeister-9907.html.

[10] Griffith, M. L., Ensz, M. T., Puskar, J. D., Robino, C. V., Brooks, J. A., Philliber, J. A., Smugeresky, J. E., and Hofmeister, W. H., 2000, "Understanding the Microstructure and Properties of Components Fabricated by Laser Engineered Net Shaping (LENS)," Mater. Res. Soc. Symp. Proc., **625**, pp. 9–20.

[11] Griffith, M. L., Schlienger, E., Harwell, L. D., Oliver, M. S., Baldwin, M. D., Ensz, M. T., Smugeresky, J. E., Essien, M., Brooks, J., Robino, C. V., Hofmeister, W. H., Wert, M. J., and Nelson, D. V., 1999, "Understanding Thermal Behavior in the LENS™ Process," Mater. Des., **20**, pp. 107–114.

[12] Griffith, M. L., Schlienger, M. E., Harwell, L. D., Oliver, M. S., Baldwin, M. D., Ensz, M. T., Smugeresky, J. E., Essien, M., Brooks, J., Robino, C. V., Hofmeister, W. H., Wert, M. J., and Nelson, D. V., 1998, "Thermal Behavior in the LENS™ Process," *Proceedings of the Solid Freeform Fabrication Symposium*, The University of Texas at Austin, Austin, TX, pp. 89–97.

[13] Wei, W., Zhou, Y., Ye, R. Q., Lee, D., Craig, J. E., Smugeresky, J. E., and Lavernia, E. J., 2002, "Investigation of the Thermal Behavior During the LENS™ Process," *International Conference on Metal Powder Deposition for Rapid Manufacturing*, San Antonio, TX, pp. 128–135.

[14] Grujicic, M., Gao, G., and Figliola, R. S., 2001, "Computer Simulations of the Evolution of Solidification Microstructure in the LENS™ Rapid Function Process," Appl. Surf. Sci., **183**, 43–57.

[15] Grujicic, M., Hu, Y., Fadel, G. M., and Keicher, D. M., 2002, "Optimization of the LENS Rapid Fabrication Process for In-flight Melting of Feed Powder," J. Mater. Synth. Process., **9**, pp. 223–233.

[16] Ye, R., Smugeresky, J. E., Zheng, B., Zhou, Y., and Lavernia, E. J., 2006, "Numerical Modeling of the Thermal Behavior During the LENS Process," Mater. Sci. Eng., A, **428**, pp. 47–53.

[17] Costa, L., Vilar, R., Reti, T., and Deus, A. M., 2005, "Rapid Tooling by Laser Powder Deposition: Process Simulation Using Finite Element Analysis," Acta Mater., **53**, pp. 3987–3999.

[18] Hoadley, A. F. A., and Rappaz, M., 1992, "A Thermal Model of Laser Cladding by Powder Injection," Metall. Trans. B, **23**, pp. 631–642.

[19] Han, L., Liou, F. W., and Phatak, K. M., 2004, "Modeling of Laser Cladding with Powder Injection," Metall. Mater. Trans. B, **35**, pp. 1139–1150.

[20] Ye, R., Zhou, Y., Wei, W., Smugeresky, J. E., and Lavernia, E. J., 2003, "Numerical Modeling of the Thermal Behavior During the LENS Process," *Materials Science and Technology 2003 Meeting*, Chicago, IL, Nov. 9–12, pp. 369–376.

[21] Wang, L., and Felicelli, S., 2006, "Analysis of Thermal Phenomena in LENS™ Deposition," Mater. Sci. Eng., A, **435–436**, pp. 625–631.

[22] Wang, L., Felicelli, S., Gooroochurn, Y., Wang, P. T., and Horstemeyer, M. F., 2008, "Optimization of the LENS™ Process for Steady Molten Pool Size," Mater. Sci. Eng., A, **474**, pp. 148–156.

[23] Faghri, A., and Zhang, Y., 2006, *Transport Phenomena in Multiphase Systems*, Elsevier, New York, p. 460.

Modeling of Convective Cooling of a Rotating Disk by Partially Confined Liquid Jet Impingement

Jorge C. Lallave

Muhammad M. Rahman

Department of Mechanical Engineering,
University of South Florida,
Tampa, FL 33620

This paper presents the results of the numerical simulation of conjugate heat transfer during a semiconfined liquid jet impingement on a uniformly heated spinning solid disk of finite thickness and radius. This study considered various disk materials, namely, aluminum, copper, silver, Constantan, and silicon; covering a range of Reynolds number (220–900), Ekman number (7.08×10^{-5}–∞), nozzle-to-target spacing ($\beta=0.25$–1.0), disk thicknesses to nozzle diameter ratio ($b/d_n=0.25$–1.67), and Prandtl number (1.29–124.44) using ammonia (NH_3), water (H_2O), flouroinert (FC-77), and oil (MIL-7808) as working fluids. The solid to fluid thermal conductivity ratio was 36.91–2222. A higher thermal conductivity plate material maintained a more uniform interface temperature distribution. A higher Reynolds number increased the local heat transfer coefficient. The rotational rate also increased the local heat transfer coefficient under most conditions.
[DOI: 10.1115/1.2945898]

Keywords: semiconfined liquid jet impingement, free surface flow, conjugate heat transfer

Introduction

Jet impingement has been demonstrated to be effective in processes such as annealing of metal and plastic sheets, tempering glass, chemical vapor deposition, avionics cooling, cooling of turbine blades, and drying of textiles. The rotation is an effective way to generate secondary flow and therefore enhance convective heat transfer. The interaction of rotation and impingement creates a complex and powerful flow capable of improving heat transfer processes considerably.

McMurray et al. [1] studied convective heat transfer to an impinging plane jet from a uniform heat flux wall. To fit their data, they based heat transfer correlations on the stagnation flow in the impingement zone and on the flat plate boundary layer in the uniform parallel flow zone. Metzger et al. [2] experimentally studied the effects of Prandtl number on heat transfer to a liquid jet for a uniform surface temperature boundary condition. Hung and Lin [3] proposed an axisymmetric subchannel model for evaluating the local surface heat flux for confined and unconfined cases. Webb and Ma [4] presented a comprehensive review of studies on jet impingement heat transfer. Garimella and Nenaydykh [5], Fitzgerald and Garimella [6], Li et al. [7], and Rahman et al. [8] all considered a confining top wall such as the one used at the present study for a submerged liquid jet. However, no rotation was used. These studies covered a number of working fluids including flouroinert (FC-77) and ammonia (NH_3) at different volumetric flow rates. Li and Garimella [9] experimentally investigated the influence of fluid thermo-physical properties on heat transfer from confined and submerged impinging jets. Generalized correlations for heat transfer were proposed based on their results. Ichimiya and Yamada [10] studied the heat transfer and flow characteristics of a single circular laminar impinging jet, including buoyancy effect in a narrow space with a confining wall. Dano et al. [11] investigated the flow and heat transfer characteristics of semiconfined jet array impingement with cross-flow.

The jet impingement on a rotating disk adds more complexity to the flow field. Carper and Deffenbaugh [12] and Carper et al. [13] conducted experiments to determine the average heat transfer coefficient at the rotating disk with uniform temperature cooled by a single liquid jet of oil impinging normal to the surface. Metzger et al. [14] employed a liquid crystal for mapping the local heat transfer distribution on a rotating disk with jet impingement. Thomas et al. [15] measured the film thickness across a stationary and rotating horizontal disk using the capacitance technique, where the liquid was delivered to the disk by a controlled semiconfined impinging jet. Rahman and Faghri [16,17] and Faghri et al. [18] experimentally, analytically, and numerically studied the heat transfer effect from a heated stationary or rotating horizontal disk to a liquid film from a controlled impinging jet under a partially confined condition for different volumetric flow rates and inlet temperatures for both supercritical and subcritical regions. Hung and Shieh [19] reported experimental measurements of heat transfer characteristics of jet impingement onto a horizontally rotating ceramic-based multichip disk. Ozar et al. [20] measured the thickness of the liquid film on the disk surface by an optical method, including the characterization of the hydraulic jump, and Rice et al. [21] presented an analysis of the liquid film and heat transfer characteristics of a free surface controlled liquid jet impingement onto a rotating disk.

Although the above investigations provided very useful information, only a few attempted to produce a local heat transfer distribution for a rotating disk in combination with a confined liquid jet impingement. The intent of this research is to study this effect with a steady laminar flow over a solid spinning disk partially confined by a plate under five different flow rates or jet Reynolds numbers, six spinning rates or Ekman numbers, five different disk thicknesses, and four nozzle-to-target spacings. A broad range of Prandtl numbers was covered with the use of four working fluids, namely, water (H_2O), ammonia (NH_3), flouroinert (FC-77), and MIL-7808 lubricating oil. The thermal conductivity effect was studied with the implementation of five different disk materials: aluminum, Constantan, copper, silicon, and silver. The

Contributed by the Heat Transfer Division of ASME for publication in the JOURNAL OF HEAT TRANSFER. Manuscript received April 18, 2007; final manuscript received January 8, 2008; published online August 6, 2008. Review conducted by Gautam Biswas. Paper presented at the 2007 ASME Solar Energy Division and Advanced Energy Systems Division Conference (ES2007) Long Beach, CA, June 27–29, 2007.

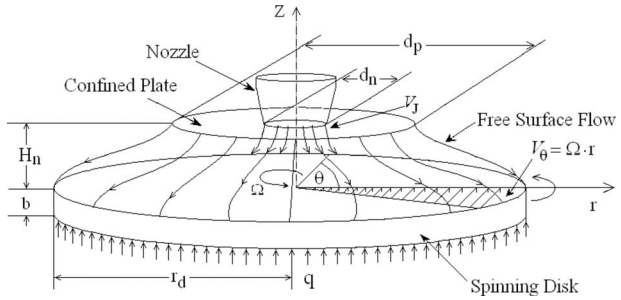

Fig. 1 3D schematic of axisymmetric semiconfined liquid jet impingement on a uniformly heated spinning disk

results offer a better understanding of the fluid mechanics and heat transfer behavior of semiconfined liquid jet impingement.

Mathematical Formulation

A schematic of the physical problem is shown in Fig. 1. An axisymmetric liquid jet is discharged through a nozzle and impinges at the center of a solid uniformly heated circular disk. The top plate acts as an insulated partially confined boundary that ends, allowing the free surface boundary condition exposure of the fluid. The present study considered an incompressible, Newtonian, and axisymmetric laminar flow under a steady state condition. The variation of fluid properties with local temperature was taken into account. Due to rotational symmetry of the problem, the $\partial/\partial\theta$ terms could be omitted. The equations describing the conservation of mass, momentum (r, θ, and z directions, respectively), and energy can be written as [22]

$$\frac{1}{r}\frac{\partial}{\partial r}(\rho_f r V_r) + \frac{\partial}{\partial z}(\rho_f V_Z) = 0 \tag{1}$$

$$\rho_f\left(V_r\frac{\partial V_r}{\partial r} + V_Z\frac{\partial V_r}{\partial z} - \frac{V_\theta^2}{r}\right) = -\frac{\partial p}{\partial r} + \frac{1}{r}\frac{\partial}{\partial r}\left[\frac{2}{3}\mu_f r\left(2\frac{\partial V_r}{\partial r} - \frac{V_r}{r} - \frac{\partial V_Z}{\partial z}\right)\right] + \frac{\partial}{\partial z}\left[\mu_f\left(\frac{\partial V_r}{\partial z} + \frac{\partial V_Z}{\partial r}\right)\right] + \frac{2}{3}\frac{\mu_f}{r}\left(\frac{\partial V_r}{\partial r} + \frac{\partial V_Z}{\partial z} - \frac{2V_r}{r}\right)\Bigg] \tag{2}$$

$$\rho_f\left(V_r\frac{\partial V_\theta}{\partial r} + V_Z\frac{\partial V_\theta}{\partial z} + \frac{V_r V_\theta}{r}\right) = \frac{1}{r^2}\frac{\partial}{\partial r}\left[r^2\mu_f\left[r\frac{\partial}{\partial r}\left(\frac{V_\theta}{r}\right)\right]\right] + \frac{\partial}{\partial z}\left[\mu_f\left(\frac{\partial V_\theta}{\partial z}\right)\right] \tag{3}$$

$$\rho_f\left(V_r\frac{\partial V_Z}{\partial r} + V_Z\frac{\partial V_Z}{\partial z}\right) = -\rho_f g - \frac{\partial p}{\partial z} + \frac{1}{r}\frac{\partial}{\partial r}\left[r\mu_f\left(\frac{\partial V_r}{\partial z} + \frac{\partial V_Z}{\partial r}\right)\right] + \frac{\partial}{\partial z}\left[\frac{2}{3}\mu_f\left(2\frac{\partial V_Z}{\partial z} - \frac{V_r}{r} - \frac{\partial V_r}{\partial r}\right)\right] \tag{4}$$

$$\rho_f\left(V_r\frac{\partial (Cp_f T_f)}{\partial r} + V_Z\frac{\partial (Cp_f T_f)}{\partial z}\right) = \left[\frac{1}{r}\frac{\partial}{\partial r}\left(k_f r\frac{\partial T_f}{\partial r}\right) + \frac{\partial}{\partial z}\left(k_f\frac{\partial T_f}{\partial z}\right)\right] + 2\mu_f\left[\left(\frac{\partial V_r}{\partial r}\right)^2 + \left(\frac{V_r}{r}\right)^2 + \left(\frac{\partial V_Z}{\partial z}\right)^2 + \frac{1}{2}\left(\frac{\partial V_\theta}{\partial r} - \frac{V_\theta}{r}\right)^2 + \frac{1}{2}\left(\frac{\partial V_\theta}{\partial z}\right)^2 + \frac{1}{2}\left(\frac{\partial V_r}{\partial z} + \frac{\partial V_Z}{\partial r}\right)^2 - \frac{1}{3}\left(\frac{\partial V_r}{\partial r} + \frac{V_r}{r} + \frac{\partial V_Z}{\partial z}\right)^2\right] \tag{5}$$

The variation of thermal conductivity of solids with temperature is not significant. Therefore, the conservation of energy inside the solid can be characterized by the following equation:

$$\frac{\partial^2 T_S}{\partial r^2} + \frac{1}{r}\left(\frac{\partial T_S}{\partial r}\right) + \frac{\partial^2 T_S}{\partial z^2} = 0 \tag{6}$$

The following boundary conditions were used:

$$\text{At } r = 0, \quad -b < z < 0: \ \frac{\partial T_S}{\partial r} = 0 \tag{7}$$

$$\text{At } r = 0, \quad 0 < z < H_n: \ V_\theta = V_r = 0, \quad \frac{\partial V_Z}{\partial r} = 0, \quad \frac{\partial T_f}{\partial r} = 0 \tag{8}$$

$$\text{At } r = r_d, \quad -b < z < 0: \ \frac{\partial T_S}{\partial r} = 0 \tag{9}$$

$$\text{At } r = r_d, \quad 0 < z < \delta: \ p = p_{\text{atm}} \tag{10}$$

$$\text{At } z = -b, \quad 0 \leq r \leq r_d: \ -k_S\frac{\partial T_S}{\partial z} = q \tag{11}$$

$$\text{At } z = 0, \quad 0 \leq r \leq r_d: \ V_r = V_Z = 0, \quad V_\theta = \Omega r, \quad T_S = T_f \tag{12}$$

$$k_S\frac{\partial T_S}{\partial z} = k_f\frac{\partial T_f}{\partial z}$$

$$\text{At } z = H_n, \quad 0 \leq r < \frac{d_n}{2}: \ V_Z = -V_j, \quad V_r = V_\theta = 0, \quad T_f = T_J \tag{13}$$

$$\text{At } z = H_n, \quad \frac{d_n}{2} \leq r < r_p: \ V_\theta = V_r = V_Z = 0, \quad \frac{\partial T_f}{\partial z} = 0 \tag{14}$$

The boundary condition at the free surface can be expressed as

$$\text{At } z = \delta, \quad r_p \leq r \leq r_d: \ \frac{\partial \delta}{\partial r} = \frac{V_z}{V_r}, \quad p = p_{\text{atm}} - \frac{\sigma\dfrac{d^2\delta}{dr^2}}{\left[1 + \left(\dfrac{d\delta}{dr}\right)^2\right]^{3/2}}, \quad \frac{\partial V_S}{\partial n} = 0, \quad \frac{\partial T_f}{\partial n} = 0 \tag{15}$$

where V_S is the fluid velocity component along the free surface and n is the coordinate normal to the free surface. It may be noted that boundary conditions at the free surface were obtained by satisfying the kinematic condition relating the slope of the free surface with velocity components as well as from the balance of normal and shear stresses at the free surface. For steady flow of a Newtonian fluid, the normal stress balance essentially reduces to an equation relating the pressure and surface tension, as shown in Ref. [23]. The shear stress encountered from the ambient gaseous medium is expected to be negligible. Similarly, the heat transfer from the free surface to the ambient gas is also assumed to be negligible. The average heat transfer coefficient can be defined as

$$h_{\text{av}} = \frac{2}{r_d^2(\bar{T}_{\text{int}} - T_J)}\int_0^{r_d} hr(T_{\text{int}} - T_J)dr \tag{16}$$

where $\bar{T}_{\text{int}}$ is the average temperature at the solid-liquid interface.

The characteristics of the flow are controlled by three major physical parameters: the Reynolds number, $\text{Re}_J = V_J d_n/\nu_f$, the dimensionless nozzle-to-target spacing ratio, $\beta = H_n/d_n$, and the Ekman number, $\text{Ek} = \nu_f/4\Omega r_d^2$. The values of the Reynolds number were limited to a maximum of 900, to stay within the laminar region. The nozzle opening and the heated target disk have radii of

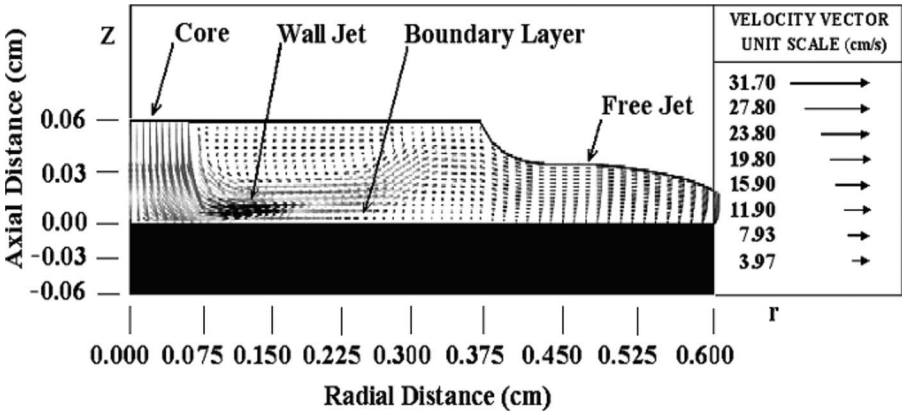

Fig. 2 Velocity vector distribution for a semiconfined jet impingement on a silicon disk with water as the cooling fluid (Re=475, Ek=4.25×10^{-4}, $r_p/r_d=0.5$, $\beta=0.5$, and $b/d_n=0.5$)

0.6 mm and 6.0 mm, respectively. The heat flux (q) was kept constant at 125 kW/m^2. The incoming fluid jet temperature (T_J) was 310 K for water and FC-77, 303 K for ammonia (at a pressure of 20 bars), and 373 K for MIL-7808. The thickness of the disk was varied over the following values: 0.3 mm, 0.6 mm, 1.0 mm, 1.5 mm, and 2.0 mm. The jet impingement height or the distance between the nozzle and disk was set at the following values: 3×10^{-4} m, 6×10^{-4} m, 9×10^{-4} m, and 1.2×10^{-3} m. The spinning rate (Ω) was varied from 0 rad/s to 78.54 rad/s or from 0 rpm to 750 rpm. The flow rate was varied from 6.65×10^{-7} m^3/s to 2.72×10^{-6} m^3/s. The ranges for the Reynolds number and the Ekman number were Re=220–900 and Ek $=7.08\times10^{-5}-\infty$. The possibility of getting into a turbulent flow due to disk rotation was checked. Using the laminar-turbulent transition criterion used by Popiel and Boguslawski [24] and Vanyo [25], all runs used in this paper checked out to be laminar.

The solid and fluid properties were obtained from Özisik [26], Bejan [27], and Bula [28]. The fluid properties were correlated according to the following equations. For water between 300 K $<T<$ 411 K: $Cp_f=9.5\times10^{-3}T^2-5.9299T+5098.1$, $k_f=-7.0\times10^{-6}T^2+5.8\times10^{-3}T-0.4765$, $\rho_f=-2.7\times10^{-3}T^2+1.3104T+848.07$, and $\ln\mu_f=-3.27017-0.0131T$. For ammonia between 273.15 K$<T<$370 K: $Cp_f=0.083T^2-40.489T+9468$, $k_f=1.159-2.30\times10^{-3}T$, $\rho_f=579.81+1.6858T-0.0054T^2$, and $\ln\mu_f=-5.33914-0.0115T$. For MIL-7808 between 303 K$<T<$470 K: $Cp_f=903.8+3.332T$, $k_f=0.18-1\times10^{-4}T$, $\rho_f=1181-0.708T$, and $\ln\mu_f=3.2436-0.0229T$. For FC-77 between 273 K$<T<$380 K: $Cp_f=589.2+1.554T$, $k_f=0.0869-8\times10^{-5}T$, $\rho_f=2507.2-2.45T$, and $\ln\mu_f=-2.38271-0.0145T$. In these correlations, the absolute temperature T is in K.

Numerical Computation

The governing equations (1)–(6) along with the boundary conditions (7)–(15) were solved using the Galerkin finite element method [29]. Four node quadrilateral elements were used. In each element, the velocity, pressure, and temperature fields were approximated, which led to a set of equations that defined the continuum. The size of the elements near the solid-fluid interface was made smaller to adequately capture large variations in the velocity and the temperature in that region. Due to the nonlinear nature of the governing differential equations, the Newton–Raphson method was used to arrive at the solution for the velocity and temperature fields. The approach used to solve the free surface problem described here was to introduce a new unknown δ representing the position of the free surface in the global system of equations. In order to start the computation, initial values of δ were assigned to all nodes at the free surface. A linear distribution with $\delta=H_n$ at $r=r_p$ to $\delta\approx H_n/2$ at $r=r_d$ was used as the initial guess. Then, conservation of mass and momentum equations (1)–(4) along with the corresponding boundary conditions were solved to determine the velocity distribution in the flow field. At the free surface, the second and third conditions in Eq. (15) were used as part of this solution process. These conditions represented the normal and shear stress balances at the free surface. Then, the velocity components at the free surface were used to check the fulfillment of the kinematic condition (the first condition in Eq. (15)). The value of δ was upgraded by applying a correction obtained from the required slope of the free surface at each free surface node. In order to preserve the numerical stability during this iterative solution for δ, a relaxation factor of 0.1 was used. Once a new location for the free surface node has been determined, the locations of all fluid nodes underneath the free surface extending to the solid-fluid interface were adjusted, keeping the same grid ratio. It may be noted that the adjustment was done only in the vertical direction (along the z axis) and only in the region of $r_p<r<r_d$ and $0<z<\delta$. The iterative solution for the determination of the free surface height distribution was continued by solving the conservation of mass and momentum equations and upgrading the grid structure at and underneath the free surface. A final free surface height distribution was obtained when the kinematic condition was satisfied at each free surface node and no further change in δ was needed. Then, the energy equation (5) was solved along with the mass and momentum conservation equations (1)–(4) to determine the final distribution of velocity, pressure, and temperature distributions. The solution was considered converged when a relative change in field values from a particular iteration to the next, and the sums of the residuals for each variable became less than 10^{-6}. The conservation of mass was independently checked by calculating the flow rate at the outlet ($r=r_d$) from the computed velocity field and comparing that with the fluid intake at the nozzle ($z=H_n$). The difference was essentially zero. The number of elements required for an accurate numerical solution was determined from a systematic grid-independence study. It was found that the numerical solution becomes grid independent when the number of divisions equal to 28×63 in the axial (z) and radial (r) directions, respectively, is used. Comparing the numerical results for the 32×72 and 45×100 grids with a 28×63 grid showed an average difference of 0.72%. A comparison of the average heat transfer coefficients was done with the experimental data of Carper and Deffenbaugh [12] and Carper et al. [13]. The agreement was found to be quite good. In addition, a comparison of local Nusselt numbers was made with the experimental data obtained by Ozar et al. [20] at various rotational speeds. The difference was in the range 0.79–22.07% with an average difference of 12.33%.

Results and Discussion

A typical velocity vector distribution is shown in Fig. 2. It can

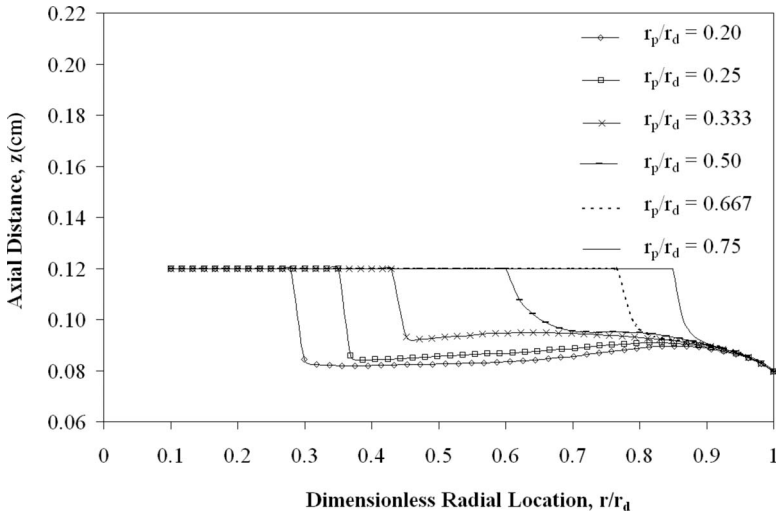

Fig. 3 Free surface height distribution for different plate-to-disk confinement ratios with water as the cooling fluid (Re=450, Ek=4.25×10^{-4}, β=0.5, and b/d_n=0.5)

be seen that the velocity remains almost uniform at the potential core region of the jet. The velocity decreases as the fluid jet expands in the radial direction as it approaches the target plate during the impingement process. The direction of motion of the fluid particles shifts by as much as 90 deg. After this, the fluid accelerates creating a region of high-velocity wall jet within the confined fluid medium. It can be noticed that as the boundary layer thickness increases downstream, the frictional resistance from the walls are eventually transmitted to the entire film thickness. This effect is observed once the fluid leaves the confined region and moves downstream with a free surface on the top. The vectors in the viscous zone show a parabolic profile going from a minimum value at the solid-fluid interface to a maximum at the free surface. The boundary layer develops rapidly and the velocity of the fluid decreases as it spreads radially along the disk. It may be noted, however, that due to spinning, streamlines are not aligned along the disk radius, rather the fluid moves at an angle based on the rate of rotation. The three different regions observed in the present investigation are in agreement with the experiments of Liu et al. [30].

Figure 3 presents the free surface height distribution for different plate-to-disk confinement ratios when the jet strikes the center of the disk while it is spinning at a rate of 125 rpm (Ek=4.25 $\times 10^{-4}$). It can be seen that the fluid spreads out radially as a thin film. The film thickness decreases as the plate-to-disk confinement ratio decreases under the same spinning rate and flow rate. This behavior occurs due to the dominance of surface tension and gravitational forces that form the free surface as the fluid leaves the confinement zone and moves downstream. When r_p is increased, the frictional resistance from both walls slows down the momentum and results in a higher film thickness. For the conditions considered in the present investigation, a sudden drop in the fluid height occurs for $r_p/r_d < 0.333$ because the equilibrium film height for free surface motion is significantly lower than the confinement height. In this situation, the liquid may not cover all the way to the end of the confinement disk and a free surface may start to form within the confinement region to provide a smooth streamline for the free surface. At $r_p/r_d \geq 0.5$, the confinement region is fully covered with fluid and a smooth transition is seen in the film height distribution after exit.

Figure 4 shows the local Nusselt number and the dimensionless interface temperature variation for different Reynolds numbers under a rotational rate of 125 rpm (Ek=4.25×10^{-4}). The plots reveal that the dimensionless interface temperature decreases with the jet velocity (or Reynolds number). At any Reynolds number, the dimensionless interface temperature has the lowest value at the stagnation point (underneath the center of the axial opening) and increases radially downstream reaching the highest value at the end of the disk. This is due to the development of a thermal boundary layer as the fluid moves downstream from the center of the disk. The thickness of the thermal boundary layer increases with the radius and causes the interface temperature to increase. All local Nusselt number distributions are half-bell shaped with a peak at the stagnation point. Figure 4 confirms to us how an increasing Reynolds number contributes to a more effective cooling. Similar profiles have been documented by Garimella and Nenaydykh [5] and Ma et al. [31].

Figure 5 plots the average Nusselt number as a function of the Reynolds number for low, intermediate, and high Ekman numbers. It may be noted that the average Nusselt number increases with the Reynolds number. As the flow rate (or Reynolds number) increases, the magnitude of fluid velocity near the solid-fluid interface that controls the convective heat transfer rate increases. Furthermore, at a particular Reynolds number, the Nusselt number gradually increases with the increment of the disk spinning rate. This behavior confirms the positive influence of the rotational rate on the average Nusselt number down to Ek=1.25×10^{-4}, which corresponds to a spinning rate of 425 rpm. It may be also noticed that the average Nusselt number plots get closer to each other as the Reynolds number increases, indicating that curves will intersect at higher Reynolds numbers. These intersections indicate the presence of a liquid jet momentum-dominated region at higher Reynolds numbers. From the numerical results, it was observed that the heat transfer is dominated by impingement when ReEk >0.124 and dominated by disk rotation when ReEk<0.092. In between their limits, both of these effects play an important role in determining the variations of the average Nusselt number. This type of behavior is consistent with the experimental results of Brodersen et al. [32] where the ratio of the jet and rotational Reynolds numbers was used to characterize the flow regime.

The rotational rate effects on the local Nusselt number and the dimensionless interface temperature are illustrated in Fig. 6 for a Reynolds number of 540 and a dimensionless nozzle-to-target spacing (β) equal to 0.25. It may be noted that the rotational effect increases the local Nusselt number and generates a lower temperature over the entire solid-fluid interface with somewhat less intensity in comparison with the Reynolds number effect. Figure 6 shows that as the Ekman number decreases from ∞ to 7.08

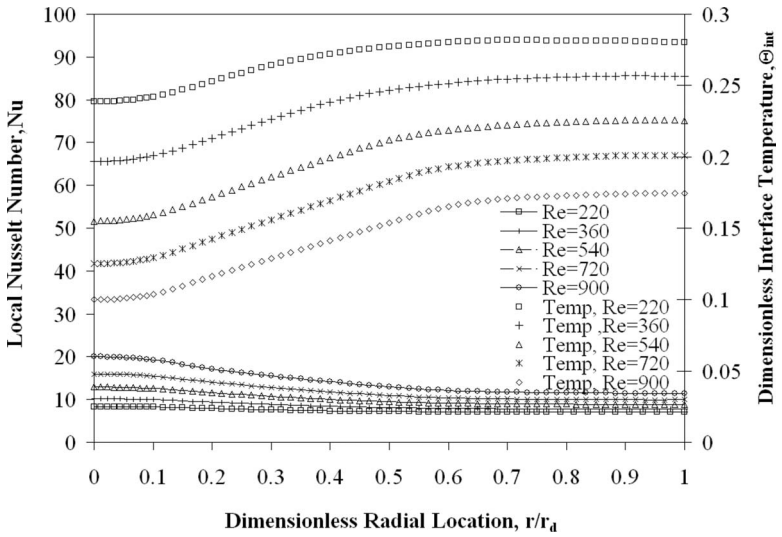

Fig. 4 Local Nusselt number and dimensionless interface temperature distributions for a silicon disk with water as the cooling fluid for different Reynolds numbers (Ek=4.25×10^{-4}, β=0.5, b/d_n=0.5, and r_p/r_d=0.667)

$\times 10^{-5}$ the local Nusselt number increases by an average of 24.02% and the dimensionless interface temperature decreases by an average of 8.34%. The enhancement of the Nusselt number due to rotation is primarily caused by the enhancement of the local fluid velocity adjacent to the rotating disk surface. The tangential velocity due to rotation combined with the axial and radial velocities due to jet momentum increases the magnitude of the velocity vector starting from the center of the disk.

The effects of the disk thickness variation on the dimensionless interface temperature and the local Nusselt number are shown in Fig. 7. The dimensionless interface temperature increases from the impingement region all the way to the end of the disk. It may be noted that the curves intersect with each other at a dimensionless radial distance of r/r_d=0.55. The thicker disks generate a more uniform dimensionless interface temperature due to a larger radial conduction within the disk. The local Nusselt number plots change slightly with the variation of disk thickness. In all cases, it is evident that the Nusselt number is more sensitive to the solid thickness at the core region where higher values are obtained. For a lower stagnation temperature, the outlet temperature tends to be relatively higher under constant flow rate and heat flux conditions. This is quite expected because of the overall energy balance of the system. This phenomenon has been documented by Lachefski et al. [33].

Three different nozzle-to-target spacing ratios (β) from 0.25 to 1 were modeled and the results are shown in Fig. 8. It may be noticed that the impingement height quite significantly affects the Nusselt number distribution. A higher local Nusselt number is obtained when the nozzle is brought very close to the heated disk (β=0.25). The smaller gap between the nozzle and the target disk avoids the loss of momentum as the jet travels through the confined fluid medium and results in a larger fluid velocity and therefore a larger rate of convective heat transfer. As the nozzle is moved away from the disk, the local Nusselt number decreases. This observation is in-line with the previous study by Hung and Lin [3] for a confined jet impingement on a stationary disk.

Figure 9 compares the dimensionless interface temperature and

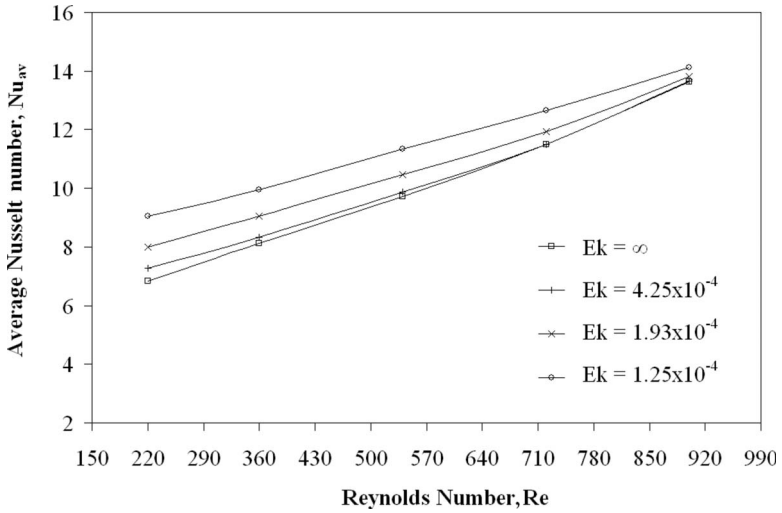

Fig. 5 Average Nusselt number variations with Reynolds number at different Ekman numbers for a silicon disk with water as the cooling fluid (β =0.5, b/d_n=0.5, and r_p/r_d=0.667)

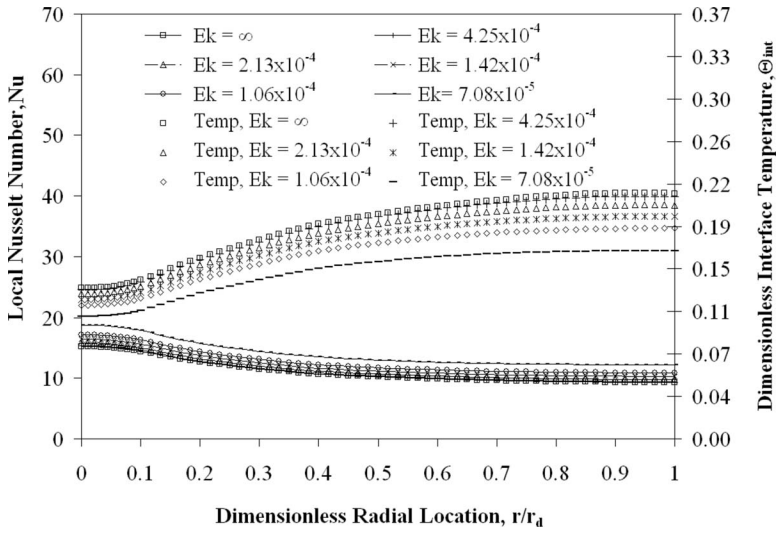

Fig. 6 Local Nusselt number and dimensionless interface temperature distributions for a silicon disk with water as the cooling f1uid at different Ekman numbers (Re=540, β=0.25, b/d_n=0.5, and r_p/r_d=0.667)

local Nusselt number results of the present working fluid (water) with three other coolants, namely, ammonia (NH_3), flouroinert (FC-77), and oil (MIL-7808) under a Reynolds number of 750. Even though the rotational rate (Ω) for the impingement disk was set at 350 rpm, the variation of Ekman numbers occurred since the density (ρ) and dynamic viscosity (μ) are different for each fluid. It may be noticed that MIL-7808 presents the highest dimensionless interface temperature and water has the lowest value. Ammonia shows the most uniform distribution of temperature along the radius of the disk. MIL-7808 presents the highest local Nusselt number values over the entire radial distance. Ammonia, on the other hand, provides the lowest Nusselt number. Higher Prandtl number fluids lead to a thinner thermal boundary layer and therefore a more effective heat removal rate at the interface. Present working fluid results are in agreement with the findings of Li et al. [7] where a larger Prandtl number corresponded to a higher recovery factor.

Figure 10 shows the dimensionless interface temperature and local Nusselt number distribution plots as a function of the dimensionless radial distance (r/r_d) measured from the axisymmetric impingement axis for different solid materials with water as the working fluid. The dimensionless temperature distribution plots reveal how the thermal conductivity affects the heat flux distribution. Constantan shows the lowest temperature at the impingement zone or stagnation point and the highest dimensionless temperature at the outlet in comparison with other solid materials. Copper and silver show a more uniform distribution and higher temperature values at the impingement zone due to their higher thermal conductivity. The dimensionless temperature and local Nusselt number distributions of these two materials are almost identical due to their similar thermal conductivity values. The crossover of curves for all five materials occurred due to a constant fluid flow

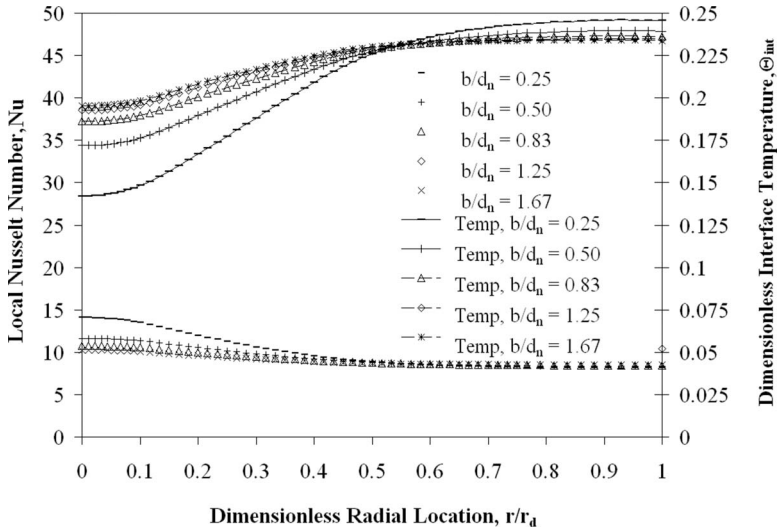

Fig. 7 Local Nusselt number and dimensionless interface temperature distributions for different silicon disk thicknesses with water as the cooling fluid (Re=450, Ek=4.25×10^{-4}, β=0.5, and r_p/r_d=0.667)

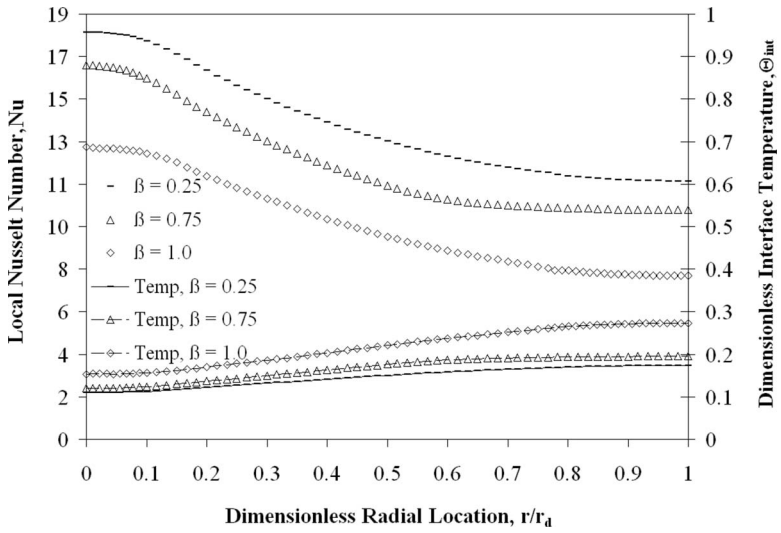

Fig. 8 Local Nusselt number and dimensionless interface temperature distributions for a silicon disk with water as the cooling fluid for different nozzle-to-target spacing (Re=750, Ek=4.25×10^{-4}, b/d_n=0.5, and r_p/r_d =0.667)

and heat flux rate that reaches a thermal energy balance. A solid material with lower thermal conductivity shows a higher maximum local Nusselt number.

Six different plate-to-disk confinement ratios (r_p/r_d) from 0.2 to 0.75 were modeled for water as the coolant and silicon as the disk material. The effects of the plate-to-disk confinement ratio on the dimensionless interface temperature and the local Nusselt number are shown in Fig. 11. The dimensionless interface temperature increases with the increment of the plate-to-disk confinement ratio (r_p/r_d). This increment coincides with the increment of the liquid film thickness in the free jet region as seen in Fig. 3. Under the same spinning and flow rates, when r_p is increased, the higher frictional resistance from the confinement disk slows down the fluid momentum. In addition, a thinner film thickness for the same flow rate results in a higher fluid velocity near the solid-fluid interface resulting in a higher rate of convective heat transfer. This is seen in the distribution of the local Nusselt number, which increases with the decrease of the plate-to-disk confinement ratio.

A correlation for the average Nusselt number was developed as a function of the confinement ratio, thermal conductivity ratio, dimensionless nozzle-to-target spacing ratio, Ekman number, and Reynolds number to accommodate most of the transport characteristics of a semiconfined liquid jet impingement cooling process. The correlation that best fitted the numerical data can be placed in the following form:

$$\mathrm{Nu}_{\mathrm{av}} = 1.94282\beta^{0.1}\mathrm{Re}^{0.75}\mathrm{Ek}^{-0.1}\varepsilon^{-0.7}(r_p/r_d)^{-0.05} \tag{17}$$

In developing this correlation, all average Nusselt number data corresponding to the variation of different parameters were used. Only data points corresponding to water as the fluid were used because the number of average heat transfer data for other fluids was small. The least square curve-fitting technique was used in developing this equation. The signs of the exponents were determined from the trend of variation of the Nusselt number with each parameter. Then, values were obtained by the least square fit of the corresponding logarithmic equation. Figure 12 gives the com-

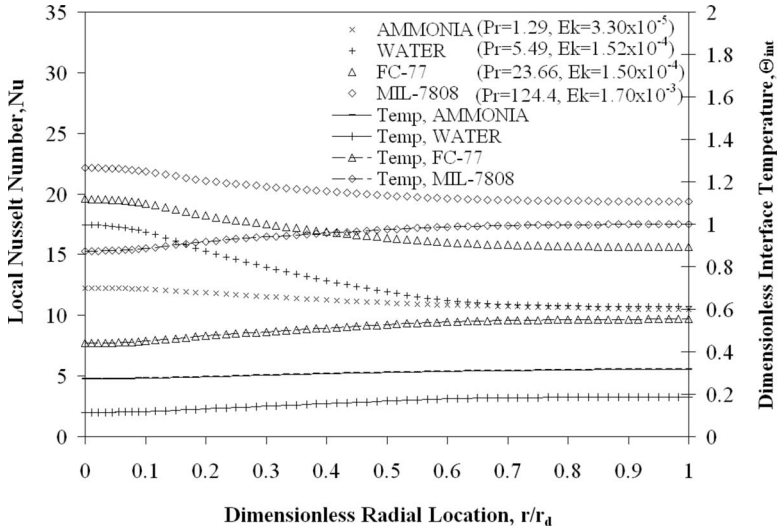

Fig. 9 Local Nusselt number and dimensionless interface temperature distributions for different cooling fluids for silicon as the disk material (Re =750, β=0.5, b/d_n=0.5, and r_p/r_d=0.667)

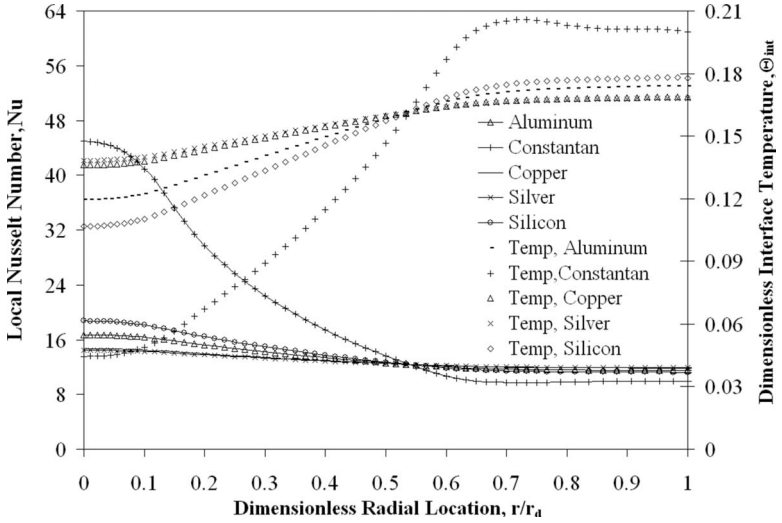

Fig. 10 Local Nusselt number and dimensionless interface temperature distributions for different solid materials with water as the cooling fluid (Re=875, Ek=4.25×10^{-4}, β=0.5, b/d_n=0.5, and r_p/r_d=0.667)

parison between the numerical average Nusselt numbers to the average Nusselt numbers predicted by Eq. (17). The average Nusselt number deviates in a range −15.13% to +15.61% from the one predicted by Eq. (17). The mean deviation is 6.94%. The ranges of the dimensionless variables in this study are the following: $360 \leq \mathrm{Re} \leq 900$, $1.06\times10^{-4} \leq \mathrm{Ek} \leq 4.25\times10^{-4}$, $0.25 \leq \beta \leq 1$, $0.2 \leq r_p/r_d \leq 0.75$, Pr=5.49, and $227.6 \leq \varepsilon \leq 627.6$. It should be noted from Fig. 12 that a large number of data points are very well correlated with Eq. (17). This correlation provides a convenient tool for the prediction of the average heat transfer coefficient for a partially confined liquid jet impingement on top of a spinning disk.

Conclusions

The solid-fluid dimensionless interface temperature and the local Nusselt number showed a strong dependence on the (1) Reynolds number, (2) rotational rate, (3) disk thickness, (4) nozzle-to-target spacing or impingement height, (5) plate-to-disk confinement ratio, (6) fluid properties, and (7) solid material properties. The increment of the Reynolds number increases the local heat transfer coefficient distribution over the entire solid-fluid interface. In general, rotation increases the local Nusselt number distribution values over the entire solid-fluid interface for Ek $>7.08\times10^{-5}$. A higher disk thickness provides a more uniform distribution of the interface temperature and heat transfer coefficient. As the nozzle-to-target distance increases from β=0.25 to 1, the existing fluid column between the target and the confinement diminishes the liquid jet momentum and therefore the heat removal rate. A decrease in the plate-to-disk confinement ratio increases the local Nusselt number at all locations in the disk. A higher Prandtl number fluid leads to a thinner thermal boundary layer and provides a more effective heat removal rate at the interface. Plate materials with higher thermal conductivity maintained a lower thermal resistance within the solid and therefore a more uniform temperature distribution happens at the interface. A correlation for average Nusselt number under partially confined liq-

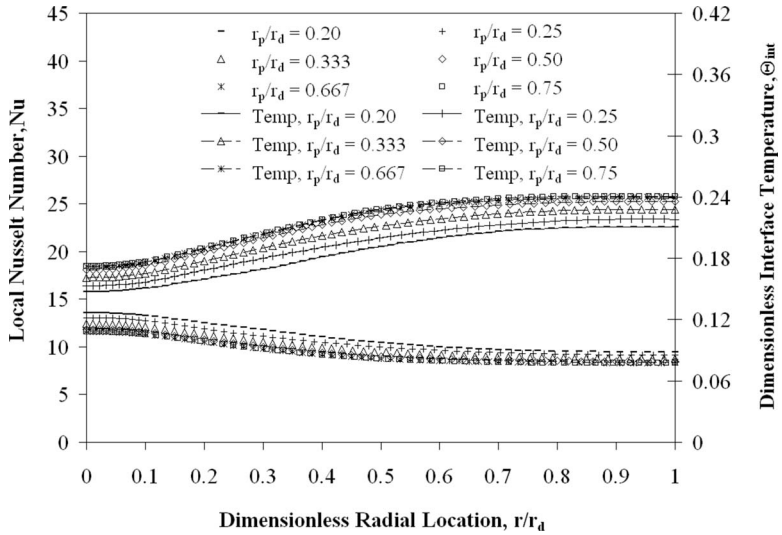

Fig. 11 Local Nusselt number and dimensionless interface temperature distributions for different plate-to-disk confinement ratios (Re=450, Ek =4.25×10^{-4}, β=0.5, and b/d_n=0.5)

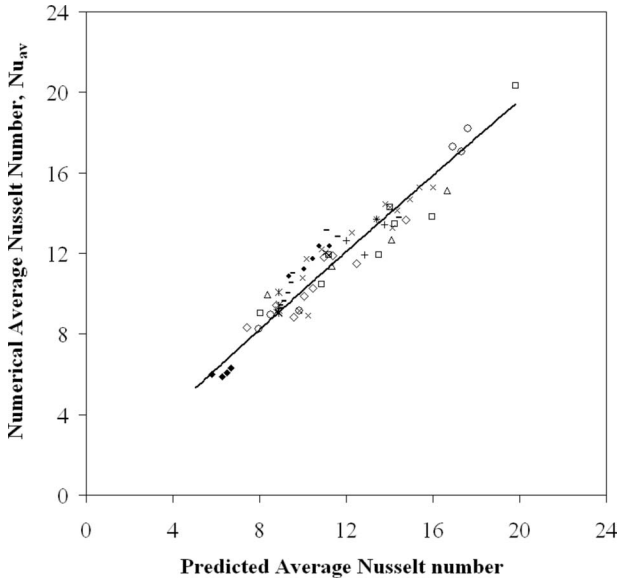

Fig. 12 Comparison of the predicted average Nusselt number (Eq. (17)) with numerical data

uid jet impingement over a spinning target is proposed in terms of the Reynolds number, Ekman number, dimensionless nozzle-to-target spacing ratio, thermal conductivity ratio, and confinement plate-to-disk radius ratio. The differences between the numerical and predicted values are in the range from −15.13% to +15.61%. The mean value of the error is 6.94%.

Nomenclature

b = disk thickness (m)
Cp = specific heat (J/kg K)
d_n = diameter of nozzle (m)
g = acceleration due to gravity (m/s^2)
Ek = Ekman number, $\nu_f/(4\Omega r_d^2)$
h = heat transfer coefficient (W/m^2 K), $q/(T_{int} - T_J)$
H_n = distance of the nozzle from the plate (m)
k = thermal conductivity (W/m K)
Nu = Nusselt number, $(hd_n)/k_f$
Nu_{av} = average Nusselt number, $(h_{av}d_n)/k_f$
p = pressure (Pa)
Pr = Prandtl number, $(\mu_f Cp_f)/k_f$
q = heat flux (W/m^2)
r = radial coordinate (m)
r_d = disk radius (m)
r_p = plate radius (m)
r_p/r_d = confinement plate-to-disk radius ratio (confinement ratio)
Re = Reynolds number, $(V_J d_n)/\nu_f$
T = temperature (K)
$\bar{T}_{int}$ = average interface temperature (K), $2/r_d^2 \int_0^{r_d} T_{int} r dr$
V_J = jet velocity (m/s)
$V_{r,z,\theta}$ = velocity component in the r, z, and θ directions (m/s)
z = axial coordinate (m)

Greek Symbols

β = dimensionless nozzle-to-target spacing, H_n/d_n
δ = free surface height (m)
ε = thermal conductivity ratio, k_S/k_f
μ = dynamic viscosity (kg/m s)
ν = kinematic viscosity (m^2/s)
θ = angular coordinate (rad)
Θ = dimensionless temperature, $2k_f(T_{int} - T_J)/(qd_n)$
ρ = density (kg/m^3)
σ = surface tension (N/m)
Ω = angular velocity (rad/s)

Subscripts

atm = ambient
av = average
f = fluid
int = interface
j = jet or inlet
n = nozzle
s = solid

References

[1] McMurray, D. C., Myers, P. S., and Uyehara, O. A., 1966, "Influence of Impinging Jet Variables on Local Heat Transfer Coefficients Along a Flat Surface With Constant Heat Flux," *Proceedings of the Third International Heat Transfer Conference*, Chicago, IL, Vol. 2, pp. 292–299.

[2] Metzger, D. E., Cammings, K. N., and Ruby, W. A., 1974, "Effects of Prandtl Number on Heat Transfer Characteristics of Impinging Liquid Jets," *Proceedings of the Fifth International Heat Transfer Conference*, Tokyo, Vol. 2, pp. 20–24.

[3] Hung, Y. H., and Lin, Z. H., 1994, "Effect of Confinement Plate on Heat Transfer Characteristics of a Circular Jet Impingement," *Proceedings of the ASME Fundamentals of Heat Transfer in Forced Convection*, HTD, Vol. 285, pp. 101–109.

[4] Webb, B. W., and Ma, C. F., 1995, "Single-Phase Liquid Jet Impingement Heat Transfer," Adv. Heat Transfer, **26**(1), pp. 105–117.

[5] Garimella, S. V., and Nenaydykh, B., 1996, "Nozzle-Geometry Effects in Liquid Jet Impingement Heat Transfer," Int. J. Heat Mass Transfer, **39**(14), pp. 2915–2923.

[6] Fitzgerald, J. A., and Garimella, S. V., 1998, "A Study of the Flow Field of a Confined and Submerged Impinging Jet," Int. J. Heat Mass Transfer, **41**(8–9), pp. 1025–1034.

[7] Li, D. Y., Guo, Z. Y., and Ma, C. F., 1997, "Relationship Between the Recovery Factor and the Viscous Dissipation in a Confined, Impinging, Circular Jet of High-Prandtl Number Liquid," Int. J. Heat Fluid Flow, **18**(6), pp. 585–590.

[8] Rahman, M. M., Dontaraju, P., and Ponnappan, R., 2002, "Confined Jet Impingement Thermal Management Using Liquid Ammonia as the Working Fluid," *Proceedings of the ASME International Mechanical Engineering Congress and Exposition*, New Orleans, LA, pp. 1–10.

[9] Li, C. Y., and Garimella, S. V., 2001, "Prandtl-Number Effects and Generalized Correlations for Confined and Submerged Jet Impingement," Int. J. Heat Mass Transfer, **44**(18), pp. 3471–3480.

[10] Ichimiya, K., and Yamada, Y., 2003, "Three-Dimensional Heat Transfer of a Confined Circular Impinging Jet With Buoyancy Effects," ASME J. Heat Transfer, **125**(2), pp. 250–256.

[11] Dano, B., Liburdy, J. A., and Kanokjaruvijit, K., 2005, "Flow Characteristics and Heat Transfer Performances of a Semi-Confined Impinging Array of Jets: Effect of Nozzle Geometry," Int. J. Heat Mass Transfer, **48**(3–4), pp. 691–701.

[12] Carper, H. J., Jr., and Deffenbaugh, D. M., 1978, "Heat Transfer From a Rotating Disk With Liquid Jet Impingement," *Sixth International Heat Transfer Conference*, Toronto, ON, Hemisphere Public, Washington, DC, Vol. 4, pp. 113–118.

[13] Carper, H. J., Jr., Saavedra, J. J., and Suwanprateep, T., 1986, "Liquid Jet Impingement Cooling of a Rotating Disk," ASME J. Heat Transfer, **108**(3), pp. 540–546.

[14] Metzger, D. E., Bunker, R. S., and Bosh, G., 1991, "Transient Liquid Crystal Measurement of Local Heat Transfer on a Rotating Disk With Jet Impingement," ASME J. Turbomach., **113**(1), pp. 52–59.

[15] Thomas, S., Faghri, A., and Hankey, W. L., 1991, "Experimental Analysis and Flow Visualization of a Thin Liquid Film on a Stationary and Rotating Disk," ASME J. Fluids Eng., **113**(1), pp. 73–80.

[16] Rahman, M. M., and Faghri, A., 1992, "Numerical Simulation of Fluid Flow and Heat Transfer in a Thin Liquid Film Over a Rotating Disk," Int. J. Heat Mass Transfer, **35**(6), pp. 1441–1453.

[17] Rahman, M. M., and Faghri, A., 1992, "Analysis of Heating and Evaporation From a Liquid Film Adjacent to a Horizontal Rotating Disk," Int. J. Heat Mass Transfer, **35**(10), pp. 2655–2664.

[18] Faghri, A., Thomas, S., and Rahman, M. M., 1993, "Conjugate Heat Transfer From a Heated Disk to a Thin Liquid Film Formed by a Controlled Impinging Jet," ASME J. Heat Transfer, **115**(1), pp. 116–123.

[19] Hung, Y. H., and Shieh, Y. R., 2001, "Convective Heat Transfer From a Rotating Ceramic-Based Multichip Disk With Round Jet Impingement," *Proceedings of the National Heat Transfer Conference*, Anaheim, CA, Vol. 1, pp. 97–103.

[20] Ozar, B., Cetegen, B. M., and Faghri, A., 2004, "Experiments on Heat Transfer in a Thin Liquid Film Flowing Over a Rotating Disk," ASME J. Heat Transfer,

126(2), pp. 184–192.
[21] Rice, J., Faghri, A., and Cetegen, B. M., 2005, "Analysis of a Free Surface Film From a Controlled Liquid Impinging Jet Over a Rotating Disk Including Conjugate Effects, With and Without Evaporation," Int. J. Heat Mass Transfer, **48**(25–26), pp. 5192–5204.
[22] Burmeister, L. C., 1993, *Convective Heat Transfer*, 2nd ed., Wiley, New York, pp. 581–590.
[23] White, F. M., 1999, *Fluid Mechanics*, 4th ed., McGraw-Hill, New York, pp. 234–236.
[24] Popiel, C. O., and Boguslawski, L., 1986, "Local Heat Transfer From a Rotating Disk in an Impinging Round Jet," ASME J. Heat Transfer, **108**(2), pp. 357–364.
[25] Vanyo, J. P., 1993, *Rotating Fluids in Engineering and Science*, Butterworth-Heinemann, MA, Chap. 14, pp. 233–264.
[26] Özisik, M. N., 1993, *Heat Conduction*, 2nd ed., Wiley, New York, pp. 657–660.
[27] Bejan, A., 1995, *Convection Heat Transfer*, 2nd ed., Wiley, New York, pp. 595–602.
[28] Bula, A. J., 1999, "Numerical Modeling of Conjugate Heat Transfer During Free Liquid Jet Impingement," Ph.D. thesis, University of South Florida, Tampa, FL.
[29] Fletcher, C. A. J., 1984, *Computational Galerkin Methods*, Springer, New York, pp. 27 and 205.
[30] Liu, X., Lienhard, J. H., and Lombara, J. S., 1991, "Convective Heat Transfer by Impingement of Circular Liquid Jets," ASME J. Heat Transfer, **113**(3), pp. 571–582.
[31] Ma, C. F., Zheng, Q., Lee, S. C., and Gomi, T., 1996, "Impingement Heat Transfer and Recovery Effect With Submerged Jets of Large Prandtl Number Liquid 2. Initially Laminar Confined Slot Jets," Int. J. Heat Mass Transfer, **40**(6), pp. 1491–1500.
[32] Brodersen, S., Metzger, D. E., and Fernando, H. J. S., 1996, "Flows Generated by the Impingement of a Jet on a Rotating Surface, Part 1: Basic Flow Patterns," ASME J. Fluids Eng., **118**(1), pp. 61–67.
[33] Lachefski, H., Cziesla, T., Biswas, G., and Mitra, K., 1996, "Numerical Investigation of Heat Transfer by Rows of Rectangular Impinging Jets," Numer. Heat Transfer, Part A, **30**(1), pp. 87–101.

Keunhan Park
George W. Woodruff School of Mechanical Engineering,
Georgia Institute of Technology,
Atlanta, GA 30332

Graham L. W. Cross
School of Physics and Centre for Research on Adaptive Nanostructures and Nanodevices (CRANN),
Trinity College Dublin,
Dublin 2, Ireland

Zhuomin M. Zhang[1]
George W. Woodruff School of Mechanical Engineering,
Georgia Institute of Technology,
Atlanta, GA 30332
e-mail: zhuomin.zhang@me.gatech.edu

William P. King[1]
Department of Mechanical Science and Engineering,
University of Illinois Urbana-Champaign,
Urbana, IL 61801
e-mail: wpk@uiuc.edu

Experimental Investigation on the Heat Transfer Between a Heated Microcantilever and a Substrate

This work describes the heat transfer process from a heated microcantilever to a substrate. A platinum-resistance thermometer with a 140 nm width was fabricated on a SiO_2-coated silicon substrate. The temperature coefficient of resistance estimated from the measurement was 7×10^{-4} K^{-1}, about one-fifth of the bulk value of platinum. The temperature distribution on the substrate was obtained from the thermometer reading, as the cantilever raster scanned the substrate. Comparison between the measurement and calculation reveals that up to 75% of the cantilever power is directly transferred to the substrate through the air gap. From the force-displacement experiment, the effective tip-specimen contact thermal conductance was estimated to be around 40 nW/K. The findings from this study should help understand the thermal interaction between the heated cantilever and the substrate, which is essential to many nanoscale technologies using heated cantilevers. [DOI: 10.1115/1.2953238]

Keywords: atomic force microscope, heated microcantilever, micro-/nanoscale heat transfer, nanoscale thermometer

1 Introduction

Since its invention for thermomechanical data storage [1], the applications of a heated microcantilever have expanded to thermal dip-pen nanolithography [2,3], thermochemical nanolithography [4], nanometer-scale thermal analysis [5,6], and thermally sensed nanotopography [7–9]. Because most of these applications make use of the thermal interaction between a heated cantilever and a substrate, the heat transfer process must be well understood to further improve these technologies based on heated cantilevers. Significant efforts have been made to understand the thermal, electrical, and mechanical behaviors of heated cantilevers in various operation conditions [10,11] and environments [12,13]. However, these studies focused on the cantilever itself, without a detailed heat transfer analysis of the substrate. Although some studies considered a substrate when performing the design analysis of heated cantilevers for thermomechanical data storage [14] and thermally sensed topography [15], to date, no experimental investigation on the cantilever-to-substrate heat transfer has been reported.

A probe equipped with a temperature-sensing tip has long been incorporated in a scanning probe microscope (SPM) platform for the development of scanning thermal microscopy (SThM) [16–20]. With the help of SThM, remarkable progress has been made in understanding complicated heat transfer mechanisms at nanoscale contacts and their thermal conductances [17,21,22]. However, an understanding of the heat transfer mechanisms in SThM cannot be directly applied to the cantilever-to-substrate heat transfer for the following reasons. In SThM, the substrate is usually heated to several tens of degrees above room temperature, whereas the heated cantilever is typically operated at much higher temperatures from several hundreds to sometimes above 1300 K. Moreover, the heated cantilever has a relatively large heater area, e.g., 8×16 μm^2. As a consequence, a substantial amount of heat will be transferred via air conduction to the substrate [7].

In the present study, a resistive thermometer with a submicron spatial resolution was fabricated on the substrate to obtain the surface temperature at various locations with respect to the cantilever position. In the following, the experimental setup is described first. A semianalytical model is developed to predict the surface temperature distribution on the substrate. Comparison between the experiment and the modeling not only reveals the mechanisms of heat transfer from the cantilever to the substrate but also allows an estimation of the resultant substrate temperature changes.

2 Experiment

The heated cantilever is made from doped single-crystal silicon. It features a "U" shape to accommodate electrical current flow and has a heater integrated at the free end, as shown in Fig. 1(*a*). The cantilever tip has a height between 500 nm and 1 μm, with a tip radius of 20–50 nm. The cantilever used in the experiment has a heater size of 8×16 μm^2. The heater region was phosphorus doped with a concentration around 10^{17} cm^{-3}. The legs of the cantilever acted as electrical leads, and thus were heavily phosphorus doped to around 10^{20} cm^{-3} to achieve low resistivity. The length and width of each leg are 85 μm and 15 μm, respectively. When an electrical current flows through the cantilever, more than 90% of the power is dissipated in the highly resistive heater region, resulting in a temperature increase that can exceed 1300 K [10]. The thickness of the cantilever was designed to be around 1 μm. While each cantilever has a nearly uniform thickness, the cantilever thickness can vary slightly over a given batch due to etch nonuniformity. A thermal constriction region, with a length of 15 μm and a width of 6.5 μm between the heater and each leg, helps confine to some extent the thermal energy to the heater region [23].

[1]Corresponding authors.

Contributed by the Heat Transfer Division of ASME for publication in the JOURNAL OF HEAT TRANSFER. Manuscript received July 25, 2007; final manuscript received November 12, 2007; published online August 8, 2008. Review conducted by Minking Chyu. Paper presented at the 2007 ASME-JSME Thermal Engineering Conference and Summer Heat Transfer Conference (HT2007), Vancouver, British Columbia, Canada, July 8–12, 2007.

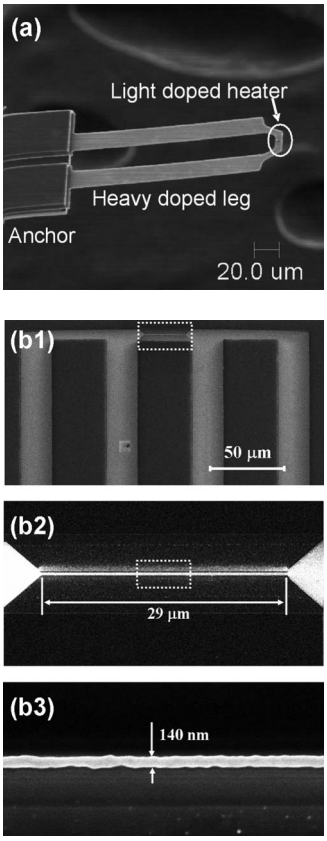

Fig. 1 (*a*) **SEM image of a heated microcantilever. The cantilever is made of single-crystal silicon, with a high phosphorus concentration in the leg region and a low phosphorus concentration in the heater region. (*b*) Top views of the fabricated PRT, obtained with SEM with different magnifications. The sensing probe is 140 nm in width and 29 μm in length. The thickness is approximately 35 nm.**

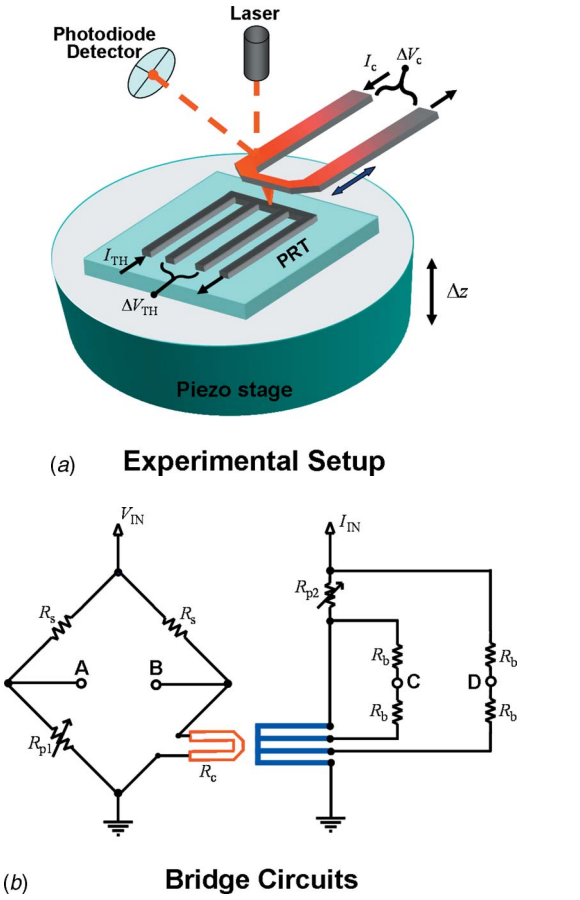

Fig. 2 (*a*) **The experimental setup in an AFM platform. While the cantilever scans the specimen, the AFM controller simultaneously measures the surface topography, the cantilever voltage, and the PRT resistance. (*b*) The bridge circuits used in the measurements of the cantilever (left) and PRT (right).**

A surface micromachined thermometer with a submicron spatial resolution is well suited to measure the substrate temperature. Recently, Au/Ni thin-film thermocouples with a submicron junction have been developed to measure the surface temperature change during electron-beam resist heating [24,25]. Although a thermocouple can achieve good spatial resolution, its low sensitivity is a serious drawback. For example, the Seebeck coefficient of the thermocouple in Ref. [25] is 6–7 μV/K, which is too small to accurately measure a temperature change that is less than 10 K. A resistive thermometer has a relatively high sensitivity, although the achievable spatial resolution is somewhat lower than that of a thermocouple junction. In the present study, a thin-film platinum-resistance thermometer (PRT) with a submicron sensing probe was fabricated. After deposition of a 1-μm-thick SiO_2 layer on a Si substrate of 500 μm thickness, a platinum layer of 35 nm thickness was deposited by e-beam evaporation. The submicron PRT was then fabricated using a focused-ion-beam (FIB) milling process. After the PRT was fabricated, a 5 nm Al_2O_3 layer was deposited to prevent electrical interface with the cantilever tip. The thermometer has a four-wire configuration for accurate measurements of its electrical resistance. Based on the scanning electron microscopic (SEM) images shown in Fig. 1(*b*), the length and width of the sensing probe are measured to be 29 μm and 140 nm, respectively, with an uncertainty of 10%. Due to its negligibly small thermal resistance in the vertical direction and very large thermal resistance in the lateral direction, the presence of PRT has little influence on the substrate temperature.

The experiment was performed in a commercial atomic force microscope (AFM) platform (Asylum MFP-3D), illustrated in Fig. 2(*a*). The AFM was operated in oscillatory ac mode to prevent the PRT from any possible damage by the contact force of the cantilever tip [9]. While the cantilever scans the surface of the PRT specimen, a topographical image can be obtained with the AFM instrument using its built-in laser and a position-sensing photodiode detector. Even though the cantilever is operated in ac mode, it remains in a thermal steady state because the oscillating frequency (75.6 kHz) is much higher than the inverse of the cantilever's thermal time constant (0.3 ms) [9,11]. Thus, the cantilever voltage can be easily measured without any frequency-domain instrumentation. By monitoring the resistance of PRT during the scan, the temperature change of the substrate surface can be determined. A multichannel 16 bit analog-to-digital (A/D) converter embedded in the AFM controller was used to simultaneously measure the cantilever and PRT voltage signals.

Both the cantilever and PRT signals were measured in bridge circuits, illustrated in Fig. 2(*b*), to remove any dc offset that could be more than 1000 times the actual signal. The cantilever voltage change was measured using a Wheatstone bridge through the potential difference between A and B, i.e., $\Delta V_C = V_B - V_A$. During the experiment, the total input voltage, V_{in}, was feedback controlled to maintain the cantilever resistance at a prescribed value. For real-time control, an NI PCI-6052 data acquisition system measured the voltage drops across the cantilever and the sense resistor with a sampling rate of 2000 data per second. The LABVIEW program was implemented to develop the proportional-integral-derivative (PID) control of V_{in}. For the PRT measurement, we used a modified Wheatstone bridge that is compatible with its

four-wire configuration. The voltage change of the sensing probe can be expressed from the voltage difference between C and D as $\Delta V_{\text{th}}=1.94(V_C-V_D)$, where the coefficient 1.94 comes from the lead resistances of the PRT; if the lead resistances are negligibly small, the coefficient would become 2. The resistance change of the sensing probe can thus be obtained from $\Delta R_{\text{th}}=\Delta V_{\text{th}}(R_{p2}/V_{p2})$, where R_{p2} is the potentiometer resistance adjusted to be the same as the base thermometer resistance and V_{p2} is the voltage drop across the potentiometer. In the experiment, 1 kΩ and 5.16 kΩ resistors with 1% tolerance were used for the cantilever and thermometer bridge circuits, respectively.

Before the cantilever is engaged on the specimen, the operation condition and electrical properties of the PRT were examined. The driving current I_{in} was set to 0.2 mA, providing the base thermometer resistance of 3.58 kΩ. The power dissipation is then 70.3 μW, resulting in a temperature rise of less than 0.03 K. The resistivity of the Pt strip can be estimated from the measured resistance and its geometry: 35 nm thick, 140 nm wide, and 29 μm long. The estimated resistivity of 5.63×10^{-5} Ω cm is about five times that of bulk platinum, i.e., 1.06×10^{-5} Ω cm. In a previous study [26], the resistivity of an electrodeposited 70-nm-diameter Pt nanowire was reported to be three times of the bulk resistivity. It is expected that the rough boundaries formed during the FIB milling process might enhance boundary scattering, giving rise to the large resistivity.

3 Thermal Model

Thermal and electrical coupling of the heated cantilever and the thermometer complicate the analysis of the experimental results. However, this complication can be substantially relieved by the appropriate numerical modeling. Thermal and electrical behaviors of the heated cantilever have been numerically studied when it is under the steady heating [10,12,27] and periodic heating [11]. However, all of these studies considered only the heated cantilever, assuming no thermal interaction with a substrate. Although some works investigated the heat transfer from the heated cantilever to a substrate [15,28], the assumption that the substrate maintains at room temperature has prevented further insight into heat transfer to the substrate. A different approach that computes the temperature distribution of not only the cantilever but also the substrate is thus required.

This section describes the calculation of the temperature distribution along the cantilever as well as that of the substrate when the cantilever is placed above the substrate with a small and parallel gap, as illustrated in Fig. 3(*a*). As for the cantilever, the present analysis adopts a simplified one-dimensional (1D) heat conduction model. The thermal resistance across the cantilever thickness and width is very small compared to that along or from the cantilever, validating the 1D steady thermal modeling given by

$$\frac{d}{ds}\left(k_c A_c \frac{dT_c}{ds}\right)+\dot{q}A_c-q_a'-q_g'=0 \tag{1}$$

where s is the coordinate along the axis of the cantilever, k_c and A_c are the thermal conductivity and the cross sectional area of the cantilever, and $\dot{q}$ is the volume density of heat generation. In Eq. (1), $q_a'=G_a'(T_c-T_\infty)$ and $q_g'=G_g'(T_c-T_s)$ are, respectively, the heat transfer rate to the ambient air and that through the air gap to the surface of the specimen per unit length, where G_a' and G_g' are the corresponding thermal conductances, T_∞ is the ambient temperature, and T_s is the surface temperature of the specimen. Due to symmetry, only half of the cantilever was modeled. The opposite end was assumed to be fixed at room temperature (T_∞) because the silicon base can be taken as a heat sink. The cantilever tip was not considered in the thermal analysis, since the amount of heat transferred through the tip will be negligibly small compared to that through the air gap. G_a' was calculated from the effective heat transfer coefficient h using $G_a'=h(w_c+2d_c)$, where w_c and d_c are,

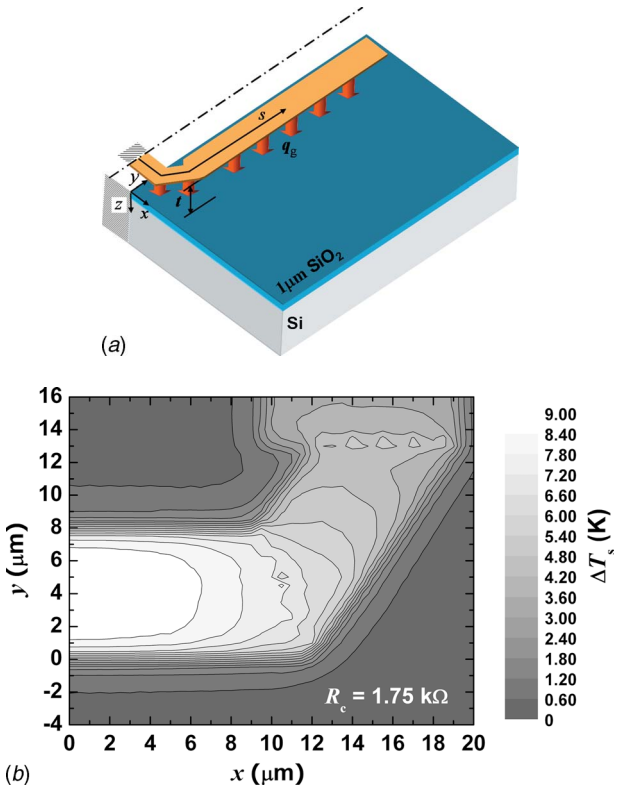

Fig. 3 (*a*) Schematic of the cantilever and the specimen (not to scale). The air gap between the cantilever and the specimen is assumed to be parallel, through which q_g is transferred to the SiO_2 film and eventually the Si substrate. (*b*) The calculation results of the specimen surface temperature distribution when the cantilever resistance is 1.75 kΩ.

respectively, the width and thickness of the cantilever. Note that h is mainly due to heat conduction of the air and is on the order of 1000 W/m^2 K, as explained in previous studies [10–12]. Since the cantilever-substrate gap is in the transition regime between the continuum and free molecular flow, G_g' can be written as a function of the gap [29],

$$G_g'=\frac{w}{t}\frac{k_a}{\Lambda}\left(\frac{1}{\Lambda}+\frac{C}{t}\right)^{-1} \tag{2}$$

where k_a is the mean thermal conductivity of the bulk air between two parallel plates; Λ is the mean free path of the air; t is the width of the air gap; and C is a coefficient, which is on the order of 1 as estimated from rarefied gas dynamics [30]. Near-field thermal radiation was not considered here because the heat transfer rate due to the near-field radiation is less than 1% of the air conduction when the cantilever-specimen gap is near 1 μm [31]. The thermal conductivity of the cantilever was taken from previous studies considering the doping level, temperature, and boundary scattering [13,27,32,33].

Computing the substrate temperature distribution is complicated because of heat transfer from the U-shaped cantilever and the presence of the SiO_2 film. While the finite-element method (FEM) can handle geometric complications, it is computationally intensive, particularly when iteration is required. A semianalytical approach is thus adopted based on a double-integral Fourier transform [34] and a matrix formulation [35]. Because the air gap is much smaller than the width of the cantilever, the heat transfer through the gap may be treated as 1D. In essence, the specimen was treated as being subjected to a cantilever-shaped heat source

on its top surface. When the heat source is divided into N rectangular segments, the temperature at any given location on the specimen surface can be expressed as [34]

$$T_s(x,y) = T_\infty + \frac{4}{\pi^2}\sum_{i=1}^{N}\int_0^\infty\int_0^\infty \tilde{\Theta}_i(\alpha,\beta)\cos(\alpha X_i)\cos(\beta Y_i)d\alpha d\beta \tag{3}$$

where $\tilde{\Theta}_i(\alpha,\beta)$ is a Fourier-transformed temperature change due to the ith segment [35]:

$$\tilde{\Theta}_i(\alpha,\beta) = \frac{q_i''[k_m\tanh(\gamma d_f) + k_f\tanh(\gamma d_m)]}{\alpha\beta\gamma[k_m k_f + k_f^2\tanh(\gamma d_f)\tanh(\gamma d_m)]}\sin(\alpha l)\sin(\beta w) \tag{4}$$

Here, (X_i, Y_i) is a translated position of (x,y) based on the center of the ith segment; q_i'' is the heat flux; $\gamma=(\alpha^2+\beta^2)^{1/2}$; k_m and d_m are, respectively, the thermal conductivity and thickness of the Si substrate; k_f and d_f are those of the SiO_2 film; and l and w are, respectively, the half-length and half-width of the segment. It should be noted that Eqs. (3) and (4) were formulated under the boundary condition that the bottom of the substrate maintains at room temperature. From the temperature distribution of the substrate, the mean temperature of the PRT sensing probe can be obtained by

$$T_{\text{th}} = \frac{1}{L}\int_L T_s(x,y)dl \tag{5}$$

where L is the length of the sensing probe and dl is either dx or dy depending on the thermometer alignment.

Equations (1)–(4) are coupled together and should be solved concurrently. The temperature distribution along the cantilever and that on the specimen surface were iteratively calculated until the cantilever-to-specimen heat transfer rate, q_g, converged within 0.1%. It should be noted that q_g can be obtained by the integration of q_g' in Eq. (1) along the cantilever. Similarly, the heat transfer rate to the air, q_a, can be calculated from q_a'. Once q_g is determined, the temperature distribution on the specimen surface can be easily calculated from Eqs. (3) and (4). Figure 3(*b*) shows an example of the surface temperature distribution around the cantilever heater region when the cantilever resistance is 1.75 kΩ. It is clear that the mean temperature of the PRT can be determined from the calculated surface temperature distribution.

4 Results and Discussion

The heated cantilever was electrically and thermally characterized when the cantilever was either far off the specimen or engaged on the specimen surface. Figure 4(*a*) shows the cantilever resistance as a function of the heater temperature, which was measured with a micro-Raman spectrometer with a spatial resolution near 1 μm [36]. The curve is nonlinear, and the slope becomes negative when $T_H > 900$ K [24]. In Fig. 4(*b*), the cantilever resistance is plotted against the cantilever power dissipation. When compared to the off-specimen case, the resistance curve of the on-specimen case is largely shifted to the high power dissipation. This is because the heat transfer rate is enhanced due to the presence of the specimen. The calculation results based on the measured resistance-temperature relation are shown as solid curves in Fig. 4(*b*). In the off-specimen data analysis, the cantilever thickness was taken as a fitting parameter and a value of $d_c=620$ nm was obtained. The thickness value is consistent with earlier studies where the thickness was measured with a SEM [10,11]. As shown in Fig. 4(*b*), the calculation agrees with the measurement within 0.5% in the off-specimen case. In the on-specimen analysis, the air gap t was taken as a fitting parameter. The calculated cantilever resistance agrees with the measurements within 1.0%. The air gap is estimated to be 770 nm, which is comparable to the

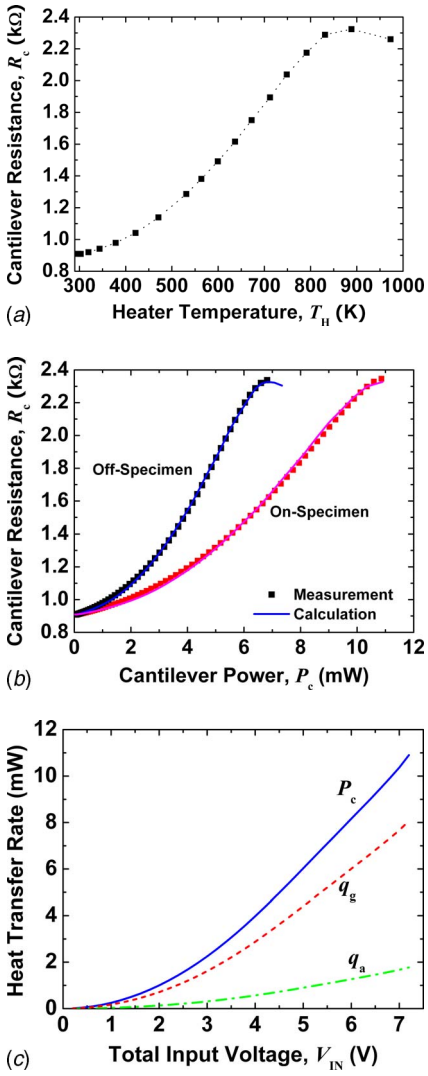

Fig. 4 The characteristics of the heated cantilever when it is off the specimen and on the specimen. (*a*) The cantilever resistance versus heater temperature measured with a micro-Raman spectroscope. (*b*) The cantilever dc characteristic curves are compared between the off-specimen and on-specimen cases. (*c*) The calculation reveals that up to 75% of the cantilever power is transferred to the substrate via the air gap and SiO_2 film.

cantilever tip height (~600 nm) measured with SEM. A little overestimation of the air gap can be explained with two reasons. The first reason is that in the actual measurement, the cantilever is not parallel to the substrate but tilted about 11 deg. Because of the difficulty in the iterative processes, the effect of tilting was not considered in the modeling. However, since most of heat is transferred near the free end of the cantilever, the effect of tilting would not provide significant difference on the results. Another reason may be because the modeling did not consider the trench next to the PRT in the real thermometer specimen, as shown in Fig. 6(*a*). Due to the trench whose depth is approximately 60 nm, the effective air gap will be greater than the cantilever tip height. Figure 4(*c*) shows the calculated cantilever power dissipation and heat transfer rates as functions of the total input voltage. The heat transfer to the substrate q_g is responsible for 70–75% of the cantilever power dissipation, whereas the heat transfer to the air q_a accounts for 10–15%. The remaining 10–20% of heat dissipated in the cantilever is transferred by conduction along the legs. Be-

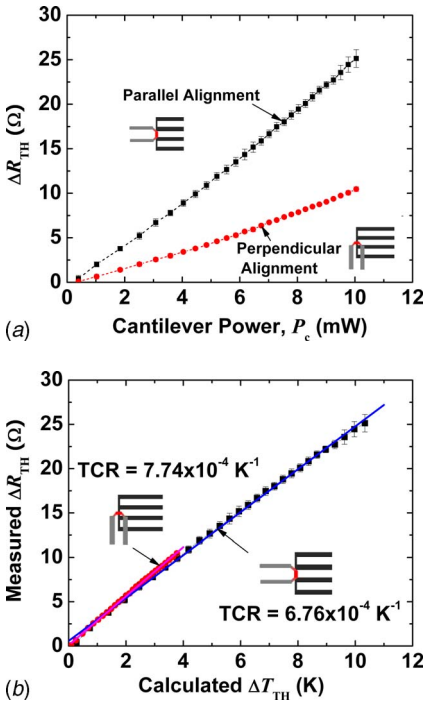

Fig. 5 The characteristics of the PRT. (*a*) The thermometer resistance change is linearly proportional to the cantilever power. The slope difference between parallel and perpendicular alignments is attributed to the effective heat transfer area. (*b*) By comparison of the measurement and the calculation, the TCR of the thermometer is estimated to be between 6.76×10^{-4} K^{-1} and 7.74×10^{-4} K^{-1}.

cause the thermal conductivity of heavily doped silicon is lower toward higher temperatures, the rate of heat transfer via the cantilever legs decreases with increasing V_{in}.

The PRT was characterized by placing the heated cantilever on the thermometer with two different directions: parallel alignment, and perpendicular alignment, as illustrated in Fig. 5. Figure 5(*a*) shows the resistance change of the PRT, ΔR_{th}, as the cantilever power increases. The thermometer resistance increases more steeply when the cantilever is aligned in parallel with the PRT sensing probe than when the cantilever is aligned perpendicular to it. This is because more area of the thermometer is underneath the cantilever. Figure 5(*b*) plots the measured thermometer resistance against the calculated average thermometer temperature rise. The temperature coefficient of resistance (TCR) was estimated to be 6.76×10^{-4} K^{-1} from the parallel alignment and 7.74×10^{-4} K^{-1} from the perpendicular alignment. These values are near one-fifth of the TCR of bulk platinum, which is 0.0039 K^{-1}. The difference of the thermometer TCR for the two alignments may be attributed to the presence of the trench in the specimen. As mentioned earlier, the presence of the trench may increase the effective cantilever-PRT air gap. Following the trench orientation, the effective air gap for the perpendicular alignment will be smaller than that for the parallel alignment; this results in a slightly higher substrate surface temperature increase for a given cantilever power. Since our calculation did not consider the presence of the trench, the calculated substrate temperature increase for the perpendicular alignment could be lower than the true value, yielding a somewhat higher TCR. Another reason may be caused by the misalignment of the cantilever, particularly in the perpendicular case, where oblique alignment of the cantilever will cover relatively a larger area of the sensing probe and thus yield a higher estimated TCR. The temperature-dependent electrical resistance of nanostructured platinum has been reported by several research groups. The TCR of microfabricated Pt structures depends strongly on the characteristic length as well as on the fabrication method. Marzi et al. [26] obtained 0.0014 K^{-1} as the TCR of an electrodeposited Pt nanowire of 70 nm in diameter, and Zhang et al. [37] measured the TCR of a polycrystalline Pt nanofilm of 62 nm in thickness to be 0.0013 K^{-1}. The lower TCR values obtained for the PRT in the present study may be consistent with its higher resistance values. An experimental calibration of the fabricated PRT was originally planned but could not be materialized due to the damage occurring in the PRT after several measurements.

Figure 6(*a*) shows the topographic image, obtained in ac mode, of the specimen around the PRT. The upper plot is the line scan along AA', where the sharp peak in the middle is associated with the Pt strip. Around the peak was a nearly 60-nm-deep trench, indicating that the FIB milling has overetched the sample. The overetching is unavoidable to guarantee the complete removal of the residue platinum and its adverse effect on the temperature measurement. Figure 6(*b*) shows the scanned cantilever voltage change while the cantilever resistance is maintained at 1.75 kΩ. The cantilever voltage image is inverse to the topographic image, because more power is needed to maintain the cantilever temperature as it moves closer to the substrate. The estimated sensitivity of the voltage signal change is approximately 130 μV/nm, which is similar to the previous experiment [9]. However, when compared to Ref. [9] that did not use feedback control, Fig. 6(*b*) exhibits higher noise. Due to the limited computation speed of real-time control, the sampling rate was set to 2000 data per second, yielding 0.5 ms interval between adjacent data points. This interval is comparable to the thermal time constant of the cantilever and thus cannot perfectly control the cantilever resistance, resulting in a higher noise floor. The noise will be suppressed in the actual measurement by averaging over a large number of samples.

The resistance change of the PRT is shown in Fig. 6(*c*) for parallel alignment as a function of the position (x,y) of the cantilever tip with respect to the Pt strip. When the tip is in the middle of the PRT, the average temperature of the PRT is the highest. The scanning speed was set to 0.5 Hz for scanning a line of 35 μm. With 256 points per line, the spatial resolution is about 140 nm, and it takes about 4 ms to measure each point. If the specimen is assumed as a semi-infinite medium with a point heat source, the thermal time constant of the specimen is about 10 μs. Hence, the scanning speed is slow enough for steady state to be established in the substrate. The maximum resistance increase is near 17 Ω, which can be converted to 7.0 K temperature rise. Although the cantilever heater is maintained at about 670 K and transfers 4.8 mW to the substrate, this small temperature rise at the specimen surface is because the heat is quickly spread into the silicon substrate due to its large thermal conductivity. After the cantilever passes the PRT, its resistance gradually decreases. However, heat transfer from the cantilever leg affects the substrate temperature, resulting in the asymmetric resistance curve. For comparison, the calculated resistance is plotted against the measurement on the top graph of Fig. 6(*c*) when the AFM scans across the AA' line. The calculated resistance change is steeper than that from the experiment. This suggests that the 1D model of heat transfer through the air gap may be an oversimplified approach and the lateral heat spread from the cantilever heater should be further considered.

Figure 6(*d*) shows the PRT contour and curves along the AA' line when the cantilever is in perpendicular alignment. When compared to Fig. 6(*c*), the resistance profile becomes much flatter because the thermometer is still exposed to the cantilever heater although the cantilever tip has been moved away from the Pt strip. However, the area of the PRT underneath the cantilever heater is only about half of that in the parallel alignment, resulting in about a half of the resistance increase in Fig. 6(*c*). The calculation agrees very well with the measurement. Although Fig. 6(*c*) shows a discrepancy between the calculated resistance change and the measured one, they occupy the almost the same area under their

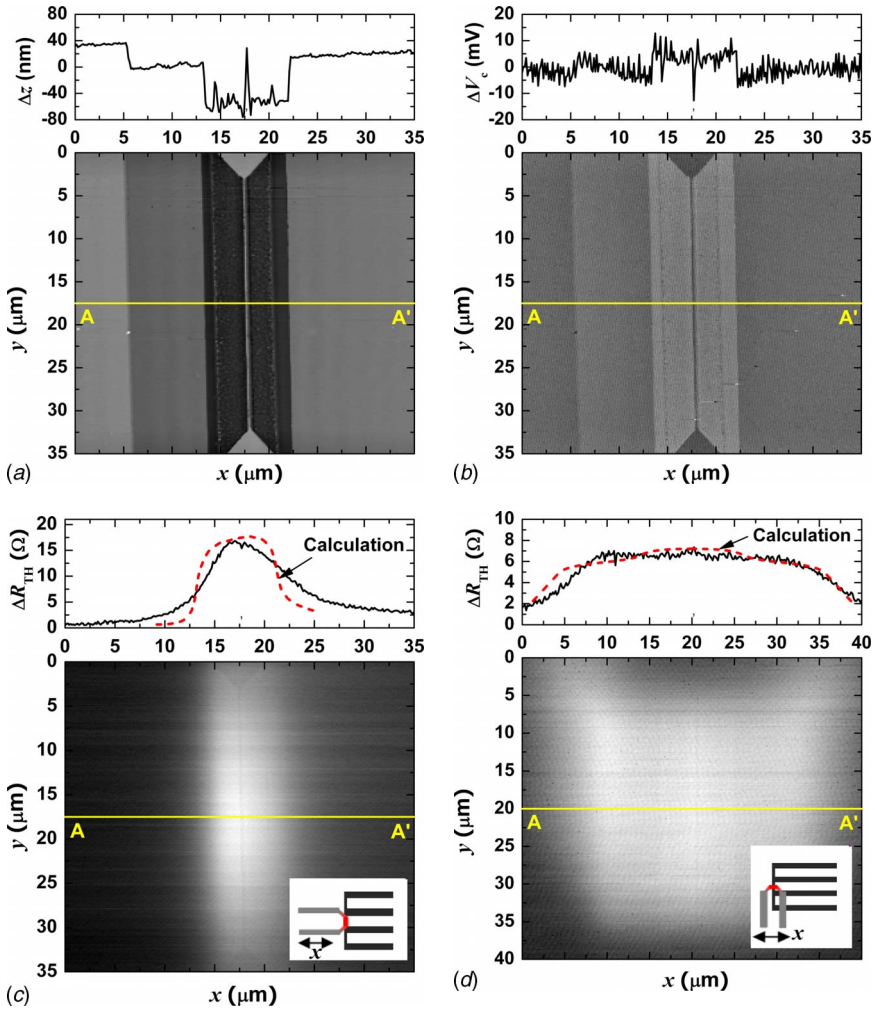

Fig. 6 AFM images when the cantilever scans over the thermometer in parallel and perpendicular alignments while maintaining its resistance at 1.75 kΩ. (*a*) The thermometer topographic image, (*b*) cantilever voltage image, (*c*) thermometer resistance image in parallel alignment, and (*d*) thermometer resistance image in perpendicular alignment. The calculation results of the thermometer resistance are shown together in (*c*) and (*d*).

curves within 5%. Provided that the thermometer signal is the averaged one over the thermometer length, the averaged temperature for the perpendicular alignment should not differ significantly between the calculation and the measurement.

Figure 7 shows the cantilever voltage and resistance (and the corresponding average temperature) of the PRT during a single-line scan for various cantilever resistances from 1.0 kΩ to 2.0 kΩ. The corresponding heater temperatures are 400 K, 520 K, 600 K, 670 K, and 740 K. The measurement was performed 128 times for each cantilever resistance setting across the same scan line (i.e., the center of the sensing probe), and the average of the 128 runs is plotted. Figure 7(*a*) shows the cantilever voltage curves in the same figure by ignoring the dc offset. When the cantilever is operated at higher resistances, the cantilever voltage changes more prominently due to the increasing slope of the resistance-temperature curve in this range. The sensitivity of the cantilever voltage signal versus the cantilever height is around 200 μV/nm at R_C=2.0 kΩ.

Figure 7(*b*) shows the PRT response during the scan in parallel alignment. The uncertainty in the PRT resistance is estimated to be around 0.40–0.45 Ω. The estimated uncertainty is a Type A standard uncertainty arising from random effects during 128 measurements, determined based on 95% confidence level; a Type B uncertainty arising from a systematic effect was assumed to be negligibly small. The right scale indicates the converted average temperature rise of the PRT. The small dip near the peak of the curve corresponds well with the cantilever voltage dip shown in Fig. 7(*a*). When the cantilever moves from trenches to the middle of the PRT Pt strip, the cantilever-specimen gap increases by as large as 95 nm, resulting in the decrease in the heat transfer rate to the specimen. A dip depth of the PRT signal at R_C=2.0 kΩ is around 1.0 Ω, corresponding to 0.25 K temperature decrease. The magnitude of this temperature decrease suggests that even though the nanoscale heat transfer near the tip may be important for local heating of the substrate [14], air conduction is the dominant mechanism in the cantilever-to-substrate heat transfer process. The uneven topography of the fabricated PRT in the present study does not allow measurement of the temperature rise due to heat transfer near the tip. In future work, this localized temperature rise needs to be measured with a thermometer that has a spatial resolution comparable to the tip radius. However, it should be noted that the electrical resistance and the TCR of the thermometer will decrease as the probe size is reduced, degrading the measurement sensitivity. The trade-off between sensitivity and spatial resolution must be carefully considered when designing a nanoscale thermometer.

The perpendicular-aligned scanning results are shown in Fig. 7(*c*), with uncertainties of around 0.40 Ω at R_c=1.0 kΩ and

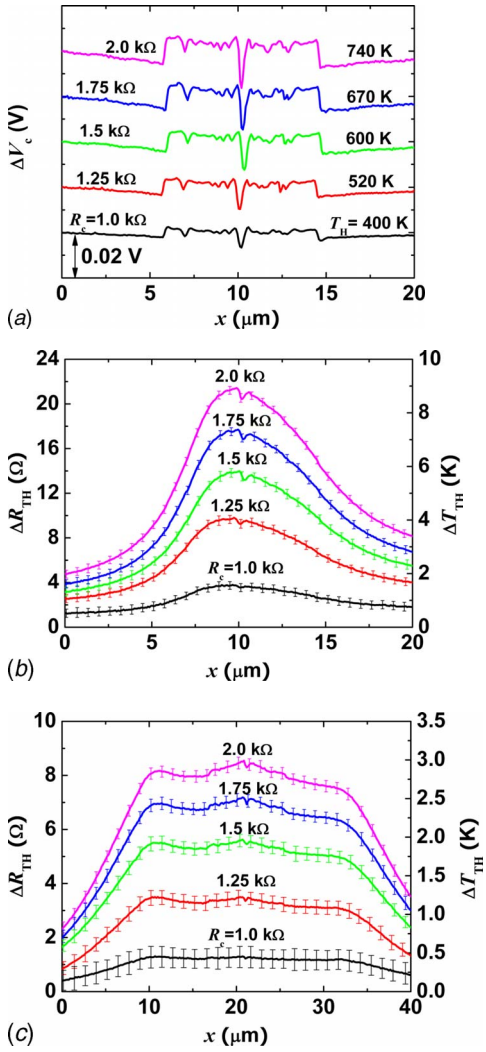

Fig. 7 The cantilever signals and thermometer signals when the cantilever resistance is controlled with different values. As the cantilever is maintained with higher resistance, more heat is transferred between the cantilever and substrate, resulting in (*a*) an increase in ΔV_C, (*b*) an increase in ΔR_{th} for parallel alignment, and (*c*) an increase in ΔR_{th} for perpendicular alignment.

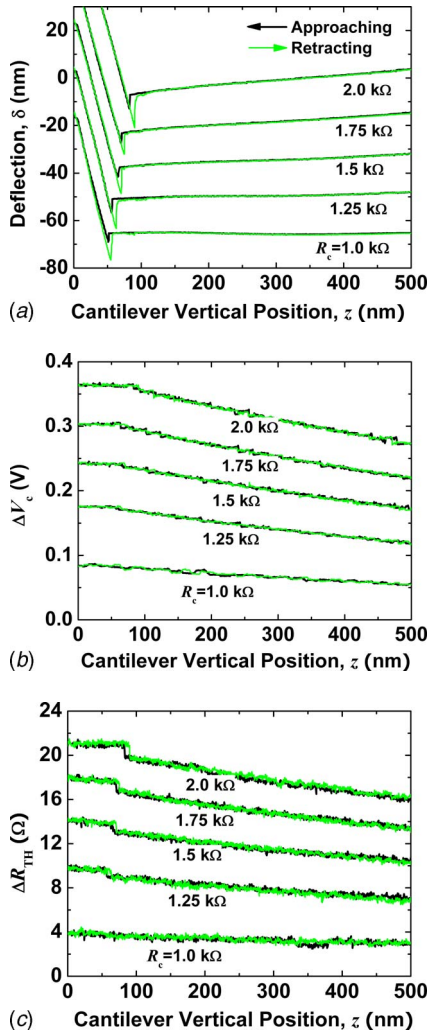

Fig. 8 The force-displacement experiment results when the cantilever is aligned with the nanothermometer in parallel and controlled with the cantilever resistance. (*a*) The deflection signal shows that as the cantilever resistance increases, the cantilever bends down due to electrostatic and thermal forces. (*b*) The cantilever voltage increases as the cantilever approaches the substrate to maintain the temperature. (*c*) As a result, the thermometer resistance increases as the cantilever approaches the substrate.

0.20–0.25 Ω at other operation conditions. As already observed in Fig. 6(*d*), there exists a flat region on the order of the cantilever heater width. The resistance of the PRT experiences a small increase for x from approximately 17 μm to 26 μm; this is due to the presence of the trench that causes the cantilever to be closer to the specimen. Right at the middle of the Pt strip, the cantilever is raised and the resistance or temperature of the PRT exhibits a dip. The curves are slightly asymmetric, which is mostly likely caused by the uneven mount of the cantilever. Another possibility is that the cantilever temperature profile may be asymmetric due to thermoelectric effects. Recently, Jungen et al. [38] demonstrated that the Thomson effect becomes important when the device dimension is significantly reduced, causing the asymmetric temperature profile of the device.

Since the scanning experiment cannot measure the localized heat transfer near the tip due to the uneven topography of the PRT, an alternative approach should be considered. To this end, the so-called force-displacement experiment was performed. In the experiment, the cantilever deflection, cantilever voltage, and thermometer resistance were simultaneously recorded while the heated cantilever approached and retracted from the thermometer aligned in parallel with the cantilever. Figure 8(*a*) shows the cantilever deflection for different cantilever resistances. When the cantilever approaches the substrate, the cantilever deflection signal remains nearly unchanged until the cantilever contacts the thermometer. The cantilever then "jumps" to contact with the thermometer due to the attractive force between the tip and thermometer. This attractive force is also responsible for the "snapping" out of contact when the cantilever retracts from the thermometer. Since the temperature in all cases is well above the saturation temperature of water, we presume that the heated cantilever locally evaporates most or all of the adsorbed water near the tip. Thus, the attractive force may not originate from the capillary effect of the water film formed between the cantilever tip and thermometer, as is the case of the SThM experiment at near room temperature [21,39]. The attractive force may be the combination of the electrostatic force and the thermal force [40]. Figures 8(*b*) and 8(*c*), respectively, show the cantilever voltage and thermometer resistance change during the force-displacement experiment. When the cantilever approaches the thermometer, both the cantilever and thermometer signals increase because more heat is transferred to the substrate. Upon contact, both the cantilever and

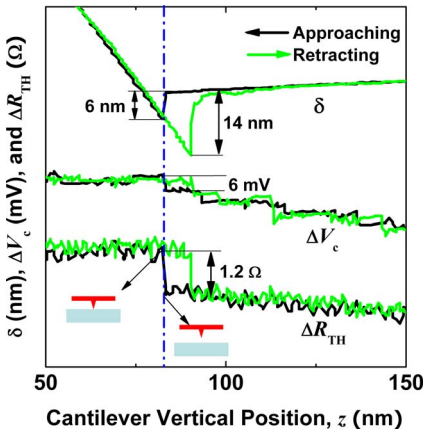

Fig. 9 The force-displacement experiment result at R_c =2.0 kΩ, which is magnified on the moment of contact. There is a jump on the cantilever and thermometer signals when the cantilever contacts the substrate, from which the effective contact conductance can be estimated to be around 40 nW/K.

PRT signals make stepwise changes and remain almost constant afterward, as the air gap does not change anymore.

For the quantitative investigation of the tip-specimen conduction, the force-displacement results at R_c=2.0 kΩ are replotted in Fig. 9. At the moment the cantilever contacts the PRT, the thermometer resistance jumps up by 1.2 ± 0.1 Ω, which corresponds to 0.50 ± 0.04 K temperature rise. At the same time, the cantilever voltage changes by 6.0 ± 0.6 mV, corresponding to 17.3 ± 0.5 μW cantilever power change. When considering the aforementioned cantilever voltage sensitivity (i.e., 200 μV/nm at R_c=2.0 kΩ), the cantilever jump-in and resultant change of its vertical displacement (i.e., 6 nm) would correspond to only 1.2 mV in the cantilever voltage change. Thus, a significant amount of the cantilever voltage change is due to the heat transfer through the nanocontact between the cantilever tip and the specimen. The effective contact thermal conductance estimated from the simple thermal network analysis is G_b=40 $\pm$ 10 nW/K. This estimated contact thermal conductance falls into the range of what was suggested by previous works [6,17,21]; they estimated the contact thermal conductance to be 10–100 nW/K, depending on the contacting area. The estimated contact thermal conductance may include other thermal resistances such as tip resistance and spread resistance in the substrate [6]. It should be noted that the thermal conductance due to the air conduction from the cantilever heater to the specimen is estimated to be around 14.9 μW/K at R_c=2.0 kΩ, which is still two orders of magnitude larger than the contact conductance.

5 Conclusions

The heat transfer between a heated microcantilever and a substrate is investigated by measuring the surface temperature rise with a fabricated PRT on a SiO_2-coated Si substrate. The estimated TCR of the thermometer is around 7×10^{-4} K^{-1}, approximately one-fifth of the bulk value for platinum. The use of the PRT in an AFM platform enables the determination of the surface temperature change while the heated cantilever scans. Simultaneous measurements of the surface topography, cantilever temperature, and the substrate surface temperature provide the accurate cantilever-substrate heat transfer rate. When the cantilever is engaged on the specimen, up to 75% of the cantilever power is transferred to the substrate. However, the surface temperature increase is less than 10 K due to the high thermal conductivity of the Si substrate. From the force-displacement experiment, the effective contact thermal conductance is estimated to be around 40 nW/K, which is still two orders of magnitude smaller than that of the cantilever-substrate air conduction. This indicates that the air conduction is the dominant heat transfer mechanism between the heated cantilever and the substrate. The obtained results will facilitate further understanding of the thermal behavior of the heated cantilever during the actual operation and the resulting heating effect on the substrate.

Acknowledgment

This work was sponsored by the National Science Foundation (CTS-0327117, and CAREER CTS-0338888), the Office of Naval Research, and DARPA.

Nomenclature

A = surface area (m^2)
A_c = cross sectional area of the cantilever (m^2)
d = thickness (m)
G' = thermal conductance per unit length (W/m K)
G_b = effective tip-specimen conductance (W/K)
h = effective heat transfer coefficient (W/m^2 K)
I = electrical current (A)
k = thermal conductivity (W/m K)
L = length of the PRT
q = heat flow rate (W)
q' = heat flow rate per unit length (W/m)
q'' = heat flux (W/m^2)
$\dot{q}$ = volume density of heat generation (W/m^3)
R = electrical resistance (Ω)
s = coordinate along the axis of the cantilever (m)
T = temperature (K)
T_∞ = ambient or room temperature (K)
t = air gap between the cantilever and the substrate (m)
V = voltage (V)
w_c = cantilever width (m)

Greek Symbols

δ = cantilever deflection (m)
Λ = mean free path of air (m)

Subscripts

a = air
c = cantilever
f = SiO_2 film
g = gap
H = cantilever heater
m = substrate
s = surface of the specimen
th = PRT

References

[1] Binnig, G., Despont, M., Drechsler, U., Haberle, W., Lutwyche, M., Vettiger, P., Mamin, H. J., Chui, B. W., and Kenny, T. W., 1999, "Ultrahigh-Density Atomic Force Microscopy Data Storage With Erase Capability," Appl. Phys. Lett., **74**, pp. 1329–1331.
[2] Sheehan, P. E., Whitman, L. J., King, W. P., and Brent, A. N., 2004, "Nanoscale Deposition of Solid Inks via Thermal Dip Pen Nanolithography," Appl. Phys. Lett., **85**, pp. 1589–1591.
[3] Nelson, B. A., King, W. P., Laracuente, A. R., Sheehan, P. E., and Whitman, L. J., 2006, "Direct Deposition of Continuous Metal Nanostructures by Thermal Dip-Pen Nanolithography," Appl. Phys. Lett., **88**, p. 033104.
[4] Szoszkiewicz, R., Okada, T., Jones, S. C., Li, T. D., King, W. P., Marder, S. R., and Riedo, E., 2007, "High-Speed, Sub-15 nm Feature Size Thermochemical Nanolithography," Nano Lett., **7**, pp. 1064–1069.
[5] King, W. P., Saxena, S., Nelson, B. A., Pitchimani, R., and Weeks, B. L., 2006, "Nanoscale Thermal Analysis of an Energetic Material," Nano Lett., **6**, pp. 2145–2149.
[6] Nelson, B. A., and King, W. P., 2007, "Measuring Material Softening With Nanoscale Spatial Resolution Using Heated Silicon Probes," Rev. Sci. Instrum., **78**, p. 023702.
[7] King, W. P., Kenny, T. W., and Goodson, K. E., 2004, "Comparison of Thermal and Piezoresistive Sensing Approaches for Atomic Force Microscopy Topography Measurements," Appl. Phys. Lett., **85**, pp. 2086–2088.

[8] Kim, K. J., Park, K., Lee, J., Zhang, Z. M., and King, W. P., 2007, "Nanotopographical Imaging Using a Heated Atomic Force Microscope Cantilever Probe," Sens. Actuators, A, **136**, pp. 95–103.
[9] Park, K., Lee, J., Zhang, Z. M., and King, W. P., 2007, "Nanotopographical Imaging With a Heated Atomic Force Microscope Cantilever in Tapping Mode," Rev. Sci. Instrum., **78**, p. 043709.
[10] Lee, J., Beechem, T., Wright, T. L., Nelson, B. A., Graham, S., and King, W. P., 2006, "Electrical, Thermal, and Mechanical Characterization of Silicon Microcantilever-Heaters," J. Microelectromech. Syst., **15**, pp. 1644–1655.
[11] Park, K., Lee, J., Zhang, Z. M., and King, W. P., 2007, "Frequency-Dependent Electrical and Thermal Response of Heated Atomic Force Microscope Cantilevers," J. Microelectromech. Syst., **16**, pp. 213–222.
[12] Lee, J., Wright, T. L., Abel, M. R., Sunden, E. O., Marchenkov, A., Graham, S., and King, W. P., 2007, "Thermal Conduction From Microcantilever Heaters in Partial Vacuum," J. Appl. Phys., **101**, p. 014906.
[13] Park, K., Marchenkov, A., Zhang, Z. M., and King, W. P., 2007, "Low Temperature Characterization of Heated Microcantilevers," J. Appl. Phys., **101**, p. 094504.
[14] King, W. P., Kenny, T. W., Goodson, K. E., Cross, G. L. W., Despont, M., Dürig, U. T., Rothuizen, H., Binnig, G., and Vettiger, P., 2002, "Design of Atomic Force Microscope Cantilevers for Combined Thermomechanical Writing and Thermal Reading in Array Operation," J. Microelectromech. Syst., **11**, pp. 765–774.
[15] King, W. P., 2005, "Design Analysis of Heated Atomic Force Microscope Cantilevers for Nanotopography Measurements," J. Micromech. Microeng., **15**, pp. 2441–2448.
[16] Williams, C. C., and Wickramasinghe, H. K., 1986, "Scanning Thermal Profiler," Appl. Phys. Lett., **49**, pp. 1587–1589.
[17] Luo, K., Shi, Z., Varesi, J., and Majumdar, A., 1997, "Sensor Nanofabrication, Performance, and Conduction Mechanisms in Scanning Thermal Microscopy," J. Vac. Sci. Technol. B, **15**, pp. 349–360.
[18] Muller-Hirsch, W., Kraft, A., Hirsch, M. T., Parisi, J., and Kittel, A., 1999, "Heat Transfer in Ultrahigh Vacuum Scanning Thermal Microscopy," J. Vac. Sci. Technol. A, **17**, pp. 1205–1210.
[19] Shi, L., Kwon, O., Miner, A. C., and Majumdar, A., 2001, "Design and Batch Fabrication of Probes for Sub-100 nm Scanning Thermal Microscopy," J. Microelectromech. Syst., **10**, pp. 370–378.
[20] Lee, D. W., Ono, T., and Esashi, M., 2002, "Fabrication of Thermal Microprobes With a Sub-100 nm Metal-to-Metal Junction," Nanotechnology, **13**, pp. 29–32.
[21] Shi, L., and Majumdar, A., 2002, "Thermal Transport Mechanisms at Nanoscale Point Contacts," ASME J. Heat Transfer, **124**, pp. 329–337.
[22] Lefevre, S., Volz, S., and Chapuis, P. O., 2006, "Nanoscale Heat Transfer at Contact Between a Hot Tip and a Substrate," Int. J. Heat Mass Transfer, **49**, pp. 251–258.
[23] Chui, B. W., Stowe, T. D., Ju, Y. S., Goodson, K. E., Kenny, T. W., Mamin, H. J., Terris, B. D., and Ried, R. P., 1998, "Low-Stiffness Silicon Cantilever With Integrated Heaters and Piezoresistive Sensors for High-Density Data Storage," J. Microelectromech. Syst., **7**, pp. 69–78.
[24] Chu, D., Bilir, D. T., Pease, R. F. W., and Goodson, K. E., 2002, "Submicron Thermocouple Measurements of Electron-Beam Resist Heating," J. Vac. Sci. Technol. B, **20**, pp. 3044–3046.
[25] Chu, D., Wong, W.-K., Goodson, K. E., and Pease, R. F. W., 2003, "Transient Temperature Measurements of Resist Heating Using Nanothermocouples," J. Vac. Sci. Technol. B, **21**, pp. 2985–2989.
[26] Marzi, G. D., Iacopino, D., Quinn, A. J., and Redmond, G., 2004, "Probing Intrinsic Transport Properties of Single Metal Nanowires: Direct-Write Contact Formation Using a Focused Ion Beam," J. Appl. Phys., **96**, pp. 3458–3462.
[27] Chui, B. W., Asheghi, M., Ju, Y. S., Goodson, K. E., Kenny, T. W., and Mamin, H. J., 1999, "Intrinsic-Carrier Thermal Runaway in Silicon Microcantilevers," Microscale Thermophys. Eng., **3**, pp. 217–228.
[28] Dürig, U., 2005, "Fundamentals of Micromechanical Thermoelectric Sensors," J. Appl. Phys., **98**, p. 044906.
[29] Masters, N., Ye, W., and King, W. P., 2005, "The Impact of Sub-Continuum Gas Conduction on the Sensitivity of Heated Atomic Force Microscope Cantilevers," Phys. Fluids, **17**, p. 100615.
[30] Zhang, Z. M., 2007, *Nano/Microscale Heat Transfer*, McGraw-Hill, New York.
[31] Fu, C. J., and Zhang, Z. M., 2006, "Nanoscale Radiation Heat Transfer for Silicon at Different Doping Levels," Int. J. Heat Mass Transfer, **49**, pp. 1703–1718.
[32] Fortier, D., and Suzuki, K., 1976, "Effect of *p*-Donors on Thermal Phonon Scattering in Si," J. Phys. (Paris), **37**, pp. 143–147.
[33] Liu, W., and Asheghi, M., 2006, "Thermal Conductivity Measurements of Ultra-Thin Single Crystal Silicon Layers," ASME J. Heat Transfer, **128**, pp. 75–83.
[34] Palisoc, A. L., and Lee, C. C., 1988, "Thermal-Properties of the Multilayer Infinite-Plate Structure," J. Appl. Phys., **64**, pp. 410–415.
[35] Carslaw, H. S., and Jaeger, J. C., 1959, *Conduction of Heat in Solids*, 2nd ed., Clarendon, Oxford.
[36] Abel, M. R., Graham, S., Serrano, J. R., Kearney, S. P., and Phinney, L. M., 2007, "Raman Thermometry of Polysilicon Microelectro-Mechanical Systems in the Presence of an Evolving Stress," ASME J. Heat Transfer, **129**, pp. 329–334.
[37] Zhang, Q. G., Cao, B. Y., Zhang, X., Fujii, M., and Takahashi, K., 2006, "Size Effects on the Thermal Conductivity of Polycrystalline Platinum Nanofilms," J. Phys.: Condens. Matter, **18**, pp. 7937–7950.
[38] Jungen, A., Pfenninger, M., Tonteling, M., Stampfer, C., and Hierold, C., 2006, "Electrothermal Effects at the Microscale and Their Consequences on System Design," J. Micromech. Microeng., **16**, pp. 1633–1638.
[39] Gomes, S., Trannoy, N., and Grossel, P., 1999, "DC Thermal Microscopy: Study of the Thermal Exchange Between a Probe and a Sample," Meas. Sci. Technol., **10**, pp. 805–811.
[40] Gotsmann, B., and Dürig, U., 2005, "Experimental Observation of Attractive and Repulsive Thermal Forces on Microcantilevers," Appl. Phys. Lett., **87**, p. 194102.

Measurement of the Thermal Conductivity and Heat Capacity of Freestanding Shape Memory Thin Films Using the 3ω Method

Ankur Jain[1]
e-mail: ankurjain@stanfordalumni.org

Kenneth E. Goodson

Department of Mechanical Engineering,
Stanford University,
Stanford, CA 94305

An accurate measurement of the thermophysical properties of freestanding thin films is essential for modeling and predicting thermal performance of microsystems. This paper presents a method for simultaneous measurement of in-plane thermal conductivity and heat capacity of freestanding thin films based on the thermal response to a sinusoidal electric current. An analytical model for the temperature response of a freestanding thin film to a sinusoidal heating current passing through a metal heater patterned on top of the thin film is derived. Freestanding thin-film samples of silicon nitride and nickel titanium (NiTi), a shape memory alloy, are microfabricated and characterized. The thermal conductivity of thin-film NiTi, which increases linearly between 243 K and 313 K, is 40% lower than the bulk value at room temperature. The heat capacity of NiTi also increases linearly with temperature in the low temperature phase and is nearly constant above 280 K. The measurement technique developed in this work is expected to contribute to an accurate thermal property measurement of thin-film materials. Thermophysical measurements on NiTi presented in this work are expected to aid in an accurate thermal modeling of microdevices based on the shape memory effect. [DOI: 10.1115/1.2945904]

Keywords: thermal conductivity, thin film, 3ω method, shape memory effect, thermal characterization, microfabrication, heat capacity

1 Introduction

Freestanding thin films are used in a variety of microelectromechanical systems (MEMS)–based applications such as micropumps [1], gas sensors [2], pressure sensors [3], microvalves [4], and microactuators [5]. The performance of such MEMS-based systems is often linked to thermal conduction phenomena in the device. For example, in a thin-film microheater device, the response time and maximum temperature reached are functions of the heat capacity and thermal conductivity of the thin-film material. Thermophysical properties of thin films deviate significantly from the bulk-form value due to a variety of reasons including boundary effects [6]. Apart from thickness, there is also a strong dependence on the method of deposition of the thin film [7,8] and on temperature [9,10]. *In situ* thermophysical measurement is thus essential for accurate modeling and performance prediction of thermal-based microdevices.

There are a broad variety of electrical and optical methods for the measurement of thermal properties of thin films [11,12]. Methods based on electrical heating are among the most popular and use either steady-state or transient heating. The steady-state electrical methods involve passing direct current through a metal heater and measuring the temperature rise, either by using a separate temperature sensor or by using the heater itself as a thermometer. The temperature rise may be used to determine the thermal conductivity of the material of interest using, for example, the Fourier law of heat conduction. Transient methods typically measure either the time response of the material of interest to a heating signal or the thermal response to sinusoidal heating generated by an alternating current. Apart from electrical methods, techniques based on other phenomena such as reflectance [13,14] and photoacoustics [15,16] have also been used.

The thermophysical properties of thin films deposited on a thick substrate of well-known thermal properties have been measured in a number of papers using a variety of methods [17–19]. For example, the 3ω method has been used to determine thin-film thermal conductivity by assuming the thermal resistances through the thin film and the substrate to add up in series [20]. The thermal conductivity is then determined by measuring the thermal response of a film-on-substrate system and comparing it with the thermal response expected in the absence of the thin film. However, such a measurement does not take into account the thermal contact resistance between the thin film and substrate, which is known to play a significant role in heat transfer in microstructures. In addition, the heat capacity of the thin-film material cannot be measured using this method. While there is a wide literature on thermal measurements on a thin film deposited on a substrate, only a limited number of measurements have been made on freestanding thin films [21–23].

This paper develops a variation of the 3ω method for a simultaneous measurement of in-plane thermal conductivity and heat capacity of freestanding thin films. The method is applied to silicon nitride and nickel titanium (NiTi) films of thickness near 1 μm. NiTi is a shape memory alloy that has attracted much research in the MEMS community due to its interesting mechanical properties [24,25]. The capability of shape memory alloys to recover large thermal strains has been used in actuation-based microdevices such as micropumps and microvalves. [1,5]. The work output of thin-film shape memory based actuation is superior to other comparable actuation technologies [24]. More recently, the excellent chemical resistance and biocompatibility of shape memory alloys have led to the development of exciting biomedical applications, including stents and drug delivery [26], tissue fixation [27], etc.

[1]Present address: Freescale Semiconductor, Austin, TX 78754.

Contributed by the Heat Transfer Division of ASME for publication in the JOURNAL OF HEAT TRANSFER. Manuscript received June 4, 2007; final manuscript received January 11, 2008; published online August 8, 2008. Review conducted by Yogendra Joshi.

NiTi is a nearly stoichiometrically equal alloy of Ni and Ti. While NiTi has been widely used in its bulk form, its application to MEMS was long hindered by difficulties in depositing thin films of NiTi with accurately controlled stoichiometric ratio of Ni and Ti [28]. This led to problems in reproducing the shape memory effect, which is extremely sensitive to the ratio of the constituent elements in the shape memory alloy. Robust techniques based on two-source sputter deposition have recently been developed for obtaining good quality thin films of NiTi [29]. This, combined with other microfabrication capabilities makes thin-film shape memory alloys very attractive for actuation related MEMS applications, including micropumps, microgrippers, etc.

While the electric and mechanical properties of shape memory alloys have been well investigated, there has been relatively lesser work in characterizing their thermophysical properties. Since the actuation of shape memory microdevices occurs by temperature modulation due to electrical heating, the thermophysical properties of the thin-film shape memory material play an important role in determining its performance characteristics. While some thermal conductivity measurements of shape memory materials have been reported [30–32], none of this work addresses the thin-film form. Thus, an investigation of thermophysical properties of thin-film shape memory alloys may lead to a better understanding of their thermomechanical behavior and the development of more accurate performance prediction tools for shape memory based microdevices.

The next section presents the derivation of the 3ω response of a freestanding thin film to a sinusoidal electric current passed through a metal heater patterned on top of it. Design and microfabrication of MEMS-based freestanding thin-film structures are described next, followed by a discussion of the experimental data and comparison with the analytical model.

2 Theory

The 3ω method [17] is a powerful tool for thermophysical property measurement and has been used extensively for a wide variety of materials including dielectrics [18,33], superlattice materials [34], complex alloys [19], etc. The 3ω method is based on the temperature-dependent electrical resistivity of metals. A thin metal line is deposited on the material of interest, and a small sinusoidal electric current is passed through it. Since the electric current is sinusoidal at frequency ω, the resultant Joule heating, and hence the temperature of the metal line, has a component that oscillates at a frequency of 2ω. The amplitude of this temperature oscillation is a function of the heating power, geometry, and thermophysical properties of the material of interest. Thus, the measurement of the 2ω temperature oscillation amplitude provides a means of determining the thermal properties of the material. This measurement is performed indirectly by measuring the 3ω voltage induced due to the electric current that oscillates at frequency ω and the temperature-dependent electrical resistance of the metal heater, which oscillates at frequency 2ω. The two quantities are related by the following equation [17,35]:

$$\Delta T_{2\omega} = 2\frac{dT}{dR}\frac{R}{V}V_{3\omega} \tag{1}$$

The 3ω method was first used for measurements on a substrate that was much thicker than the thermal penetration depth of the thermal wave produced by the sinusoidal current. In this case, a semi-infinite assumption was used to simplify and solve the governing energy equation. This method fails for freestanding thin films since the current frequency would have to be unrealistically high to still satisfy the semi-infinite assumption. The 3ω method has been modified for measuring thermal properties of thin films deposited on a substrate with well-known properties [20]. In this case, the thermal resistances through the thin film and the substrate are assumed to add up in series. Thus, the temperature oscillation amplitude with the thin film exhibits a constant frequency-independent difference from the value expected if only the substrate were present. This difference is used to determine the thermal conductivity of the thin film. This method cannot measure the heat capacity of the thin film. In addition, the boundary thermal resistance between the thin film and substrate remains unaccounted for. Some work has also been done on using numerical simulations for applying the 3ω method for freestanding thin films [36]. However, the development of an analytical method for thermal measurements remains highly desirable.

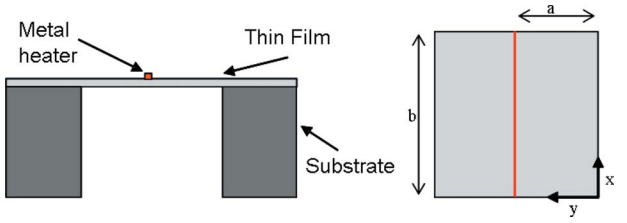

Fig. 1 Schematic showing the geometry of the freestanding thin film suspended on a substrate

Consider the geometry shown in Fig. 1. The thin-film membrane is supported all around by a substrate material. While the method outlined in this work may be used for any geometry, a rectangular membrane with dimensions $2a$ and $2b$ is considered in detail here. The thickness of the membrane is t_m. A metal heater of width w and height h is patterned in the center of the membrane. w and h are both small compared to the membrane dimensions. Thus, heat transfer within the metal may be neglected and the metal heater may be treated as a line source of heat. The metal heater is assumed to carry sinusoidal electric current of amplitude I and frequency ω. The electrical resistance of the metal heater is R. The out-of-plane thin-film thermal resistance is assumed to be small compared to the in-plane thermal resistance, so that the thin film may be treated as isothermal in the z-direction. Further simplification may be obtained by assuming convection and radiation to be negligible compared to conduction in the membrane plane. Under these assumptions, the governing energy equation may be simplified to

$$\frac{\partial^2\theta}{\partial x^2} + \frac{\partial^2\theta}{\partial y^2} = \frac{\dot{q}'''}{k} + \frac{1}{\alpha}\frac{\partial\theta}{\partial t} \tag{2}$$

where θ represents the temperature rise over the substrate temperature. Note that $\dot{q}^m$ is the volumetric heat generation rate and α is the thermal diffusivity.

In order to solve the energy equation, the membrane is divided into two equal parts separated by the metal heater. Thus the metal heater forms one of the domain boundaries, and heat generation in the metal heater may be modeled as a heat flux boundary condition. The membrane boundaries may be assumed to be isothermal due to the large thermal mass of the substrate material. Thus, the boundary conditions and initial condition for Eq. (2) may be written as

$$\theta(0,y,t) = \theta(b,y,t) = \theta(x,0,t) = 0$$

$$\frac{\partial\theta}{\partial y}^{y=a} = \frac{I^2\sin^2(\omega t)R}{2k(t_m b)} = \frac{I^2R}{2k(t_m b)}\left(\frac{1-\cos(2\omega t)}{2}\right) \tag{3}$$

$$\theta(x,y,0) = 0$$

The governing energy equation derived here is a linear time-dependent partial differential equation (PDE) with all homogeneous boundary conditions except one. In order to solve this PDE, the solution is assumed to be the sum of a steady-state component $\theta_{ss}(x,y)$ corresponding to the steady component of Joule heating due to the sinusoidal current and a time-dependent component $\theta_{tr}(x,y,t)$ that consists of the transient and sinusoidal terms. The

solution for the steady-state component is easily determined using the method of separation of variables to be

$$\theta_{ss}(x,y)=\sum_{n=1}^{\infty}-\frac{I^2R(1-\cos(n\pi))}{2kt_m(n\pi)^2\cosh\left(\frac{n\pi a}{b}\right)}\sin\left(\frac{n\pi x}{b}\right)\sinh\left(\frac{n\pi y}{b}\right) \tag{4}$$

The method of integral transforms [37] is used to derive the solution for the transient component. This method involves assuming the solution of the nonhomogeneous problem to be a linear combination of the general solutions of the corresponding homogeneous problems and deriving ODEs for the time-dependent coefficients in the linear combination. The solution for the transient temperature response is found out to be

$$\theta_{tr}(x,y,t)=\sum_{m=1}^{\infty}\sum_{n=1}^{\infty}C_{m,n}(t)\sin\left(\frac{n\pi x}{b}\right)\sin\left(\frac{(m+1/2)\pi y}{a}\right) \tag{5}$$

where

$$C_{m,n}(t)=\frac{4\omega^2}{\gamma_{m,n}^2+4\omega^2}\frac{\zeta_{m,n}}{2\gamma_{m,n}}e^{-\gamma_{m,n}t}+\frac{\zeta_{m,n}}{2\sqrt{\gamma_{m,n}^2+4\omega^2}}\sin(2\omega t+\varphi_{m,n}) \tag{6}$$

The phase angle $\varphi_{m,n}$ may be expressed in terms of the input parameters as follows:

$$\varphi_{m,n}=\tan^{-1}\left(\frac{\gamma_{m,n}}{2\omega}\right) \tag{7}$$

Note that in Eqs. (6) and (7) above,

$$\zeta_{m,n}=(-1)^{m+1}(1-(-1)^n)\frac{4\alpha}{n\pi a}\frac{I^2R}{2kt_mb}$$
$$\gamma_{m,n}=\alpha\pi^2\left[\left(\frac{m+1/2}{a}\right)^2+\left(\frac{n}{b}\right)^2\right] \tag{8}$$

Equations (4) and (5) represent the solution of the energy equation that governs the temperature profile on the thin-film membrane. The steady-state component of the temperature solution varies linearly with the input power, with the slope being related to the thermal conductivity of the thin film. The sinusoidal component oscillates at a frequency that is twice that of the heating current. In order to extract measurable quantities from this thermal model, the steady-state and sinusoidal temperature components are averaged along the heater by integration to yield the following average quantities for the metal heater:

$$\bar{\theta}_{av}=\sum_{n=1}^{\infty}\frac{I^2R}{2kt_m(n\pi)^3}(1-\cos(n\pi))^2\tanh\left(\frac{n\pi a}{b}\right)$$
$$\bar{\theta}_{2\omega}=\sum_{n=1}^{\infty}\sum_{m=1}^{\infty}-\frac{\zeta_{m,n}}{2\sqrt{\gamma_{m,n}^2+4\omega^2}}\frac{\sin((m+1/2)\pi)(1-\cos(n\pi))}{n\pi} \tag{9}$$

While $\bar{\theta}_{av}$ represents the average heater temperature rise due to Joule heating, $\bar{\theta}_{2\omega}$ represents the amplitude of the temperature oscillation at 2ω frequency due to the sinusoidal nature of heating. Measurement of these quantities provides two equations from which two thermophysical properties, namely, thermal conductivity and thermal diffusivity (or heat capacity), may be determined. Note that only thermal conductivity appears in the equation for $\bar{\theta}_{av}$. It is relatively easier to measure $\bar{\theta}_{av}$ and $\bar{\theta}_{2\omega}$ indirectly by measuring the related voltage harmonics. The relationship between the temperature quantities and voltage harmonics is as follows:

$$V_\omega=IR+I\frac{dR}{dT}\bar{\theta}_{av}$$
$$V_{3\omega}=2I\frac{dR}{dT}\bar{\theta}_{2\omega} \tag{10}$$

Note that from Eq. (9),

$$\bar{\theta}_{2\omega}\to 0 \quad \text{as } \omega\to\infty, \quad \frac{d\bar{\theta}_{2\omega}}{d\omega}\to 0 \quad \text{as } \omega\to 0 \tag{11}$$

i.e., at large frequencies, the temperature oscillation becomes too small to be measured accurately, while at the low frequency end, it is a weak function of frequency. The temperature oscillation is most sensitive to frequency in a specific frequency window where ω is comparable to γ. Physically, the high frequency behavior is explained by the fact that at large frequencies, the thermal penetration depth becomes comparable to the membrane thickness, as a result of which the boundary condition at the other side of the thin film begins to play an important role in the heat transfer problem. On the other hand, at low frequencies, the thin film has sufficient time to equilibrate, and thus the sinusoidal effect of the heating current is lost, resulting in the loss of sensitivity of the temperature oscillation to frequency.

The next section discusses the design and microfabrication of freestanding thin-film structures using MEMS technology. Thermophysical measurements using the analytical model derived in this section are described next.

3 Microfabrication and Experimental Setup

3.1 Design and Microfabrication. Freestanding thin-film structures based on MEMS technology are designed and microfabricated. Two thin-film materials are investigated—silicon nitride and NiTi. Some of the important design considerations for the thin-film structures include the material and film thickness, and the dimensions and material of the metal features. Freestanding thin films of materials such as silicon oxide tend to crumple and often break due to the high compressive stress in the oxide films. On the other hand, silicon nitride films do not show this behavior due to the tensile stress in these films. However, if the tensile stress in the films is too high, they may be prone to cracking. It is well known that the residual stress in deposited films may be controlled by changing the chemical composition of the film.

The metal heaters patterned on top of the thin film are designed to be 10 μm wide and 0.1 μm thick. These dimensions ensure high electrical resistance and reasonably low current density during operation. The film is chosen to be around 1.0 μm thick in all experiments in order to have sufficient mechanical robustness when released from the substrate. While NiTi is inherently compressive in nature, the process conditions for silicon nitride are chosen in order to result in a film with a small amount of tensile stress.

Microfabrication is carried out at the Stanford Nanofabrication Facility (SNF). 4 in., 300 μm thick, double side polished Si wafers are used. A thin layer of thermal oxide is first grown on the wafers in order to electrically passivate the thin film of interest from the silicon substrate. This step is omitted when the thin-film material is an insulator. This is followed by deposition of the thin film of interest. The silicon nitride film is deposited in a low pressure chemical vapor deposition (LPCVD) furnace at 850°C. A high ratio of dichlorosilane to ammonia of 14:1 ensures a silicon-rich film with low residual tensile stress. The NiTi film is sputter deposited at less than 100°C in an argon atmosphere at a base pressure of 10^{-7} Torr. Following the film deposition, the wafers are annealed at 500°C in vacuum for a few minutes and allowed to cool down to room temperature. NiTi deposition is carried out by the TiNi Alloy Company, San Leandro, CA. Phase transformation temperature of the sputtered NiTi films is around

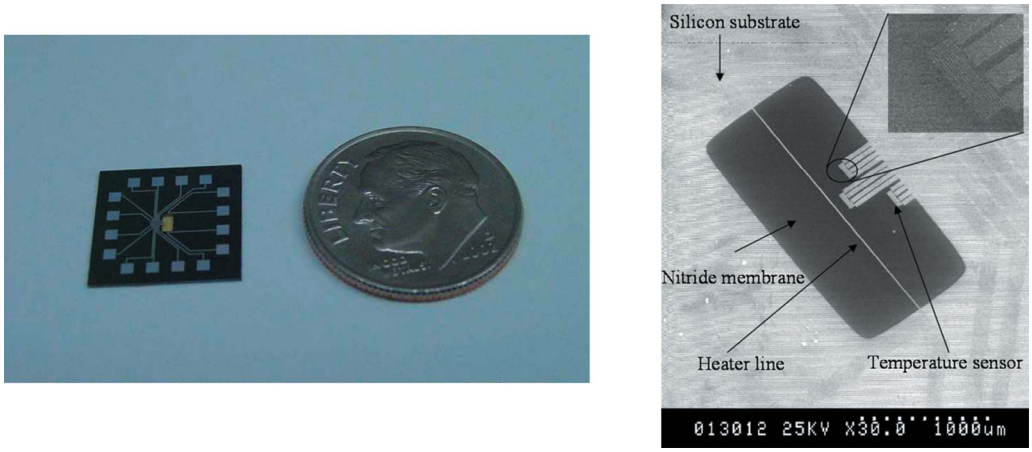

Fig. 2 A picture and SEM showing the silicon nitride freestanding thin-film microdevice

0°C. Following sputtering, the NiTi film is passivated by a 0.4 μm low temperature oxide (LTO) film deposited in a LPCVD furnace at 400°C. 0.1 μm aluminum is then sputtered on the wafers. Metal features are defined using photolithography and metal etch in a plasma etcher. Front-to-backside photolithography is then performed in order to define features to be etched on the wafer backside. Following the attachment of a backing wafer using photoresist, the wafers are etched from the backside in a deep reactive ion etcher. Due to nonuniform etching across the wafer, the etching is stopped when about 10–20 μm silicon is left, and the wafers are diced. Individual devices are then separately etched to completion. This minimizes overetching of the thin film of interest. Photoresist is washed off in acetone, and individual devices are packaged in a ceramic chip carrier. Electrical contact pads are wire bonded. Figure 2 shows a picture and scanning electron micrograph (SEM) of a silicon nitride thin-film structure microfabricated in this manner. Note that the film is stretched out due to the residual tensile stress in silicon nitride. On the other hand, NiTi is compressive in nature, and thus the NiTi thin films are wavy in nature, as shown in Fig. 3.

3.2 Experimental Setup. Figure 4 shows a schematic of the experimental setup used for thermophysical characterization of freestanding thin films. The setup consists of a vacuum chamber with a temperature-controlled platform. A proportional-integral-derivative (PID) controller maintains the desired platform temperature using liquid nitrogen and a Joule heater. The ceramic package carrying the MEMS device is attached to the platform. Wires soldered to gold pads on the ceramic package are used to electrically probe the MEMS device. The chamber is connected to a vacuum pump capable of delivering a pressure of 10 mTorr. All experiments are performed at 10 mTorr or less in order to rule out convective effects. Radiative losses are also negligible due to the small temperature rise in the samples. An SRS 830 lock-in amplifier is used for supplying sinusoidal electric current and for measuring voltage harmonics V_ω and $V_{3\omega}$ generated across the metal heater. An HP 3458A multimeter is used for current measurement. Since the third harmonic of voltage is much smaller than the first harmonic, an accurate measurement of the former requires the arrangement of the metal heater as one of the arms of a Wheatstone bridge. The bridge is balanced using a variable resistor arm. The third harmonic of voltage is then easily measured across the balanced bridge, while the first harmonic of voltage is directly measured across the metal heater.

4 Results and Discussion

As a first step, the electrical resistance of the metal heater is measured as a function of temperature. The test current is chosen

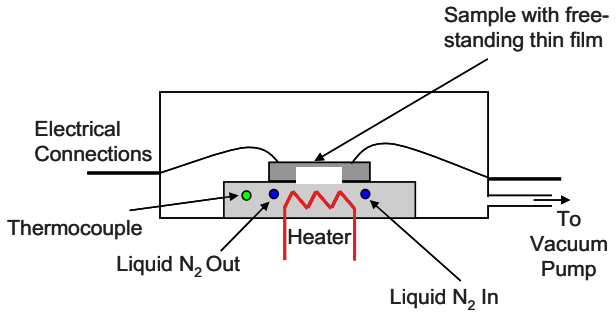

Fig. 4 A schematic of the experimental setup used for temperature-dependent thermophysical measurements on freestanding thin films

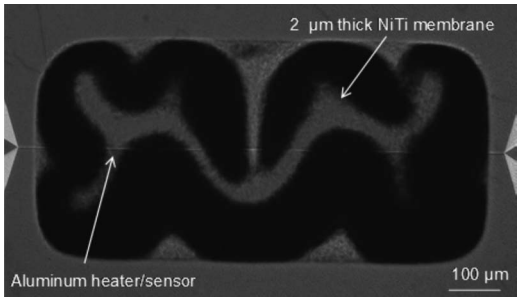

Fig. 3 An image of the freestanding NiTi thin film. Note the ridgy membrane surface due to the compressive residual stress in the film.

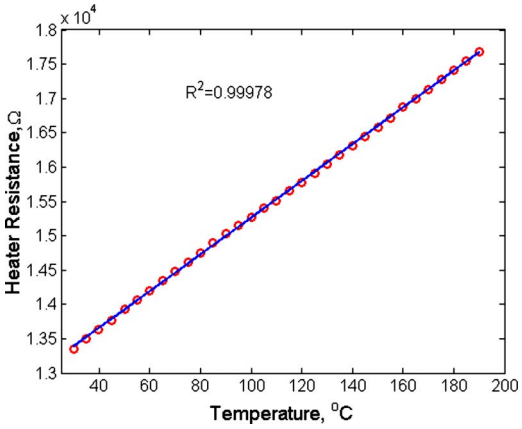

Fig. 5 Plot of the heater electrical resistance as a function of temperature. A linear temperature dependence is observed as expected.

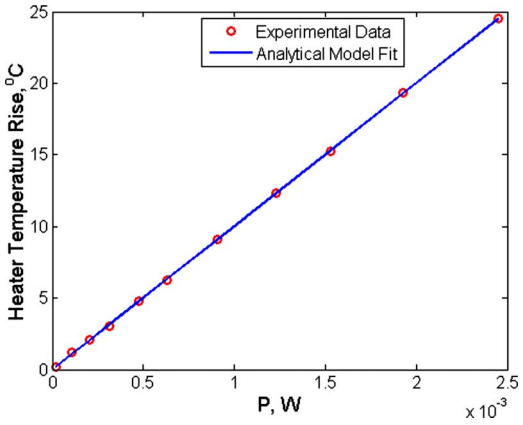

Fig. 6 Heater temperature rise as a function of the input heating power. As expected, the temperature rise depends linearly on the heating power. There is a good agreement between the experimental data and the analytical model. Thermal conductivity of the freestanding thin film may be determined from the slope of the plot.

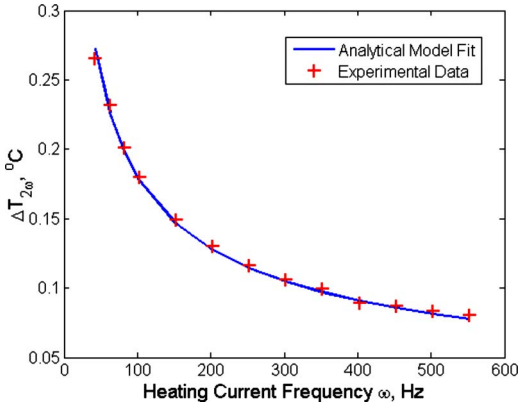

Fig. 7 2ω temperature oscillation amplitude as a function of the frequency of heating current. Experimental data agree well with the analytical model. Using the thermal conductivity value determined from the temperature rise data, least-squares fitting of experimental data with Eq. (9) yields the value of thermal diffusivity of the freestanding thin film.

to be small enough to not cause significant self-heating. As shown in Fig. 5, the electrical resistance is found to be a linear function of temperature, with a temperature coefficient of 0.0022 K^{-1}. Next, the heater temperature rise is measured as a function of heating power. Figure 6 shows a plot of the average temperature rise as a function of the heating power. As expected, the average temperature rise has a linear dependence on the heating power. There is a good agreement between experimental data and the analytical model presented in Sec. 2. Thermal conductivity of the freestanding thin film may be determined from the slope of the least-squares fit of the analytical model to the experimental data. Once the thermal conductivity has been determined, the amplitude of 2ω temperature oscillation is measured and plotted as a function of the frequency of the electric current. As shown in Fig. 7, there is a good agreement between the experimental data and the analytical model represented by Eq. (9). The temperature oscillation is most sensitive to frequency in a window of roughly 40–1000 Hz. With the thermal conductivity already determined using the average heater temperature rise, least-squares fitting of experimental data for the 2ω temperature oscillation is used to determine the thermal diffusivity of the thin film. Heat capacity of the film can also be determined by combining the two measurements. Using the temperature-controlled platform, the measurements are repeated over a large temperature range, thus yielding temperature-dependent data for thermal conductivity and heat capacity of the freestanding thin film. 10 minutes are allowed before each measurement in order for the temperature to become steady. Figure 8 shows a plot of the thermal conductivity and heat capacity of a 1.5 μm silicon nitride film between −200°C and 200°C. Both thermal conductivity and heat capacity increase with temperature, with the temperature dependence of thermal conductivity being stronger. This measured temperature data are consistent with previous measurements [18,38].

The experimental procedure is also used for thermophysical characterization of thin-film NiTi. Figure 9 shows the thermal conductivity and heat capacity of 1.7 μm thick NiTi film over a temperature range of −40°C and 40°C. Thermal conductivity of NiTi is observed to increase linearly as a function of temperature. On the other hand, heat capacity increases with temperature from −30°C to about 0°C, following which it remains constant. This may be related to the phase change that occurs in the NiTi film at around 0°C. While the heat capacity of one of the NiTi phases increases with temperature, the other phase has a much weaker temperature dependence of the heat capacity. Table 1 summarizes the room-temperature measurements of thermal conductivity and heat capacity of thin-film silicon nitride and NiTi.

Thermophysical measurements on thin-film shape memory alloys have not been reported in the past. The thermal conductivity

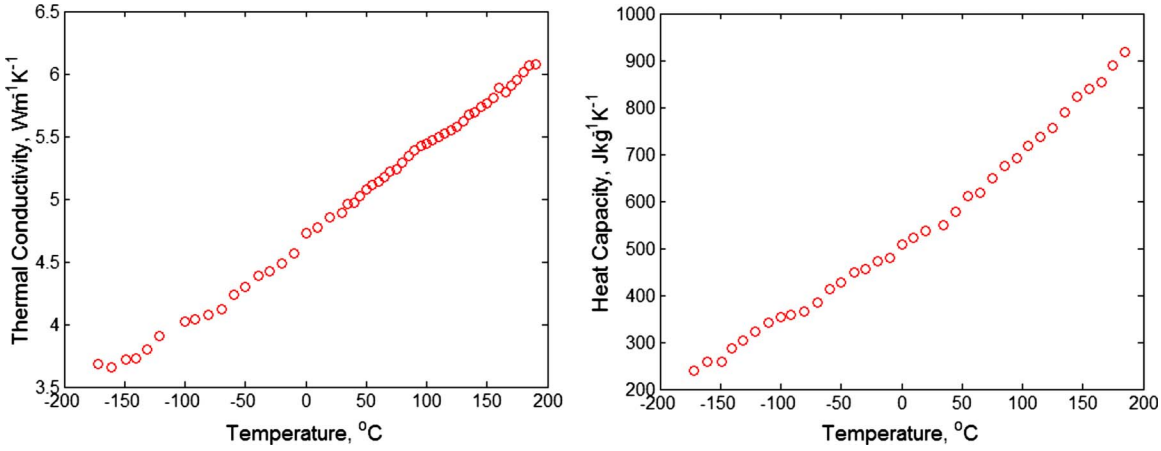

Fig. 8 Temperature dependence of thermal conductivity and heat capacity for 1.5 μm silicon nitride film

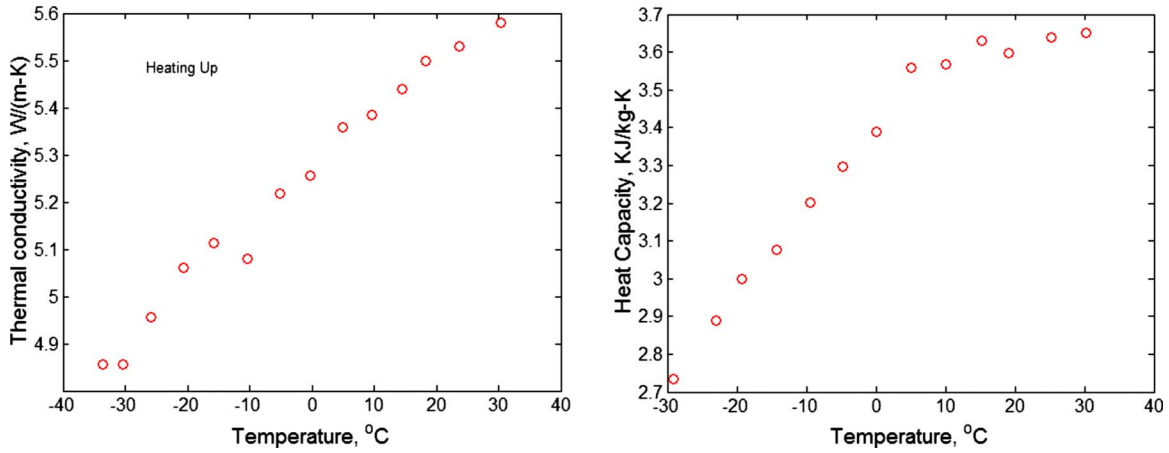

Fig. 9 Temperature dependence of thermal conductivity and heat capacity for 1.7 μm NiTi film. Note that the phase transformation temperature of NiTi is around 0°C.

Table 1 Summary of the room-temperature thermophysical thin-film data measured in this work

	Thermal conductivity, W m^{-1} K^{-1}	Heat capacity, J kg^{-1} K^{-1}
Silicon nitride	4.9 ± 0.7	523.2 ± 78.5
NiTi	5.5 ± 0.8	3612.3 ± 581.3

of NiTi measured in this work is about 40% smaller than the well-known bulk value [30]. The thermal conductivity reduction underlines the importance of measuring thin-film properties *in situ* instead of using previously measured bulk-form values when developing analytical or numerical models for predicting the performance of shape memory alloy based MEMS devices. The mechanism behind this significant reduction in thermal conductivity is currently under investigation. It is possible that this deviation from bulk value is due to a different stoichiometric composition compared to the previous work. Shape memory material properties are known to be extremely sensitive to composition. If the bulk samples used by Goff [30] were crystalline, it is possible that defects in the thin-film form, augmented by an offset in the stoichiometric ratio, may be playing a role in the thermal conductivity reduction.

Uncertainty in the film thickness measurement is the largest source of uncertainty in the absolute measured value of thermal conductivity and heat capacity. Film thickness is measured using a Nanospec system based on noncontact spectroreflectometry. The expected error in film thickness measurements using the Nanospec is around 10%. In addition, error analysis shows that a higher electric current results in a lower uncertainty in the measured value of thermal conductivity and heat capacity. However, a higher electric current also leads to higher self-heating, which causes the averaging out of each measurement over a larger temperature range. A tradeoff between these conflicting parameters is reached by using a maximum electric current of around 0.5 mA and 6 mA for the silicon nitride and NiTi measurements, respectively, wherein the uncertainty in thermal conductivity and heat capacity measurements is around 12–15% and the maximum temperature rise in the thin film is limited to around 2°C.

5 Conclusion

The availability of accurate thermophysical data for thin-film materials plays an important role in the development of modeling tools for microsystems. The present work extends the 3ω method to freestanding thin films and develops a technique for measuring both thermal conductivity and heat capacity simultaneously. The method presented here offers several advantages over other possible methods for measuring thermal properties of freestanding thin films. The measured value of the thermal conductivity of thin-film NiTi is significantly smaller than the bulk-form value, which reinforces the need for direct thin-film measurements instead of using bulk values when developing thermal models for microsystems. The thermophysical measurements on thin-film NiTi presented here are likely to throw new light on a promising material for MEMS.

Acknowledgment

The authors would like to acknowledge financial support from the Stanford Graduate Fellowship Program (SGF), the Semiconductor Research Corporation (SRC) and a NSF NIRT Award. Microfabrication work presented in this paper was performed at the Stanford Nanofabrication Facility (SNF). Useful discussions with Kevin Ness and Xuejiao Hu are gratefully acknowledged.

Nomenclature

a = membrane width
b = membrane breadth
h = heater height
I = electric current
k = thermal conductivity
R = electrical resistance
t = time
t_m = membrane thickness
T = temperature
V = voltage
w = heater width
α = thermal diffusivity
φ = phase change
θ = temperature rise
ω = frequency

Subscripts

av = average
ss = steady state
tr = transient

References

[1] Benard, W. L., Kahn, H., Heuer, A. H., and Huff, M., 1998, "Thin-Film Shape Memory Alloy Actuated Micropumps," J. Microelectromech. Syst., **7**, pp. 245–251.
[2] Sberveglieri, G., Hellmich, W., and Müller, G., 1997, "Silicon Hotplates for Metal Oxide Gas Sensor Elements," Microsyst. Technol., **3**, pp. 183–190.
[3] Eaton, W. P., and Smith, J. H., 1997, "Micromachined Pressure Sensors: Re-

view and Recent Developments," Smart Mater. Struct., **6**, pp. 530–539.
[4] Kohl, M., Dittmann, D., Quandt, E., Winzek, B., Miyazaki, S., and Allen, D. M., 1999, "Shape Memory Microvalves Based on Thin Films or Rolled Sheets," Mater. Sci. Eng., A, **273–275**, pp. 784–788.
[5] Krulevitch, P., Lee, A. P., Ramsey, P. B., Trevino, J. C., Hamilton, J., and Northrup, M., 1996, "Thin Film Shape-Memory Alloy Micro-Actuators," J. Microelectromech. Syst., **5**(4), pp. 270–282.
[6] Cahill, D. G., Ford, W. K., Goodson, K. E., Mahan, G. D., Majumdar, A., Maris, H. J., Merlin, R., and Phillpot, S. R., 2003, "Nanoscale Thermal Transport," J. Appl. Phys., **93**(2), pp. 793–818.
[7] McConnell, A. D., Uma, S., and Goodson, K. E., 2001, "Thermal Conductivity of Doped Polysilicon Layers," J. Microelectromech. Syst., **10**(3), pp. 360–369.
[8] Ju, Y. S., and Goodson, K. E., 1999, "Process-Dependent Thermal Transport Properties of Silicon Dioxide Films Deposited Using Low-Pressure Chemical Vapor Deposition," J. Appl. Phys., **85**, pp. 7130–7134.
[9] Goodson, K. E., Flik, M. I., Su, L. T., and Antoniadis, D. A., 1993, "Annealing-Temperature Dependence of the Thermal Conductivity of LPCVD Silicon-Dioxide Layers," IEEE Electron Device Lett., **14**(10), pp. 490–492.
[10] Asheghi, M., Touzelbaev, M. N., Goodson, K. E., Leung, Y. K., and Wong, S. S., 1998, "Temperature-Dependent Thermal Conductivity of Single-Crystal Silicon Layers in SOI Substrates," ASME J. Heat Transfer, **120**(1), pp. 30–36.
[11] Cahill, D. G., Goodson, K. E., and Majumdar, A., 2002, "Thermometry and Thermal Transport in Micro/Nanoscale Solid-State Devices and Structures," ASME J. Heat Transfer, **124**(2), pp. 223–241.
[12] Goodson, K. E., and Ju, Y. S., 1999, "Heat Conduction in Novel Electronic Films," Annu. Rev. Mater. Sci., **29**, pp. 261–293.
[13] Paddock, C. A., and Eesley, G. L., 1986, "Transient Thermoreflectance From Thin Metal Films," J. Appl. Phys., **60**, pp. 285–290.
[14] Chu, D. C., Touzelbaev, M., Goodson, K. E., Babin, S., and Pease, R. F. W., 2001, "Thermal Conductivity Measurements of Thin-Film Resist," J. Vac. Sci. Technol. B, **19**(6), pp. 2874–2877.
[15] Govorkov, S., Ruderman, W., Horn, M. W., Goodman, R. B., and Rothschild, M., 1997, "A New Method for Measuring Thermal Conductivity of Thin Films," Rev. Sci. Instrum., **68**(10), pp. 3828–3834.
[16] Rajan, M. A. J., Vivekanandam, T. S., Ramakrishnan, S. K., Ramachandran, K., and Umapathy, S., 2004, "Heat Transfer in Poly(Methyl Acrylate) by Photoacoustic Measurements," J. Appl. Polym. Sci., **93**(3), pp. 1071–1076.
[17] Cahill, D. G., 1990, "Thermal Conductivity Measurement From 30 K to 750 K—the 3-Omega Method," Rev. Sci. Instrum., **61**, pp. 802–808.
[18] Lee, S.-M., Cahill, D. G., and Allen, T. H., 1995, "Thermal Conductivity of Sputtered Oxide Films," Phys. Rev. B, **52**, pp. 253–257.
[19] Liu, W., and Balandin, A. A., 2005, "Thermal Conduction in $Al_xGa_{1-x}N$ Alloys and Thin Films," J. Appl. Phys., **97**, p. 073710.
[20] Cahill, D. G., Katiyar, M., and Abelson, J. R., 1994, "Thermal Conductivity of *a*-Si:H Thin Films," Phys. Rev. B, **50**, pp. 6077–6081.
[21] Kurabayashi, K., Asheghi, M., Touzelbaev, M., and Goodson, K. E., 1999, "Measurement of the Thermal Conductivity Anisotropy in Polyimide Films," J. Microelectromech. Syst., **8**(2), pp. 180–191.
[22] Völkein, F., and Baltes, H., 1992, "A Microstructure for Measurement of Thermal Conductivity of Polysilicon Thin Films," J. Microelectromech. Syst., **1**, pp. 193–196.
[23] Rogers, J. A., Yang, Y., and Nelson, A., 1994, "Elastic Modulus and Inplane Thermal Diffusivity Measurements in Thin Polyimide Films Using Symmetry-Selective Real-Time Impulsive Stimulated Thermal Scattering," Appl. Phys. A: Solids Surf., **58**, pp. 523–534.
[24] Fu, Y., Du, H., Huang, W., Zhang, S., and Hu, M., 2004, "TiNi-Based Thin Films in MEMS Applications: A Review," Sens. Actuators, A, **A112**(2–3), pp. 395–408.
[25] Kahn, H., Huff, M. A., and Heuer, A. H., 1998, "The TiNi Shape-Memory Alloy and Its Applications for MEMS," J. Micromech. Microeng., **8**, pp. 213–221.
[26] Reynaerts, D., Peirs, J., and Van Brussel, H., 1997, "An Implantable Drug-Delivery System Based on Shape-Memory Alloy Micro-Actuation," Sens. Actuators, A, **A61**, pp. 455–462.
[27] Xu, W., Frank, T. G., Stockham, G., and Cuschieri, A., 1999, "Shape Memory Alloy Fixator System for Suturing Tissue in Minimal Access Surgery," Ann. Biomed. Eng., **27**, pp. 663–669.
[28] Wolf, R. H., and Heuer, A. H., 1995, "TiNi (Shape Memory) Films on Silicon for MEMS Applications," J. Microelectromech. Syst., **4**, pp. 206–212.
[29] Shih, C. L., Lai, B. K., Kahn, H., Philips, S. M., and Heuer, A. H., 2001, "A Robust Co-Sputtering Fabrication Procedure for TiNi Shape-Memory Alloys for MEMS," J. Microelectromech. Syst., **10**, pp. 69–79.
[30] Goff, J. F., 1964, "Thermal Conductivity, Thermoelectric Power, and the Electrical Resistivity of Stoichiometric TiNi in the 3 to 300 K Temperature Range," J. Appl. Phys., **35**, pp. 2919–2927.
[31] Terada, Y., Ohkubo, K., Nakagawa, K., Mohri, T., and Suzuki, T., 1995, "Thermal Conductivity of B2-Type Aluminides and Titanides," Intermetallics, **3**, pp. 347–355.
[32] Faulkner, M. G., Amalraj, J. J., and Bhattacharyya, A., 2000, "Experimental Determination of Thermal and Electrical Properties of Ni-Ti Shape Memory Wires," Smart Mater. Struct., **9**, pp. 643–639.
[33] Ju, Y. S., Kurabayashi, K., and Goodson, K. E., 1999, "Thermal Characterization of Anisotropic Thin Dielectric Films Using Harmonic Joule Heating," Thin Solid Films, **339**, pp. 160–164.
[34] Yang, B., Liu, W. L., Liu, J. L., Wang, K. L., and Chen, G., 2002, "Measurements of Anisotropic Thermoelectric Properties in Superlattices," Appl. Phys. Lett., **81**(19), pp. 3588–3590.
[35] Cahill, D. G., 2002, "Errata—Thermal Conductivity Measurement From 30 K to 750 K—The 3-Omega Method," Rev. Sci. Instrum., **73**(10), pp. 3701–3701.
[36] Jacquot, A., Lenoir, B., Dauscher, A., Stolzer, M., and Meusel, J., 2002, "Numerical Simulation of the 3ω Method for Measuring the Thermal Conductivity," J. Appl. Phys., **91**(7), pp. 4733–4738.
[37] Myers, G. E., 1998, *Analytical Methods in Conduction Heat Transfer*, 2nd ed., AMCHT, Madison, WI.
[38] Mastrangelo, C. H., Tai, Y.-C., and Muller, R. S., 1990, "Thermophysical Properties of Low-Residual Stress, Silicon-Rich, LPCVD Silicon Nitride Films," Sens. Actuators, A, **A21–A23**, pp. 856–860.

Flows Between Rotating Cylinders With a Porous Lining

M. Subotic
Graduate Research Assistant
Mem. ASME

F. C. Lai
Associate Professor
Fellow ASME

School of Aerospace and Mechanical Engineering,
University of Oklahoma,
Norman, OK 73019

Flow and temperature fields in an annulus between two rotating cylinders have been examined in this study. While the outer cylinder is stationary, the inner cylinder is rotating with a constant angular speed. A homogeneous and isotropic porous layer is press fit to the inner surface of the outer cylinder. The porous sleeve is saturated with the fluid that fills the annulus. The Brinkman-extended Darcy equations are used to model the flow in the porous layer while the Navier–Stokes equations are used for the fluid layer. The conditions applied at the interface between the porous and fluid layers are the continuity of temperature, heat flux, tangential velocity, and shear stress. Analytical solutions have been attempted. Through these solutions, the effects of Darcy number, Brinkman number, and porous sleeve thickness on the velocity profile and temperature distribution are studied. [DOI: 10.1115/1.2953305]

Keywords: annular flow, forced convection, heat transfer, porous media

Introduction

In the past few decades, interactions in flow between a fluid layer and a porous medium have received considerable attention for their important applications in engineering. For a planar system, the problem has been studied by several researchers [1–5]. However, for a radial system, the problem has not received much attention despite that it is involved in many important applications. For the present study, our interest is related to the application in lubrication where a porous bearing is in use. Porous bearings are often used in rotational machinery because of their ability to retain lubricant.

Previous studies often employed the assumption of an infinitely long porous bearing with which it can greatly simplify the analysis. Capone [6] was the first to develop such a model. He also provided guidelines to determine when the assumption is valid. Diprima and Stuart [7] studied the effects of eccentricity on the flow between rotating cylinders. They derived curvature and inertial corrections for the flow in a journal bearing as a preliminary analysis for Taylor-vortex stability. While Cusano [8] studied the effect of variable permeability of a porous sleeve in journal bearing, Gururajan and Prakash [9] studied the effect of surface roughness on the performance of infinitely long porous journal bearings. In a related study, Channabasappa et al. [10] investigated the linear stability of viscous flow in a porous annulus bounded by two concentric circular cylinders in which the inner cylinder was stationary and the outer was rotational. Their results revealed that the critical Taylor number increases with a decreasing permeability of the porous medium. Chang [11] also investigated the hydrodynamic stability of Taylor–Dean flow in a porous annulus between rotating cylinders with radial flow. He considered both inward and outward radial flows. He found that the superimposed radial flow can produce either stabilizing or destabilizing effect depending heavily on the ratio between the average pumping velocity and the rotation velocity.

Although extensive research has been devoted to porous bearings, most of the previous works have considered lubricant and porous bearing separately. To adequately address the problem involved, one needs to consider both systems simultaneously. Clearly, it is rather challenging to deal with a combined system with a fluid layer overlaying a porous layer. One of the great challenges encountered in a problem like this is the specification of the interface conditions between the fluid and porous layers. In the past, an empirical condition proposed by Beavers and Joseph [12], which matches Darcy's law for the porous medium with the Navier–Stokes equations for the fluid layer through an empirical slip-flow interface condition, has been widely employed. Neale and Nader [13] showed that the empirical interface condition mentioned above can be derived independently from Brinkman's extension of Darcy's law for the porous medium. This enables the use of continuities in velocity and shear stress at the interface. They also showed that their predictions agreed well with experimental data. Recently, Ochoa-Tapia and Whitaker [14,15] proposed an interface condition that permits a jump in the shear stress at the interface region. The interface condition that they proposed has been applied by Kuznetsov in several subsequent studies [16–18]. Alazmi and Vafai [19] examined various interfacial conditions that had been proposed in the literature and their effects on the velocity and temperature solutions. They showed that these interface conditions generally have greater effects on the velocity field than the temperature field.

For the present study, analytical solutions have been attempted for the flow and temperature fields in an annulus with a porous sleeve between two rotating cylinders. Through the solutions obtained, the effects of various governing parameters on the velocity profile and temperature distribution are carefully examined. These solutions also serve as a foundation for the future study of hydrodynamic stability for flow in the annulus with a porous sleeve.

Formulation and Numerical Method

The geometry considered is an annulus between two infinitely long concentric cylinders (Fig. 1). While the outer cylinder of radius c is stationary, the inner cylinder of radius a is rotating. In addition, the surface of the outer cylinder is maintained at a constant temperature T_c while that of the inner cylinder is assumed adiabatic. The annular space between the cylinders is filled with an incompressible Newtonian fluid. Since the inner cylinder is rotating with a constant angular velocity of ω, the flow in the annulus is induced by this rotational motion. A homogeneous and isotropic porous layer is press fit to the inner wall of the outer cylinder. The porous layer is saturated with the same fluid in the annulus.

With the assumption of steady, two-dimensional laminar flow in the annulus, the governing equations for the fluid region are given by

Contributed by the Heat Transfer Division of ASME for publication in the JOURNAL OF HEAT TRANSFER. Manuscript received August 18, 2007; final manuscript received February 27, 2008; published online August 7, 2008. Review conducted by Peter Vadasz. Paper presented at the 2007 International Mechanical Engineering Congress & Exposition (IMECE2007), Seattle, WA, November 11–15, 2007.

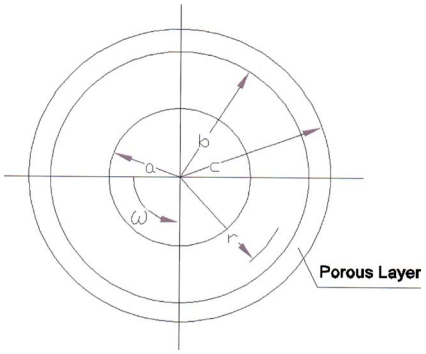

Fig. 1 Annular flow between two rotating cylinders with a porous lining

$$\frac{d}{dr}\left(r\frac{du_{\theta 1}}{dr}\right)-\frac{u_{\theta 1}}{r}=0 \tag{1}$$

$$\frac{\alpha}{r}\frac{d}{dr}\left(r\frac{dT_1}{dr}\right)+\frac{\nu}{c_{p,f}}\left(\frac{du_{\theta 1}}{dr}-\frac{u_{\theta 1}}{r}\right)^2=0 \tag{2}$$

Similarly, the governing equations for flow in the porous region based on Brinkman-extended Darcy law are given by

$$\frac{1}{\phi}\left(\frac{d^2u_{\theta 2}}{dr^2}+\frac{1}{r}\frac{du_{\theta 2}}{dr}-\frac{u_{\theta 2}}{r^2}\right)-\frac{u_{\theta 2}}{K}=0 \tag{3}$$

$$\frac{\alpha_e}{r}\frac{d}{dr}\left(r\frac{dT_2}{dr}\right)+\Phi=0 \tag{4}$$

In the above equations, ϕ and K are the porosity and permeability of the porous medium, respectively; α_e is the effective thermal diffusivity of the porous medium and Φ is the viscous dissipation function. Also note that in the above equations, subscript 1 represents the flow in the fluid region, while subscript 2 refers to the flow in the porous region.

Nield [20] has suggested that the viscous dissipation function should take the following form when Brinkman formulation is considered.

$$\Phi=\frac{\nu u_{\theta 2}^2}{Kc_{p,f}}-\frac{\mu_e u_{\theta 2}}{\rho_f c_{p,f}}\left(\frac{\partial^2 u_{\theta 2}}{\partial r^2}+\frac{1}{r}\frac{\partial u_{\theta 2}}{\partial r}-\frac{u_{\theta 2}}{r^2}\right) \tag{5}$$

On the other hand, Al-Hadhrami et al. [21] have proposed a different form shown below, which has a similar expression like that derived from the Navier–Stokes equation for a Newtonian fluid.

$$\Phi=\frac{\nu u_{\theta 2}^2}{Kc_{p,f}}+\frac{\mu_e}{\rho_f c_{p,f}}\left(r\frac{\partial}{\partial r}\left(\frac{u_{\theta 2}}{r}\right)\right)^2 \tag{6}$$

For the two dissipation functions shown above, μ_e is the effective viscosity associated with the Brinkman formulation. Since μ_e has to be determined by experiment and there are limited data of this quantity in the literature, it has been assumed $\mu_e=\mu$ in the present study. It is also clear that the first term in the above two equations is derived from Darcy's law and the second term is the result due to the Brinkman-extended Darcy formulation. Although these two expressions for the viscous dissipation function are different, Nield et al. [5] have shown that the second term (Brinkman term) is of the order of Darcy number (Da) in comparison with the first term (Darcy term). As such, in the case of small Darcy numbers (the range that the present study is concerned), the two formulations are, in fact, reduced to that of Darcy term. For this reason, the Brinkman term is neglected in the present study.

The solutions of the above governing equations (1)–(4) depend on the boundary and interface conditions imposed. For the present study, no-slip boundary conditions are applied to the surfaces of the inner and outer cylinders while continuities of velocity, velocity gradient, temperature, and heat flux are imposed on the interface between the fluid and porous regions.

The formulations of boundary and interface conditions are presented below.

For $r=a$,

$$u_{\theta 1}=a\omega \tag{7a}$$

$$\frac{dT_1}{dr}=0 \tag{7b}$$

For $r=c$,

$$u_{\theta 2}=0 \tag{7c}$$

$$T_2=T_c \tag{7d}$$

For $r=b$,

$$u_{\theta 1}=u_{\theta 2} \tag{7e}$$

$$\frac{d}{dr}\left(\frac{u_{\theta 2}}{r}\right)-\frac{d}{dr}\left(\frac{u_{\theta 1}}{r}\right)=\beta\frac{u_\theta}{K^{1/2}} \tag{7f}$$

$$T_1=T_2 \tag{7g}$$

$$k_1\frac{dT_1}{dr}=k_e\frac{dT_2}{dr} \tag{7h}$$

where β is an empirical coefficient and k_e is the effective thermal conductivity of the porous medium. Note that Eq. (7*f*) describes a jump in the shear stress at the interface as suggested by Ochoa-Tapia and Whitaker [14,15]. Although this interface condition has been successfully applied in the studies by Kuznetsov [16–18], it requires experimentally determined value of β for real applications, which is currently scarce in the literature. In addition, after examining various interface conditions proposed, Alazmi and Vafai [19] have concluded that for most practical applications, the discrepancy in the results predicted by these various interface conditions is negligible. In view of the above arguments, the jump condition in the shear stress is relaxed in the present study for simplicity. As such, Eq. (5) is reduced to that proposed by Neale and Nader [13] (i.e., $\beta=0$).

The governing equations as well as the boundary and interface conditions can be normalized using the following dimensionless variables:

$$R=\frac{r}{c},\quad V=\frac{u_\theta}{a\omega}=\frac{u_\theta}{U_a},\quad \Theta=\frac{T-T_c}{T_s-T_c} \tag{8}$$

where T_s $(=U_a^2/c_{p,f}+T_c)$ is the stagnation temperature. In the dimensionless form, the governing equations for the fluid and porous regions are given, respectively, by the following.

In Fluid region,

$$\frac{d}{dR}\left(R\frac{dV_1}{dR}\right)-\frac{V_1}{R}=0 \tag{9}$$

$$\frac{1}{R}\frac{d}{dR}\left(R\frac{d\Theta_1}{dR}\right)+Br\left(\frac{dV_1}{dR}-\frac{V_1}{R}\right)^2=0 \tag{10}$$

In Porous region,

$$\frac{d^2V_2}{dR^2}+\frac{1}{R}\frac{dV_2}{dR}-\left(\frac{1}{R^2}+\frac{\phi}{\mathrm{Da}}\right)V_2=0 \tag{11}$$

$$\frac{1}{R}\frac{d}{dR}\left(R\frac{d\Theta_2}{dR}\right)+\frac{\mathrm{Br}_e}{\mathrm{Da}}{V_2}^2=0 \tag{12}$$

where Da in the above expression is the Darcy number, which represents a relative measure of the permeability of the porous sleeve. Also appearing in the above equations are the Brinkman

numbers Br and Br_e (=$\mathrm{Br}\cdot k/k_e$) for the fluid and porous medium, respectively. The Brinkman number is a product of Prandtl and Eckert numbers and it represents the ratio of viscous dissipation to heat conduction. If its value is greater than unity, then viscous dissipation is significant.

The boundary and interface conditions are also normalized to give the following:

For $R=a/c$,

$$V_1 = 1 \tag{13a}$$

$$\frac{d\Theta_1}{dR} = 0 \tag{13b}$$

For $R=1$,

$$V_2 = 0 \tag{13c}$$

$$\Theta_2 = 0 \tag{13d}$$

For $R=b/c$,

$$V_1 = V_2 \tag{13e}$$

$$\frac{d}{dR}\left(\frac{V_1}{R}\right) = \frac{d}{dR}\left(\frac{V_2}{R}\right) \tag{13f}$$

$$\Theta_1 = \Theta_2 \tag{13g}$$

$$k_f\frac{d\Theta_1}{dR} = k_e\frac{d\Theta_2}{dR} \tag{13h}$$

Analytical solutions have been attempted for the above equations (9)–(12) subject to the boundary conditions and interface conditions (13*a*)–(13*h*). The general solution for the velocity in the fluid region is given by

$$V_1 = C_1R + \frac{C_2}{R} \tag{14}$$

and that for the porous region is given by

$$V_2 = AI_1\left[R\sqrt{\frac{\phi}{\mathrm{Da}}}\right] + BK_1\left[R\sqrt{\frac{\phi}{\mathrm{Da}}}\right] \tag{15}$$

where I_1 and K_1 are the modified Bessel functions of the first order, and A, B, C_1, and C_2 are the coefficients to be determined by the boundary and interface conditions.

After implementing the boundary and interface conditions, one obtains the velocity in the fluid region in the following form:

$$V_1 = \frac{a}{b^2-a^2}\left(\frac{b^2}{cR} - cR\right) + \frac{2ab^2(c^2R^2-a^2)}{R(b^2-a^2)}M \tag{16}$$

and that in the porous region is given by

$$V_2 = \left\{I_1\left(\sqrt{\frac{\phi}{\mathrm{Da}}}\right)K_1\left(R\sqrt{\frac{\phi}{\mathrm{Da}}}\right) - K_1\left(\sqrt{\frac{\phi}{\mathrm{Da}}}\right)I_1\left(R\sqrt{\frac{\phi}{\mathrm{Da}}}\right)\right\}N \tag{17}$$

where M and N are the complicated expressions involving the modified Bessel functions and are given below.

$$M = \frac{I_1\left(\sqrt{\frac{\phi}{\mathrm{Da}}}\right)K_1\left(\frac{b}{c}\sqrt{\frac{\phi}{\mathrm{Da}}}\right) - K_1\left(\sqrt{\frac{\phi}{\mathrm{Da}}}\right)I_1\left(\frac{b}{c}\sqrt{\frac{\phi}{\mathrm{Da}}}\right)}{b(b^2-a^2)\sqrt{\frac{\phi}{\mathrm{Da}}}\left[K_1\left(\sqrt{\frac{\phi}{\mathrm{Da}}}\right)I_2\left(\frac{b}{c}\sqrt{\frac{\phi}{\mathrm{Da}}}\right) + I_1\left(\sqrt{\frac{\phi}{\mathrm{Da}}}\right)K_2\left(\frac{b}{c}\sqrt{\frac{\phi}{\mathrm{Da}}}\right)\right] + 2a^2c\left[I_1\left(\sqrt{\frac{\phi}{\mathrm{Da}}}\right)K_1\left(\frac{b}{c}\sqrt{\frac{\phi}{\mathrm{Da}}}\right) - K_1\left(\sqrt{\frac{\phi}{\mathrm{Da}}}\right)I_1\left(\frac{b}{c}\sqrt{\frac{\phi}{\mathrm{Da}}}\right)\right]} \tag{18}$$

$$N = \frac{2abc}{b(b^2-a^2)\sqrt{\frac{\phi}{\mathrm{Da}}}\left[K_1\left(\sqrt{\frac{\phi}{\mathrm{Da}}}\right)I_2\left(\frac{b}{c}\sqrt{\frac{\phi}{\mathrm{Da}}}\right) + I_1\left(\sqrt{\frac{\phi}{\mathrm{Da}}}\right)K_2\left(\frac{b}{c}\sqrt{\frac{\phi}{\mathrm{Da}}}\right)\right] + 2a^2c\left[I_1\left(\sqrt{\frac{\phi}{\mathrm{Da}}}\right)K_1\left(\frac{b}{c}\sqrt{\frac{\phi}{\mathrm{Da}}}\right) - K_1\left(\sqrt{\frac{\phi}{\mathrm{Da}}}\right)I_1\left(\frac{b}{c}\sqrt{\frac{\phi}{\mathrm{Da}}}\right)\right]} \tag{19}$$

From Eq. (16), one can calculate the first derivative of the fluid velocity in the fluid region, which is given by

$$\frac{dV_1}{dR} = \frac{a}{b^2-a^2}\left(-\frac{b^2}{cR^2} - c\right) + \left[\frac{2ab^2c^2}{b^2-a^2} + \frac{2a^3b^2}{(b^2-a^2)R^2}\right]M \tag{20}$$

Given Eqs. (16) and (20), the general solution for the temperature field in the fluid region can be found to be

$$\Theta_1 = -\frac{\mathrm{Br}}{4R^2}\left[-\frac{2ab^2}{c(b^2-a^2)} + \frac{4a^3b^2}{b^2-a^2}M\right]^2 + E\ln R + F \tag{21}$$

where E and F are the integration constants to be determined by the boundary and interface conditions. For example, constant E is determined from the boundary condition Eq. (13*b*) and is given by

$$E = -\frac{\mathrm{Br}}{2}\left(\frac{c^2}{a^2}\right)\left[-\frac{2ab^2}{c(b^2-a^2)} + \frac{4a^3b^2}{b^2-a^2}M\right]^2 \tag{22}$$

Constant F is determined from the interface condition Eq. (13*g*) and is given by

$$F = \frac{\mathrm{Br}}{4}\left[-\frac{2ab^2}{c(b^2-a^2)} + \frac{4a^3b^2}{b^2-a^2}M\right]^2\left(\frac{c^2}{b^2} + 2\frac{c^2}{a^2}\ln\frac{b}{c}\right) + \Theta_2\Big|_{R=b/c} \tag{23}$$

Thus, the complete solution of the temperature field in the fluid region is given by

$$\Theta_1 = \frac{\mathrm{Br}}{4}\left[-\frac{2ab^2}{c(b^2-a^2)} + \frac{4a^3b^2}{b^2-a^2}M\right]^2\left(\frac{c^2}{b^2} - \frac{1}{R^2} + 2\frac{c^2}{a^2}\ln\left(\frac{b}{Rc}\right)\right) + \Theta_2\Big|_{R=b/c} \tag{24}$$

Substitute V_2 from Eq. (17) to the energy equation for the porous layer, Eq. (14), one obtains

$$\frac{1}{R}\frac{d}{dR}\left(R\frac{d\Theta_2}{dR}\right) + \frac{\mathrm{Br}_e}{\mathrm{Da}}\left[I_1\left(\sqrt{\frac{\phi}{\mathrm{Da}}}\right)K_1\left(R\sqrt{\frac{\phi}{\mathrm{Da}}}\right) - I_1\left(R\sqrt{\frac{\phi}{\mathrm{Da}}}\right)K_1\left(\sqrt{\frac{\phi}{\mathrm{Da}}}\right)\right]^2N^2 = 0 \tag{25}$$

Integrating twice, one obtains the following solution:

$$\Theta_2 = -\frac{\mathrm{Br}_e}{\mathrm{Da}} N^2 \left[I_1^2\left(\sqrt{\frac{\phi}{\mathrm{Da}}}\right) F_1(R) - 2I_1\left(\sqrt{\frac{\phi}{\mathrm{Da}}}\right) K_1\left(\sqrt{\frac{\phi}{\mathrm{Da}}}\right) F_2(R) + K_1^2\left(\sqrt{\frac{\phi}{\mathrm{Da}}}\right) F_3(R) \right] + G \ln R + H \tag{26}$$

where G and H are the integration constants and F_1, F_2, and F_3 involve the integration of the modified Bessel functions and their expressions are given below.

$$f_1(R) = \int R K_1^2\left(R\sqrt{\frac{\phi}{\mathrm{Da}}}\right) dR \tag{27a}$$

$$f_2(R) = \int R I_1\left(R\sqrt{\frac{\phi}{\mathrm{Da}}}\right) K_1\left(R\sqrt{\frac{\phi}{\mathrm{Da}}}\right) dR \tag{27b}$$

$$f_3(R) = \int R I_1^2\left(R\sqrt{\frac{\phi}{\mathrm{Da}}}\right) dR \tag{27c}$$

$$F_1(R) = \int \frac{1}{R} f_1(R) dR = \int \left[\frac{1}{R} \int R K_1^2\left(R\sqrt{\frac{\phi}{\mathrm{Da}}}\right) dR \right] dR \tag{27d}$$

$$F_2(R) = \int \frac{1}{R} f_2(R) dR = \int \left[\frac{1}{R} \int R I_1\left(R\sqrt{\frac{\phi}{\mathrm{Da}}}\right) K_1\left(R\sqrt{\frac{\phi}{\mathrm{Da}}}\right) dR \right] dR \tag{27e}$$

$$F_3(R) = \int \frac{1}{R} f_3(R) dR = \int \left[\frac{1}{R} \int R I_1^2\left(R\sqrt{\frac{\phi}{\mathrm{Da}}}\right) dR \right] dR \tag{27f}$$

Constant G in Eq. (26) is calculated from the interface condition, Eq. (13h), and is given by

$$G = \frac{b}{c}\frac{k_1}{k_e}\frac{\mathrm{Br}_e}{2}\left[-\frac{2ab^2}{c(b^2-a^2)} + \frac{4a^3b^2}{b^2-a^2} M \right]^2 \left(\frac{c^3}{b^3} - \frac{c^3}{a^2 b}\right) + \frac{\mathrm{Br}e}{\mathrm{Da}} N^2 \left[I_1^2\left(\sqrt{\frac{\phi}{\mathrm{Da}}}\right) f_1(R)_{R=b/c} - 2I_1\left(\sqrt{\frac{\phi}{\mathrm{Da}}}\right) K_1\left(\sqrt{\frac{\phi}{\mathrm{Da}}}\right) f_2(R)_{R=b/c} + K_1^2\left(\sqrt{\frac{\phi}{\mathrm{Da}}}\right) f_3(R)_{R=b/c} \right] \tag{28}$$

Similarly, constant H in Eq. (26) is calculated from the boundary condition, Eq. (13d), to give

$$H = \frac{\mathrm{Br}_e}{\mathrm{Da}} N^2 \left[I_1^2\left(\sqrt{\frac{\phi}{\mathrm{Da}}}\right) F_1(R)_{R=1} - 2I_1\left(\sqrt{\frac{\phi}{\mathrm{Da}}}\right) K_1\left(\sqrt{\frac{\phi}{\mathrm{Da}}}\right) F_2(R)_{R=1} + K_1^2\left(\sqrt{\frac{\phi}{\mathrm{Da}}}\right) F_3(R)_{R=1} \right] \tag{29}$$

Results and Discussion

With the analytical solutions obtained above, we can now examine the effect of each governing parameter. Before doing so, we can first verify the assumption that we made earlier about the dissipation functions. Indeed, we find that the Brinkman term is at least one order smaller than that of the Darcy term for the range of the parameters considered in the present study. As such, it justifies the neglect of the Brinkman term in the dissipation function. The effect of each governing parameter is then discussed separately below.

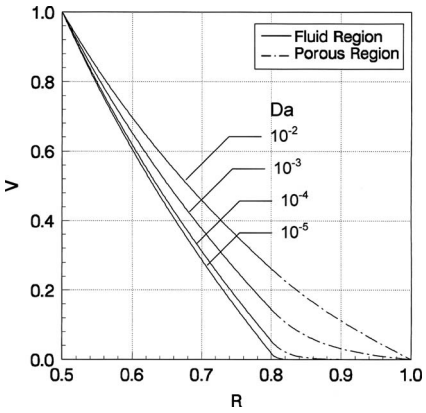

Fig. 2 Effects of Darcy number on the velocity profile (ϕ=0.2, a=0.5, b=0.8, and c=1)

Effects of Darcy Number. The effects of Darcy number on the flow and temperature fields can be examined from Figs. 2 and 3 for a given geometry (a=0.5, b=0.8, and c=1). Also fixed for comparison are the porosity of the porous sleeve (i.e., ϕ=0.2), Brinkman number (Br=1) as well as thermal conductivity ratio (k_1/k_e=1). In this case, one observes that the slip velocity at the interface increases with an increase in the Darcy number (Fig. 2). Consequently, the flow penetration to the porous sleeve also increases with the Darcy number. Recall that the Darcy number is defined as K/c^2. Thus, for a fixed geometry, a large Darcy number implies that the porous sleeve is more permeable. As such, the trend observed above is reasonable. Another interesting phenomenon observed is that the velocity gradient at the interface increases with a reduction in the Darcy number, which means that the shear stress experienced at the interface increases when the permeability of the porous sleeve reduces, which also implies that the power required to maintain the inner cylinder running at the same velocity will increase.

The effect of Darcy number on the temperature distribution of flow in the annulus can be examined from Fig. 3. One observes that the maximum temperature occurs at the surface of the inner cylinder. In addition, the maximum temperature increases with a reduction in the Darcy number. As observed earlier (Fig. 2), the velocity gradient increases with a reduction in the Darcy number, which leads to a greater viscous dissipation and thus a higher fluid

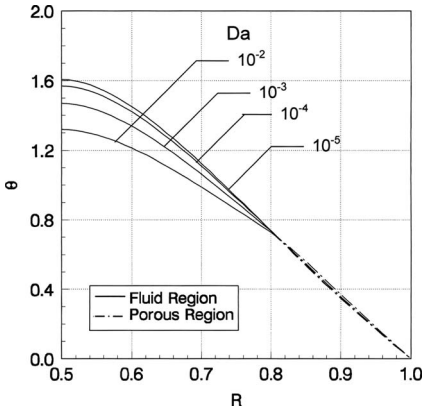

Fig. 3 Effects of Darcy number on the temperature distribution (ϕ=0.2, a=0.5, b=0.8, and c=1)

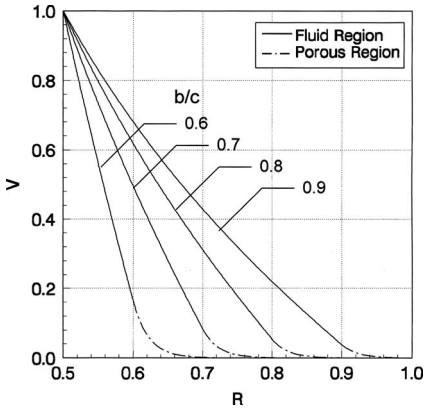

Fig. 4 Effects of porous sleeve thickness on the velocity profile (ϕ=0.2, a=0.5, and Da=10^{-4})

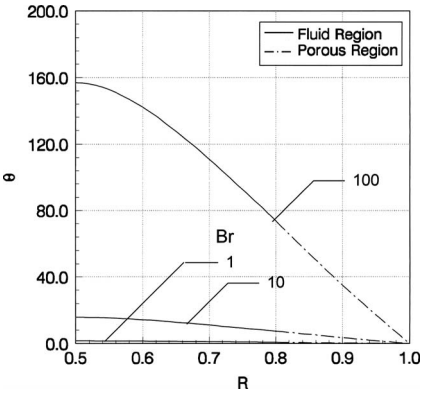

Fig. 6 Effects of Brinkman number on the temperature distribution (ϕ=0.2, Da=10^{-4}, a=0.5, b=0.8, and c=1)

temperature at the inner cylinder. It is interesting to note that the variation of Darcy number causes a larger temperature difference in the fluid region than that in the porous sleeve. The Darcy number appears to have little influence on the temperature distribution in the porous sleeve.

Effects of Porous Sleeve Thickness. The effects of porous sleeve thickness on the flow and temperature fields can be examined from Figs. 4 and 5 for a given Darcy number (Da=10^{-4}), thermal conductivity ratio (k_1/k_e=1), and a fixed gap width of the annulus (a=0.5 and c=1). In this case, an increase in the thickness of the porous sleeve leads to a reduction in the fluid layer thickness. As observed from Fig. 4, the slip velocity and velocity gradient at the interface all increase with an increase in the porous sleeve thickness (i.e., a reduction in b/c). This has significant influence on the fluid temperature distribution inside the annulus as the viscous dissipation is proportional to the velocity gradient. It is indeed that a higher temperature profile is observed when the porous sleeve thickness increases. Also noted, a larger temperature difference is experienced in the fluid layer than the porous sleeve when the porous sleeve thickness increases.

Effects of Brinkman Number. As described earlier, the Brinkman number signifies the effect of viscous dissipation. In many applications involving rotational cylinders, viscous dissipation is of a great concern. In the absence of thermal buoyancy, viscous dissipation has no influence on the velocity profile but has a significant effect on the temperature distribution, as is evident from Fig. 6. As observed, when the Brinkman number is small (Br $\leq$1), the effect of viscous dissipation is negligible. For a large Brinkman number (Br$>$1), the maximum fluid temperature resulted from the viscous dissipation increases with an increase in the Brinkman number. In addition, one notices that the maximum fluid temperature is directly proportional to the Brinkman number.

Effects of Thermal Conductivity Ratio. All the discussion above is based on the assumption that the thermal conductivity of fluid is the same as that of the porous medium (i.e., k_1/k_e=1). For applications involving porous bearings, the thermal conductivity of the porous sleeve (which is usually made from sintered metal powder) can be substantially different from that of the lubricant. Again, the thermal conductivity ratio has no effect on the velocity profile in the absence of thermal buoyancy but can modify the temperature distribution significantly, as shown in Fig. 7 where the temperature profiles are shown for a given Darcy number (Da=10^{-4}), Brinkman number (Br=1) and a fixed gap width of the annulus (a=0.5 and c=1). As one observes, a smaller value of the thermal conductivity ratio (i.e., the thermal conductivity of porous sleeve is significantly larger than that of fluid) leads to a reduction in the maximum fluid temperature. This can be attributed to the effectiveness in heat dissipation by conduction through the porous sleeve. As the thermal conductivity ratio decreases, one observes a more uniform temperature distribution in the porous sleeve.

Conclusion

Analytical solutions have been presented for velocity profiles and temperature distributions for laminar flows in an annulus between the two rotating cylinders. The annulus is partially occupied by a porous sleeve. The effects of several governing parameters

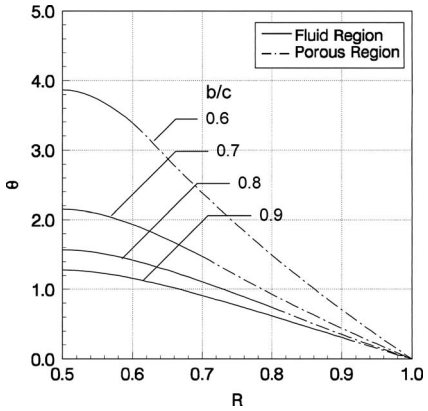

Fig. 5 Effects of porous sleeve thickness on the temperature distribution (ϕ=0.2, a=0.5, and Da=10^{-4})

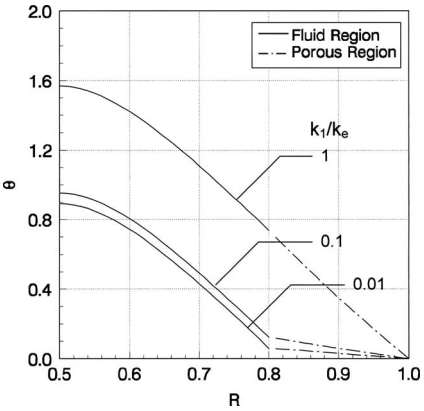

Fig. 7 Effects of thermal conductivity ratio on the temperature distribution (ϕ=0.2, Da=10^{-4}, a=0.5, b=0.8, and c=1)

(such as Darcy number, Brinkman number, porous sleeve thickness, as well as thermal conductivity ratio) on the flow and temperature fields are closely examined. It has been found that the slip velocity and flow penetration at the interface increase with an increase in both the Darcy number and the porous sleeve thickness. However, the velocity gradient at the interface shows an opposite trend. Since the viscous dissipation is proportional to the velocity gradient, this has led to an increase in the maximum fluid temperature with a reduction in the Darcy number and the fluid layer thickness. It is also found that viscous dissipation can significantly increase the maximum fluid temperature for Brinkman numbers greater than unity. The maximum fluid temperature resulted from viscous dissipation is found to be directly proportional to the Brinkman number. In addition, it is found that a smaller thermal conductivity ratio between the fluid and the porous medium leads to a reduction in the maximum fluid temperature as the heat is more effectively dissipated through conduction by the porous sleeve.

While the present study has examined a fundamental problem in fluid flow and heat transfer involving rotating cylinders with a porous sleeve, the results obtained have important implications for many practical applications. The analytical solutions presented not only help identify critical parameters for design consideration but also lay the foundation for studies on the hydrodynamic stability, which await further investigation in the future.

Acknowledgment

The support of this work through GAANN fellowship program provided by the Department of Education is gratefully acknowledged.

Nomenclature

a = radius of the inner cylinder (m)
b = radial distance of the interface (m)
Br = Brinkman number of fluid, $\nu U_a^2/\alpha c_{pf}(T_s-T_c)$
Br_e = Brinkman number of porous medium, $\nu U_a^2/\alpha_e c_{pf}(T_s-T_c)$
c = radius of the outer cylinder (m)
c_p = specific heat, (kJ/kg K)
Da = Darcy number, K/c^2
Ec = Eckert number, $U_a^2/c_{pf}(T_s-T_c)$
K = permeability (m^2)
k = thermal conductivity of fluid (W/m K)
k_e = effective thermal conductivity of porous medium (W/m K)
Pr = Prandtl number of fluid, ν/α
Pr_e = Prandtl number of porous medium, ν/α_e
r = radial distance (m)
R = dimensionless radial distance, r/c
T = temperature (K)
T_c = temperature at the surface of the outer cylinder (K)
T_s = stagnation temperature (K)
U_a = tangential velocity at the surface of the inner cylinder, $a\omega$ (m/s)
u_θ = velocity in the angular direction (m/s)
α = thermal diffusivity of fluid, $\mathrm{k}/\rho c_p$ (m^2/s)
α_e = effective thermal diffusivity of porous medium, $k_e/(\rho c_p)_f$ (m^2/s)
β = empirical coefficient of Brinkman dissipation function
μ = dynamic viscosity of fluid ($\mathrm{kg/m\cdot s}$)
μ_e = effective viscosity in Brinkman formulation (kg/m s)
ν = kinematic viscosity (m^2/s)
Θ = dimensionless temperature, $(T-T_c)/(T_s-T_c)$
ρ = density ($\mathrm{kg/m}^3$)
Φ = viscous dissipation function
ω = angular velocity (rad/s)

Subscripts

e = effective property
f = fluid
1 = fluid
2 = porous medium

References

[1] Vafai, K., and Kim, S. J., 1990, "Analysis of Surface Heat Transfer Enhancement by a Porous Substrate," ASME J. Heat Transfer, **112**, pp. 700–706.
[2] Huang, P. C., and Vafai, K., 1994, "Analysis of Flow and Heat Transfer Over an External Boundary Covered With a Porous Substrate," ASME J. Heat Transfer, **116**, pp. 768–771.
[3] Kuznetsov, A. V., 2000, "Fluid Flow and Heat Transfer Analysis of Couette Flow in a Composite Duct," Acta Mech., **140**, pp. 163–170.
[4] Nield, D. A., and Kuznetsov, A. V., 2003, "Boundary-Layer Analysis of Forced Convection With a Plate and Porous Substrate," Acta Mech., **166**, pp. 141–148.
[5] Nield, D. A., Kuznetsov, A. V., and Xiong, M., 2003, "Thermally Developing Forced Convection in a Porous Medium: Parallel Plate Channel With Walls at Uniform Temperature, With Axial Conduction and Viscous Dissipation Effects," Int. J. Heat Mass Transfer, **46**, pp. 643–651.
[6] Capone, E., 1970, "Lubrication of Axially Undefined Porous Bearings," Wear, **15**, pp. 157–170.
[7] Diprima, R. C., and Stuart, W. H., 1972, "Flow Between Eccentric Rotating Cylinders," ASME J. Lubr. Technol., **94**, pp. 266–274.
[8] Cusano, C., 1973, "The Effects of Variable Permeability on the Performance Characteristics of Porous Bearings," Wear, **23**, pp. 55–62.
[9] Gururajan, K., and Prakash, J., 1999, "Surface Roughness Effects in Infinitely Long Porous Journal Bearings," ASME J. Tribol., **121**, pp. 139–147.
[10] Channabasappa, M. N., Ranganna, G., and Rajappa, B., 1984, "Stability of Viscous Flow in a Rotating Porous Medium in the Form of an Annulus: The Small-Gap Problem," Int. J. Numer. Methods Fluids, **4**, pp. 803–811.
[11] Chang, M.-H., 2003, "Hydrodynamic Stability of Taylor–Dean Flow Between Rotating Porous Cylinders With Radial Flow," Phys. Fluids, **15**, pp. 1178–1188.
[12] Beavers, G. S., and Joseph, D. D., 1967, "Boundary Conditions at a Naturally Permeable Wall," J. Fluid Mech., **30**, pp. 197–207.
[13] Neale, G., and Nader, W., 1974, "Practical Significance of Brinkman Extension of Darcy's Law. Coupled Parallel Flow Within a Channel and a Bounding Porous Medium," Can. J. Chem. Eng., **52**, pp. 475–478.
[14] Ochoa-Tapia, J. A., and Whitaker, S., 1995, "Momentum Transfer at the Boundary Between a Porous Medium and a Homogeneous Fluid—I. Theoretical Development," Int. J. Heat Mass Transfer, **38**, pp. 2635–2646.
[15] Ochoa-Tapia, J. A., and Whitaker, S., 1995, "Momentum Transfer at the Boundary Between a Porous Medium and a Homogeneous Fluid—II. Comparison With Experiment," Int. J. Heat Mass Transfer, **38**, pp. 2647–2655.
[16] Kuznetsov, A. V., 1997, "Influence of the Stress Jump Condition at the Porous-Medium/Clear-Fluid Interface on a Flow at a Porous Wall," Int. Commun. Heat Mass Transfer, **24**, pp. 401–410.
[17] Kuznetsov, A. V., 1998, "Analytical Investigation of Coette Flow in a Composite Channel Partially Filled With a Porous Medium and Partially Filled With a Clear Fluid," Int. J. Heat Mass Transfer, **41**, pp. 2556–2560.
[18] Kuznetsov, A. V., 1999, "Fluid Mechanics and Heat Transfer in the Interface Region Between a Porous Medium and a Fluid Layer: A Boundary Layer Solution," J. Porous Media, **2**, 309–321.
[19] Alazmi, B., and Vafai, K., 2001, "Analysis of Fluid Flow and Heat Transfer Interfacial Conditions Between a Porous Medium and a Fluid Layer," Int. J. Heat Mass Transfer, **44**, pp. 1735–1749.
[20] Nield, D. A., 2000, "Resolution of a Paradox Involving Viscous Dissipation and Nonlinear Drag in a Porous Medium," Transp. Porous Media, **41**, pp. 349–357.
[21] Al-Hadhrami, A. K., Elliott, L., and Ingham, D. B., 2003, "A New Model for Viscous Dissipation in Porous Media Across a Range of Permeability Values," Transp. Porous Media, **53**, pp. 117–122.

The Solution of Transient Radiative Transfer With Collimated Incident Serial Pulse in a Plane-Parallel Medium by the DRESOR Method

Qiang Cheng
Wuhan National Laboratory for Optoelectronics,
Huazhong University of Science and Technology,
Wuhan 430074, P.R.C;
State Key Laboratory of Coal Combustion,
Huazhong University of Science and Technology,
Wuhan 430074, P.R.C.

Huai-Chun Zhou
e-mail: hczhou@mail.hust.edu.cn

Zhi-Feng Huang

State Key Laboratory of Coal Combustion,
Huazhong University of Science and Technology,
Wuhan 430074, P.R.C.

Yong-Lin Yu

De-Xiu Huang

Wuhan National Laboratory for Optoelectronics,
Huazhong University of Science and Technology,
Wuhan 430074, P.R.C.

A time-dependent distribution of ratios of energy scattered by the medium or reflected by the boundary surfaces (DRESOR) method was proposed to solve the transient radiative transfer in a one-dimensional slab. This slab is filled with an absorbing, scattering, and nonemitting medium and exposed to a collimated, incident serial pulse with different pulse shapes and pulse widths. The time-dependent DRESOR values, representing the temporal response of an instantaneous, incident pulse with unit energy and the same incident direction as that for the serial pulse, were proposed and calculated by the Monte Carlo method. The temporal radiative intensity inside the medium with high directional resolution can be obtained from the time-dependent DRESOR values. The transient incident radiation results obtained by the DRESOR method were compared to those obtained with the Monte Carlo method, and good agreements were achieved. Influences of the pulse shape and width, reflectivity of the boundary, scattering albedo, optical thickness, and anisotropic scattering on the transient radiative transfer, especially the temporal response along different directions, were investigated. [DOI: 10.1115/1.2945906]

Keywords: transient radiative transfer, DRESOR method, Monte Carlo method, serial pulse

1 Introduction

Much attention has been devoted to the study of short pulse laser radiative transfer in a strongly scattering medium during the past decade [1,2], because of its wide applications to medical diagnosis [3], remote sensing [4], laser material processing of microstructures [5], and optical tomography [6]. Several theoretical analyses and numerical models of transient radiative transfer have been used to solve the transient radiative transfer equation (TRTE), such as integral equation (IE) formulation [6], modified differential approximation [7], discrete ordinates method (DOM) [8], Monte Carlo method (MCM) [9–11], finite-volume method (FVM) [12], and finite element method (FEM) [13,14]. In most of the studies mentioned, laser pulses were limited to simple shapes, such as a square or Gaussian temporal profile. The incident radiation was used to examine the effect of scattering albedo, optical thickness, anisotropic scattering, and reflective boundary on the transmitted temporal signals, reported with Brewster and Yamada [15], Hasegawa et al. [16], Hsu [9], and Zhou and Cheng [17].

Currently, more complex pulses, such as pulse train or serial pulses, have been used to carry out scientific research [18–22]. A pulse train or a serial pulse consists of "bursts" or "trains" at a separation time of a few milliseconds to microseconds. For instance, micromachining was controlled by the use designed pulse trains of a laser [18]. Heat accumulated at the irradiation site from successive pulses affects the quality and size of the features. The appropriate time interval between pulses and proper number of pulses per burst can improve the quality of features. The temporal variation of radiative intensity in a scattering medium is far more complex, which can be exposed to serial pulse with different pulse shapes and widths, either continuous or discontinuous. It is desirable to develop a numerical model to help our understanding of the transient radiative transfer for incident serial pulse.

The distribution of ratios of energy scattered by the medium or reflected by the boundary surfaces (DRESOR) method based on the MCM has been proposed to treat the steady and transient radiative transfer problems in one-dimensional medium [23,17] or with collimated irradiation [24]. By this method, the angular distribution of intensity with high directional resolution can be obtained, which plays a key role in most inverse radiative transfer issues and in radiative image processing in some industrial applications, for example, monitoring of temperature distributions in industrial combustion furnaces [25].

The purpose of this study was to simulate the transient radiative transfer for collimated incident serial pulse with different pulse shapes and widths in an absorbing, nonemitting, isotropic/anisotropic scattering, plane-parallel medium by using the DRESOR method. In the following section, the formulas of a time-dependent DRESOR method are given, and the transient results for a single Gaussian incident pulse in an isotropic scattering medium as well as related validation are presented. Then, various collimated incident serial-pulse cases are studied to analyze the effects of pulse shape and width, boundary reflectivity, and medium properties. Finally, concluding remarks are given.

2 Formulas of the Time-Dependent DRESOR Method

2.1 Basic Description of the Time-Dependent DRESOR Method. The considered physical cases in this paper are all absorbing, nonemitting, isotropic/anisotropic scattering, plane-parallel media, as shown in Fig. 1. The radiative properties of the media and the boundary remain unchanged during the transient process. The TRTE can be written as [6,9,26]

Contributed by the Heat Transfer Division of ASME for publication in the JOURNAL OF HEAT TRANSFER. Manuscript received March 25, 2007; final manuscript received January 15, 2008; published online August 6, 2008. Review conducted by Bengt Sunden.

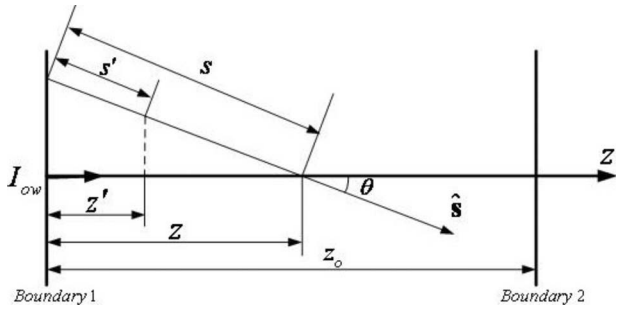

Fig. 1 The geometry and coordinate system

$$\frac{dI(z,\hat{\mathbf{s}},t)}{ds}=\frac{\partial I(z,\hat{\mathbf{s}},t)}{c\partial t}+\frac{\partial I(z,\hat{\mathbf{s}},t)}{\partial s}=-\beta I(z,\hat{\mathbf{s}},t)+\frac{\sigma_s}{4\pi}\int_{4\pi}I(z,\hat{\mathbf{s}}_i,t)\Phi(\hat{\mathbf{s}}_i,\hat{\mathbf{s}})d\Omega_i \quad (1)$$

Integration of Eq. (1) leads to

$$I(z,\hat{\mathbf{s}},t)=I_{ow}\left(z_w,\hat{\mathbf{s}},t-\frac{s}{c}\right)\exp\left[-\int_0^s\beta ds'\right]+\int_0^s S\left(z',\hat{\mathbf{s}},t-\frac{s-s'}{c}\right)\exp\left[-\int_{s'}^s\beta ds''\right]\beta ds' \quad (2)$$

where I_{ow} denotes the incident intensity at the boundary. The source function S is given as

$$S\left(z',\hat{\mathbf{s}},t-\frac{s-s'}{c}\right)=\frac{\omega}{4\pi}\left[\int_{4\pi}I\left(z',\hat{\mathbf{s}},t-\frac{s-s'}{c}\right)\Phi(\hat{\mathbf{s}},\hat{\mathbf{s}})d\Omega_i\right] \quad (3)$$

Equations (2) and (3) show that the radiative intensity at time t depends on the entire time history from $t=0$, $t-s/c$ or $t-((s-s')/c)$, and it is determined from the distance between the location under consideration and the contribution location.

To avoid duplication of the details, only the salient features of the time-dependent DRESOR method are given here. Details can be found in a previous work by the authors [17,19]. The new formula for S in the time-dependent DRESOR method was

$$S\left(z',\hat{\mathbf{s}},t-\frac{s-s'}{c}\right)=\frac{1}{4\pi}\int_0^{t-((s-s')/c)}\left[\int_W\pi I_{ow}(z_w,\hat{\mathbf{s}},t')\times R_d^s\left(z_w,z',\hat{\mathbf{s}},t-\frac{s-s'}{c}-t'\right)dA\right]dt' \quad (4)$$

where W denotes the irradiated area at the boundary. Substituting Eq. (4) into Eq. (2) leads to a new formula for TRTE,

$$I(z,\hat{\mathbf{s}},t)=I_{ow}\left(z_w,\hat{\mathbf{s}},t-\frac{s}{c}\right)\exp\left[-\int_0^s\beta ds'\right]+\frac{1}{4\pi}\int_0^s\int_0^{t-((s-s')/c)}\int_W\pi I_{ow}(z_w,\hat{\mathbf{s}},t')\times R_d^s\left(z_w,z',\hat{\mathbf{s}},t-\frac{s-s'}{c}-t'\right)dAdt'\times\exp\left[-\int_{s'}^s\beta ds''\right]\beta ds' \quad (5)$$

$R_d^s(z,z',\hat{\mathbf{s}},t)$ is the so called transient DRESOR value. It denotes the ratio of the energy scattered by the medium in a unit volume or by the boundary on a unit area around the point z' into a unit solid angle around the direction $\hat{\mathbf{s}}$ at the time t multiplied by 4π to the energy emitted from point z on the boundary or in the medium. It is like a temporal response function of an instantaneous pulse with unit energy, and the detailed definition of the DRESOR value can be referred to Refs. [17,23,24,27].

From Eq. (5), it is obvious that, for the given distributions of scattering and absorbing coefficients, once all the DRESOR values $R_d^s(z_w,z',\hat{\mathbf{s}},t)$ are known, the spatial and temporal distribution of the radiative intensity, $I(z,\hat{\mathbf{s}},t)$, with high directional resolution at any point in the medium can be expressed as a function of the incident intensity at the boundary I_{ow}.

2.2 Calculation of the DRESOR Values for Anisotropic Scattering Media. For the calculation of the DRESOR values, the assumed incident radiation is an infinitesimal (a Dirac delta) pulse with zero temporal width in this study, i.e., all the bundles are emitted at the same time. The Heaviside unit step function as the transient input at the boundary $z_w=0$. The incident energy bundles start their travel with the initially normalized energy $E_0=1$ for each bundle. The tracking procedure for every bundle is based on the path-length method following the general procedure of radiation energy absorption distributions (READ) method, a MCM [17,23,24]. The calculation of the transient DRESOR values for the anisotropic scattering media will be discussed below.

All the DRESOR values are set to zero at the beginning of the calculation. Once ΔR_d^s, an update for a DRESOR value, is obtained, R_d^s can be renewed by

$$R_{d,\text{new}}^s=R_{d,\text{old}}^s+\Delta R_d^s \quad (6)$$

$\Delta R_d^s(z_w,j_z,\theta_i,t)$ can be calculated for an anisotropic scattering medium by

$$\Delta R_d^s(z_w,j_z,\theta_i,t)=C_0\frac{E_0}{N_0}\{1-\exp[-s\sigma_s(j_z)]\}\Phi(\theta_{i'},\theta_i) \quad (7)$$

where N_0 is the total number of the energy bundles, z_w refers to the initial position, j_z the position being passed, and s the travel distance in the j_z element being passed. $\Phi(\theta_{i'},\theta_i)$ is the scattering phase function. The phase function for linear anisotropic scattering has the form of [26]

$$\Phi(\theta_{i'},\theta_i)=1+a\cos\theta_{i'}\cos\theta_i \quad (8)$$

Positive and negative values of the coefficient a ($a\leq 1$) correspond to forward scattering and backward scattering media, respectively. It is stated that in the DRESOR method, it is not difficult to deal with different scattering phase functions, for example, the truncated Legendre polynomials for the scattering phase function were used previously in Ref. [23]. $\theta_{i'}$ denotes the incident polar angle direction and θ_i the scattering direction. Since the problem is restricted to one-dimensional radiative transfer, the phase function does not depend on angle φ, i.e., it has azimuthal symmetry.

It is noted that the calculation for Eq. (7) is repeated for the total M scattering directions, which means M can be taken arbitrarily, for example, as 100, 1000, or even 10,000, and determines the directional resolution of the present method. $\Delta R_d^s(z_w,j_z,\theta_i,t)$ is calculated for M times in the M "possible" scattering directions. After that, only one actual direction is taken for tracking the flight of the energy bundle, and there is no need to continue tracking the energy bundle in all M scattering directions. Therefore, the increase in number of discrete directions only results in an increase in the executing time for Eq. (7), but does not sharply increase the computation time for tracking the energy bundles. Compared with other methods, such as DOM, if the same directional and spatial resolutions are required for the intensity, the DRESOR method may be efficient in the computational time. Actually, it is doubt that if DOM can provide intensity with such directional resolution

Table 1 The boundary conditions, the radiative property, and different collimated incident serial pulses for test problems

Case	Linear coefficient in scattering phase function a	Scattering albedo ω	Reflectivity of boundary 2 ρ	Optical thickness τ	Serial pulse
A1	0	0.5	0	1.0	Single Gaussian
A2	0	0.5	0	1.0	Continuous square
B1	0	0.9	0	1.0	Periodic square
B2	0	0.9	1.0	1.0	Periodic square
B3	0	0.9	0	1.0	Periodic Gaussian
B4	0	0.9	1.0	1.0	Periodic Gaussian
C1	0	0.05	0	1.0	Periodic Gaussian
C2	0	0.35	0	1.0	Periodic Gaussian
C3	0	0.70	0	1.0	Periodic Gaussian
C4	0	0.95	0	1.0	Periodic Gaussian
D1	0	0.9	0	0.1	Periodic Gaussian
D2	0	0.9	0	1.0	Periodic Gaussian
D3	0	0.9	0	5.0	Periodic Gaussian
D4	0	0.9	0	10.0	Periodic Gaussian
E1	0	0.9	0	1.0	Periodic Gaussian
E2	0.9	0.9	0	1.0	Periodic Gaussian
E3	−0.9	0.9	0	1.0	Periodic Gaussian

in this paper. This is an attractive feature of the method. The calculation method for tracking the flight of energy bundles in an anisotropic scattering medium in detail can be referred to Ref. [27], which dealt with a steady state radiative transfer problem.

During the bundle tracing, regardless whether the bundle travels along a straight line or it changes its direction due to scattering, the DRESOR value for the passed element should be updated by Eqs. (6) and (7). The residual energy of the bundle is reduced due to absorption,

$$E_{0,\text{new}} = E_{0,\text{old}} \exp[-s\kappa(j_z)] \tag{9}$$

The bundle's tracing will be over when the residual energy becomes small enough, such as 10^{-5}.

For the calculation of $\Delta R_d^s(z_w, j_z, \theta_i, t)$ by the MCM, the statistical errors should be maintained at a relatively lower level, such as below 1%, for a reasonable balance between the accuracy and the computation time. For the isotropic scattering case, which is independent of direction, $R_d^s(z_w, j_z, \theta_i, t)$ reduces to $R_d^s(z_w, j_z, t)$.

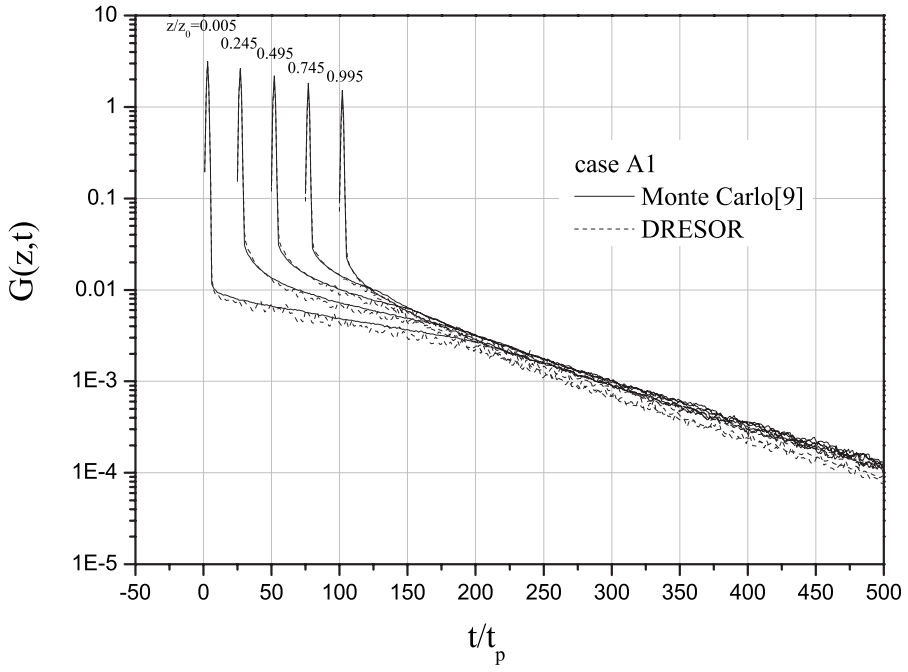

Fig. 2 Validation by comparison of the transient incident radiation obtained by the DRESOR method and MCM for Case A1

Table 2 Test of the number bundles needed in a unit time step for Case A2

No. of energy bundles	Computation time (s) For DRESOR values	Total	G (z/z_0=0.005, t/t_p=300) DRESOR	MC	IE
10,000	0.781	186.312	1.21183		
50,000	3.513	187.891	1.21154		
100,000	7.281	194.141	1.21162	1.21273	1.2143
500,000	34.91	221.209	1.21165		
1,000,000	67.23	255.187	1.21167		

Table 3 The width and shape for three kinds of serial pulse

Serial pulse	t_p (ps) τ=0.1	τ=1.0	τ=10.0	Pulse width	Interval	Duration t
Continuous square	3.336	33.36	333.6	t_p	0	∞
Periodic Gaussian	3.336	33.36	333.6	$50t_p$	$45t_p$	∞
Periodic square	3.336	33.36	333.6	$50t_p$	$49t_p$	∞

2.3 Validation for Single Incident Pulse Case. Tan and Hsu [6], Hsu [9], Zhou and Cheng [17], and Sakami et al. [28] studied boundary incidence problem with a single pulse in an isotropic scattering medium, where two boundaries were kept at black and cold and medium properties were σ_s=0.5 m^{-1}, β=1.0 m^{-1}, and $\tau=\beta z_0$=1.0. System geometry is shown in Fig. 1. The medium is uniformly divided into N elements numbered by j_z, where $j_z=1,2,\ldots,N$. The optical coordinate for the j_zth element is $\tau_j=(j_z-0.5)\tau/N$. The range of polar angle θ in $[0,\pi]$ is uniformly divided into M parts, $\theta_i=i\pi/M$, $i=0,1,2,\ldots,M$. After solving for the intensity in all directions at every time step and location, the time-resolved transmittance $T(z,t)$ at boundary 2 ($z=z_0$), reflectance $R(z,t)$ at boundary 1 (z=0), and incident radiation $G(z,t)$ can be computed by

$$T(z_0,t)=2\pi\int_0^1 I(z_0,\mu,t)\mu d\mu \tag{10}$$

$$R(0,t)=2\pi\int_{-1}^0 I(0,\mu,t)\mu d\mu \tag{11}$$

$$G(z,t)=2\pi\int_{-1}^1 I(z,\mu,t)d\mu \tag{12}$$

In Ref. [17], two cases were studied to validate the transient DRESOR method, where there was diffuse emission at Boundary 1 and with or without reflection at Boundary 2, as shown in Fig. 1, respectively. In order to further verify the DRESOR method developed in this study, the result of Case A1 with a single Gaussian incident pulse (see definition in Table 1) solved by the DRESOR method was compared with that by the MCM. The temporal distribution of incident radiation at different locations for Case A1 is plotted in Fig. 2. It can be seen that the results by the DRESOR method and the MCM agree very well. The results demonstrate the dominant effect of pulse shape on the time response right after the pulse, and a series of slopes following the passed pulse is observed in the transient response curves.

A rigorous test of the number bundles needed in a unit time step for Case A2 with collimated constant emission is shown in Table 2. It was determined that 100,000 energy bundles in a unit time step is the best compromise between the accuracy and computational time requirements. All calculations were conducted on an Intel Celeron 2.4 GHz PC with the total time step t/t_p=500. When the energy bundle number was chosen as 100,000, the typical execution time was about 7.281 s for calculation of the DRESOR values. The total execution time was about 194.141 s to compute the intensity, incident radiation, and heat flux including the DRESOR values at the location z/z_0=0.005. It should be noted that incident radiation G (z/z_0=0.005, t/t_p=300) in Table 2 was calculated by integration of the radiative intensity over 180 directions. It is not necessary to calculate DRESOR values again when computing the intensities at other locations; thus, the computation time is considerably acceptable. That is one of the characteristics for the DRESOR method.

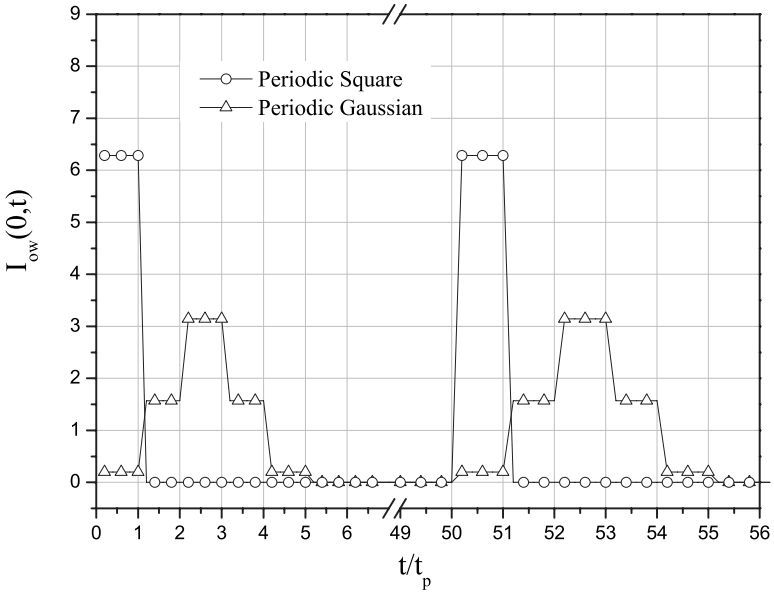

Fig. 3 The intensity distributions of collimated incident serial pulse for periodic Gaussian and square

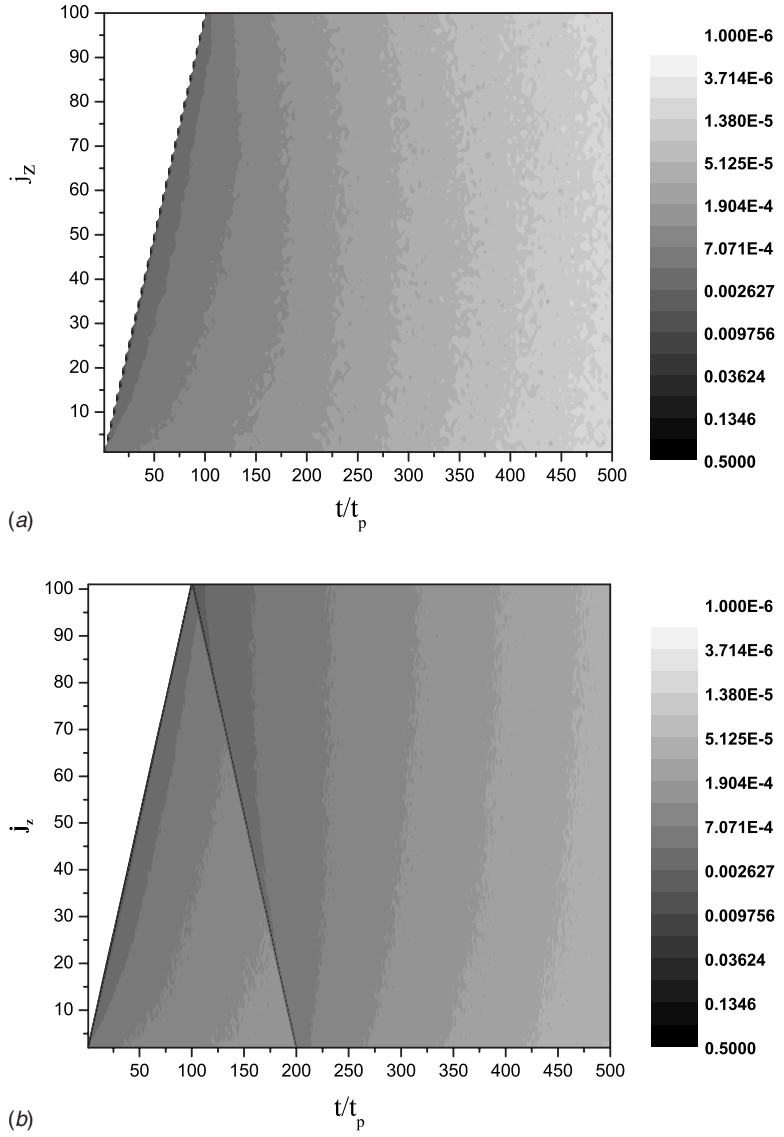

Fig. 4 DRESOR values for Cases B1 (*a*) and B2 (*b*)

3 Calculation for Serial Pulse

Different kinds of serial pulses with various pulse widths and shapes were considered in this paper, as shown in Table 3. Functions of the different kinds of serial pulse, such as continuous square, periodic Gaussian, and periodic square, are, respectively, defined as follows:

$$I_{ow1}(0,\mu,t) = 2\pi I_0 \delta(\mu - 1), \quad nT_1 < t \le nT_1 + t_p, \quad T_1 = t_p \tag{13}$$

$$I_{ow2}(0,\mu,t) = \begin{cases} \pi I_0 \delta(\mu - 1)\exp\left[-\ln 2\left(\dfrac{t}{t_p} - 2.5\right)^2\right], & nT_2 < t \le nT_2 + 5t_p, \\ 0, & nT_2 + 5t_p < t \le (n+1)T_2, \end{cases} \qquad T_2 = 50t_p \tag{14}$$

$$I_{ow3}(0,\mu,t) = \begin{cases} 2\pi I_0 \delta(\mu - 1), & nT_3 < t \le nT_3 + t_p, \\ 0, & nT_3 + t_p < t \le (n+1)T_3, \end{cases} \qquad T_3 = 50t_p \tag{15}$$

where $n = 0, 1, 2, \ldots, \infty$, it means that the duration is infinity for the three incident serial pulses. The interval in Table 3 denotes the time between two incident pulses. I_0 is the normalized collimated incident intensity, which is equal to 1. In order to compare, equal amount of energy is emitted for a single Gaussian and a single square pulse during their different temporal widths. Therefore, the

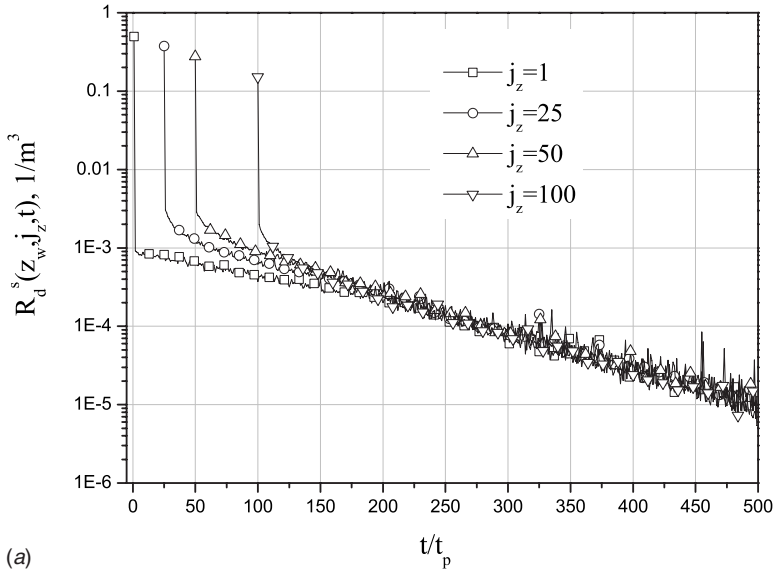

(*a*)

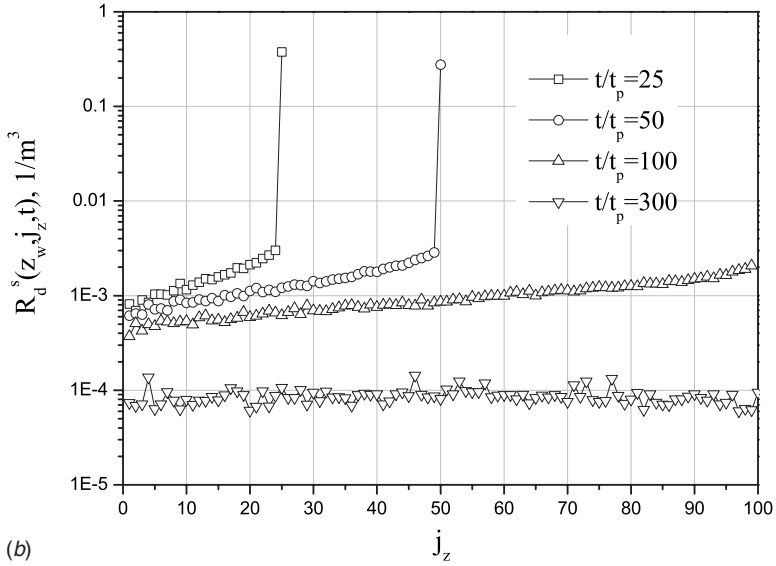

(*b*)

Fig. 5 DRESOR distributions for Case B1 at different locations (*a*) and different times (*b*)

height of the square pulse is taller than that of the Gaussian pulse, since the same amount of radiative energy is deposited in a shorter time interval, t_p versus $5t_p$. The collimated incident serial-pulse intensity distributions for periodic Gaussian, periodic square from $t=0$ to $56t_p$ are shown in Fig. 3, respectively. In Fig. 3, a distorted five-step shape was used to simulate the Gaussian profile, as used in Ref. [9].

3.1 DRESOR Values. The DRESOR values are most important in the DRESOR method, which will be explained here. Figures 4(*a*) and 4(*b*) show the DRESOR values for the discrete volume elements at different time steps for Cases B1 and B2, respectively. They display the energy distribution scattered by the discrete volume elements at different time steps for collimated radiation with initial energy $E_0=1$. There is a similar triangle zone with zero DRESOR value in the two cases, which means the bundles have not arrived at these zones before certain time steps. The effect of boundary reflection to the DRESOR values is clearly observed in an evident line in Fig. 4(*b*), which records the bundles (or wave front) reflected by Boundary 2 traveling back into the medium at different locations and times.

The DRESOR values at locations $j_z \geq 1$, 25, 50, and 100 for Case B1 are plotted in Fig. 5(*a*). It shows that the transient pulse sequentially strikes the locations $j_z=1$, 25, 50, and 100 at and after times $t/t_p \geq 1$, 25, 50, and 100, respectively, during the propagation of the radiation. After the pulse passes through a location, there is continuous scattering radiation energy contributed to the location due to the scattering from the surrounding medium. However, the collimated radiation incidence into the medium with $\theta=0$ deg has much less chance to be scattered into other directions than the diffuse incident radiation. Thus, the scattered energy of transient pulse sharply decreases after the collimated irradiation arrives at locations and more radiation directly penetrates the medium along the incident direction. Due to the increased attenuation by the absorption of medium, the DRESOR values for all locations decrease close to zero at large time steps. The DRESOR values at different time steps $t/t_p=25$, 50, 100, and 300 for Case B1 are shown in Fig. 5(*b*). It can be seen that at time steps $t/t_p=25$ and 50, there are nonzero DRESOR values among the regions $j_z \leq 25$ and $j_z \leq 50$, respectively. At time step $t/t_p=100$, the pulse has propagated through the whole medium, and the

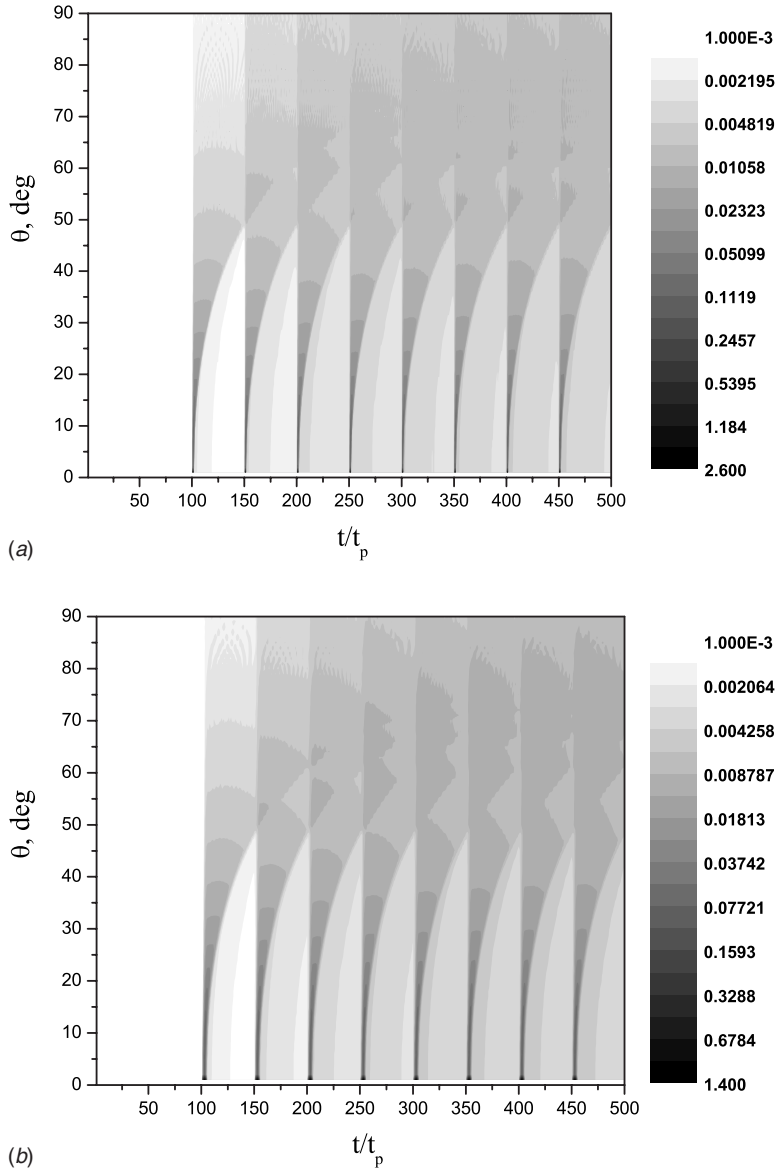

Fig. 6 The transient intensity distributions in all directions within [0 deg, 90 deg) at boundary 2 ($z=z_0$) for Cases B1 (*a*) and B3 (*b*)

DRESOR values have nonzero values at all locations in the medium. At time step $t/t_p=300$, the DRESOR values sharply decrease due to attenuation by the medium.

In the DRESOR method, by calculating the time-dependent DRESOR values for a unit short-pulse radiation incident into a scattering media, the solution of intensity can be determined by integrating DRESOR values for a series of incident pulses with different shapes and widths in Eq. (5). So there is no difficulty for solving the transient radiative transfer with different incident pulse shapes and widths, even in the anisotropic scattering medium.

DRESOR values are dominated by the directional feature of the pulse, the radiative property and geometry of the medium, and the boundary conditions, but have nothing to do with the strength, the shape, and the width of the incident pulse. Thus, the DRESOR values in Cases B1 and B3 are identical, and those in Cases B2 and B4 with the reflective boundary are also equal.

3.2 Effect of Serial-Pulse Width. The transient radiative intensity distributions in all directions within [0 deg, 90 deg) at Boundary 2 ($z=z_0$) for Cases B1 and B3 are shown in Figs. 6(*a*) and 6(*b*), respectively. The temporal radiative intensity caused by the collimated incident serial pulse comes from the overlapped temporal responses of the different pulses, it changes periodically, and the width of the pulse does not change during the transmission in the scattering media. As shown in Figs. 6(*a*) and 6(*b*), it takes $t/t_p=100$ time steps for the first pulse front to reach Boundary 2 from the incident source, and at large time steps, the transient intensity at every direction reaches a special periodic profile with the same period time as that for the incident pulse, and a distinct, repeatable shape. The discrimination of pulse width for different serial pulses can also be observed from the two figures, for example, the temporal response width of Gaussian pulse $5t_p$ and square pulse t_p can be identified in the curves. The maximum intensities in Fig. 6(*a*) are larger than those in Fig. 6(*b*), since the same amount of energy is emitted during a pulse width, and the square pulse width is shorter than the Gaussian width.

Figures 7(*a*) and 7(*b*) show the temporal radiative intensity at Boundary 2 with $\theta=0$ deg, 1 deg, 5 deg, 15 deg, 30 deg, and 45 deg for Case B1 with collimated periodic square serial-pulse incidence and with $\theta=0$ deg, 1 deg, 10 deg, 20 deg, 40 deg, and

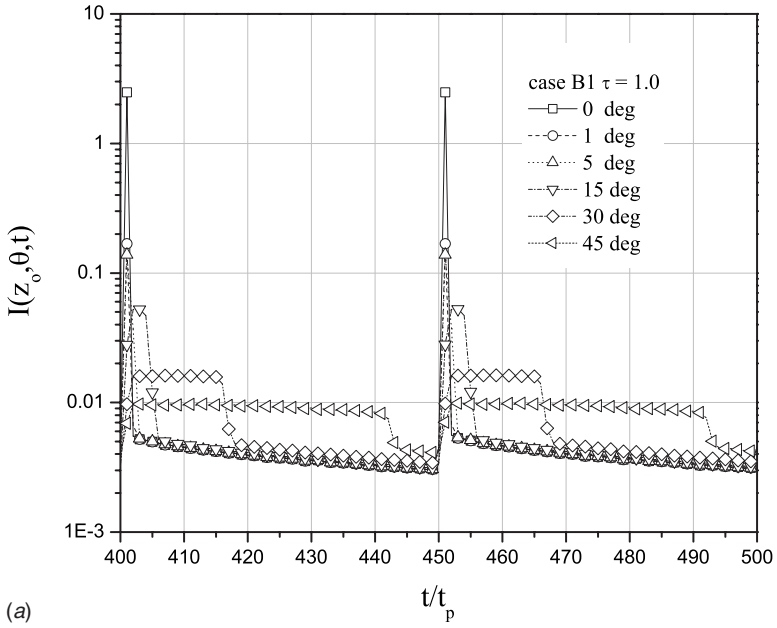

(*a*)

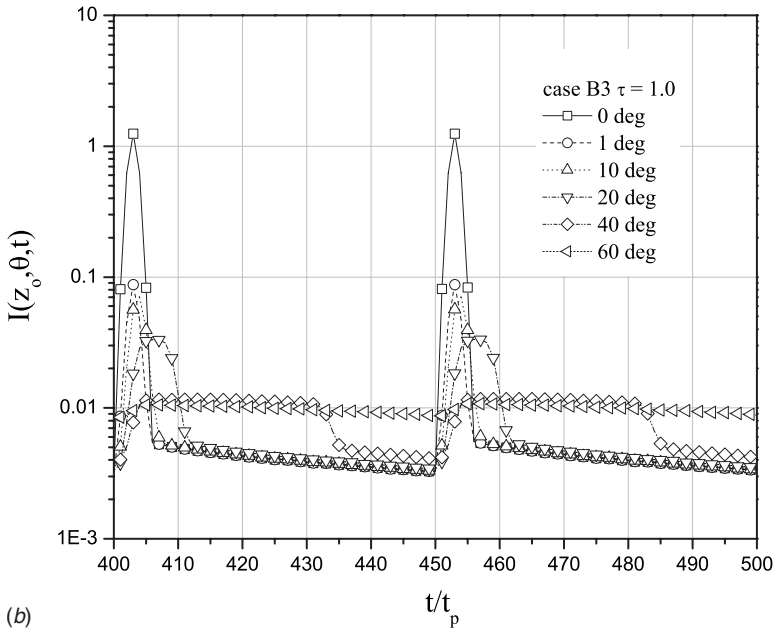

(*b*)

Fig. 7 The temporal radiative intensity at Boundary 2 with θ=0 deg, 1 deg, 5 deg, 15 deg, 30 deg, and 45 deg for Case B1 with collimated periodic square serial-pulse incidence (*a*), with θ=0 deg, 1 deg, 10 deg, 20 deg, 40 deg, and 60 deg for Case B3 with collimated periodic Gaussian serial-pulse incidence (*b*)

60 deg for Case B3 with collimated periodic Gaussian serial-pulse incidence, respectively. From the two figures, it can be seen that the intensity along θ=0 deg is obviously larger than those along the other directions. The profiles of the temporal intensity for the two different types of incident pulse with the same energy are identical in the same directions during the time interval between the adjacent pulses, as shown in Figs. 7(*a*) and 7(*b*), due to the overlapped scattering for a series of incident pulses. The results reveal that the shape of pulse has a little effect on the extended temporal spread of intensity. For periodic square serial-pulse incidence when $\theta > 5$ deg, the response widths of the pulse in those directions are obviously broaden in Fig. 7(*a*). For the collimated periodic Gaussian serial-pulse incidence in Fig. 7(*b*), when $\theta > 10$ deg, the response widths of the pulse are larger than $5t_p$, and when θ=60 deg, the response width for incident pulse even is so broadened out that it continues into the next pulse.

3.3 Effect of Boundary Reflectivity. The effect of boundary reflectivity on the transient radiative transfer with serial pulse as incident radiation is examined. The temporal reflectance at Boundary 1 for Cases B2 and B4 with specular reflection at Boundary 2 compared with those for Cases B1 and B3 are shown in Fig. 8. For Cases B1 and B3, due to the backward scattering of medium, the reflectance continuously increases to approach a periodic profile. For Cases B2 and B4 with specular reflection at Boundary 2, the reflectance is the same as those for Cases B1 and

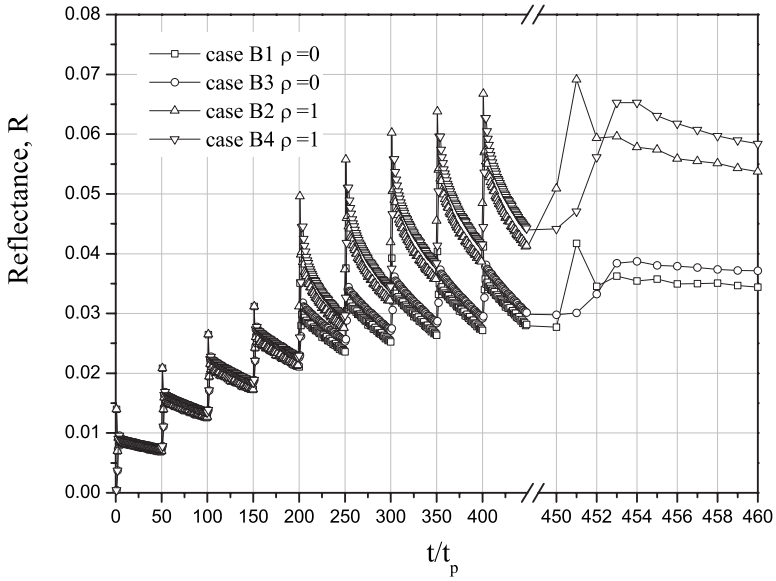

Fig. 8 The temporal reflectance at Boundary 1 for Cases B2 and B4 with specular reflection of Boundary 2 compared with those for Cases B1 and B3

B3 when $t/t_p < 200$. When $t/t_p \geq 200$, the reflectance continues to rise evidently due to the reflectivity of Boundary 2. However, at large time steps, the reflectance in Cases B2 and B4 would also approach a periodic profile, which is higher than those for Cases B1 and B3.

Figure 9 shows the comparison for temporal intensity in directions $\theta = 180$ deg and 179 deg at Boundary 2 with and without reflection with collimated periodicGaussian serial-pulse incidence. From Fig. 9, it can be observed that the intensity in directions $\theta = 180$ deg and 179 deg with reflection at boundary 2 ($\rho = 1$) are larger than those without reflection at Boundary 2 ($\rho = 0$). However, on the same condition at Boundary 2 the intensity in $\theta = 180$ deg and 179 deg is the same csince the intensity along (90 deg, 180 deg] comes from the isotropic scattering of collimated incidence.

3.4 Effect of Scattering Albedo. The effect of different scattering albedos on the transmittance at Boundary 2 for collimated incident serial pulse is shown in Fig. 10. As scattering albedo increases while the attenuation coefficient remains constant, $\kappa + \sigma_s = 1.0\ \mathrm{m}^{-1}$, less energy is absorbed during the pulse propagation, resulting in an obvious increase in transmittance within a period of pulse, and a slight increase in the peak. It can be seen

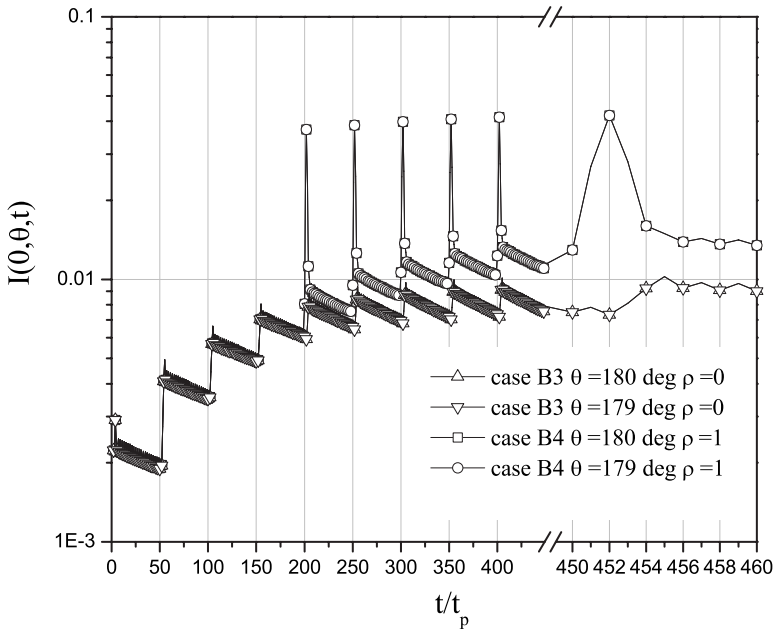

Fig. 9 The temporal intensity distributions along directions $\theta = 180$ deg and 179 deg at Boundary 1 for Cases B3 and B4

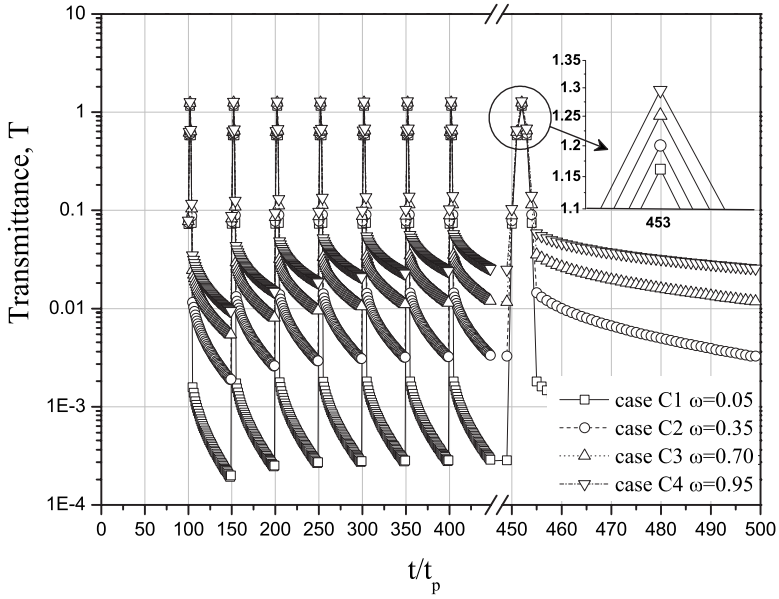

Fig. 10 The temporal transmittance at Boundary 2 for collimated periodic Gaussian incident serial pulse with different scattering albedos

that at large time steps, such as $t/t_p \geq 300$, the temporal output transmittance does not increase anymore and almost reach a periodic profile with different levels as the scattering albedo changes.

Figure 11 depicts the temporal radiative intensity along $\theta = 0$ deg and 1 deg at Boundary 2 with $\omega = 0.05$ and 0.95. It can be seen that when scattering albedo increases, the intensity in all directions increases. The temporal radiative intensity along $\theta = 0$ deg is larger than that along $\theta = 1$ deg in the peak response of serial pulse for both $\omega = 0.05$ and 0.95. However, during the extended temporal spread time, the temporal radiative intensity along $\theta = 0$ deg and 1 deg is the same. This again indicates that the pulse shape has a little effect on the in-between pulse response, but the multiple scattering of the medium has the dominant effect.

3.5 Effect of Optical Thickness. The influence of different optical thicknesses on the temporal transmittance at Boundary 2 for Cases D1, D2, D3, and D4 with $\tau = 0.1$, 1.0, 5.0, and 10.0, respectively, is shown in Fig. 12. When optical thickness increases, the peak response of transmittance decreases due to the increasing attenuation of medium. However, when optical thickness increases from $\tau = 0.1$ to $\tau = 1.0$, the extended temporal spread of transmittance also increases due to the increased scattering. When optical thickness continues to increase, the attenuation also increases. Therefore, at $\tau = 5.0$ and 10.0, the extended temporal spread of transmittance decreases. So there exists the largest extended temporal spread of transmittance for a certain optical thickness due to the different effects of scattering in conjunction

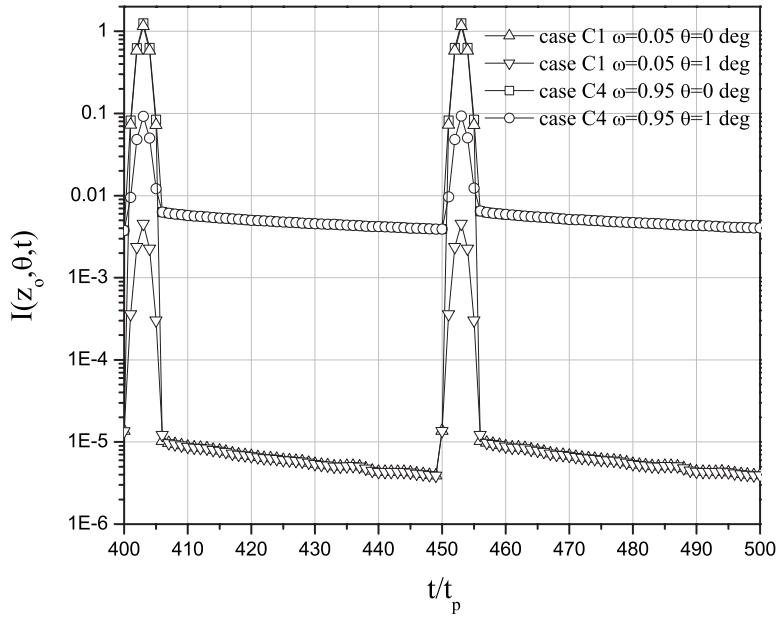

Fig. 11 The temporal radiative intensity along directions $\theta = 0$ deg and 1 deg at Boundary 2 with $\omega = 0.05$ and 0.95

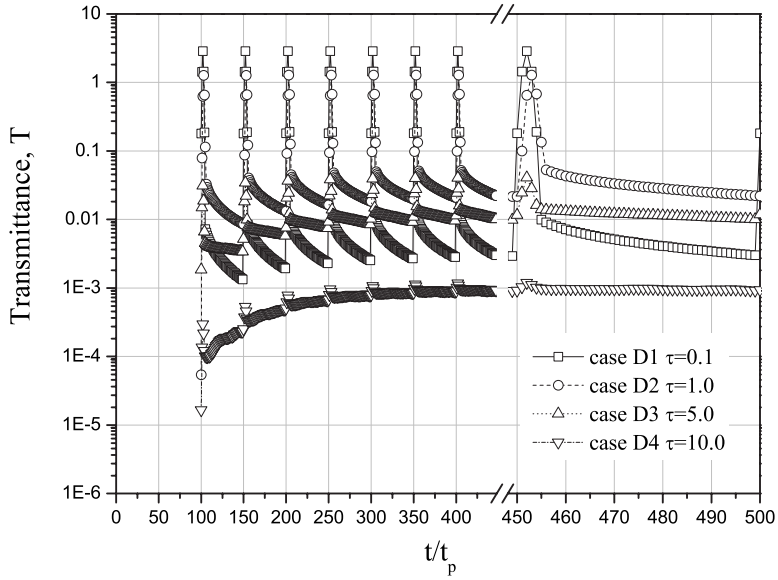

Fig. 12 The temporal transmittance at Boundary 2 for Cases D1, D2, D3, and D4 with different optical thicknesses

with optical thickness. Figure 13 testifies that when $2.4<\tau<2.6$, the largest extended temporal spread of transmittance appears. From Figure 12 it can also be seen that the peak of pulse could not be recognized in the medium with $\tau=10$ and $\omega=0.9$, since the attenuated pulse is masked by the multiple scattering.

The temporal radiative intensity along $\theta=0$ deg, 1 deg, 10 deg, 20 deg, 40 deg, and 60 deg at Boundary 2 for Case D1 with $\tau=0.1$ is shown in Fig. 14. The intensity in directions $\theta=0$ deg, 1 deg, 10 deg, 20 deg, 40 deg, and 60 deg with $\tau=0.1$ is smaller than those in Fig. 7(*b*) with $\tau=1.0$, because of medium with thinner optical thickness having smaller scattering ability. However, the intensity along $\theta=0$ deg with $\tau=0.1$ is larger than that in Fig. 7(*b*) with $\tau=1.0$ due to smaller attenuation by the medium. It also can be seen that only when $\theta<10$ deg the response width is almost equal to the incident serial pulse. When $\theta>10$ deg, the response width for incident pulse is broadened. When $\theta>60$ deg, the response width for the incident pulse cannot be recognized.

The temporal incident radiation distributions at five different locations with large optical thickness $\tau=10$ are shown in Fig. 15. It can be seen that as the optical thickness increases, the attenuation increases and the incident radiation decreases. During the whole radiative transfer process, the temporal incident radiation curves also vary periodically with the incident serial pulse. Nevertheless, at large optical thickness, the effect of incident pulse shape on the incident radiation weakens, and the peak of the incident radiation tends to disappear.

3.6 Effect of Anisotropic Scattering. Figures 16(*a*) and 16(*b*) show the temporal radiative intensity along $\theta=0$ deg, 1 deg, 10 deg, 20 deg, and 30 deg at Boundary 2 in the forward scattering medium with $a=0.9$ for Case E2 and in the backward scattering medium with $a=-0.9$ for Case E3, respectively. Compared

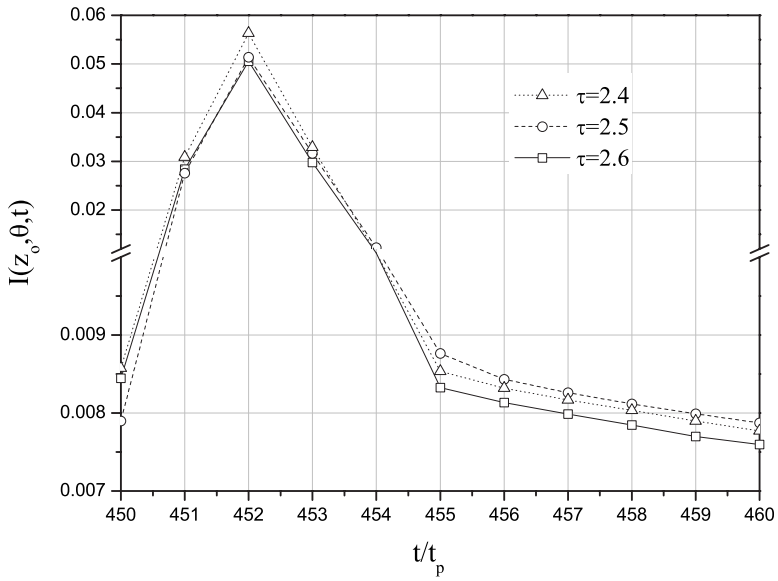

Fig. 13 The largest extended temporal spread of transmittance appearing when $2.4<\tau<2.6$

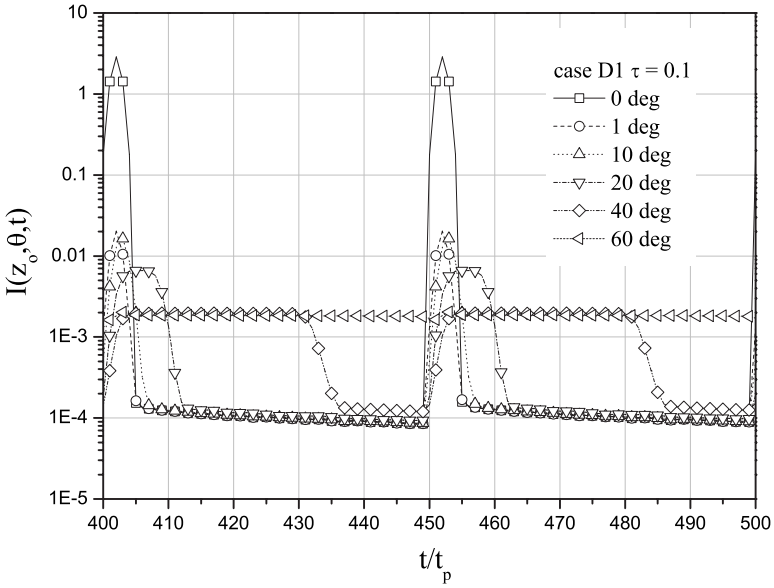

Fig. 14 The temporal radiative intensity along directions θ=0 deg, 1 deg, 10 deg, 20 deg, 40 deg, and 60 deg at Boundary 2 for Case D1 with τ=0.1

with Fig. 7(*b*), it can be seen that the scattering phase function causes significant differences on the relative intensity distributions at τ=1.0. The forward scattering evidently increase the response along directions within [0 deg, 90 deg). In the forward scattering medium with collimated radiation along the direction 0 deg, most of the energy bundles travel in the forward directions [0 deg, 90 deg), which enable the energy bundles to penetrate the layer more rapidly. On the contrary, in the backward scattering medium, the energy bundles always propagate back and forth inside the medium, leading to more energy being absorbed and less energy arriving at Boundary 2, so the temporal responses for radiative intensity are smallest along all directions within [0 deg, 90 deg).

Figure 17 shows the temporal transmittance at Boundary 2 with ω=0.9, τ=1.0 for Cases E1, E2, and E3 with three different scattering phase functions, respectively. It can be seen that forward scattering makes obviously larger temporal transmittance than those by the isotropic and backward scattering media, and the temporal transmittance is smallest in the backward scattering medium. The shape and width of the transient incident radiation do not change in the three scattering functions.

4 Concluding Remarks

The time-dependent DRESOR method was utilized to solve transient radiative transfer in a one-dimensional slab filled with an absorbing, scattering, and nonemitting medium and exposed to

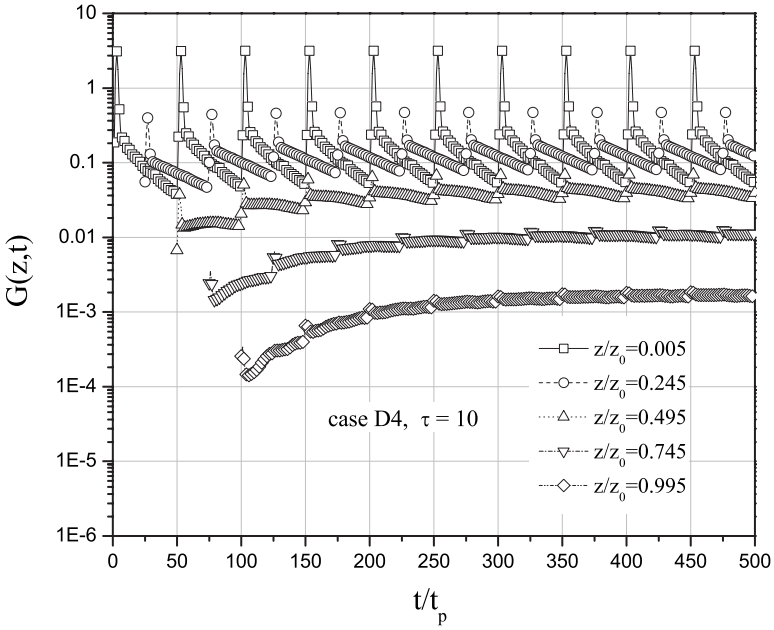

Fig. 15 The transient incident radiation distributions $G(z,t)$ at different locations for Case D4 with optical thickness τ=10

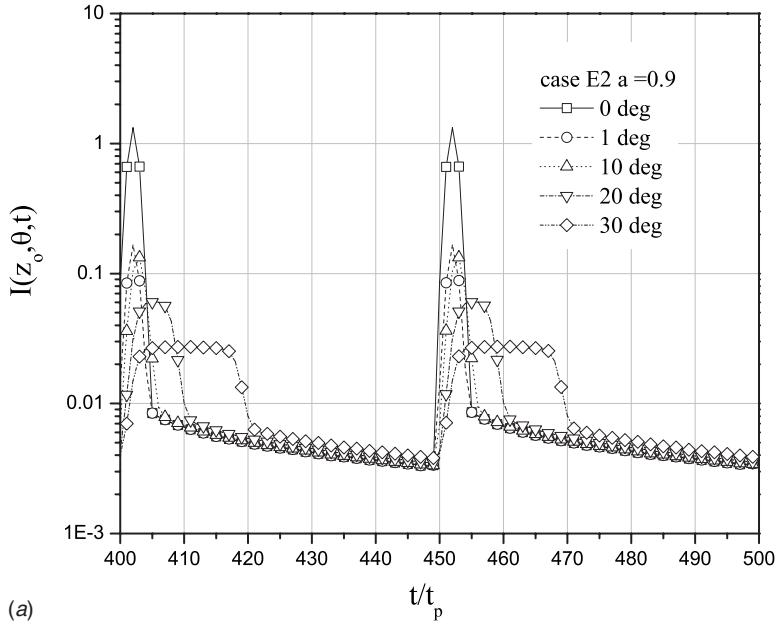

(*a*)

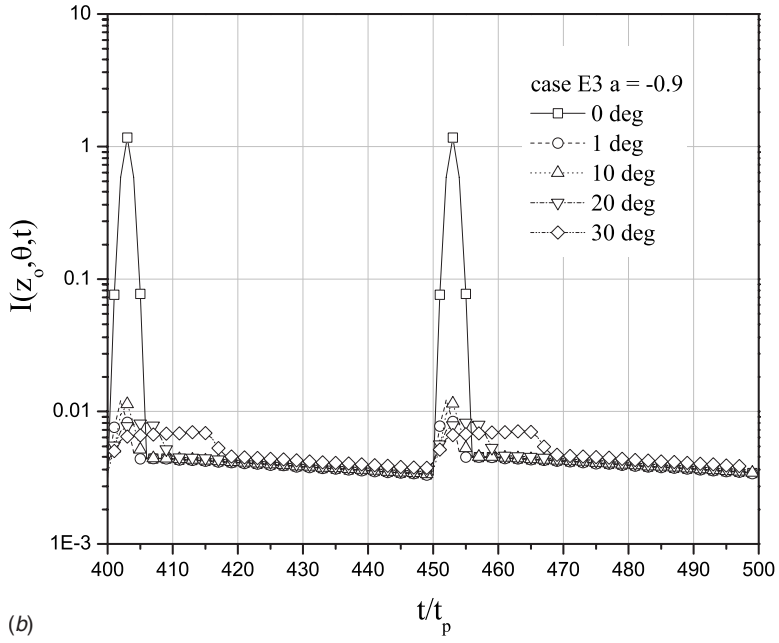

(*b*)

Fig. 16 The temporal radiative intensity along θ=0 deg, 1 deg, 10 deg, 20 deg, and 30 deg at Boundary 2 in the forward scattering medium with *a*=0.9 for Case E2 (*a*), and in the backward scattering medium with *a* =−0.9 for Case E3 (*b*)

collimated incident serial pulse with different pulse shapes and widths. With the time-dependent DRESOR values, representing the temporal response of an instantaneous, incident pulse with unit energy and the same incident direction as that for the serial pulse proposed and calculated by the MCM, the temporal radiative intensity with fine directional resolution was obtained. To verify the time-dependent DRESOR algorithm, the transient results obtained by the DRESOR method were compared to the results with the MCMs, and good agreements were achieved.

The influences of pulse width, reflective boundary, scattering albedo, optical thickness, and anisotropic scattering on the transient radiative intensity, especially along different directions were investigated. It was shown that the pulse shape and width dominate the temporal response right after pulse; however, the multiple scattering of the medium has the dominant effect on the in-between pulse response. The temporal radiative intensity caused by collimated incident serial pulse comes from the overlapped temporal response of serial pulse, and also changes periodically. The observing angle within $\theta < 10$ deg was suggested to study the width effect of pulse on the radiative transfer. The boundary reflectivity and scattering albedo of media can evidently promote the response of the serial pulse. For the cases with smaller optical thickness, such as 1.0, the temporal curves of the incident radiation approach the shape of incident serial pulse, and the pulse width does not change during the transmission in the scattering media. However, for the cases with larger optical thickness, such as 10.0, the acutely attenuated incident radiation is masked by the

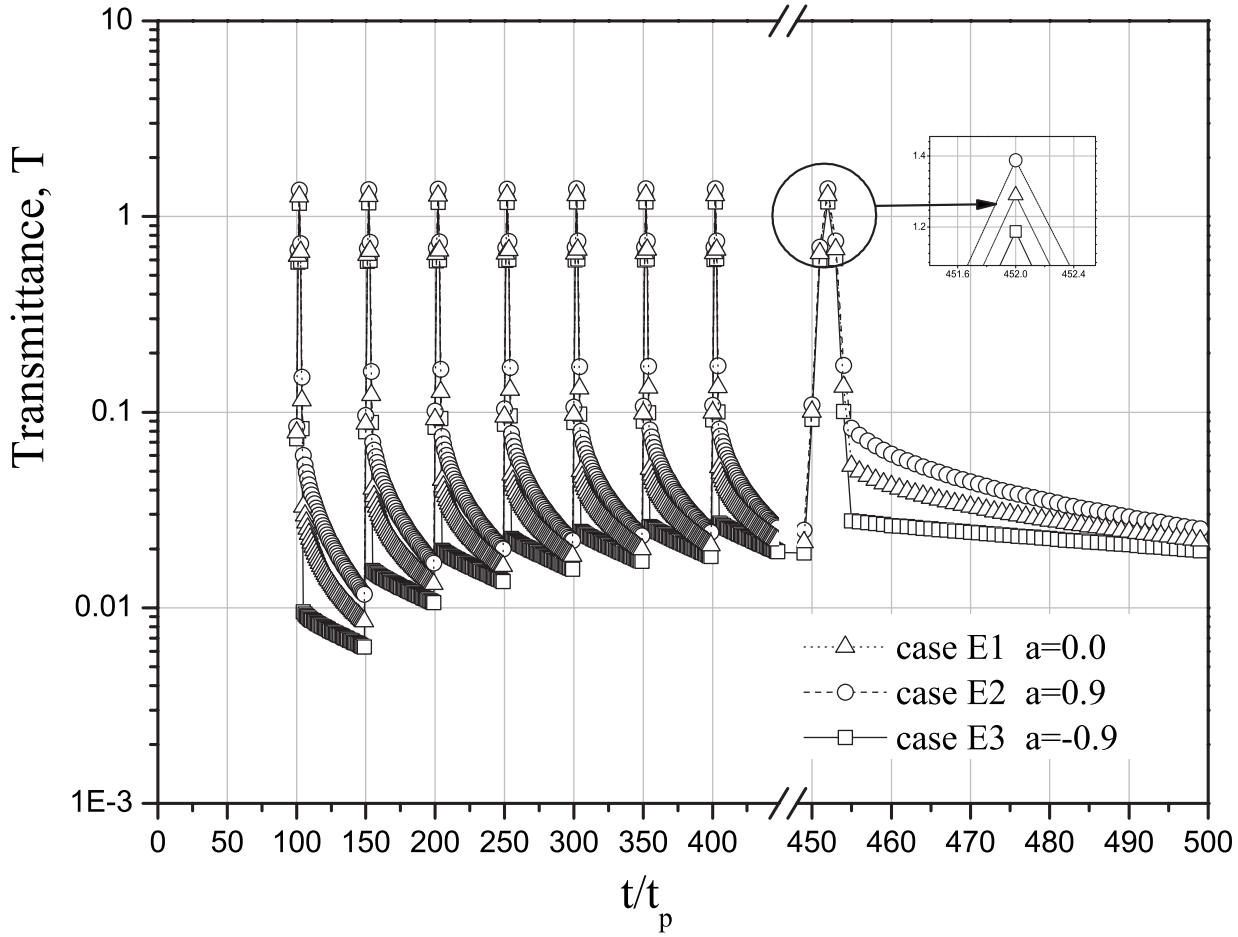

Fig. 17 The temporal transmittance distributions for Cases E1, E2, and E3 with three different scattering phase functions

multiple scattering, and its shape becomes invisible. In the linearly anisotropic scattering medium, compared with the backward scattering, the forward scattering enhances the radiative transfer across the medium and thus increases the incident radiation inside the medium.

Although the present work focused on the theoretical research, it seems especially helpful to promote the study of micromachining with serial pulse or pulse train incident radiation. One of the advantages of the DRESOR method is to provide the directional intensity with good accuracy, which is useful to develop some inverse techniques based on radiative measurements at several angles. The numerical results presented in this paper might have potential for testing other codes, such as DOM, which may suffer from numerical diffusion especially in oblique directions.

Acknowledgment

This study was supported by the National Natural Science Foundation of China (Nos. 50636010 and 50721005) and the Programme of Introducing Talents of Discipline to Universities ("111" Project No. B06019), China. The reviewers' comments on the manuscript were appreciated. Professor Pei-feng Hsu from Florida Institute of Technology helped us revise this paper when he visited Huazhong University of Science and Technology during June to July, 2007, and he was also gratefully acknowledged.

Nomenclature

A = area, m^2
c = propagation speed of the radiation inside the medium, m/s
E_0 = relative energy of energy bundles
G = incident radiation, W/m^2
I = radiative intensity, $W/(m^2\ sr)$
I_{ow} = the incident radiative intensity, $W/(m^2\ sr)$
j_z = the volume element
N = number of discrete volume elements
N_0 = number of energy bundles used in the DRESOR method
M = number of discrete polar angles
R = time-resolved reflectance
R_d^s = DRESOR values, $1/m^3$ or $1/m^2$
S = source function
s = distance, m
$\hat{\mathbf{s}}$ = direction vector
T = time-resolved transmittance
t = time of bundle traveling, s
t_p = a unit time step, s
z = location in z axis, m
z_0 = thickness of the one-dimensional layer, m
κ = absorption coefficient, m^{-1}
σ_s = scattering coefficient, m^{-1}
β = extinction coefficient, m^{-1}
θ = polar angle, rad
ω = scattering albedo
τ = optical thickness
μ = cosine of the polar angle
Ω = solid angle
Φ = scattering phase function

Subscripts

W, w = wall surface

z = axis of the rectangular coordinate system

References

[1] Trivedi, A., Basu, S., and Mitra, K., 2005, "Temporal Analysis of Reflected Optical Signals for Short Pulse Laser Interaction With Nonhomogeneous Tissue Phantoms," J. Quant. Spectrosc. Radiat. Transf., **93**, pp. 337–348.

[2] Mitra, K., and Kumar, S., 1997, HTD-Vol. 353, Proc. ASME Heat Transfer Division, Vol. 3, pp. 359–365.

[3] Longtin, J. P., and Tien, C. L., 1996, "Saturable Absorption During High-Intensity Laser Heating of Liquids," ASME J. Heat Transfer, **118**, pp. 924–930.

[4] Liu, F., Yoo, K. M., and Alfano, R. R., 1993, "Ultrafast Laser-Pulse Transmission and Imaging Through Biological Tissues," Appl. Opt., **32**(4), pp. 554–558.

[5] Mitra, K., and Kumar, S., 1993, "Development and Comparison of Models for Light Pulse Transport Through Scattering-Absorbing Media," Appl. Opt., **38**, pp. 188–196.

[6] Tan, Z. M., and Hsu, P. F., 2001, "An Integral Formulation of Transient Radiative Transfer," ASME J. Heat Transfer, **123**, pp. 466–475.

[7] Wu, C. Y., and Ou, N. R., 2002, "Differential Approximations for Transient Radiative Transfer Through a Participating Medium Exposed to Collimated Irradiation," J. Quant. Spectrosc. Radiat. Transf., **73**, pp. 111–120.

[8] Ayranci, I., and Selçuk, N., 2004, "MOL Solution of DOM for Transient Transfer in 3-D Scattering Media," J. Quant. Spectrosc. Radiat. Transf., **84**, pp. 409–422.

[9] Hsu, P. F., 2001, "Effects of Multiple Scattering and Reflective Boundary on the Transient Radiative Transfer Process," Int. J. Therm. Sci., **40**, pp. 539–549.

[10] Guo, Z. X., Aber, J., Garetz, B. A., and Kumar, S., 2002, "Monte Carlo Simulation and Experiments of Pulsed Radiative Transfer," J. Quant. Spectrosc. Radiat. Transf., **73**, pp. 159–168.

[11] Lu, X. D., and Hsu, P. F., 2005, "Reverse Monte Carlo Simulations of Light Pulse Propagation in Nonhomogeneous Media," J. Quant. Spectrosc. Radiat. Transf., **93**, pp. 349–367.

[12] Chai, J. C., 2003, "One-Dimensional Transient Radiation Heat Transfer Modeling Using a Finite-Volume Method," Numer. Heat Transfer, Part B, **44**(2), pp. 187–208.

[13] An, W., Ruan, L. M., Tan, H. P., Qi, H., and Lew, Y. M., 2007, "Finite Element Simulation for Short Pulse Light Radiative Transfer in Homogeneous and Nonhomogeneous Media," ASME J. Heat Transfer, **129**(3), pp. 353–362.

[14] Liu, L. H., and Liu, L. J., 2007, "Discontinuous Finite Element Approach for Transient Radiative Transfer Equation," ASME J. Heat Transfer, **129**(8), pp. 1069–1074.

[15] Brewster, M. Q., and Yamada, Y., 1995, "Optical Properties of Thick, Turbid Media From Picosecond Time-Resolved Light Scattering Measurement," Int. J. Heat Mass Transfer, **38**, pp. 2569–2581.

[16] Hasegawa, Y., Yamada, Y., Tamura, M., and Nomura, Y., 1991, "Monte Carlo Simulation of Light Transmission Through Living Tissues," Appl. Opt., **30**, pp. 4515–4520.

[17] Zhou, H. C., and Cheng, Q., 2006, "The DRESOR Method for the Transient Radiative Transfer in an Isotropic Scattering Gray Plane-Parallel Medium," *Proceedings of Eurotherm78—Computational Thermal Radiation in Participating Media II*, D. Lemonier, N. Selçuk, and P. Lybaert, eds., Poitiers, France, Apr. 5–7, pp. 105–114.

[18] Ilie, D., Mullan, C., Connor, G., TFlaherty, T., and Glynn, T., 2007, "Controlled Process for Polymer Micromachining Using Designed Pulse Trains of a UV Solid State Laser," Appl. Surf. Sci., **254**(4), pp. 845–849.

[19] Chowdhury, I. H., Xu, X. F., and Weiner, A. M., 2003, "Ultrafast Pulse Train Micromachining," Proc. SPIE, **4978**, pp. 138–146.

[20] Jiang, L., and Tsai, H. L., 2005, "Repeatable Nanostructures in Dielectrics by Femtosecond Laser Pulse Trains," Appl. Phys. Lett., **87**, pp. 151104–151106.

[21] Jiang, L., and Tsai, H. L., 2006, "Energy Transport and Nanostructuring of Dielectrics by Femtosecond Laser Pulse Trains," ASME J. Heat Transfer, **128**(9), pp. 926–933.

[22] Spyridaki, M., Koudoumas, E., Tzanetakis, P., Fotakis, C., Stoian, R., Rosenfeld, A., and Hertel, I. V., 2003, "Temporal Pulse Manipulation and Ion Generation in Ultrafast Laser Ablation of Silicon," Appl. Phys. Lett., **83**, pp. 1474–1476.

[23] Zhou, H. C., Chen, D. L., and Cheng, Q., 2004, "A New Way to Calculate Radiative Intensity and Solve Radiative Transfer Equation Through Using the Monte Carlo Method," J. Quant. Spectrosc. Radiat. Transf., **83**, pp. 459–481.

[24] Cheng, Q., and Zhou, H. C., 2007, "The DRESOR Method for a Collimated Irradiation on an Isotropically Scattering Layer," ASME J. Heat Transfer, **129**(5), pp. 634–645.

[25] Zhou, H. C., Lou, C., Cheng, Q., Jiang, Z. W., He, J., Huang, B. Y., Pei, Z. L., and Lu, C. X., 2005, "Experimental Investigations on Visualization of Three-Dimensional Temperature Distributions in a Large-Scale Pulverized-Coal-Fired Boiler Furnace," Proc. Combust. Inst., **30**(1), pp. 1699–1706.

[26] Modest, M. F., 2003, Radiative Heat Transfer, 2nd ed., Academic, New York.

[27] Zhou, H. C., Cheng, Q., Huang, Z. F., and He, C., 2007, "The Influence of Anisotropic Scattering on the Radiative Intensity in a Gray, Plane-Parallel Medium Calculated by the Dresor Method," J. Quant. Spectrosc. Radiat. Transf., **104**(1), pp. 99–115.

[28] Sakami, M., Mitra, K., and Hsu, P. F., 2000, "Transient Radiative Transfer in Anisotropically Scattering Media Using Monotonicity-Preserving Schemes," *Proceedings of IMECE 2000*, Orlando, FL, Nov. pp. 5–10.

Two-Phase Flow Simulation of Mist Film Cooling on Turbine Blades With Conjugate Internal Cooling

Xianchang Li[1]

Ting Wang[2]
e-mail: twang@uno.edu

Energy Conversion and Conservation Center,
University of New Orleans,
New Orleans, LA 70148-2220

Effective cooling of gas turbine combustor liners, combustor transition pieces, turbine vanes (nozzles), and blades (buckets) is a critical task to protect these components from the flue gas at extremely high temperature. Air film cooling has been successfully used to cool these hot sections for the past half century. However, the net benefits from the traditional methods seem to be incremental, but the temperature of working gas is continuously increasing to achieve high thermal efficiency. Therefore, new cooling techniques need to be developed. One of the promising techniques is to enhance film cooling with mist injection. While the previous study reported the effect of mist on the cooling effectiveness with an adiabatic wall, this paper focuses on the effect of mist injection on heat transfer of film cooling with a nonadiabatic flat wall, using the commercial computational fluid dynamics software package FLUENT. Both 2D and 3D cases are considered with a 2D slot and diffusive compound-angle holes. Modeling of the interaction of a droplet with a uniformly cooled wall as well as conjugate heat conduction inside the solid base are conducted. Different mist droplet sizes and mist concentrations are adopted. Conditions both in a gas turbine operating environment (15 atm and 1561 K) and in a laboratory environment (1 atm and 450 K) are considered. Results show that injecting 2–10% mist reduces the heat transfer coefficient and the wall temperature. Especially, mist has the prolonged effect of cooling the region downstream for 15 jet hole diameters, where conventional air film cooling is not effective. [DOI: 10.1115/1.2944247]

Keywords: film cooling, mist cooling, blade cooling, heat transfer enhancement, two-phase flow

1 Introduction

To improve the thermal efficiency of gas turbines (GTs), the turbine inlet temperature is usually elevated higher than the metal melting point. Effective cooling of GT combustor liners, combustor transition pieces, turbine vanes (nozzles), and blades (buckets) is a critical task to protect these components from the hot flue gas. Air film cooling as well as airfoil internal cooling have been successfully used in GT applications for the past half century. To make the cooling more effective, significant effort has been expended and research has been conducted. Many flow and geometric parameters affect the performance of film cooling, such as jet hole shape and coolant injection angle, blowing ratio, inlet velocity profile, turbulence intensity, and coolant-supply plenum configuration. These parameters have to be optimized to achieve good cooling performance (Brittingham and Leylek [1]; Jia et al. [2]). For example, the injection angle is mostly less than 35 deg to reduce the jet separation and flow recirculation. Studies also found that lateral or forward diffusive holes perform better than simple forward holes. A well-designed diffusive hole can mimic the performance of a slot jet (Brittingham and Leylek [1]). Turbulence intensity can either upgrade or downgrade film-cooling performance depending on the blowing ratio and flow structure (Mayhew et al. [3]). Further studies were also conducted on some specific parameters, such as the effect of surface roughness on film cooling (Rutledge et al. [4]) and the cooling of trailing edge cutback (Martini et al. [5]).

Selection and validation of turbulence modelings are vital in predicting film-cooling performance. Turbulence models adopted include V2F k-ε by Jia et al. [2], the standard k-ε model by Brittingham and Leylek [1], k-ω model by Heidmann et al. [6], and large eddy simulation (LES) by Tyagi and Acharya [7]. In general, numerical simulation can provide ideal boundary conditions but may fail to accurately predict such physical phenomena as flow separation.

Film-cooling technology has become quite mature during the past five decades. The net benefits from further improvement seem to be marginally incremental. New cooling techniques need to be developed to surpass the current limits. To this end, this paper proposes to simulate injecting water mist into the air coolant to improve the film-cooling performance. By injecting water mist into the coolant flow, each droplet acts as a heat sink. Droplet evaporation reduces the flow temperature near the surface and thus provides better protection for the surface. The cooling effectiveness can also be enhanced due to direct contact between the droplets and the wall. Other enhancing mechanisms include high-temperature gradient near the wall, augmented mixing by droplet-air interactions, and increased specific heat. In addition, the residence time needed for droplet evaporation postpones the cooling enhancement into the downstream region where single-phase air film cooling becomes less powerful. By taking advantage of the aforementioned heat transfer mechanisms, mist has been employed in GT inlet air fog cooling (Chaker et al. [8]), overspray cooling through wet compression (Petr [9]), and airfoil internal cooling (Guo et al. [10]).

[1]Present address: Lamar University, TX.
[2]Corresponding author.

Contributed by the Heat Transfer Division of ASME for publication in the JOURNAL OF HEAT TRANSFER. Manuscript received July 10, 2007; final manuscript received November 28, 2007; published August 8, 2008. Review conducted by Louis C. Burmeister.

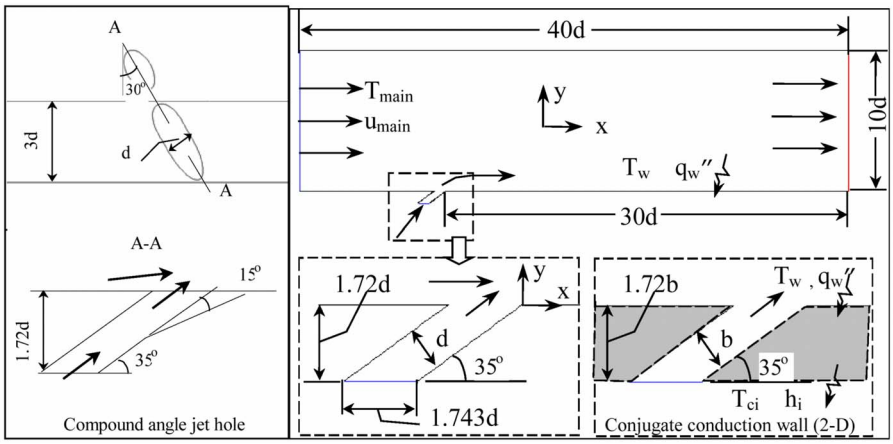

Fig. 1 Computational domain and cooling hole configurations

Li and Wang [11,12] evaluated the effect of mist injection on film cooling with numerical simulation under low temperature, velocity, and pressure. It was shown that a small amount of mist injection (2% of the coolant mass flow rate) could increase the adiabatic cooling effectiveness by about 30–50%. Further study indicated that smaller droplets and higher mist concentration result in a better enhancement. Afterward, Wang and Li [13] examined the performance of mist film cooling under GT operational conditions, featured by high pressure (15 atm), velocity (128 m/s), and temperature (1561 K). The enhancement of the adiabatic cooling effectiveness was found less attractive than the cases with low pressure, velocity, and temperature conditions. However, due to high surface temperature under GT operating conditions, the additional wall temperature reduction could achieve 60 K even though the enhancement of adiabatic cooling effectiveness is only 5%. This temperature reduction can be critical to the airfoil life expectancy of GTs.

Previous studies (Li and Wang [11–13]) reported only the effect of mist on the adiabatic cooling effectiveness. As a continuation of mist film cooling studies, this paper focuses on mist film cooling heat transfer coefficient with a nonadiabatic surface. A 2D slot and 3D diffusive compound-angle holes are considered in this study with both a uniformly cooled wall at a constant heat flux and a conjugate inner wall cooled by an internal cooling flow.

2 Numerical Model

2.1 Geometric Configurations and Physical Model. Recognizing that a diffusive compound-angle hole generally provides a good cooling performance, it was employed first in this study. Figure 1 shows the details of the diffusive compound-angle hole. The forward angle is 35 deg with an extra diffusive angle of 15 deg, and the inclination angle in the direction perpendicular to the mainstream is 30 deg. The nominal diameter (d) of the injection hole is 1 mm. The vertical height of the jet hole is $1.72d$, which gives an actual jet hole length of $3d$. The computational domain is $40d$ in the mainstream direction and $3d$ in the spanwise direction. The domain has a height of $10d$. The distance between the mainstream inlet and the coolant jet injection hole is $10d$.

To more closely simulate the real turbine airfoil cooling including both the external film and the internal channel flow cooling, a 2D slot with a slot width (b) of 4 mm is employed, as shown in Fig. 1. The slot width was chosen to be consistent with previous studies. In this conjugate cooling arrangement, the solid metal wall with a uniform thickness of $1.72d$ is included in the computational domain. Below the base wall bottom surface, an internal cooling channel flow is imposed with an internal heat transfer coefficient h_i and a coolant flow temperature T_{ci}.

There are 360,000 cells for the 3D case. An unstructured grid with tetrahedron elements is applied to the coolant passage of the compound-angle jet and a small volume in the main domain close to the jet exit. The rest of the domain is meshed to structured but nonuniform grids with hexahedron elements. Figure 2 shows the grid of the coolant passage wall as well as the cooled base surface. Finer grids are generated in the region close to the jet hole and the base wall. For the 2D slot case, a near-wall grid was adapted to examine the grid independence. Adaptation refines the grid in both streamwise and spanwise directions. The y^+ value reaches 1 in most of the areas. A detailed discussion of near-wall mesh effect on mist film cooling is referred to a previous study (Li and Wang [12]).

A feasible method to simulate film cooling with mist injection is to consider the droplets as a discrete phase since the volume fraction of the liquid is usually small (less than 1%). The trajectories of the dispersed phase (droplets) are calculated by the Lagrangian method. The impacts of the droplets on the continuous phase are considered as source terms to the governing equations of mass, momentum, energy, and species equations. Three species (oxygen, nitrogen, and water vapor) are simulated in mist film cooling flow. The standard k-ε model is used with enhanced near-wall treatment to the continuous phase (air). The governing equations as well as the turbulence model have been explained in Ref. [12] and are summarized in Table 1 without further explanation.

The droplet trajectory is traced by applying Newton's second law. The energy balance for each droplet can be given as

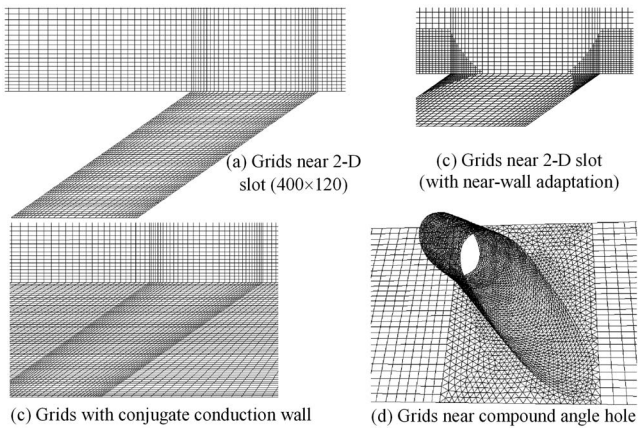

Fig. 2 Validation of numerical procedure

Table 1 Governing equations and k-ε turbulence model

$\partial/\partial x_i(\rho u_i)=S_m$	$\partial/\partial x_i(\rho u_i k)=\partial/\partial x_i[(\mu+\mu_t/\sigma_k)\partial k/\partial x_i]+G_k-\rho\varepsilon$
$\partial/\partial x_i(\rho u_i u_j)=\rho\vec{g}_j-\partial P/\partial x_j+\partial/\partial x_i(\tau_{ij}-\rho\overline{u_i' u_j'})+F_j$	$\partial/\partial x_i(\rho u_i \varepsilon)=\partial/\partial x_i[(\mu+\mu_t/\sigma_\varepsilon)\partial\varepsilon/\partial x_i]+C_{1\varepsilon}G_k\varepsilon/k-C_{2\varepsilon}\rho\varepsilon^2/k$
$\partial/\partial x_i(\rho c_p u_i T)=\partial/\partial x_i(\lambda\partial T/\partial x_i-\rho c_p\overline{u_i' T'})+\mu\Phi+S_h$	$\mu_t=\rho C_\mu k^2/\varepsilon$
$\partial/\partial x_i(\rho u_i C_j)=\partial/\partial x_i(\rho D_j\partial C_j/\partial x_i-\rho\overline{u_i' C_j'})+S_j$	$\lambda_{\text{eff}}=\lambda+c_p\mu_t/\text{Pr}_t$ $D_{\text{eff}}=D+\mu_t/\text{Sc}_t$

$$m_p c_p \frac{dT}{dt} = \pi d^2 h_d (T_\infty - T) + \frac{dm_p}{dt} h_{fg} \tag{1}$$

where h_{fg} is the latent heat. The convective heat transfer coefficient (h_d) can be obtained with an empirical correlation (Ranz and Marshall [14]). The mass change rate/vaporization rate (dm_p/dt) is governed by concentration difference between droplet surface and air stream,

$$-\frac{dm_p}{dt} = \pi d^2 k_c (C_s - C_\infty) \tag{2}$$

where k_c is the mass transfer coefficient, C_s is the vapor concentration at the droplet surface, and C_∞ is the vapor concentration of the bulk flow. When the droplet temperature reaches the boiling point, its evaporation rate will be evaluated by (Kuo [15])

$$-\frac{dm_p}{dt} = \pi d^2 \left(\frac{\lambda}{d}\right)(2.0 + 0.46\ \text{Re}_d^{0.5}) \ln(1 + c_p(T_\infty - T)/h_{fg})/c_p \tag{3}$$

where λ is the gas/air heat conductivity and c_p is its specific heat.

Stochastic method is used to consider the effect of turbulence dispersion on droplet tracking. The droplet trajectories are calculated with the instantaneous flow velocity ($\bar{u}+u'$), and the velocity fluctuations are then given as

$$u' = \varsigma(\overline{u'^2})^{0.5} = \varsigma(2k/3)^{0.5} \tag{4}$$

where ς is a normally distributed random number. This velocity will apply during the characteristic lifetime of the eddy (t_e), a time scale calculated from the turbulence kinetic energy and dissipation rate. After this time period, the instantaneous velocity will be updated with a new ς value until a full trajectory is obtained. A more detailed discussion of the stochastic method is given by Li and Wang [12], and more numerical details are given in FLUENT [16].

2.2 Boundary Conditions and Operational Parameters. To explore the physics of mist film cooling under a real GT operating environment, simulation needs to be conducted under high-pressure and high-temperature conditions, which is difficult and expensive for experimental studies. The parameters simulating the GT operating environment are listed in Table 2 (3D case). Note that these parameters represent a general condition in an F-frame type GT without trying to match the specific condition of any brand or model. Periodic boundary condition is assigned in the spanwise direction. All other walls are adiabatic and have a nonslip velocity boundary condition. The upper boundary is specified as a slip wall; i.e., the wall shear is zero (or the velocity gradient normal to the wall is zero). The slip-wall boundary condition is justified because the upper boundary ($10d$) is outside the boundary layer, which is about $2d-3d$ thick. The mean flow is in the potential core and the flow shear is negligible.

Also listed in Table 2 is another set of 2D slot flow conditions with low temperature, pressure, and velocity for typical laboratory experiments that are similar to those used in many other literatures. For the 2D conjugate cases, the solid wall is assumed to be an alloy steel with a density of 8030 kg/m^3, a heat conductivity of 16.27 W/m K, and a specific heat of 502 J/kg K. A heat transfer coefficient of h_i=20 W/m^2 K and an internal coolant flow temperature of T_{ci}=375 K are assigned to the internal cooling flow, which is located at the bottom of Fig. 1. For a convenient comparison with the 3D case, the boundary condition of a constant cooling flux is also assigned to the 2D case.

Based on the experimental results in Guo and Wang [10], uniform droplet sizes ranging from 5 μm to 20 μm are simulated. In a real condition, the droplet sizes are not uniform, and the results should be a combination of the results bounded by different uniform sizes. Mist is injected uniformly from a surface perpendicular to the jet hole axis and close to the jet inlet. The total trajectories traced are about 10,000. Two different boundary conditions of droplets at walls are simulated: "reflect" and "trap."

Table 2 Parameters used in simulation for different cases

		3D hole	2D hole	
Operational pressure	P (atm)	15	1	
	T_{main} (K)	1561	450	1561 K=2350°F
Main stream inlet	u_{main} (m/s)	128	10	Uniform
(Dry air)	Tu (%)	5	5	Turbulence intensity
	$\text{Re}_1\times10^{-6}$	1.5	0.062	1=0.2 m
	T_c (K)	644	375	644 K=700°F
Jet inlet	u_j (m/s)	106	15	Uniform
(Saturated air)	Tu (%)	1	1	Turbulence intensity
	$\text{Re}_d\times10^{-3}$	26.8	1.69	
$M=(\rho u)_c/(\rho u)_g$	M	2	1.2	
Outlet	P (atm)	15	1	Constant pressure
Uniformly cooled wall	q (W/m^2)	2×10^5	2000	Constant heat flux
Conjugate cooling wall	T_{ci} (K)	NA	375	
	h_i (W/m^2 K)		20	
Droplet size	d (μm)	5, 10, 20	5, 10, 20	Uniform
Mist concentration	m_l/m_0 (%)	10, 20	2	
Injection temperature	T_d (K)	472	373	Saturation temperature

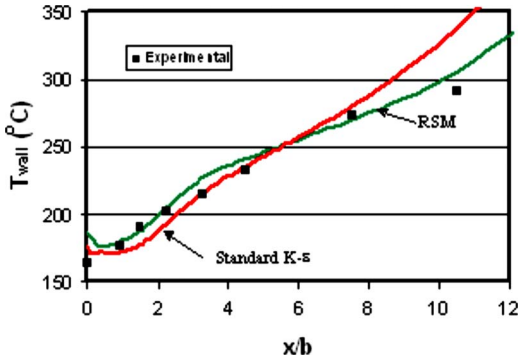

Fig. 3 Computational meshes

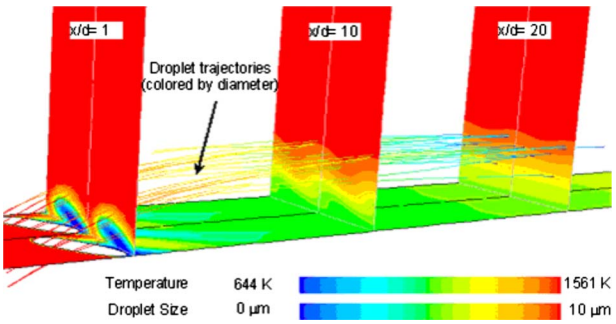

Fig. 4 Temperature field and droplet trajectories with the 3D compound-angle hole

Reflect means the droplets elastically bounce off once they reach the wall, while trap means they "adhere to the wall and evaporate completely." The real situation will be bounded by these two cases as a hybrid condition. Based on the wall temperature and droplet parameters, some droplets may stick to the wall and evaporate, while others may bounce away from the wall with partial evaporation.

2.3 Numerical Method and Model Qualification. FLUENT (v. 6.2.16), a commercial software package, is used in this study. The simulation uses the segregated solver, which employs an implicit pressure-correction scheme (FLUENT [16]). Second order upwind scheme is used for spatial discretization of the convective terms and species. Iteration proceeds alternatively between the continuous and discrete phases, and the droplet trajectories are updated every ten iterations in the continuous phase. Results are converged after the specified residuals are met. A converged result renders a mass residual of 10^{-4}, an energy residual of 10^{-6}, and momentum and turbulence kinetic energy residuals of 10^{-5}. These residuals are the summation of the imbalance for each cell, scaled by the flow rate. Typically, 1000–2000 iterations are needed to obtain a converged result, which takes 1–2 h on a 2.8 GHz Pentium 4 personal computer for 2D cases and 10–20 h for 3D cases.

The numerical procedure and methodology in this paper follow those in the studies of Refs. [11,12], in which the numerical results were qualified by comparing with the experimental data with air-only film cooling. In Ref. [12], the effect of various models on the computational results was examined. These models include the turbulence models, dispersed-phase model, different force models, trajectory tracking model, near-wall grid arrangement, and mist injection scheme. In addition, the effects of flow inlet boundary conditions, inlet turbulence intensity, and near-wall grid density on simulation results were also considered. Since there are no mist film cooling experimental data available in the public domain, the modeling of water droplets in this study is qualified by comparing the computational fluid dynamics (CFD) results with the experimental mist impingement jet data from Li et al. [17]. Figure 3 shows both the standard k-ε and Reynolds stress (RSM) turbulence models predicting well (within 5%) in comparison with the experimental results of wall temperature distribution on the target wall.

2.4 Grid Sensitivity and Uncertainty. In the 3D cases, the grid sensitivity study started from 150,000 meshes until the result of film-cooling effectiveness changed less than 1% when the mesh number was increased from 240,000 to 360,000. We felt comfortable with this result and did not continue to refine the mesh over 360,000. The uncertainty from the key factors is estimated as follows: 10% for different turbulence models, 5% for turbulence length scales, 3% for the resolution of second order central and upwind methods, 1% for convergence resolution, 3% for the effect of grid size, and 3% for the near-wall grid effect. The overall uncertainty for cooling effectiveness is estimated to be 12%. Since no experimental data in the public domain could be found to be compared with the current computational results under the simulated conditions, the above uncertainty is estimated from the computational results under low temperature and pressure conditions in Refs. [11,17]. Therefore, the estimated uncertainty is not based on the true value; rather it represents the uncertainty excursion of the results that are attributed to the computational model and scheme.

3 Results and Discussion

3.1 Baseline Case of Mist Film Cooling With the Compound-Angle Diffuse Hole. As a baseline case, Fig. 4 shows the temperature field and droplet trajectories of the 3D case with the compound-angle diffuse hole at elevated operational conditions (1561 K, 15 atm, and 128 m/s) with a blowing ratio of 2, mist concentration at 10%, and 10 μm water droplets. The jet flow does not detach from the wall but creates a cold film layer with a thickness of about one jet diameter, which blankets the wall surface quite uniformly. The film coolant flow is not shown, but the coolant-affected area can be recognized by the temperature field. The relatively uniform cold blanket with the compound-angle hole can be interpreted by the flow behavior in the cross section perpendicular to mainstream direction. As shown in Fig. 5, the compound-angle hole provides a well-organized flow close to the wall in the downstream region, which makes the coverage uniform in the spanwise direction.

The droplet trajectories are also shown in Fig. 4, and these trajectories are only a small fraction of those traced in simulation. It can be seen that rather than following the streamline, the droplets move to the top of the coolant-affected area, away from the wall and the coolant flow. As found in Wang and Li [13], this uplift droplet behavior under the elevated operating conditions downgrades the mist enhancement on film cooling. Even with this downgraded performance, water droplets still play an important role to keep the cooling surface temperature low.

The film-cooling performance is usually evaluated by the adiabatic film-cooling effectiveness, $\eta_a=(T_g-T_{aw})/(T_g-T_c)$, with the base wall being insulated. This approach provides a useful reference with a well-controlled boundary condition. However, in real applications, the cooling of airfoils is usually a conjugate heat transfer accompanied with internal airfoil cooling. Heat transfer coefficient (h) is usually reported for nonadiabatic cases. The appropriate way to determine the h-value is not straightforward. Two options can be considered: First, it is defined as

$$h_o = q''_w(x)/(T_w - T_{aw}) \tag{5}$$

This definition provides an appropriate scaling for the h-value when different wall cooling or heating fluxes are employed, but it cannot fairly show the cooling enhancement induced by mist because T_{aw} of the mist case is lower than the air-only case, so lower T_w of the mist case is not fairly reflected through the h-value. Furthermore, to calculate h_0, an additional computation needs to

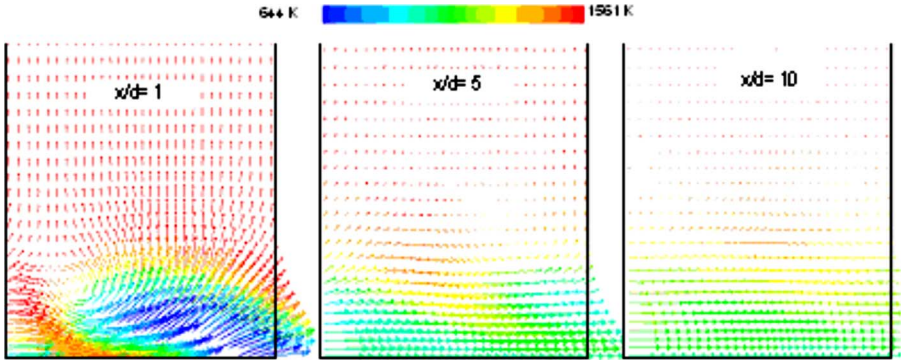

Fig. 5 Flow field on planes perpendicular to the mainstream direction for the 3D compound-angle hole case (colored by temperature)

be conducted to obtain T_{aw} under the adiabatic-wall condition. Therefore, for the convenience of comparing the film-cooling performance between air and mist film cooling in this study, a second consideration is given to the local heat transfer coefficient defined as

$$h = q''(x)/(T_w - T_g) \tag{6}$$

where the h-value is a function of coolant temperature and wall heat flux in addition to the function of the aerodynamics and surface conditions as the conventional heat transfer coefficient is.

Methods have been previously developed to relate the adiabatic cooling effectiveness to the wall heat flux with the intention to keep the h-value as a function of aerodynamics and surface conditions only. For example, Metzger et al. [18] developed a method to absorb the functionality of T_c into the nondimensional temperature $\theta=(T_c-T_g)/(T_w-T_g)$ and proved that h is a linear function of θ bounded by two conditions: no heat flux (i.e., $T_w=T_{aw}$) and $\theta=0$ (i.e., $T_c=T_g$). Eckert [19] and Choe et al. [20] developed a superposition method with $h_o=q''_w(x)/(T_w-T_{aw})$ and other h-values with the coolant ejected at the mainstream temperature (i.e., $T_c=T_g$) to determine the actual local heat transfer coefficient as a function of θ. In this paper, we choose to use the definition of Eq. (6) because T_c and T_g are fixed for all cases. Thus, the comparison of h-values obtained from Eq. (6) is adequate and unique. Furthermore, for conjugate heat transfer boundary conditions, two more factors are introduced: the internal heat transfer coefficient, h_i, and the internal coolant temperature, T_{ci}. The h-value defined by Eq. (6) is the most convenient way to compare air and mist film-cooling performances when both h_i and T_{ci} are also fixed.

The heat transfer result of film cooling with the 3D compound-angle hole jet is shown in Fig. 6, and a constant heat flux is applied to the base cooled wall for this case. To allow readers to compare the differences between the two heat transfer coefficients, both h_o and h are shown in Fig. 6. It can be seen that the heat transfer coefficient (h_o), defined by Eq. (5), for film cooling with and without mist injection is almost the same, while the heat transfer coefficient (h), defined by Eq. (6), is reduced because of mist injection, especially at larger x/d. In this case with the constant heat flux as the boundary condition, a lower h-value indicates a lower surface temperature, as shown in Fig. 6(b). The h-value defined by Eq. (6) adequately shows this reduced heat transfer phenomenon, whereas h_0 defined by Eq. (5) does not. In real GT applications, the actual wall temperature reduction is important. The mist film cooling results show that the wall temperature reduction increases from 15 K to 45 K downstream of $x/d=15-30$ in Fig. 6(b). This is exactly what we really want because the downstream wall is hotter and needs more cooling. The prolonged effect of mist cooling provides this needed service.

3.2 Effects of Water Droplet Sizes, Mist Concentration, and Droplet-Wall Interaction Model on Film-Cooling Performance. Three different water droplet sizes (5 μm, 10 μm, and 20 μm) are simulated. Figure 7(a) shows that the droplet size does not make a difference within $x/d<5$, but the smaller droplets can provide better cooling enhancements (lower h-values and low surface temperatures) downstream of $x/d=5$. The plausible explanation is that the higher surface to volume ratio of small droplets makes droplet evaporation more rapidly and effectively than that of large droplets. In addition, smaller droplets follow the jet flow better, and the evaporation occurs more adjacent to the wall as supported by the particle tracing results, which are not shown here due to limited space.

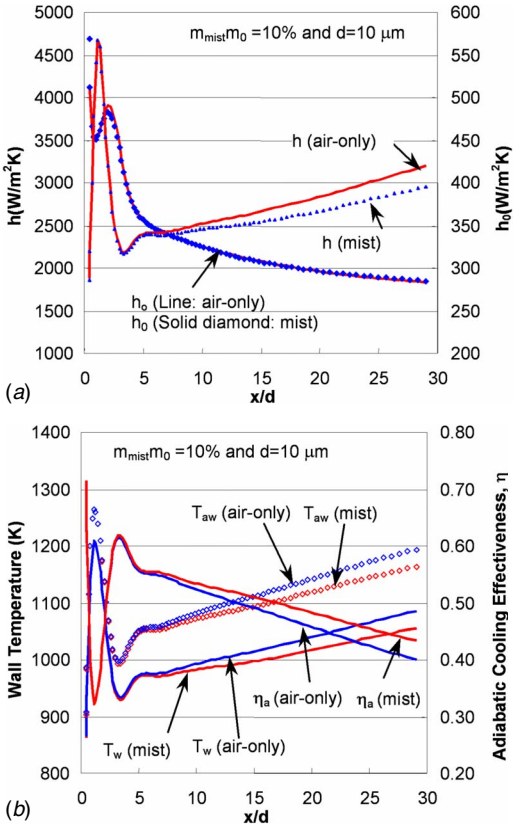

Fig. 6 Heat transfer results of the 3D case with the compound-angle hole over a uniformly cooled base wall under GT operating conditions (15 atm and 1561 K)

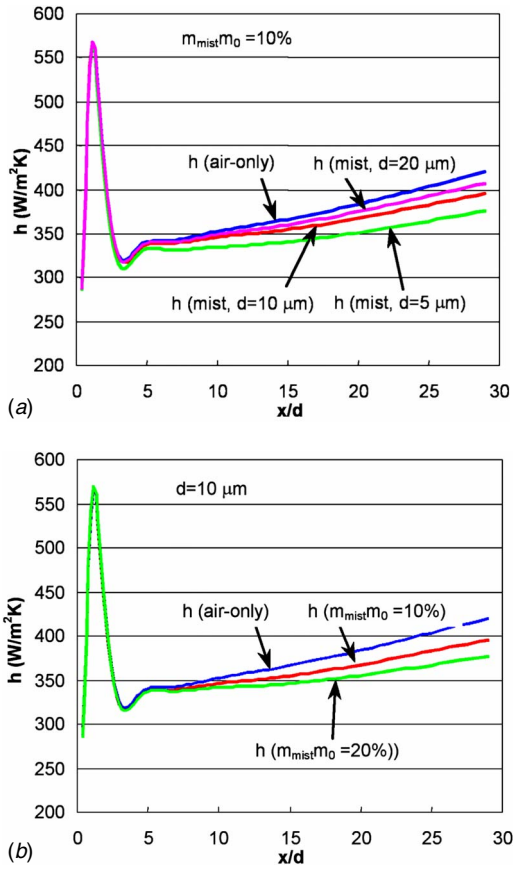

Fig. 7 Effects of (*a*) droplet size and (*b*) mist concentration on film cooling with the compound-angle diffuse hole over a uniformly cooled base wall under GT operating conditions (15 atm and 1561 K)

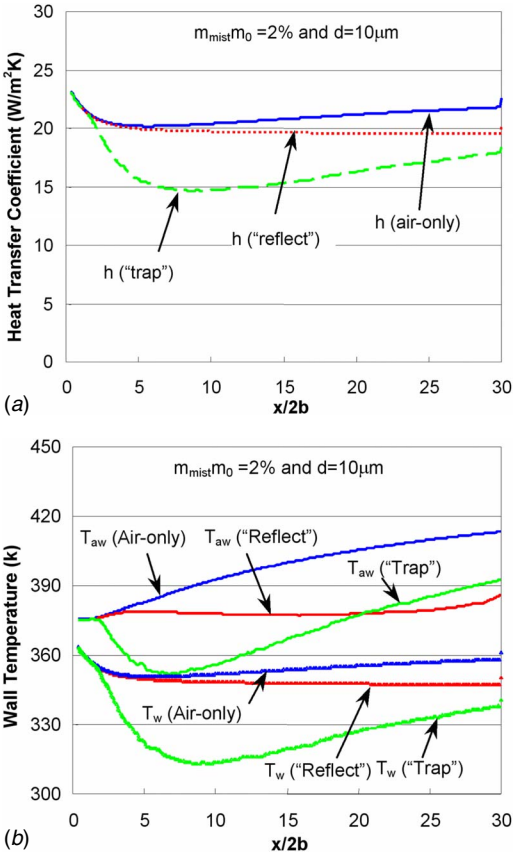

Fig. 8 Heat transfer result of the 2D slot case at low operational conditions (1 atm and 450 K)

The droplet trajectory of 10% mist concentration (Fig. 4) shows that all the droplets evaporate before the mainstream exit at $x/d=30$ due to the high main flow temperature. By adding more mist up to 20% of the coolant mass flow rate, the result in Fig. 7(*b*) shows an approximately 10% decrease downstream of $x/d=30$ for the *h*-value, which corresponds to an additional drop of wall temperature of approximately 28 K from the 10% mist case and 55 K from the air-only case.

Another factor that may affect mist film cooling is the boundary condition of droplets on the wall (i.e., droplet-wall interactions). In all the cases above, the reflect condition is applied, which means the droplet will bounce from the wall elastically. On the opposite end of the extreme case, the trap condition assumes that the droplets adhere to the wall and evaporate completely once they hit the wall. The true condition shall fall within these two extreme conditions. Both reflect and trap conditions have been employed, and numerical results indicate that these two different conditions produce almost no difference on heat transfer coefficient. The reason is that only few droplets (less than 1%) have a chance to hit the wall in these film cooling cases.

3.3 Heat Transfer of Mist Film Cooling at Low Operational Conditions With a 2D Slot Jet. Figure 8 shows the results of the 2D case at low operational conditions (1 atm and 450 K). Due to mist injection, the heat transfer coefficient (*h*) decreases for both reflect and trap boundary conditions. The wall temperature is reduced significantly, and the intensive evaporation with trap condition results in a wall temperature below coolant temperature. At low operational conditions, the droplets stay more closely to the wall, following the streamline, which makes the cooling enhancement more effective.

3.4 Effect of Conjugate Heat Transfer on Mist Film Cooling (2D Slot Jet). Conjugate wall condition mimics more closely the actual blade cooling with both internal passage cooling and external film cooling. Figure 9 shows the temperature field of the 2D film cooling with conjugate heat transfer. The temperature distribution in the *y* direction (cross stream) is relatively uniform in the conduction region. However, the large temperature gradient in the *x* direction indicates that there is a strong axial heat conduction, especially in the proximity of the jet hole. As seen in Fig. 9(*b*), the temperature in the solid wall at $x/2b=1$ is higher than the local flow temperature. Figure 9 also shows some droplet trajectories. Under the low operating conditions, the droplets stay more closely to the wall, following the streamline. Turbulence random tracking method allows individual trajectory to divert from its time-averaged track and mimics the actual instantaneous turbulence flow fluctuations more adequately.

Figure 10 shows the result of the 2D conjugate heat transfer with internal cooling. Injecting mist lowers the temperature of both internal and external walls. The heat flux transferred to the internal flow with mist injection is gladly found to be much lower than the air-only case because the reduced internal cooling means that more energy will remain in the main flow. The positive heat flux in the neighborhood of jet hole with $x/2b<5$ indicates a strong axial heat conduction from downstream to upstream due to the large axial wall temperature gradient. It is interesting to see that the heat flows back to the mainstream (actually to the jet flow that is cooler than the wall, as shown in Fig. 9(*b*)), rather than moves to the internal cooling flow through the inner wall. Generally speaking, heat flux through the wall is reduced significantly by mist injection. The heat flux losses to the internal flow are almost zero between $x/b=10-25$. With the conjugate heat transfer modeling, mist injection can be seen to reduce the heat transfer coefficient (*h*), the wall heat flux, and the wall temperature.

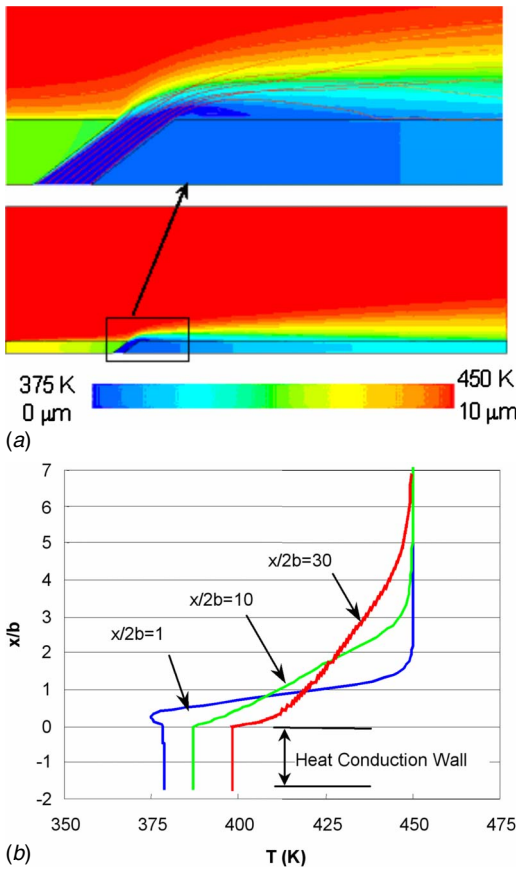

Fig. 9 Temperature distribution of 2D film cooling with conjugate heat transfer

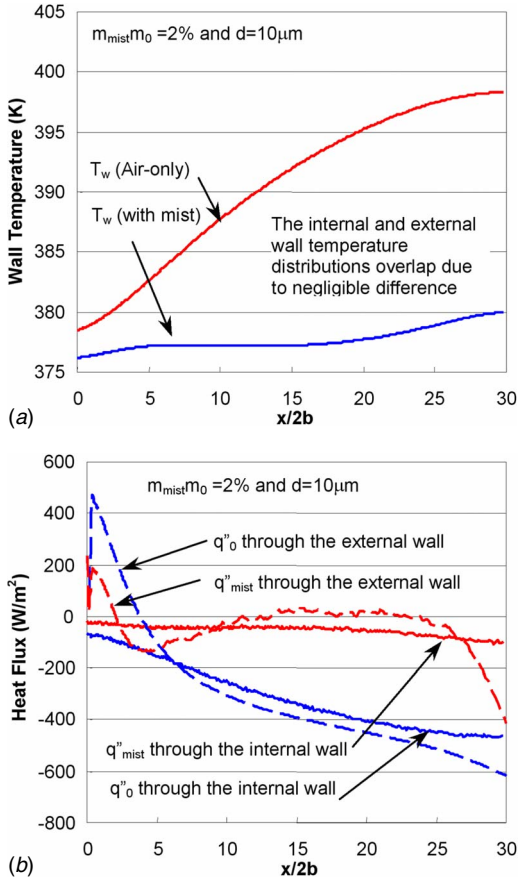

Fig. 10 Heat transfer result of mist film cooling of a 2D slot jet with a conjugate wall cooling

4 Conclusions

As an effort to develop an advanced film-cooling scheme, this paper studies heat transfer of film cooling with mist injection. Both low laboratory conditions and realistic GT operating conditions at high temperature, pressure, and Reynolds number (velocity) are considered with different wall heating conditions. The conclusions are as follows:

- Under GT operating conditions with a compound-angle diffuse hole, mist injection reduces the heat transfer coefficient (h) as well as the wall temperature, especially at the downstream region. The heat transfer coefficient (h_0) has little changes with mist injection.
- Due to a large temperature difference between the main flow and the coolant flow under GT operating conditions, injecting 10% (weight) mist results in 8% (4% point) reduction of heat transfer coefficient (h) and approximately 40 K reduction in wall temperature. Injecting mist provides prolonged cooling and results in more effective cooling in the downstream region ($x/d>15$) where air-only film cooling is less effective.
- Smaller droplets and higher mist concentration result in a stronger surface cooling protection, indicated by a smaller heat transfer coefficient (h) under the same wall heat flux.
- The droplet boundary conditions of reflect and trap give nearly identical results at GT operating conditions because most droplets do not have a chance to hit the wall.
- Under low temperature, pressure, and Reynolds number laboratory conditions, the results of the 2D slot jet with conjugate internal cooling show that injecting 2% mist (mass) reduces heat transfer coefficient (h), wall heat flux about 400 W/m^2, and wall temperature about 15 K.
- The result of the conjugate 2D cases indicates that heat conduction from downstream to upstream along the solid wall is strong. Heat flux through the wall is reduced significantly due to mist injection. The heat flux losses to the internal flow are almost zero in the range $x/b=10-25$. The streamwise heat even conducts back to the film-cooling jet flow in the neighborhood of the jet hole within $x/b<5$.

Acknowledgment

This study was supported by the Louisiana Governor's Energy Initiative via the Clean Power and Energy Research Consortium (CPERC) and was administered by the Louisiana Board of Regents.

Nomenclature

b = slot width (m)
C = concentration (kg/m^3)
d = diameter (m)
k = turbulence kinetic energy (m^2/s^2)
k_c = mass transfer coefficient (m/s)
M = blowing ratio, $(\rho u)_c/(\rho u)_g$
q''_w = wall heat flux
S = source term
Tu = turbulence intensity

Greek

ε = turbulence dissipation rate (m^2/s^3)
η_a = adiabatic film-cooling effectiveness, $(T_g-T_{aw})/(T_g-T_c)$
λ = thermal conductivity (W/m K)

Subscripts

aw = adiabatic wall
c = coolant or jet flow
i = internal cooling
p = particle or droplet

References

[1] Brittingham, R. A., and Leylek, J. H., 2000, "A Detailed Analysis of Film Cooling Physics—Part IV: Compound-Angle Injection With Shaped Holes," ASME J. Turbomach., **122**, pp. 133–145.

[2] Jia, R., Sunden, B., Miron, P., and Leger, B., 2005, "Numerical and Experimental Study of the Slot Film Cooling Jet With Various Angles," ASME J. Turbomach., **127**, pp. 635–645.

[3] Mayhew, J. E., Baughn, J. W., and Byerley, A. R., 2004, "Adiabatic Effectiveness of Film Cooling With Compound Angle Holes—The Effect of Blowing Ratio and Freestream Turbulence," ASME J. Heat Transfer, **126**, pp. 501–502.

[4] Rutledge, J. L., Robertson, D., and Bogard, D. G., 2005, "Degradation of Film Cooling Performance on a Turbine Vane Suction Side Due to Surface Roughness," *Proceedings of the ASME Turbo Expo 2005*, Nevada, Jun. 6–9.

[5] Martini, P., Schulz, A., and Bauer, J. H., 2005, "Film Cooling Effectiveness and Heat Transfer on the Trailing Edge Cut-Back of Gas Turbine Airfoils With Various Internal Cooling Designs," *Proceedings of the ASME Turbo Expo 2005*, Nevada, Jun. 6–9.

[6] Heidmann, J. D., Rigby, D. L., and Ameri, A. A., 2000, "A Three-Dimensional Coupled Internal/External Simulation of a Film-Cooled Turbine Vane," ASME J. Turbomach., **122**, pp. 348–359.

[7] Tyagi, M., and Acharya, S., 2003, "Large Eddy Simulation of Film Cooling Flow From an Inclined Cylindrical Jet," ASME J. Turbomach., **125**(4), pp. 734–742.

[8] Chaker, M., Meher-Homji, C. B., and Mee, M., 2002, "Inlet Fogging of Gas Turbine Engines—Part A: Fog Droplet Thermodynamics, Heat Transfer and Practical Considerations," *Proceedings of the ASME Turbo Expo 2002*, Vol. 4, pp. 413–428.

[9] Petr, V., 2003, "Analysis of Wet Compression in GTs," *Proceedings of the International Conference on Energy and the Environment*, Vol. 1, pp. 489–494.

[10] Guo, T., Wang, T., and Gaddis, J. L., 2000, "Mist/Steam Cooling in a Heated Horizontal Tube, Part 1: Experimental System, Part 2: Results and Modeling," ASME J. Turbomach., **122**, pp. 360–374.

[11] Li, X., and Wang, T., 2006, "Simulation of Film Cooling Enhancement With Mist Injection," ASME J. Heat Transfer, **128**, pp. 509–519.

[12] Li, X., and Wang, T., 2007, "Effects of Various Modeling on Mist Film Cooling," ASME J. Heat Transfer, **129**, pp. 472–482.

[13] Wang, T., and Li, X., 2006, "Simulation of Mist Film Cooling at Gas Turbine Operating Conditions," ASME Paper No. GT2006-90742.

[14] Ranz, W. E., and Marshall, W. R., Jr., 1952, "Evaporation From Drops, Part I," Chem. Eng. Prog., **48**, pp. 141–146.

[15] Kuo, K. Y., 1986, *Principles of Combustion*, Wiley, New York.

[16] Fluent Manual, 2005, Version 6.2.16, Fluent, Inc.

[17] Li, X., Gaddis, J. L., and Wang, T., 2001, "Mist/Steam Heat Transfer in Confined Slot Jet Impingement," ASME J. Turbomach., **123**, pp. 161–167.

[18] Metzger, D. E., Carper, H. J., and Swank, L. R., 1968, "Heat Transfer With Film Cooling Near Nontangential Injection Slots," ASME J. Eng. Power, **90**, pp. 157–163.

[19] Eckert, E. R. G., 1984, "Analysis of Film Cooling and Full-Coverage Film Cooling of Gas Turbines Blades," ASME J. Eng. Gas Turbines Power, **106**, pp. 206–213.

[20] Choe, H., Kays, W. M., and Moffat, R. J., 1974, "The Superposition Approach to Film-Cooling," ASME Paper No. 74-WA/HT-27.

Assessment of the Single-Mixture Gas Assumption for the Correlated *K*-Distribution Fictitious Gas Method in H_2O-CO_2-CO Mixture at High Temperature

C. Caliot
e-mail: cyril.caliot@promes.cnrs.fr

G. Flamant

Processes, Materials and Solar Energy,
PROMES CNRS,
66120 Odeillo-Font-Romeu, France

M. El Hafi
Centre de Recherche d'Albi en génie des Procédés des Solides Divisés,
De l'Energie et de l'Environnement,
Ecole des Mines d'Albi Carmaux,
81000 Albi, France

Y. Le Maoult
Centre de Recherche Outillages, Matériaux et Procédés,
Ecole des Mines d'Albi Carmaux,
81000 Albi, France

This paper deals with the comparison of spectral narrow band models based on the correlated-K (CK) approach in the specific area of remote sensing of plume signatures. The CK models chosen may or may not include the fictitious gas (FG) idea and the single-mixture-gas assumption (SMG). The accuracy of the CK and the CK-SMG as well as the CKFG and CKFG-SMG models are compared, and the influence of the SMG assumption is inferred. The errors induced by each model are compared in a sensitivity study involving the plume thickness and the atmospheric path length as parameters. This study is conducted in two remote-sensing situations with different absolute pressures at sea level (10^5 Pa) and at high altitude (16.6 km, 10^4 Pa). The comparisons are done on the basis of the error obtained for the integrated intensity while leaving a line of sight that is computed in three common spectral bands: 2000–2500 cm^{-1}, 3450–3850 cm^{-1}, and 3850–4150 cm^{-1}. In most situations, the SMG assumption induces negligible differences. Furthermore, compared to the CKFG model, the CKFG-SMG model results in a reduction of the computational time by a factor of 2. [DOI: 10.1115/1.2946475]

Keywords: radiative heat transfer, high temperature plume signature, remote sensing, spectral narrow band models, parametric study

Introduction

Modeling of plume signatures involves two main issues. On the one hand, the radiative properties of the combustion gases at high temperatures are necessary to compute the radiative heat transfer. This is an active research area (Refs. [1–4] and references therein). On the other hand, fast and accurate methods are required to describe the radiative heat transfer inside the plume and through the atmosphere. This paper addresses this issue. This study deals with the comparison of spectral narrow band models, based on the correlated-*K* (CK) approach [5,6] in the specific area of remote sensing of plume signatures. The evaluation of the accuracy of each narrow band model is done with the use of line-by-line (LBL) reference calculations.

In the long range sensing of plume signature, high temperature combustion gases, such as CO_2, H_2O, and CO, are also present in the atmosphere. In this type of application, emission is mainly due to the plume at high temperature, whereas absorption occurs principally in the atmosphere between the plume and a sensor. Contrary to the LBL model, the spectral interval of narrow band models includes many lines. Each of these line intensities depends on temperature. As the line location inside a narrow band is blurred, the CK approach can lead to a large overestimate of the atmospheric absorption.

To avoid this source of discrepancy, several models, including the fictitious gas (FG) idea, were developed [5,7–9]. The present authors [10] have proposed to extend the single-mixture-gas assumption (SMG) of Fu and Liou [11] used in meteorological applications to the remote sensing of plume signature in order to increase the computational efficiency of the CKFG model. The CKFG-SMG model considers the H_2O-CO_2-CO mixture as a single complex gas, which is divided into FGs. As Fu and Liou [11] pointed out, the SMG assumption induces additional blurring in the narrow band because the radiation emitted by the lines belonging to one real gas can be absorbed by the lines of another gas. The SMG assumption leads to an overcorrelation of lines belonging to different real gases. This source of error has been studied in Refs. [10,12] with academic cases. In Ref. [10], the CK-SMG and CKFG-SMG models were presented and compared to a LBL reference calculation in academic configurations at the sea level pressure. As expected, the CKFG-SMG method achieved better accuracy than the CK-SMG method, especially when long atmospheric path lengths were involved. Moreover, in the test cases of Ref. [10], the SMG assumption resulted in negligible errors.

In this paper, we propose to compare the computational time and accuracy of narrow band models. These comparisons are conducted in two remote-sensing situations in which the altitude and the absolute pressure are different. The results of the CK, CKFG, CK-SMG, and CKFG-SMG models are compared to a LBL reference calculation. Furthermore, the validity of the SMG assumption is investigated for ground level and high altitude remote-sensing applications.

Description of the Radiative Transfer Method and the Spectral Models

To compute the plume signature with the different spectral models cited previously, the radiative transfer equation has to be solved in a typical remote-sensing application. To evaluate the accuracy of spectral models, the medium is considered to contain only gases; scattering is not taken into account. The ray tracing method is well suited to compute the infrared intensity leaving a line of sight.

First, the ray tracing method is presented. Then, the CK and the CKFG models are presented, and special features of the CK-SMG and the CKFG-SMG models are given. The LBL approach is not detailed here because it is exposed and validated in Ref. [10].

Ray Tracing Model. The ray tracing method allows one to compute the intensity leaving a line of sight [5,8,10]. In the case of plume signatures, such a line of sight goes through a nonhomogeneous and nonisothermal medium containing a H_2O-CO_2-CO mixture. Taking into account successive emis-

Contributed by the Heat Transfer Division of ASME for publication in the JOURNAL OF HEAT TRANSFER. Manuscript received March 24, 2007; final manuscript received February 22, 2008; published online August 6, 2008. Review conducted by Walter W. Yuen.

sions and absorptions occurring along a line of sight passing through N_c homogeneous and isothermal layers, the monochromatic intensity, I_ν, leaving a line, is written as follows:

$$I_\nu = \sum_{n=1}^{N_c} I_{b\nu}(T_n)[\tau_\nu(n,N_c) - \tau_\nu(n-1,N_c)] \quad (1)$$

where $I_{b\nu}(T_n)$ is the monochromatic blackbody intensity at the temperature T_n of the layer n, and the transmittivity $\tau_\nu(n,N_c)$ is the monochromatic transmittivity of layers from n to N_c, that is defined by the following equation:

$$\tau_\nu(n,N_c) = \prod_{n'=n}^{N_c} \tau_{\nu n'} = \exp\left(-\sum_{n'=n}^{N_c} \kappa_{\nu n'} \ell_{n'}\right) \quad (2)$$

with $\kappa_{\nu n'}$ the monochromatic absorption coefficient of the gas mixture in the layer n' having a thickness $\ell_{n'}$. The LBL method solves Eq. (1) to find the monochromatic intensity I_ν and requires monochromatic radiative properties, such as the monochromatic absorption coefficient of each gas present in the layer. In order to compare the intensities computed with the LBL approach and the narrow band models, the intensity spectrum obtained with the LBL (Eq. (1)) is averaged over a narrow band. Concerning the narrow band models, average radiative properties over a narrow band are used to compute the average intensity, $\bar{I}$, leaving the line of sight. For each narrow band, the expression for this intensity is written, as in Ref. [5].

$$\bar{I} = \sum_{n=1}^{N_c} \bar{I}_b(T_n)[\bar{\tau}(n,N_c) - \bar{\tau}(n-1,N_c)] \quad (3)$$

The transmittivity $\bar{\tau}(n,N_c)$ is a mean value in a narrow band of the transmittivity of layers from n to N_c. The computation of $\bar{\tau}(n,N_c)$ is detailed in the following sections for each model. The main steps shared by all approaches are summarized below:

$$\tau_{ij}(n,N_c) = \exp\left[-\sum_{n'=n}^{N_c} k_j(g_i)\ell_{n'}\right] \quad (4)$$

$$\bar{\tau}_j(n,N_c) = \sum_{i=1}^{N_q} \omega_i \tau_{ij}(n,N_c) \quad (5)$$

$$\bar{\tau}(n,N_c) = \prod_{j=1}^{N} \bar{\tau}_j(n,N_c) \quad (6)$$

where $k_j(g_i)$ is the K-distribution parameter for the gas j at the quadrature abscissa g_i, which corresponds to the quadrature weight ω_i. N_q and N, are, respectively, the total number of quadrature points and the total number of gases. The K-distribution parameters ($k_j(g_i)$) of each real gas (CK) or fictitious gas (CKFG) are computed from their line spectra. The $k_j(g_i)$ are then determined from the LBL spectra using a bisection method. They are obtained for a ten-point Gauss–Legendre quadrature and the width of a narrow band is fixed to $\Delta\nu = 25\ \text{cm}^{-1}$.

Correlated *K* Model and Correlated *K* Model With Fictitious Gases. The CK model considers each real gas of the mixture. The CKFG method consists of dividing one real gas into N_{FG} FGs, which include lines from the same interval of lower-state energy of transition, $\Delta E''$. Furthermore, in the CKFG approach, each real gas is divided into three FGs ($N_{\text{FG}}=3$). FGs of H_2O and CO_2 consist of lines with their E'' in the intervals $\Delta E''$, $0-2000\ \text{cm}^{-1}$, $2000-3000\ \text{cm}^{-1}$, and $3000\ \text{cm}^{-1}-\infty$. For CO, the three FGs classes are $0-900\ \text{cm}^{-1}$, $900-3000\ \text{cm}^{-1}$, and $3000\ \text{cm}^{-1}-\infty$. Considering Eqs. (4)–(6) for the CK model, the subscript j represents the three real gases of the gas mixture and $N=N_g=3$. With the CKFG model, the subscript j represents the FGs used for the gas mixture. If the mixture contains three real gases, then the total number of FGs is $N=N_g \times N_{\text{FG}}=9$.

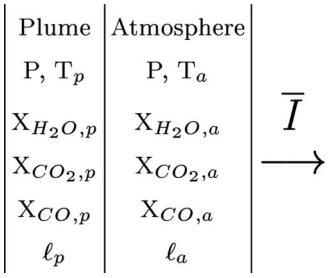

Fig. 1 Schematic description of the intensity leaving a line of sight, which goes through two layers, the high temperature plume and the atmosphere, both constituted of H_2O-CO_2-CO mixture at the same pressure but with different temperatures and layer thicknesses

Correlated *K* Model and Correlated *K* Model With Fictitious Gases and the Single-Mixture Gas Assumption. The idea of Fu and Liou [11], who computed K-distribution parameters for a CK-SMG model, is extended to decrease the total number of FGs involved with the CKFG model and, consequently, enhance computational efficiency. The lines of H_2O, CO_2, and CO gases are grouped to create three ($N_{\text{GF}}=3$) FGs of the mixture. The first FG is constituted of the lines from H_2O and CO_2 gases belonging to the $\Delta E''$ class, $0-2000\ \text{cm}^{-1}$ and from CO gas with lines having their E'' in the $0-900\ \text{cm}^{-1}$ range. The second and third FGs of the mixture are obtained similarly with the $\Delta E''$ classes cited previously. The CKFG-SMG model is used to compute Eqs. (4)–(6). In these equations, the subscript j stands for a FG from the mixture where the total number of FGs is $N=N_{\text{GF}}=3$. For the CK-SMG model, the subscript j represents only the mixture, $N=1$.

In the following section, a specific situation of remote-sensing application is described.

Description of the Remote-Sensing Configurations

The applications of remote sensing considered in this paper are assumed to take place in a subarctic summer atmosphere. The remote sensing of plume signatures is conducted at two altitudes where the absolute pressure and the atmospheric concentration of H_2O are different. The line of sight is composed of two layers (see Fig. 1), the high temperature plume and the atmosphere with respective thicknesses, ℓ_p and ℓ_a. The atmosphere for both altitudes is summarized in Table 1. The molar fractions of CO_2 and CO are identical at both altitudes, and the temperature, pressure, and H_2O molar fraction are obtained from the standard model of the subarctic summer [13]. Moreover, the high temperature value of the gaseous plume is $T_p=2000$ K, and the concentrations of the combustion gases inside the plume are representative of typical combustion products; the molar fractions are then, $X_{\text{H}_2\text{O},p}=0.2$, $X_{\text{CO}_2,p}=0.1$, and $X_{\text{CO},p}=0.05$. Also, the plume pressure is assumed to be the atmospherical pressure (depending on the cases in Table

Table 1 Description of the atmosphere composition in two remote-sensing cases with different altitudes

Case No.	Altitude (km)	Pressure P (Pa)	Temperature T_a (K)	Composition		
				$X_{\text{H}_2\text{O},a}$	$X_{\text{CO}_2,a}$	$X_{\text{CO},a}$
Case 1	0	10^5	287	0.012	370×10^{-6}	2×10^{-5}
Case 2	16.6	10^4	225	7×10^{-6}	370×10^{-6}	2×10^{-5}

Table 2 Number of τ_{ij} needed for each spectral model in different spectral intervals

Spectral intervals (cm^{-1})	Resolution Nos.				
	LBL	CK	CKFG	CK-SMG	CKFG-SMG
2000–2500	10^6	530	1590	210	630
3450–3850	8×10^5	340	1020	170	510
3850–4150	6×10^5	240	720	120	360

Table 3 Spectral intervals where the gases H_2O, CO_2, and CO overlap ($\Delta\nu$=25 cm^{-1})

Spectral intervals (cm^{-1})	Gaseous mixture	No. of narrow band
1950–2325	H_2O-CO_2-CO	16
2350–2425	H_2O-CO_2	4
2450–3200	H_2O	31
3225–3775	H_2O-CO_2	23
3800–4350	H_2O-CO	23

1). For both altitudes, the intensity leaving a line of sight is computed with the LBL, CK, CKFG, CK-SMG, and CKFG-SMG models in three spectral intervals given in Table 2. As Beier and Lindermeir [14] specified, these spectral intervals are frequently used for missile detection.

In Table 2, the computational time required for each model is evaluated. Because the time of computation depends on the computer and programming, the number of transmittivity $\tau_{ij}(n,N_c)$ (Eq. (5)) required in a spectral interval is chosen as an indicator for the computation time. In a spectral interval, such as [2000–2500 cm^{-1}], the number of $\tau_{ij}(n,N_c)$ required in a narrow band depends on the number of overlapping gases. The spectral intervals where the gases overlap are given in Table 3. Furthermore, in order to find an equivalent indicator for the LBL method, the number of monochromatic transmittivity $\tau_\nu(n,N_c)$ needed to compute the narrow band intensities is also presented in Table 2 (the resolution of the LBL spectra is 5×10^{-4} cm^{-1}). Table 2 illustrates the time savings when the spectral narrow band models are used. Moreover, for the spectral intervals considered in this study, the SMG assumption reduces the computation time by at least half.

In the following, the accuracy of each narrow band model is investigated in two cases: the remote sensing of high temperature plume at sea level (Case 1, Table 1) and at high altitude (Case 2, Table 1). Considering three spectral intervals (Table 2), the accuracy of a narrow band model is evaluated with the R ratio defined as the average difference of the intensity between the narrow band model and the reference model. Its expression is as follows:

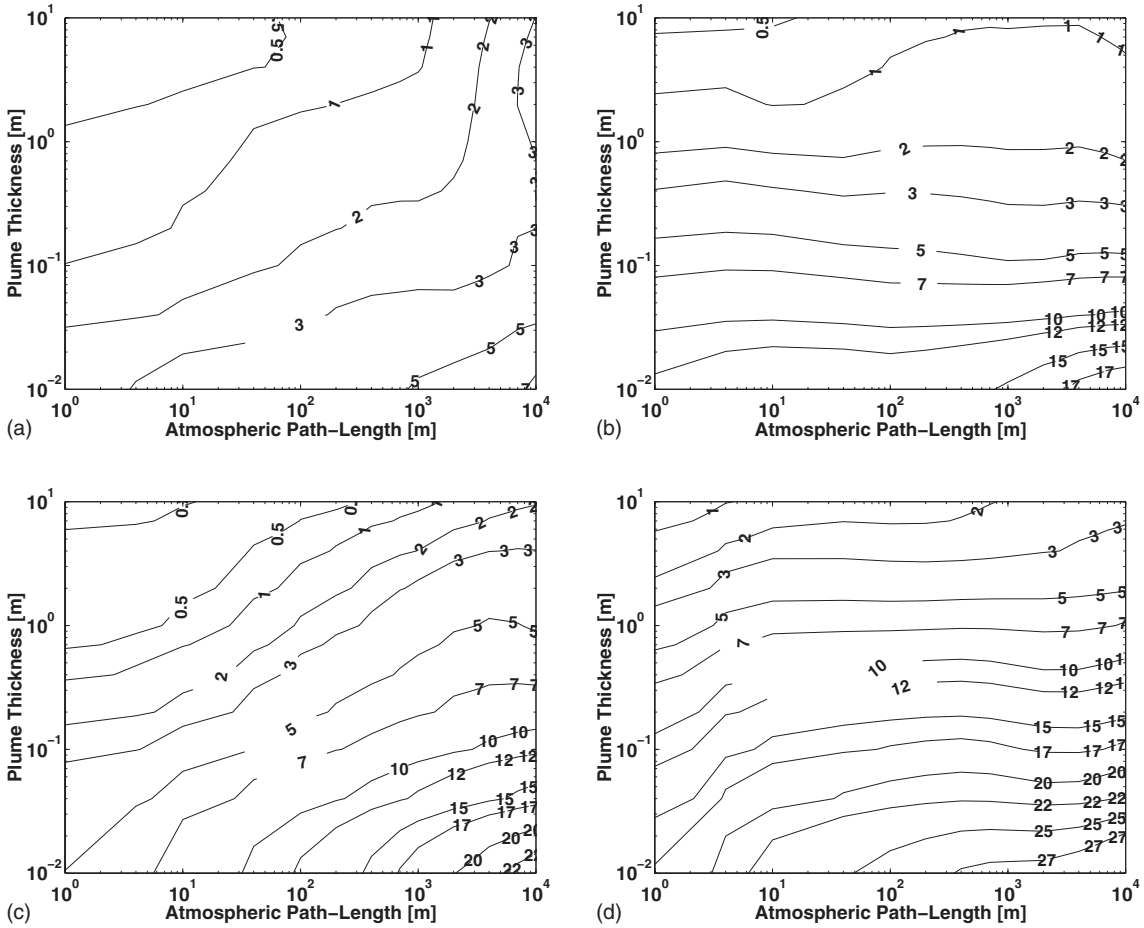

Fig. 2 Mappings of the R ratio in the spectral interval 2000–2500 cm^{-1} versus the atmospheric path-length and the plume thickness (*a*) CKFG-SMG and CKFG in Case 1, (*b*) CKFG-SMG and CKFG in Case 2, (*c*) CK-SMG and CK in Case 1, and (*d*) CK-SMG and CK in Case 2

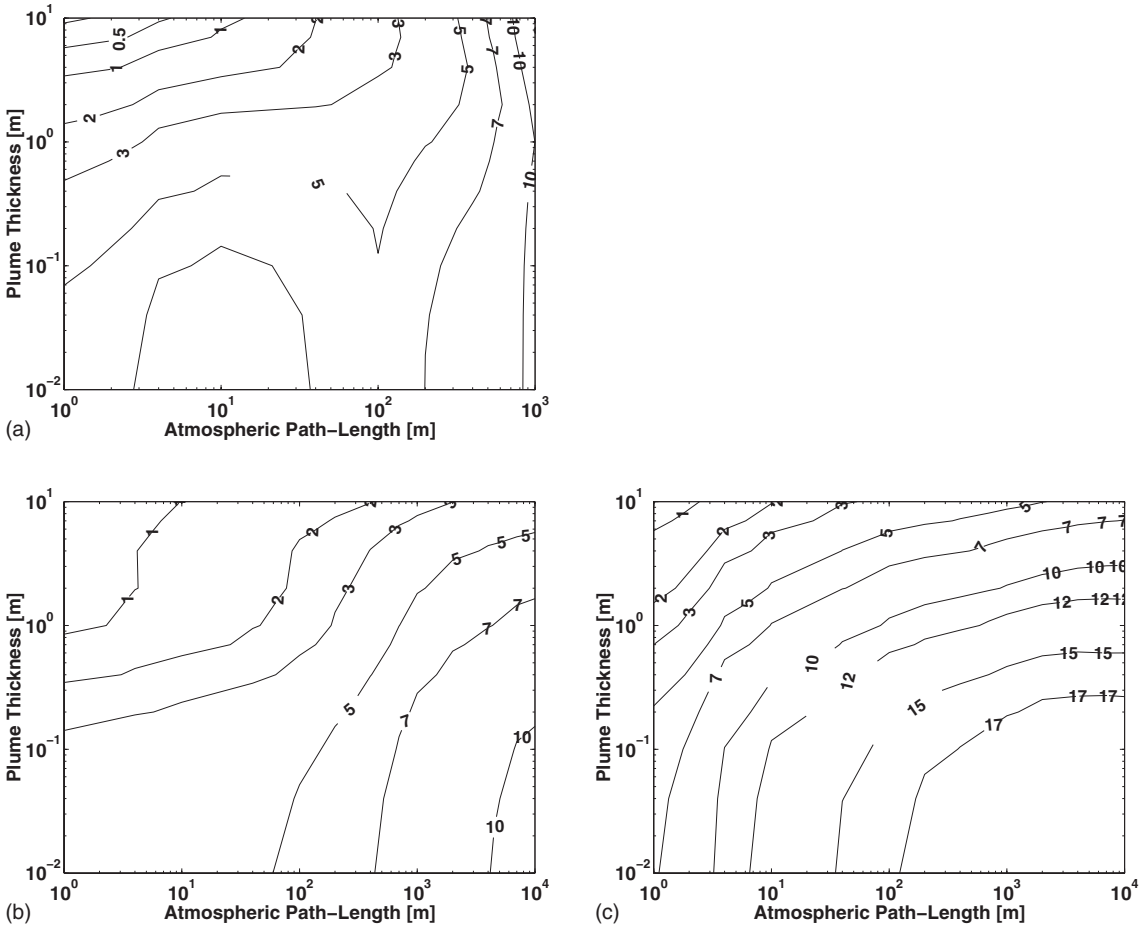

Fig. 3 Mappings of the *R* ratio in the spectral interval 3450–3850 cm^{-1} versus the atmospheric path-length and the plume thickness for (*a*) CKFG-SMG and CKFG in Case 1, (*b*) CKFG in Case 2, and (*c*) CKFG-SMG in Case 2

$$R = 100\left(\sum_{k=1}^{N_b} \bar{I}_{\mathrm{LBL},k}\right)^{-1} \sum_{k=1}^{N_b} |\bar{I}_{\mathrm{LBL},k} - \bar{I}_{\mathrm{NB},k}| \tag{7}$$

where N_b is the number of bands included in the spectral intervals (Table 2). $\bar{I}_{\mathrm{LBL},k}$ and $\bar{I}_{\mathrm{NB},k}$ are, respectively, the average intensity, in the kth narrow band, obtained with the reference LBL approach and the intensity computed with a narrow band model (Eq. (3)) such as CK, CK-SMG, CKFG, or CKFG-SMG. The absolute value of the error due to the narrow band model is considered in Eq. (7) in order to avoid a balancing effect of the integrated error in the spectral interval. R is not the relative error induced by a narrow band model on the integrated intensity in the spectral interval but is an indicator of the difference between a narrow band model and the LBL.

Results and Discussion

From Figs. 2–4, the mappings of the R ratio are represented versus the atmospheric path length (ℓ_a) and the plume thickness (ℓ_p). The dependence of the R ratio on the atmospheric path length and the plume thickness is investigated by covering a wide range of remote sensing configurations. The mappings in Fig. 2 show the spectral interval 2000–2500 cm^{-1}, and the mappings in Figs. 3 and 4 show the spectral intervals 3450–3850 cm^{-1} and 3850–4150 cm^{-1}, respectively.

The figures of the R ratio highlight four sources of discrepancies between the narrow band models and the LBL. First, the increase in the plume thickness results in an enlargement of the line wing contribution to the emitted radiation by the plume. The overlapping of several line wings create a continuum, which helps to decrease the overcorrelation effects between lines from different lower-state energies. Consequently, the errors of the narrow band models tend to be smaller when the plume thickness increases. The second source of discrepancies is illustrated by the higher value of R for the low pressure case. At low pressure, the collision broadening of the lines is weak, and the optical thickness of the corresponding line wings is almost zero. For the spectra involved in Case 2, the lines are more spaced and the emitted radiation is concentrated at the center of the lines. The errors due to the correlation of lines from different lower-state energies are enhanced, and R-values are greater at high altitude than at sea level. The third source of discrepancies is the overestimate of the atmospheric absorption, due to the spectral correlations. In summary, long atmospheric path length and low pressure result in the increase in the R ratio. In contrast, the increase in the plume thickness tends to reduce the R ratio. If the effects of the atmospheric path length and the plume thickness are competitive, the mappings show curved isolines of R. When one of these effects prevails, the isolines of R are either vertical if the effect of atmospheric path length is dominant or horizontal if the effect of the plume thickness is predominant. The fourth source of discrepancies affects only the models with the SMG assumption since it is related to the overcorrelation of lines belonging to different real gases.

In Fig. 2, each frame represents the results of two models: CKFG-SMG and CKFG, shown in Figs. 2(*a*) and 2(*b*), and CK

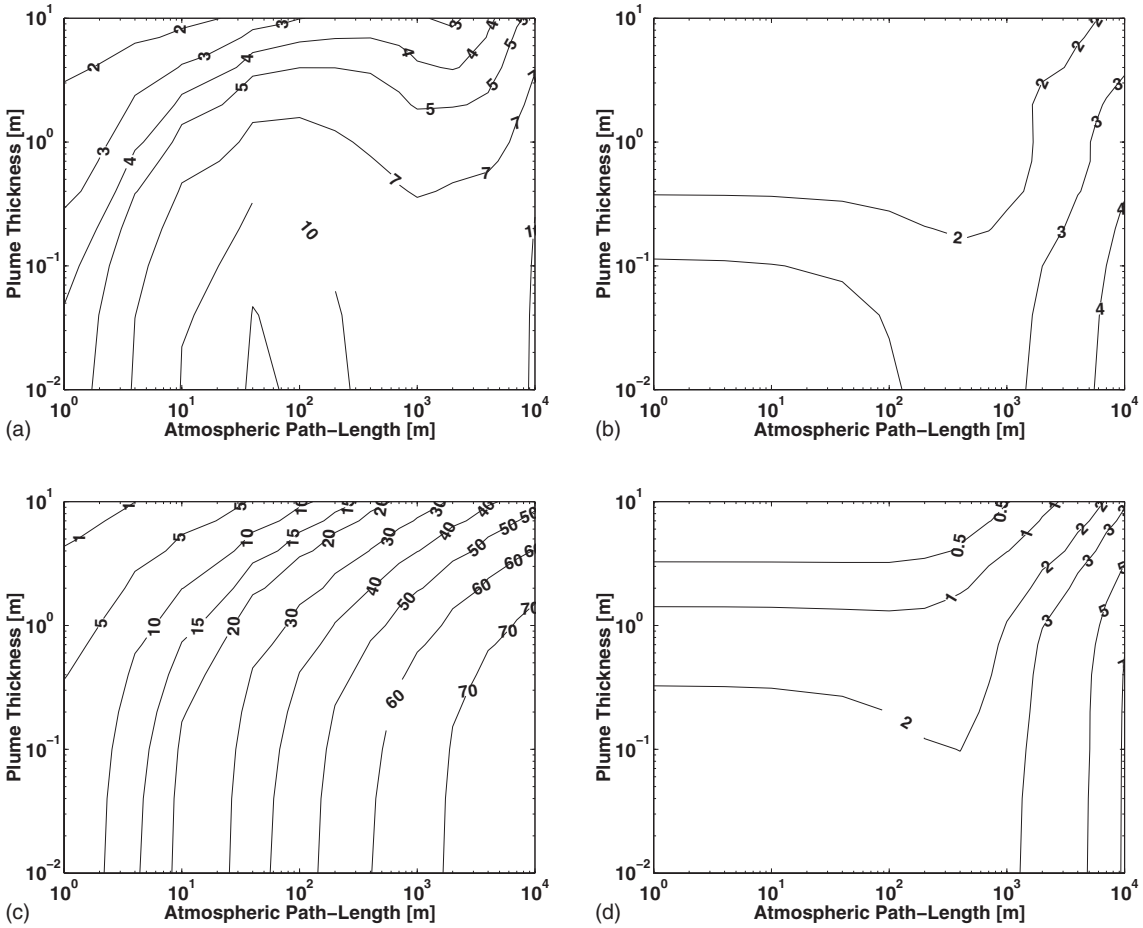

Fig. 4 Mappings of the *R* ratio in the spectral interval 3850–4150 cm^{-1} versus the atmospheric path-length and the plume thickness for (*a*) CKFG-SMG and CKFG in Case 1, (*b*) CKFG-SMG and CKFG in Case 2, (*c*) CK-SMG and CK in Case 1, and (*d*) CK-SMG and CK in Case 2

and CK-SMG models, shown in Figs. 2(*c*) and 2(*d*). Indeed, in such cases, both models give similar results. There are two reasons for this, which are due to the specificity of the spectral distribution of the lines in this interval. First, the lines of H_2O and CO_2 do not overlap in the atmospheric spectrum (cold lines). Second, H_2O cold lines only absorb the intensity emitted by the H_2O lines of the high temperature spectrum. In the same manner, the CO_2 cold lines absorb principally the intensity emitted by the CO_2 lines. That is why the SMG assumption does not introduce a supplementary error and the two models give identical results. Moreover, the contribution of CO to the overall atmospheric absorption is negligible in view of its low concentration. At sea level, CKFG and CKFG-SMG reach a good accuracy since $R \leqslant 7\%$. At high altitude, both models give also good results ($R \leqslant 5\%$) if the plume thickness is greater than 0.1 m. As the plume thickness increases, the *R* ratio decreases. The comparison of the *R* values involved in Figs. 2(*a*) and 2(*b*) shows the role of the pressure on *R*, which enhances the spectral overcorrelation effects. In the spectral interval [2000–2500 cm^{-1}], the CK-SMG and CK models can be used ($R \leqslant 7\%$) if the plume thickness is greater than 1 m.

For the remote-sensing application at sea level, Fig. 3(*a*) represents the mapping of the *R* ratio obtained either with the CKFG-SMG model or the CKFG model, in the spectral interval 3450–3850 cm^{-1}. In this figure, the atmospheric path length is truncated to 1 km (10^3 m); beyond this value, the average intensity in the spectral interval is not significant. Figure 3(*a*) shows that both models, considering FGs, lead to a difference compared to the reference (LBL) of 5–10% when the atmospheric path increases. For the high altitude case, the mappings of *R* for the CKFG and CKFG-SMG models are, respectively, presented in Figs. 3(*b*) and 3(*c*). In this spectral interval, H_2O and CO_2 lines overlap. Then, the SMG assumption introduces additional errors due to the change in mole fraction. It is for this reason that the CKFG model ($R < 10\%$) has better accuracy than the CKFG-SMG model ($R < 17\%$). Although the SMG assumption introduces supplementary errors, both models reach values of the *R* ratio greater than 5%. The models do not give a sufficiently good accuracy when the long atmospheric path is considered. The results for the CK and CK-SMG models are not shown in this case because of their low accuracy. For this spectral interval, 3450–3850 cm^{-1}, the LBL approach is recommended if a very high accuracy is necessary. If an *R* ratio close to 10% is a tolerable accuracy, the CKFG-SMG model should be used for applications at sea level; at high altitude, the CKFG model is recommended.

Figures 4(*a*)–4(*d*) represent the mapping of the *R* ratio obtained with the narrow band models in the spectral interval 3850–4150 cm^{-1}. The results computed with the CKFG model are similar to those computed with the CKFG-SMG model. In the same manner, the results of the CK model are identical to those obtained with the CK-SMG model. Figure 4(*a*) shows that the *R* ratio reaches values around 10% for the remote-sensing case at the sea level, whereas for the high altitude case (Fig. 4(*b*)), the *R* ratio takes values lower than 5%. At the sea level, the models using the FGs do not seem to be accurate enough. This is due to the optical thickness of H_2O, which is larger at sea level than at high altitude.

In addition, when FGs are not used, e.g., with the CK and CK-SMG models in Fig. 4(*c*), the *R* ratio exceeds 50%. Comparing Figs. 4(*c*) and 4(*d*), the same conclusions can be drawn. The influence of H_2O concentration leads to a better accuracy of the CK and CK-SMG models at high altitude than at the sea level.

Summary and Conclusion

The present study evaluates the accuracy of the narrow band models in two specific applications: the remote sensing of a high temperature plume at sea level and at high altitude. In the spectral ranges studied, 2000–2500 cm^{-1}, 3450–3850 cm^{-1}, and 3850–4150 cm^{-1}, the CKFG and the CKFG-SMG models are found to have identical accuracies in remote-sensing applications. However, an exception occurs for the high altitude case in the spectral interval 3450–3850 cm^{-1}. At high altitude, the CKFG model gives an *R* ratio lower than 10%, which is better than the CKFG-SMG, which reaches 17%. In this particular case, the SMG assumption provokes an additional difference. Overall, this study shows that the error induced by the SMG assumption is almost negligible. However, if the two models are compared in terms of computing time, the CKFG-SMG needs half of the computational time required by the CKFG model. In most cases, the CKFG-SMG model is the most efficient narrow band model, among the ones studied in this paper, for the remote sensing of a high temperature plume.

References

[1] Rothman, L. S., Wattson, R. B., Gamache, R. R., Schroeder, and J., and McCann, A., 1995, "HITRAN HAWKS and HITEMP High-Temperature Molecular Database," Proc. SPIE, **2471**, pp 105–111.

[2] Partridge, H., and Schwenke, D. W., 1997, "The Determination of an Accurate Isotope Dependent Potential Energy Surface for Water From Extensive Ab Initio Calculations and Experimental Data," J. Chem. Phys., **106**, pp. 4618–4639.

[3] Tashkun, S. A., Perevalov, V. I., Teffo, J.-L., Bykov, A. D., and Lavrentieva, N. N., 2003, "CDSD-1000, the High-Temperature Carbon Dioxide Spectroscopic Databank," J. Quant. Spectrosc. Radiat. Transf., **82**, pp. 165–196.

[4] Bharadwaj, S. P., and Modest, M. F., 2007, "Medium Resolution Transmission Measurements of CO_2 at High Temperature: An Update," J. Quant. Spectrosc. Radiat. Transf., **103**, pp. 146–155.

[5] Taine, J., and Soufiani, A., 1999, "Gas IR Radiative Properties: From Spectroscopic Data to Approximate Models," Adv. Heat Transfer, **33**, pp. 295–341.

[6] Lacis, A., Wang, W. C., and Hansen, J., 1979, "Correlated K-Distribution Method for Radiative Transfer in Climate Models: Application to Effect of Cirrus Clouds on Climate," NASA Conf. Publ., **2076**, pp. 309–314.

[7] Ludwig, C. B., Malkmus, W., Reardon, J. E., and Thomson, J. A.L., 1973, "Handbook of Infrared Radiation From Combustion Gases," NASA SP-3080.

[8] Rivière, P., Soufiani, A., and Taine, J., 1992, "Correlated-K and Fictitious Gas Methods for H_2O Near 2.7 μm," J. Quant. Spectrosc. Radiat. Transf., **48**, pp. 187–203.

[9] Levi Di Leon, R., and Taine, J., 1986, "A Fictive Gas-Method for Accurate Computations of Low Resolution, IR Gas Transmissivities: Application to the 4.3 μm CO_2 Band," Rev. Phys. Appl., **21**, pp. 825–831.

[10] Caliot, C., Le Maoult, Y., El Hafi, M., and Flamant, G., 2006, "Remote Sensing of High Temperature H_2O–CO_2–CO Mixture With a Correlated K-Distribution Fictitious Gas Method and the Single Mixture Gas Assumption," J. Quant. Spectrosc. Radiat. Transf., **102**, pp. 304–315.

[11] Fu, Q., and Liou, K. N., 1992, "On the Correlated K-Distribution Method for Radiative Transfer in Nonhomogenous Atmospheres," J. Atmos. Sci., **49**, pp. 2139–2156.

[12] Caliot, C., 2006, "Modélisation et Simulation de l'Emission Energétique et Spectrale d'un Jet Réactif Composé de Gaz et de Particules à Haute Température Issus de la Combustion d'un Objet Pyrotechnique." Ph.D. thesis, Institut National Polytechnique de Toulouse, Toulouse.

[13] Mc Clatchey, R. A., Fenn, R. W., Selby, J. E.A., Voltz, F. E., and Garing, J. S., 1971, "Optical Properties of the Atmosphere," Air Force Cambridge Res Lab, Tech Report No. AFCRL-71-0279.

[14] Beier, K., and Lindermeir, E., 2007, "Comparison of Line-by-Line and Molecular Band IR Modeling of High Altitude Missile Plume," J. Quant. Spectrosc. Radiat. Transf., **105**, pp. 111–127.

Effect of Velocity and Temperature Boundary Conditions on Convective Instability in a Ferrofluid Layer

C. E. Nanjundappa
Department of Mathematics,
Dr. Ambedkar Institute of Technology,
Bangalore 560 056, India
e-mail: cenanju@hotmail.com

I. S. Shivakumara[1]
UGC-Centre for Advanced Studies in Fluid Mechanics,
Department of Mathematics,
Bangalore University,
Bangalore 560 001, India
e-mail: isshivakumara@hotmail.com

A variety of velocity and temperature boundary conditions on the onset of ferroconvection in an initially quiescent ferrofluid layer in the presence of a uniform magnetic field is investigated. The lower boundary of the ferrofluid layer is assumed to be rigid-ferromagnetic, while the upper boundary is considered to be either rigid-ferromagnetic or stress-free. The thermal conditions include a fixed heat flux at the lower boundary and a general convective, radiative exchange at the upper boundary, which encompasses fixed temperature and fixed heat flux as particular cases. The resulting eigenvalue problem is solved using the Galerkin technique and also by the regular perturbation technique when both boundaries are insulated to temperature perturbations. It is observed that an increase in the magnetic number and the nonlinearity of fluid magnetization as well as a decrease in Biot number are to destabilize the system. Further, the nonlinearity of fluid magnetization is found to have no effect on the onset of ferroconvection in the absence of the Biot number.
[DOI: 10.1115/1.2952742]

Keywords: ferroconvection, constant heat flux, Galerkin technique, regular perturbation technique

1 Introduction

Ferromagnetic fluids are colloidal suspensions of fine magnetic monodomain nanoparticles (diameter of the particles is typically 10 nm) in nonconducting carrier liquids such as water, ester, hydrocarbon, etc. These fluids are not found in nature but are artificially synthesized due to their widespread interest in diverse applications (see Refs. [1–3]). Besides, heat transfer through ferrofluids has received the attention of many researchers in the recent past because of its many technological applications. Finlayson [4] was the first to study the linear stability of ferroconvection in a horizontal layer of ferrofluid heated from below in the presence of a uniform vertical magnetic field, which is the generalization of the classical Rayleigh–Benard problem. Thermoconvective instability of ferrofluids without considering buoyancy effects has been investigated by Lalas and Carmi [5], whereas Shliomis [6] has analyzed the linear relation for magnetized perturbed quantities at the limit of instability. A similar analysis, but with the fluid confined between ferromagnetic plates, was carried out by Gotoh and Yamada [7] using the linear stability analysis. Schwab et al. [8] have conducted experiments and their results are found to be in good agreement with those in Ref. [4]. Recently, Kaloni and Lou [9] have studied convective instability in a horizontal layer of magnetic fluid by considering the relaxation time and the rotational viscosity effects.

All the above mentioned studies dealt with isothermal boundary conditions at the surfaces of the ferrofluid layer. However, consideration of actual situations suggests that these conditions may be too restrictive [10]. For instance, if the heating at the lower surface is by passing an electric current through a thin metallic foil, then the appropriate boundary condition would be a fixed heat flux rather than a fixed temperature. Therefore, the aim of the present study is to investigate analytically the condition for the onset of convection in a ferrofluid layer for different hydrodynamic boundaries (i.e., both boundaries rigid, lower-rigid, and upper-free boundaries) with fixed heat flux and convective-radiative exchange conditions at lower and upper boundaries, respectively.

2 Mathematical Formulation

We consider an infinite horizontal layer of an electrically nonconducting Boussinesq ferrofluid of depth d in the presence of a uniform magnetic field H_0 acting normal to the boundaries. A Cartesian coordinate system (x,y,z) is used with the origin at the bottom of the surface and the z-axis vertically upward. At the lower boundary $z=0$, a constant heat flux condition of the form

$$-k_1\frac{\partial T}{\partial z}=q_0 \tag{1}$$

is used, while at the upper boundary $z=d$, a radiative type of condition of the form

$$-k_1\frac{\partial T}{\partial z}=h_t(T-T_\infty) \tag{2}$$

is invoked. In the above equations, T is the temperature, q_0 is the conductive thermal flux, k_1 is the overall thermal conductivity, h_t is the heat transfer coefficient, and T_∞ is the temperature in the bulk of the environment. It is clear that there exists the following solution for the quiescent basic state:

$$\mathbf{q}_b=0,\quad p_b(z)=p_0-\rho_0 gz-\frac{1}{2}\rho_0\alpha_t g\beta z^2-\frac{\mu_0 M_0\kappa\beta}{1+\chi}z-\frac{\mu_0\kappa^2\beta^2}{2(1+\chi)^2}z^2$$

$$T_b(z)=T_0-\beta z,\quad \mathbf{H}_b(z)=\left[H_0-\frac{K\beta z}{1+\chi}\right]\hat{k} \tag{3}$$

$$\mathbf{M}_b(z)=\left[M_0+\frac{K\beta z}{1+\chi}\right]\hat{k}$$

where $\hat{k}$ is the unit vector in the z-direction, $\beta=q_0/k_1$ is the temperature gradient, $T_0=T_\infty+q_0/h_t(1+h_t d/k_1)$, and the subscript b denotes the basic state. To study the stability of the basic state, we perturb all the variables in the form

$$\mathbf{q}=\mathbf{q}',\quad p=p_b(z)+p',\quad T=T_b(z)+T'$$
$$\mathbf{H}=\mathbf{H}_b(z)+\mathbf{H}',\quad \mathbf{M}=\mathbf{M}_b(z)+\mathbf{M}' \tag{4}$$

where $\boldsymbol{q}'$, p', T', $\boldsymbol{H}'$, and $\boldsymbol{M}'$ are perturbed variables and are assumed to be small.

Following the standard linear stability analysis procedure [4] and assuming the principle of exchange of stability is valid, the resulting dimensionless equations are then found to be

$$(D^2-a^2)^2W=-\mathrm{R}a^2[M_1D\Phi-(1+M_1)\Theta] \tag{5}$$

$$(D^2-a^2)\Theta=-(1-M_2)W \tag{6}$$

[1]Corresponding author.

Contributed by the Heat Transfer Division of ASME for publication in the JOURNAL OF HEAT TRANSFER. Manuscript received January 2, 2007; final manuscript received March 22, 2008; published online August 6, 2008. Review conducted by Cholik Chan.

Table 1 Comparison of R_c and a_c for different values of Bi with $M_1=0$

	Sparrow et al. [10]				Present analysis			
	Rigid-rigid		Rigid-free		Rigid-rigid		Rigid-free	
Bi	R_c	a_c	R_c	a_c	R_c	a_c	R_c	a_c
0	720. 000	0.00	320.000	0.000	720.000	0.000	320.000	0.000
0.1	807.676	1.23	381.665	1.015	807.676	1.2281	381.665	1.0151
1	974.173	1.94	513.792	1.64	974.172	1.9427	513.790	1.6438
10	1204.571	2.44	725.150	2.11	1204.57	2.4367	725.147	2.1055
100	1284.263	2.53	804.973	2.20	1284.28	2.5394	804.972	2.2029
∞	1295.781	2.55	816.748	2.21	1295.78	2.5490	816.744	2.2147

$$(D^2 - a^2 M_3)\Phi = D\Theta \tag{7}$$

Here, $D=d/dz$ is the differential operator, W is the amplitude of vertical component of velocity, Θ is the amplitude of temperature, Φ is the amplitude of magnetic potential, $a=\sqrt{\ell^2+m^2}$ is the overall horizontal wave number, $R=\alpha_t g\beta d^4/\nu\kappa$ is the Rayleigh number, $M_1=\mu_0 K^2\beta/(1+\chi)\alpha_t\rho_0 g$ is the magnetic number, $M_2=\mu_0 T_0 K^2/(1+\chi)\rho_0 C_0$ is the magnetic parameter, and $M_3=(1+M_0/H_0)/(1+\chi)$ is the measure of nonlinearity of fluid magnetization. The typical value of M_2 for magnetic fluids with different carrier liquids turns out to be of the order of 10^{-6} and hence its effect is neglected as compared to unity.

Equations (5)–(7) are solved using the following boundary conditions:

$$W = DW = \Phi = D\Theta = 0 \quad \text{(on the lower rigid boundary)} \tag{8}$$

$$W = DW = \Phi = D\Theta + \mathrm{Bi}\Theta = 0 \quad \text{(if the upper boundary is rigid)} \tag{9}$$

$$W = D^2W = D\Phi = D\Theta + \mathrm{Bi}\Theta = 0 \quad \text{(if the upper boundary is free)} \tag{10}$$

where $\mathrm{Bi}=h_t d/k_1$ is the Biot number. The cases $\mathrm{Bi}=0$ and $\mathrm{Bi}\to\infty$, respectively, correspond to constant heat flux and isothermal conditions at the upper boundary.

3 Solution

Equations (5)–(7) together with the chosen boundary conditions constitute an eigenvalue problem, which has been solved by the Galerkin method. Accordingly, W, Θ, and Φ are written as

$$W(z) = \sum_{i=1}^{N} A_i W_i(z), \quad \Theta(z) = \sum_{i=1}^{N} C_i \Theta_i(z), \quad \Phi(z) = \sum_{i=1}^{N} D_i \Phi_i(z) \tag{11}$$

where A_i, C_i, and D_i are unknown constants to be determined. The base functions $W_i(z)$, $\Theta_i(z)$, and $\Phi_i(z)$ are generally chosen such that they satisfy the corresponding boundary conditions [4]. For rigid-rigid as well as lower-rigid and upper-free boundaries, they are chosen as

$$W_i = (z^4 - 2z^3 + z^2)T^*_{i-1}, \quad \Theta_i = z^2(1 - 2z/3)T^*_{i-1}$$
$$\Phi_i = (z^2 - z)(z-2)T^*_{i-1} \tag{12}$$

$$W_i = (2z^4 - 5z^3 + 3z^2)T^*_{i-1}, \quad \Theta_i = z^2(1 - 2z/3)T^*_{i-1}$$
$$\Phi_i = z^2(1 - 2z/3)T^*_{i-1} \tag{13}$$

where T^*_i's are the modified Tchebychev polynomials. The above trial functions satisfy all the boundary conditions except the natural one, namely, $D\Theta+\mathrm{Bi}\Theta=0$ at $z=1$, but the residual from this condition is included as residual from the differential equation. Multiplying Eq. (5) by $W_j(z)$, Eq. (6) by $\Theta_j(z)$, and Eq. (7) by $\Phi_j(z)$, performing the integration by parts with respect to z between $z=0$ and $z=1$, and using the boundary conditions, we obtain a system of linear homogeneous algebraic equations in A_i, C_i, and D_i. Nontrivial solution exists if and only if a given characteristic determinant is equal to zero. This leads to a relation involving the characteristic parameters R, Bi, M_1, M_3, and a in the form

$$f(\mathrm{R}, \mathrm{Bi}, M_1, M_3, a) = 0 \tag{14}$$

4 Numerical Calculations and Discussion

The numerical procedure used is validated first by comparing the critical Rayleigh number R_c, and the corresponding wave number a_c with those obtained by Sparrow et al. [10] for different values of Bi under the limiting case of $M_1=0$ (i.e., ordinary viscous fluid) for rigid-rigid and rigid-free boundary conditions in Table 1. We note that an excellent agreement between both approaches and thus verifies the accuracy of the numerical procedure used in the investigation.

Figures 1 and 2 show the variation of R_c as a function of Bi for different values of M_1 (=0,1,5) with $M_3=1$, and for different values of M_3 (=1,10,∞) when $M_1=5$, respectively. The results are shown for rigid-rigid as well as lower-rigid and upper-free boundaries. We note that an increase in M_1 and M_3 is to hasten, while an increase in Bi is to delay the onset of ferroconvection. Moreover, R_c is found to be independent of M_3 when $\mathrm{Bi}=0$. In other words, the nonlinearity of magnetization (i.e., M_3) has no influence on the onset of ferroconvection if the boundaries are insulated to temperature perturbations. Besides, the critical Rayleigh numbers of rigid-rigid and rigid-free boundaries become closer as the value of M_1 increases. As expected on physical grounds, the critical Rayleigh numbers for rigid-rigid boundaries are found to be greater than those of rigid-free boundaries.

The complementary effects of the buoyancy and the magnetic forces are made clear in Fig. 3 by displaying the loci of R_c and Rm_c, where $Rm(=RM_1)$ is the magnetic Rayleigh number, for different values of M_3 when $\mathrm{Bi}=2$ for both types of velocity boundary conditions. It is seen that R_c is inversely proportional to Rm_c. As $M_3\to\infty$, irrespective of the boundaries considered, the data fit the following relation exactly:

$$\frac{R_c}{R_{c0}} + \frac{Rm_c}{Rm_{c0}} = 1 \tag{15}$$

where R_{c0} is the critical Rayleigh number in the nonmagnetic case ($Rm=0$) and Rm_{c0} is the critical magnetic Rayleigh number in the nongravitational case ($R=0$).

Figures 4 and 5 illustrate the variation of a_c as a function of Bi for different boundary conditions and also for different values of M_1 and M_3. From these two figures, it is evident that increase in M_1 is to decrease a_c and thus its effect is to increase the size of convection cells (see Fig. 4). Whereas, an increase in Bi and M_3 is

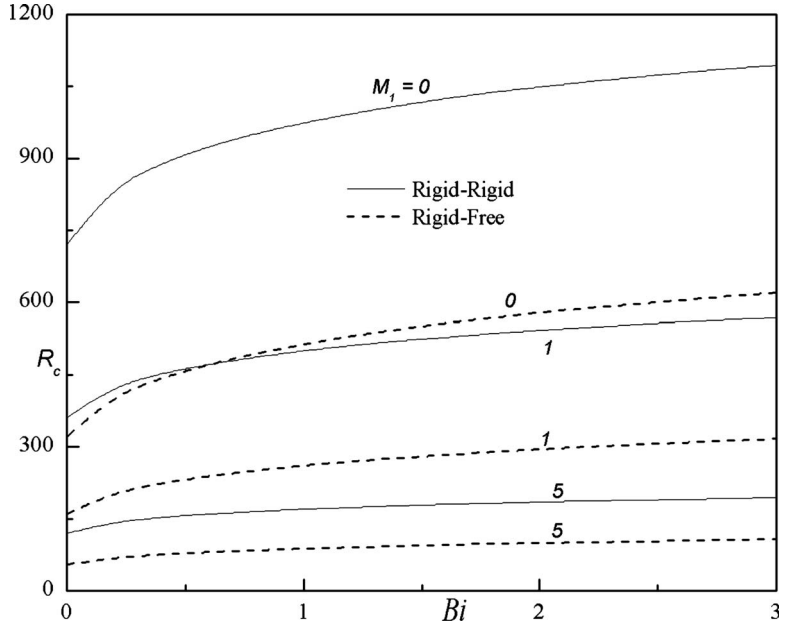

Fig. 1 Variation of R_c as a function of Bi when $M_3=1$

to increase a_c indicating that their effect is to reduce the dimension of convection cells (see Fig. 5). Further, the critical wave numbers for rigid-rigid boundaries are higher than those of rigid-free boundaries.

Since the critical wave number is negligibly small when the boundaries are insulated to temperature perturbations (i.e., $D\Theta = 0$ at $z=0,1$), the eigenvalue problem is also solved analytically using the regular perturbation technique with wave number a as a perturbation parameter. Accordingly, W, Θ, and Φ are expanded in powers of a^2 as

$$(W,\Theta,\Phi) = (W_0,\Theta_0,\Phi_0) + a^2(W_1,\Theta_1,\Phi_1) + \cdots \tag{16}$$

Equation (16) is substituted into Eqs. (5)–(7) as well as in the boundary conditions, and the terms of different orders are collected and solved. The solution to the zeroth order equations for rigid-rigid and rigid-free boundaries is found to be

$$W_0 = 0, \quad \Theta_0 = 1, \quad \text{and } \Phi_0 = 0 \tag{17}$$

The solution for velocity at the first order for rigid-rigid and rigid-free boundary conditions is then found as follows:

$$W_1 = \mathrm{R}(1 + M_1)(z^4 - 2z^3 + z^2)/24 \tag{18}$$

$$W_1 = \mathrm{R}(1 + M_1)(z^4 - 5z^3/2 + 3z^2/2)/24 \tag{19}$$

An expression for the critical Rayleigh number for rigid-rigid and rigid-free boundary conditions is obtained from the solvability condition

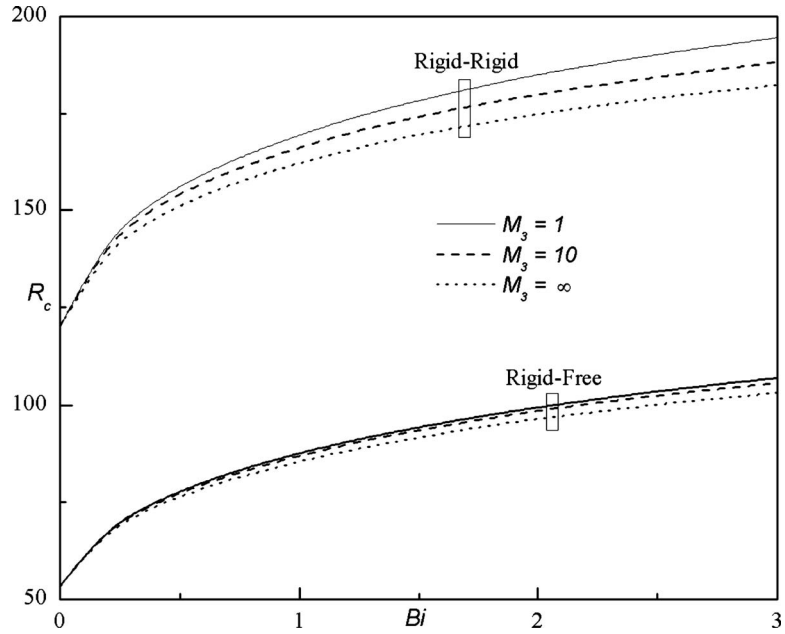

Fig. 2 Variation of R_c as a function of Bi when $M_1=5$

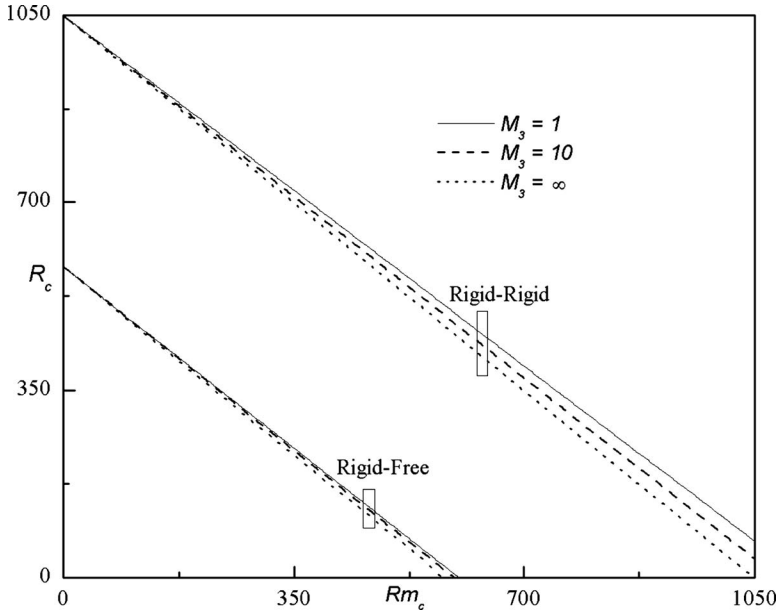

Fig. 3 Variation of R_c as a function of Rm_c when Bi=2

$$1 = \int_0^1 W_1 dz \tag{20}$$

in the forms

$$R_c = 720/(1 + M_1) \tag{21}$$

and

$$R_c = 320/(1 + M_1) \tag{22}$$

respectively. When $M_1=0$, Eqs. (21) and (22), respectively, reduce to $R_c=720$ and $R_c=320$, which are the known exact values for an ordinary viscous fluid layer [10]. From Eqs. (21) and (22), it is further observed that the critical Rayleigh numbers are independent of M_3 and thus corroborate the numerically obtained results in the previous section, but inversely proportional to M_1. It is important to note here that the results obtained from the simple regular perturbation technique coincide exactly with those obtained from time consuming numerical methods and thus provide a justification for the analytically obtained results for the prescribed heat flux conditions (i.e., Bi=0) at the boundaries.

5 Conclusions

From the foregoing study, it is observed that an increase in the values of M_1 and M_3 is to destabilize, while an increase in Bi is to stabilize the ferrofluid motion against convection. The nonlinearity of fluid magnetization has no influence on the onset of ferroconvection if the boundaries of the ferrofluid layer are insulated to temperature perturbations. Further, an increase in M_1, and a decrease in Bi and M_3 are to decrease the critical wave number.

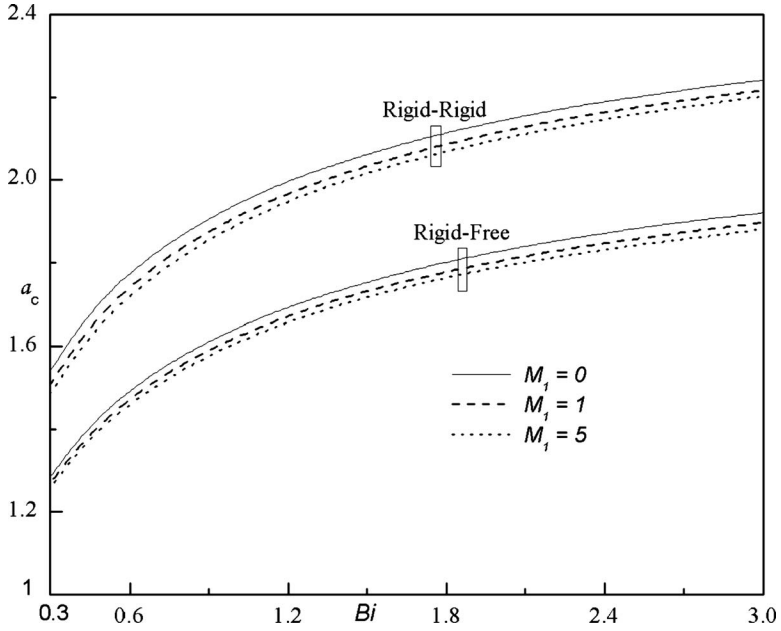

Fig. 4 Variation of a_c as a function of Bi when M_3=1

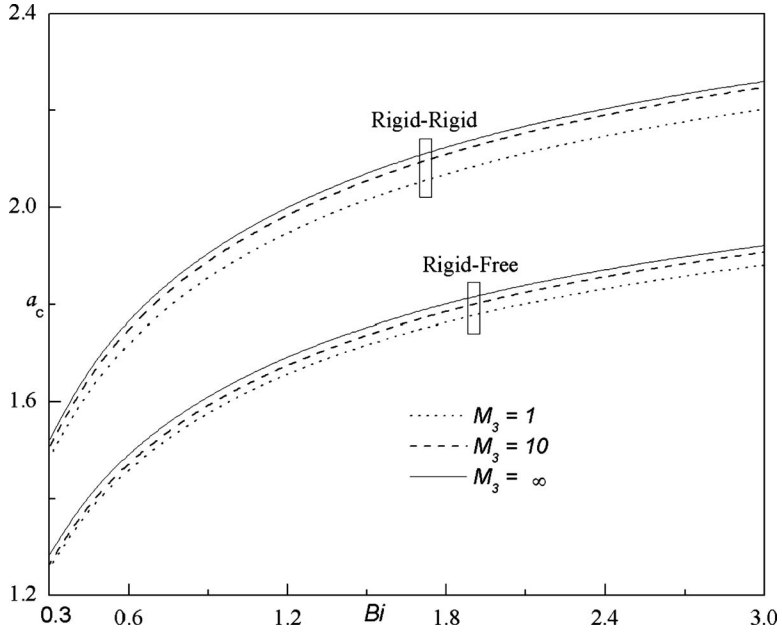

Fig. 5 Variation of a_c as a function of Bi when $M_1 = 5$

Also, $(R_c \text{ and } a_c)_{\text{rigid–rigid}} > (R_c \text{ and } a_c)_{\text{rigid–free}}$. The numerically and analytically obtained results complement each other for the case of insulated boundaries.

Acknowledgment

This work was supported by the UGC-Centre for Advanced Studies in Fluid Mechanics, Bangalore. We thank the reviewers for their useful comments.

References

[1] Rosensweig, R. E., 1985, *Ferrohydrodynamics*, Cambridge University Press, Cambridge, London.
[2] Berkovsky, B. M., Medvedev, V. F., and Krakov, M. S., 1973, *Magnetic Fluids, Engineering Applications*, Oxford University Press, New York.
[3] Bashtovoy, V. G., Berkovsky, B. N., and Vislovich, A. N., 1988, *Introduction to Thermo-Mechanics of Magnetic Fluids*, Hemisphere, Washington, DC.
[4] Finlayson, B. A., 1970, "Convective Instability in Magnetic Fluids," J. Fluid Mech., **40**, pp. 753–767.
[5] Lalas, D. P., and Carmi, S., 1971, "Thermoconvective Stability of Ferrofluids," Phys. Fluids, **4**, pp. 436–437.
[6] Shliomis, M. I., 1974, "Magnetic Fluids," Sov. Phys. JETP, **17**, pp. 153–169.
[7] Gotoh, K., and Yamada, M., 1982, "Thermal Convection in a Horizontal Layer of Magnetic Fluids," J. Phys. Soc. Jpn., **51**, pp. 3042–3048.
[8] Schwab, L., Hildebrandt, U., and Stierstadt, K., 1987, "Magnetic Benard Convection," J. Magn. Magn. Mater., **65**, pp. 315–319.
[9] Kaloni, P. N., and Lou, J. X., 2004, "Convective Instability of Magnetic Fluids," Phys. Rev. E, **70**, pp. 026313.
[10] Sparrow, E. M., Goldstein, R. J., and Jonsson, U. K., 1964, "Thermal Instability in a Horizontal Fluid Layer: Effect of Boundary Conditions and Non-Linear Temperature Profile," J. Fluid Mech., **18**, pp. 513–528.

Modeling the Natural Convection Heat Transfer and Dryout Heat Flux in a Porous Debris Bed

R. Sinha
Graduate Student
Department of Mechanical Engineering,
S.P. College of Engineering,
Mumbai 400058, India

A. K. Nayak
Reactor Engineering Division,
Bhabha Atomic Research Centre,
Trombay, Mumbai 400085, India
e-mail: arunths@barc.gov.in

B. R. Sehgal
Nuclear Power Safety Division,
Royal Institute of Technology,
Stockholm SE-10044, Sweden

An empirical model for natural convection heat transfer for film-boiling condition has been developed for volumetrically heated particulate debris beds when flooded with water at the top of the bed. The model has been derived from the quenching data generated in the POMECO facility located at KTH, Stockholm. A dryout model is also developed for countercurrent flooding limiting condition when the heat generating saturated debris bed is flooded with water from the top. The model is in good agreement with the experimental data over a wide range of particle size and porosity as compared to the existing models. The implication of the models with respect to quenching of porous debris bed formed during postulated severe accident condition is discussed.
[DOI: 10.1115/1.2952756]

Keywords: natural convection, boiling, quenching, debris bed, severe accident, nuclear reactor, dryout heat flux

1 Introduction

During a postulated severe accident in a nuclear power plant, the core melt can fail the reactor vessel and relocate into the containment. In the Swedish boiling water reactors (BWRs) and the Westinghouse pressurized water reactors (PWRs), the vessel cavity is flooded with water before the vessel failure, resulting in formation of a particulate debris bed on the cavity floor due to the melt breakup in water. If no more water is available, the existing water will evaporate in time resulting in a dry particulate bed, which still generates decay heat. The coolability of the debris bed on the containment floor is essential to prevent the failure of the penetrations in the floor and the eventual failure of the basemat, which can cause radioactivity release and land contamination.

A convenient accident management scheme to cool the debris bed is to flood the bed with water from top of it. The cooling of debris bed may proceed by heat transfer from the heat generating particles to the overlying water by conduction, single-phase convection, and boiling. As long as cooling is adequate to remove the heat from all portions of the debris bed, the temperature in the debris remains stabilized or keeps on reducing. In this condition, due to the high temperature difference between the particles and the surrounding fluid, film boiling prevails and the rate of heat removal is limited by the corresponding heat transfer behavior in the debris bed. Once the temperature falls to a low value, nucleate boiling is initiated and the heat is removed at a much faster rate than that in film-boiling condition. In view of this, the most important phenomenon to be considered in order to quantify the coolability of the debris bed is that occurring at film-boiling condition. However, if the heat generation rate is sufficiently high, a point is reached where the boiling process and associated convection can no longer carry away all the heat generated in the bed and the bed begins to dry out.

In the analysis of postaccident heat removal, it is important to know whether porous bed can be adequately cooled by natural convection of boiling water. Hardee and Nilson [1] proposed a model for conduction and single-phase convection heat transfer characteristics of fluid saturated porous media for the case of uniform internal heat generation with cooling from the top. However, to the authors' knowledge, there are almost no models available in literature on convective film-boiling heat transfer in porous debris bed with heat generation and flooded from the top. In this paper, an effort has been made to develop a model for natural convection heat transfer for film boiling from the quenching characteristics of a volumetrically heated homogeneous particulate bed with top flooding. For this, the quenching test data obtained from the POMECO facility [2] were used. From the experimental data, an empirical model was developed for the calculation of local heat transfer coefficient in terms of Rayleigh number and Nusselt number applicable to particulate debris bed.

As said before, the most important physical phenomenon in the particulate debris bed is the prediction of limiting heat flux above which local dryout can occur, leading to remelting of the debris. Such a process can occur when vapor bubbles leaving the top surface of the bed do not allow the counterflow of the cold liquid, which is necessary to quench the bed. In this paper, a dryout model has been developed from the countercurrent flooding limitation criteria. The model was compared to the existing models for dryout in particulate debris bed with top flooding condition. The proposed model compares well with the experimental data for a wide range of particle sizes and porosities relevant to the conditions of light water reactors (LWRs).

2 Physical Model and Equations

2.1 Natural Convection Model. The model has been developed from the measured data in the POMECO facility. A detailed description of the POMECO facility is given in Ref. [2] and hence will not be discussed here. Only a brief description of the facility is given below.

2.1.1 POMECO Experiment. To simulate the corium debris bed formed in a LWR during a postulated severe accident, experiments were conducted with sand having a particle size of 0–2 mm (mean size of 0.2 mm) and a porosity of 0.4, which is closer to the actual debris formed in a nuclear reactor accident [3]. The sand bed was located in a rectangular test section with dimension $350\times350\times450$ mm^3. The test section was flooded with water from the top by keeping the water in an upper tank just above the test section. The dimension of the upper tank is $350\times350\times900$ mm^3. The bed was heated almost uniformly by employing electrical heaters. After the bed was heated to an average temperature of approximately 450 °C, water at a temperature of around 90 °C was added to the top of the bed. The height of the water column above the bed was nearly 0.5 m, which was kept constant throughout the test. The power input to the bed was 4.6 kW. The radial and axial temperature distributions in the bed were measured by 33 K type thermocouples.

Figure 1 shows a typical temperature distribution in the bed when the bed is flooded from the top. The top of the bed is

Contributed by the Heat Transfer Division of ASME for publication in the JOURNAL OF HEAT TRANSFER. Manuscript received April 9, 2007; final manuscript received March 28, 2008; published online August 7, 2008. Review conducted by Raj M. Manglik.

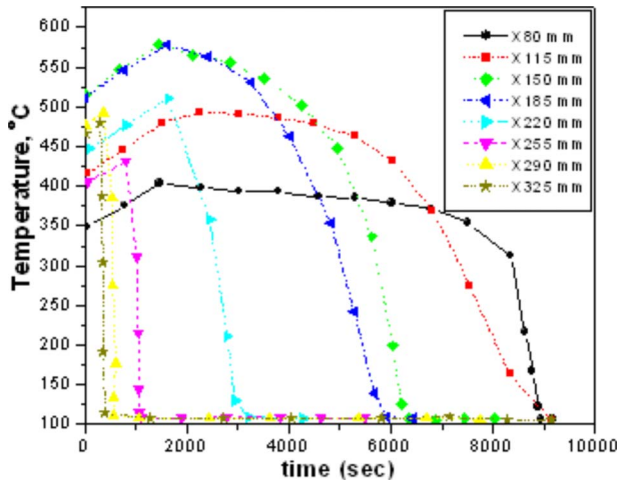

Fig. 1 Temperature distribution in the porous debris bed during the quenching test

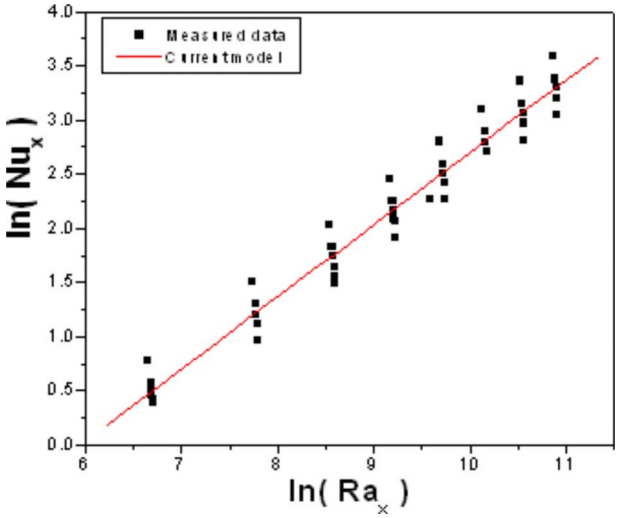

Fig. 2 Relationship between Nu_x versus Ra_x for film boiling in porous debris bed

quenched first and the quench front propagates from the top to the bottom of the bed as observed from the temperature distribution in the figure.

2.1.2 Model Development. The fluid flow and heat transfer characteristics of a heat generating porous medium are strongly dependent on conditions at the boundaries of the region. Since the wall would be cooler than the bed, a descending boundary layer flow can develop at the walls. If the walls of the containing vessel have negligible thermal mass and conductivity, they can be treated as adiabatic surfaces, and the balance between buoyant and viscous forces determines the onset of convection

The local Rayleigh number [4], which characterizes the relative magnitude of buoyant forces and viscous forces, is defined as follows:

$$\mathrm{Ra}_x = \frac{[\rho g \beta X \kappa (QX^2/K_m)]}{\mu \alpha_m} \tag{1}$$

The local Nusselt number [4] for the particulate bed is defined as

$$\mathrm{Nu}_x = \frac{QX^2}{[K_m(T_s - T_\infty)]} \tag{2}$$

In the above definitions, Q is the heat generation rate per unit volume of the sand bed. For the porous debris bed formed in the severe nuclear reactor accident,

$$Q = Q_V(1-\varepsilon) \tag{3}$$

The physical properties in the particulate bed are calculated as follows.

In the absence of measured data, the thermal conductivity, K_m, is calculated by mixing rule as [4]

$$K_m = [(\varepsilon K_f) + (1-\varepsilon)K_s] \tag{4}$$

As the thermal conductivity of particle bed is very low, the error caused by the difference between the measured and calculated thermal conductivities can be ignored.

The permeability, κ, is calculated directly using the Kozeny–Carmen equation [5], as follows:

$$\kappa = \frac{d^2\varepsilon^3}{[180(1-\varepsilon)^2]} \tag{5}$$

The thermal diffusivity, α_m, of the porous bed was calculated from mixing rule by the following equation:

$$\alpha_m = \frac{K_m}{[\varepsilon(\rho C_p)_f + (1-\varepsilon)(\rho C_p)_s]} \tag{6}$$

From the general correlation between the Nusselt number (Nu) and the Rayleigh number (Ra),

$$\mathrm{Nu} = c\mathrm{Ra}^n$$

where c is the constant coefficient and n is the constant exponent in the equation.

From the temperature distribution in the bed during the quenching process, the local Rayleigh and local Nusselt numbers were calculated from quasisteady temperature data in the film-boiling region. The local Rayleigh number and the local Nusselt number so obtained from the test data are plotted in Fig. 2. From best fitting of 51 data points by linear regression, the following relationship is obtained:

$$\mathrm{Nu}_x = 0.0189\mathrm{Ra}_x^{0.667} \tag{7}$$

2.2 Dryout Heat Flux Model. A state-of-the-art review of the coolability of particulate debris bed has been provided recently by Bürger and Berthoud [6]. They have highlighted the discrepancies of current models to capture the complex dryout phenomena in particulate debris bed.

In this work, the dryout model is developed on the basis of the countercurrent flooding condition criteria. In the flooding model, the liquid-vapor counterflow is limited by the drag between the liquid and the vapor. For the flooding limit of steam flowing upward and water downward, the Wallis model [7] can be used as

$$(J_v^*)^{1/2} + (mJ_l^*)^{1/2} = C \tag{8}$$

In Eq. (8) m and C are the constants. For relatively larger diameter particles ($d > 1$ mm), for which both the liquid and the vapor flow are turbulent, constant m in Wallis model can be taken as 1 [7]. So Eq. (8) reduces to

$$(J_v^*)^{1/2} + (J_l^*)^{1/2} = C \tag{9}$$

expressing J_v^* and J_l^* as

$$J_v^* = J_v[\rho_v/gD(\rho_l - \rho_v)\varepsilon^2]^{1/2} \tag{10}$$

and

$$J_l^* = J_l[\rho_l/gD(\rho_l - \rho_v)\varepsilon^2]^{1/2} \tag{11}$$

The effect of surface tension is assumed negligible since the heat flux is assumed to vary with the one-eighth of the surface tension.

In steady state evaporation, the mass flow rate for inflowing liquid prior to dryout must equal the rate at which vapor leaves the surface. For relatively larger particles for which flooding is applicable, the equation of continuity is

$$\rho_v J_v = \rho_l J_l \tag{12}$$

Equations (9)–(12) can be combined to yield the vapor flux at flooding condition as

$$J_{v,f} = \frac{C^2[gD\varepsilon^2(\rho_l - \rho_v)/\rho_v]^{1/2}}{[1 + (\rho_v/\rho_l)^{1/4}]^2} \tag{13}$$

Since the vapor flux is maximum at the top of the bed, the dryout heat flux at the top of the bed, q_d, is given by

$$q_d = \rho_v h_{lv} J_{v,f} \tag{14}$$

where h_{lv} is the latent heat of vaporization of liquid. The value of D depends on how tightly packed the bed is; however, the tightness of the packed bed depends on the ratio of the flow volume to the particle surface area, which can be expressed as

$$D = \frac{\varepsilon}{(1-\varepsilon)s} \tag{15}$$

For the case of particles of uniform spheres of diameter d, the specific surface s can be expressed as the particle surface area to the volume ratio. For the spherical particle of radius r,

$$s = \frac{4\pi r^2}{\frac{4}{3}\pi r^3} = \frac{3}{r} = \frac{6}{d}$$

For irregularity of the shape, the average diameter (d_{av}) is multiplied by a shape factor (Ω), as given in Ref. [8].

Hence, the dryout heat flux can be expressed as

$$q_d = \frac{C^2 h_{lv}[g\varepsilon^3(\rho_l - \rho_v)\rho_v/s(1-\varepsilon)]^{1/2}}{[1 + (\rho_v/\rho_l)^{1/4}]^2} \tag{16}$$

For the commonly used conditions for a system pressure of 1 bar and the expected particulate debris during severe accident in a nuclear power plant, a mean porosity ε of about 0.39 may be assumed. For relatively large particles, the dryout heat flux varies with square root of particle diameter.

From the dryout heat flux data of various authors [9–14], the coefficient C in Eq. (16) has been evaluated considering the variation of dryout heat flux versus the particle diameter and porosity using a linear regression analysis. The constant C so obtained is 1.149 and the dryout heat flux is given by

$$q_d = 0.539 h_{lv} \frac{[(\rho_l - \rho_v)\rho_v g d\varepsilon^3/(1-\varepsilon)]^{1/2}}{[1 + (\rho_v/\rho_l)^{1/4}]^2} \tag{17}$$

3 Discussions and Concluding Remarks

This paper contains development of models for boiling natural convection in a porous particulate bed and dryout heat flux. The models have been developed from quenching and dryout data applicable to nuclear reactors in a low probable severe accident condition.

3.1 Natural Convection Model. In the analysis of postaccident heat removal, it is important to know whether the bed can be adequately cooled by natural convection of coolant liquid. The natural convection model, Eq. (7), can be used to estimate the film-boiling heat transfer coefficient during the debris bed cooling at any location of the debris bed formed during severe accident condition. Due to the complex quenching behavior of the debris bed, the data obtained from quenching tests were scattered (Fig. 1) and the model so generated using these data predicted with a standard deviation of ~18% and a regression factor (R)=0.984 (Fig. 2). Considering the complexity in the thermal hydraulics involved in the severe accident phenomena, the correlation currently developed can be used to compute the heat removal rate by natural convection with reasonable accuracy.

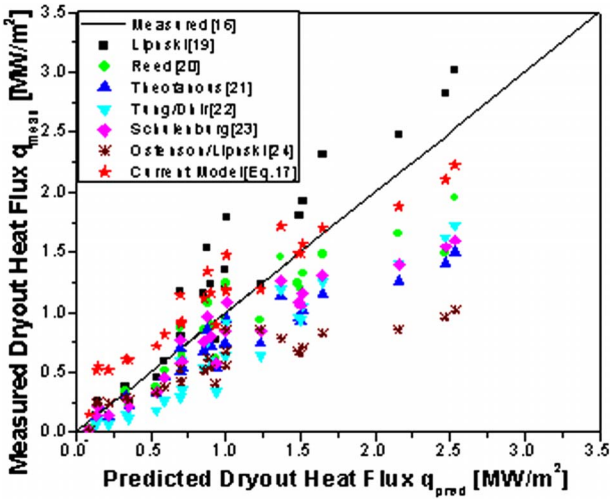

Fig. 3 Comparison of different models for dryout heat flux in porous debris bed

3.2 Dryout Heat Flux Model. The summary of some previous experiments investigating the dryout heat fluxes in particle beds with top flooding conditions is detailed in literature [15]. Several models are available in literature for the prediction of dryout heat flux [16]. The prediction of Eq. (17) and other classical models are compared with the dryout measurements of Refs. [9–14,17,18] in Fig. 3. Because of the large number of independent variables (diameter, porosity, and material properties), the data are plotted in terms of predicted versus measured dryout flux. A comparison among the predictions due to these models shows large-scale differences (Fig. 3) among them [19].

The dependence of dryout heat flux on particle size and porosity measured by various authors for a system pressure of 1 bar is shown in Fig. 4. In general, it can be seen that the different experiments yield some spread in the published data. This is due to the different experimental sets and measurement procedures [20]. A general statement on the validity of the models only based on these values is not possible. However, the tendency to predict

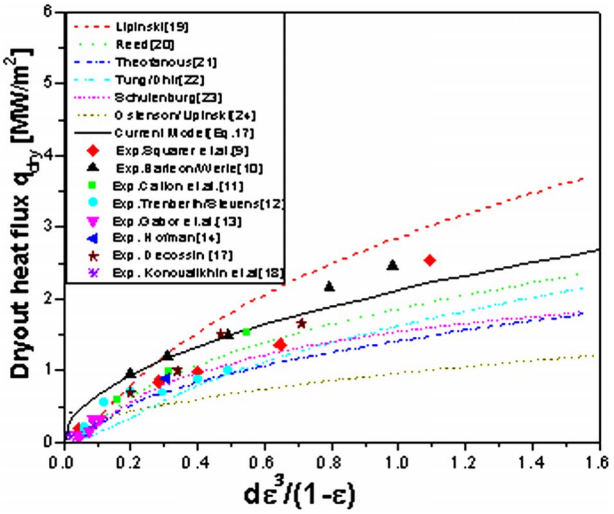

Fig. 4 Dependence of dryout heat flux with particle size and bed porosity

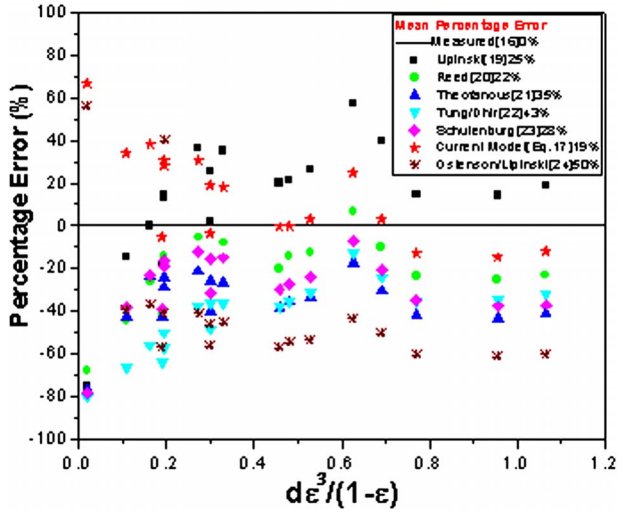

Fig. 5 Percentage error of different models versus particle size and bed porosity

lower dryout heat flux than the measured ones with increasing diameter and porosity can be seen in the classical models from Lipinski over Reed to Theofanous. For large diameter particles, classical Lipinski model predicts higher dryout heat flux than the experimental data. However, other classical models predict lower dryout heat flux than the experimental data for larger size particles [21]. The gross higher or lower predictions (as compared with the experimental data) by the established models of the dryout flux for the large particles are expected to be even worse as the particle diameter increases [22–24]. To further assess the applicability of these models, the errors between the measured and predicted values of these models have been calculated and are shown in Fig. 5. A mean percentage error has also been calculated as

$$\%\text{mean error} = \frac{\sum_{i=1}^{N} (q_{m,i} - q_{p,i})/q_{m,i}}{N} \times 100$$

where $q_{m,i}$ and $q_{p,i}$ are the measured and predicted dryout fluxes, respectively, and N is the number of points. For the current, Lipinski, Reed, Theofanous, Tung/Dhir, Schulenberg, and Ostenson/Lipinski models, the mean percentage errors are found to be nearly 19.0, 25.0, 22.0, 35.0, 43.0, 28.0, and 50.0, respectively, considering 18 experimental data (Fig. 5).

Such a large nonconservatism is not desirable in nuclear reactor safety assessment, and useful consideration of the appropriate model should be made for the particle diameters in excess of ~1 mm. In this perspective, the present dryout model, Eq. (17), is found to be closer to the measured values as compared with others and applicable for a wide range of particle diameter and porosity of the debris bed.

Nomenclature

C_p = specific heat (J/kg K)
d = particle diameter (m)
g = acceleration due to gravity (m/s^2)
h_{lv} = latent heat of vaporization of water (J/kg)
J_v^* = dimensionless superficial velocity of vapor
J_l^* = dimensionless superficial velocity of liquid
J_v = upward vapor flux (m/s)
J_l = downward liquid flux (m/s)
$J_{v,f}$ = vapor flux at flooding condition (m/s)
K = thermal conductivity (W/m K)
Nu_x = local Nusselt number
Q_V = heat generation rate per unit volume in the solid fraction (W/m^3)
Q = heat generation rate per unit volume of the bed (W/m^3)
q_d = dryout heat flux (W/m^2)
Ra_x = local Rayleigh number
T_∞ = fluid temperature (°C)
T_s = surface temperature (°C)
X = distance from the bottom of the bed (m)

Greek Symbols

α = thermal diffusivity (m^2/s)
β = thermal expansion coefficient of the fluid (K^{-1})
ε = porosity
κ = permeability (m^2)
μ = dynamic viscosity (N s/m^2)
ρ = density (kg/m^3)

Subscripts

f = fluid
m = medium (sand bed)
l = liquid
s = sand (surface)
v = vapor

References

[1] Hardee, H. C., and Nilson, R. H., 1977, "Natural Convection in Porous Media With Heat Generation," Nucl. Sci. Eng., **63**, pp. 119–132.
[2] Sehgal, B. R., Konovalikhin, M. J., Yang, Z. L., Kazachkov, I. V., Amjad, M., and Li, G. J., 2001 "Experimental Investigation on Porous Media Coolability: KTH Report," Division of Nuclear Power Safety, Royal Institute of Technology.
[3] Nayak, A. K., Sehgal, B. R., and Stepanayan, A., 2006, "An Experimental Study on Quenching of a Radially Stratified Heated Porous Bed," Nucl. Eng. Des., **236**, pp. 2189–2198.
[4] Kakac, S., Aung, W., and Viskanta, R., 1985, *Natural Convection Fundamentals and Applications*, Hemisphere, Washington, DC, pp. 500–511.
[5] Bau, H., and Torrance, K. E., 1982, "Boiling in Low Permeability Porous Materials," Int. J. Heat Mass Transfer, **25**, pp. 45–55.
[6] Bürger, M., and Berthoud, G., 2006, "Basic Laws and Coolability of Particulate Debris: Comments on the Status and Present Contributions," Nucl. Eng. Des., **236**, pp. 2049–2059.
[7] Wallis, J. B., 1969, *One Dimensional Two Phase Flow*, McGraw-Hill, New York, pp. 336–340.
[8] Gorham-Bergeron, E., 1983, "Remaining Uncertainties in Predicting the Coolability Limits of a Degraded Reactor Core," *Proceedings of the International Meeting of Light Water Reactor Severe Accident Evaluation*, Cambridge, MA, Aug. 28–Sept. 1.
[9] Squarer, D., Pieczynski, A. T., and Hochreiter, L. E., 1982, "Effect of Debris Bed Pressure, Particle Size and Distribution on Degraded Nuclear Reactor Core Coolant," Nucl. Sci. Eng., **80**, pp. 2–13.
[10] Barleon, L., and Werle, H., 1981, "Dependence of Dryout Heat Flux on Particle Diameter for Volume and Bottom-Heated Debris Beds," Kernforschungszentrum, Technical Report No. KfK-3138.
[11] Catton, I., Dhir, V. K., and Somerton, C. W., 1983, "An Experimental Study of Debris Bed Coolability Under Pool Boiling Conditions," University of California, Technical Report.
[12] Trenberth, R., and Stevens, G. F., 1980, "An Experimental Study of Boiling Heat Transfer and Dryout in Heated Particulated Beds," Winfrith, Technical Report No. UKAEA.
[13] Gabor, J. D., 1980, "Status Report on Limiting Heat Fluxes in Debris Beds," Argonne National Laboratory, Technical Report No. ANL/RAS 80-21.
[14] Hofmann, G., 1984, "On the Location and Mechanisms of Dryout in Top-Fed and Bottom-Fed Particulate Beds," Nucl. Technol., **65**, pp. 36–45.
[15] Lindholm, I., Holmström, S., Miettinen, J., Lestinen, V., Hyvärinen, J., Pankakoski, P., and Sjövall, H., 2006, "Dryout Heat Flux Experiments With Deep Heterogeneous Particle Bed," Nucl. Eng. Des., **236**, pp. 2060–2074.
[16] Schmidt, W., 2004, "Influence of Multidimensionality and Interfacial Friction on the Coolability of Fragmented Corium," Ph.D. thesis, University of Stuttgart, Stuttgart.
[17] Décossin, É., 1999, "Numerical Investigation on Particulate Debris Bed Coolability: Critical Analysis of the Silfide Experimental Project," *Proceedings: The Ninth International Topical Meeting on Nuclear Reactor Thermal Hydraulics (NURETH-9)*, San Francisco, CA, Oct. 3–8.
[18] Konovalikhin, M. J., Yang, Z. L., Amjad, M., and Sehgal, B. R., 2000, "On Dryout Heat Flux of a Particles Debris Bed With a Downcomer," Technical Report No. ICONE-8.
[19] Lipinski, R. J., 1984, "A Coolability Model for Post Accident Nuclear Reactor

Debris," Nucl. Technol., **65**, pp. 53–66.
[20] Reed, A. W., 1982, "The Effect of Channeling on the Dryout of Heated Particulate Beds Immersed in a Liquid Pool," Ph.D. thesis, Massachusetts Institute of Technology, Cambridge, MA.
[21] Hu, K., and Theofanous, T. G., 1991, "On the Measurement and Mechanism of Dryout in Volumetrically Heated Coarse Particle Beds," Int. J. Multiphase Flow, **17**, pp. 519–532.
[22] Tung, V. X., and Dhir, V. K., 1988, "A Hydrodynamic Model for Two-Phase Flow Through Porous Media," Int. J. Multiphase Flow, **14**, pp. 47–65.
[23] Schulenberg, T., and Müller, U., 1986, "A Refined Model for the Coolability of Core Debris With Flow Entry From the Bottom," *Proceedings of the Sixth Information Exchange Meeting on Debris Coolability*, University of California, Los Angeles, Mar., Paper No. EPRI NP-4455.
[24] Ostenson, R. W., and Lipinski, R. J., 1981, "A Particle Bed Dryout Model Based on Flooding," Nucl. Sci. Eng., **79**, pp. 110–140.

Soret and Dufour Effects on Free Convection Heat and Mass Transfer From a Horizontal Flat Plate in a Darcy Porous Medium

P. A. Lakshmi Narayana

P. V. S. N. Murthy[1]
e-mail: pvsnm@maths.iitkgp.ernet.in

Department of Mathematics,
Indian Institute of Technology, Kharagpur,
Kharagpur, 721 302 West Bengal, India

The effect of Soret and Dufour parameters on free convection from a horizontal flat plate in a Darcian fluid saturated porous medium is analyzed using the similarity solution technique. With constant wall temperature and concentration, the similarity solution is possible even when Soret and Dufour effects are considered in the medium. The transformed coupled systems of ordinary differential equations involve parameters such as the buoyancy ratio parameter N and diffusivity ratio Le in addition to the Soret Sr and Dufour Df parameters. The effect of all these parameters on the convective transport has been analyzed, and the variation of heat and mass transfer coefficients with Dufour and Soret parameters is presented through computer generated graphs.
[DOI: 10.1115/1.2789716]

Keywords: free convection, heat transfer, mass transfer, boundary layer, Soret effect, Dufour effect, Darcy porous media

Introduction

Coupled heat and mass transfer phenomenon in porous media is gaining attention due to its interesting applications. The flow phenomenon in this case is relatively more complex than that in the pure thermal/solutal convection process. Processes involving heat and mass transfer in porous media are often encountered in the chemical industry, in reservoir engineering in connection with thermal recovery process, and in the study of the dynamics of hot and salty springs of a sea. Underground spreading of chemical waste and other pollutants, grain storage, evaporation cooling, and solidification are few other application areas where combined thermosolutal convection in porous media can be observed. Due to the coupling of temperature and concentration, new parameters such as buoyancy ratio and Lewis number (diffusion ratio) arise, and they influence the convective transport to a greater extent. Bansod [1] analyzed the coupled heat and mass transfer from a horizontal flat surface immersed in a Darcy porous medium under boundary layer assumptions. A review of both natural and mixed convection boundary layer flows in Darcy fluid saturated porous media is given in Nield and Bejan [2].

In processes involving vigorous free convection heat and mass transfer in clear fluids as well as porous media, there may be augmentation of the heat transfer coefficient because of the concentration gradients and the mass transfer coefficient due to the thermal gradients. The Soret effect corresponds to species differentiation developing in an initially homogeneous mixture submitted to a thermal gradient, and Dufour effect corresponds to the diffusion of heat caused by concentration gradients. In several earlier studies, Soret and Dufour effects are neglected on the basis that they are of a smaller order of magnitude than the effects described by Fourier's and Fick's laws. These effects are considered as second order phenomena and may become significant in areas such as hydrology, petrology, geosciences, etc.

However, Eckert and Drake [3] indicated the processes where the Dufour effect becomes significant in the medium. Anghel et al. [4] analyzed both the Soret and Dufour effects on free convection boundary layer over a vertical surface embedded in a porous medium and noticed an appreciable change in the flow field. Postelnicu [5] analyzed the influence of magnetic field considering Soret and Dufour effects from a vertical surface in porous medium. Partha et al. [6] studied the effect of magnetic field and double dispersion on free convective heat and mass transport considering the Soret and Dufour effects in a non-Darcy porous medium. Recently, Postelnicu [7] analyzed the influence of chemical reaction on flow field considering Soret and Dufour effects from a vertical surface in a porous medium. The effect of Soret and Dufour parameters on free convection heat and mass transfers from a vertical surface in a doubly stratified Darcian porous medium has been reported by Lakshmi Narayana and Murthy [8]. The influence of Soret and Dufour parameters on free convective heat and mass transport from a horizontal plate in a non-Darcy porous medium has been analyzed by Murthy and Lakshmi Narayana [9] considering power law variation for the temperature and concentration at the wall.

It was reported in Postelnicu [5], Partha et al. [6], and Lakshmi Narayana and Murthy [8] that a large difference in the values of the Dufour and Soret parameters results in the change in sign of the nondimensional heat and mass transfer coefficients. For certain combinations of these parameters, heat reversal is observed inside the boundary layer region, and the heat/mass transfer coefficient has been found to be negative for some other combinations of these parameters. The objective of the present study is to investigate the presence of such peculiarities in free convection heat and mass transfers from a horizontal surface with uniform wall temperature and concentration in a fluid saturated Darcian porous media with Soret and Dufour effects.

Governing Equations

Consider the free convection heat and mass transfers from a horizontal plane surface in a fluid saturated Darcy porous medium with Soret and Dufour effects (Fig. 1). Viscous resistance due to the solid boundary is neglected under the assumption that the medium is with low permeability. The governing equations for the flow, heat and mass transfers under the boundary layer, and Boussinesq approximations are given by

$$\frac{\partial u}{\partial x}+\frac{\partial v}{\partial y}=0 \tag{1}$$

$$\frac{\partial u}{\partial y}=\frac{-Kg\beta_T}{\nu}\left(\frac{\partial T}{\partial x}+\frac{\beta_c}{\beta_T}\frac{\partial C}{\partial x}\right) \tag{2}$$

$$u\frac{\partial T}{\partial x}+v\frac{\partial T}{\partial y}=\alpha\frac{\partial^2 T}{\partial y^2}+\frac{Dk}{C_sC_p}\frac{\partial^2 C}{\partial y^2} \tag{3}$$

$$u\frac{\partial C}{\partial x}+v\frac{\partial C}{\partial y}=D\frac{\partial^2 C}{\partial y^2}+\frac{Dk}{C_sC_p}\frac{\partial^2 T}{\partial y^2} \tag{4}$$

The boundary conditions are given by

$$y=0:\ v=0 \quad T=T_w \quad C=C_w \tag{5a}$$

$$y\to\infty:\ u\to 0 \quad T=T_\infty\ (\text{const}) \quad C=C_\infty\ (\text{const}) \tag{5b}$$

Here, x and y are the Cartesian coordinates along and normal to the plate, respectively, u and v are the averaged velocity compo-

[1]Corresponding author.

Contributed by the Heat Transfer Division of ASME for publication in the JOURNAL OF HEAT TRANSFER. Manuscript received September 26, 2006; final manuscript received July 17, 2007; published online August 7, 2008. Review conducted by Jose L. Lage.

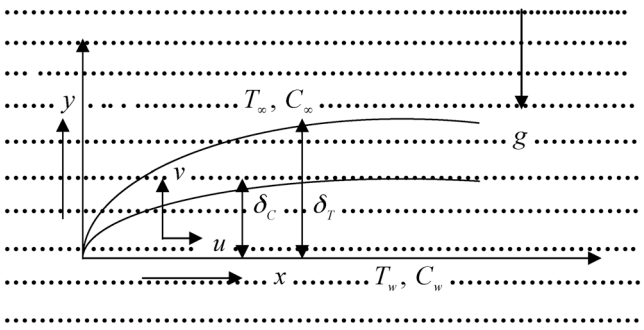

Fig. 1 Schematic of the problem

nents in x and y directions, respectively, T and C are the temperature and concentration, respectively, β_T and β_C are the coefficients of thermal and solutal expansion, respectively, ν is the kinematic viscosity of the fluid, c is the inertia coefficient, K is the permeability, g is the acceleration due to gravity, α and D are the thermal and solutal diffusivities of the medium, k is the thermal diffusion ratio, C_p is the specific heat at constant pressure, and C_s is the concentration susceptibility. The suffix ∞ indicates the conditions in the ambient medium.

Using the similarity transformation,

$$\eta = \frac{y}{x}\mathrm{Ra}_x^{1/3} \quad \psi = \alpha \mathrm{Ra}_x^{1/3} f(\eta) \quad T - T_\infty = \theta_w \theta(\eta)$$

$$C - C_\infty = \phi_w \phi(\eta) \tag{6}$$

the governing Eqs. (1)–(4) reduce to the following set of ordinary differential equations:

$$f'' = \frac{2}{3}\eta(\theta' + \phi') \tag{7}$$

$$\theta'' + \mathrm{Df}\phi'' = -\frac{1}{3} f\theta' \tag{8}$$

$$\phi'' + \mathrm{SrLe}\theta'' = -\frac{\mathrm{Le}}{3} f\phi' \tag{9}$$

the boundary conditions (Eqs. (5*a*) and (5*b*)) are transformed to

$$\eta = 0 \quad f = 0 \quad \theta = 1 \quad \phi = 1 \tag{10a}$$

$$\eta \to \infty \quad f' \to 0 \quad \theta \to 0 \quad \phi \to 0 \tag{10b}$$

Here, $\theta_w = T_w - T_\infty$, $\phi_w = C_w - C_\infty$, and $\mathrm{Ra}_x = Kg\beta_T\theta_w x/\alpha\nu$ is the Rayleigh number defined based on the thermal conditions. The parameters involved in the present study are the diffusivity ratio $\mathrm{Le} = \alpha/D$ and buoyancy ratio $N = \beta_c\phi_w/\beta_T\theta_w$ ($N > 0$ indicates aiding buoyancy where both the thermal and solutal buoyancies are in the same direction and $N < 0$ indicates opposing buoyancy where the solutal buoyancy is in the opposite direction to the thermal buoyancy). Also, $\mathrm{Df} = Dk\phi_w/C_sC_p\alpha\theta_w$ and $\mathrm{Sr} = Dk\theta_w/C_sC_p\alpha\phi_w$ are Dufour and Soret parameters. The nondimensional heat transfer coefficient (Nusselt number) and the nondimensional mass transfer coefficient (Sherwood number) are given by

$$\frac{\mathrm{Nu}_x}{\mathrm{Ra}_x^{1/3}} = -\theta'(0) \quad \text{and} \quad \frac{\mathrm{Sh}_x}{\mathrm{Ra}_x^{1/3}} = -\phi'(0)$$

Results and Discussion

The resulting ordinary differential equations (Eqs. (7)–(9)) along with the boundary conditions (Eqs. (10*a*) and (10*b*)) are integrated by giving appropriate initial guess values for $f'(0)$, $\theta'(0)$, and $\phi'(0)$ to match the solutions with the corresponding boundary conditions at $f'(\infty)$, and $\theta(\infty)$, and $\phi(\infty)$, respectively. The solution procedure is explained in Partha et al. [6] and is not repeated here for brevity. Extensive calculations have been performed to obtain the flow, temperature and concentration fields for the following range of parameters: $0 < \mathrm{Le} \leq 30$, $-0.2 \leq N \leq 1$, $0 \leq \mathrm{Sr} \leq 15$, and $0 \leq \mathrm{Df} < 0.5$. The results obtained here are accurate up to the fourth decimal place. The numerical results are analyzed and presented for aiding and opposing buoyancies in the presence and absence of the Dufour and Soret parameters in the Darcy porous media.

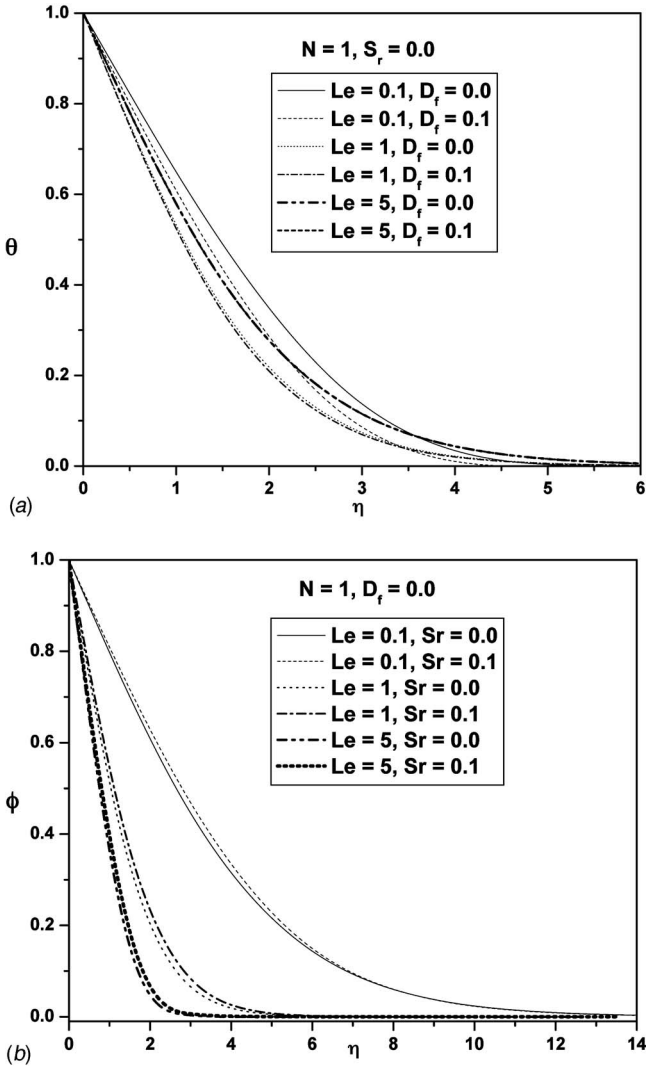

Fig. 2 (*a*) Variation of θ with η for fixed N for varying Le and Df in the absence of Sr. (*b*) Variation of ϕ with η for fixed N for varying Le and Sr in the absence of Df.

Aiding Buoyancy. The Dufour parameter Df represents the amount of heat added to the system because of the concentration gradients, and thus it will be more reasonable to discuss the variation of the temperature and nondimensional heat transfer coefficient with this parameter. The nondimensional temperature θ and concentration ϕ inside the boundary layer are plotted against η in Figs. 2(*a*) and 2(*b*) for analyzing the influence of Dufour and Soret parameters independently on the thermal and concentration fields in the Darcy porous medium. From Fig. 2(*a*), it is evident that increase in Df decreases the temperature distribution in the

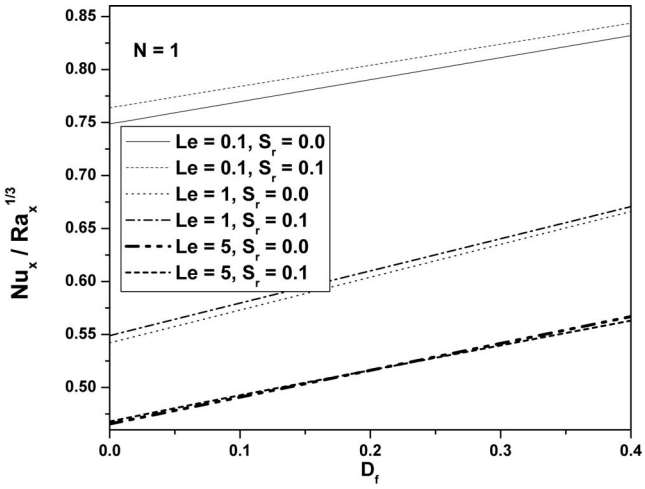

Fig. 3 Variation of nondimensional heat transfer coefficient with Df for varying Le and Sr for fixed *N*

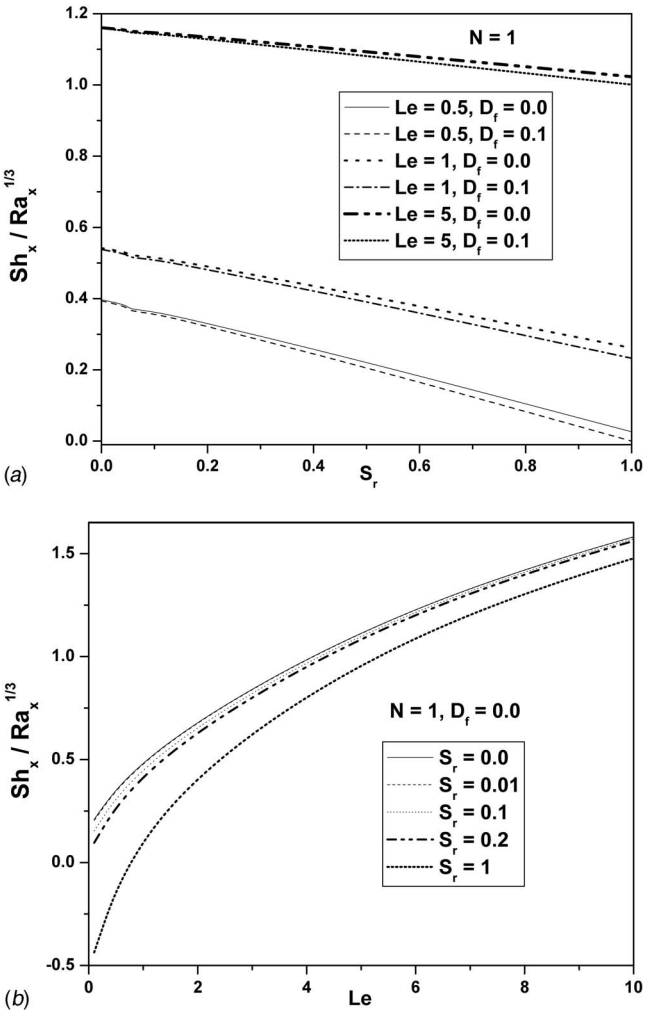

Fig. 4 (*a*) Variation of nondimensional mass transfer coefficient with Sr for varying Le and Df for fixed *N*. (*b*) Variation of nondimensional mass transfer coefficient with Le with varying Sr for fixed *N* in the absence of Df.

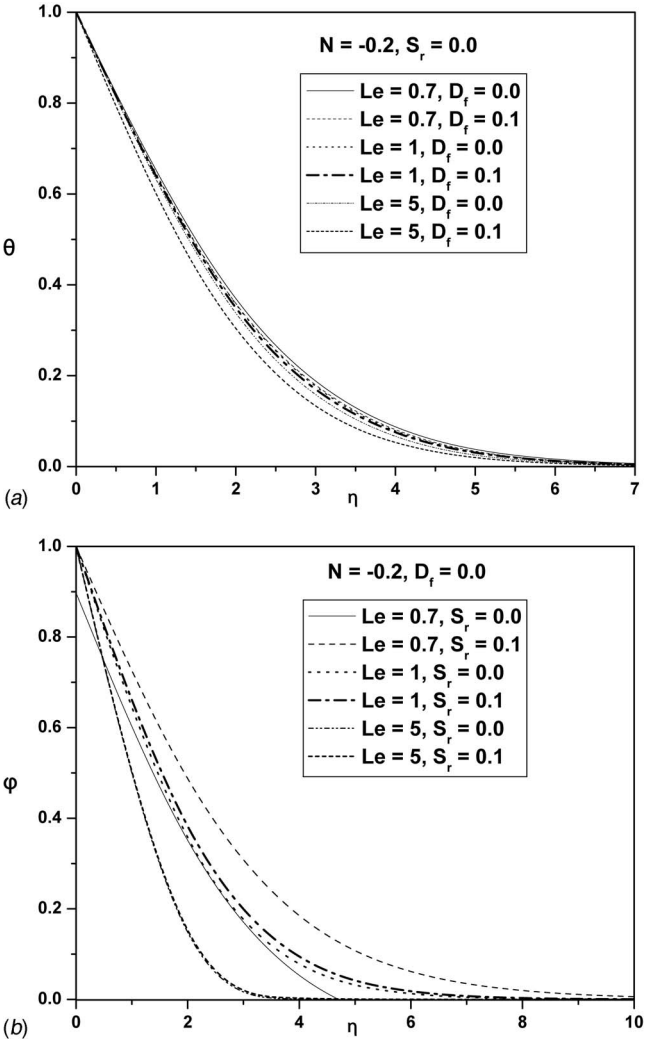

Fig. 5 (*a*) Variation of θ with η for fixed *N* for varying Le and Df in the absence of Sr. (*b*) Variation of ϕ with η for fixed *N* for varying Le and Sr in the absence of Df.

medium when Sr=0. It is also noted from the results obtained that when Df=0=Sr, as Le increases, the nondimensional temperature decreases in the medium. When Df=0 and Sr=0, as Le increases, the nondimensional concentration is found to decrease in the medium. When Df=0, the nondimensional concentration decreases with increasing values of the Lewis number, and this is evident from Fig. 2(*b*), for varying Sr. Also, it is observed that the nondimensional concentration increases with increasing values of the Soret parameter.

The Nusselt number is plotted against Df for different values of Le and Sr with fixed *N* in Fig. 3. It is clear that the Nusselt number increases linearly with Df. However, it decreases nonlinearly with increasing value of Le. The heat transfer coefficient increases as Sr increases in the medium; also, it is seen that as Le increases, the difference between the nondimensional heat transfer coefficient gets magnified with increasing value of the Sr.

The Sherwood number is plotted against the Soret parameter Sr for different values of Le, with fixed *N* and Df in Fig. 4(*a*), and against the Lewis number for different values of Sr with fixed values of *N* and Df in Fig. 4(*b*). From these figures, it is seen that the Sherwood number decreases with increasing value of the Soret parameter Sr, while it increases with Le in a nonlinear fashion, and this is seen in Fig. 4(*b*). Also, for nonzero values of the Dufour parameter, the value of the Sherwood number is less when

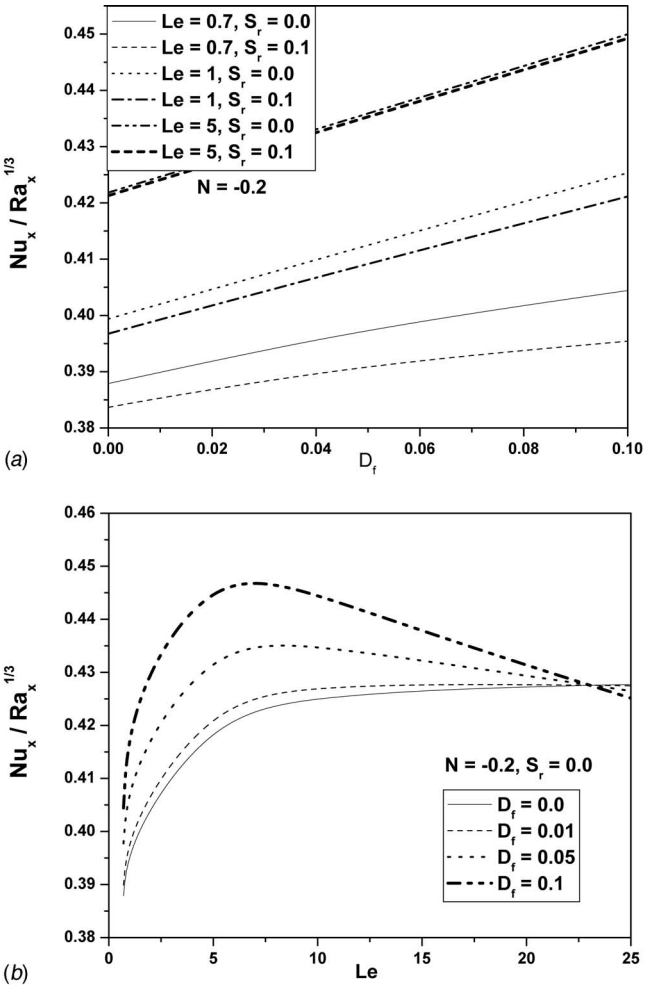

Fig. 6 (*a*) Variation of nondimensional heat transfer coefficient with Df for varying Le and Sr for fixed *N*. (*b*) Variation of nondimensional heat transfer coefficient with Le for fixed *N* with varying Df in the absence of Sr.

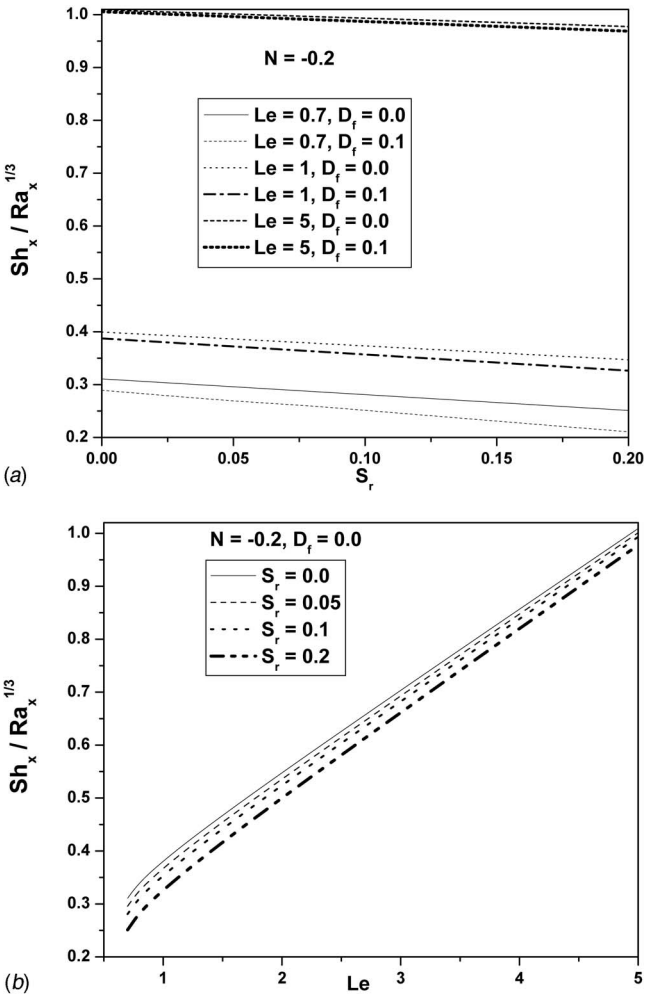

Fig. 7 (*a*) Variation of nondimensional mass transfer coefficient with Sr for varying Le and Df for fixed *N*. (*b*) Variation of nondimensional mass transfer coefficient with Le for fixed *N* with vaying Sr in the absence of Df.

Df=0 and it decreases with increasing values of Df. From Eq. (9), it is clear that Le Sr is the parameter that is responsible for the increase in the mass transfer coefficient because of thermal gradients. Thus, for large values of Le (>1), the value of the mass transfer coefficient is more as when Le is less than 1, the curves corresponding to the mass transfer coefficient lie below those of Le greater than or equal to 1. Thus, when the product Le Sr increases, the mass transfer coefficient is enhanced, as it should be. It is observed that the mass transfer coefficient increases with increasing Le in the medium. It is also observed that the nondimensional mass transfer coefficient becomes negative for large values of the Soret parameter in the absence and presence of the Dufour effect in the medium.

Opposing Buoyancy. In the opposing buoyancy case where the solutal buoyancy opposes the thermal buoyancy, the thermal and solutal variations with respect to the nondimensional parameters are significantly different from those in the aiding buoyancy case. The nondimensional temperature θ is plotted against η in Fig. 5(*a*), in the absence of the Soret effect for fixed *N*. Like in the aiding buoyancy, here also, it is observed that the Dufour parameter decreased the temperature distribution in the medium, and this reduction is further lowered as the value of the Lewis number increases. Variation of the nondimensional concentration ϕ with η is plotted in Fig. 5(*b*) for different values of Le and Sr with Df =0. From this figure, it is evident that increase in Sr increased the nondimensional concentration in the medium. However, it is observed that the nondimensional concentration decreases with increasing values of Le.

The nondimensional heat transfer coefficient plotted against Df for varying Le and Sr in the Darcy medium in Fig. 6(*a*) indicates that the heat transfer coefficient increases with both Df and Le, while a reduction in the heat transfer coefficient is seen with increasing Sr. Contrary to what has been observed in the aiding buoyancy case, in the opposing buoyancy case, when Sr=0 and Df=0, the Nusselt number increases steeply up to a value of Le and a steady raise is seen as Le is increased further. As the value of Df increases, a similar behavior is seen for small values of Le, but the Nusselt number is observed to decrease in the medium as Le is increased further. This is clearly seen from Fig. 6, where the curves are plotted for the buoyancy ratio $N=-0.2$. This phenomenon can also be seen with other values *N* in the opposing buoyancy case.

The nondimensional mass transfer coefficient is plotted against Sr for varying Le and Df in Fig. 7(*a*), and this figure indicates clearly that the mass transfer coefficient is decreases with both Sr and Df, while it increases as Le increases. This confirms the fact that even in the opposing buoyancy case, as the value of the product of the parameters Le and Sr increases, the mass transfer coefficient increases. The variation of the mass transfer coefficient against the Lewis number for different values of the parameter Sr

Table 1 Critical values of Sr for which the Sherwood number becomes negative when $N=1$

Le	Df	Sr
	0	0.5
0.1	0.01	0.5
	0.1	0.5
	0	1.9
1	0.01	1.8
	0.1	1.7
	0	6.9
5	0.01	6.6
	0.1	6.2

is presented in Fig. 7(*b*). From these curves, it is evident that the mass transfer coefficient increased with the Lewis number, while a marginal decrease is seen as the value of the Soret parameter is increased.

As observed in the earlier studies on convective transport from a vertical surface in porous media by Postelnicu [5], Partha et al. [6], and Lakshmi Narayana and Murthy [8], in the present study it has also been observed that for certain combinations of Df and Sr, the Sherwood number becomes negative depending on the values of the Lewis number. A list of values of Df and Sr for which the Sherwood number continues to become negative is presented in Tables 1 and 2 for aiding and opposing buoyancies, respectively. The Dufour parameter is given very small values, as it is indicated in the literature that its impact is seen mostly in gaseous media. The Soret parameter is given higher values (refer to Tables 1 and 2) to bring out the instances where there is a change in the sign of the Sherwood number. The practicality of these high values for Sr may be questionable, but the qualitative behavior of $\phi'(\eta)$ clearly changes with large values of Sr in both aiding and opposing buoyancies for all values of the Lewis number.

Table 2 Critical values of Sr for which the Sherwood number becomes negative when $N=-0.2$

Le	Df	Sr
	0	0.9
0.7	0.01	0.9
	0.1	0.9
	0	1.6
1	0.01	1.5
	0.1	1.4
	0	6.8
5	0.01	6.8
	0.1	5.9

Conclusions

The effect of Soret and Dufour parameters on free convection heat and mass transfers from a horizontal flat plate in a Darcy porous medium has been analyzed. The results are presented in both aiding and opposing buoyancy cases for various values of the flow governing parameters via the diffusivity ratio Le, buoyancy ratio N, Dufour parameter Df, and Soret parameter Sr. It is observed that the nondimensional heat and mass transfer coefficients are changed to an extent by the Soret and Dufour effects. In aiding buoyancy, the Nusselt number increases linearly with Df. However it decreases nonlinearly with increasing value of Le, whereas the Sherwood number decreases linearly with increasing value of the Soret parameter Sr and it increases with Le in a nonlinear fashion. When the product Le Sr increases, the mass transfer coefficient is enhanced. Contrary to what has been observed in the aiding buoyancy case, in the opposing buoyancy case, an increase in the heat transfer coefficient is observed with increasing values of Le in the absence of the Dufour effect and also for small values of the Dufour parameter, but as the value of this parameter is increased, a reduction in the heat transfer coefficient is seen with the Lewis number. Even in the opposing buoyancy case so, as the value of the product of the parameters Le and Sr increases, the mass transfer coefficient increases. A change in the sign of the Sherwood number is noticed for certain combinations of Df and Sr values, and these are tabulated in both aiding and opposing buoyancies.

References

[1] Bansod, V. J., 2003, "The Darcy Model for Boundary Layer Flows in a Horizontal Porous Medium Induced by Combined Buoyancy Forces," J. Porous Media, **6**, pp. 273–281.

[2] Nield, D. A., and Bejan, A., 2006, *Convection in Porous Media*, Springer-Verlag, New York.

[3] Eckert, E. R. G., and Drake, R. M., 1972, *Analysis of Heat and Mass Transfer*, McGraw-Hill, New York.

[4] Anghel, M., Takhar, H. S., and Pop, I., 2000, "Dufour and Soret Effects on Free Convection Boundary-Layer Flow Over a Vertical Surface Embedded in a Porous Medium," Stud. Univ. Babes-Bolyai, Math., **XLV**, pp. 11–21.

[5] Postelnicu, A., 2004, "Influence of a Magnetic Field on Heat and Mass Transfer by Natural Convection From Vertical Surfaces in Porous Media Considering Soret and Dufour Effects," Int. J. Heat Mass Transfer, **47**, pp. 1467–1472.

[6] Partha, M. K., Murthy, P. V. S. N., and Raja Sekhar, G. P., 2006, "Soret and Dufour Effects in Non-Darcy Porous Media," ASME Trans. J. Heat Transfer, **128**, pp. 605–610.

[7] Postelnicu, A., 2007, "Influence of Chemical Reaction on Heat and Mass Transfer by Natural Convection From a Vertical Surfaces in Porous Media Considering Soret and Dufour Effects," Heat Mass Transfer, **43**, pp. 595–602.

[8] Lakshmi Narayana, P. A., and Murthy, P. V. S. N., 2007, "Soret and Dufour Effects in a Doubly Stratified Darcy Porous Medium," J. Porous Media, **10**, pp. 613–624.

[9] Murthy, P. V. S. N., and Lakshmi Narayana, P. A., "Soret and Dufour Effects on Free Convection Heat and Mass Transfer From a Horizontal Plate in Non-Darcy Porous Media," Int. J. Fluid Mech. Res., accepted.

Heating and Ignition of Metal Particles in the Transition Heat Transfer Regime

Salil Mohan

Mikhaylo A. Trunov

Edward L. Dreizin

Department of Mechanical Engineering,
New Jersey Institute of Technology,
Newark, NJ 07102

This paper considers the heating and ignition of small metallic particles in hot gases for a range of Knudsen numbers, for which the continuum description of heat transfer is not valid. Modified Fuchs' model for the transition heat transfer analysis was adapted to treat diatomic gas with properties changing as a function of temperature. The dimensionless heat transfer coefficient, Nusselt number, was calculated as a function of the particle diameter for the transition heat transfer regime. Heat transfer rates in the transition regime are somewhat different from one another for the cases of particle heating and cooling while the absolute values of the particle-gas temperature difference are the same. This effect does not exist for the continuum heat transfer model. It is observed that the applicability of the continuum heat transfer model for particles of different sizes depends on pressure and particle-air temperature difference. For example, for particles at 300 K heated in air at 2000 K, the continuum heat transfer model can be used for particle diameters greater than 10 μm and 1 μm at the pressures of 1 bar and 10 bars, respectively. Transition heat transfer model must be used for the analysis of heat transfer for nanosized particles. For calculating the ignition delay, the continuum model remains useful for particle diameters greater than 18 μm and 2 μm for 1 bar and 10 bars, respectively. The sensitivity of the transition heat transfer model to the accommodation coefficient is evaluated. It is found that for metallic particles, the accommodation coefficient has a relatively weak effect on the heat transfer rate. [DOI: 10.1115/1.2945881]

Keywords: transition regime heat transfer, ignition delay, energetic particle, magnesium ignition

Introduction

Problems involving the heat transfer between spherical particles and quiescent gas are ubiquitous in such applications as laser-induced incandescence (LII) [1–3], solid propellant combustion [4–7], metal powder explosions in air [8–10], etc. Such problems also need to be considered in multiple laboratory experiments, such as powder ignition in shock tube experiments [11,12] and laser ignition of aerosol particles [13,14]. In many cases, the particle sizes are of the order of microns and the treatment of the surrounding fluid (gas) as a continuum medium becomes invalid. Typically, the transition heat transfer regime is recommended when Knudsen number, Kn, defined as $\mathrm{Kn}=\lambda/D$, where λ is the mean free path in gas and D is the particle diameter, is in the range of 0.01–10 [15]. Figure 1 shows two constant Knudsen number lines for Kn=0.01 and Kn=10, in the coordinates of particle diameter and temperature of air at atmospheric pressure. Conditions of heat transfer for most micron-sized particles in the applications mentioned above should be described by the transition regime.

The transition heat transfer regime has been dealt with extensively in the literature [15–17]. Various quasisteady analytical solutions [17,18] as well as interpolation-based approaches [19–22], describing heat transfer, have been proposed. In most of the suggested models, such as based on T-jump approximation [21] and others, a small temperature difference between the particle and the quiescent ambient gas is assumed. This assumption makes the respective models unacceptable for applications listed above, where a particle is typically heated to a temperature exceeding that of the surrounding gas by thousands of degrees. For a two-layer model proposed by Fuchs [23] and modified by Wright [24], the assumption of a small temperature difference between the particle and gas is less critical and can be relaxed. Recently, Fuchs' model has been validated using direct Monte Carlo simulation [16]. The model has been shown to be advantageous compared to other proposed approaches [15,16] and is recommended for use in many related applications. The model is relatively simple and readily implemented, but it still requires an iterative evaluation of the temperature at the boundary between the "free-molecular layer" and "continuum" surrounding. Thus, for each specific application, it is desirable to determine the range of particle sizes and experimental conditions when the use of this model is necessary. This study focuses on the applications dealing with particle ignition. In this case, the most readily detectable experimental parameter is an ignition delay for a heated particle. The discrepancy between the ignition delays predicted by the modified Fuchs model and by the continuum heat transfer calculation is determined and discussed for particles of different sizes. In addition, the version of the Fuchs model that was validated in Ref. [16] has been further modified to account for a diatomic gas with thermal properties varied as a function of temperature. The effects of the transition regime heat transfer on the heating and cooling of particles of different diameters are considered and compared to each other. Finally, the sensitivity of the predicted heat transfer rate to a usually poorly known accommodation coefficient is considered.

Transition Heat Transfer Model by Fuchs Modified for Diatomic Gas

A model describing the heat transfer for a sphere in the transition regime was proposed by Fuchs [23]. The model introduced a so-called Langmuir layer with thickness δ adjacent to the particle. The heat transfer within the Langmuir layer is assumed to occur in the free-molecular regime, while outside the layer, the heat transfer is described by a continuum model. The free-molecular expression for the heat transfer rate within the Langmuir layer is given as [16]

$$\dot{q} = \dot{q}_{\text{free molecular}} = \alpha \pi D^2 P_g \sqrt{\frac{k_B T_\delta}{8\pi m_g}} \frac{\gamma^* + 1}{\gamma^* - 1} \left(\frac{T_p}{T_\delta} - 1 \right) \tag{1}$$

where α is the accommodation coefficient, m_g is the mass of a gas molecule, k_B is the Boltzmann constant, D is the particle diameter, P_g is the ambient gas pressure, T_P is the particle surface temperature, T_δ is the gas temperature at the boundary of the Langmuir layer, i.e., at a distance of $(D/2+\delta)$ from the center of the particle, and γ is the adiabatic index of the ambient gas. The superscript " *" indicates that the value of γ is averaged over the temperature range of $(T_P - T_\delta)$ [16], calculated as

$$\frac{1}{\gamma^* - 1} = \frac{1}{T_P - T_\delta} \int_{T_\delta}^{T_P} \frac{dT}{\gamma - 1} \tag{2}$$

In the region outside Langmuir's layer, heat transfer is calculated using the continuum regime expression [15]

Contributed by the Heat Transfer Division of ASME for publication in the JOURNAL OF HEAT TRANSFER. Manuscript received April 27, 2007; final manuscript received December 27, 2007; published online August 7, 2008. Review conducted by Walter W. Yuen.

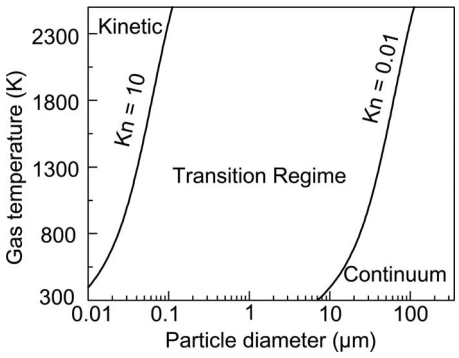

Fig. 1 Constant Knudsen number lines as a function of particle temperature and gas temperature

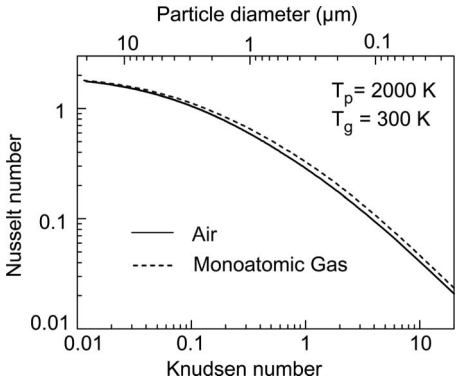

Fig. 2 Nusselt number as a function of Knudsen number (and particle diameter) calculated for the transition regime heat transfer using Fuchs' model for monoatomic gas [16] and for air considering air properties as a function of temperature

$$\dot{q} = \dot{q}_{\text{continuum}} = 4\pi[D/2 + \delta(T_\delta)]\int_{T_\delta}^{T_g} k(T)dT \tag{3}$$

where k is the gas thermal conductivity. Langmuir's layer thickness $\delta(T_\delta)$ is approximately equal to the mean free path $\lambda(T_\delta)$ [15,24].

The value of λ is calculated for a monoatomic gas in Ref. [16] as

$$\lambda(T_\delta) = \frac{4}{5}\frac{k(T_\delta)}{P_g}\sqrt{\frac{m_g T_\delta}{2k_B}} \tag{4}$$

The effect of any pressure difference between the gas in Langmuir's layer and the ambient gas is neglected. Note that Eq. (4) is different from a more general equation reported in Refs. [15,25] and describes the mean free path in polyatomic ideal gases (see Eq. (5) below). Equations (1) and (3) can be solved iteratively for T_δ, so that the rate of heat transfer can be determined.

Modified Fuchs' model described above has been validated using direct Monte Carlo simulations [22] in Refs. [15,16] for a hypothetical monoatomic gas. In order to use this result for air, which is a diatomic gas, air properties, such as the thermal conductivity and the adiabatic index [26], should be used instead of the monoatomic gas properties. In addition, Eq. (4) used for the mean free path calculation should be replaced by an equation appropriate for a diatomic gas. As noted above, a more generic equation for the mean free path is available and given, for example, by Refs. [15,25]:

$$\lambda'(T_\delta) = \frac{k(T_\delta)}{P_g}\left[\frac{\gamma(T_\delta) - 1}{9\gamma(T_\delta) - 5}\right]\sqrt{\frac{8\pi m_g T_\delta}{k_B}} \tag{5}$$

When applied to a monoatomic gas, i.e., $\gamma = 5/3$ Eq. (5) is different from Eq. (4) by a constant factor of $\sqrt{\pi}/3$. While Eq. (5) allows one to account for the polyatomic gas properties depending on the specific heat ratio, γ, the direct validation of Fuchs' model was performed in Ref. [16] using Eq. (4). Thus, in order to use Fuchs' model validated in Ref. [16] to describe the heat transfer in a polyatomic gas, Eq. (5) replaced Eq. (4) while being corrected by the factor of $3/\sqrt{\pi}$.

Figure 2 shows the dimensionless heat transfer coefficient or Nusselt number as a function of Knudsen number and as a function of the particle diameter for a selected fixed combination of particle and air temperatures. The accommodation coefficient is assumed to be equal to 1. The value of the Nusselt number approaches "2" for bigger particles indicating the approaching continuum regime. The dashed curve is for the hypothetical monoatomic gas used in Ref. [16]. Note that the scale is logarithmic so the difference between the curves for monoatomic and diatomic gases is not insignificant. The Nusselt number is defined here as

$$\text{Nu} = \frac{q}{\pi D\bar{k}(T_p - T_g)} \tag{6}$$

where

$$\bar{k} = \frac{1}{T_p - T_g}\int_{T_g}^{T_P} k(T)dT \tag{7}$$

In the continuum regime, heat transfer is independent of pressure. However, when the continuum regime analysis stops being applicable, the rate of heat transfer becomes a strong function of pressure.

In the continuum regime, heat transfer rates are of the same magnitude for the heating and cooling of a particle in hot and cold gases, respectively, when the absolute value of the particle-gas temperature difference is the same. This is no longer the case for transition and free-molecular regimes, where the magnitudes of heat transfer rates for particle heating and cooling become different even when the absolute values of the particle-gas temperature difference are the same. Indeed, the transition regime heat transfer rate depends on Langmuir's layer thickness, δ, which is effectively equal to the mean free path at T_δ. The value of T_δ is not a simple average of the particle and gas temperatures and the thicknesses of Langmuir's layers are different for the cold and hot particles of the same sizes placed in hot and cold gases, respectively. Furthermore, for small particles, T_δ is closer to the gas temperature than to the particle temperature, while the opposite is true for large particles. Thus, the difference between the heat transfer coefficients for heating and cooling reverses around a specific particle size, depending on particle-gas temperatures and gas pressure. Figure 3 shows the Nusselt number defined by Eq. (6) and calculated as a function of particle diameter for the particle's heating and cooling in air. When a colder particle is being heated in air for the considered air and particle temperatures, the heat transfer rate should be calculated using Fuchs' model for particles less than about 10 μm and 1 μm for pressures of 1 bar and 10 bars, respectively. When a hotter particle is being cooled in air, Fuchs' model must be used for particles smaller than about 50 μm and 5 μm for pressures of 1 bar and 10 bars, respectively. The above cutoff limits were calculated while allowing a 5% deviation from the value of Nu=2 corresponding to the continuum heat transfer regime. The difference between the transition and continuum heat transfer approximations is more pronounced for the particle cooling than for its heating, for micron-sized particles and vice versa for smaller particle sizes.

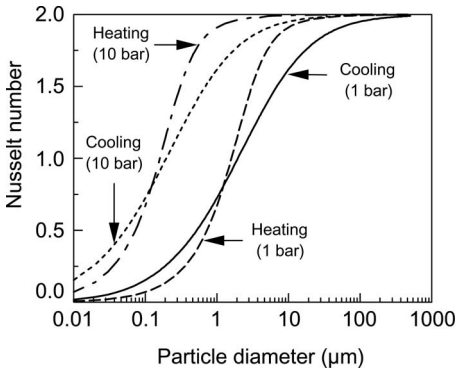

Fig. 3 Nusselt number calculated as function of the particle diameter and pressure for the transition heat transfer regime at pressures of 1 bar and 10 bars. Particle heating: T_g=2000 K and T_p=300 K. Particle cooling: T_g=300 K and T_p=2000 K.

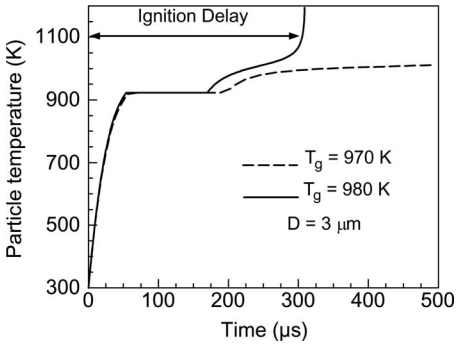

Fig. 4 Temperature histories for Mg particle inserted in air at the air temperatures just above (solid line) and just below (dashed line) of the ignition threshold. The ignition delay is measured from time t=0, the moment when the particle is exposed to hot air.

Ignition Delays for Particles Heated in the Transition Regime

For many experimental situations, ignition can be modeled based on the heat balance analysis for an igniting particle. For example, for an experiment in which particles are ignited in a shock wave [11,12], the heat balance can be written as

$$MC\frac{\partial T_p}{\partial t} = \dot{Q}_{\text{chemical}} + \dot{Q}_{\text{convection}} + \dot{Q}_{\text{radiation}} \tag{8}$$

where M is the particle mass, C is its specific heat, and T_p is its temperature; $\dot{Q}_{\text{chemical}}$ is the chemical heat generation rate, which is the term describing an exothermic process responsible for ignition, and $\dot{Q}_{\text{radiation}}$ and $\dot{Q}_{\text{convection}}$ are the radiation and convection heat transfer rates, respectively. The two latter terms can lead to particle heating when it is below the environment temperature (and below the temperature of the surrounding walls) and to its cooling when the particle starts self-heating above the environment gas temperature due to the chemical heat generation. The radiation term is readily determined from the Stefan–Boltzmann law shown below:

$$\dot{Q}_{\text{radiation}} = \varepsilon\sigma_{\text{SB}}(\pi D^2)(T_p{}^4 - T_w^4) \tag{9}$$

where ε is the emissivity, σ_{SB} is the Stefan–Boltzmann constant, and T_p and T_w are the particle and surrounding wall temperatures, respectively. It is assumed that the ambient gas temperature, T_g, is equal to the wall temperature, T_g=T_w.

The convection term, $\dot{Q}_{\text{convection}}$, is calculated using the transition regime heat transfer model described above. For comparison, the convection term is also calculated using the continuum model and the neglecting particle slip, i.e., assuming that Nusselt number, Nu=2.

$$\dot{Q}_{\text{convection}}^{\text{continuum}} = 2\pi D\int_{T_P}^{T_g} k(T)dT \tag{10}$$

The chemical heat generation rate term needs to be specifically described for each material. In this paper, the simplest Arrhenius-type model was used. The specific model used in calculations was suggested for the description of the ignition of the spherical magnesium particles [6,27,28]

$$\dot{Q}_{\text{chemical}} = A_r\Delta H_{\text{ox}}\pi D^2\exp\left[-\frac{E_a}{RT_p}\right] \tag{11}$$

where A_r is the Arrhenius preexponent, A_r=10^{10} kg m^{-2} s^{-1} [27], ΔH_{ox} is the heat of oxidation for magnesium, E_a is the activation energy, E_a=215 kJ/mol [6,27,28], and R is the universal gas constant. Note that the specific values of the activation energy and the preexponent employed here were reported in the literature based on ignition experiments for micron-sized particles. Such a description is expected to provide a reasonable accuracy for the calculations presented in this paper, while it clearly neglects the effect of the transition regime heat and mass transfer processes on the rate of chemical reaction. In the future, such effect will need to be considered and a modified expression for the rate of heat generation due to the chemical reaction will need to be derived.

The event of ignition was defined by the particle temperature runaway due to a rapid heat release by magnesium oxidation. Figure 4 shows the temperature histories predicted for a magnesium particle inserted in air at air temperatures just below and just above the ignition threshold. Ignition delay is defined as the time required to reach the temperature runaway. When the environment temperature is below the ignition threshold, the temperature runaway is never observed.

Two parallel sets of calculations for ignition delays were performed, one using modified Fuchs' model and the other using the continuum regime model for the heat transfer analysis. Ignition delays were calculated for magnesium particles with an initial temperature of 300 K heated in a quiescent air at 2000 K. Figure 5 shows the ignition delays calculated as a function of particle diameter at the pressures of 1 bar and 10 bars. Due to a slower heat transfer predicted by the transition regime model as compared to the continuum case, much longer ignition delays are predicted for submicron-sized particles heated in the transition regime. The effect diminishes as the particle size increases. The effect is also reduced for elevated pressures. It is observed that for

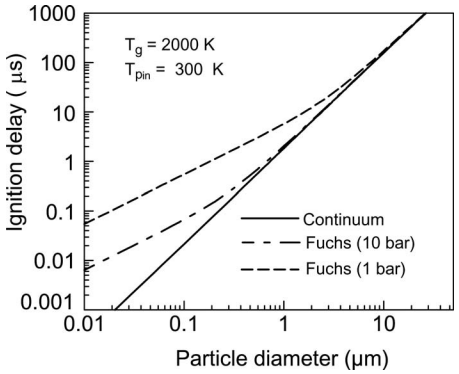

Fig. 5 Calculated ignition delay of Mg particle at 300 K inserted in air at 2000 K as a function of particle diameter and pressure

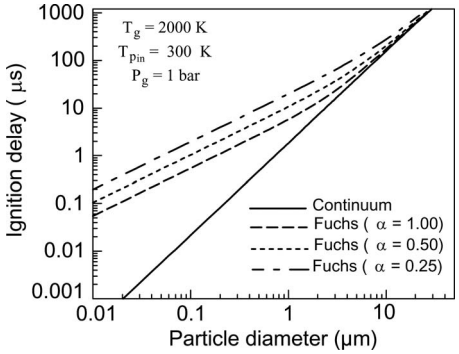

Fig. 6 Calculated ignition delay of Mg particle at 300 K inserted in air at 2000 K as a function of particle diameter and accommodation coefficient

the specific air and particle temperatures considered, the continuum model can be used to predict ignition delays for particles greater than 18 μm and 2 μm for pressures of 1 bar and 10 bars, respectively. The particle size cutoff was calculated allowing 5% errors in the ignition delays predicted by the continuum regime calculations. Note that the ignition delay calculation considers the particle at a continuously increasing temperature. The initial part of the heating process, when the particle-gas temperature difference is the greatest, affects the predicted ignition delays most significantly.

The sensitivity of ignition delay to the accommodation coefficient, α, used in describing the free-molecular heat transfer in Eq. (1) was also considered. Figure 6 shows the ignition delay as a function of the particle diameter at an air pressure of 1 bar for different accommodation coefficients. The breakdown of the continuum model occurs at larger particle diameters for smaller values of the accommodation coefficients. The accommodation coefficient for metal particles usually varies in the range of 0.5–0.95 [29]. Thus, according to Fig. 6, the practical calculations of ignition delays would be relatively insensitive to uncertainties in the value of the accommodation coefficient used in the transition model.

Conclusions

Modified Fuchs' model for the transition regime heat transfer was expanded to account for the properties of diatomic gases as a function of temperature. The dimensionless heat transfer coefficient, Nusselt number, was calculated as a function of particle diameter using this expanded Fuchs' model. Heat transfer rates predicted by the model are somewhat different from one another for the cases of particle heating and cooling while the absolute values of the particle-gas temperature difference are the same. This effect is not predicted by the continuum heat transfer calculations. It is observed that the applicability of the continuum heat transfer model for the description of heating or cooling of particles of different sizes depends on pressure. For processes involving particle heating by laser, particle ignition, and similar processes, the continuum heat transfer model can be used for particles with diameters greater than about 10 μm at 1 bar, and for particles greater than about 1 μm at 10 bars. The transition heat transfer model must always be used for the analysis of heat transfer for nanosized particles. For calculating the ignition delay, the continuum model remains useful for particle diameters greater than 18 μm and 2 μm for 1 bar and 10 bars, respectively. A usually poorly known accommodation coefficient is observed to have a relatively small effect on the heat transfer rate in the transition regime for metallic particles.

Nomenclature

A_r = Arrhenius preexponent (kg m^{-2} s^{-1})
C = particle specific heat (J kg^{-1} K^{-1})
D = particle diameter (m)
E_a = activation energy (J mol^{-1})
ΔH_{ox} = magnesium oxidation enthalpy (J kg^{-1})
Kn = Knudsen number
k = gas thermal conductivity (J m^{-1} s^{-1} K^{-1})
k_B = Boltzmann constant (J K^{-1})
M = particle mass (kg)
m_g = mass of gas molecule (kg)
Nu = Nusselt number
P_g = ambient gas pressure (kg m^{-1} s^{-2})
$\dot{Q}_{chemical}$ = chemical heat release in the particle (J s^{-1})
$\dot{Q}_{convection}$ = convection heat transfer by Fuchs' model (J s^{-1})
$\dot{Q}_{radiation}$ = radiation heat transfer (J s^{-1})
$\dot{Q}^{continuum}_{convection}$ = convection heat transfer by continuum model (J s^{-1})
$\dot{q}$ = heat transfer rate between particle and gas (J s^{-1})
$\dot{q}_{continuum}$ = continuum heat transfer for a sphere (J s^{-1})
$\dot{q}_{free\ molecular}$ = free-molecular heat transfer for a sphere (J s^{-1})
R = universal gas constant (J mol^{-1} K^{-1})
T_p = particle temperature (K)
T_w = surrounding wall temperature (K)
T_δ = gas temperature at Langmuir's layer (K)

Greek

α = accommodation coefficient
δ = Langmuir layer's thickness (m)
ε = particle surface emissivity
γ = gas adiabatic index
γ^* = average gas adiabatic index
λ = molecular mean free path for monatomic gas (m)
λ' = molecular mean free path for polyatomic gas (m)
σ_{SB} = Stefan–Boltzmann constant (J m^{-2} s^{-1} K^{-4})

References

[1] Ni, T., Pinson, J. A., Gupta, S., and Santoro, R. J., 1995, "Two-Dimensional Imaging of Soot Volume Fraction by the Use of Laser-Induced Incandescence," Appl. Opt., **34**, pp. 7083–7091.
[2] Shaddix, C. R., and Smyth, K. C., 1996, "Laser-Induced Incandescence Measurements of Soot Production in Steady and Flickering Methane, Propane, and Ethylene Diffusion Flames," Combust. Flame, **107**, pp. 418–452.
[3] Hofmann, M., Bessler, W. G., Schulz, C., and Jander, H., 2003, "Laser-Induced Incandescence for Soot Diagnostics at High Pressures," Appl. Opt., **42**(12), pp. 2052–2062.
[4] Krishnan, S., and George, P., 1998, "Solid Fuel Ramjet Combustor Design," Prog. Aerosp. Sci., **34**(3–4), pp. 219–256.
[5] Galfetti, L., De Luca, L. T., Severini, F., Meda, L., Marra, G., Marchetti, M., Regi, M., and Bellucci, S., 2006, "Nanoparticles for Solid Rocket Propulsion," J. Phys.: Condens. Matter, **18**(33), pp. S1991-S2005.
[6] Fedorov, A. V., and Gosteev, Y., 1998, "A Physical-Mathematical Investigation of Magnesium Particle Ignition," Arch. Combust., **16**(3–4), pp. 137–152.
[7] Bocanegra, P. E., Chauveau, C., and Gökalp, I., 2007, "Experimental Studies on the Burning of Coated and Uncoated Micro and Nano-Sized Aluminum Particles," Aerosp. Sci. Technol., **11**(1), pp. 33–38.
[8] Mitsui, R., and Tanaka, T., 1973, "Simple Models of Dust Explosion. Predicting Ignition Temperature and Minimum Explosive Limit in Terms of Particle Size," Ind. Eng. Chem. Process Des. Dev., **12**(3), pp. 384–389.
[9] Going, J. E., and Snoeys, J., 2002, "Explosion Protection With Metal Dust Fuels," Process Saf. Prog., **21**(4), pp. 305–312.
[10] Dreizin, E. L., and Hoffmann, V. K., 2000, "Experiments on Magnesium Aerosol Combustion in Microgravity," Combust. Flame, **122**(1–2), pp. 20–29.
[11] Gauthier, B. M., Davidson, D. F., and Hanson, R. K., 2004, "Shock Tube Determination of Ignition Delay Times in Full-Blend and Surrogate Fuel Mixtures," Combust. Flame, **139**(4), pp. 300–311.
[12] Bazyn, T., Krier, H., and Glumac, N., 2006, "Combustion of Nano-Aluminum at Elevated Pressure and Temperature Behind Reflected Shock Waves," Com-

bust. Flame, **145**(4), pp. 703–713.
[13] Legrand, B., Marion, M., Chauveau, C., Gökalp, I., and Shafirovich, E., 2001, "Ignition and Combustion of Levitated Magnesium and Aluminum Particles in Carbon Dioxide," Combust. Sci. Technol., **165**(1), pp. 151–174.
[14] Cain, J., and Brewster, M. Q., 2006, "Radiative Ignition of Fine Ammonium Perchlorate Composite Propellants," Propellants, Explos., Pyrotech., **31**(4), pp. 278–284.
[15] Liu, F., Daun, K. J., Snelling, D. R., and Smallwood, G. J., 2006, "Heat Conduction from a Spherical Nano-Particle: Status of Modeling Heat Conduction in Laser-Induced Incandescence," Appl. Phys. B: Lasers Opt., **83**, pp. 355–382.
[16] FIlipov, A. V., and Rosner, D. E., 2000, "Energy Transfer Between an Aerosol Particle and Gas at High Temperature Ratios in the Knudsen Transition Regime," Int. J. Heat Mass Transfer, **43**, pp. 127–138.
[17] McCoy, B. J., and Cha, C. Y., 1974, "Transport Phenomena in the Rarefied Gas Transition Regime," Chem. Eng. Sci., **29**(2), pp. 381–388.
[18] Kennard, E. H., 1938, *Kinetic Theory of Gases, With an Introduction to Statistical Mechanics*, McGraw-Hill, New York.
[19] Williams, M. M. R., and Loyalka, S. K., 1991, *Aerosol Science: Theory and Practice*, Pergamon, New York.
[20] Bhatnagar, P. L., Gross, E. P., and Krook, M., 1954, "A Model for Collision Processes in Gases. I. Small Amplitude Processes in Charged and Neutral One-Component Systems," Phys. Rev., **94**(3), pp. 511–525.
[21] Kullmer, R., 1996, "Heat Transfer From Small Tungsten Spheres Into an Ambient H_2 Atmosphere," Appl. Phys. B: Lasers Opt., **62**(2), pp. 191–196.
[22] Bird, G. A., 1994, *Molecular Gas Dynamics and the Direct Simulation of Gas Flows*, Clarendon, Oxford.
[23] Fuchs, N. A., 1963, "On the Stationary Charge Distribution on Aerosol Particles in a Bipolar Ionic Atmosphere," Geofis. Pura Appl., **56**, pp. 185–193.
[24] Wright, P. G., 1960, "On the Discontinuity Involved in Diffusion Across an Interface (the Δ of Fuchs)," Discuss. Faraday Soc., **30**, pp. 100–112.
[25] Lees, L., 1965, "Kinetic Theory Description of Rarefied Gas Flow," J. Soc. Ind. Appl. Math., **13**, pp. 278–311.
[26] Lide, D. R., 2003, *Handbook of Chemistry and Physics*, CRC, New York.
[27] Ward, T. S., Trunov, M. A., Schoentiz, M., and Dreizin, E. L., 2006, "Experimental Methodology and Heat Transfer Model for Identification of Ignition Kinetics of Powdered Fuels," Int. J. Heat Mass Transfer, **49**(25–26), pp. 4943–4954.
[28] Roberts, T. A., Burton, R. L., and Krier, H., 1993, "Ignition and Combustion of Aluminum/Magnesium Alloy Particles in Oxygen at High Pressures" Combust. Flame, **92**(1–2) pp. 125–143.
[29] Saxena, S. C., and Joshi, R. K., 1989, *Thermal Accommodation and Adsorption Coefficients of Gases*, Hemisphere, New York.

Experiments in Single-Phase Natural Circulation Miniloops With Different Working Fluids and Geometries

Pietro Garibaldi

Mario Misale
e-mail: misale@diptem.unige.it

Dipartimento di Ingegneria della Produzione,
Termoenergetica e Modelli Matematici DIPTEM-Tec,
University of Genoa,
Via all'Opera Pia 15a,
16145 Genova, Italy

The aim of this work is to analyze experimentally the influence of geometrical parameters and fluid properties on the thermal performances of rectangular single-phase natural circulation miniloops, which could be used for cooling of electronic devices. The present paper analyzes two experimental campaigns performed on two rectangular miniloops (ML1 and ML2), characterized by different heights, when two working fluids (water and FC43) are employed. The temperature trends are measured for different combinations of miniloop inclination and power, and the associated fluid velocities are calculated by means of an enthalpy balance. The experimental data are compared with Vijayan's model, developed for large scale loops in steady-state conditions, corrected with a parameter that takes into account the loop inclination. The dynamical behavior is always stable. The time of the initial transient is long at high miniloop inclination (close to horizontal) and at low power, while the temperature overshoot grows up with increasing power and inclination. Results show that at the same power the velocity of FC43 is almost twice than that of water, but the thermal performances are worse because FC43 is characterized by low specific heat. Moreover, the velocities of the tallest miniloop are the lowest, probably because the enhancement of shear stresses overcomes the increase in buoyancy forces. For both fluids, the velocity grows almost linearly with power. Experimental data show a good agreement with the modified Vijayan's model. [DOI: 10.1115/1.2948393]

Keywords: single-phase, natural circulation, miniloop, loop inclination, reduced gravity, water, dielectric fluid

Introduction

Natural circulation is a fluid flow phenomenon, which occurs in case of density gradients inside a fluid. Even if its thermal efficiency is lower than in case of forced convection, natural circulation guarantees good reliability and low costs of maintenance as it does not need any mechanical moving part. Therefore, its main industrial applications are in the field of nuclear power plants, solar heaters, and passive cooling systems of engines, turbines, and electronic components.

Most researchers focused their attention on large scale systems, with particular consideration to performance optimization and stability analysis, while there are only a few studies about natural circulation inside small scale devices, which were studied until now only in case of two-phase flow, particularly for computer cooling applications.

Grief [1] and Vijayan et al. [2] reviewed single-phase natural circulation in large scale thermosyphons and their applications, studying, in particular, transient and stable flow and models for predicting the stability behavior of the system with different heating and cooling conditions. Other parameters such as loop inclination and pipe materials were analyzed by Misale et al. [3] in a large scale loop. Muhkherjee and Mudawar [4,5] and Tuma and Mortazavi [6] studied a two-phase miniloop for cooling electronic devices. Moreover, Fantozzi et al. [7] compared the performances of a pulsated two-phase mini thermosyphon (PTPT) with a classical two-phase thermosyphon, both characterized by internal diameter of the tubes of 4 mm.

This paper describes the experiments performed on two miniloops with different working fluids. Results were analyzed with the first campaign made by Misale et al. [8], and compared with Vijayan's correlation [9] proposed for large scale vertical single-phase natural circulation loops, modified with a correction factor in order to take into account the reduction in buoyancy forces due to miniloop inclination.

Experiments

Experimental Setup. The experimental setup consists of two rectangular single-phase natural circulation miniloops (ML1 and ML2). Figure 1 shows a scheme of the miniloops, whereas the geometrical dimensions of ML1 and ML2 are summarized in Table 1.

All the tubes are made of copper (99.9%) and are connected by means of four glass bends. The heater, placed at the bottom side of the miniloop, is made by a Nichrome wire, rolled around the horizontal tube, connected to a dc power supply. The cooler is a coaxial heat exchanger at the top of the miniloop, and it is connected to a cryostat, which provides a mixture of 50% water and 50% glycol. Since the cryostat flow rate is high (1 l/min), the temperature along the cooler can be considered constant. Heater, cooler, and vertical tubes are thoroughly insulated. Heat losses estimated with classical literature correlations are lower than 5% of the supplied power. The boundary conditions are of imposed power at the heater and imposed temperature at the cooler.

The fluid temperatures were measured by four *K*-type calibrated ($\pm 0.1\,^{\circ}$C) and shielded thermocouples (O.D. of 0.2 mm), placed in the vertical legs in the middle of the cross sections at a distance of 40 mm from the horizontal tube axis (Fig. 1). The presence of thermocouples inside the tube reduces the cross-sectional area of 3.2%. This value is sufficiently small to neglect the consequent increase in pressure losses [10]. Two additional *T*-type calibrated ($\pm 0.1\,^{\circ}$C) thermocouples were utilized to measure the temperature of the cryostat and of the ambient, respectively. Temperature data were stored at the acquisition frequency of 1 Hz for 5400 s by means of a high speed data acquisition system.

The miniloop is placed on a plate, which can rotate. With an inclined miniloop, the buoyancy forces are reduced by a $\cos(\alpha)$ factor. Neglecting the three-dimensional effects inside the flow, the miniloop inclination could simulate reduced gravity.

Every run started from stagnant condition: the working fluid and the coolant inside the cooler were at room temperature, while the cryostat was at $0\,^{\circ}$C. Acquisition began, and after 100 s power was supplied and, at the same time, cooling flow rate started.

Experimental Campaigns. Two experimental campaigns were done with the same inclination angles but different powers (Table 2). For ML1 with FC43 power inputs are the same of the ones in case of water [8], while for ML2 (water) they are double than in the case of ML1, because with a taller miniloop a greater power should be transferred at similar mean fluid temperatures.

FC43 (Table 3) is characterized by density being almost twice

Contributed by the Heat Transfer Division of ASME for publication in the JOURNAL OF HEAT TRANSFER. Manuscript received September 13, 2007; final manuscript received February 25, 2008; published online August 14, 2008. Review conducted by Yutaka Asako.

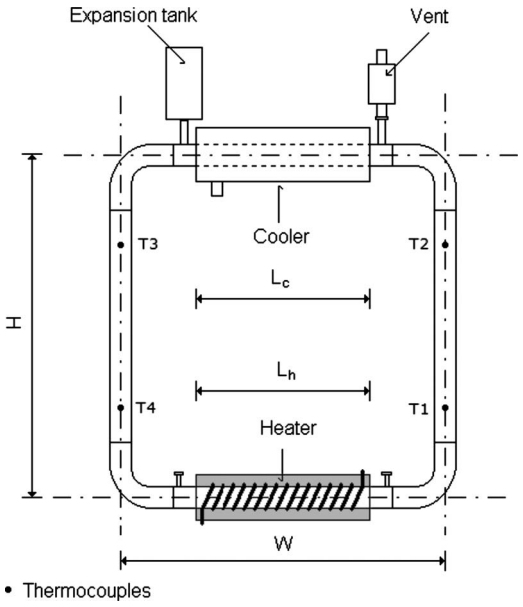

Fig. 1 Scheme of the miniloops

than that of water, while its specific heat is about one-quarter compared to water. Moreover, its isothermal expansion coefficient and Prandtl number are one order of magnitude higher than water, so that at the same boundary conditions the velocity and the mean fluid temperature of FC43 should be higher than those of water. Dynamic viscosity of FC43 is high and should cause smooth initial temperature transients.

For each combination of inclination and power, three tests from stagnant condition were performed. Tests at the same boundary conditions are depicted in the same plot and show good repeatability.

Results

Experimental Data. For each run, the temperature differences across heater and cooler as well as the fluid velocities were calculated. Since the vertical legs were thoroughly insulated, the differences between the two ΔT's were always lower than 5%; for this reason, only the ΔT_h (across the heater) was considered for the analysis.

In Figs. 2–4, the transient behaviors of ΔT_h data, for the three miniloop inclinations, are compared together, whereas Fig. 5 resumes the steady-state velocities of the runs. The time scale of the runs at $\alpha=0$ deg and $\alpha=30$ deg (Figs. 2 and 3) is 1000 s, while in the case of $\alpha=75$ deg (Fig. 4), as the transients are very slow, the temperature trends of the first 2500 s are plotted. As the tests of ML1 were already analyzed and reported in Ref. [8], only the average trend of ΔT_h of ML1 with water is plotted, and it is compared with the runs of ML1 with FC43 at the same power and with the runs of ML2 with water at double power. Since the sign of ΔT depends only on the circulation direction (clock- or counterclockwise), the absolute values were plotted. ML2 ($\alpha=0$ deg) at 30 W and 50 W showed a 20% difference in ΔT_h between clockwise and counterclockwise directions. This discrepancy could be explained both with small asymmetries of the apparatus and with slightly different positions of temperature sensors. Therefore, the blue asymptotes in Figs. 2(*b*) and 2(*c*) have two different values. In all other cases, the circulation flowed always in the same direction, with coincident asymptotic value of ΔT_h for the repeated runs.

The thermohydraulic behavior of the miniloops was always stable. In fact, for such a small internal diameter, the shear stresses stabilize the circulation induced by the buoyancy forces, avoiding any flow instabilities, which might appear in large scale loops.

Generally, it can be noted that the more inclined is the miniloop, the longer are the initial quiescent state as well as the transient time, in particular, at low power. In case of $\alpha=0$ deg (vertical) and $\alpha=30$ deg inclinations, the transient of water in ML1 is the fastest, probably because of the high viscosity of FC43 and of high inertia of ML2, even if in the latter case data are compared with double power. At $\alpha=75$ deg, the transition to steady state is very slow, and for ML2 the initial temperature overshoot is very high. In every run FC43 shows smooth temperature transient, characterized by just one oscillation, while for ML2, due to high power and slow initial motion, the temperature peak is very sharp.

Concerning the steady-state temperatures at the same power in ML1, ΔT of FC43 is always higher than that of water, because of its low specific heat, even if its velocity is higher than that of water (Fig. 5).

The steady-state velocities as a function of power and loop inclination were calculated by means of the enthalpy balance across the heater. The velocity trends are almost linear with power; however, the investigated power range was limited, in order to avoid the establishment of two-phase flow. For water, the circulation is faster in ML1 than in ML2. In particular, with $\alpha=0$ deg and $\alpha=30$ deg inclinations, the fluid velocities in ML1 are 20% higher than in ML2, while at $\alpha=75$ deg the difference rises up to 60%, even if the buoyancy forces are higher with the taller miniloop. This result could be explained with an unwanted increase in shear stresses, which are dominant in case of laminar flow with such small internal diameter.

In case of $\alpha=0$ deg in ML2 at 30 W and 50 W, there are different velocities, corresponding to the different ΔT_h mentioned above. At the same power input, the velocity of FC43 in ML1 is

Table 2 Experimental campaigns

α (deg)	ML1 power (W)	ML2 power (W)
0	5, 15, 25	10, 30, 50
30	2.5, 7.5, 10	5, 15, 20
75	2.5, 7.5, 10	5, 15, 20

Table 1 Geometrical dimensions (mm) and characteristics of the miniloops

	ML1	ML2
D	4	4
W	180	180
H	151	264
$L_h=L_c$	100	100
L_{tot}	662	888
L_{tot}/D	166	222
H/W	0.84	1.47

Table 3 Thermophysical properties of water and FC43 at 25°C, 1 atm

	Water[a]	FC43[b]	FC43/Water
ρ (kg/m^3)	997.1	1859	1.86
μ (kg/ms)	8.9$E-4$	5.4$E-3$	6.08
β (l/K)	2.5$E-4$	1.2$E-3$	4.8
c_p (J/kg K)	4183	1042	0.25
Pr	6.3	85.0	13.6

[a]Reference [11].
[b]Reference [12].

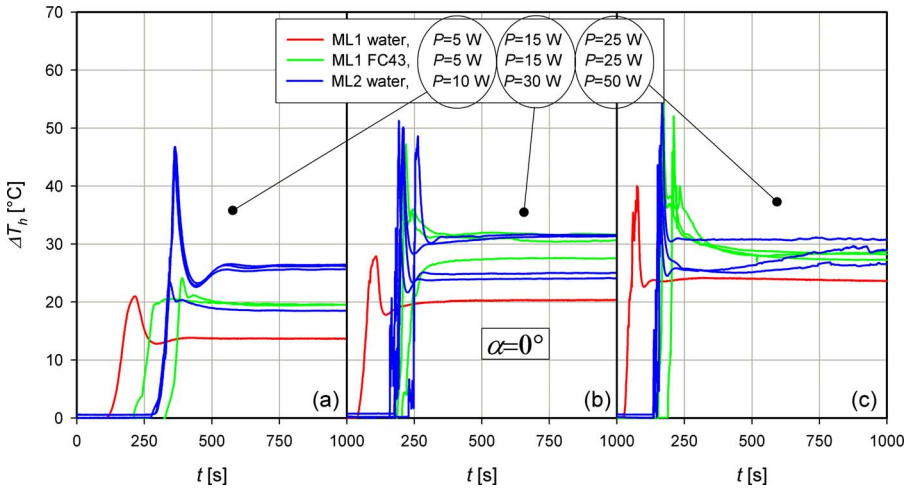

Fig. 2 Transient behaviors of ΔT_h for α=0 deg

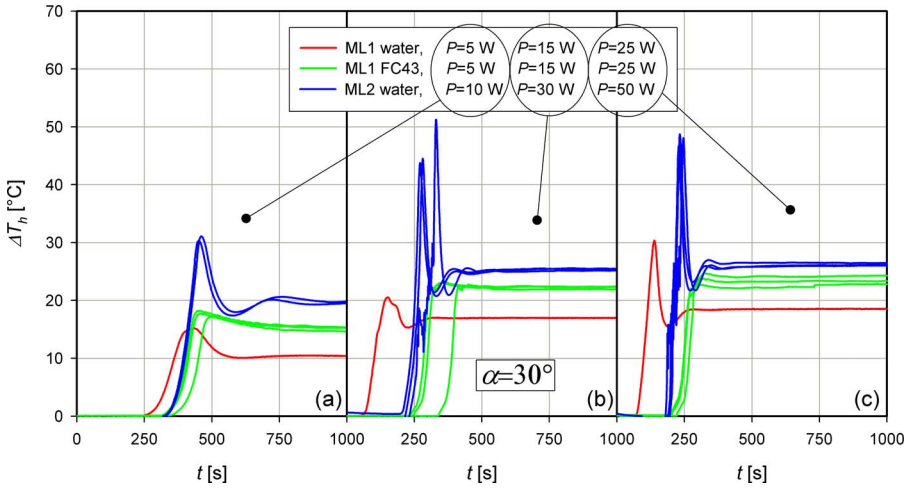

Fig. 3 Transient behaviors of ΔT_h for α=30 deg

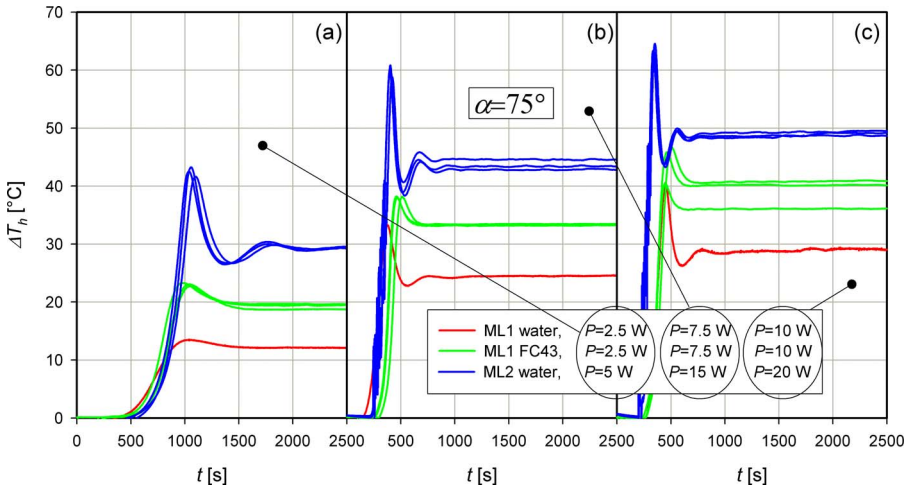

Fig. 4 Transient behaviors of ΔT_h for α=75 deg

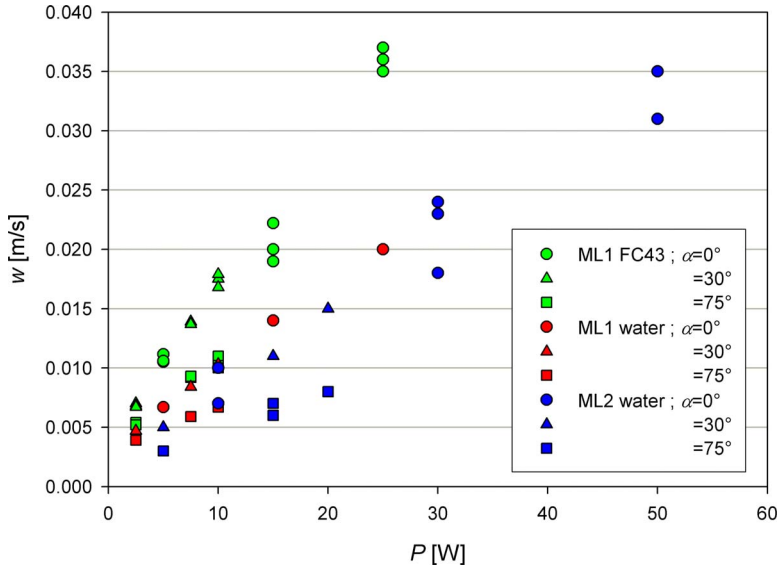

Fig. 5 Steady-state fluid velocities

almost twice than that of water. $\alpha=0$ deg and $\alpha=30$ deg data lie approximately on the same line for each fluid, while $\alpha=75$ deg data show a velocity reduction of 25–40% in case of FC43, and of 40–50% in case of water.

Finally, in case of $\alpha=0$ deg, Table 4 reports the maximum power density calculated on the internal heater surface, the maximum temperature overshoot and the maximum asymptotic temperature after the transient, respectively.

Table 4 Power density and maximum temperatures, $\alpha=0$ deg

	Maximum power density (kW/m^2)	Maximum temperature overshoot (°C)	Maximum asymptotic temperature (°C)
ML1 water	19.9	85.4	63.5
ML1 FC43	19.9	81.6	73.4
ML2 water	39.8	96.1	77.2

Even if FC43, because of its low specific heat, is characterized by a higher fluid temperature at steady state, the temperature overshoot is lower than in case of water, probably because FC43 is characterized by high thermal conductivity. In ML2, the overshoot is close to single-phase limit; however, the steady-state maximum temperature is close to the one of FC43 with half power input.

Steady-State Data Analysis. As for the present miniloops, all the runs lead to stable condition with asymptotic values of fluid temperatures, a one-dimensional steady-state analysis was carried out following Vijayan's model [9] developed for large scale natural circulation loops.

In case of stable flow, as the gravitational forces balance the shear stresses, it is possible to obtain a correlation between Re_{ss}, the steady-state Reynolds number, and Gr_m, a modified Grashof number. For the present analysis, the corrective parameter $\cos(\alpha)$ term is introduced in Gr_m to take into account the reduction in buoyancy forces due to the miniloop inclination α as follows:

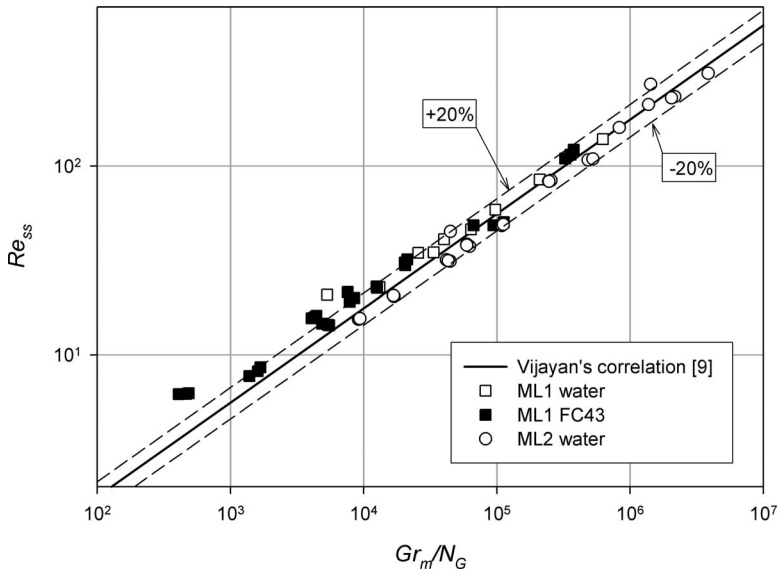

Fig. 6 Comparison between experimental data and Vijayan's correlation

$$\mathrm{Re}_{ss} = \frac{wD}{\nu}, \quad \mathrm{Gr}_m = \frac{D^3\rho^2 PH}{A\mu^3 c_p}\beta g \cos(\alpha) \tag{1}$$

For brevity, the analytical model is not reported (see Ref. [9]). The final correlation for laminar flow is

$$\mathrm{Re}_{ss} = 0.1768\left[\frac{\mathrm{Gr}_m}{N_G}\right]^{0.5} \tag{2}$$

N_G is a dimensionless parameter related to geometrical dimensions and the ratio between concentrated and uniform pressure losses,

$$N_G = \left(\frac{L_{\mathrm{tot}}}{D} + \frac{k}{f}\right) \tag{3}$$

where $f = 64/\mathrm{Re}$ and k was evaluated (by us) with Ref. [13].

The experimental data from the previous campaign [8] with the data of the two present campaigns are compared with the modified Vijayan correlation for laminar flow (Fig. 6). All the experimental data follow the correlation line with good agreement. The data range of the first campaign (ML1 water) was expanded both to lower and to higher dimensionless numbers. Experimental data of ML2, which lie at higher Gr_m, are moderately overestimated, while data of the FC43 campaign lie slightly over the correlation line. In particular, with ML1 displaced at $\alpha = 75$ deg, with both FC43 and water, the small disagreement could be due to three-dimensional effects, which cause uncertainty on the mean temperature of the fluid at the thermocouple section, and consequently on the calculated velocity.

Conclusions

Single-phase natural circulation was experimentally investigated in two miniloops, characterized by the same width and internal diameter but different heights. FC43 and water were used as working fluids. Miniloop inclination and power input were varied during the experimental campaigns.

Conclusions can be summarized as follows:

- The thermohydraulic behavior of the miniloops is always stable. In fact, for such a small internal diameter, the shear stresses stabilize the circulation induced by the buoyancy forces, avoiding any flow instabilities, which might appear in large scale loops.
- With FC43, the initial temperature transient is smooth but slow due to its high viscosity. The steady-state maximum temperature is higher than in case of water, even if the fluid velocity is almost twice, because of its low specific heat. Heat transfer performances are therefore worse than those of water.
- With taller miniloop (ML2), the steady-state velocities are slightly (20%) lower than in ML1 because, for such a small internal diameter, with longer pipes shear stresses increase more than buoyancy forces. Moreover, the circulation starts later because of higher inertia so that at similar power the initial temperature overshoot is higher than in ML1. However, when single-phase flow is established, the increased height avoids any temperature disturbance and makes the system more stable. Actually with ML2 it is possible to transfer up to 40 $\mathrm{kW/m^2}$, while, in the previous campaign with ML1, at half maximum flux temperatures fluctuations started to appear.
- The fluid velocity depends strongly on the working fluid (FC43 is twice faster than water); it is slightly affected by miniloop geometry and grows almost linearly with power in the range investigated. The inclination drops down the velocity only if the miniloop is close to horizontal (25–50% of velocity reduction at $\alpha = 75$ deg).
- Experimental data were compared with Vijayan's correlation [9], developed for large scale vertical loops, showing good agreement. A corrective parameter was introduced in order to take into account the miniloop inclination. The dimensionless numbers data range (Re_{ss} and Gr_m) of the first campaign [8] was expanded by selecting a different working fluid and by modifying the geometrical dimensions of the miniloop.

Acknowledgment

This paper was supported by Grant No. 2005094817_004 (Ministero dell'Università e della Ricerca).

Nomenclature

A = flow area, $\mathrm{m^2}$
D = pipe internal diameter, m
Gr_m = modified Grashof number
H = loop height, m
L_c = cooler length, m
L_h = heater length, m
L_{tot} = total length, m
N_G = dimensionless parameter
P = power, W
Pr = Prandtl number
Re_{ss} = steady-state Reynolds number
T = temperature, °C
ΔT_h = temperature difference across the heater, °C
W = loop width, m
c_p = specific heat, J/kg K
f = friction factor
k = concentrated pressure loss coefficient
t = time, s
w = fluid velocity, m/s

Greek Symbols

α = loop inclination, deg
β = thermal expansion coefficient, $1/\mathrm{K}$
μ = dynamic viscosity, kg/ms
ρ = density, $\mathrm{kg/m^3}$

References

[1] Greif, R., 1998, "Natural Circulation Loops," ASME J. Heat Transfer, **110**, pp. 1243–1257.
[2] Vijayan, P. K., Nayak, A. K., Pilkhwal, D. S., Saha, D., and Verkat Raj, V., 1992, "Effect of Loop Diameter on the Stability of Single-Phase Natural Circulation in Rectangular Loops," Nureth, **5**, pp. 61–267.
[3] Misale, M., Devia, F., and Garibaldi, P., 2005, "Some Considerations on the Interaction Between the Fluid and Wall Tube During Experiments in a Single-Phase Natural Circulation Loops," IASME Trans., **9**(2), pp. 1717–1722.
[4] Mukherjee, S., and Mudawar, I., 2003, "Smart Pumpless Loop for Micro-Channel Electronic Cooling Flat and Enhanced Surfaces," IEEE Trans. Compon. Packag. Technol., **26**(1), pp. 99–109.
[5] Mukherjee, S., and Mudawar, I., 2003, "Pumpless Loop for Narrow Channel and Micro-Channel Boiling," ASME J. Electron. Packag., **125**, pp. 431–441.
[6] Tuma, P. E., and Mortazavi, H. R., 2006, "Indirect Thermosyphons for Cooling Electronic Devices," Electronic Cooling, **12**(1), pp. 26–32.
[7] Fantozzi, F., Filippeschi, S., and Latrofa, E. M., 2004, "Upward and Downward Heat and Mass Transfer With Miniature Periodically Operating Loop Thermosyphons," Superlattices Microstruct., **35**, pp. 339–351.
[8] Misale, M., Garibaldi, P., Passos, J. C., and Ghisi de Bitencourt, G., 2007, "Experiments in a Single-Phase Natural Circulation Mini-Loop," Exp. Therm. Fluid Sci., **31**, pp. 1111–1120.
[9] Vijayan, P. K., 2002, "Experimental Observations on the General Trends of the Steady State and Stability Behaviour of Single-Phase Natural Circulation Loops," Nucl. Eng. Des., **215**, pp. 139–152.
[10] Misale, M., and Frogheri, M., 2001, "Stabilization of a Single-Phase Natural Circulation Loop by Pressure Drops," Exp. Therm. Fluid Sci., **25**(5), pp. 277–282.
[11] Bejan, A., 1993, *Heat Transfer*, Wiley, New York.
[12] 3M™ NOVEC™ Engineered Fluids, 3M Center, St. Paul, MN.
[13] Idelchik, I. E., 1996, *Handbook of Hydraulic Resistance*, 3rd ed., Begell House, Redding, CT.